ISSN 2434-1088

KURNS-EKR-5

アジア原子炉物理国際会議 2019 論文集

Proceedings of
Reactor Physics Asia Conference 2019
(RPHA19)

開催日：2019 年 12 月 2 日および 3 日

(December 2 and 3, 2019)

編集： 卞　哲浩、大岡靖典、辻田浩介、山中正朗

Edited by: Cheol Ho Pyeon, Yasunori Ohoka,

Kosuke Tsujita and Masao Yamanaka

京都大学複合原子力科学研究所

Institute for Integrated Radiation and Nuclear Science, Kyoto University

Preface

Establishing this RPHA (**R**eactor **PH**ysics **A**sia) conference series was agreed by the Reactor Physics Divisions (and/or mathematics and computation) of nuclear (or atomic energy) societies of Korea, China and Japan to promote knowledge and information exchange between the nuclear reactor physics related groups of the nuclear industry, academia, and research sectors in Asian countries. With the growing need for the safe and effective utilization of nuclear energy in the Asian region which lacks abundant sources of cheap and clean energy, the outcomes of the *theoretical*, *experimental*, *computational*, and *operational* reactor physics research and developments of the Asian reactor physics related groups could play an instrumental role in the stable and expanded use of nuclear power. RPHAs, which will take place every two years by rotating the host among the three countries, could provide a very efficient meeting ground for sharing technical information and encouraging mutual collaboration. The regional closeness and the cultural similarities of the Asian countries would be another important benefits of the RPHA meetings as well.

The RPHA19 (Reactor PHysics Asia Conference 2019) will be held at the Osaka International House Foundation in Japan on December 2 and 3, 2019, organized by the Reactor Physics Division of the Atomic Energy Society of Japan, the Reactor Physics & Mathematical Computational Division of the Korean Nuclear Society, and the Mathematical Computational Division of the Chinese Nuclear Society, and supported by the Kindai University Atomic Energy Research Institute, and the Institute for Integrated Radiation and Nuclear Science, Kyoto University.

Finally, we would like to give special thanks for their support and patience, by all members of the Organizing committees in RPHA19, to hold this conference.

Cheol Ho Pyeon (KURNS)
Yasunori Ohoka (Nuclear Fuel Industries, Ltd.)
Kosuke Tsujita (Nuclear Engineering, Ltd.)
Masao Yamanaka (KURNS)

November 2019

Keywords:
Reactor physics, Mathematic and Computation, Nuclear data

要旨

アジア原子炉物理国際会議 RPHA（Reactor PHysics Asia）は，アジア諸国の原子力産業や研究開発機関における原子炉物理学の情報交換を促進するため，韓国，中国，日本の原子力学会炉物理部会（及び計算科学部会）によって設立されたものであり，3 ヵ国間でホストを交代しながら 2 年毎に開催している原子炉物理学に特化した国際会議である。経済的でクリーンなエネルギー源に乏しいアジア地域において，原子力エネルギーの安全で効率的な利用に関するニーズは高まりに伴い，アジア諸国の原子炉物理学に基づく理論や実験，解析手法，原子炉の運用手法といった研究開発は，原子力エネルギー利用の拡大に対し重要な役割を果たすことができる。RPHA は，そのようなニーズに応えるため，最新の研究成果を共有し，相互協力を促進するために有効な会議体であり，加えてアジア諸国の地理的な近さや文化的な類似性に関してもまた RPHA における重要な利点である。

2019 年 12 月 2 日および 3 日に大阪国際交流センターにおいて開催される RPHA19（Reactor PHysics Asia 2019 Conference）は、日本原子力学会 炉物理部会，韓国原子力学会炉物理 計算科学部会，中国原子力学会 計算科学部会が主催し，近畿大学 原子力研究所，京都大学 複合原子力科学研究所の後援を受けている。

最後に，RPHA19 組織委員会のメンバーに心より感謝申し上げます。

京都大学複合原子力科学研究所　卞 哲浩
原子燃料工業株式会社　大岡 靖典
（株）原子力エンジニアリング　辻田 浩介
京都大学複合原子力科学研究所　山中 正朗

2019 年 11 月

キーワード：
炉物理，計算科学，核データ

Contents

目次

SS-01 Advanced Monte Carlo Modeling

Proceedings of the Reactor Physics Asia 2019 (RPHA19) Conference
Osaka, Japan, Dec. 2-3, 2019

MCS Multi-group Cross Sections Generation for Fast Reactor Analysis

Tung Dong Cao Nguyen, Hyunsuk Lee, Xianan Du, Vutheam Dos, Tuan Quoc Tran and Deokjung Lee*
Ulsan National Institute of Science and Technology (UNIST)
50 UNIST-gil, Ulsan 44919, Republic of Korea
*Corresponding author: deokjung@unist.ac.kr

Abstract

Current work introduces a brief methodology for multi-group (MG) cross sections (XSs) generation by Monte Carlo (MC) code MCS, which can be compatible with nodal diffusion code, PARCS. The applicability of the methodology is quantified on the sodium fast reactor ABR-1000 design with a metallic fuel loaded. The MG XSs generated by MCS with a 2D sub-assembly are well consistent with those of SERPENT 2. Furthermore, the solutions of beginning-of-cycle steady-state MG calculation of MCS/PARCS for a whole-core problem, including the core k_{eff} and power profiles, are compared to those of the MCS MC code. Overall, the code-to-code comparison indicates a reasonable agreement between deterministic and stochastic codes, with the difference in k_{eff} less than 100 pcm and the root-mean-square error in assembly power less than 1.15%. Therefore, it is successfully demonstrated the employment of the MCS MG XSs generation for PARCS is a promising system to accurately perform neutronic analyses for fast reactors.

Key Words: **Monte Carlo, multi-group cross sections, fast reactor, MCS**

1. Introduction

In general, a Monte Carlo (MC) code or a deterministic code is to be employed to simulate the nuclear reactor. The main advantages of MC codes are in the accuracy in geometry simulation and neutron interactions. However, those are counterweighted with the high computational cost due to a complex and detail level of a certain model. On the other hand, deterministic code's capability is to provide an adequately accurate result, which requires less computational demand. Nevertheless, their disadvantage is the simplicity in geometry and transport/diffusion physics. Recently, the combination of both stochastic and deterministic codes has become more and more attractive in the framework of establishing the basic viability of the advanced fast reactor. This approach ensures the superposition of the benefits of these methods. The major purpose of a code system is to achieve accurate evaluation and analysis in a systematic manner for a wide variety of fast reactor. Therefore, current research is focused on the use of both MC and deterministic codes for 2D/3D fast reactor simulation and analysis. In this work, the generation of the multi-group (MG) cross sections (XSs) data by MC method is implemented in the in-house UNIST MC code MCS. These XSs data is then converted into the compatible database that is able to be used in nodal diffusion code PARCS.

2. Computer Codes

3.1 UNIST Monte Carlo code MCS

MCS is a 3D continuous-energy neutron-physics code for particle transport based on the MC method, under development at UNIST since 2013 [1-2]. MCS can conduct criticality runs for reactivity calculations and fixed-source runs for shielding problems. MCS has been designed from scratch since 2013 to conduct whole-core criticality simulation with pin-wise depletion and thermal/hydraulic feedback. MCS neutron transport capability is verified and validated against several benchmark problems, including the BEAVRS benchmark, ~300 cases from the International Criticality Safety Benchmark Experimental Problem (ICSBEP) and the Jordan Research and Training Reactor (JRTR).

3.2 SERPENT 2

The SERPENT MC code [3] is a continuous energy MC reactor physics burnup code with recent applications in radiation shielding, multi-physics, and fusion neutronics. It is currently employed for reactor physics applications, including homogenized group constant generation, burnup calculations, the modeling of small research reactor cores and multi-physics calculations. SERPENT has been developed at VTT Technical Research Centre of Finland since 2004 and the current development version, SERPENT 2, has notably diversified the applications of the code.

3.3 PARCS

PARCS is a 3D reactor core simulator, which solves the steady-state and time-dependent, MG neutron diffusion and SP3 transport equations in square and hexagonal geometries [4].

3. Multi-group Cross Sections Generation with Monte Carlo Method

A general goal of the MC code is to estimate the average neutron flux for a certain geometrical region and for a number of energy ranges (energy group) [5]:

$$\phi_g = \frac{1}{V}\int_V \int_{E_g}^{E_{g-1}} \phi(r,E)\mathrm{d}E\mathrm{d}V \quad , \tag{1}$$

where

$\phi(r,E)$ = the space and energy dependent flux

V = volume for averaging flux region and

g = group index.

From this, the specific reaction rates can be obtained by multiplying flux estimates by an interest XS:

$$R_x = \frac{1}{V}\int_V \int_{E_g}^{E_{g-1}} \Sigma_x(r,E)\phi(r,E)\mathrm{d}E\mathrm{d}V \quad , \tag{2}$$

Division of these two quantities gives the MG XS for a certain reaction type x and energy group g:

$$\Sigma_{x,g} = \frac{\frac{1}{V}\int_V \int_{E_g}^{E_{g-1}} \Sigma_x(r,E)\phi(r,E)\mathrm{d}E\mathrm{d}V}{\phi_g} \quad , \tag{3}$$

As discussed, the generated XSs are to be utilized in MG nodal diffusion code, the required data are therefore the total XS, the absorption XS, the fission and fission production XS, fission spectrum, scattering matrix and transport XS. It is noted that the Pn scattering matrix in this study is only weighted by the scalar flux:

$$\Sigma^l_{s,g\to g'} = \frac{\frac{1}{V}\int_V \int_{E_g}^{E_{g'}} \Sigma^l_s(r,E\to E')\phi(r,E)dEdV}{\phi_g} \quad , \tag{4}$$

where l = scattering order, which is also the l^{th} order Legendre polynomial coefficient.

The transport XS is estimated by using the outer-scatter approximation:

$$\Sigma_{tr,g} = \Sigma_{t,g} - \sum_{g'=1}^{G} \Sigma^1_{s,g\to g'} \quad , \tag{5}$$

where G = the total number of groups.

4. Numerical Results

First, the XS set for 4-group energy structure and for a 2D assembly problem is generated by MCS and compared to those of SERPENT 2. Then, the XS set for 24-group energy structure [7] is obtained by MCS and converted into a compatible database that can be used in the nodal diffusion code PARCS for the fast reactor 3D core problem. The two energy structures are listed in Tables I and II. The ENDF/B-VII.0 library is used, where the fuel and other material temperature is set 900K and 600K, respectively.

Table I. 4-group Energy Structure.

No.	Upper E (MeV)	Lower E (MeV)
1	1.41910E+01	1.11090E-01
2	1.11090E-01	1.72230E-03
3	1.72230E-03	2.67030E-05
4	2.67030E-05	1.00000E-11

Table II. 24-group Energy Structure.

No.	Upper E (MeV)	Lower E (MeV)
1	1.96403E+01	1.00000E+01
2	1.00000E+01	6.06531E+00
3	6.06531E+00	3.67879E+00
4	3.67879E+00	2.23130E+00
5	2.23130E+00	1.35335E+00
6	1.35335E+00	8.20850E-01
7	8.20850E-01	4.97871E-01
8	4.97871E-01	3.01974E-01
9	3.01974E-01	1.83156E-01
10	1.83156E-01	1.11090E-01
11	1.11090E-01	6.73795E-02
12	6.73795E-02	4.08677E-02
13	4.08677E-02	2.47875E-02
14	2.47875E-02	1.50344E-02
15	1.50344E-02	9.11882E-03
16	9.11882E-03	5.53084E-03
17	5.53084E-03	3.35463E-03
18	3.35463E-03	2.03468E-03
19	2.03468E-03	1.23410E-03
20	1.23410E-03	7.48518E-04
21	7.48518E-04	4.53999E-04
22	4.53999E-04	3.04325E-04
23	3.04325E-04	1.48625E-04
24	1.48625E-04	1.00001E-11

4.1 Multi-group cross section comparison between MCS and SERPENT 2

Since the original aim of this work is to serve in the fast reactor analysis and development, the fuel sub-assembly of a typical sodium fast reactor, ABR-1000 [6], is employed in this analysis. Fig. 1 illustrates the 2D layout of the ABR-1000 sub-assembly [6]. Table III summarizes the 4-group flux and XSs generated by MCS compared to those of SERPENT 2. It is seen that MCS solution is well agreed with SERPENT 2 solution, and it also notice that the considered error at group 4 is due to the poor uncertainties as lack of neutrons in the small energy ranges. Figs. 2 and 3 shown the P0 and P1 scattering and their uncertainties (in %) between MCS and SERPENT 2. The index in the green row stands for the departure energy

group, while the vertical orange column indicates the arrival energy group. All the group-wise scattering XSs by MCS are well consistent with those of SERPENT 2, except group 4 as a result of the lack of neutron in the thermal energy range of a fast reactor assembly.

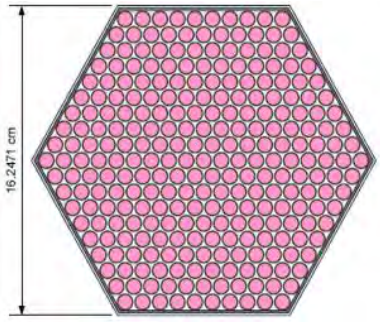

Fig. 1. ABR-1000 fuel sub-assembly geometry.

Table III. Summary of 4-group Flux and XSs [cm^{-1}].

Parameter	G	MCS		Diff. vs. SERPENT 2 (%)	
		Value	SD (%)	Value	SD
Flux	1	1.18E+02	7.46E-03	0.22	0.01
	2	6.53E+01	1.08E-02	0.21	0.01
	3	1.12E+00	7.46E-02	0.29	0.11
	4	3.03E-06	2.74E+01	-11.31	45.63
Total	1	2.08E-01	1.21E-03	0.00	0.00
	2	3.02E-01	2.11E-03	0.02	0.00
	3	3.91E-01	6.40E-03	-0.01	0.02
	4	5.51E-02	2.34E+01	-93.11	24.38
Abs[a]	1	4.39E-03	2.95E-03	0.02	0.01
	2	6.93E-03	3.85E-03	0.02	0.01
	3	2.67E-02	2.50E-02	-0.03	0.05
	4	2.51E-02	3.90E+01	-90.54	44.04
NSF[b]	1	8.79E-03	5.06E-03	0.01	0.01
	2	6.62E-03	2.05E-03	0.02	0.01
	3	2.13E-02	2.64E-02	-0.07	0.06
	4	3.29E-02	5.92E+01	-91.47	64.77
Chi[c]	1	9.85E-01	1.90E-03	0.00	0.00
	2	1.46E-02	1.28E-01	0.24	0.18
	3	2.87E-05	3.04E+00	-0.09	4.30
	4	5.01E-08	7.06E+01	-44.60	97.40
Transport	1	1.71E-01	2.72E-03	0.01	0.00
	2	2.89E-01	2.73E-03	0.02	0.00
	3	3.87E-01	1.00E-02	-0.01	0.02
	4	2.21E-02	2.24E+01	-97.33	25.31

[a]Absorption, [b]Fission production, [c]Fission spectrum

Error (%)	1	2	3	4
1	0.01	--	--	--
2	0.05	0.02	--	--
3	-2.65	0.14	-0.02	--
4	-62.01	152.98	26.76	-95.27
SD (%)	1	2	3	4
1	0.00	--	--	--
2	0.02	0.00	--	--
3	3.07	0.09	0.03	--
4	62.96	75.01	51.58	28.60

Fig. 2. P0 scattering matrix error, MCS vs. SERPENT 2.

Error (%)	1	2	3	4
1	-0.01	--	--	--
2	0.01	0.02	--	--
3	14.05	0.11	-0.44	--
4	-117.12	-101.91	214.67	-103.86
SD (%)	1	2	3	4
1	0.02	--	--	--
2	0.09	0.05	--	--
3	23.63	0.19	1.26	--
4	115.76	5681.69	107.31	166.93

Fig. 3. P1 scattering matrix error, MCS vs. SERPENT 2.

4.2 ARB-1000 analysis by MCS/PARCS

The radial core layout of the ABR-1000 is shown in Fig. 4 [6]. XSs for fuel sub-assemblies are generated using a single 2D model of a fuel sub-assembly with reflective boundary conditions, as in Fig. 1. All MG XSs for non-multiplying regions are generated using 2D super-cell models as shown in Fig. 5 [7]. Those regions are located at the center of the model and surrounded by fuel assemblies to approximate the flux that those experience in a core. The k_{eff} for 2D/3D core calculation at beginning-of-cycle (BOC) all rod out (ARO) by MCS/PARCS and MCS is summarized in Table IV. The radial assembly-wise power distributions by MCS/PARCS and MCS are shown in Figs. 6-8. It is clearly seen that a great agreement is achieved due to the difference in k_{eff} less than 100 pcm and the root-mean-square (RMS) in power error is less than 1.15% and the maximum error is less than 2.5% for radial power and 4.73% for axial power.

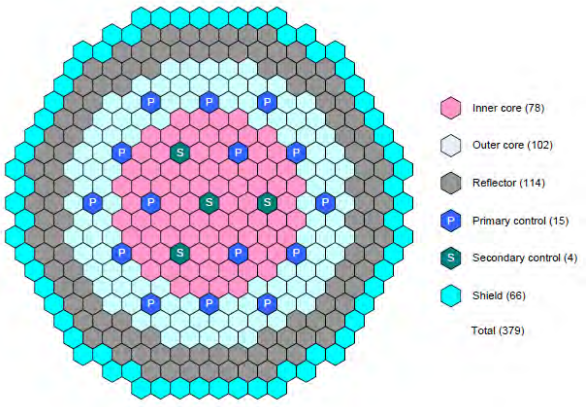

Fig. 4. ABR-1000 radial core layout.

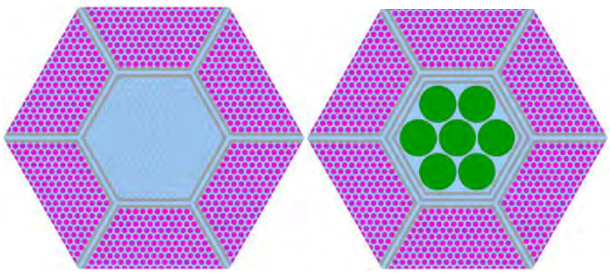

Fig. 5. Example for super-cell models.

Table IV. Summary of k_{eff}, MCS/PARCS vs. MCS.

Case	MCS	MCS/ PARCS	Diff. (pcm)
2D core	1.22120±0.00010	1.22129	9
3D core	1.03011±0.00011	1.03104	93

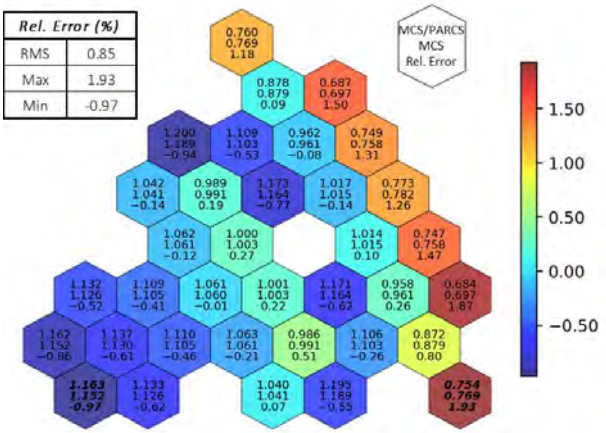

Fig. 6. Normalized assembly radial power distribution for 2D core, MCS/PARCS vs MCS.

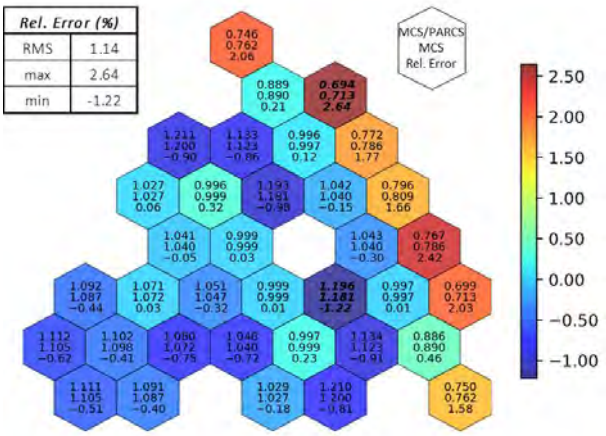

Fig. 7. Normalized assembly radial power distribution for 3D core, MCS/PARCS vs MCS.

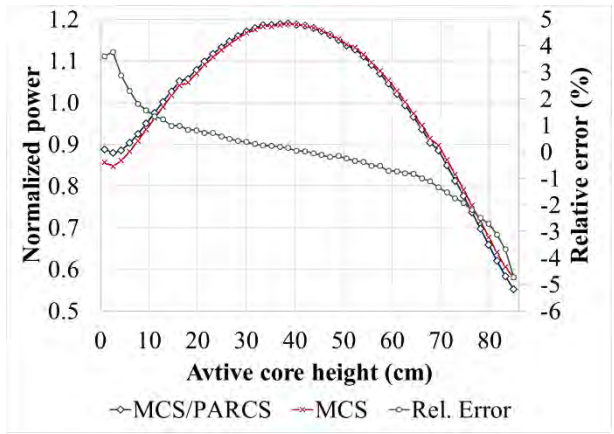

Fig. 8. Normalized axial power distribution, MCS/PARCS vs MCS.

5. Conclusions

In this study, the feasibility of using the MCS MC code for generating MG XSs at BOC for fast spectrum 2D/3D simulation with the PARCS simulator is investigated. The 4-group XSs by MCS are compared with SERPENT 2 results, and a great agreement is achieved. The final step is to perform steady-state analysis with PARCS using the 24-group XS data generated by MCS and conduct a comparison in k_{eff} and power distributions. Results point out a reasonable consistency, mainly explained by the difference between deterministic and stochastic code. The outcome of this study proves the MCS can be a promising tool for MG XSs generation for fast reactor analysis. The future work is focused on the application of MCS for temperature dependent and coolant density dependent MG XSs for thermal-hydraulics feedback for fast reactor.

Acknowledgements

This work was supported by the National Research Foundation of Korea (NRF) grant funded by the Korea government (MSIT). (No.NRF-2017M2A8A2018595)

References

1. Lee H et al., “MCS – A Monte Carlo Particle Transport Code for Large-scale Power Reactor Analysis,” *Annuals of Nuclear Energy* (2019). (Under review)
2. Jang J et al., “Validation of UNIST Monte Carlo code MCS for Criticality Safety Analysis of PWR Spent Fuel Pool and Storage Cask,” *Annuals of Nuclear Energy*, **114**, 495-509 (2018).
3. Leppänen J et al., “The Serpent Monte Carlo Code: Status, Development and Applications in 2013,” *Annals of Nuclear Energy*, **82**, 142-150 (2015).
4. Downar T, “PARCS v2.7 U.S. NRC Core Neutronics Simulator USER MANUAL,” U.S. NRC (2006).
5. Hoogenboom J et al., "Generation of Multi-group Cross Sections and Scattering Matrices with the Monte Carlo Code MCNP5," Proc. Joint International Topical Meeting on Mathematics & Computation and Supercomputing in Nuclear Applications, Monterey, California, April 15-19, p.15-19 (2007).
6 Bernnat W et al., "Benchmark for Neutronic Analysis of Sodium-Cooled Fast Reactor Cores with Various Fuel Types and Core Sizes," Nuclear Energy Agency Technical Report, NEA/NSC (2015).
7 Pereira G et al., "Applying the Serpent-DYN3D Code Sequence for the Decay Heat Analysis of Metallic Fuel Sodium Fast Reactor," *Annals of Nuclear Energy*, **125**, 291-306 (2019).

Proceedings of the Reactor Physics Asia 2019 (RPHA19) Conference
Osaka, Japan, Dec. 2-3, 2019

A Systematic Way to Determine Neutron Generation Size in Monte Carlo Simulation Accelerated by the CMFD

Inhyung Kim[a] and Yonghee Kim[a*]
[a]*KAIST, Daehak-ro 291, Daejeon, Republic of Korea (34141)*
[*]Corresponding author: yongheekim@kaist.ac.kr

Abstract

A modified particle ramp-up (m-PRUP) method was suggested and improved to systematically determine the minimum generation size, optimum generation size, and number of inactive cycles in a Monte Carlo simulation for an efficient and accurate calculation. This paper describes the concept and algorithm for the m-PRUP method in details. It provides a guideline for source convergence conditions. It also explains how to determine the minimum generation size based on probability and statistics. The m-PRUP method was applied to a simple reactor problem to characterize its numerical performance compared to the standard MC calculation. The convergence behavior was examined, and the multiplication factor, computing time, and figure-of-merits (FOMs) were evaluated and compared for each method.

Key Words: **m-PRUP method, Minimum generation size, Optimum generation size**

1. Introduction

In a Monte Carlo (MC) simulation, generation size, i.e. the number of histories per cycle, is a significant factor which can influence the reliability of the solution and the efficiency of the calculation. If generation size is huge, the calculation can be inefficient due to a waste of time in unnecessary calculations during inactive cycles to determine a converged fission source distribution (FSD). On the other hand, if the generation size is too small, the solution may contain a bias due to generation-correlation [1]. In addition, in the CMFD-assisted by MC calculation, it may result in numerical instability and inconsistency in the deterministic solution [2].

The modified particle ramp-up (m-PRUP) method was proposed to give a guideline for an optimum generation size [3]. In this work, this method was further improved to suggest a minimum generation size which enhances the calculation efficiency and guarantees the numerical stability. Moreover, it can judge the convergence of the FSD and systematically switch to the active MC calculation. In this paper, the concept of the m-PRUP is introduced in detail, and the method is applied to a benchmark problem to characterize its performance.

2. Modified Particle Ramp-up Method

2.1 Concept and algorithm

The m-PRUP method [3-4] is an algorithm for providing a minimum generation size, an optimum generation size, and the number of inactive cycles in a systematic way. This method begins with a small number of histories. The small generation size can quickly reach the rough convergence of the FSD and thus decrease the unnecessary computing time in the inactive cycle. After the rough convergence is achieved, the number of histories increases. With new generation size, another stationary distribution is searched. This procedure continues until the convergence of the FSD is achieved with the final generation size.

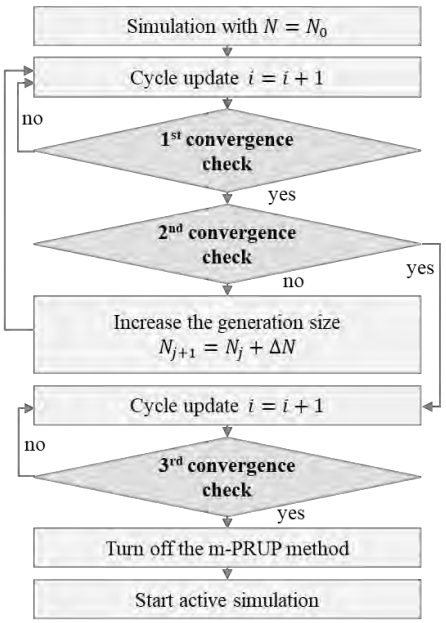

Fig. 1 Flowchart of the m-PRUP method

The algorithm of the m-PRUP method is shown in Fig. 1. In the figure, N_0 is the initial generation size, i is

the cycle number, and ΔN is the increment of the generation size. The convergence check is carried out by evaluating Shannon entropy [5]. If the difference of the entropy values is within the criterion, the method increases the generation size (1st check), finds the optimal generation size (2nd check), and automatically switches to the active simulation (3rd check).

The entropy is estimated by taking the average of cycle-wise entropies such as

$$\bar{e}_i^1 = \frac{1}{c}\sum_{k=i-c+1}^{i} e_k, \tag{1}$$

and

$$\bar{e}_i^0 = \frac{1}{c}\sum_{k=i-2c+1}^{i-c} e_k, \tag{2}$$

where c is the cycle-accumulation length. If the relative error of two quantities is within the first criterion such as

$$\left|\frac{\bar{e}_j^1 - \bar{e}_j^0}{\bar{e}_j^1}\right| < \varepsilon_1, \tag{3}$$

where j is the index for the generation size, and ε_1 is the convergence criterion, then the generation size increases by the increment ΔN. If the error of the entropies with two different generation sizes is within the second criterion such as

$$\left|\frac{\bar{e}_j^1 - \bar{e}_{j-1}^1}{\bar{e}_j^1}\right| < \varepsilon_2, \tag{4}$$

where ε_2 is the stopping criterion, then the generation size is determined and fixed. Last, if the difference of the entropies with the final (optimal) generation size is within the last criterion such as

$$\left|\frac{\bar{e}_j^1 - \bar{e}_j^0}{\bar{e}_j^1}\right| < \varepsilon_2, \tag{5}$$

then the simulation turns off the m-PRUP method and moves into the active calculation.

2.2 Convergence criteria

Because the Shannon entropy is a statistical parameter, it follows the intrinsic nature of stochastic parameters in the MC simulation that the uncertainty decreases inversely proportional to the square root of the number of histories. Therefore, the convergence criteria are determined based on the function of the generation size.

The constant, C, for the criteria is derived by trial and error based on numerous simulations. The inconsistent conclusion may be drawn depending on the constant C, but many tests and simulations demonstrated that the adequate constant for the m-PRUP method was almost invariant regardless of the problems.

In the m-PRUP method, it is not necessary to accomplish a strict convergence of the FSD in the first convergence check. Too tight convergence condition may not be achieved depending on the initial generation size, or may lessen the calculation efficiency. However, the stopping criterion should be relatively tight for a reliable convergence of the FSD. In this regard, the stopping criterion is more rigorous than the convergence criterion.

Table I. Convergence criteria for the m-PRUP method

	Criterion
ε_1	$3C/\sqrt{N}$
ε_2	$1C/\sqrt{N}$

* $C = 0.03$ and N is the current generation size

2.3 Minimum generation size

Initial generation size for the m-PRUP method is also an important variable to enhance the calculation efficiency. If the initial generation size is pointlessly large, an amount of numerical effort would be wasted to determine the converged FSD due to an inaccurate flat source data. On the contrary, too small generation size can lead to numerical instability and inconsistency. Therefore, it is important to find the proper minimum generation size for the m-PRUP method.

For a reactor core problem, zero flux or zero current physically does not make sense. The given neutron particles per cycle should at least yield non-zero reactor parameters. In this respect, the probability of crossing all neighboring surfaces with *N* neutrons per node was estimated based on the Buffon's needle problem [6].

According to the Buffon's needle problem, the probability that a neutron traveling length l crosses any of parallel lines each distance t apart can be obtained by

$$p_{cross} = \frac{2l}{\pi t} - \frac{2}{\pi t}\sqrt{l^2 - t^2} + 1 + \frac{2}{\pi}\sin^{-1}(t/l) \tag{6}$$

A neutron track-length can be approximated by a crow flight distance (CFD) of the neutron which is defined as a straight root-mean-square distance from birth to death. The CFD of the neutron is given by

$$l = \sqrt{6}L, \tag{7}$$

where $L = \sqrt{D/\Sigma_a}$ is the diffusion length. The diffusion coefficient and absorption cross section can be obtained by the group condensation and spatial homogenization over the active core. The fast group constants could draw the conservative conclusion, but the one-group constant also can yield sufficiently acceptable results. In this analysis, the one-group diffusion coefficient and absorption cross section were used.

The probability of crossing each surface (i.e. *x*, *y*, and *z*) can be estimated with consideration of radial and axial node size. One neutron randomly distributed on a lattice grid can encounter total 8 cases including no surface crossing (p), 3 cases with only one surface crossing (p_x, p_y, and p_z), 3 cases with two surfaces crossing (p_{xy}, p_{yz}, and p_{zx}), and crossing all surfaces simultaneously (p_{xyz}).

Therefore, the probability of crossing all surfaces with one neutron can be calculated as

$$\begin{aligned} p_{cross}^{1} &= \frac{p_{xyz}}{p + p_x + p_y + p_z + p_{xy} + p_{yz} + p_{zx} + p_{xyz}} \\ &= p_{xyz} \\ &= p_i \cdot p_j \cdot p_k \end{aligned} \tag{8}$$

which is the only one case among 8 cases under the assumption that the probability of crossing each surface is independent.

Next, the crossing probability with two neutrons can be considered. Combination of two neutrons can make total of 8^2 cases. Among them, the cases which two neutrons cross all surrounding surfaces are estimated as 27 cases.

$$\begin{aligned} p_{cross}^{2} = 2\times(&p \cdot p_{xyz} + p_x \cdot p_{yz} + p_y \cdot p_{zx} + p_z \cdot p_{xy} \\ &+ p_{xy} \cdot p_{yz} + p_{yz} \cdot p_{zx} + p_{zx} \cdot p_{yx} + p_x \cdot p_{xyz} \\ &+ p_y \cdot p_{xyz} + p_z \cdot p_{xyz} + p_{xy} \cdot p_{xyz} + p_{yz} \cdot p_{xyz} \\ &+ p_{zx} \cdot p_{xyz}) + p_{xyz} \cdot p_{xyz}. \end{aligned} \tag{9}$$

In this manner, the probability of crossing all surfaces with N neutrons can be calculated. However, the number of cases and combinations exponentially increases with increasing the number of neutrons considered. Therefore, a simple computer code was developed to numerically calculate the cases and probabilities for a given condition. The computing time for the calculation of the cases and probability is almost negligible compared to the MC simulation. It only requires less than 10 seconds with the given data such as the reactor type, the problem size, and so on.

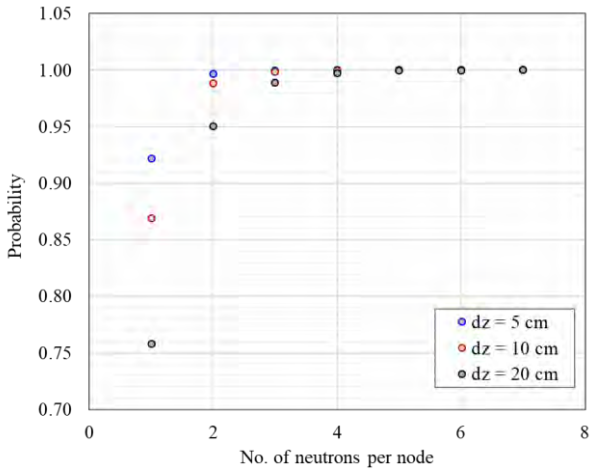

Fig. 2 Probability of crossing all surfaces with N neutrons as a function of axial node sizes

For a standard PWR type reactor core where the low-enriched uranium fuel is loaded and the pin pitch size is 1.26 cm, the probability of crossing all surfaces can be calculated as a function of the axial node size and the number of neutrons per node (Fig. 2). The probability dramatically increases with increasing the number of neutrons and decreasing the axial node size.

Using a fitting curve based on the data points, the number of neutrons per node can be derived to have non-zero surface parameters at a probability less than 0.01%. Therefore, in the PWR type reactor core problem, at least 4 to 5 neutrons per node are necessary for the efficient and reliable MC calculation.

Table II. No. of neutrons per node depending on the axial node size

Axial node size	No. of neutrons per node
5 cm	4.62
10 cm	4.73
20 cm	4.81

The higher probability indicates that fewer neutrons are required per node to make sure that the surface parameters are non-zero in the MC simulation. That is, when 5 cm of axial node size is used for a mesh grid, the number of neutrons per node can be smaller. However, in terms of the whole core simulation, the total number of nodes increases with decreasing the node size because of the many axial division. As a result, the total number of neutrons required for a whole core simulation will be higher with the smaller axial node size.

3. Results and Discussion

3.1 Problem description

A simple reactor core problem was analyzed to verify the numerical performance of the m-PRUP method in the MC simulation. The full core consists of 8 by 8 homogeneous uranium fuel assemblies surrounded by a reflector as shown in Fig. 3. The radial assembly pitch size is 21.42 cm, and the height of the core is 64.26 cm. The core is axially divided into three regions for the entropy calculation.

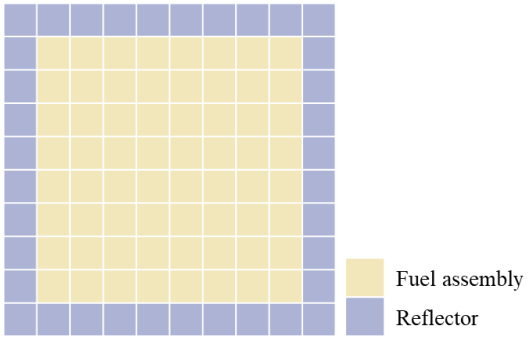

Fig. 3 Configuration of a reactor core

3.2 Minimum generation size

Because each assembly contains 17 by 17 pin nodes, the total number of pin node in this problem can be estimated to be 36,992 nodes. Therefore, according to the m-PRUP method, the necessary minimum generation size for this problem is 177,931 by multiplying the total number of nodes and the necessary neutrons per node (4.81).

The MC simulation started with the 180,000 initial (minimum) histories, and the increment of the generation size (ΔN) is also determined to be 180,000. The final (optimum) generation size and the number of inactive cycles

are automatically obtained with the m-PRUP method.

3.3 Convergence behavior

Fig. 4 compares the convergence behavior of the FSD for the standard MC calculation and the m-PRUP method application. The m-PRUP method begins with smaller histories (i.e. 170,000) and allows a quick source convergence. When the difference of the entropies is small enough, it increases the generation size and searches another stationary state with the new generation size. After several increments, the optimum generation size is finally evaluated to be 540,000 histories per cycle and the simulation moves into the active calculation at cycle 47. On the other hand, the standard MC calculation which uses 540,000 histories per cycle from the beginning shows the slow convergence in the FSD and reaches the stationary level at around cycle 70.

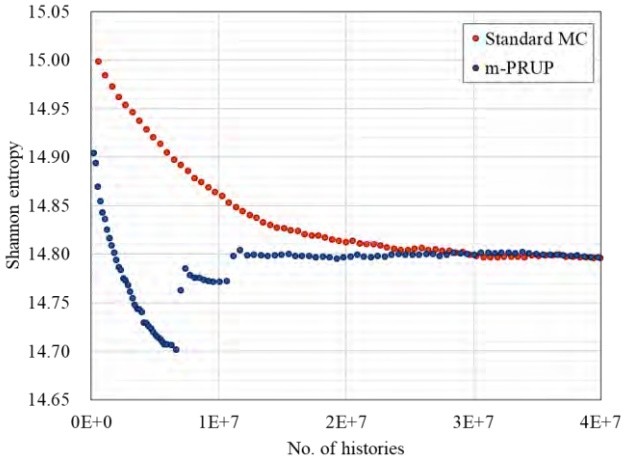

Fig. 4 Shannon entropy of the MC calculation

Table III demonstrates the numerical performance of each method through the FOM estimation. Both calculations show a good agreement of the multiplication factor each other, and have a similar statistical error. However, because the m-PRUP method uses much smaller histories to obtain the converged source distribution, it can reduce the numerical cost during the inactive cycle. As a result, the total computing time is shortened, and thus the m-PRUP gives the higher FOM than the standard MC calculation.

Table II. Comparison of reactor parameters

Parameters		Standard MC	m-PRUP
k_{eff}		1.38376	1.38376
SD (pcm)		10.3	10.7
Computing time (min)	Inactive	48	13
	Active	59	55
	Total	106	68
FOM		14710	21401

4. Conclusions

The m-PRUP method was suggested and improved to provide a guideline for systematically determining the minimum generation size, the optimum generation size, and the number of inactive cycles in a MC calculation. From the numerical analysis, the m-PRUP method properly estimated the target variables and increased the calculation efficiency by reducing the total number of histories necessary to determine the converged FSD. This method can be applied to the CMFD-assisted MC simulation which often suffers from some divergence or bias depending on the mesh grid system, problem size, and the generation size etc. The m-PRUP method can stabilize the calculation by the ramp-up technique and the algorithm to generate the optimal generation size.

Acknowledgements

This work was supported by the National Research Foundation of Korea Grant funded by the Korean government NRF-2016R1A5A1013919.

References

1. Ely M. Gelbard, “Biases in Monte Carlo Eigenvalue Calculations”, invited paper for the *International Symposium on Scientific Computing and Mathematical Modeling (IMACS)*, Bangalore, India, December 7-11, (1992).
2. YuGwon Jo & Nam Zin Cho, “Acceleration and Real Variance Reduction in Continuous Energy Monte Carlo Whole-Core Calculation via p-CMFD Feedback”, *Nuclear Science and Engineering*, Vol. 189 (1), pp. 26-40, (2018).
3. Inhyung Kim & Yonghee Kim, “A Study on Deterministic Truncation of Monte Carlo Transport Calculation”, *Reactor Physics (PHYSOR 2018)*, Cancun, Mexico, April 22-26, (2018).
4. Amanda L. Lund Paul K. Romano, and Andrew R. Siegel, "Accelerating Source Convergence in Monte Carlo Criticality Calculations Using a Particle Ramp-up Technique," in *International Conference on Mathematics & Computational Methods Applied to Nuclear Science & Engineering (M&C 2017)*, Jeju, Korea, (2017).
5. Forrest B. Brown, "On the Use of Shannon Entropy of the Fission Distribution for Assessing Convergence of Monte Carlo Criticality Calculations," in *Reactor Physics (PHYSOR 2016)*, Vancouver, BC, Canada, (2006).
6. Schroeder L., “Buffon’s Needle Problem: An Exciting Application of Many Mathematical Concepts”, *Mathematics Teacher*, Vol. 67 (2), pp. 183-6, (1974).

Proceedings of the Reactor Physics Asia 2019 (RPHA19) Conference
Osaka, Japan, Dec. 2-3, 2019

Validation of Activation Analysis Method on RV/RVI of Kori Unit 1 Using McCARD/ORIGEN2

Young In Kim, Sang Hoon Jang, Dong Hyuk Lee and Hyung Jin Shim*
Seoul National University, 1 Gwanak-ro, Gwanak-gu, Seoul 08826, Korea
* Corresponding author: shimhj@snu.ac.kr

Abstract

Activation analysis on Reactor Vessel and Reactor Vessel Internal of Kori Unit 1 is conducted for the planning of decommission. Unlike conventional activation analysis methods that calculate radioactivity of radioactive isotopes conservatively for convenience of calculation, this study pursued more accurate calculation while keeping efficiency. Representative cores which can represent the full cycle is selected and the calculation results are compared with the case which reflects full operating history. It is evaluated whether such a method is valid by comparing the time plot of the specific activity.

Key Words: **Activation Analysis, Kori Unit 1, McCARD, ORIGEN2, Specific Activity**

1. Introduction

In the reactor decommissioning process, RV (Reactor Vessel) and RVI (Reactor Vessel Internal) need to be dismantled which are impossible to dispose of in their original form. For the planning of the dismantling process, high-performance high-precision volumetric activation analysis must precede which enables classifying of the radioactive waste level. Conventionally, activation analysis is conducted in two-step procedure which calculates neutron flux and reaction cross sections at the desired location by neutron transport code and calculates radioactivity of RI(radioactive isotope) using depletion code. The most precise way to get neutron flux is tracing the full cycle operating history of the power plant and reflecting the fuel loading pattern of each cycle to the whole core neutron transport analysis. But it takes a lot of calculation time and is a burden to perform in this way while getting neutron flux with a sufficiently small statistical error. So several conventional methods choose to get a conservative result rather than a precise result. The radioactivity calculation using neutron flux obtained from the last working core in the operating history gives conservative results because neutron flux increases over time in a cycle of operation. When calculating neutron flux using neutron transport code, assuming low burnup fuel assemblies are located on the periphery of the core also gives conservative results due to maximized leakage caused by the arrangement. Although these methods can reduce the computational burden, they overestimate the radioactivity of RI.

This paper aims to devise activation method which guarantees the accuracy of result with efficient calculation. For the efficient activation analysis of Kori Unit1, representative cores that can represent the full cycle operating history are selected and radioactivity is calculated by using McCARD, a Monte Carlo (MC) particle transport analysis code, and the ORIGEN2 code. The radioactivity is compared with the result using the most precise way which traces the full cycle operating history.

2. Modeling of Kori Unit 1

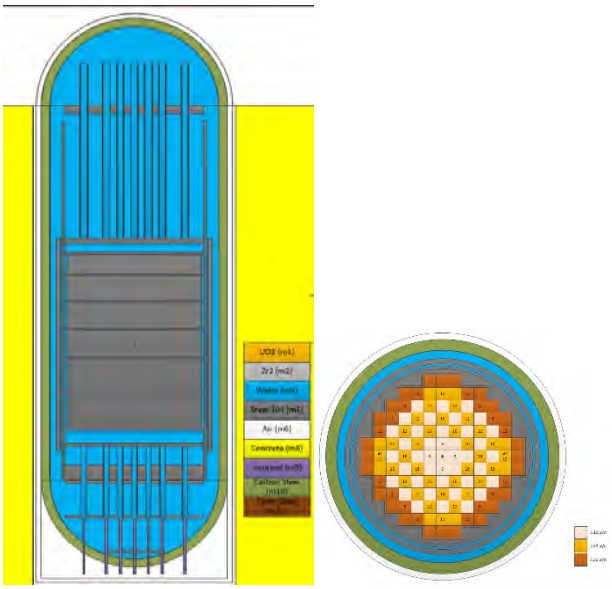

Fig. 1. Top view and side view of Kori Unit 1

The left side of Fig. 1 illustrates a top view of Kori Unit1. It consists of 11×11 fuel assemblies, baffle, former, thermal shield, reactor vessel, and insulation. Fuel enrichment, burnable poison rad and loading pattern were considered for modeling of Kori Unit 1 core. The Right side of Fig. 1 illustrates a side view of Kori Unit1. Various guide tubes, instrument tubes, support plates were

implemented in the geometry modeling. Leg nozzles and simplified concrete structures are also modeled which are not fully shown in the figure.

3. Methodology

To get the most accurate neutron flux and cross-sections at the structures, several feedback effects were applied to McCARD calculation. The calculation is performed in a state where the temperature gradient of fuel and coolant, boron concentration and xenon concentration are converged at each burnup step by using the critical boron concentration search module, the thermal-hydraulic feedback module, and the equivalent xenon module.

3.1 Whole core tracking calculation method

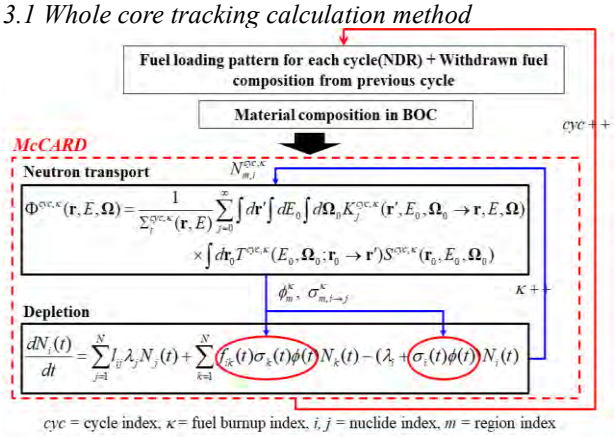

Fig. 2. Calculation procedure of whole core tracking method

The whole core tracking calculation method can produce a reference solution to the activation analysis because it is a method to simulate the lifetime of a reactor as it is. The calculation of each cycle repeats neutron transport calculation and depletion calculation using McCARD according to burnup step given in nuclear data report and updates the composition of fuel and structure. The structural information for fuel assemblies and burnable poison rods was also acquired from the nuclear design report.

At the end of a cycle calculation, discharged fuel is reloaded according to the core loading pattern or new fuel is loaded. Then the whole core tracking calculation is performed following the previous cycle.

3.2 Simple Core tracking calculation method

While the whole core tracking method can produce a reference solution with no approximation, it requires long computing time and is challenging. Therefore, we carried out activation analysis using a simple core tracking method which assumes that the MOC(middle of the cycle) core represents a cycle without performing burnup calculation according to detailed burnup steps. So a total of 32 cores was modeled for simple core tracking calculation.

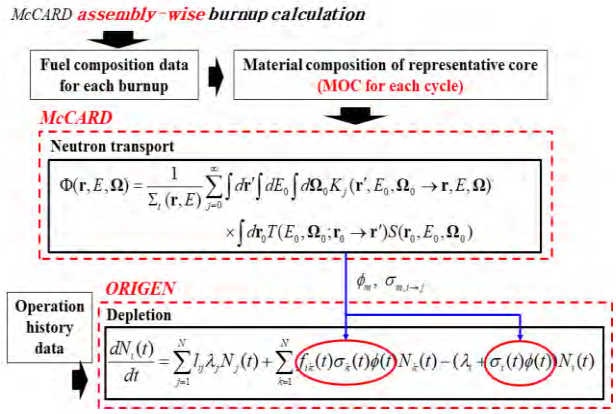

Fig. 3. Calculation procedure of simple core tracking method

The fuel composition of the MOC core was calculated in two steps. First, the composition of a fuel assembly for detailed burnup steps was calculated by McCARD assembly-wise burnup calculation. Then, the composition of the MOC core was acquired by interpolation according to burnup. Activation calculation was performed using McCARD / ORIGEN2 system which calculates neutron flux and cross sections at the desired location with McCARD and conducts depletion calculation with ORIGEN2.

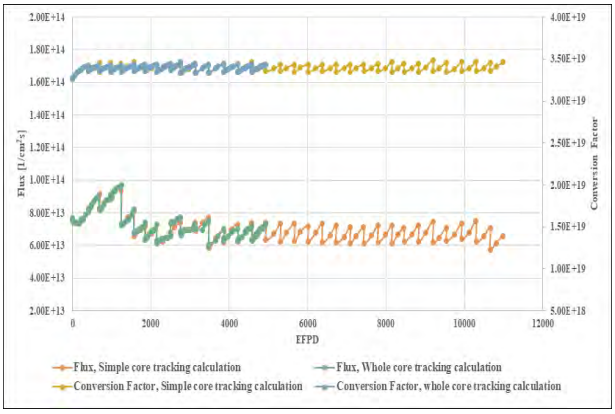

Fig. 4. Neutron flux and conversion factor at baffle

Figure 4 illustrates neutron flux and conversion factor, which is ratio of real flux to estimated flux from MC calculation, calculated using a simple core tracking method and whole core tracking method.
As a result of the comparison up to 15 cycles, neutron flux and the conversion factor evaluated by the simple core tracking method were well followed by the results of the whole core tracking method and the validity of the simple core tracking method was verified.

3.3 Representative core calculation method

Simple core tracking calculation is still a burdensome method. Therefore, the final calculation is carried out by the representative core calculation method which selects the cores that can represent the whole cycle. Based on the

results of neutron flux calculation using a simple core tracking method, cores that have neutron flux equivalent to mean neutron flux of each section were selected as the representative core. This considers that the radioactivity of structure is proportional to fluence, the total amount of neutrons irradiated on the structure over a given time.

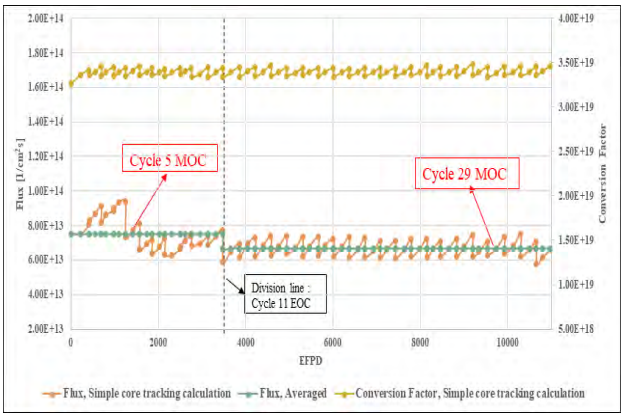

Fig. 5. Decision of representative core with neutron flux at baffle

As shown in Fig. 5, Results of simple core tracking calculations show that the transition of neutron flux is highly fluctuated in the anterior cycle and reaches equilibrium state after a certain cycle. Therefore, selection of representative core was performed by selecting two cores representing the transient cycle of 1 to 11 cycles and a core representing the equilibrium cycle of 12 to 32 cycles, each of which was determined as cycle 5 and cycle 29.

4. Calculation Results

Radioactivity of various radioactive isotope at RV/RVI was calculated using three different methods. Whole core tracking calculation was performed up to cycle 14 and the value of remaining cycles are obtained by extrapolation. Figures 6 and 7 show that the representative core calculation method using MOC core eventually follows the result of a simple core tracking calculation. It can be inferred that the results obtained from extrapolation are inaccurate and actually be deduced to follow the result of simple core tracking calculation. Table Ⅰ shows the specific activity of Fe-55, Ni-59, Co-60, Ni-63 at three different regions after 10 years from when the reactor operation stopped. The specific activity ratio of the representative core calculation method is alike a simple core tracking method, and it also backs the claim that the representative core calculation method is valid. It can be also shown that the results of whole core tracking method are about 10% higher than those of other methods and it is explained as inaccuracy resulting from extrapolation.

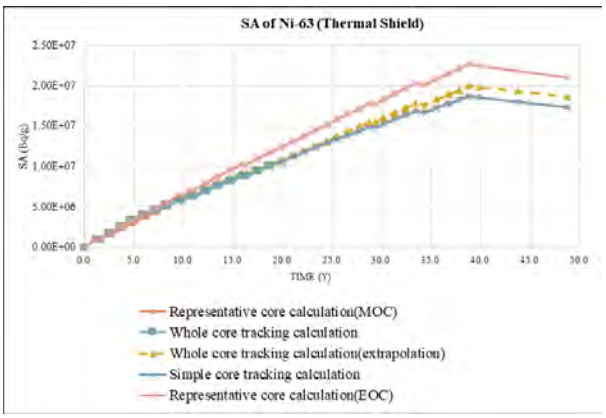

Fig. 6. Specific activity of Ni-63 at thermal shield

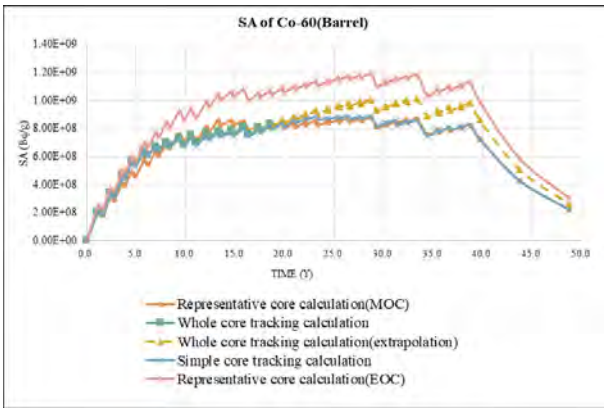

Fig. 7. Specific activity of Co-60 at barrel

Table I. Comparison of the specific activity of radioactive isotopes at the barrel, thermal shield, a reactor vessel

		Specific Activity (Bq/g)				
Region	RI	Whole core tracking (A)	Representative core (B)	Simple core tracking (C)	Ratio (B/A)	Ratio (C/A)
Barrel	Fe55	7.27E+07	6.15E+07	6.28E+07	0.85	0.86
	Ni59	9.65E+05	8.16E+05	8.58E+05	0.85	0.89
	Co60	2.64E+08	2.21E+08	2.22E+08	0.84	0.84
	Ni63	1.25E+08	1.10E+08	1.13E+08	0.88	0.90
Thermal Shield	Fe55	1.11E+07	9.99E+06	9.86E+06	0.90	0.89
	Ni59	1.47E+05	1.38E+05	1.37E+05	0.94	0.93
	Co60	4.57E+07	4.20E+07	4.13E+07	0.92	0.90
	Ni63	1.87E+07	1.74E+07	1.73E+07	0.93	0.93
Reactor Vessel	Fe55	4.69E+05	3.77E+05	3.91E+05	0.80	0.83
	Ni59	2.90E+02	2.53E+02	2.64E+02	0.87	0.91
	Co60	8.92E+04	7.93E+04	7.88E+04	0.89	0.88
	Ni63	3.68E+04	3.14E+04	3.27E+04	0.85	0.89

5. Conclusions

Activation analysis of RV/RVI in Kori Unit1 is performed using McCARD. Three different methods, whole core tracking calculation method, simple core tracking calculation method, representative core calculation method are applied to calculate specific activity of various radioactive isotopes. For precise calculation, critical boron concentration, thermal- hydraulic effect, xenon concentration were considered at all of the methods. The transition of the specific activity of isotope according to time was compared. The most simplified method, representative core calculation method, showed similar results to other methods and estimated to be sufficiently valid. For the representative core calculation method, we have to decide which core states can represent whole cycles and simple core tracking calculation should be preceded. But it still holds its efficiency when we roughly obtain neutron flux trend through cycles with relatively small number of histories, and conduct main calculation with selected representative core with a larger number of histories.

References

1. B. Roque et al. "International Comparison of a Depletion Calculation Benchmark on Fuel Cycle Issues", NEA/NSC/DOC(2013)1.
2. H. J. Shim, et al. "McCARD: Monte Carlo code for advanced reactor design and analysis." Nuclear Engineering and Technology 44.2 (2012): 161-176.
3. MJ Bell, “ORIGEN: the ORNL isotope generation and depletion code”, No. ORNL—4628. Oak Ridge National Lab., Tenn.(USA), 1973.
4. DE Peplow, et al. "Monaco/MAVRIC: Computational Resources for Radiation Protection and Shielding in SCALE." TRANSACTIONS-AMERICAN NUCLEAR SOCIETY 95 (2006): 669.
5. Sanghwa Shin and Jooho Whang, "A Study on Source Term Assessment of the Kori unit-1 Reactor Vessel", Journal of NUCLEAR SCIENCE and TECHNOLOGY, Supplement 4, p. 86-89, March, 2004.
6. Yong IL Kim, "Application of SCALE 6.1 MAVRIC Sequence for Activation Calculation in Reactor Primary Shield Concrete", Transactions of Korean Nuclear Society, Jeju, Korea, 2014.
7. NUREG/CR-3474, J. C. Evans et al., "Long-Lived Activation Products in Reactor Material," NUREG/CR-3474, Pacific Northwest Laboratory (1984).
8. Kontogeorgakos, D., F. Tzika, and I. E. Stamatelatos, "Neutron Activation Study of the GRR-1 Research Reactor Core Supporting Plate," Nuclear Technology, 175[2], 435, 2011.
9. Ben Volmert, Elena Tamaseviciute, Manuel Pantelias, Pavol Zvoncek and Beat Bitterli, "MCNP neutron streaming investigations from the reactor core to regions outside the reactor pressure vessel for a Swiss PWR", Progress in Nuclear Science and Technology, Vol 4, pp. 481-485, 2014.

Proceedings of the Reactor Physics Asia 2019 (RPHA19) Conference
Osaka, Japan, Dec. 2-3, 2019

UNCERTAINTY QUANTIFICATION OF NEUTRONICS CHARACTERISTICS IN THERMAL SYSTEMS USING RANDOM SAMPLING AND CONTINUOUS ENERGY MONTE-CARLO METHODS

Hiroya OIKE*, Ryoichi KONDO, Tomohiro ENDO, and Akio YAMAMOTO
Nagoya University, Furo-cho, Chikusa-ku, Nagoya-shi, 464-8603, Japan,
*Corresponding author: h-oike@fermi.energy.nagoya-u.ac.jp

Abstract

Uncertainty quantification of neutronic characteristics using the random sampling (RS) technique and a continuous energy Monte-Carlo code(MCNP) for thermal neutron systems is conducted. The RS code of the ACE-format cross section is used, which is developed in Nagoya University using the modules of FRENDY. In this study, all reactions in multi-group covariance data of SCALE 6.2.3 are considered. Through perturbation of nuclear data and statistical processing of k_{eff} obtained by MCNP6.2, the uncertainty quantification of k_{eff} is conducted. Comparison of the present result and the deterministic result obtained by the first-order perturbation theory (TSUNAMI-1D) showed that the uncertainty quantification results in thermal neutron systems using random sampling and MCNP are adequate.

Key Words: **Uncertainty Quantification, Random Sampling, MCNP, FRENDY, TSUNAMI-1D, Thermal Neutron Systems**

1. Introduction

The aim of the present paper is the uncertainty quantification of neutronics characteristics in thermal systems using the random sampling and a continuous energy Monte-Carlo methods. An analysis result of a reactor core inevitably includes the uncertainty. To improve the reliability of core analysis, uncertainty quantification of prediction results is important [1]. The uncertainties of predicted results mainly come from analysis methods and input parameters. The former is classified into modeling approximations in a deterministic method and statistical error of a probabilistic method. Examples of the later source are fuel composition, reactor/fuel geometry, and nuclear data. Recently, the random sampling method has been used to evaluate the uncertainty of core characteristics in light water reactor cores [2].

In the deterministic method, various approximations are used in a core analysis such as discretization of space, angle, and energy to solve the Boltzmann transport equation. By contrast, in the probabilistic method, especially in the continuous energy Monte-Carlo method, fewer approximations are used. Therefore, the probabilistic method is considered to be more accurate than the deterministic method. In the previous study, the RS method has been used with a deterministic code and multi-group cross section covariance of nuclear data [2]. However, from the viewpoint of accuracy, application of the RS with a probabilistic method and continuous energy cross section is desirable.

Perturbation of cross sections is necessary for the RS method. Kondo et al. developed an RS code for the ACE (A Compact ENDF) cross section files [3]. This code uses the functional modules of the FRENDY [4] code, which is a nuclear data processing system developed by Tada et al.

In the previous research[3], the RS method was applied to the Godiva core, which is a simple and bare sphere of ^{235}U, with MCNP, and its validity was confirmed through comparison with the deterministic method(TSUNAMI-1D). However, the validity of the RS method in a complicated thermal system with light nuclides, moderators and reflectors has not been confirmed yet.

The first purpose of this study is the investigation of the validity of the RS method using the continuous energy Monte-Carlo method in the thermal systems containing light nuclides.

The second purpose of this study is decomposition of total uncertainties obtained by the RS method. Usually, the RS method can quantify only total uncertainties even if there are many sources of uncertainties. When breakdown of uncertainties is necessary, the RS method should be repeatedly used for each source of uncertainty. When the number of uncertainty sources is large, it will be impractical. Therefore, possibility of uncertainty decomposition using a set of random sampling calculations considering all sources of uncertainty is pursued in the present study [5].

2. Random Sampling-based Uncertainty Quantification Method using MCNP

This section describes outline of the uncertainty quantification using the RS method and MCNP [2][3].

Firstly, multi-group relative variance-covariance matrix of nuclear data **R** is created. The diagonal elements of this matrix contain variances for nuclear data and the off-diagonal elements represent covariances among them.

Secondly, *I* sets of perturbation factors **f**, which are the factors to make perturbations on cross sections, are generated. Note that dimension of **f** is (number of nuclide × number of energy groups × number of reaction types). The cross sections are assumed to obey a Gaussian distribution. Using the matrix **R** and the multivariate normal random numbers **z** in Eq. (1), the perturbed cross sections can be obtained considering the variance and covariance of cross sections.

$$\mathbf{f} = \mathbf{A}\mathbf{z} + \boldsymbol{\mu}, \tag{1}$$

where **z** is a vector of random number obeying the standard normal distribution, $\boldsymbol{\mu}$ is a vector whose elements are 1, **A** is the matrix satisfying Eq. (2).

$$\mathbf{R} = \mathbf{A}\mathbf{A}^{\boldsymbol{T}}, \tag{2}$$

where $\boldsymbol{T}$ denotes a matrix transpose.

The perturbed cross sections are obtained by multiplying **f** to the original(unperturbed) cross sections. If negative value(s) is contained in the perturbation vector **f**, this vector is discarded and regenerated. This treatment may lead to positive bias on the result. However, negative perturbation factors are generated for cross sections with large uncertainty, which would be cross sections of minor nuclides. Generally, such nuclides have minor impact on the results and our experiences in the previous studies support this expectation.

Thirdly, the generated perturbation factors are multiplied to continuous energy cross section data in the ACE-format for MCNP to make perturbed cross sections. The RS code for ACE-format cross sections was used [3][4]. Note that the created matrix **R** is multi-group, thus continuous energy cross sections are uniformly perturbed within the energy range of a multi-group.

Fourthly, neutronics calculations using MCNP is carried out using perturbed ACE-format cross sections [6].

Finally, *I* output parameters, specifically the effective multiplication factors, are obtained and the relative standard deviations are calculated in order to estimate the uncertainty of multiplication factor.

3. Decomposition Method of Total Uncertainty

This section describes outline of the decomposition method of total uncertainty into contribution from each nuclide.

An estimation method of sensitivity coefficients of neutronics parameters using the RS method was proposed in the previous study [5]. When the sensitivity coefficients are available, the partial uncertainty owing to specific nuclear data can be calculated by Eq. (3) or Eq. (4).

$$V_{\tilde{\sigma}}^{k} = \mathbf{S}_{\tilde{\sigma}}^{k^T}\mathbf{V}_{\tilde{\sigma},\tilde{\sigma}}^{true}\mathbf{S}_{\tilde{\sigma}}^{k}, \tag{3}$$

$$V_{\tilde{\sigma}}^{k} = \boldsymbol{S}_{\tilde{\sigma}}^{k^T}\boldsymbol{V}_{\tilde{\sigma},\tilde{\sigma}}\boldsymbol{S}_{\tilde{\sigma}}^{k}, \tag{4}$$

where $\tilde{\sigma}$ is specific nuclear data, $V_{\tilde{\sigma}}^{k}$ is uncertainty due to $\tilde{\sigma}$, which is extracted from total uncertainty; and $\mathbf{V}_{\tilde{\sigma},\tilde{\sigma}}^{true}$ is the multi-group covariance of nuclear data and $\mathbf{V}_{\tilde{\sigma},\tilde{\sigma}}$ is a sample covariance matrix of nuclear data obtained by the RS calculations. $\mathbf{S}_{\tilde{\sigma}}^{k}$ is a sensitivity coefficients of neutronics parameter k with respect to $\tilde{\sigma}$, and is calculated in Eq. (5).

$$\mathbf{S}_{\tilde{\sigma}}^{k} = \mathbf{V}_{\tilde{\sigma},\tilde{\sigma}}^{-1}\mathbf{V}_{k,\tilde{\sigma}}, \tag{5}$$

where $\mathbf{V}_{k,\sigma}$ is a sample covariance vector between k and $\tilde{\sigma}$. We attempt to decompose total uncertainty into contributions from individual nuclides using Eq. (3) or (4) and Eq. (5).

4. Calculation Conditions

In this study, multi-group relative variance-covariance matrix is taken from the 56 energy group covariance data of SCALE6.2.3 (56groupcov7.1) [7].

ENDF/B-VII.1 in the ACE-format is used for MCNP[8].

If the effective rank of covariance matrix $\mathbf{V}_{\tilde{\sigma},\tilde{\sigma}}$ is smaller than that of matrix size, the singular value decomposition and the low-rank approximation, or pseudoinverse can be used to avoid a numerical issue to calculate $\mathbf{V}_{\tilde{\sigma},\tilde{\sigma}}^{-1}$. Note that the pseudoinverse is used in the present study [5].

A sphere composed of high enriched uranium oxyfluoride solution in the ICSBEP handbook (HEU-SOL-THERM-012) [9] is calculated in this study. Number densities of the core are shown in Table I. Hydrogen to Uranium-235 ratio is 1272. Radius of the core and volume are 27.9244 cm and 91.21 liters, respectively. The core is surrounded by 0.2 cm thick spherical 1100 aluminum tank and 15 cm thick water reflector. The benchmark system is under room temperature. The measured k_{eff} is 0.9999 ± 0.0058.

All nuclides and reactions having the covariance data, which are shown in Table II, were perturbed in this study.

Firstly, four sets of RS calculations were carried out making the perturbation for ^{1}H, ^{16}O, ^{235}U, and all nuclides. The sample size is 100 for each set because the available computational time was limited. Total number of neutron histories was 50 million, i.e., numbers of neutron histories per cycle, active cycles, and skip cycles are 10000, 5025, and 25, respectively, for one sample.

Table I. Compositions of HEU-SOL-THERM-012 core

Elements	atoms/barn-cm
^{234}U	5.5393×10^{-7}
^{235}U	5.2444×10^{-5}
^{236}U	2.8022×10^{-7}
^{238}U	2.9675×10^{-6}
^{19}F	1.1249×10^{-4}
^{16}O	3.34603×10^{-2}
^{17}O	1.27197×10^{-5}
^{1}H	6.6722×10^{-2}

Table II. All Nuclides and reactions considered in the calculation.

Reaction	Nuclide
Elastic	^{1}H
(n, n′)	^{16}O
(n, 2n)	^{17}O
Fission	^{19}F
(n, γ)	^{27}Al
(n, p)	^{28}Si
(n, d)	^{29}Si
(n, t)	^{30}Si
(n, ^{3} He)	^{55}Mn
(n, α)	^{63}Cu
(n, ν_{total})	^{65}Cu
Fission spectrum	^{234}U
	^{235}U
	^{236}U
	^{238}U

Secondly, 2000 RS calculations are carried out to decompose total uncertainty into contribution from each nuclide. In this case, the sample size is determined to reduce statistical error of estimated covariance matrix $\mathbf{V}_{k,\tilde{\sigma}}$. In these calculations, number of active cycles are reduced to 525 to shorten computation time.

5. Numerical Results

Figure 1 shows the distributions of effective multiplication factors obtained by RS for ^{1}H, ^{16}O, ^{235}U, and all nuclides.

Table III provides the comparison of the uncertanities obtained by the present RS calculations and by the deterministic method based on the first-order perturbation theory(TSUNAMI-1D)[7]. The 95 % confidence interval obtained by the bootstrap method with 10000 bootstrap samples is also shown in Table III [10][11].

Table III indicates that the results obtained by the RS and the deterministic method agree within the range of statistical error, which shows the validity of the present method in the thermal neutron system.

Table III Comparison of relative k_{eff} uncertainty

	TSUNAMI-1D	RS	95% conf. interval
All nuclides	0.81	0.81	0.698-0.919
^{1}H	0.44	0.44	0.371-0.496
^{16}O	0.10	0.10	0.090-0.116
^{235}U	0.67	0.60	0.511-0.693

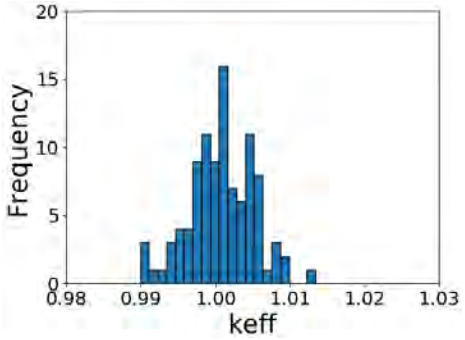

(a)^{1}H

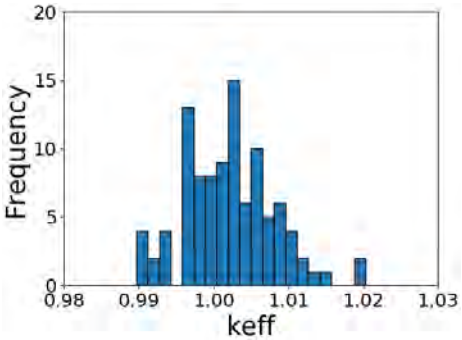

(b)^{235}U

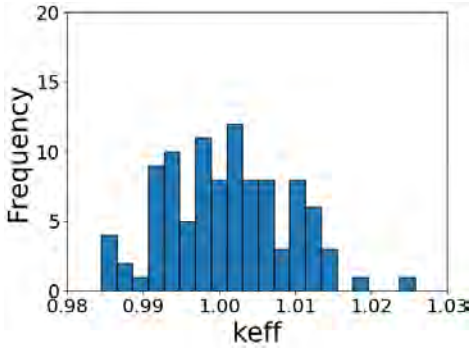

(c)All nuclides

Fig. 1 The histogram of 100 k_{eff} in the RS method for 3 cases. The number of bins in the histograms is 20.

Table IV shows the decomposition results of total uncertainty using Eq. (3) or (4) and Eq. (5) with 2000 samples and deterministic classification results of each nuclide uncertainty.

The "Total all nuclide uncertainty" in Table IV was calculated by Eq. (3) or Eq. (4) considering all nuclear data. The "Sum up each nuclide uncertainty" was summation of Eq. (3) or Eq. (4) for individual nuclides. The covariance matrix obtained by the RS calculations is used for the results in $\mathbf{V}_{\tilde{\sigma},\tilde{\sigma}}$ column calculated by Eq. (3) while the true covariance matrix $\mathbf{V}_{\tilde{\sigma},\tilde{\sigma}}^{true}$ is used for the results in $\mathbf{V}_{\tilde{\sigma},\tilde{\sigma}}^{true}$ column calculated by Eq. (4).

Table IV Breakdown of uncertainty of k_{eff}

Nuclide	relative standard deviation (Δk/k%)		
	$\mathbf{V}_{\tilde{\sigma},\tilde{\sigma}}$	$\mathbf{V}^{true}_{\tilde{\sigma},\tilde{\sigma}}$	TSUNAMI -1D
^{27}Al	0.02	0.01	0.00
^{63}Cu	0.03	0.03	0.00
^{65}Cu	0.03	0.03	0.00
^{19}F	0.02	0.02	0.00
^{1}H	0.44	0.44	0.44
^{55}Mn	0.03	0.02	0.00
^{16}O	0.10	0.10	0.10
^{17}O	0.03	0.01	0.00
^{28}Si	0.02	0.02	0.00
^{29}Si	0.02	0.02	0.00
^{30}Si	0.02	0.02	0.00
^{234}U	0.04	0.03	0.00
^{235}U	0.64	0.67	0.67
^{236}U	0.03	0.03	0.00
^{238}U	0.04	0.03	0.00
Total of all nuclide uncertainties	0.76	0.81	0.81
Sum up of each nuclide uncertainty	0.78	0.81	

Table IV indicates that the decomposition results of total uncertainty were appropriately estimated except for minor contributors. The statistical error of the MCNP in this calculation conditions is about 0.025 %; thus decomposition of minor contributors having small uncertainty was not accurate.

Table IV also indicates that the results using $\mathbf{V}^{true}_{\tilde{\sigma},\tilde{\sigma}}$ column are closer to the deterministic results than those using $\mathbf{V}_{\tilde{\sigma},\tilde{\sigma}}$ since $\mathbf{V}^{true}_{\tilde{\sigma},\tilde{\sigma}}$ utilizes the true covariance. Even if the number of samples increases, $\mathbf{V}_{\tilde{\sigma},\tilde{\sigma}}$ is not equal to $\mathbf{V}^{true}_{\tilde{\sigma},\tilde{\sigma}}$ because perturbation factor **f** has positive bias.

The values "Total of all nuclide uncertainties" and "Sum up of each nuclide uncertainty" using $\mathbf{V}^{true}_{\tilde{\sigma},\tilde{\sigma}}$ are close; thus correlation among nuclides is sufficiently small. Therefore, "Total of all nuclide uncertainties" and "Sum up of each nuclide uncertainty" using $\mathbf{V}_{\tilde{\sigma},\tilde{\sigma}}$ will be closer when the number of samples increases.

6. Conclusions

The uncertainty quantification of neutronics characteristics in the thermal system is carried out using the continuous energy Monte-Carlo code MCNP and the RS method. Comparison of the results by the RS method and the deterministic method (TSUNAMI-1D) indicates the validity of present method. Decomposition of total uncertainty is also tried and the results are promising; the uncertainties by the major contributors can be accurately decomposed.

The present study clarifies the applicability of the RS method coupled with accurate continuous energy Monte-Carlo method. The present approach is flexible, accurate and general, and can be used to obtain the reference value of uncertainty.

References

1. Cacuci DG, *Sensitivity and Uncertainty Analysis: Theory*, Vol. 1, Chapman and Hall/CRC, Florida, USA (2003).
2. Yamamoto A, Kinoshita K, Watanabe T, et al., "Uncertainty Quantification of LWR Core Characteristics Using Random Sampling Method," *Nucl. Sci. Eng*., **181**, *2*, 160 (2015).
3. Kondo R, Endo T, Yamamoto A, et al., " Implementation of Random Sampling for Ace-Format Cross Sections using FRENDY and Application to Uncertainty Reduction," *Proc. M&C 2019*, Portland, OR, Aug.25-29, 2019, American Nuclear Society (2019).
4. Tada K, Nagaya Y, Kunieda S, et al., "Development and Verification of a New Nuclear Data Processing System FRENDY," *J. Nucl. Sci. Technol*., **54**, *7*, 806 (2017).
5. Chiba G, Kawamoto Y, Tsuji M, et al., "Estimation of Neutronics Parameter Sensitivity to Nuclear Data in Random Sampling-Based Uncertainty Quantification Calculations," *Ann. Nucl. Energy,* **75,** 395 (2015)
6. Werner CJ (Ed.), "MCNP User's Manual Code Version 6.2," LA-UR-17-29981, Los Alamos National Laboratory (2018).
7. Rearden BT, Jessee MA (Eds.), "SCALE Code System," ORNL/TM-2005/39 Version 6.2.3, Oak Ridge National Laboratory (2018).
8. Chadwick MB, Herman M, Obložinský P, et al., "ENDF/B-VII.1 Nuclear Data for Science and Technology: Cross Sections, Covariances, Fission Product Yields and Decay Data," *Nucl. Data Sheets*, **112**, *12*, 2887 (2011).
9. Pitts M, Rahnema F, Williamson TG, et al., "Water-Reflected 91-Liter Sphere of Enriched Uranium Oxyfluoride Solution," NEA/NSC/DOC/(95)03/II, HEU-SOL-THERM-012, OECD Nuclear Energy Agency (2004).
10. Efron B, "Bootstrap Methods: Another Look at the Jackknife," *Ann. Stat.*, **7**, *1*, 1 (1979).
11. Endo T, Yamamoto A, Watanabe T, "Confidence Interval Estimation by Bootstrap Method for Uncertainty Quantification using Random Sampling Method," *J. Nucl. Sci. Technol*., **52**,*7*, 993 (2015).

SS-02 Source-Driven Subcritical System

Proceedings of the Reactor Physics Asia 2019 (RPHA19) Conference
Osaka, Japan, Dec. 2-3, 2019

Experimental Analyses of Spallation Neutrons by 100 MeV Protons and Lead-Bismuth Target at Kyoto University Criticality Assembly

Kota Morioka[a,*], Masao Yamanaka[b], Kimihiko Sugiura[a], Cheol Ho Pyeon[b]
[a] *Technological Systems, Mechanical Engineering Course, Osaka Prefecture University College of Technology, 26-12 Saiwai-cho, Neyagawa, Osaka 572-8572, Japan;*
[b] *Research Center for Safe Nuclear System, Institute for Integrated Radiation and Nuclear Science, Kyoto University, Asashiro-nishi, Kumatori-cho, Sennan-gun, Osaka 590-0494, Japan;*
*Corresponding author: f18022@osaka-pct.ac.jp

Abstract

Irradiation experiments are carried out at the Kyoto University Criticality Assembly aimed at revealing the accuracy of numerical calculations of spallation reactions by 100 MeV protons and a lead-bismuth target. The neutron yield and the spectrum of spallation neutrons are obtained by reaction rate analyses of an aluminum, an indium and a bismuth foils. The experimental analyses are performed by using PHITS3.10 together with a nuclear model INCL and several neutron data libraries. The results show the agreement of the neutron yield and the neutron spectrum within the relative difference of 10% and 20% between measured and calculated reaction rates. Finally, the accuracy of calculations is revealed through a series of the irradiation experiments.

***Key Words*: Spallation neutron, Reaction rate analysis, neutron spectrum, Neutron yield, KUCA**

1. Introduction

The accelerator-driven system (ADS) was proposed aiming at a large amount transmutation of minor actinides and long-lived fission products by operating subcritical rector with spallation neutrons generated by high-energy proton injections onto a heavy metal (lead-bismuth (Pb-Bi)) target [1-2]. At the Kyoto University Critical Assembly (KUCA), the basic research on feasibility of ADS has been accumulated with the combined use of subcritical cores and spallation neutrons generated by 100MeV protons, revealing that the neutronic characteristics are varied by the spectrum of spallation neutrons [3]. Furthermore, for the ADS design, the study of the neutron source is emphasized quite important since the power of the reactor could be affected by the neutron yield that is the number of neutrons generated by injecting a proton onto a target.

The spectrum analysis was conducted for spallation neutrons generated by high-energy (150, 190 and 235 MeV) protons and tungsten target with reaction rates of bismuth (Bi) [4-5]. In previous study [5], the spectrum of spallation neutrons was correctly evaluated by Bi foils in good agreement within the relative difference of 10% between the calculation (MCNPX) and the experiment. Also, the analyses have been conducted on reaction rates in the research at the KUCA. Although the Pb-Bi target was employed in the ADS experiments since the target is planned to be used in actual ADS, the analyses of spallation neutrons by Pb-Bi target are a remained to reveal the accuracy of analyses of ADS experiments with Pb-Bi target.

The purpose of this study was to examine the accuracy of spallation calculations on the neutron yield and the neutron spectrum through the comparison between calculated and measured reaction rates.

2. Experimental Settings

Irradiation experiments were carried out at the beam dump to obtain the reaction rate on the yield and the spectrum of the spallation neutrons. In case of the measurement of the neutron yield, an aluminum (Al) and an indium foils (10×10×1 mm) were used for obtaining reaction rates by protons and neutrons by attaching onto the upper stream and the downstream of the Pb-Bi target (50 mm diam. and 18 mm thick; **Fig. 1**), respectively. In case of the neutron spectrum, the Bi foil (50 mm diam. and 2 mm thick) was attached on to the downstream of the target.

The proton beam was injected by an operation of proton (FFAG) accelerator at pulsed frequency of 30 Hz, and 300 pA and 1 nA during irradiation time of 2.5 and 4 hours in irradiation experiments of Al and In foils, and of Bi foil, respectively.

Reaction rates of irradiated foils were measured by the saturated activities D_∞ ($s^{-1}\cdot cm^{-3}$) deduced from γ-ray measurements with the use of the highly-purified germanium detector as follows:

$$D_\infty = \frac{\lambda T_C C \rho}{\varepsilon_D \varepsilon_E \{1-\exp(-\lambda T_i)\} \cdot \exp(-\lambda T_w) \cdot \{1-\exp(-\lambda T_C)\} \cdot M} \quad , \qquad (1)$$

where λ indicates the decay constant, T_c the counting time, C the count rate, ε_D the detection efficiency, ε_E the emission rate, T_i the irradiation time, T_w the waiting time before the start of the decay measurement, ρ the density, and M the mass of the foil, respectively. Here, the fundamental characteristics of irradiation foils used in experiment are shown in **Table I**.

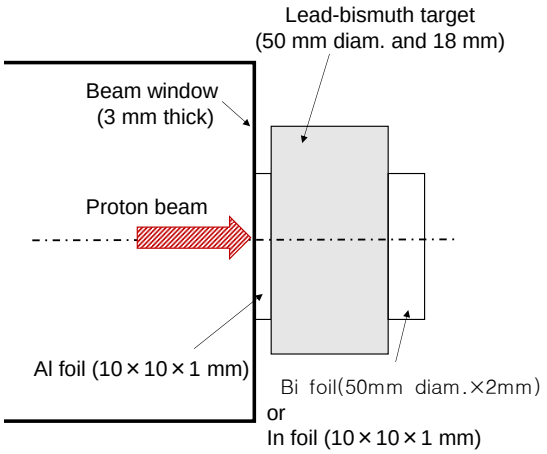

Fig. 1 Schematic of irradiation experiments.

Table I. Specification of measured reactions and γ-ray.

Reaction, (Threshold energy)	Half life	Energy [keV] (Emission rate [-])
^{27}Al (p, n+3p) (3.25MeV)	15.00 h	1368.6 (1.00)
^{115}In(n, n') (0.34 MeV)	4.486 h	336.2 (0.37)
^{209}Bi(n, 4n) (22.56 MeV)	6.243 d	803.1 (0.99)
^{209}Bi(n, 5n) (29.63 MeV)	15.31 d	703.5 (0.31)
^{209}Bi(n, 6n) (38.08 MeV)	11.22 h	374.8 (0.82) 670.7 (0.11)
^{209}Bi(n, 7n) (45.34 MeV)	11.76 h	822.7 (0.45) 1679.6 (0.09) 1847.3 (0.12)
^{209}Bi(n, 8n) (54.24 MeV)	1.71 h	422.1 (0.84) 657.5 (0.02) 960.7 (0.99)

3. Analyses of Spallation Neutrons

Experimental analyses were performed by PHITS 3.10 code [6] with cross sections by the nuclear model INCL [7] for proton and neutrons (above 20 MeV) and JENDL-4.0 [8] for neutrons (under 20 MeV). The transport calculation was conducted with 5×10^5 total histories. The proton spectrum injected into Bi foil indicated by mono-energy around 100 MeV and moderated spectrum, as shown in **Fig. 2**. The combined spectrum was caused by scattering attributed to injecting 100 MeV protons onto beam window (3 mm thick) before the Bi foil. By the injection of the protons onto the Pb-Bi target, the spallation neutrons with wide range of spectrum were generated with two components: a most dominant spectrum similar to that by fission reactions and a unique high-energy spectrum ranging between 10 and 100 MeV. The reaction rate analysis was conducted by multiplying calculated neutron or proton spectra and target cross sections with PHITS3.10 code. Here, ENDF/B-VI.8 [9], JENDL/D-99 [10] and JENDL/HE-2007 [11] were used for reaction rates of ^{27}Al(p, n+3p)^{24}Na, ^{115}In(n, n')^{115m}In and ^{209}Bi(n, xn)$^{210-x}$Bi (n = 4 to 8) reactions, as shown in **Fig.3**.

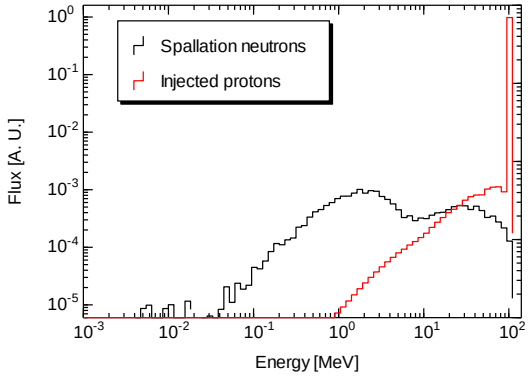

Fig. 2 Spectra of injected protons on to Bi foil and generated spallation neutrons.

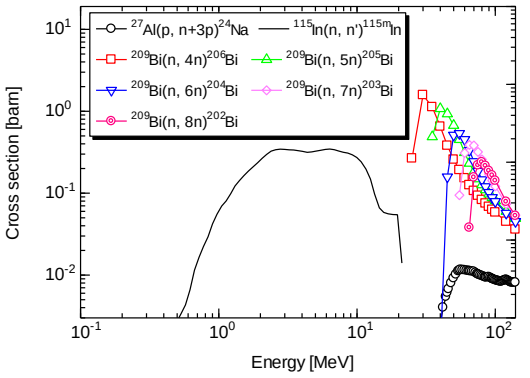

Fig. 3 Cross sections of ^{27}Al(p, n+3p)^{24}Na, ^{115}In(n, n')^{115m}In and ^{209}Bi(n, xn)$^{210-x}$Bi (x = 4 to 8) reactions.

3.1 Neutron yield

The neutron yield (number of generated neutrons by the injection of a proton) was investigated through the comparison of reaction rates by ^{27}Al(p, n+3p)^{24}Na and ^{115}In(n, n')^{115m}In reactions for measuring the number of protons and neutrons respectively, at the location of Pb-Bi target.

Measured ^{115}In(n, n')^{115m}In reaction rates were

normalized by the measured ^{27}Al(p, n+3p)^{24}Na ones so as to represent the neutron yield in the experiment. Here, ^{115}In(n, n')^{115m}In indicates constant cross section ranging between 2.5 and 10 MeV (Fig. 3), predicting to play the role of a neutron detector for dominant neutron spectrum of spallation neutrons (Fig. 2). The experimental analyses agreed with the measured neutron yield within a relative difference of 13%, as show in **Table II**, indicating the validity of the calculated spallation neutron spectrum and the cross section of ^{27}Al(p, n+3p)^{24}Na reaction.

Table II. Comparison between the calculation and the experiment in terms of neutron yield.

Neutron / proton	Calculation	Experiment	C/E
^{115}In(n,n') ^{115m}In/ ^{27}Al (p, n+ 3p)^{24}Na	0.210±0.002	0.185±0.004	1.13±0.03

3.2 Neutron spectrum

The irradiation experiment was carried out on the spectrum evaluation of spallation neutrons with Bi foil. Measured reaction rates were normalized by ^{209}Bi(n, 4n)^{206}Bi reaction rate for organizing reaction rates in terms of neutron spectrum. Here, ^{209}Bi(n, xn)$^{210-x}$Bi cross sections cover neutron energy ranging between 20 and 100 MeV for the high-energy component of the spallation neutron spectrum in Fig. 2.

The results of experimental analyses indicated agreement between measured and calculated reaction rates within a relative difference of 20% except for ^{209}Bi(n, 7n)^{206}Bi cross section, as shown in **Table III**. A discrepancy of ^{209}Bi(n, 7n)^{206}Bi reaction was attributed to the nuclear cross section since the cross section of ^{209}Bi(n, xn)$^{210-x}$Bi reaction overlaps in very narrow energy and no drastic variation was observed in the spectrum of the spallation neutrons ranging between 20 to 100 MeV. Further investigation was considered necessary for spectrum estimation by comparison between various cross sections for protons in a future work. Additionally, elaboration of the beam spot modeling needs to be considered since cylindrical spot was approximately used in this study.

Table III. Reaction rates and comparison between the calculation and the experiment in terms of neutron spectrum

Reaction	Measured reaction rate [1/cm^3/s]	C/E
^{209}Bi(n, 4n)	(8.22±0.09)×10^4	-
^{209}Bi(n, 5n)	(4.29±0.42)×10^4	0.84±0.09
^{209}Bi(n, 6n)	(2.23±0.02)×10^4	1.20±0.03
^{209}Bi(n, 7n)	(1.42±0.04)×10^4	1.44±0.06
^{209}Bi(n, 8n)	(3.54±0.09)×10^3	1.01±0.05

4. Conclusions

Irradiation experiments were carried out so as to examine the prediction accuracy of the spectrum and the yield of spallation neutrons with 100 MeV proton accelerator and the Pb-Bi target. The experimental analyses of reaction rates were numerically analyzed by PHITS3.10 together with INCL and nuclear data libraries.

Calculated reaction rate of the neutron yield compared with measured one within the relative difference of 13%. Furthermore, the reaction rates on spallation neutron spectrum indicated agreement within 20% except for ^{209}Bi(n, 7n)^{206}Bi reaction, demonstrating the validity of spallation neutron calculations and nuclear data libraries. For comprehensive evaluation of spallation calculations, various nuclear data libraries are examined in experimental analyses of the neutron spectrum and the neutron yield to evaluate accuracy of the series of reaction rate analysis as the future work. Also, the calculation model is planned to be elaborated for the beam spot.

References

1. Rubbia C, et. al., "A Conceptual Design of a Fast Neutron Operated High Power Energy Amplifier," CERN/AT95-44 ET, Switzerland (1995).4.
2. Sugawara T, et. al., "Research and Development Activities for Accelerator-Driven System in JAEA," *Prog. Nucl. Energy*, **106**, 27 (2018).
3. Pyeon CH, et. al., "Neutron Characteristics of Solid Targets in Accelerator-Driven System at Kyoto University Critical Assembly," *Nucl. Technol.*, **192**, 181 (2015).
4. Kim E, et. al., "Measurement of Neutron Spallation Cross Sections of ^{12}C and ^{209}Bi in the 20- to 150-MeV Energy Range," *Nucl. Sci. Eng.*, **129**, 209 (1998).
5. Pyeon CH, et. al., "Reaction Rate Analysis of Nuclear Spallation Reactions Generated by 150, 190, and 235 MeV Protons," *J. Nucl. Sci. Technol.*, **47**, 1090 (2010).
6. Sato T, et. al., "Features of Particle and Heavy Ion Transport code System (PHITS) version 3.02," *J. Nucl. Sci. Technol*. **55**, 684 (2018).
7. Boudard A, et. al., "New Potentialities of the Liège Intranuclear Cascade Model for Reactions Induced by Nucleons and Light Charged Particles," *Physical Review C87*, 014606 (2013).
8. Shibata K, et. al., "JENDL-4.0: A New Library for Nuclear Science and Technology," *J. Nucl. S ci. Technol*. **48**, 1 (2011)..
9. "Evaluated Nuclear Data File," ENDF/B-VI, *National Nuclear Data Center*, Brookhaven National Laboratory (1990).
10. Kobayashi K, et. al., "JENDL Dosimetry File 99 (JENDL/D-99)," JAERI 1344, Japan Atomic Energy Agency (2002).
11. Takada H, et. al., "Validation of JENDL High-Energy File Through Analyses of Spallation Experiments at Incident Proton Energies from 0.5 to 2.83 GeV," *J. Nucl. Sci. Technol.*, **46**, 589 (2009).

Proceedings of the Reactor Physics Asia 2019 (RPHA19) Conference
Osaka, Japan, Dec. 2-3, 2019

Applicability of Extended Kalman Filter Technique to Reactivity Monitoring at Kyoto University Criticality Assembly

Masao Yamanaka[a, *], Cheol Ho Pyeon[a]
[a] *Research Center for Safe Nuclear System, Institute for Integrated Radiation and Nuclear Science, Kyoto University, Asashiro-nishi, Kumatori-cho, Sennan-gun, Osaka 590-0494, Japan;*
[*]Corresponding author: m-yamanaka@rri.kyoto-u.ac.jp

Abstract

Transient experiments with external neutron source are carried out at the Kyoto University Criticality Assembly with the variation of subcriticality, so as to investigate applicability of the extended Kalman filter (EKF) technique to on-line monitoring of subcriticality. The external neutron source is generated by an injection of 100 MeV protons onto a lead-bismuth target, observed inherent instability (beam swing and intense oscillation) in beam current. In the EKF technique, two different state space models are prepared for an estimation of only reactivity and a simultaneous estimation of reactivity and beam current. The result of subcriticality estimation is revealed accurate for reference subcriticality by MCNP6.2, indicating the applicability of EKF technique to reactivity monitoring.

***Key Words*: On-line monitoring of subcriticality, Extended Kalman filter, Transient experiment, Spallation neutron source, KUCA**

1. Introduction

The Kalman filter technique has been adopted for accurately evaluating reactivity variation by combined use of measured data and theoretical modeling in a framework of data assimilation [1]. The reactivity variation could be directly recognized by the response of neutron detectors. The reactivity variation is easily observed by the filtering technique even when the detector count is very poor. For accurate subcriticality monitoring, the particle filter was introduced as a strong tool so as to take into account the non-linearity in the state space model based on the one-point kinetic equation [2]. Among the filtering techniques, the extended Kalman filter (EKF) treats 1st-order approximation of the nonlinearity with slight calculation cost.

The EKF was applied to the subcriticality monitor only in rod drop transient in critical experiments and subcritical experiments with a stable neutron source [3-4]. Here, subject was remained to accurately estimate the subcriticality when varying the neutron source intensity, such as beam trip and restart behavior in an accelerator-driven system. Then, two different state space models were attempted to examine the capability for single parameter (reactivity) estimation and simultaneous estimation of reactivity and neutron source intensity.

The purpose of this study was to investigate applicability of the EKF technique to the subcriticality monitor even with unstable neutron source.

2. Extended Kalman Filter

The EKF was proposed to be applicable to indirectly estimating parameters of the non-linear system from the Kalman filter. On the basis of the one-point kinetic equation, the state space model and the observation equation were prepared as follows:

$$\boldsymbol{x}(k+1)=\boldsymbol{f}\left(\boldsymbol{x}(k)\right)+\boldsymbol{b}v(k)\ , \tag{1}$$

$$y(k)=h\left(\boldsymbol{x}(k)\right)+w(k)\ , \tag{2}$$

where $\boldsymbol{x}$ is state space variable, $\boldsymbol{y}$ observation matrix, $\boldsymbol{f}$ a matrix expressing the state space, $\boldsymbol{b}$ a vector distributing system noise, v system noise, h a the observability matrix, and w observation noise. The non-linearity was considered by derivative $\boldsymbol{A}$ and $\boldsymbol{c}^T$, as follows:

$$\boldsymbol{A}(k)=\left.\frac{\partial \boldsymbol{f}\left(\boldsymbol{x}(k)\right)}{\partial \boldsymbol{x}}\right|_{\boldsymbol{x}=\hat{\boldsymbol{x}}^{-}(k)}\ , \tag{3}$$

$$\boldsymbol{c}^{T}(k)=\left.\frac{\partial h\left(\boldsymbol{x}(k)\right)}{\partial \boldsymbol{x}}\right|_{\boldsymbol{x}=\hat{\boldsymbol{x}}^{-}(k)}\ , \tag{4}$$

where $\hat{x}^{-}$ is a priori estimate. The priori estimate is evaluated with the use of state estimate $\hat{x}$ in previous time step, as follows:

* Corresponding author, E-mail: m-yamanaka@rri.kyoto-u.ac.jp

$$\boldsymbol{x}^{-}(k)=\boldsymbol{f}\left(\boldsymbol{x}(k-1)\right) \quad . \tag{5}$$

The priori error covariance matrix $\boldsymbol{P}^{-}$ is evaluated, as follows:

$$\boldsymbol{P}^{-}(k)=\boldsymbol{A}(k)\boldsymbol{P}(k-1)\boldsymbol{A}^{\mathrm{T}}(k)+\sigma_v^{2}\boldsymbol{b}\boldsymbol{b}^{\mathrm{T}} \quad , \tag{6}$$

where $\boldsymbol{P}$ is a posteriori error covariance matrix. The Kalman gain $\boldsymbol{g}$ is determined, as follows:

$$\boldsymbol{g}^{-}(k)=\boldsymbol{P}^{-}(k)\boldsymbol{C}(k)\left(\boldsymbol{C}^{T}(k)\boldsymbol{P}^{-}(k)\boldsymbol{C}(k)+\sigma_w^{2}\right)^{-1}. \tag{7}$$

The state estimate is evaluated with the use of observation results and the priori state estimate by the most likelihood parameter $\boldsymbol{g}$, as follows:

$$\boldsymbol{x}(k)=\boldsymbol{x}^{-}(k)+\boldsymbol{g}(k)\left\{y(k)-h\left(\boldsymbol{x}^{-}(k)\right)\right\} \quad . \tag{8}$$

Finally, for next time step, the posteriori error covariance matrix is prepared, as follows:

$$\boldsymbol{P}(k)=\left\{\boldsymbol{I}-\boldsymbol{g}(k)-\boldsymbol{C}^{T}(k)\right\}\boldsymbol{P}^{-}(k) \quad . \tag{9}$$

In this study, simultaneous estimation of reactivity and neutron source intensity was attempted besides single estimation of reactivity. In case of single (reactivity) estimation model, the $\boldsymbol{x}$, $\boldsymbol{y}$ and $\boldsymbol{f}$ were expressed as follows:

$$\boldsymbol{x}(k)={}^{t}\left(n\ C_1\ C_2\ C_3\ C_4\ C_5\ C_6\ \rho\right) \quad , \tag{10}$$

$$\boldsymbol{y}(k)={}^{t}\left(n\right) \quad , \tag{11}$$

$$\boldsymbol{f}(\boldsymbol{x}(k))=\begin{pmatrix} n(k)+T\left(\frac{\rho(k)-\beta_{eff}}{\Lambda}n(k)+\sum_{i=1}^{6}\lambda_i C_i(k)+\varepsilon I(k)\right) \\ C_1(k)+T\left(\frac{\beta_{eff,1}}{\Lambda}n(k)-\lambda_1 C_1(k)\right) \\ C_2(k)+T\left(\frac{\beta_{eff,2}}{\Lambda}n(k)-\lambda_2 C_2(k)\right) \\ C_3(k)+T\left(\frac{\beta_{eff,3}}{\Lambda}n(k)-\lambda_3 C_3(k)\right) \\ C_4(k)+T\left(\frac{\beta_{eff,4}}{\Lambda}n(k)-\lambda_4 C_4(k)\right) \\ C_5(k)+T\left(\frac{\beta_{eff,5}}{\Lambda}n(k)-\lambda_5 C_5(k)\right) \\ C_6(k)+T\left(\frac{\beta_{eff,6}}{\Lambda}n(k)-\lambda_6 C_6(k)\right) \\ \rho(k) \end{pmatrix} , \tag{12}$$

where n is the neutron count, ρ reactivity, $\beta_{eff,\,i}$ effective delayed neutron fraction of i-th group, λ_i delayed neutron decay constant of i-th group, C_i density of delayed neutron precursor, ε source efficiency (determined by initial subcriticality and neutron count), and I observed beam current source T the time step. The transient experiments were initiated at stable state first. Then, initial values in $x(0)$ were set by solving the one-point kinetic equation in stable state with measured neutron count at time = 0 s.

In case of simultaneous (reactivity and beam intensity) estimation, observed current and differential of the current in time step were appended to Eqs. (10), (11) and (12), as follows:

$$\boldsymbol{x}(k)={}^{t}\left(n\ C_1\ C_2\ C_3\ C_4\ C_5\ C_6\ \rho\ S\ \omega\right) \quad , \tag{13}$$

$$\boldsymbol{y}(k)={}^{t}\left(n\ S\ \omega\right) \quad , \tag{14}$$

$$\boldsymbol{f}(\boldsymbol{x}(k))=\begin{pmatrix} n(k)+T\left(\frac{\rho(k)-\beta_{eff}}{\Lambda}n(k)+\sum_{i=1}^{6}\lambda_i C_i(k)+\varepsilon S(k)\right) \\ C_1(k)+T\left(\frac{\beta_{eff,1}}{\Lambda}n(k)-\lambda_1 C_1(k)\right) \\ C_2(k)+T\left(\frac{\beta_{eff,2}}{\Lambda}n(k)-\lambda_2 C_2(k)\right) \\ C_3(k)+T\left(\frac{\beta_{eff,3}}{\Lambda}n(k)-\lambda_3 C_3(k)\right) \\ C_4(k)+T\left(\frac{\beta_{eff,4}}{\Lambda}n(k)-\lambda_4 C_4(k)\right) \\ C_5(k)+T\left(\frac{\beta_{eff,5}}{\Lambda}n(k)-\lambda_5 C_5(k)\right) \\ C_6(k)+T\left(\frac{\beta_{eff,6}}{\Lambda}n(k)-\lambda_6 C_6(k)\right) \\ \rho(k) \\ S(k)+\omega(k)T \\ \omega(k) \end{pmatrix} , \tag{15}$$

where S is beam current and ω slope in the variation of beam current.

3. Experimental Settings

Transient experiments were carried out by combining subcritical cores and an external neutron source generated by an injection of 100 MeV protons on to a lead-bismuth (Pb-Bi) target. The subcritical cores were constituted by lead-loaded fuel rods "f" (central region: highly-enriched uranium (HEU) plate and lead plate; both sides: HEU plate and polyethylene moderator) and normal fuel rod "F" (HEU plate and polyethylene moderator) as shown in **Figs. 1** and **2**. The core spectrum in the central region of fuel rod "f" was approximated to that of a fast rector by loading lead plates. Furthermore, the core spectrum in the normal fuel region had relative hard spectrum by H/U ratio of approximately 50 in polyethylene-moderated cores at KUCA.

The proton beam was generated by an operation of proton (FFAG) accelerator at pulsed frequency of 20 Hz, and varied beam current by the accelerator instability: swing and rapid oscillation. The spallation neutrons were generated with Pb-Bi target placed at [A, 15; Figs. 1 and 2], and its intensity of the neutron source was differed by the variation of the beam current (approximately10 to 70 pA).

In transient experiments, control rods and safety rods were inserted during the variation of beam current for two

different subcritical cores so as to investigate the applicability of EKF technique to the monitoring in a wide range of subcriticality and variation of the neutron source intensity. Here, the subcriticality was numerically obtained by using MCNP6.2 together with ENDF/B-VII.1, as shown in **Table I**.

Time evolution of neutron signals was recoded for a BF_3 detector placed at [Q, 5; Figs. 1 and 2] to prevent the variation of detector efficiency and neutron source efficiency during transient experiments. In addition to neutron signals, the time series data on the proton beam current were obtained for the observable parameter in the EKF. The time resolution in on-line monitoring was 1 s.

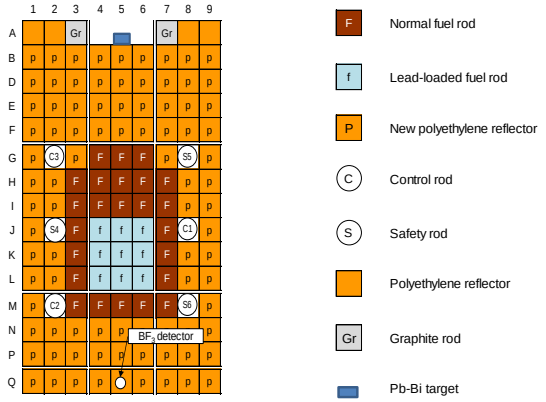

Fig. 1 Subcritical core (HEU: 3960 plates) for beam swing transient experiment.

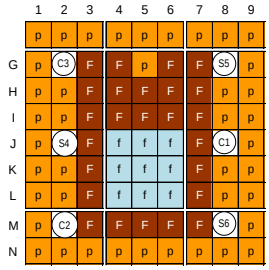

Fig. 2 Subcritical core (HEU: 4080 plates) for beam oscillation transient experiment.

Table I. Condition of transient experiments.

Case	Fuel plates	Inserted control rod	Subcriticality [pcm]
I-1	3960	-	4633
I-2	3960	C1	5796
I-3	3960	C1, C2, C3	6790
I-4	3960	C1, C2, C3 S4, S5, S6	9010
II-1	4080	-	4160
II-2	4080	C1	5296
II-3	4080	C1, C2, C3	6314

4. Transient Analyses

Proton beam transient experiments were carried out for different type of variation in the beam current: swing and intense oscillation involving short beam trip. With the use of these transient experiments, the applicability of the reactivity monitor was revealed by comparing the accuracy between different modeling for the state space with and without estimation of the source intensity as described in Sec. 2.

4.1 Swing of proton beam current

Beam swing transient experiment were conducted by gradually varying the beam current. The neutron count rate was varied as shown in **Fig. 3** by the beam transient as shown in **Fig. 4**. The beam transient actually involved spiked beam trip and restart, however, the focus was placed on the global variation of the beam swing.

The subcriticality was also varied during the beam swing by an actuator-driven insertion of control and safety rods through Cases I-1 to I-4 (Table I) between 1000 and 1900 s. From the count rate distribution (Fig. 3), reactivity variation could be recognized only at 1200 s and 1800 s because of beam current increase (Fig. 4). However, the emphasis should be placed where reactivity monitoring correctly indicated subcriticality variation compared with reference subcriticality during the beam swing. Furthermore, the accuracy was revealed that the simultaneous estimation is better than the single (reactivity) estimation in the beam swing transient.

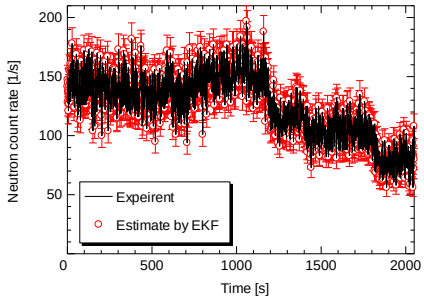

Fig. 3 Measured neutron count rate and its estimation result by simultaneous estimation model in beam swing transient experiment.

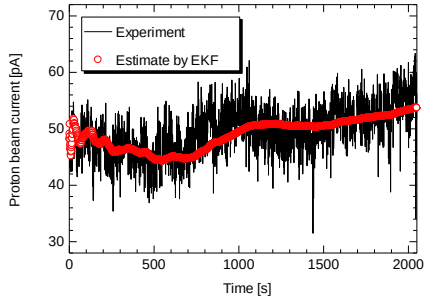

Fig. 4 Measured beam current and its estimation result by simultaneous estimation model in beam swing transient experiment.

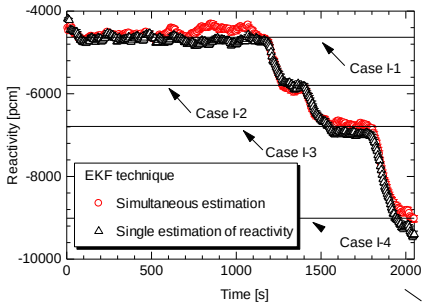

Fig. 5 Comparison of reactivity estimations in beam swing transient experiment.

4.2 Oscillation of proton beam current

The beam oscillation transient experiment was conducted, when the accelerator was unstably resulted in intense oscillation of count rate (**Fig. 6**), by insertion of control and safety rods during 650 s and 1000 s in **Fig. 7** through Cases II-1 to II-3 (Table I).

For unrecognizable subcriticality variation from the count rate distribution (Fig. 6), subcriticality monitoring was performed by the EKF technique with simultaneous estimation and single (reactivity) estimation (**Fig. 8**). The result of simultaneous estimation was revealed difficult to follow the intense current oscillation as shown in Fig. 7, indicating difficult to deduce correct subcriticality caused by inaccurate estimation of the beam current.

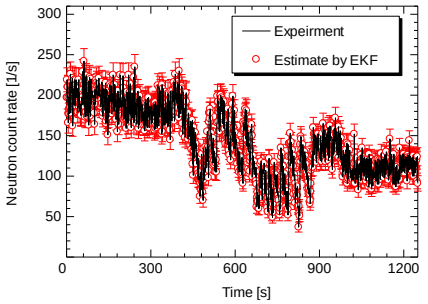

Fig. 6 Measured neutron count rate and its estimation result by simultaneous estimation model in beam oscillation transient experiment.

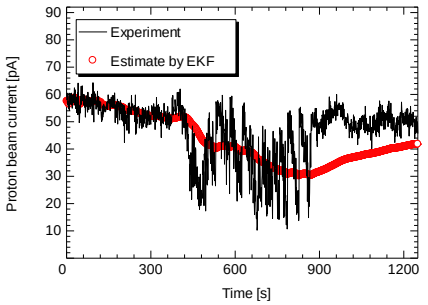

Fig. 7 Measured beam current and its estimation result by simultaneous estimation model in beam oscillation transient experiment.

Conversely, single (reactivity) estimation was revealed applicable even for intensely unstable neutron source. The correct estimation was attributed to accurately measured current and discontinuous trend, and was considered unnecessary to estimate by EKF technique. In other method, time resolution (1s) should be increased to follow the current variation.

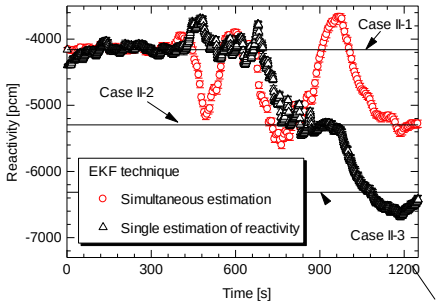

Fig. 8 Comparison of reactivity estimations in beam oscillation transient experiment.

5. Conclusions

Transient experiments with external neutron source and subcriticality were carried out at KUCA so as to investigate applicability of EKF technique to subcriticality monitoring. Among two types of transient experiments, the simultaneous estimation of reactivity and beam intensity was very accurate for beam swing transient even in deep subcriticality (9%dk/k) by comparing the reference by MCNP6.2. In case of intense beam oscillation, no simultaneous estimation was worked to follow rapid variation of the current. Conversely, the single (reactivity) estimation indicated accurate subcriticality variation during unstable neutron source. For simultaneously estimating beam current, time resolution is considered to be increased.

Acknowledgements

The authors are grateful to Prof. T. Endo of Nagoya University for his advice in the extended Kalman filter.

References

1. Venerus JC, et. al., “Estimation of the Dynamic Reactivity Using Digital Kalman Filtering,” *Nucl. Sci. Eng.*, **40**, 199 (1970).
2. Ikeda T, et. al., “Estimation of Subcriticality Using Particle Filter Method,” *Trans. Am. Nucl. Soc.*, **118**, 851 (2018).
3. Shimazu Y, “Qualitative Performance Comparison of Reactivity Estimation between the Extended Kalman Filter technique and the inverse point kinetic method,” *Ann. Nucl. Energy*, **66**, 161 (2014).
4. Yamanaka M, et. al., “Subcriticality Estimation by Extended Kalman Filter Technique in Transient Experiment with External Neutron Source at Kyoto University Critical Assembly,” *Eur. Phys. J. Plus* (2019) [to be submitted].

Proceedings of the Reactor Physics Asia 2019 (RPHA19) Conference
Osaka, Japan, Dec. 2-3, 2019

Core design of accelerator driven system with reactivity control method using thorium

Kentaro Nakamura, Hideki Saito, Naoto Aizawa, Tomohiko Iwasaki
Tohoku University, 6-6-01-2, Aoba, Aramaki, Aoba-ku, Sendai 980-8579, Japan
*Corresponding author: kentaro_nakamura062@neutron.qse.tohoku.ac.jp

Abstract

Accelerator-driven system (ADS) is planned to be operated at stable thermal power by increasing the beam current to compensate the fuel burnup, but the burden of core components increases with the beam current increase. The research on the reactivity control method using burnable poison for ADS has been conducted to minimize the increment of beam current. However, the burnable poison-loaded core has a potential to reach criticality by the unexpected withdrawal of burnable poison. The present study works on the reactivity control method with thorium to take advantage of its characteristics as fertile. Three types of thorium-loaded core are discussed from the aspect of the core homogeneity to study the effective reactivity control: homogeneous core, heterogeneous core and heterogeneous fuel assembly-loaded core. The homogeneous core is composed of single fuel assembly and all fuel pins are the mixture of original ADS fuel ((MA+Pu)N) and thorium. The heterogeneous core is consisted of two fuel assemblies: MA-bearing fuel assembly and thorium-only fuel assembly. The heterogeneous fuel assembly-loaded core is composed of single fuel assembly and the assembly is composed of MA-bearing fuel pins and thorium fuel pins. The core designs are performed by changing the amount of thorium for each core model. The heterogeneous fuel assembly-loaded core which the assembly contains 85 thorium pins out of the 391 pins shows the best reactivity control among the three core models, and 97% decrease of the burnup reactivity compared to that of original ADS is achieved.

Key Words: **Core design, ADS, reactivity control**

1. Introduction

Accelerator-Driven System (ADS) has been studied to transmute Minor Actinides (MA) and long-lived fission products in a high level radioactive waste effectively for the mitigation of the burdens related to the disposal of the waste. ADS consists of a high-intensity proton accelerator, a spallation target, and a subcritical core. The thermal power of ADS is maintained at a constant level by changing the beam current in a normal operation condition, and the beam current increases as the operation progresses to compensate the fuel burnup. However, the increase of beam current leads to grow the burden of reactor components. The large damage is considered to occur in the beam window, which is the important division wall between the accelerator beam duct and the spallation target and is in very severe conditions such as an external pressure, a heat generation by the proton beam and an irradiation damage. Therefore, it is desired that the extra load on the beam window is avoided and the increment of the beam current from the initial state is minimized.

The core design to decrease the maximum beam current has been performed by the introduction of burnable poison of gadolinium to increase the reactivity at the end of the operation cycle in the past studies. The various cores with gadolinium were designed with using various moderators of zirconium hydride, zirconium deuteride and beryllium oxide [1-3]. A series of core designs revealed that the burnup reactivity loss was decreased up to 0.75 %Δk/k with the use of gadolinium hydride as a result of optimizations whereas the loss in the reference core (no poison-loaded core) was 4.3 %Δk/k. However, the gadolinium-loaded core had the inherent characteristic that the unexpected withdrawal of burnable poison leads to reach criticality because these cores suppressed the excess reactivity by the poison at the beginning of cycle.

In the present study, the core design with reactivity control method which can eliminate the potential for criticality was conducted by the use of thorium to decrease the potential excess reactivity and take advantage of its characteristics as fertile. The core characteristics were also calculated to evaluate the influence of the use of thorium. In Section 2, the reference core model was introduced, and the method of the core

design was described. Section 3 presented the result of burnup reactivity performance and the core characteristics. Finally, the present study was summarized in Section 4

2. Analysis condition

2.1 Reference core design

The reference core design employed in this studies was JAEA-proposed 800 MWt lead-bismuth cooled ADS core [4-5]. Figure 1 shows the schematic view of the core, and the basic specifications are presented in Table 1. The fuel is composed of the mixed plutonium-minor actinide nitride ((Pu + MA)N) and the inert matrix of zirconium nitride (ZrN). The coolant and the spallation target is lead-bismuth eutectic. The proton beam accelerator is assumed the linac and its beam energy is 1.5 GeV. The thermal output is maintained at 800 MWt by adjusting the proton beam current (about 10 -20 mA in the reference design) throughout the operation cycle.

Table I. Basic specification of reference ADS design

Plant	Thermal Power	800 MWt
	initial k_{eff}	0.97
	Fuel	(Pu + MA)N+ZrN
	Coolant and Target	Lead-Bismuth eutectic
	Coolant inlet temperature	300 °C
	Coolant velocity	2.0 m/s
Fuel	Assembly pitch	233.9 mm
	Flat to Flat	232.9 mm
	Active fuel length	1000 mm
	Pu ratio in (Pu + MA)N	36.2 vol%
	ZrN ratio of reference core fuel	67.1 vol%
Accelerator	Accelerator type	linac
	Proton energy	1.5GeV

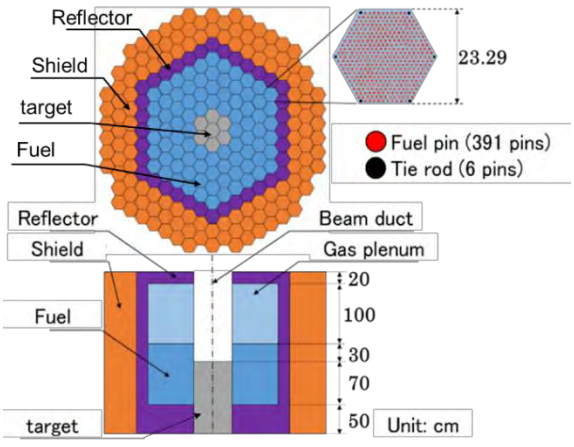

Fig. 1. Reference ADS core design

2.2 Core design of Thorium-loaded core

Thorium-loaded core was designed on the basis of the reference ADS core. For the design of thorium-loaded core, the following design requirements were set:

- The chemical form of the thorium was assumed the nitride (ThN).
- The structure of fuel assembly was the same as the reference design.
- One type of fuel assembly and thorium-only assembly were employed in the core.
- The number of fuel pins was conserved.
- No moderators (such as hydride) in the core
- The initial k_{eff} was set to 0.97 by changing the ratio of ZrN in the fuel.

There are many ways to load thorium in the core, and three types of the core were designed in this study from the aspect of the core homogeneity to study the effective reactivity control. Each loading pattern is shown in Figs. 2-4. The core which was composed of single fuel assembly and whose fuel was the homogeneous mixture of (Pu + MA + Th)N and ZrN (hereafter called homogeneous core) is shown in Fig, 2. The ratio of ZrN was decreased to compare with the reference core, and ThN was added instead of ZrN. The ratio of thorium was changed from 10 to 50 %. The heterogeneous core in Fig. 3 was consisted of two fuel assemblies: MA-bearing fuel ((Pu + MA)N + ZrN) assembly and thorium-only (ThN) assembly. The heterogeneous core introduced thorium-only assemblies in addition to the MA-bearing fuel assembly, and therefore, the core size was enlarged to conserve the number of fuel pins. The number of thorium-only assembly was changed from 12 to 48 in the process of the optimizations. The heterogeneous fuel assembly-loaded core is composed of the single fuel assembly, and the assembly is composed of MA-bearing fuel ((Pu + MA)N + ZrN) pins and thorium (ThN) pins. The number of pins in the assembly was 391, and the number of thorium pin was changed from 48 to 144. The chemical form of thorium in all core designs was assumed the nitride as listed in the design requirements since the homogeneous core should adopt the nitride to consider the manufacture process of the original fuel.

The analysis of the designed core was performed with the use of the PHITS [6], MVP [7] and MVP-BURN [8]. The external neutron source was calculated by using PHITS which carried out the transport calculations until the spallation neutrons generated by 1.5 GeV protons were below 20 MeV. The MVP calculations were performed on the basis of the external neutron source data obtained by PHITS. The nuclear data library employed in MVP was the JENDL-4.0 [9], and the burnup calculation was based on the chain data including actinides and 50 fission products. The calculation was performed with the time interval of 200 days in the burnup calculations, and the total history at each time step was set to 1,000,000 in the fixed-source calculation of MVP.

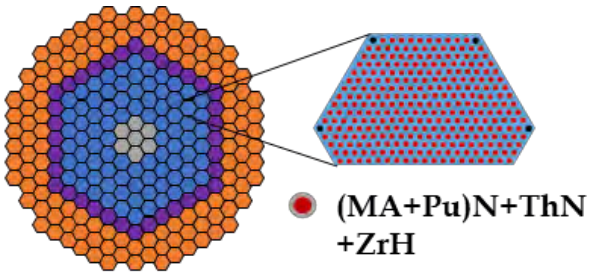

Fig. 2. Homogeneous core (type1)

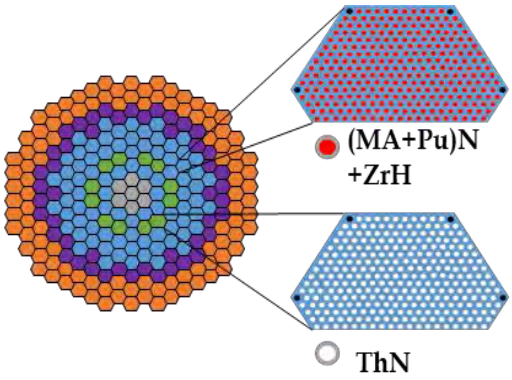

Fig. 3. Heterogeneous core (type2)

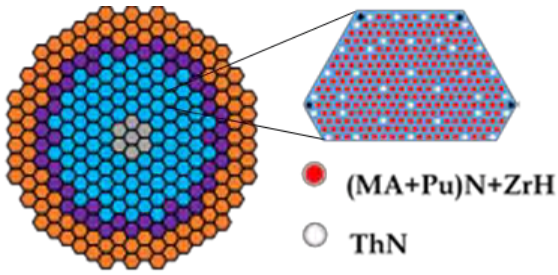

Fig. 4. Heterogeneous fuel assembly-loaded core (type3)

3. Analysis result

Figure 5 shows the time variation of the k_{eff} with the optimal core designs in each pattern of thorium-loaded core. In the homogeneous core, the burnup reactivity tended to decrease as the ratio of thorium in the fuel increased. When the ratio was 10%, the burnup reactivity was 2.49 %Δk/k, and the k_{eff} showed almost flat curve thorough the cycle when the ratio of thorium was 25 %. The k_{eff} exceeded 0.97 of the design requirement over 30 % of the ratio of thorium. As for the heterogeneous core, the effect of the burnup reactivity control depended on the location of thorium assembly, and the core with the thorium assembly at the second innermost fuel region from the target made most effective reactivity control. The optimal case of 18 assemblies at second innermost fuel region showed the minimum burnup reactivity loss of 0.70 %Δk/k in the heterogeneous core. In the heterogeneous fuel assembly-loaded core, the minimum burnup reactivity of 0.15 %Δk/k was obtained when 85 of the 391 fuel pins in the fuel assembly are replaced with thorium pin, and that showed the most effective burnup reactivity control among the three cores.

From the aspect of core performances, the amount of transmutation and the radial peaking factor deteriorated in any of the cores compared to that in the reference core design as described in Table II. The peaking factor was large enough even in the reference core but it was worsened in the all thorium-loaded core design. The mitigation of the peaking factor was also the issue in the thorium-loaded core design.

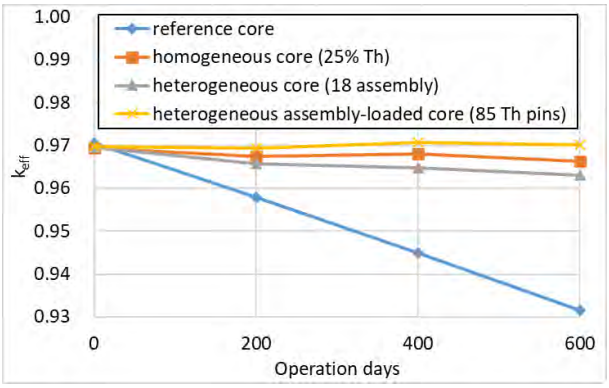

Fig. 5. Time variation of k_{eff} with three types of thorium-loaded ADS core

Table II. The summary of burnup reactivity and core characteristics in each pattern of thorium-loaded core

	Burnup reactivity loss [%Δk/k]	Transmutation amount [kg]	Radial peaking factor*
Homogeneous core	0.31	447.6	2.17
Heterogeneous core	0.70	438.2	2.31
Heterogeneous fuel assembly-loaded core	0.15	454.3	2.33
Reference core	4.32	484.7	1.89

* The ratio of the maximum radial neutron flux to the average radial neutron flux

4. Summary

The reactivity control method using thorium for ADS is studied. Three types of thorium-loaded core are discussed from the aspect of the core homogeneity to study the effective reactivity control. The heterogeneous fuel assembly-loaded core which the assembly has 85 thorium pins out of the 391 pins shows the most effective reactivity control among the three core models, and 97% decrease of the burnup reactivity compared to the original ADS is achieved.

References

1. Aizawa N, et al., "Study of Reactivity Control Method by the Application of Gadolinium Hydride to Accelerator-Driven System," *J. Nucl. Sci. Technol.*, **53**, *2*, 240, (2016)
2. Yamaguchi H, et al., "Study of Reactivity Contro l Method by Metallic Deuteride Burnable Poison for Accelerator Driven System," *Proc. RPHA15*, Jeju, Korea, Sep. 16-18, 2015, Korean Nuclear Society (2015) (on website)
3. Aizawa N, et al., "Study of Reactivity Control Method for Acceleratory-Driven System by the Use of Burnable Poison Oxide," *Proc. TCADS-3*, Mito, Japan, Sep. 6-9, 2016, OECD/NEA (2017)
4. Tsujimoto K, et al., "Accelerator-driven system for transmutation of highlevel waste," *Progress in Nuclear Energy*, **37**, 339, (2000)
5. Tsujimoto T, et al., "Neutronics design for lead-bismuth cooled accelerator-driven system for transmutation of minor actinide," *J. Nucl. Sci. Technol.*, **41**, *1*, 21, (2004)
6. Sato T, et al., "Particle and Heavy Ion Transport Code System PHITS, Version 2.52", *J. Nucl. Sci. Technol.* **50**, *9*, 913 (2013)
7. Nagaya Y, et al., "MVP/GMVP II: general purpose Monte Carlo codes for neutron and photon transport calculations based on continuous energy and multigroup methods," JAERI 1348, Tokai-mura(Japan): Japan Atomic Energy Research Institute (2005).
8. Okumura K, "Validation of a continuous-energy Monte Carlo burn-up code MVP-BURN and its application to analysis of post irradiation experiment," *J. Nucl. Sci. Technol.*, **37**, *2*, 128, (2000)
9. Shibata K, et. al., "JENDL-4.0: a new library for nuclear science and engineering," Journal of Nuclear Science and Technology, **48**, *1*, 1, (2011)

SS-04 Fukushima Challenge

Proceedings of the Reactor Physics Asia 2019 (RPHA19) Conference
Osaka, Japan, Dec. 2-3, 2019

Peak Power Characteristics of Postulated Criticality in Fuel Debris

Yuichi Yamane*
Japan Atomic Energy Agency, 2-4 Shirakata, Tokai-mura, Naka-gun, Ibaraki 319-1195, Japan
*Corresponding author: yamane.yuichi@jaea.go.jp

Abstract

For safe operation at the retrieval of fuel debris in Fukushima Daiichi Nuclear Power Plant, inadvertent criticality should be considered and the prediction of its peak power is important for the evaluation of the shielding between the fission source and operators, while measured data or analytical values in past criticality accidents are quite rare. Characteristics of the peak power under a postulated criticality accident condition have been investigated. One-point kinetics basis analysis of a postulated criticality in the fuel debris in comparison with that of JCO criticality accident showed its dependency on the parameters such as excess reactivity, delayed neutron fraction, neutron generation time, etc. In conclusion, the difference of the peak power values is mainly from heat capacity, and the key factor is the size of fuel debris at criticality.

Key Words: **Criticality accident, Fuel debris, Fukushima Daiichi NPP, Peak power, One-point kinetics**

1. Introduction

For safe operation at the retrieval of fuel debris in Fukushima Daiichi Nuclear Power Plant (NPP), inadvertent criticality should be considered. The retrieval work should be planned to be conducted in a subcritical state, while the countermeasure and evacuation procedure against inadvertent criticality should be ready, because the property of the fuel debris such as the composition, inner structure and outmost geometry is not clear.

For the operator's safety, the prediction of its peak power is important for the evaluation of the shielding between the fission source and operators. Exposure to direct radiation of the neutron and gamma-ray from the fissions is the dominant factor of the operator's dose. The shielding between them and the fuel debris reduces their dose. The effect of shielding should be evaluated before starting the work.

Data of the peak power in past criticality accidents are very little. Many critical accidents and estimated number of the fissions are reported [1], but the peak power is not. A paper reports an estimated power profile at the JCO criticality accident [2]. The importance of such data has been not recognized enough and the characteristics of the peak powers have been not often discussed.

In this study, the characteristics of the peak power under a postulated criticality accident condition have been investigated, in order to find the important factors which should be considered in the prediction and estimation of peak power for better evaluation of shielding. Semi-quantitative analysis was done because it is known that the non-stochastic effect of direct radiation depends on the order of dose [3,4].

Equations derived from one-point kinetics equation were used with the analysis parameters of fuel debris in Fukushima Daiichi NPP and JCO criticality accident. It is reported that numerical calculation by using one-point kinetics code AGNES [5] reproduced power profiles which showed good agreements with TRACY experimental data [6]. That indicates one-point kinetics describes the power profile very well. Therefore, a meaningful result is expected from the analysis based on the one-point kinetics.

2. Parameters of Fuel Debris and JCO Accident

For the purpose of highlighting the difference between solid and solution systems, the calculation conditions of the fuel debris [7] and JCO accident [8] were compared. From many calculations done for those, a typical case for each was chosen for comparison. A case of fresh UO_2 fuel was chosen for fuel debris for simplicity.

In the study, it was assumed that 3.0$ of excess reactivity was instantaneously inserted. When a portion of debris is being removed, the operation must be slowly done to keep the reactivity insertion rate very small, and the fission power reaches the 1st peak by temperature feedback reactivity soon after the excess reactivity exceeds 1$. For the excess reactivity close to 1$, there is no simple expression of the peak power and more than 3$ would give rise to boiling of the fuel solution in the JCO condition. For simplicity of the study, 3.0$ was chosen as the representative of other lower excess reactivity cases.

Some parameters were in the same order to each other as shown in Table I, in other words, those values were

similar to each other from the point of semi-quantitative view. The nominal value of the temperature feedback reactivity of fuel debris linearly increased as the increase in temperature and was smaller than that of the solution system as shown in Fig. 1.

The differences were seen in the 2nd order coefficient of temperature feedback reactivity and reciprocal heat capacity. The 2nd order coefficient of temperature feedback reactivity was much smaller than the 1st and it was neglected in the following calculation for the fuel debris condition. The value of the reciprocal heat capacity of fuel debris was an order of magnitude smaller than that of the solution system and the ratio of them was 7.6 (=3.7 $\times 10^{-5}$/4.9$\times 10^{-6}$), i.e. the ratio of heat capacities was 0.13 (=1/7.6).

Table I. A typical value of analysis parameters

parameter			fuel debris	solution system
excess reactivity (-)		$\boldsymbol{\rho_0}$	2.1$\times 10^{-2}$ (3.0$)	2.4$\times 10^{-2}$ (3.0$)
neutron generation time (s)		$\boldsymbol{\ell}$	5.4$\times 10^{-5}$	3.0$\times 10^{-5}$
effective delayed neutron fraction (-)		$\boldsymbol{\beta}$	6.9$\times 10^{-3}$	7.9$\times 10^{-3}$
reactivity temperature feedback coefficient	1st (1/K)	$\boldsymbol{\alpha_1}$ ($\boldsymbol{\alpha}$)	-1.2$\times 10^{-4}$	-2.3$\times 10^{-4}$
	2nd (1/K^2)	$\boldsymbol{\alpha_2}$	4.6$\times 10^{-8}$	-1.4$\times 10^{-6}$
reciprocal heat capacity (K/J)		$\boldsymbol{K}$	3.7$\times 10^{-5}$	4.9$\times 10^{-6}$

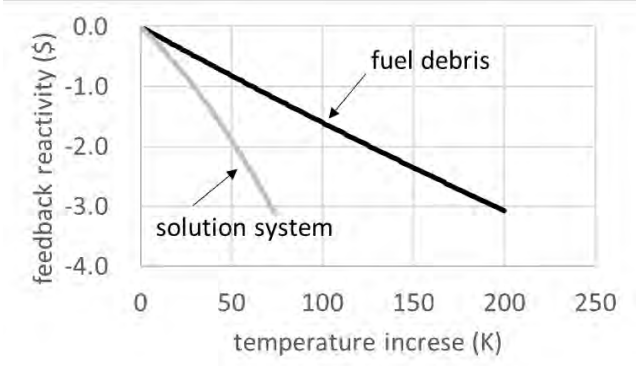

Fig. 1. Temperature feedback reactivity calculated with the values from Table I.

3. Equations Used for Analysis

For the analysis, two equations of the peak power for $\boldsymbol{\rho_0 \gg \beta}$ derived from the one-point kinetics equation were used instead of numerical calculation code for clear visibility.

One was the equation derived by Nordheim and Fuchs for linear temperature feedback system [9-11],

$$\mathbf{P}_d = \frac{(\boldsymbol{\rho_0 - \beta})^2}{\mathbf{2\alpha K \ell}}\,, \qquad (1)$$

where $\boldsymbol{P_d}$ was the peak power, $\boldsymbol{\rho_0}$, excess reactivity, $\boldsymbol{\beta}$, effective delayed neutron fraction, $\boldsymbol{\alpha}$, nominal value of reactivity temperature feedback coefficient, $\boldsymbol{K}$, reciprocal heat capacity, $\boldsymbol{\ell}$, neutron generation time.

Another denoted by $\boldsymbol{P_s}$ was derived by Yamane for non-linear temperature feedback system [12],

$$\mathbf{P}_s = \frac{\mathbf{2}}{\mathbf{3}\sqrt{\boldsymbol{\alpha_2}}\mathbf{K\ell}}(\boldsymbol{\rho_0 - \beta + \alpha_2 A^2})^{\frac{3}{2}} \times \left[\mathbf{1} - \frac{\mathbf{3}}{\mathbf{2}}\left(\frac{\boldsymbol{\alpha_2 A^2}}{\boldsymbol{\rho_0 - \beta + \alpha_2 A^2}}\right)^{\frac{1}{2}} + \frac{\mathbf{1}}{\mathbf{2}}\left(\frac{\boldsymbol{\alpha_2 A^2}}{\boldsymbol{\rho_0 - \beta + \alpha_2 A^2}}\right)^{\frac{3}{2}}\right], \qquad (2)$$

where

$$\mathbf{A} = \frac{\boldsymbol{\alpha_1}}{\mathbf{2}\boldsymbol{\alpha_2}}\,, \qquad (3)$$

and $\boldsymbol{\alpha_1}$ and $\boldsymbol{\alpha_2}$ were the nominal values of the 1st and 2nd order coefficients of reactivity temperature feedback.

Equation (1) was applied to the fuel debris because the 2nd order coefficient was much smaller than the 1st and was ignored. Equation (2) was applied to the solution system because its 2nd coefficient was not too small to be ignored compared to the 1st. In the calculation by using Eq.(1), the value of $\boldsymbol{\alpha}$ was set as 1.2$\times 10^{-4}$.

4. Comparison and Result

Eqs. (1) and (2), show that peak power is proportional to the inverse of neutron generation time and the inverse of reciprocal heat capacity, i.e. heat capacity.

The calculated peak power by using those two equations and values shown in Table I is shown in Table II, in which the peak power of fuel debris is an order of magnitude smaller than that of the solution system. The ratio of them is 0.14 (=4.2$\times 10^8$/3.0$\times 10^9$) and that is very close to the ratio of their heat capacities, 0.13.

Table II. Calculated peak power

case	fuel debris	solution system
peak power (W)	4.2$\times 10^8$	3.0$\times 10^9$

That implies the difference in heat capacity is the main cause of the difference in peak power.

Specific heat $\boldsymbol{C_{p(sol)}}$ $\boldsymbol{(J/(gK))}$ of uranyl nitrate solution is expressed as a function of uranium concentration [13] as,

$$\boldsymbol{C_{p(sol)} = 4.186(0.998 - 9.630 \times 10^{-4} \times C_u - 4.850 \times 10^{-2} \times C_N)} \qquad (4)$$

where $\boldsymbol{C_u}$ is uranium concentration (g/Lit) and $\boldsymbol{C_N}$ is acidity (*mol*/Lit) and $\boldsymbol{C_{p(sol)}}$ is in the order of $\boldsymbol{O(10^0)}$ for $\boldsymbol{C_u = 370}$ (g/Lit) and $\boldsymbol{C_N = 0.5}$ (mol/Lit). Specific heat of uranium di-oxide and SUS are in the order of $\boldsymbol{O(10^{-1})}$ and smaller than that of aqueous solutions as shown in table III.

Table III. Specific heat of UO_2 and SUS

Material	UO_2 [14]	SUS304 [15]
Specific heat (J/(gK))	0.24 (300K) 0.29 (600K)	0.50 (293K)

And a homogeneous mixture of such solids has the same order of magnitude of their specific heat. Therefore, if the size of the debris at criticality and that of a solution system are close to each other, the difference in their specific heat must be the main cause of the difference in their heat capacity.

For a single homogeneously mixed fuel debris with similar parameter values to that of UO_2 fuel, the order of $\boldsymbol{\beta}$ and $\boldsymbol{\ell}$ are expected to be $\boldsymbol{O(10^{-3})}$ and $\boldsymbol{O(10^{-5})}$, respectively, and that of $\boldsymbol{\alpha}$ is $\boldsymbol{O(10^{-4})}$[7].

From the consideration above, it is reasonable for the first rough estimation that the peak power in a postulated criticality of the fuel debris is in one order of magnitude lower than that of the solution system like the JCO criticality accident and that an extremely larger peak power than that we have ever experienced from the criticality accidents like the JCO will not appear in an advertent criticality if the operation is cautiously conducted so that the reactivity insertion rate is very low.

The effect of surrounding fuel debris is the next issue to be taken into account, while it may not significantly change the order of magnitude of the peak power because the total reactivity of each is negative.

The concerned heat capacity, however, depends on the mass or volume under criticality condition and the degree of mixture of the materials. Therefore, the range of the size is important and a sample of the fuel debris would provide the information useful to estimate its size under criticality condition.

5. Conclusion

For the first rough estimation, the peak power in a postulated criticality of the fuel debris is in one order of magnitude lower than that of the solution system like the JCO criticality accident. The difference of the peak power value of the fuel debris from the solution system is mainly from its low heat capacity and the key factor for the safety of the operators is the size of the fuel debris under criticality condition.

References

1. McLaughlin TP, Monahan SP, Pruvost NL, Frolov VV, Ryazanov BG, Sviridov VI, “A Review of Criticality Accidents,” LA-13638, Los Alamos National Laboratory (2008).
2. K. Tonoike, T. Nakamura, Y. Yamane, Y. Miyoshi, “Power profile evaluation of the JCO precipitation vessel based on the record of the γ-ray monitor,” *Nucl Technol*, **143**, 364 (2003).
3. Rechet P, Andrews GA, Auxier JA, Dousset M, Duncan KP, Stevens DJ, Strambi E, Wald N, “The principles and general procedures for handling emergency and accidental exposures of workers,” ICRP Publication 28, ICRP (1978).
4. Upton AC, Brown JM, Casarett GW, Field SB, Lincoln TA,Withers HR, “Nonstochastic effects of ionizing radiation,” ICRP Publication 41, ICRP (1984).
5. Nakajima K, Yamane Y, Miyoshi Y, “A kinetics code for criticality accident analysis of fissile solution systems: AGNES2,” JAERI-Data/Code 2002-004, Japan Atomic Research Institute (2002).
6. Miyoshi Y, Yamane Y, Okubo K, Reverdy L, Grivot P, Konishi H, Mitake S, Liem PH, “Inter-code comparison exercise for criticality excursion analysis: benchmarks phase I: pulse mode experiments with uranyl nitrate solution using the TRACY and SILENE experimental facilities,” Report No.06285, OECD NEA, (2009).
7. Yamane Y, Numata Y, Tonoike K, “Exploratory Investigation for Estimation of Fuel Debris Criticality Risk,” *Proc. ICNC2019*, Paris, France, September 15-20, 2019, OECD/NEA (2019) (CD-ROM).
8. Yamane Y, Nakajima K, Yamamoto T, Nakamura T, Miyoshi Y, “Analysis of TRACY Experiment and JCO Criticality Accident by Using AGNES Code,” JAERI-Conf 2000-012, Japan Atomic Research Institute, (2000) [in Japanese].
9. Fuchs K, “Efficiency for very slow assembly,” LA-596, Los Alamos National Laboratory (1946).
10. Nordheim LW, “Pile kinetics,” MDDC-35, Oak Ridge National Laboratory (1946).
11. Hetrick DL. *Dynamics of nuclear reactors*, p.164, American Nuclear Society, La Grange Park, Illinois (1993).
12. Yamane Y, “Improvement in estimation of maximum first peak power based on non-linear temperature feedback reactivity in criticality accident with instantaneous reactivity insertion," *J. Nucl. Sci. Technol.* **52**, *11*, 1425 (2015).
13. Sugikawa S, Umeda M, Izawa N, Yamagami S, Ota K, Hosoya N, “Performance analysis of uranium evaporator by evaporator simulation code (I),” *Proc. the Atomic Energy Society of Japan Spring Meeting 1997*, Tokyo, Japan, Mar 24-26, 1997, *Atomic Energy Society of Japan* (1997) [in Japanese].
14. Yamane Y, Sakai M, Abe H, Yamamoto T, Okuno H, Miyoshi Y, “Material Data for Criticality Transient Phenomena Analysis of MOX Powder System -Data of MOX and Zinc Stearate Powders-,” JAEA-Data/Code 2006-021, Japan Atomic Energy Agency, (2006) [in Japanese],
15. Peckner D, Bernstein IM, “Handbook of Stainless Steel,” McGraw-Hill Book Company, New York, USA (1977).

Proceedings of the Reactor Physics Asia 2019 (RPHA19) Conference
Osaka, Japan, Dec. 2-3, 2019

Development of Integral Kinetic Model with Delayed Neutrons Effect for Criticality Accident Analysis of Fukushisma Daiichi NPP Fuel Debris

Hiroki Takezawa[a*], Delgersaikhan Tuya[b] and Toru Obara[c],
[a]*Tokyo City University, 1-28-1 Tamazutsumi, Setagaya-ku, Tokyo, Japan*
[b]*Japan Atomic Energy Agency, 2-4 Shirakata, Tokai-mura, Ibaraki, Japan*
[c]*Tokyo Institute of Technology, 2-12-1-N1-19 Ookayama, Meguro-ku, Tokyo, Japan*
[*]Corresponding author: takezawa@tcu.ac.jp

Abstract

Multi-region integral kinetic code MIK with a capability of handling delayed neutrons effect has been under development for criticality accident analysis of Fukushisma Daiichi NPP defueling activities. Cumulative secondary-fission distribution function of delayed neutrons that is essential for MIK code was calculated for Godiva core without delay of emission by modifying continuous energy neutron transport Monte Carlo calculation code MVP3.0. Calculation result was consistent with experimental delayed neutron fractions.

Key Words: **Space-dependent kinetic analysis, Integral Kinetic Model, Criticality accident, Fuel debris.**

1. Introduction

Fuel debris of Fukushima Daiichi NPP will remain uncertain in composition and spatial distribution. Hence, it is necessary to establish counter measures for anticipated re-criticality accident in addition to avoiding re-criticality associated with defueling activities. One-point kinetic model (PKM) is generally used for criticality accident analysis. However, the model is not applicable to some fuel debris systems that consists of fragmented fuel debris with water surrounded by re-solidified fuel debris bed, i.e. the combination of thermal and fast spectrum regions as shown in Fig. 1 as an example.

On the other hand, integral kinetic model (IKM) [1] and transient fission matrix approach (TFM) [2] are space-dependent kinetic models and are applicable to so called coupled reactors including such a fuel debris system. IKM and TFM are the same in mathematical foundation. Multi-region integral kinetic code MIK [3] that has been developed on IKM has more general feedback treatment than TFM. However, MIK code has been developed only for super prompt-criticality transient analysis. MIK code with a capability of handling delayed neutrons effect has been under development. This paper shares a part of the development progress.

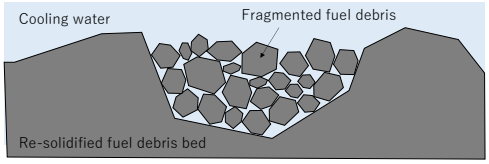

Fig. 1. An example of fuel debris system.

2. Method

IKM calculates fission rate in region i at the present time t $N_i(t)$ [fissions/sec] by taking all past fission contributions in region j into account using Eq. (1):

$$N_i(t) = \sum_j \left\{ \int_{-\infty}^{t} \left(\alpha_{ij}^{p}(\tau) + \alpha_{ij}^{d}(\tau) \right) N_j(t')dt' \right\} \quad (1),$$

where
$\alpha_{ij}^{p/d}(\tau)$: probability density function of secondary-fissions in region i triggered by prompt neutrons or delayed neutrons originates from a source fission in region j with time difference $\tau \equiv t - t'$ [secondary-fissions@i/source fission@j/sec].

Eq. (1) is numerically solved simply by forward calculation method using the cumulative secondary-fission distribution function $C_{ij}(\tau)$ [cumulative secondary-fissions@i/source fission@j] defined as follows:

$$C_{ij}(\tau) = \int_0^{\tau} \alpha_{ij}(\tau')d\tau' \quad (2).$$

Continuous energy neutron transport Monte Carlo calculation code MVP3.0[4] was modified to calculate $C_{ij}(\tau)$ of delayed neutrons without delay of emission. Delay of emission is included in the forward calculation module in MIK code. In this paper, $C_{ij}(\tau)$ of delayed neutrons without delay of emission was calculated for Godiva core [5]. The calculation was performed by an eigenvalue calculation of MVP3.0 with nuclear data library JENDL-4.0 [6]. Calculation conditions are

summarized in Table I and II.

Table I. MVP3.0 calculation conditions

Number of history per batch	500,000
Total batches (skip)	100 (50)

Table II. Godiva core specification

Core division	2 (Inner/Outer)
Radius	Inner (ID=1) 5.0 cm Outer (ID=2) 8.85 cm
Mass density	18.71 g/cm^3
Composition	U234 1.0 wt% U235 93.7 wt% U238 5.3 wt%
Temperature	293 K

3. Result

Cumulative secondary-fission distribution functions $C_{ij}(\tau)$ of prompt (dashed lines) and delayed neutrons (solid lines) for Godiva core are shown in Fig. 2. Difference in neutron spectrum between prompt and delayed neutrons has been considered, but delay of emission for delayed neutrons has not included in the calculation. Horizontal axis shows time between an emission of a source prompt/delayed neutron and a secondary-fission. It is shown that both prompt and delayed neutrons fission in 1.0×10^{-8} sec to 1.0×10^{-7} sec after their emission, that is consistent to prompt neutron lifetime. $C_{ij}(\tau)$ of prompt neutrons are relatively larger than $C_{ij}(\tau)$ of delayed neutrons. This difference was checked by confirming delayed neutron fractions between experimental [5] and calculated values were consistent each other.

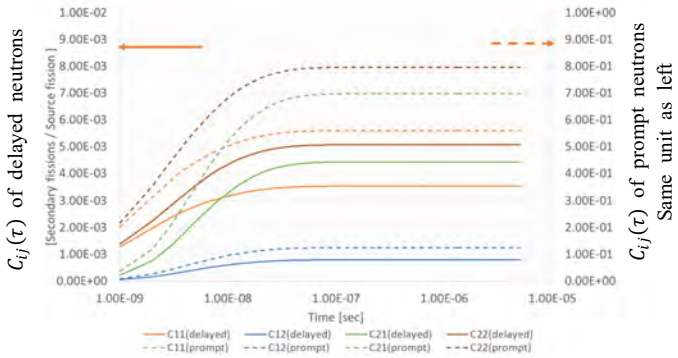

Fig. 2. An example of cumulative secondary-fission distribution functions for Godiva core.

4. Conclusions

MIK code with a capability of handling delayed neutrons effect has been under development. Cumulative secondary-fission distribution function $C_{ij}(\tau)$ of delayed neutrons was calculated without considering delay of emission by modifying continuous energy neutron transport Monte Carlo calculation code MVP3.0. $C_{ij}(\tau)$ distribution functions of prompt and delayed neutrons will be verified in comparison of MIK code calculation results with Godiva super-prompt transient experimental data considering delayed neutrons effects. Subsequent development progress will be shared in the presentation.

References

1. Gulevich A, "Methods for Calculating Coupled Reactor Systems," *At. Enegy*, **97**, 803 (2004).
2. Laureau A, "Transient Fission Matrix: Kinetic Calculation and Kinetic Parameters β_{eff} and Λ_{eff}," *Ann. Nucl. Energy*, **85**, 1035 (2015).
3. Tuya D, "Development of Monte Carlo Neutron Transport Method-Based Supercritical Transient Code with Time-Dependent Feedback Capability," *Nucl. Sci. Eng.*, **193**, 481 (2019).
4. Nagaya Y, "MVP/GMVP Version 3: General Purpose Monte Carlo Codes for Neutron and Photon Transport Calculations Based on Continuous Energy and Multigroup Methods," JAEA-Data/Code 2016-018, Japan Atomic Energy Agency (2016).
5. Peterson R. E., "Lady Godiva: An Unreflected Uranium-235 Critical Assembly," LA-1614, Los Alamos Scientific Laboratory (1953).
6. Shibata K, "JENDL-4.0: A New Library for Nuclear Science and Engineering," *J. Nucl. Sci. Technol.*, **48**, 1 (2011).

Proceedings of the Reactor Physics Asia 2019 (RPHA19) Conference
Osaka, Japan, Dec. 2-3, 2019

Radiation Dose by Criticality Accidents of Fuel Debris in Water

Kodai Fukuda, Jun Nishiyama and Toru Obara*
Laboratory for Advanced Nuclear Energy, Institute of Innovative Research, Tokyo Institute of Technology,
2-12-1-N1-19 Ookayama, Meguro-ku, Tokyo 152-8550, Japan
*Corresponding author: tobara@lane.iir.titech.ac.jp

Abstract

Removal of the fuel debris at Fukushima Dai-ichi Nuclear Power Station (1F-NPS) must be started after the evaluation of the consequences of possible criticality accidents. Especially, a prediction of radiation dose by such accidents can be crucial for the safety of machines, workers and public. In this research work, a radiation dose by possible super prompt criticality accidents was predicted in a simple fuel debris system. Particularly, we focused on the relationship between the water level surrounding the fuel debris and the radiation dose during the supercritical condition. This is according to that the water level may influence on both the reactivity and the shielding of radiation. For that, space-dependent kinetic analysis and radiation transport analysis were connected. For the space-dependent kinetic analysis, the MIK code, which is a unique methodology based on Monte Carlo neutron transport calculation, was used in order to consider special characteristics of fuel debris systems. Radiation transport analysis was performed using PHITS code. The obtained results indicated that the radiation dose during the supercritical condition can be largest when a part of fuel debris is exposed to the air, even though the total energy release is smaller compared with systems which have higher water level. These results will be useful when the water level will be determined during the removal of fuel debris.

Key Words: **Criticality safety, Space-dependent kinetic analysis, Fuel debris, Decommissioning of Fukushima Dai-ichi Nuclear Power Station**

1. Introduction

The Great East Japan Earthquake brought about a severe accident at Fukushima Dai-ichi Nuclear Power Station (1F-NPS) in 2011. As a result, a part of the reactor core melted down and fuel debris was thought to be formed [1]. To reduce long-term risk, a removal of the fuel debris is one of the most crucial operation in the decommissioning of 1F-NPS.

During the removal of fuel debris, water will be used because it has ability to shield operators and machines from radiation emitted from fission products and prevent the diffusion of radioactive dust. In that case, criticality accidents may happen because water can be a moderator for neutrons. Therefore, it is necessary to prepare measures to prevent such accidents in advance. However, it is possible to happen the criticality accidents unintentionally even if the measures are adequate. If the transient of accidents is slow, measures can be taken even after the detection of the criticality. However, in the case of prompt super criticality accidents, there is no time to take actions when the criticality is detected. Therefore, before the removal of fuel debris, the effect of such accidents should be evaluated in advance to think of effective measures to protect workers. Specifically, evaluation of radiation doses resulting from criticality accidents of fuel debris is important in this context.

In the case of criticality accidents, the water level surrounding the fuel debris is thought to give an impact on the radiation dose around the position of the criticality. This is due to that the water level affects both the reactivity and the shielding of radiation. If the fuel debris is partially in water, a higher water level will give higher reactivity. However, if the fuel debris is completely submerged in water, the radiation shielding effect will be significant. This may be an important phenomenon for predicting the radiation dose in the case of such accidents. However, no study about this relationship has not been conducted.

Therefore, the aim of this work was to make it clear that the relationship between the water level and radiation dose when fuel debris becomes prompt supercritical in water. A simple assumptive fuel debris system was considered for that. In the system, supercritical kinetic analysis was performed for different water level using the MIK code [2], which is a space-dependent kinetic code based on Monte Carlo neutron transport calculations. The detailed information of the MIK code is described in the

later section. The region-dependent number of fissions which were obtained by the MIK code was used for dose evaluation.

2. Methodology

It is necessary to perform kinetic analyses and estimate the number of fissions in the case of supercritical conditions in order to predict possible radiation doses. The characteristics of fuel debris can be different in different locations. In specific, compositions, shapes, quantities, and submerged conditions can be different in different positions. These difference may bring about a non-negligible space-dependent difference in terms of neutronics. In such system, methods based on diffusion theory, for example, traditional point-reactor kinetic model (PKM) [3] may be out of the applicable range. Hence, space-dependent kinetic analysis methods based on neutron transport theory should be used for such fuel debris systems instead.

In this work, the Multi-region Integral Kinetic Code (MIK) was applied. The MIK code makes it possible to perform space-dependent kinetic analyses based on neutron transport theory with reasonable calculation time.

The basis of the MIK code is the Integral Kinetic Model (IKM) [4]. Fundamentally, the IKM describes the fission rate at time *t* in region *i* for a system consisting of *n* fissile regions as:

$$N_i(t) = \sum_{j=1}^{n} \left(\int_{-\infty}^{t} \alpha_{ij}^{p}(t-t')N_j(t')dt' + \int_{-\infty}^{t} \alpha_{ij}^{d}(t-t')N_j(t')dt' \right), \quad (1)$$

where $N_i(t)$ is the total fission rate at time *t* in region *i* (fissions in *i*/sec), and α_{ij} is the secondary fission rate in region *i* provided by the first fission in region *j* with a time difference τ (fissions in *i*/sec /fission in *j*). Superscripts *p* and *d* show that prompt neutrons and delayed neutrons cause secondary fissions, respectively. The MIK code calculates $N_i(t)$ discretely using output data of the neutron transport calculation with the continuous-energy Monte Carlo Code MVP 2.0[5].

Detailed information about the MIK code is given elsewhere [2].

In addition, dose evaluation was performed by the PHITS code [6] (ver. 2.86) which is a radiation transport calculation code based on the Monte Carlo method.

As an input data, the number of fissions obtained by space-dependent kinetic analysis using the MIK code was used.

3. Analysis conditions

3.1 Simple spherical fuel debris system

The analysis was performed in the spherical fuel debris system shown in Fig. 1. This system was considered because spherical system is the simplest of all systems in terms of geometry. In reality, it is difficult for the fuel debris to make a spherical shape when the decommissioning is conducted. However, the spherical shape was chosen for the first step because of its simplicity.

The characteristics of the system are shown in Table 1. In the system, particles of fuel debris that assemble into a sphere are submerged in water. The composition of the fuel debris is unknown, therefore, the fuel debris was assumed to be UO_2 for simplicity. The UO_2 was set to have ordinary density and enrichment. The unit was composed of 0.1-cm-radius spherical particles. The volume-packing fraction in the unit was 0.6, representing random packing fraction. The radius of the unit was set to be that the effective multiplication factor was 1 when the half of the unit was submerged. The thickness of the water was 30 cm, representing an infinite reflector size. The bottom of the unit was considered the zero water level in the analysis. Different systems were simulated at different water levels ranging from 50 cm to 150 cm.

The systems were assumed to be at a critical state of low power, 1W. Step-wise positive reactivity was inserted by increasing the water level. The situations were simulated when the water level became a specific value in an instant. It indicates that different water levels resulted in different reactivities.

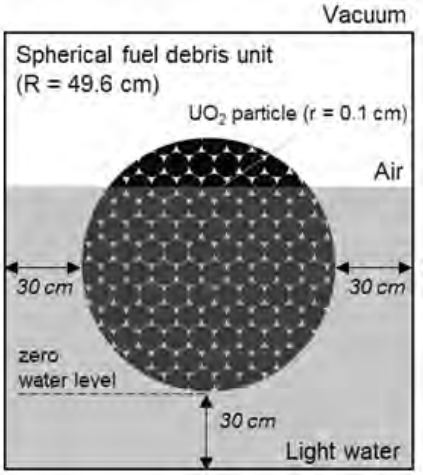

Fig. 1. Cross-sectional view of system (not to scale).

Table 1. Characteristics of the system

Particle composition	UO_2
Density of UO_2, g/cm^3	10.97
Enrichment of ^{235}U. wt%	2.95
Particle radius, cm	0.1
Volume packing fraction	0.6
Unit radius, cm	49.6
Water level, cm	50-150

3.2 Other analysis conditions

For neutron transport calculations, sixty batches (20 skipped batches + 40 active batches) with 500,000 histories/batch were used with the JENDL-4.0 nuclear data library [7]. Delayed neutrons were ignored in the calculations because the target of this work was prompt supercritical conditions. The fuel debris unit was divided

into 2 fissile regions when part of the unit was exposed to the air. It was treated as 1 fissile region when the entire unit was submerged. In the analysis, the Doppler feedback effect was considered.

The radiolysis gas and the heat transfer from the fuel debris to water were ignored. In fact, the instant evaporation of water and the production of radiolysis gas are both expected as results of the supercritical condition. However, both phenomena have a negative feedback effect. This means that the release of the power is lower when the phenomena are considered. Therefore, the approximation disregarding these factors can be regarded a conservative analysis condition.

For radiation transport calculation, one million histories were used with the JENDL-4.0 as well. The source locations are equivalent to fission regions which were considered in the space-dependent kinetic analysis. Neutrons and photons were used as source particles. A prompt neutron specrum [8] and prompt gamma ray specrum [9], which were from fissions induced by thermal neutrons, were used. They were tallied at the point 3 m above the center of the unit. The energy range of neutrons was between 10^{-3} and 10^{3} MeV in the analysis. Simiraly, that of gamma rays was between 10^{-10} and 20 MeV in the analysis. The effective dose conversion factor under the antero-posterior irradiation condition [10] was set to convert fluence to dose.

4. Results and discussion

The relationship between the water level and the prompt multiplication factor is shown in Fig.2. It should be noted that the dotted line shown in the figure indicates the water level of 99.2 cm, which is the same as the diameter of the unit. According to Fig.2, the prompt multiplication factor increased as the water level increased. This was due to the increase of fissile regions which was submerged and reacted with thermal neutrons.

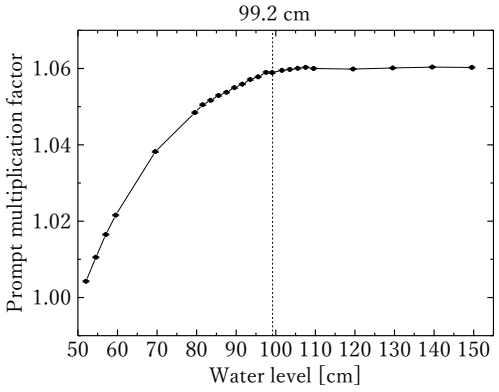

Fig. 2. Prompt multiplication factor and water level.

Fig. 3 shows the time-dependent fission rate calculated by the MIK code in which the water level was 52.1 cm as an example. As shown in Fig. 3, a pulsatile fission rate was obtained. It is observed that an increase of power caused by the insertion of positive reactivity and a decrease of power due to the Doppler feedback effect brought on by a rise of temperature of the fuel. It should be noted that the heat transfer between the fuel debris and water was not included. Thus, the temperature of the fuel debris was kept high even after the power declined and the system became subcritical. Therefore, only the first spike was obtained and later spikes could not be obtained. However, the aim of this study can be satisfied by observing the first spike. This is due to that the released energy during the first spike is dominant for the total released energy during the prompt supercritical condition according to criticality experiments [11]. Therefore, this limitation may be acceptable in this work.

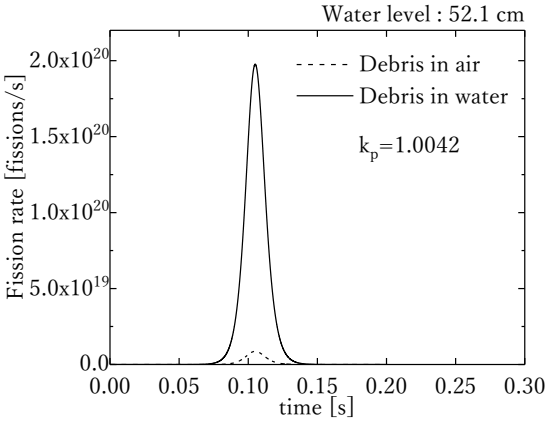

Fig. 3. Change of fission rate (water level = 52.1 cm).

By the time-integration of the pulse such as shown in Fig. 3, the number of total fissions in each region were calculated. Those values were used in dose evaluation as input values. Fig.4 shows the relationship between the radiation dose during supercritical condition and the water level. The result shows that the maximum dose was found at approximately 95 cm of water level. Therefore, in this system, the maximum dose during supercritical condition was expected in a system in which part of the fuel debris was exposed to the air.

Those results indicate that the reactivity is higher when water level is higher. However, the dose is higher in a system when water level is lower. Therefore, when the removal of fuel debris is performed at a lower water level, more attentions should be paid in the case of criticality accidents, although the total energy release may be smaller. On the other hand, a lower radiation dose can be anticipated when the water level is higher, even though the energy release and a probability of criticality may be larger.

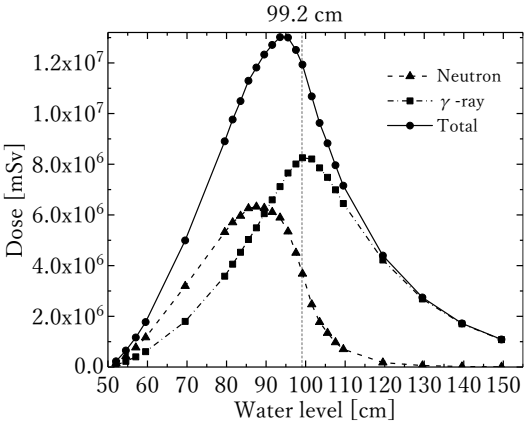

Fig. 4. Radiation dose during supercritical condition.

5. Conclusions

In order to make it clear that the relationship between the water level and radiation dose when fuel debris becomes prompt supercritical in water, connected analysis was performed and discussed. For space-dependent kinetic analysis, the MIK code, which is unique methodology based on Monte Carlo neutron transport calculation, was used. The PHITS code was utilized for radiation transport calculation with the results of space-dependent kinetic analysis as an input data.

The results mainly showed that the dose caused by supercritical condition is the largest when a part of the fuel debris is exposed to the air. Thus the dose in those systems can be greater than that in systems which the all of fuel debris is completely submerged in water.

Hence, the radiation dose caused by criticality accidents may be decreased if the removal of fuel debris is conducted with a higher water level at 1F-NPS. However, in that case, the possibility of an accident and the total energy release may be higher. These results and discussions will contribute to the consideration about the water level during the removal of fuel debris at 1F-NPS.

References

1. Tokyo Electric Power Company Holdings, "Evaluation of the situation of cores and containment vessels of Fukushima Daiichi Nuclear Power Station Units-1 to 3 and examination into unsolved issues in the accident progression," Progress Report No.1 (2013).
2. D. Tuya et al.," Improved Approach to Multiregion Supercritical Transient Analysis Based on the Integral Kinetic Model and Monte Carlo Method," *Nucl. Sci. Eng.*, **188**, 1, 33 (2017).
3. J. J. Dudestadt and L. J. Hamilton, *Nuclear reactor analysis*, John Wiley and Sons Inc (1976).
4. A. V. Gulevich and O. F. Kukharchuk, "Methods for calculating coupled reactor systems," *At. Energy*, **97**, 6, 803 (2004).
5. Y. Nagaya, "General purpose Monte Carlo Codes for Neutron and Photon Transport Calculations based on Continuous Energy and Multigroup Methods: MVP/GMVP II," JAERI-1348 (2005).
6. T. Sato et al., "Features of Particle and Heavy Ion Transport code System (PHITS) version 3.02," *J. Nucl. Sci. Technol*, **55**, 6, 684 (2018).
7. K. Shibata et al., "JENDL-4.0: A New Library for Nuclear Science and Engineering," *J. Nucl. Sci. Technol,* **48**, 1, 1 (2011).
8. Atomic Energy Society of Japan, "Neutron shielding design handbook," (1993).
9. T. E. Valentine, "MCNP-DSP USERS MANUAL," Oak Ridge, TN (United States) (2001).
10. N. Petoussi-Henss et al., "Conversion Coefficients for Radiological Protection Quantities for External Radiation Exposures," *Ann. ICRP*, **40**, 2, C. H. Clement, Ed., 1 (2010).
11. Y. Yamane et al., "Transient Characteristics Observed in TRACY Supercritical Experiments," *in ICNC2003: Proceedings of the seventh international conference on nuclear criticality safety, Challenges in the pursuit of global nuclear criticality safety* (2003).

Proceedings of the Reactor Physics Asia 2019 (RPHA19) Conference
Osaka, Japan, Dec. 2-3, 2019

Development of Criticality Safety Evaluation Method Based on the Actual Dynamic Behavior of the Fuel Debris in Water

Takeshi Muramoto[a], Jun Nishiyama[a], Toru Obara[a*],
[a] *Laboratory for Advanced Nuclear Energy, Institute of Innovative Research, Tokyo Institute of Technology, 2-12-1-N1-19, Ookayama, Meguro-ku, Tokyo 152-8550, Japan*
[*]Corresponding author: tobara@lane.iir.titech.ac.jp

Abstract

In the decommissioning of the Tokyo Electric Power Company's Fukushima Daiichi nuclear power station, criticality safety assessment taking into account the dynamic behavior of fuel debris in water is important for the safety of workers. The purpose of this study is to show that it is possible to evaluate criticality safety using a computational system combining moving particle semi-implicit method (MPS) and Monte Carlo neutron transport calculation code (MVP). Experiments and calculations were first performed to validate the accuracy of the MPS calculations. We then combined MPS and MVP and calculated the change in effective multiplication factor at each time during fuel debris falling in water. The results showed that it is possible to evaluate criticality safety taking into account the actual dynamic behavior of fuel debris in water using the computational system.

Key Words: **Criticality Safety, Fuel Debris, Moving Particle Semi-Implic it Method, Monte Carlo Neutron Transport Calculation**

1. Introduction

In the decommissioning of the Tokyo Electric Power Company's Fukushima Daiichi nuclear power station, the fuel debris retrieval work is going to start within a few years based on the Japanese government's mid- and long-term roadmap [1]. It is important to remove the fuel debris in order to reduce radiation risk. At present, it is estimated that the fuel debris is not critical. However, it may be possible to become critical if the fuel debris shape or cooling water volume changes with the fuel debris removal work. Thus, it is necessary to establish an analysis method that can perform criticality evaluation with higher accuracy for the protection of workers and public health in the decommissioning.

The conventional criticality assessment methods can evaluate only under conservative and static conditions without considering the behavior of the fuel debris in water. [2]. Thus, no study has yet been able to evaluate criticality with the actual dynamic behavior of fuel debris in water. The purpose of this study is to show that it is possible to evaluate criticality safety using the calculation system combining computational fluid dynamics (CFD) and Monte Carlo neutron transport calculation code.

2. Numerical simulation for fuel debris movement

2.1 CFD simulation method

The CFD calculation method is divided into the Eulerian method and Lagrangian method. The Lagrangian method uses calculation particles as opposed to the Eulerian method use calculation grids. The Lagrangian method is suitable for solving physical phenomena like free surfaces and large deformations compared with the Eulerian method such as finite difference method, finite volume method, and finite element method. The moving particle semi-implicit (MPS) method [3] is one of the Lagrangian methods. It can calculate multiphase flows like the dynamics behavior of debris in water and various complex boundary conditions. Thus, in this study we selected the MPS method using Particleworks [4] simulation software for computer-aided engineering (CAE) to calculate three-dimensional (3-D) solid-fluid multiphase flows. In addition, NVIDIA Tesla k40 which is one of the Graphics Processing Unit (GPU) was used as the calculator.

2.2 Validation of MPS simulation

2.2.1 Experiment of falling plate in water

In the behavior of fuel debris in water, the force from gravity and fluid is applied to the fuel debris. In order to confirm if these forces can be properly calculated by the MPS method, validation experiments of falling plates in water were performed. Because the plate shape is easily affected by the resistance from water, it is suitable for verification experiments. The plate materials were stainless steel (SS) (8.25 g/cm^3) and aluminum (2.78 g/cm^3), high- and low-density materials respectively. Although studies on the physical properties of the fuel debris were in progress, the exact density and composition have not been clarified yet. Therefore we

carried out verification experiments using these different density substances. The plates were dropped into room-temperature water by sliding down a 30-degree, 150-mm high acrylic slope. The movement of the plate was captured using a high-speed camera with a frame rate of 120 fps from the water tank until it came to rest. The calculation conditions are shown in Table 1. The discrete particles were 2 mm in diameter, and there were 460,068 total particles. The validation method was a comparison of the experimental and simulation results for the center of the gravity position of the plate as it fell in water. The experimental measurements were calculated using image data processing of the pictures filmed by the camera. Each experiment was conducted 5 times, and the standard division (σ) of the measurements was calculated as the experimental uncertainty.

Snapshots of experimental and simulation results are shown in Figure. 1. The plate fell down in water with swinging due to water resistance. The aluminum plate fell in water with more complicated behavior compared to the stainless steel plate. Qualitatively, the MPS method has been able to simulate the complex falling behavior in both of experiments. In the case of stainless steel, the simulation results were within the 1.96 σ of the experimental results. On the other hand, in the case of aluminum, the simulation results were almost within the 1.96 σ of experimental results but deviation between experiment and simulation results increased with time. It indicates that the calculation accuracy may be not well as the falling time becomes longer when calculating a light material by the MPS method. As results, the MPS method was shown to be capable of calculating gravity and the fluid resistance force well except for a long time falling phenomenon of light materials.

Table. 1 Simulation conditions of falling plate.

Water density	1,000 kg/m^3
Water kinetic viscosity	1.0×10^{-6} m^2/s
Stainless steel density	8,250 kg/m^3
Aluminum density	2,780 kg/m^3
Discrete particle diameter	2.0×10^{-3} m
Number of particles	460,068
Time step	1.0×10^{-4} s

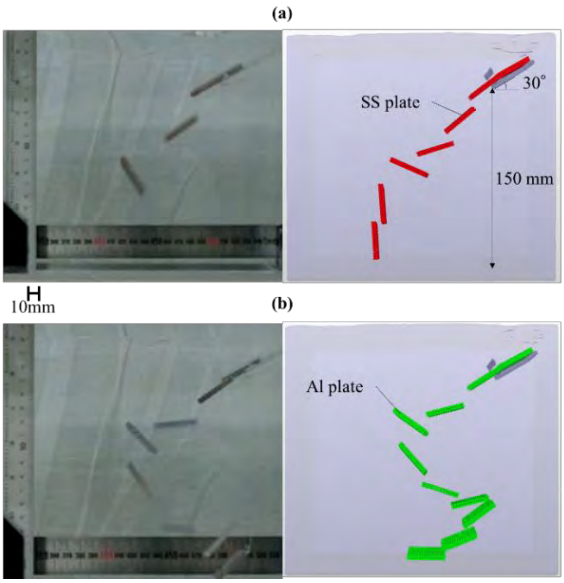

Figure. 1 Comparison between experimental (left side) and simulation (right side) results of falling plate in water. (a) Stainless steel, (b) Aluminum.

2.2.2 Experiment of sedimentation of bolts in water

In order to confirm whether the interaction between the objects can be calculated properly by MPS method, we carried out experiments of sedimentation of bolts which is hexagon head bolts (nominal diameter, 6 mm; length of head, 4 mm; nominal length, 10 mm) to simulate the debris. The experimental apparent is as follows. A concrete board formed the bottom of the water tank to simulate the environment in a reactor. The water surface was 100 mm above the concrete board. A polyvinyl chloride (PVC) pipe, 60 mm in diameter and filled with 500 bolts was dropped from 150 mm into the water by pulling up the stopper. The bolts were made of stainless steel (7.90 g/cm3) and aluminum (2.62 g/cm3). The calculation conditions are shown in Table 2. The diameter of discrete particles was 2 mm, and there were a total of 1,110,050 particles. The validation method compared the Height (H), Width (W), and Depth (D) of the sedimentation shape between the experimental and simulation results. Experimental measurements were conducted using a ruler. Each experiment was repeated 5 times, and the standard division of the measurements was calculated as the experimental uncertainty.

Table. 2 Simulation conditions of sedimentation of bolts.

Water density	1,000 kg/m^3
Water kinetic viscosity	1.0×10^{-6} m^2/s
Stainless steel density	7,900 kg/m^3
Aluminum density	2,620 kg/m^3
Friction coefficient of stainless steel	0.387
Friction coefficient of aluminum	1.09
Spring constants	0.05
Damping coefficient	0.05
Discrete particle diameter	2.0×10^{-3} m
Number of particles	125,288
Time step	1.0×10^{-4} s

Figure 2 contains snapshots of the experimental and simulation results. The simulation results for the measured values were within 1.96σ of the experimental results, except for D in the case of aluminum. In the experiment using aluminum bolts, this slight difference was made because the mountain collapsed in the D direction and this slight difference is smaller than the length of one bolt. Therefore we conclude that we can reasonably simulate sedimentation process of debris using the MPS method. We verified the simulation accuracy of the MPS method by comparing with the experiments. As a result, it clarified that MPS method can be simulated within the constant fluctuation of experimental result.

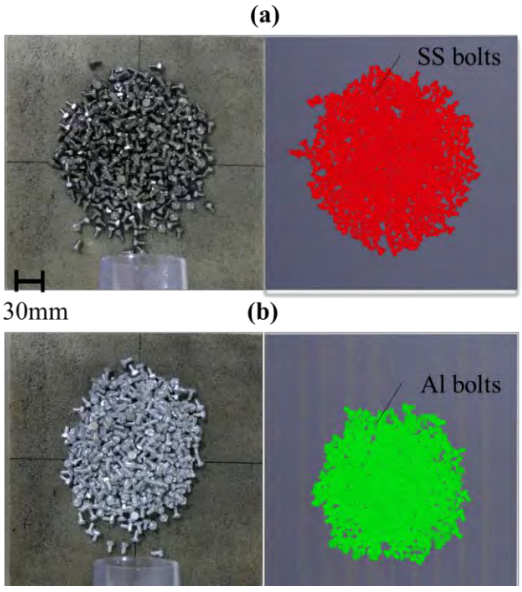

Figure. 2 Experimental (left side) and simulation (right side) results of sedimentation of 500 bolts in water. (a) Stainless steel, (b) Aluminum.

3. Analysis of criticality as fuel debris falls in water

3.1 Algorithm coupling the MPS simulation and Monte Carlo neutron transport calculation

We used the neutron transport calculation with Monte Carlo code MVP2.0 [5] and the JENDL - 4.0 [6] nuclear data library. In the calculation by MVP code, it is possible to create analysis geometry as input data by using the position of the object. In the calculation system that couples the MPS method with MVP, we first performed fluid analysis by MPS. The analysis results, such as 3-D position information and speed of all discretized particles was output as CSV data for each calculation step. Each particle had an identification (ID). Using this ID, we could track specific particles. Therefore, we could search and extract the ID of the particle discretizing the solid at each time. Using this 3-D position information, we could create MVP input data. We basically focus on evaluation of the criticality in the subcritical state and how to ensure safety. So both of thermal feedback and delayed neutron are not considered in the system at this stage.

3.2 Criticality evaluation in the fuel debris fall in water accident during removal process

The purpose of this section is clarified to that it is possible to evaluate criticality with the actual dynamic behavior of fuel debris in water by developing a calculation system. We calculated criticality evaluation in the fuel debris fall in water accident during removal process. As a specific situation, it is assumed that the collected fuel debris falls to the bottom of the pedestal where the cooling water is accumulated during the fuel debris removal. A calculation system is shown in Figure. 3. Here, 1,728 debris cubes, 50-mm per side were dropped from the funnel in water whose surface is 1 m high from the bottom of the pedestal. In addition, we calculated two cases to fall in water from two different funnels with different outlet diameters (φ1m or 0.2 m). It makes possible to evaluate the impact on the criticality by the difference in the way of falling of the fuel debris in water. The composition of the fuel debris and conditions is currently unknown and so we used UO_2 (5wt%) as the composition of the fuel debris. The diameter of discrete particles was 25 mm, and there was a total of 636,142 particles. In neutron transport calculation, the history number is 2,000,000 and the number of batches is 80 with 40 discard batches. After the calculation, the effective multiplication factor k_{eff} during the fuel debris sedimentation in water was evaluated. The criticality calculation is normal eigenvalue calculation considering delayed neutrons and prompt neutrons.

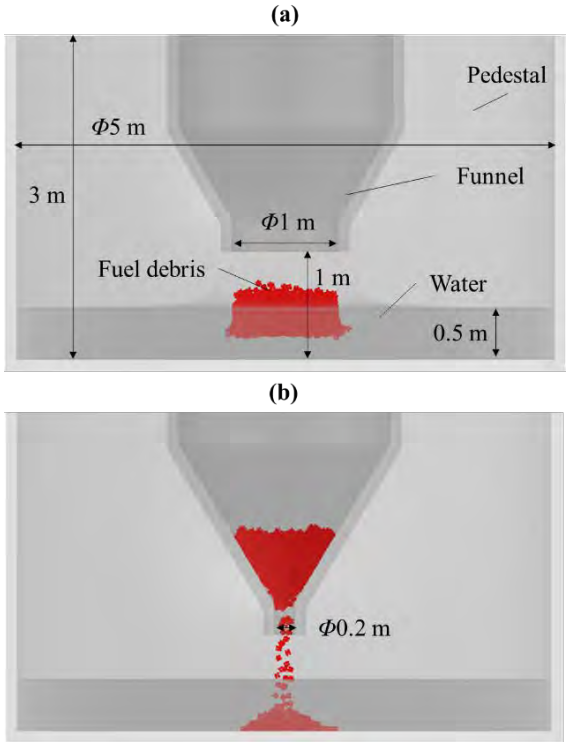

Figure. 3 The fuel debris falls to the bottom of the pedestal where the cooling water is accumulated during the fuel debris removal in case of the funnel outlet diameter (a) φ1m, (b) φ0.2m.

The time change of the effective multiplication factor k_{eff} is shown in Figure. 4. In case of the funnel outlet diameter φ1m, the fuel debris starts to sink in water about 0.3 seconds from the start of the fall from air. At the same time, k_{eff} rapidly increases because of reactivity increase.

Table. 3 Calculaion condition.

MPS	
Water density	1,000 kg/m^3
Water kinetic viscosity	1.0×10^{-6} m^2/s
Cube density	10,950 kg/m^3
Friction coefficient	0.5
Spring constants	0.8
Damping coefficient	0.8
Discrete particle diameter	2.5×10^{-2} m
Number of particles	636,142
Time step	5.0×10^{-4} s
MVP	
Number of history	2,000,000
Number of batches	80 with 40 discard batches

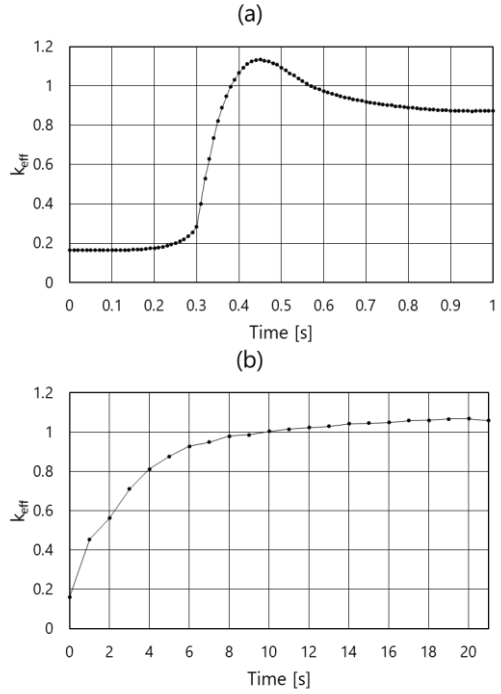

Figure. 4 Time change of effective multiplication factor in case of the funnel outlet diameter (a) φ1m, (b) φ0.2m.

The uncertainty of the effective multiplication factor was less than 0.05% by the Monte Carlo method. Therefore, the error bar is not displayed because it is too small. The uncertainty by MPS method is not evaluated.

k_{eff} reaches a maximum just before the debris clump hits the pedestal bottom. Then in the process of deposition, k_{eff} is reduced by the effect of the whole fuel debris shape becoming flat and the neutron leakage becoming large. On the other hand, In case of the funnel outlet diameter φ0.2m, the fuel debris falls little by little because the outlet of the funnel is narrow and so the increase in k_{eff} is slow. Furthermore, the maximum value of k_{eff} is smaller than in another case. These results indicate that it may be more likely to lead to a criticality accident if the collected fuel debris falls more rapidly than gradually.

These calculations are to clarify that it is possible to evaluate criticality with the actual dynamic behavior of fuel debris in water by developing a calculation system that combines MPS and MVP. Also the obtained facts was first revealed quantitatively by our developed computing system and it is an important result when considering the rational removal working method in the future.

4. Conclusions

In this study, we clarified that it is possible to evaluate criticality with the actual dynamic behavior of fuel debris in water by developing a calculation system that combines computational fluid dynamic and the Monte Carlo neutron transport calculation code.

In the future works, we will clarify what kind of the removal work conditions are safe and reasonable from the viewpoint of working cost and time in decommissioning of the TEPCO's Fukushima Daiichi nuclear power station by using our developed calculation system.

References

1. Inter-Ministerial Council for Contaminated Water and Decommissioning Issues. Mid-And-Long-Term roadmap towards the decommissioning of TEPCO's Fukushima Daiichi nuclear power station (2017). (In Japanese).
2. Hiroki Takezawa and Toru Obara., Passive measure for preventing recriticality of fuel debris dust for defueling at Fukushima Daiichi nuclear power station, Journal of Nuclear Science and Technology, Vol. 53 No. 12 pp. 1960-1967 (2016).
3. S. Koshizuka, Y. Oka, "Moving-particle semi-implicit method for fragmentation of incompressible fluid", Nuclear Sci. Eng. 123, 421-434 (1996).
4. Prometech Software「Particleworks」, http://www.prometech.co.jp/particleworks.html.
5. Yasunobu Nagaya et al. MVP/GMVP II: General purpose Monte Carlo codes for neutron and photon transport calculations based on continuous energy and multigroup method. Technical Report JAERI 1348, Japan Atomic Energy Research Institute (2005).
6. Shibata Keiichi et al. JENDL-4.0: A new library for nuclear science and engineering. Journal of Nuclear Science and Technology, 48 (2011).

TS-01 Deterministic Transport Methods and Applications

Proceedings of the Reactor Physics Asia 2019 (RPHA19) Conference
Osaka, Japan, Dec. 2-3, 2019

BEAVRS Benchmark Simulation by Using NECP-Bamboo

Jiewei Yang, Hongchun Wu and Yunzhao Li*
Xi'an Jiaotong University: 28 West Xianning Road, Xi'an, Shaanxi 710049, China
*Yunzhao Li: yunzhao@mail.xjtu.edu.cn

Abstract

NECP-Bamboo, a PWR-core fuel management calculation system developed by NECP lab from Xi'an Jiaotong University, is based on improved two-step method. By using the BEAVRS benchmark released by MIT of America based on the Watts-Bar nuclear power plant measurements, it is verified and validated in this paper. Results of this paper cover critical boron concentrations, detector signal, reactivity coefficient and control rod worth. The average absolute value of error between calculated and measured value is 10ppm, the maximum error of detector signals in BOC is 4.346%, and the maximum error of control rod wroth is -4%.

Key Words: **PWR, BEAVRS, NECP-Bamboo1.0, Verification**

1. Introduction

For large commercial PWR-core, the two-step method is still usually used in the simulation with depletion calculation, thermal-hydraulics and critical search calculation of large PWR.

Firstly, the two-dimensional fine-group lattice neutron transport calculation is carried out to obtain the few-group constants for multiple states of each assembly with reflective boundary condition. The few-group constants can then be parameterized into the function of the state parameters such as assembly burnup, boron concentration, fuel and moderator temperatures. Those typical state parameters are defined to describe the lattice state and should cover the boundary of state during the entire core operation process. The function relationships are stored in the so-called few-group constants data library. After that, three-dimensional whole core neutron diffusion calculation coupling thermal-hydraulics calculation, depletion calculation and critical search calculation will be carried out. Based on the two-step method, the PWR core nuclear design code system NECP-Bamboo [1-2] has been developed, including the two-dimensional lattice calculation code Bamboo-Lattice, three-dimensional whole-core calculation code Bamboo-Core and three dimensional whole core transient simulation code Bamboo-Transient.

This paper introduces basic theoretical models and mainly introduces the modeling of BEAVRS benchmark and the solution by NECP-Bamboo code system. The main reason for choosing this benchmark is that this benchmark has measured value and this benchmark is widely used in lots of code including deterministic and probabilistic code for the verification and validation.

2. Theoretical Models

2.1 The lattice heterogeneous calculation

With the autonomous multi-group cross section data library and depletion data library from the ENDF/VII.0. The assembly modular Method of Characteristic(MOC) is employed to solve the multi-group neutron transport equation in the entire lattice directly[3]. It can handle complex geometry including pin-cell (i.e., pellet, clad, and moderator), IFBA surrounding the fuel rod, water gap surrounding the fuel assembly, baffle or barrel, et al. Besides that, to decrease the cost of calculation, 1/4 or 1/8 modular can be described.

Before the transport calculation, the subgroup method is employed to eliminate the limitation in assembly geometry and to guarantee both accuracy and efficiency in resonance calculation.

2.2 The cross section model

Considering the fact that it is impossible to take all states during reactor operation into consideration in lattice calculation, it is necessary to provide a continuous function relationship between few-group constants and state parameters for core calculation. It is the few-group constants parameterization or cross section model.

There are lots of ways to achieve the few-group constants parameterization. The selection of state parameters type, the fitting form of state parameters, and the order in each state parameters will influence the accuracy. A general code [4] was developed to achieve the few-group constants parameterization. In this code, there is no limitation on the type and number of few-group constants, the type and number of state parameters, and the

polynomial order of the fitting function
A recommended parameterization form is given as default option in Bamboo-Core as following:

$$\Sigma\left(Bu,Tm,\sqrt{Tf},Cb\right)=f\left(Bu,Cb\right)+f\left(Bu,Tm,\sqrt{Tf}\right) \quad (1)$$

where Bu, Cb, Tm, Tf represent node-averaged depletion (MWd/Tu), soluble boron concentration (ppm), moderator temperature (K) and effective fuel temperature (K). The Σ can stand for macroscopic cross section (m^{-1}), microscopic cross section (barn), discontinuity factor and pin-power form factor, which means those variables use the same function.

2.3 The Variational Nodal Diffusion Method

Instead of using the transverse integration technique, the Variational Nodal Method (VNM) directly expand the volumetric flux and surface partial currents by using three- and two-dimensional spatial orthogonal polynomials respectively to transform the continuous neutron diffusion equation about neutron flux into a linear algebra system in terms of the expansion moments [5].

Compared with nodal methods based on integration, on one hand, the homogeneous pin-power or flux can be directly obtained by combining the expansion moments and the corresponding basis functions. On the other hand, the control rod cusping effect can be fully eliminated by using heterogeneous VNM [6].

2.4 Thermal-hydraulics Model

Ignoring the axial pressure drop and coolant mass exchange between adjacent channels, the one dimensional mass and energy conservation equations can be solved from the core bottom to the top sequentially.

For a single phase flow under the above conditions, the coolant temperature is calculated by the following mass continuity and energy conservation equation:

$$\frac{dw}{dz}=0 \quad (2)$$

and

$$\frac{d\left(hw\right)}{dz}=q \quad (3)$$

where w is the coolant mass flow (kg/s), h is the coolant enthalpy (J/kg), q is the linear power in coolant (w/m).

After that, with known coolant temperature, the fuel rod effective temperature can be obtained by solving the one dimensional heat conduction model in rod geometry. The radial heat conduction from the fuel pellet to the gap and even to the clad, and coolant can be described by the following equation:

$$\frac{1}{r}\frac{\partial}{\partial r}\left(k\left(T\right)r\frac{\partial T}{\partial r}\right)+\tilde{q}=0 \quad (4)$$

where $k(T)$ is the heat conductivity ($w\cdot cm^{-1}$) at temperature T, $\tilde{q}$ is the volumetric heat source ($w\cdot cm^{-3}$).

2.4 Critical Search Model

During the active reactor core fuel cycle operation simulation, the critical state with the effective multiplication factor of the core equal to unity has to be found by changing the concentration of the boron in the coolant or the control rod position, named as critical search. For the second generation reactor, soluble boron is more commonly used to control reactivity. Taking the boron concentration as an example.

The linear interpolation is obtained to estimate the c ritical boron concentration (CBC):

$$CB_2=CB_1+\frac{1-k_{\text{eff},1}}{Guess} \quad (5)$$
$$CB_{i+1}=CB_i+\frac{1-k_{\text{eff},i}}{k_{\text{eff},i-1}-k_{\text{eff},i}}\cdot\ CB_{i-1}-CB_i$$

where, $k_{\text{eff},i}$ represents the effective multiplication factor corresponding to boron concentration CB_i (ppm), i is number of the critical boron concentration search, Guess is initial prediction boron worth (ppm^{-1}).

3. BEAVRS Benchmark

The BEAVRS benchmark [7] is proposed by the Computational Reactor Physics Group of MIT, providing detailed measured value and information for modeling. The reactor comes from a Westinghouse four-loop PWR with 3411MWth. The core is loaded with 193 fuel assemblies with 17×17 pin arrangement and 3 enrichments in the first cycle including 1.6, 2.4 and 3.1 wt.%. High leakage loading pattern is employed.

Besides those material and geometry description, the benchmark also provides the hot zero power measurement, measured data obtained during the reactor operation and the operational power history.

The challenge of modeling the first cycle is how to deal with the complex power history. In this study, a fine power history modeling is carried out to describe the true power history and make the minimum information loss, guarantee both accuracy and efficiency.

As can be seen in Fig. 1, the black line is the real power history with 573 days data. It is complex because of the frequent shutdown and power drop. In order to describe those power history, typical days are chosen to compared with measured value. In those days, the core condition is exactly the same as real condition, including the power level, control rod position, inlet coolant temperature, core macroscopic depletion and et al. Between those typical days, extra time points were used to describe the power change and guarantee the depletion of typical days is same as real depletion.

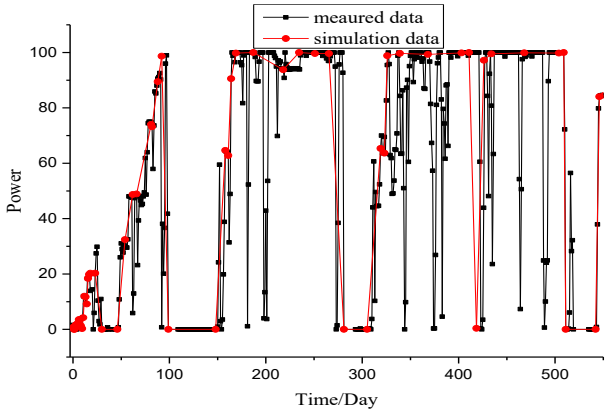

Fig. 1 power history of the first cycle (black) and the power follow approximation (red)

Finally, the number of calculation time points is 61, much less than the original 573.

4.Simulation Results

4.1 Hot Zero Power Simulation

The results in hot zero power condition include critical boron concentration, control rod worth and detector signals.

Table I shows the result of critical boron concentration. The results of NECP-Bamboo agree well with the measured values. Fig. 2 shows the results of detector response. The maximum error from measured value is 4.346% while the Root-Mean-Square (RMS) error is 1.89%. Table II provides the control rod worth in hot zero power condition. The maximum error is -31pcm, while the maximum relative error is -4%. Fig. 3 shows the results of axial detector response and the results of NECP-Bamboo agree well with the measured values.

Table I critical boron concentration results

	NECP-Bamboo	Measured value	Error/ppm
CBC	975ppm	979ppm	-4ppm

0.778	0.815	0.728	0.584				Measured Value
0.751	0.782	0.704	0.575				NECP-Bamboo1.0
-3.458	-4.074	-3.242	-1.627				Relative Error/%
1.264	0.873	1.242		0.958	0.702		RMS/%
1.242	0.850	1.249		0.952	0.719		1.89
-1.772	-2.589	0.531		-0.605	2.379		
0.935	1.168	0.984	1.307	1.196	0.852	0.702	
0.926	1.186	0.972	1.364	1.214	0.864	0.719	
-0.941	1.558	-1.189	4.346	1.480	1.397	2.379	
1.147	0.974	1.212		1.343	1.196	0.958	
1.149	0.959	1.207		1.346	1.214	0.952	
0.174	-1.540	-0.421		0.186	1.480	-0.605	
0.94	1.143	0.968	1.249		1.307		0.584
0.930	1.149	0.979	1.263		1.364		0.575
-1.106	0.542	1.105	1.129		4.346		-1.627
1.065	0.897	1.138	0.968	1.212	0.984	1.242	0.728
1.068	0.900	1.147	0.979	1.207	0.972	1.249	0.704
0.300	0.301	0.808	1.105	-0.421	-1.189	0.531	-3.242
0.779	1.011	0.897	1.143	0.974	1.168	0.873	0.815
0.779	1.020	0.900	1.149	0.959	1.186	0.850	0.782
0.026	0.880	0.301	0.542	-1.540	1.558	-2.589	-4.074
	0.779	1.065	0.94	1.147	0.935	1.264	0.778
	0.779	1.068	0.930	1.149	0.926	1.242	0.751
	0.026	0.300	-1.106	0.174	-0.941	-1.772	-3.458

Fig. 2 Radial detector response distribution and relative error between Bamboo-Core1.0 and Measured value for HZP condition

Table II Control rod worth and error between Bamboo-Core1.0 and Measured value

Control rod bank state	NECP-Bamboo	Measured value	Error/ pcm
D in	804	788	16
C with D in	1219	1203	16
B with D C in	1196	1171	25
A with D, C, B in	552	548	4
SE with D, C, B, A in	460	461	-1
SD with D, C, B, A, SE in	741	772	-31
SC with D, C, B, A, SE, SD in	1118	1099	19

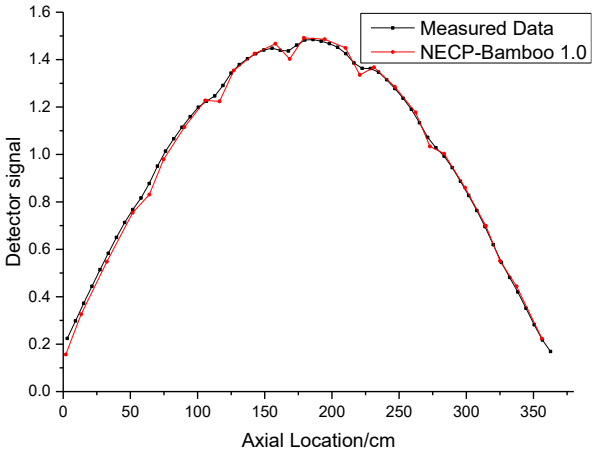

Fig. 3 Axial detector response distribution and relative error between Bamboo-Core1.0 and Measured value for HZP condition

4.2 Hot Full Power Simulation

Hot full power calculations are performed for the first cycle at 3411 MWth with all rods out of core (ARO). It can be seen that the results of NECP-Bamboo show good agreement with the reference in Fig. 4. The maximum error is 22ppm, while the average absolute error is 7ppm.

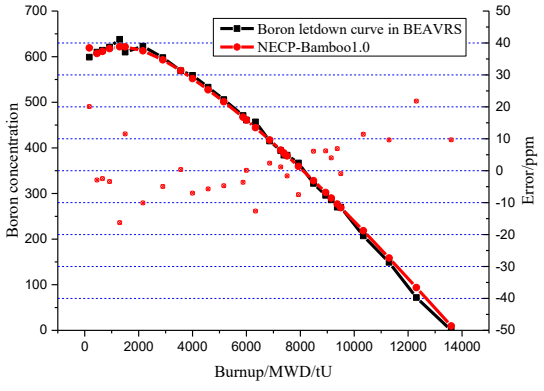

Fig. 4 Comparison of boron letdown curve with provided data in BEAVRS

At BOL of HFP condition, the pin power also can be given by NECP-Bamboo. The guide tubes, fuel rods, and absorbers can be recognized in Fig. 5.

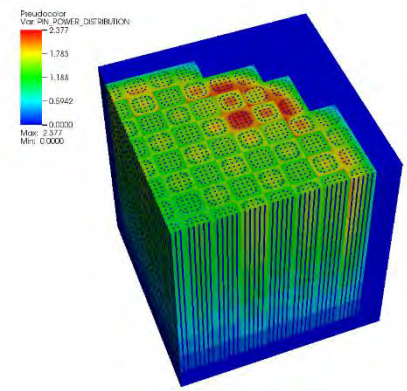

Fig. 5 Pin power of quarter core at BOL

4.3 Power History Simulation

Different with HFP condition, the power history and control rod move are considered. The simplified power history is shown in Fig. 1 as red line. The measured data is from the detector signals folder rather than BEAVRS text.

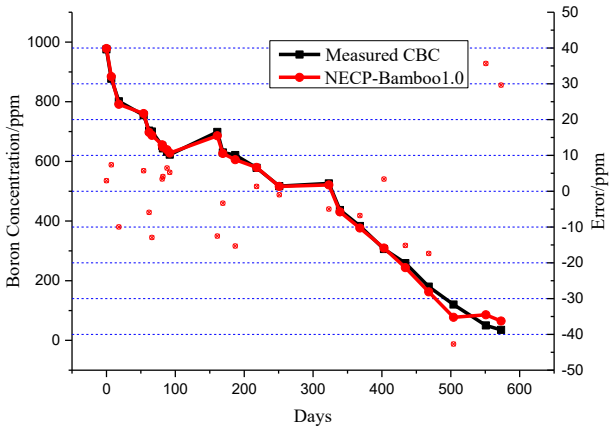

Fig. 6 Comparison of boron letdown curve with provided measured value.

Considering the complex of power history within the first 500 days, the results of NECP-Bamboo show great agreement with measured value in Fig. 6. The maximum error is less than 20ppm and the average absolute error is 7ppm. After 500 days, the error is greater than that before 500 days, but the maximum error is -42ppm, within the criteria. It is necessary to add more time points in simulation to reduce the error after 500 days.

6. Conclusions

By using the BEAVRS benchmark, NECP-Bamboo code system is verified and validated in this paper. The calculation includes HZP condition, HFP condition and power history simulation. The results of NECP-Bamboo give good accuracy within the criteria in the standard at major core properties such as critical boron concentrations, control rod worth and detector response. Besides, NECP-Bamboo can give pin power distribution, flux distribution, temperature distribution and et al.

Acknowledgements

This work is financially supported by the Project 11775171 supported by National Natural Science Foundation of China.

References

1. Y. Li, B. Zhang, et al., "Development and Verification of PWR-Core Fuel Management Calculation Code System NECP-Bamboo: Part I Bamboo-Lattice," Nuclear Engineering and Design, 335, pp.432-440 (2018).
2. Yang W, Wu HC, Li YZ, et al. "Development and verification of PWR: Core nuclear design code system NECP-Bamboo, Part II: Bamboo-Core," Accepted by Nuclear Engineering and Design.
3. C. Tian, Y. Zheng, et al., "Neutron transport study based on assembly modular ray tracing MOC method," Nuclear Power Engineering, VOL 36, pp. 157-161, June 15, (2015).
4. S. Gao. "PWR few-group constant parameterization methodology study and code development," Master Thesis, Xi'an, China: Xi'an Jiaotong Univ. (2015).
5. Y. Li. "Advanced reactor core neutronics computational algorithms based on the variational nodal and nodal SP3 Methods," PhD Thesis, Xi'an, China: Xi'an Jiaotong Univ. (2012).
6. Li Y, Liang B, Wu H, et al. "Heterogeneous Discontinuity Factor Treatment in Variational Nodal Method," Annals of Nuclear Energy (Online; DOI: 10.1016/j.anucene.2018.12.021)
7. N. HORELIK, B. HERMAN, M. ELLIS, et al. "Benchmark for Evaluation and Validation of Reactor Simulations (BEAVRS), Release rev.2.0.2", MIT Computational Reactor Physics Group (2018).

Proceedings of the Reactor Physics Asia 2019 (RPHA19) Conference
Osaka, Japan, Dec. 2-3, 2019

Optimization and Verification of PWR Pin-by-pin Fuel Management Calculation Code NECP-Bamboo2.0

Sicheng Wang, Liangzhi Cao, Yunzhao Li* and Wen Yang
Xi'an Jiaotong University: 28 West Xianning Road, Xi'an, Shaanxi 710049, P. R. China
* yunzhao@mail.xjtu.edu.cn

Abstract

As an improved two-step calculation scheme for PWR-core fuel management, pin-by-pin calculation can improve the simulation accuracy by eliminating approximations including assembly homogenization and pin-power reconstruction. Accordingly, the NECP-Bamboo2.0 code has been developed by using the approaches of two-dimensional whole-assembly direct neutron transport calculation, seven-group pin-cell homogenization and three-dimensional whole-core pin-by-pin multi-physics coupling iteration. Different from the traditional assembly-homogenization based two-step scheme, the refinement in space requires not only higher-order angular discretization, such as from diffusion to SP_3, but also the increased number of energy-group, such as from 2 to 7. Unfortunately, both the storage of the few-group constants and the computing time would be then increased dramatically. Thus, in this paper, an energy group structure optimization has been done to provide a suitable 4-group structure condensed from the 69-group WIMS library. The improved code has been verified by using a 2D multi-assembly neutron transport calculation and a 3D whole-core power-history following simulation.

Key Words: PWR, Pin-by-pin, Energy-group optimization, NECP-Bamboo

1. Introduction

There are two steps in the pin-by-pin calculation scheme, including two-dimensional lattice high-order neutron transport calculation [1] and three-dimensional whole-core low-order neutron transport calculation. The former provides a series of discrete relationships between the few-group constants of each pin-cell and its state parameters such as burnup, fuel temperature, moderator temperature and et al. After obtaining the continuous relationship between few-group constants and state parameters by parameterization in the form of few-group constants data library, multi-physics coupled iteration can be carried out in the second step, including neutron transport, thermal-hydraulics, fuel depletion, critical-state searching and et al. Different from the traditional two-step scheme with assembly homogenization, lattice is only homogenized within each pin-cell to fully eliminate the pin-power reconstruction to provide the pin-power profile for safety analysis. Based on this scheme, Nuclear Engineering Computational Physics (NECP) laboratory in Xi'an Jiaotong University has developed a new PWR-core pin-by-pin fuel management system named NECP-Bamboo2.0, including the lattice calculation code Bamboo-Lattice2.0 [2] and the steady-state pin-by-pin core calculation code Bamboo-Core2.0. [3]

Pin-cell is usually optically thin, making the pin-cell homogenized few-group constants more dependent on its environment [4], especially when the target pin locates at the assembly boundary or is adjacent to some special pin-cell like strong absorbers. Therefore, the two-group structure is insufficient to represent the coupling in pin-by-pin simulation. An increased number of energy groups, such as seven or even more, is widely used to capture the spectrum interference effect [5-6].

However, more energy groups would increase the amount of equations needed to be solved in the whole-core calculation dramatically, and then deteriorate the computational efficiency. Besides, compared with the two-group structure, the increase in storage caused by the seven-group structure is about triple. In order to keep the efficiency and to reduce the storage requirement, a suitable few-group structure, which is less than seven groups and can guarantee an acceptable accuracy at the same time, would be very meaningful. This is what would be introduced in this paper.

The rest of this paper is organized as following. The theoretical models employed in the NECP-Bamboo2.0 code are described in Section 2, including the energy-group structure optimization method and a suitable four-group structure condensed from the 69-group WIMS

library. In Section 3, verification of the improved code is introduced by using two typical calculations by comparing with one-step calculation or engineering measurements. Finally, Section 4 summarizes the conclusions.

2. Theoretical Models

In this section, the main models in NECP-Bamboo2.0 are introduced in the sequence of actual calculation scheme as following: 2D whole-assembly heterogeneous neutron transport, four-group pin-cell homogenization, Few-group cross-section parameterization and 3D whole-core multi-physics coupling iteration.

2.1 2D whole-assembly heterogeneous neutron transport

Other than the legacy equivalence theory, the subgroup method is employed in Bamboo-Lattice 2.0 to eliminate the limitations in lattice geometry and to guarantee both accuracy and efficiency. Besides, to solve the two-dimensional steady-state multi-group neutron transport equation, an assembly-modular Method of Characteristics (MOC) is employed in Bamboo-Lattice 2.0. Since the MOC method has a capability of processing complex geometry model, the code can module two-dimensional single or multiple assembly, while each assembly can be surrounded by a thin water gap and be constructed by a certain number of rectangular pins. In addition, each pin can be constructed by straight lines and circle curves.

2.2 Four-group pin-cell homogenization

Either the generalized equivalent theory or the super-homogenization technique can be utilized to obtain the few-group cross-sections after the lattice heterogeneous calculation with the reflective boundary condition [4]. The definition of the homogenized few-group cross-section in the multi-group calculation is applied as following:

$$\Sigma_{x,i,g}^{hom}=\frac{\sum_{h\in g}\sum_{m\in i}\Sigma_{x,m,h}^{het}\cdot\phi_{m,h}\cdot V_m}{\sum_{h\in g}\sum_{m\in i}\phi_{m,h}\cdot V_m} \tag{1}$$

Theoretically, if the fine-group energy spectrum used for homogenization was obtained from whole-core high-order heterogeneous calculation, few-group low-order core calculation would be expected to provide consistent results with heterogeneous calculation. Unfortunately, considering the computational cost, pin-by-pin calculation scheme can only get the homogenized few-group parameters by using the energy spectrum obtained from single-assembly calculation. Obviously, the energy spectrum obtained by the single-assembly model with reflective boundary differs from the spectrum from the whole-core calculation due to the so-called environmental effects.

It should be noted that the spectrum used in Eq. (1) is a normalized one. When energy spectrums were obtained from different calculation models, there would always exist adjacent fine-group intervals where $\frac{\phi_{single}}{\phi_{env}}$ varies gently. For those adjacent fine-group intervals, the following equalities can approximately hold:

$$\phi_{m,h}^{single}=c\cdot\phi_{m,h}^{env} \tag{2}$$

$$\Sigma_{x,i,g}^{hom,single}=\frac{\sum_{h\in g}\sum_{m\in i}\Sigma_{x,m,h}^{het}\cdot\phi_{m,h}^{single}\cdot V_m}{\sum_{h\in g}\sum_{m\in i}\phi_{m,h}^{single}\cdot V_m},\Sigma_{x,i,g}^{hom,env}=\frac{\sum_{h\in g}\sum_{m\in i}\Sigma_{x,m,h}^{het}\cdot\phi_{m,h}^{env}\cdot V_m}{\sum_{h\in g}\sum_{m\in i}\phi_{m,h}^{env}\cdot V_m},$$
$$\Sigma_{x,i,g}^{hom,single}=\frac{\sum_{h\in g}\sum_{m\in i}\Sigma_{x,m,h}^{het}\cdot\phi_{m,h}^{single}\cdot V_m}{\sum_{h\in g}\sum_{m\in i}\phi_{m,h}^{single}\cdot V_m}=\frac{\sum_{h\in g}\sum_{m\in i}\Sigma_{x,m,h}^{het}\cdot c\cdot\phi_{m,h}^{env}\cdot V_m}{\sum_{h\in g}\sum_{m\in i}c\cdot\phi_{m,h}^{env}\cdot V_m}=\Sigma_{x,i,g}^{hom,env} \tag{3}$$

where superscripts *single* and *env* stand for single-assembly and whole-core models respectively. Eq. (3) shows the fact that in those fine-group intervals which could be then condensed into a single few group, the single-assembly model and the whole-core model can provide the same few-group constants. Therefore, to find certain adjacent fine-group intervals where fine-group $\frac{\phi_{single}}{\phi_{env}}$ varies gently could be a guiding principle to determine the few-group boundary.

In this paper, the difference between the energy spectrums obtained from single-assembly model and whole-core model is analyzed. An optimized four-group energy structure is proposed in Table I finally.

Table I. The upper bounds of energy group structures

	7-group(eV)	**4-group(eV)**	**2-group(eV)**
1	1.000E+07	1.000E+07	1.000E+07
2	5.000E+05	9.118E+03	6.250E-01
3	9.118E+03	4.000E+00	
4	4.000E+00	6.250E-01	
5	6.250E-01		
6	1.400E-01		
7	5.800E-02		

2.3 Few-group cross-section parameterization

NECP-Bamboo2.0 adopts the least-squares polynomial fitting approach. A recommended few-group constants parameterization function form is given as following:

$$\Sigma\left(Bu,Tm,\sqrt{Tf},Cb\right)=f\left(Bu,Cb\right)+f\left(Bu,Tm,\sqrt{Tf}\right) \tag{4}$$

where Bu,Cb,Tf,Tm represent pin-averaged burnup (GWd/tU), boron concentration (PPM), moderator temperature (K) and effective fuel temperature respectively $\left(\sqrt{K}\right)$ Σ can stand for the macroscopic cross section, microscopic cross section, effective yield for fission products (Iodine, Xenon, Promethium, Samarium) and discontinuity factors.

2.4 3D whole-core multi-physics coupling iteration

NECP-Bamboo2.0 proposes a multi-physics coupling strategy for pin-by-pin core calculation, which is a tight coupled iterative process. Firstly, the cell homogenized parameters generated by the Bamboo-Lattice2.0 code are fitted and then the fission source iteration is performed at each burnup point. At each outer iterative process, few mesh acceleration calculation, SP_3 multi-group calculation, updated fission source and keff, critical search calculation, thermal-hydraulic feedback calculation, burnup calculation, and cross-section calculation are performed in sequence. Among them, critical search calculation, thermal-hydraulic calculation and burnup calculation are performed at certain outer iterative interval numbers *N*c, *N*t, and *N*d respectively cross-section calculation must be performed whenever any of the three calculations above is performed.

3. Verification

3.1 Verification of the new four-group structure

In order to verify the optimized four-group structure applied in the pin-by-pin calculation, four multi-assembly problems with reflective boundary conditions have been calculated. Six single assembly with different enrichment or different numbers of burnable absorbers and control rods are shown in Fig. 1. The configurations of the problems are shown in Fig. 2, and the reference solution was provided by 2D one-step transport calculation.

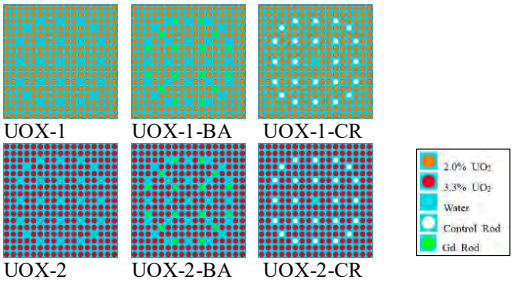

Fig. 1. Geometries of assemblies

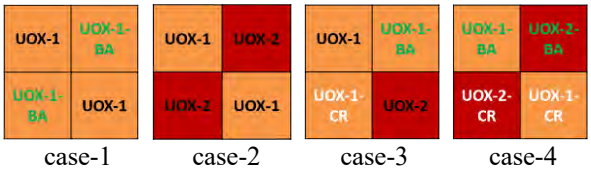

Fig. 2. Configuration of multi-assembly problems

As in Table II, better results could be obtained from the four- and seven-group structures compared with the traditional two-group structure, while k_{eff} biases of the four- and seven-group are both less than 200 pcm, which satisfies the error requirements. Moreover, Table Ⅲ shows that both computing time and storage requirement of four-group structure is almost half of those of seven-group structure. Besides, the reference pin power distribution is shown in Fig. 3.

Table Ⅱ. Eigenvalue results of multi-assembly problems

	reference (69G)	2G		4G		7G	
		k-eff	Δρ /pcm	k-eff	Δρ /pcm	k-eff	Δρ /pcm
case1	1.00388	1.00568	180	1.00473	85	1.00519	131
case2	1.18499	1.18570	71	1.18519	20	1.18513	14
case3	1.03943	1.04566	623	1.04139	196	1.04078	135
case4	0.89868	0.90100	232	0.89927	59	0.89903	35

Table Ⅲ. Storage Requirement and Calculation Time of Multi-Assembly Problems

	2G		4G		7G	
	Storage /Mb	Time /s	Storage /Mb	Time /s	Storage /Mb	Time /s
case1	1.35	6.31	2.58	8.00	4.78	17.88
case2		9.97		10.92		37.70
case3		16.30		25.26		55.81
case4		13.88		16.79		51.13

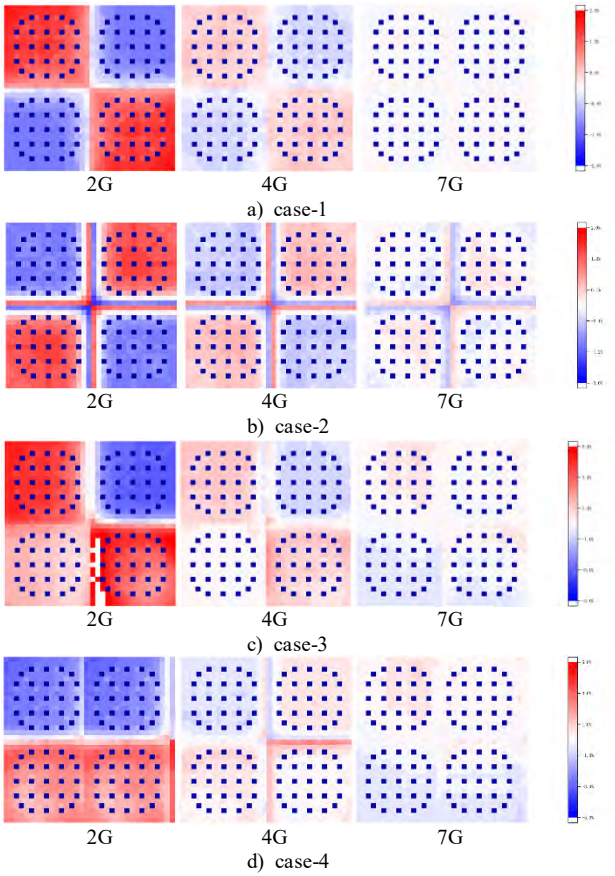

Fig. 3. Relative pin-power bias

3.2 Verification of NECP-Bamboo2.0

With the new four-group structure, a 3D whole-core power-history following simulation for a commercial pressurized water reactor currently in operation was carried out to compare with the 13 active measurements. There are 157 assemblies with different numbers of

burnable absorbers and control rods in the core. Fig. 4 shows the critical boron concentrations, while Fig. 5-7 show the assembly power distributions of BOC, MOC and EOC. What needs to be pointed out is that a simplified operating history was employed in the calculation, while the measured values comes from the actual and complex operating history.

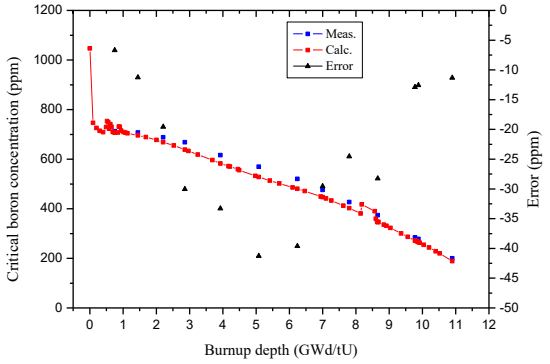

Fig. 4. Letdown curve of the cycle

0.807 0.814 0.87%	0.642 0.653 1.62%						Meas. Calc. (C-M)/M
0.857 0.846 -1.29%	1.008 1.014 0.64%	0.997 0.996 -0.08%	0.701 0.701 0.00%				
1.095 1.103 0.80%	1.050 1.039 -1.12%	1.063 1.057 -0.63%	1.042 1.035 -0.63%	0.797 0.796 -0.13%			
1.110 1.105 -0.46%	1.130 1.141 0.90%	1.019 1.007 -1.22%	1.198 1.184 -1.14%	1.075 1.059 -1.56%	0.797 0.796 -0.13%		
1.199 1.211 1.03%	1.008 1.006 -0.17%	1.211 1.214 0.23%	1.061 1.047 -1.27%	1.198 1.184 -1.14%	1.042 1.035 -0.64%	0.701 0.701 0.06%	
0.963 0.970 0.69%	1.058 1.076 1.73%	0.993 0.991 -0.16%	1.211 1.214 0.23%	1.019 1.007 -1.22%	1.063 1.056 -0.64%	0.997 0.996 -0.09%	
1.033 1.046 1.24%	0.949 0.959 1.11%	1.058 1.076 1.72%	1.008 1.006 -0.18%	1.130 1.140 0.88%	1.050 1.038 -1.14%	1.008 1.014 0.62%	0.642 0.653 1.59%
1.061 1.077 1.53%	1.033 1.046 1.24%	0.963 0.970 0.68%	1.199 1.211 1.03%	1.110 1.105 -0.48%	1.095 1.103 0.79%	0.857 0.846 -1.32%	0.807 0.813 0.84%

Fig. 5. Assembly power distribution of BOC

0.724 0.712 -1.57%	0.588 0.579 -1.45%						Meas. Calc. (C-M)/M
0.844 0.828 -1.84%	0.955 0.948 -0.72%	0.887 0.875 -1.37%	0.631 0.620 0.00%				
1.095 1.098 0.33%	1.026 1.010 -1.48%	1.041 1.032 -0.85%	0.981 0.972 -0.92%	0.714 0.706 -1.10%			
1.117 1.112 -0.49%	1.172 1.184 1.01%	1.062 1.055 -0.69%	1.139 1.135 -0.43%	0.985 0.973 -1.22%	0.714 0.706 -1.10%		
1.250 1.269 1.53%	1.111 1.116 0.45%	1.237 1.253 1.31%	1.093 1.090 -0.35%	1.139 1.135 -0.43%	0.981 0.971 -0.93%	0.631 0.620 -1.62%	
1.101 1.113 1.05%	1.190 1.218 2.36%	1.096 1.112 1.46%	1.237 1.253 1.31%	1.062 1.055 -0.69%	1.041 1.032 -0.85%	0.887 0.875 -1.37%	
1.114 1.128 1.26%	1.087 1.101 1.36%	1.190 1.218 2.36%	1.111 1.116 0.45%	1.172 1.183 1.00%	1.026 1.010 -1.49%	0.955 0.948 -0.73%	0.588 0.579 -1.45%
1.113 1.127 1.26%	1.114 1.128 1.26%	1.101 1.113 1.05%	1.250 1.269 1.53%	1.117 1.112 -0.50%	1.095 1.098 0.28%	0.844 0.828 -1.86%	0.724 0.712 -1.57%

Fig. 6. Assembly power distribution of MOC

0.765 0.753 -1.48%	0.630 0.620 -1.65%						Meas. Calc. (C-M)/M
0.925 0.909 -1.68%	1.038 1.035 -0.31%	0.911 0.901 -1.08%	0.657 0.647 0.00%				
1.139 1.149 0.88%	1.037 1.031 -0.58%	1.097 1.096 -0.08%	1.041 1.039 -0.18%	0.728 0.719 -1.18%			
1.073 1.073 0.02%	1.169 1.182 1.19%	1.062 1.061 -0.08%	1.130 1.132 0.19%	0.991 0.984 -0.63%	0.728 0.719 -1.18%		
1.173 1.186 1.13%	1.069 1.070 0.13%	1.175 1.187 1.03%	1.062 1.061 -0.07%	1.130 1.132 0.19%	1.041 1.039 -0.19%	0.657 0.647 -1.64%	
1.040 1.042 0.21%	1.147 1.160 1.17%	1.052 1.054 0.22%	1.175 1.187 1.03%	1.062 1.061 -0.08%	1.097 1.096 -0.08%	0.911 0.901 -1.08%	
0.997 1.004 0.70%	1.014 1.018 0.45%	1.147 1.160 1.17%	1.069 1.070 0.13%	1.169 1.182 1.19%	1.037 1.031 -0.59%	1.038 1.034 -0.32%	0.630 0.620 -1.66%
0.974 0.982 0.81%	0.997 1.004 0.70%	1.040 1.042 0.20%	1.173 1.186 1.12%	1.073 1.073 0.02%	1.139 1.148 0.87%	0.925 0.909 -1.68%	0.765 0.753 -1.48%

Fig. 7. Assembly power distribution of EOC

4. Conclusions

NECP-Bamboo2.0 developed by NECP in Xi'an Jiaotong University was improved by optimizing a four-group structure and verified by using a two-dimensional whole-core problem and a three-dimensional whole-core power-history following simulation. Compared with the original seven-group structure, about 60% of computing time can about of 50% of storage requirement can be saved.

Acknowledgements

This work was supported by National Natural Science Foundation of China (No. 11775171 and No.11735011).

References

1. C. Tian, Y. Zheng, et al. Neutron transport study based on assembly modular ray tracing MOC method (in Chinese), Nuclear Power Engineering, 36:157-161, 2015.
2. Y. Li, B. Zhang, et al. Development and verification of PWR-core fuel management calculation code system NECP-Bamboo: Part I Bamboo-Lattice, Nuclear Engineering and Design, 335:432-440, 2018.
3. W. Yang. Study on PWR Three-dimensional Whole-core Pin-by-pin Physical Calculation Method, Xi'an Jiaotong University, 2018.
4. B. Zhang, H. Wu, et al. Evaluation of Pin-Cell Homogenization Techniques for PWR Pin-by-Pin Calculation, Nuclear Science and Engineering, 186(2):134-146, 2016.
5. M. Tatsumia, Y. Ohokaa, et al. Verification of the AEGIS/SCOPE2 in-core fuel management system, International Conference on the Physics of Reactors, Casino-Kursaal Conference Center, Interlaken, Switzerland, September 14-19, 2008.
6. C. Beckert and U. Grundmann, Development and verification of a nodal approach for solving the multigroup SP_3 equations, Annals of Nuclear Energy 35:75–86, 2008.

Proceedings of the Reactor Physics Asia 2019 (RPHA19) Conference
Osaka, Japan, Dec. 2-3, 2019

Application of cosKERNEL code for NPP Shielding Calculation

Wen Song*, Yeshuai Sun, Shuo Li, Xing Wang, Hui Yu, Yixue Chen
Nuclear Power Software Development Center, SPICRI, Beijing, China, 102209
National Energy Key Laboratory of Nuclear Power Software
*Corresponding author: songwen@spic.com.cn

Abstract

As the basis of shielding design, radiation dose calculation is to ensure that radiation level is lower enough to satisfy a safe dose for relevant personnel. The cosKERNEL is a code to compute the dose rate of nuclear power plant system and equipment based on the point kernel integral method with considering of the various geometries and materials to make sure that the code can meet the requirements. In the paper, four examples are designed and calculated for different situation to prove that the code can be used for shielding calculation analysis of the nuclear power plant.

Key Words: **Radiation Dose, cosKERNEL, Point Kernel Integral Method**

1. Introduction

Radionuclides produced during reactor operation can be carried by coolant and flow into the system and equipment, it can cause radiation exposure to nuclear power plant workers. The calculation of radiation dose for system and equipment can ensure radiation dose safety for staff and nearby residents. The point kernel integral method is a method to calculate and process the radiation shielding problem.

The State Power Investment Corporation Research Institute Nuclear Power Software Development Center of China has developed a code package for design and analysis of Core and System INtegrated Engine (named COSINE) [1]. The radiation and shielding code system cosSHIELD [2] is a member of COSINE code package, which contains a Monte Carlo method code cosRMC, a discrete ordinate method code cosSN, a point kernel integral method code cosKERNEL and a radiation source term code cosSOURCE. This paper mainly describes the cosKERNEL code.

The cosKERNEL code is widely used for radiation shielding of the main and auxiliary circuit of nuclear power plants. It supports the definition of point source, surface source and body source. The calculated geometric space can be formed by the combination of different basic body. It can be used for containment building, nuclear auxiliary building and other shielding calculation.

This paper mainly introduces the function of cosKERNEL code, and the model calculation results are displayed.

2. Main Function

The cosKERNEL uses point kernel integral method to simulate the penetrating behavior of gamma rays in geometric space and improve the computation speed of optical distance by ray tracing means. The cosKERNEL code can calculate the photon flux and dose rate at the multi-dose point position of the multi-radiation source.

The calculation model of dose rate is as follows.

$$D_i = DF_i \cdot \iiint_V \frac{S_{r,i} \cdot e^{-L}}{4\pi \cdot r^2} \cdot B(E,L) \cdot dv \quad , \tag{1}$$

where

$S_{r,i}$= gamma source strength of source point r at energy group i, the formula is as shown in equation (2);

L= optical distance, the formula is as shown in equation (3);

r= distance between the source and the dose point;

$B(E,L)$= build-up factor, the formula is as shown in equation (4);

DF_i= flux dose conversion factor;

D_i= dose rate of energy group i.

2.1 Source Information

The input mode of source term information can be selected as nuclide activity or gamma source strength. Multiple sources can be computed simultaneously. The discrete source strength of energy group i is shown below.

$$S_{r,i} = S_r \cdot f_i \quad , \tag{2}$$

where

S_r= gamma source strength of source point r;

f_i= photon energy spectrum for each energy group.

2.2 Optical Distance

The optical distance is an important part of the calculation.

The cosKERNEL uses the ray tracing method to enhance the computing efficiency and the computational formula indicated below.

$$L = \sum_{n=1}^{N} \mu_n \cdot \Delta S_n \quad , \tag{3}$$

where

μ_n= cross section of area n;

$\triangle S_n$= pass through distance of the ray at area n.

2.3 Build-up Factors

The cosKERNEL can calculate photon flux rate and dose rate of many dose point at the same time. It covers ten kinds of materials for the build-up factors numeration. Goldstein Wilkins (GW) method [3] is used in the code to compute the build-up factors and the formula is as follows.

$$\begin{aligned} B(E,L) &= \sum_{i=0}^{3}\sum_{j=0}^{5} C_{ij} \cdot L \cdot E_s^{\,j} \\ E_s &= E, \quad (heavy\ material) \\ E_s &= 1/E, (light\ material) \end{aligned} \quad , \tag{4}$$

where

C_{ij}= parameters related to the source energy and material;

L= optical distance;

E= source energy.

3. Calculation Results

3.1 Examples description

This part shows four examples and their parameters are shown in table I. The comparison code used in this paper is cosRMC.

cosRMC is a member of COSINE code package. It is a Monte Carlo particle transport code jointly developed by State Power Investment Corporation Research Institute Nuclear Power Software Development Center of China (National Energy Key Laboratory of Nuclear Power Software) [4] and Tsinghua University [5]. cosRMC now has such functions as criticality calculation, fixed-source calculation, burnup calculation and kinetics simulations.

Table I. Parameters of four examples

Example	Description
Model I	**Source:** cylinder, 9cm (radius), 50cm (height), mixed with water (0.657 g/cm^3) and stainless steel (0.976 g/cm^3). **Shield:** cylinder, 1cm stainless steel (7.8 g/cm^3); cuboid, 20cm concrete (2.24 g/cm^3), 30cm away from the center of the source. **Dose Point:** 1-A: 5 cm from the cylinder shielding surface.1-B: 30 cm from the cuboid shielding surface.
Mode II	**Source:** cylinder, 10cm (radius), 50cm (height), water (1.0g/cm^3), the distance between each source is 7cm. **Shield:** cylinder, 1cm (radius), stainless steel (7.86 g/cm^3); cuboid, 20cm concrete (2.24 g/cm^3). The closest cylinder is 5cm away from the shield of the cuboid. **Dose Point:** 2-A, 2-B, 2-C, 2-D, 30 cm from the cuboid shielding surface.
Model III	**Source:** cuboid, 50×20×80 (cm), water (0.976 g/cm^3). **Shield:** The one that is closer to the source is stainless steel(7.86 g/cm^3) with 1cm thickness, the other is concrete (2.24 g/cm^3) with 20cm thickness. **Dose Point:** 3-A, 30cm from the shielding surface.
Model IV	**Source:** sphere, 25cm (radius), water (0.8 g/cm^3). **Shield:** cuboid, 20cm concrete (2.24 g/cm^3). **Dose Point:** 4-A, 30cm from the shielding surface.

The information of source strength and flux dose conversion factors are shown in table II. All diagrams in this section are top views and schematic. The air density is 1.29E-03 g/cm^3.

Table II. Part of Source Information

Average Energy (MeV)	Source Strength (1/cm^3•s)	Flux Dose Conversion Factors [6] (10^{-12}Sv•cm^{-2})
0.31	2.50E+03	1.319E+00
0.65	5.98E+04	2.893E+00
1.10	6.77E+04	4.666E+00
1.45	7.52E+04	5.877E+00
2.08	8.46E+03	7.791E+00
2.25	2.78E+01	8.218E+00
3.01	3.11E+01	1.012E+01
Total Source Strength (MeV/cm^3•s)		2.41E+05

The geometric model of four examples are shown in fig. 1-fig. 4.

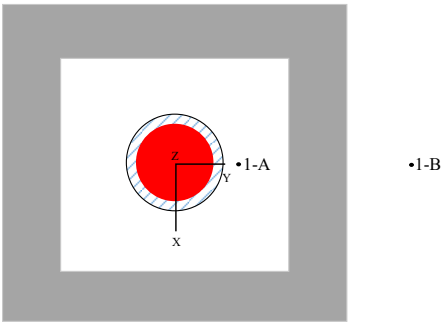

Fig. 1. Geometric model of model I.

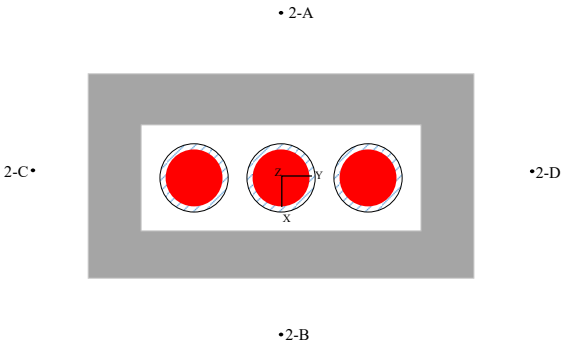

Fig. 2. Geometric model of model II.

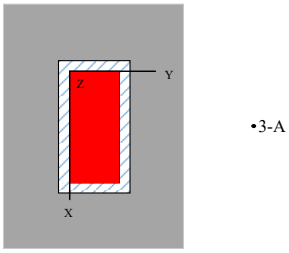

Fig. 3. Geometric model of model III.

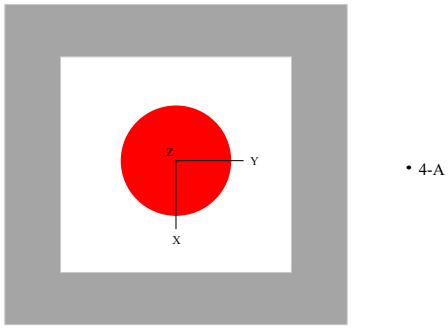

Fig. 4. Geometric model of model IV.

3.2 Calculation Results

The calculation results of the above four examples are listed in table III. The parenthesis contents shown in second column represents relative statistical error of cosRMC. The relative deviation means (cosKERNEL - cosRMC) / cosRMC×100%.

Table III. Calculation results

Dose Point	Dose Rate (mSv/h)		Relative Deviation
	cosRMC	cosKERNEL	
1-A	5.29E+00 (0.08%)	5.71E+00	7.86%
1-B	6.11E-02 (0.76%)	7.80E-02	27.72%
2-A	3.20E-01 (0.63%)	3.81E-01	19.46%
2-B	3.18E-01 (0.64%)	3.81E-01	19.81%
2-C	1.45E-01 (0.76%)	1.72E-01	18.23%
2-D	1.44E-01 (0.76%)	1.72E-01	19.15%
3-A	6.12E-01 (0.60%)	7.22E-01	17.85%
4-A	3.41E-01 (0.75%)	3.38E-01	-0.89%

From table III we can see that the relative deviation between cosKERNEL and cosRMC is less than 28%. The comparison results show that the cosKERNEL calculation results are reasonable and reliable.

4. Conclusions

This paper describes the point kernel integral code cosKERNEL in COSINE code package for plant shielding design.

The code supports the combination modeling of various geometric objects and it can calculate build-up factors of various materials. The results display that the code can be used for shielding calculation and analysis of reactor systems and equipment.

Acknowledgements

This work was supported by National Science and Technology Major Project of Large Advanced PWR and HTGR Nuclear Power Plant (2017ZX06004-002).

References

1. YIXUE CHEN, HUI YU, “Development Status of Reactor Physics Codes in COSINE Project,” *Proc. The 18th Pacific Basin Nuclear Conference*, Busan, Korea, March 18-23, 2012, Pacific Nuclear Council (2012).
2. Yeshuai Sun, Wen Song, et al, “Preliminary Application of Radiation and Shielding Code System of COSINE Code Package,” *PHYTRA4*, Marrakech, Morocco, September 17-19, 2018, Moroccan Association for Nuclear Engineering and Reactor Technology (2018) (CD-ROM).
3. Goldstein H, Wilkins J E. “Calculations of the penetration of gamma rays,” International Conference on E-business & Inform (1954).
4. Yao Qin, Hui Yu, et al, “Verification of Monte Carlo code cosRMC based on VERA core physics benchmark,” *High Power Laser and Particle beams*, 29(12), (2017).
5. Wang K , Li Z , She D , et al. “RMC – A Monte Carlo code for reactor core analysis,” *Annals of Nuclear Energy*, 82:121-129, (2015).
6. International Commission on Radiological Protection. Data for use in protection against external radiation: a report of a Task Group of Committee 3 of the International Commission on Radiological Protection [M]. Pergamon (1987).

Proceedings of the Reactor Physics Asia 2019 (RPHA19) Conference
Osaka, Japan, Dec. 2-3, 2019

GPU/CPU Concurrent Heterogeneous Parallel MOC Calculation with Asynchronous Communication Scheme

Liang Liang[a,*], Peitao Song[a], Qian Zhang[a], Zhijian Zhang[a], Qiang Zhao[a]
[a] *Fundamental Science on Nuclear Safety and Simulation Technology Laboratory, College of Nuclear Science and Technology, Harbin Engineering University, Harbin, Heilongjiang 150001, China*
[*]Corresponding author: liangliang_ls@hrbeu.edu.cn

Abstract

Recently, method of characteristics (MOC) has been widely developed as the most promise method to process the whole-core transport calculation. Meanwhile, GPU/CPU heterogeneous parallel calculation has been widely used and great performance has been achieved. In this research, GPU/CPU concurrent heterogeneous parallel MOC calculation is implemented to exploit all the computational resource in the heterogeneous high performance computer (HPC) while the asynchronous communication scheme is introduced in to improve the parallel efficiency. In order to accomplish this scheme, both MPI, OpenMP, CUDA protocols are introduced. The spatial domain decomposition (SDD) technique provides the coarse-grained parallelism with the MPI protocol while the fine-grained parallelism is exploited through OpenMP (in CPU calculated domain) and CUDA (in GPU calculated domain) based on the ray parallelization. Numerical results indicate that both the concurrent heterogeneous parallel calculation and the asynchronous communication scheme are effective to improve the performance of the parallel MOC calculation. Moreover, the CPUs/GPUs heterogeneous clusters significantly outperform the CPUs clusters, which makes the large-scale whole-core transport calculation is more practicable.

Key Words: **Whole-core Transport, GPU/CPU Concurrent Heterogeneous Parallel, MOC, Spatial Domain Decomposition, Asynchronous communication**

1. Introduction

Recently whole-core transport calculation is widely developed in reactor physics calculation to obtain high-fidelity simulation. Most of the research is based on the MOC method [1], such as CRX [2], DeCART [3], nTRACER [4], and NECP-X [5]. CPU-based large-scale parallel algorithms have been widely introduced in and deployed on the supercomputer [6]. However, the whole-core high-fidelity simulation is still time consuming, even using the newest CPU-based supercomputers.

Heterogeneous parallelization is one of the most promising approaches to improve the computational performance of the modern HPC systems. With the dramatically enhanced performance, the heterogeneous hybrid parallel MOC method is practicable to accomplish the whole-core transport calculations. Choi et al. proposed a technique to accelerate MOC calculation with anisotropic scattering source on GPUs [7]. In our former research, a 2D MOC parallel calculation based on GPU is implemented and a performance analysis model is introduced to guide the performance optimization [8].

In this paper, GPU/CPU concurrent heterogeneous parallel spatial domain decomposition (SDD) [9] MOC calculation is implemented. The SDD technique provides the coarse-grained parallelism with the MPI protocol while the fine-grained parallelism is exploited through OpenMP (in CPU calculated domain) and CUDA (in GPU calculated domain) based on the ray parallelization.

Moreover, the asynchronous communication scheme is applied to reduce the communication time. The overlapping asynchronous communication between GPU and CPU has been introduced into this research to overlap the CPU communication and the GPU transport calculation. The asynchronous data copy between GPU and CPU are processed to further improve the parallel performance.

Numerical results indicate that the GPU/CPU concurrent heterogeneous calculation is able to exploit all the computational resource in the heterogeneous nodes while the asynchronous communication scheme significantly improve the parallel efficiency.

2. Concurrent Parallel Heterogeneous MOC Calculation

2.1 MOC Basic Theory

The basic theory of MOC method is shown as below. The single group neutron transport equation is as Eq. (1) and the MOC formed neutron transport equation is as Eq. (2).

$$\varepsilon\frac{\partial\psi_{m,g}(\mathbf{r})}{\partial x}+\eta\frac{\partial\psi_{m,g}(\mathbf{r})}{\partial y}+\mu\frac{\partial\psi_{m,g}(\mathbf{r})}{\partial z}+\Sigma_{t,g}(\mathbf{r})\psi_{m,g}(\mathbf{r})=Q_g(\mathbf{r}) \quad (1)$$

Where;

ε,η,μ is the direction cosine.

m is the discrete direction.

g is the energy group.

$\psi_{m,g}(\mathbf{r})$ is the angular flux of the direction m and energy group g in the position $\mathbf{r}$.

$\Sigma_{t,g}(\mathbf{r})$ is the transport cross section of group g in the position $\mathbf{r}$.

$Q_g(\mathbf{r})$ is the total source of group g in the position $\mathbf{r}$.

$$Q_g(\mathbf{r})=\frac{\chi_g}{4\pi k_{eff}}\sum_{g'=1}^{G}\nu\Sigma_{f,g'}\phi_{g'}(\mathbf{r})+\frac{1}{4\pi}\sum_{g'=1}^{G}\Sigma_{s,g'\to g}\phi_{g'}(\mathbf{r})$$

Where;

k_{eff} is the eigenvalue.

χ_g is the fission spectrum.

$\nu\Sigma_{f,g'}$ is the fission neutron number of group g'

$\Sigma_{s,g'\to g}$ is the scatter cross section from g' to g

$\phi_{g'}$ is the scalar flux of group g'.

$$\frac{d\psi_{m,g}(s)}{ds}+\Sigma_{t,g}(\mathbf{r})\psi_{m,g}(\mathrm{s})=Q_g(\mathbf{r}) \quad (2)$$

With the flat source and the flat cross section approximation, the analytical solution of Eq. (2) can be easily obtained like Eq. (3).

$$\psi_{m,g}(s)=\psi_{m,g}^{in}e^{-\Sigma_{t,g}s}+\frac{Q_g}{\Sigma_{t,g}}(1-e^{-\Sigma_{t,g}s}) \quad (3)$$

2.2 Implementation of GPU/CPU Concurrent Heterogeneous Parallel MOC Calculation

SDD technique is important for the simulations of the whole-core transport calculation on the HPC cluster. The spatially decomposed subdomain is managed by a MPI [10] process, which will be calculated by GPU or OpenMP [11] multi-threads. The independence of those rays provides the possibility and the flexibility of massive ray parallelization. As a result, the ray parallelization involves parallelizing the loop over all rays in all discretized directions. The ray parallelization is implemented using a shared memory model (e.g. OpenMP, CUDA [12]).

According to the computational ability, the whole problem is divided into several subdomains, which is assigned to the corresponding CPU or GPU. As mentioned above, the ray parallelization is performed by OpenMP protocol in CPU and CUDA protocol in GPU.

The concurrent MPI + OpenMP/CUDA programming model is employed in this implementation to perform the concurrent CPU/GPU heterogeneous parallelization. As illustrated in Fig. 1, this is a heterogeneous cluster which contains N compute nodes connected by high-speed interconnection fabrics. Each heterogeneous node contains N_c CPU-cores and N_g GPUs, and commonly N_c is assumed to be larger than N_g. Based on this hardware model, two levels of parallelism are utilized to addressing the MOC application onto heterogeneous HPC cluster.

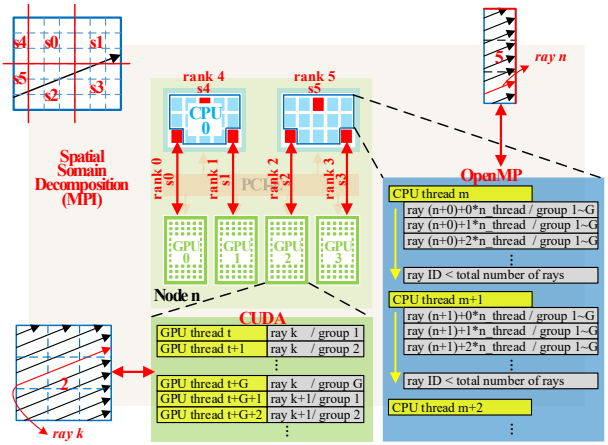

Fig. 1. MPI + OpenMP/CUDA Programming Model with Concurrent SDD and Ray Parallelization.

3. Asynchronous Communication Scheme

The communication time in GPU/CPU heterogeneous parallel calculation contains two parts: 1) the communication between each CPU process, 2) the data copy between GPU and CPU. In order to reduce the communication impact, the overlapping asynchronous communication scheme is implemented. The basic idea is that CPU processes the communication meanwhile GPU performs the calculation.

3.1 Overlapping asynchronous communication between CPU

The overlapping asynchronous communication between CPU is accomplished by starting process communication between CPU immediately after initializing the GPU. The MPI communication and the MOC sweep on GPU (CPU) are simultaneously performed. This scheme achieves the overlap between communication and the MOC sweep, which will reduce the overall runtime. The negative impact is the iteration degradation, which is negligible. In general, the overlapping asynchronous communication scheme will hide the communication time while the iteration degradation is negligible.

3.2 Asynchronous data-copy between GPU and CPU

According to the former research, the communication cost of the data-copy between GPU and CPU also have large impact on the performance of the parallel efficiency of the heterogeneous application. To address this issue, the asynchronous data-copy between GPU and CPU is implemented like shown in Fig. 2, In the original way, the GPU/CPU data-copy, GPU sweep, CPU communication are executed serially while in the overlapping asynchronous communication scheme, the communication and the computation are executed concurrently, which will reduce lots of runtime on each iteration. In this research this new scheme is implemented and the numerical results demonstrate that the great improvement is obtained.

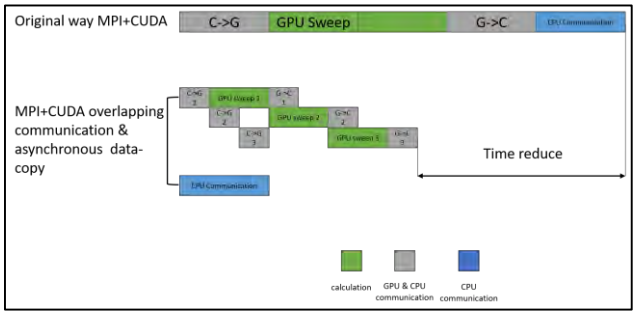

Fig. 2. the Asynchronous Communication Scheme

4. Numerical Results

The TianHe-ES supercomputer (TH-ES for short) serves as the computational platform which is deployed in the National Supercomputing Center in Tianjin. The computing subsystem of TH-ES is constructed with 40 heterogeneous nodes, each of which is configured with two Intel Xeon CPU E5-2690 v4 CPUs and two Tesla K80 GPUs.

In order to evaluate the performance of the new heterogeneous algorithm, a series of runs are performed for a 2D fictitious whole-core problem. This problem consists of 100 UO2 and MOX fuel assemblies from the C5G7 2D [13] benchmark aligned in a chessboard pattern in Fig. 3.

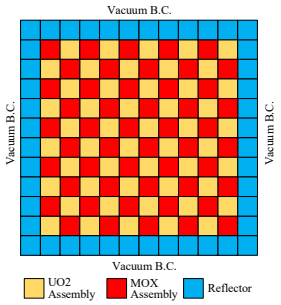

Fig. 3. The Mock Whole-core Problem.

Fig. 4 shows the runtime of each parallelization with different number of heterogeneous nodes while Fig. 5 shows the parallel efficiency. In Fig. 4, MPI+CUDA means that CPUs do not perform the MOC sweep while the MPI+CUDA+OpenMP means both CPU and GPU perform the MOC sweep concurrently. Numerical results suggest that GPU/CPU concurrent calculation is able to exploit all the computational resource in the heterogeneous node, which can bring 14.5% performance improvement when using 5 nodes. With the increase of the nodes, this value increases slightly.

Moreover, MPI+CUDA+OpenMP+Asynchronous means that the asynchronous communication scheme is also applied and 21.8% improvement is observed when using 5 nodes. Since the asynchronous communication scheme significantly reduce the communication time, the performance improvement increases with the number of the nodes arising.

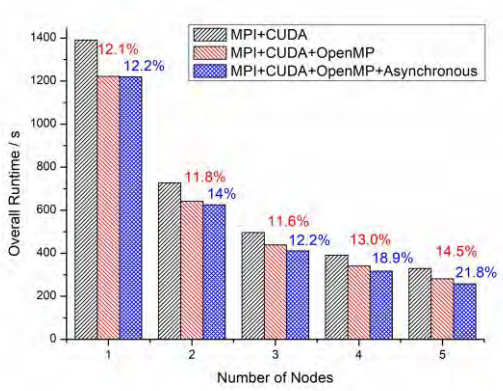

Fig. 4. Performance Comparison of Each Parallelization

With the increase of the number of the calculation nodes, all the parallel efficiency decrease. The parallel efficiency of the parallelization without asynchronous communication scheme decreases dramatically. According to Fig. 5, the asynchronous communication scheme contributes remarkable improvement. The overall parallel efficiency is 95.8% when using 5 nodes to calculate while the parallelization without asynchronous communication scheme is only 84.5%.

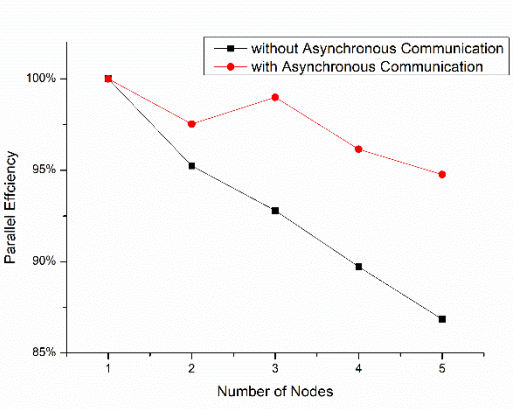

Fig. 5. Parallel Efficiency with and without Asynchronous Communication Scheme

The same C5G7 based fictitious 2D whole-core problem is also performed in the CPU nodes in TH-ES HPC system. Fig. 6 illustrates the performance comparison of the CPUs/GPUs heterogeneous nodes and CPUs nodes. The MPI parallelization is performed with 5,10, 15, and 20

CPUs nodes. As shown in Fig. 6, The CPUs/GPUs heterogeneous nodes significantly outperform the CPUs nodes, and the computing capability of one CPUs/GPUs heterogeneous node is equal to five CPUs nodes in our implementation.

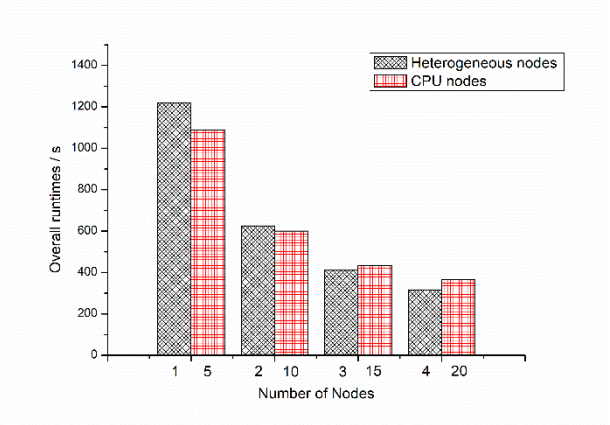

Fig. 6 Performance Comparison of the CPU/GPU Heterogeneous Node and the CPU Nodes

5. Conclusion

In this paper, GPU/CPU concurrent heterogeneous parallel SDD MOC calculation is implemented and the asynchronous communication scheme is applied to reduce the communication time. A 2D fictitious whole-core problem is calculated to analyze the performance of the new implementation.

Numerical results show that both the concurrent heterogeneous calculation and the asynchronous communication scheme are effective to reduce the overall runtime. Overall parallel performance improvement is about 21.8% when using 5 heterogeneous nodes. Numerical results also indicate that the computing capability of the CPUs/GPUs heterogeneous node is basically five times faster than the CPUs node in our implementation.

This work performs remarkable improvement, which make the large-scale whole-core transport calculation more practicable. The implementation and performance analysis of the 3D whole-core transport calculation on heterogeneous cluster will be the future focus.

Acknowledgements

This work is supported by the fund provided by the Science and Technology on Reactor System Design Technology Laboratory, the Heilongjiang Province Science Foundation for Youths [QC2018003], and Research on Key Technology of Numerical Reactor Engineering [J121217001]. This work is also supported by the project from the Nuclear Power Technology Innovation Center.

References

1. Askew JR, 1972. “A Characteristics Formulation of the Neutron Transport Equation in Complicated Geometries”. *AEEW-M*, **1108**.
2. Cho NZ, Lee GS, Park CJ. “Partial current-based CMFD acceleration of the 2D/1D fusion method for 3D whole-core transport calculations,” *Trans. Am. Nucl. Soc.*, **88**, 594-594 (2003).
3. Joo HG, Cho JY, Kim KS, et al., “Methods and performance of a three dimensional whole-core transport code DeCART,” *International conference on physics of reactors*, Chicago, Illinois, USA, Apr 25-29 (2004).
4. Jung YS, Shim CB, Lim CH, et al., “Practical numerical reactor employing direct whole core neutron transport and subchannel thermal/hydraulic solvers,” *Ann. Nucl. Energy*, **62**, 357–374 (2013).
5. Chen J, Liu ZY, Zhao C, et al., “A new high-fidelity neutronics code NECP-X,” *Ann. Nucl. Energy*, **116**, 417–428, (2018).
6. Ryu M, Jung YS, Cho HH, et al., “Solution of the BEAVRS benchmark using the nTRACER direct whole core calculation code,” *Journal of Nuclear Science and Technology*, **52**(7-8), 961-969, (2015).
7. Choi N, Kang J, Joo HG, “Massively parallel method of characteristics neutron transport calculation with anisotropic scattering treatment on GPUs,” P*roceeding of International conference on high performance computing in Asia Pacific Region*, Chiyoda, Tokyo, Japan, January 28-31. (2018).
8. Song PT, Zhang ZJ, Liang L, et al., “Implementation and performance analysis of the massively parallel method of characteristics based on GPU,” *Ann. Nucl. Energy*, **131**, 257-272, (2019).
9. Kosaka S, Saji E, “Transport theory calculation for heterogeneous multi-assembly problem by characteristics method with direct path linking technique.” *J. Nucl. Sci. Technol*, **37**, 1015-1023. (2000).
10. Mathematics and Computer Science, The Message Passing Interface (MPI) standard, http://www.mcs.anl.gov/research/projects/mpi/, (2019).
11. The OpenMP API specification for parallel programming, https://www.openmp.org/, (2019).
12. CUDA toolkit documentation, CUDA C programming guide, https://docs.nvidia.com/cuda/cuda-c-programming-guide/index.html, (2019).
13. Lewis EE, Palmiotti G, Taiwo TA, et al., “Benchmark Specifications for Deterministic MOX Fuel Assembly Transport Calculations without Spatial Homogenization,” Organization for Economic Co-operation and Development’s Nuclear Energy Agency, (2003).

Proceedings of the Reactor Physics Asia 2019 (RPHA19) Conference
Osaka, Japan, Dec. 2-3, 2019

Impact of Diffusion Coefficient and Correction Term on the Convergence of CMFD Acceleration for MOC

Yoshiki Oshima[a,*], Tomohiro Endo[a] and Akio Yamamoto[a]
[a]*Nagoya University, Furo-cho, Chikusa-ku, Nagoya-shi, 464-8603, Japan*
[*]Corresponding author: y-oshima@fermi.energy.nagoya-u.ac.jp

Abstract

The Coarse Mesh Finite Difference (CMFD) acceleration is widely used for neutron transport calculations, *e.g*., for the Method of Characteristics (MOC). However, numerical instability is observed for optically thick meshes. In the previous studies, the diffusion coefficient used in CMFD was corrected to improve the convergence. The present study tries to clarify the impact of diffusion coefficient and magnitude of correction term, which are used in CMFD, on the convergence performance of CMFD. The results indicated that the correction term became smaller when the modified diffusion coefficient, which improved the stability of CMFD, was used. However, when the diffusion coefficients were further adjusted to make correction terms smaller, further improvement of the convergence was not observed. These results imply that the limitation of the current finite difference approximation formula used for CMFD acceleration.

Key Words: **CMFD acceleration, diffusion coefficient, correction term, convergence, MOC**

1. Introduction

The neutron transport method such as the Method of Characteristics (MOC) requires longer computation time for a fuel assembly or a core analysis when no acceleration method is applied. Convergence performance of MOC depends on its scattering ratio, which is the ratio of scattering cross section to total cross section, and eigenvalue dominance ratio. Especially in a light water reactor analysis, an efficient convergence acceleration method is crucial and the Coarse Mesh Finite Difference (CMFD) acceleration method is generally used because scattering ratio and eigenvalue dominance ratio are close to 1 in a light water reactor analysis [1–3].

In CMFD, diffusion calculations are performed using the modified finite difference diffusion approximation in coarse meshes. Generally, since the net neutron current obtained by MOC is not consistent to that by a finite difference diffusion approximation, a correction term is used to reproduce the net current by MOC. Though the CMFD method is very efficient, the convergence issue is observed for optically thick meshes [4].

Various studies have been carried out to improve the stability of CMFD and it is known that a correction of the diffusion coefficient is a remedy [5]. Various methods have been proposed *e.g*., multiplying the diffusion coefficient by a constant [4], the effective diffusion coefficient [6], adding a constant to the diffusion coefficient [5] and the diffusion coefficient where transport calculation and diffusion calculation become equivalent [7]. Their effectiveness is evaluated by the linearized Fourier analysis.

These conventional studies on the stability of CMFD generally focused on the diffusion coefficient used in the finite difference approximation formula. Therefore, the magnitude of the correction term in CMFD has not been explicitly discussed. CMFD uses the finite difference approximation formula based on the diffusion theory. When the correction term is large, it deviates from the original finite difference approximation formula. Therefore, the magnitude of the correction term may have an impact on the convergence performance.

This study confirms the magnitude of the correction term for various diffusion coefficients. Impact of the correction term on the convergence property is also discussed.

2. Theory

Let us consider a two-node problem shown in Fig. 1

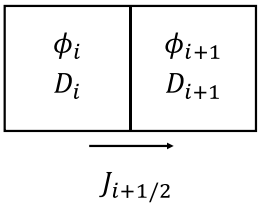

Fig. 1. ϕ, D, J in coarse meshes.

In CMFD, the scalar fluxes and the net neutron current in coarse meshes have the following relation:

$$J_{i+1/2} = -\hat{D}^{FD}_{i+1/2}(\phi_{i+1} - \phi_i) + \tilde{D}^{COR}_{i+1/2}(\phi_{i+1} + \phi_i), \quad (1)$$

where J is the net neutron current, ϕ is the scalar flux, $\tilde{D}^{COR}$ is the correction factor, $\hat{D}^{FD}_{i+1/2}$ is given by:

$$\hat{D}^{FD}_{i+1/2} = \frac{2D_iD_{i+1}}{D_i\Delta_{i+1} + D_{i+1}\Delta_i}, \quad (2)$$

where D is the diffusion coefficient, Δ is the coarse mesh size, i is an index of the coarse mesh, $i+1/2$ indicate the mesh interface between i and $i+1$.

Using $\phi^{MOC}_i, J^{MOC}_{i+1/2}$ calculated by MOC and Eq. (1), $\tilde{D}^{COR}_{i+1/2}$ is written as:

$$\tilde{D}^{COR}_{i+1/2} = \frac{J^{MOC}_{i+1/2} + \hat{D}^{FD}_{i+1/2}(\phi^{MOC}_{i+1} - \phi^{MOC}_i)}{\phi^{MOC}_{i+1} + \phi^{MOC}_i}. \quad (3)$$

In this study, diffusion coefficient D_i of the following four definitions are used:

(a) Conventional diffusion coefficient:

$$D^{Conv}_i = \frac{1}{3\Sigma_{tr,i}}, \quad (4)$$

where Σ_{tr} is macroscopic transport cross section.

(b) Artificial grid diffusion coefficient:

$$D^{AGD}_i = D^{Conv}_i + \frac{\Delta_i}{4}. \quad (5)$$

The convergence of CMFD is equivalent to that of p-CMFD when AGD is used [8].

(c) Diffusion coefficient multiplied by α:

$$D^{*}_i = \alpha D^{Conv}_i, \quad (6)$$

where α is determined to minimize $|\tilde{D}^{COR}_{i+1/2}|$ as discussed in Section 4.

(d) Diffusion coefficient added by energy group dependent $\alpha_g\Delta_i$:

$$D^{+}_i = D^{Conv}_i + \alpha_g\Delta_i, \quad (7)$$

where g is an index of the energy group. The α_g is determined in each energy group.

3. Calculation Conditions

The KAIST benchmark problem 2A shown in Fig. 2 is used for verification calculations. The fuel assemblies consist of arrays of 17×17 fuel rods. The symbols (I)–(V) represent UOX-1, UOX-2(CR), UOX-2(BA_{16}), MOX-1, and MOX-1(BA_8), respectively.

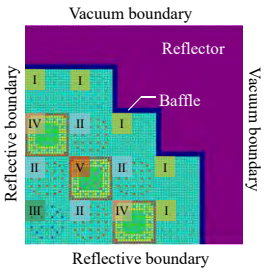

Fig. 2. KAIST benchmark problem 2A.

The GENESIS code is used for MOC calculations [9]. The calculation conditions are as follows: ray trace width is 0.1 cm, the number of azimuthal angles is 48 for 2π, the number of polar angles 4 for π (TY-quadrature), the number of energy group is 7, the number of azimuthal divisions in a pin-cell is 16, the number of radial divisions in a pin-cell is 6, the number of maximum inner iteration is 2, the number of maximum outer iteration is 50, convergence criteria for k_{eff} and ϕ of MOC are 5.0×10^{-6} and 1.0×10^{-5}, convergence criteria for k_{eff} and ϕ of CMFD are 5.0×10^{-7} and 1.0×10^{-6}. The GENESIS code can set CMFD mesh regardless of the input geometry. In this analysis, two different mesh sizes for CMFD are used: 1×1 cell and 5×5 cells for a CMFD mesh, *i.e.*, mesh sizes are 1.26 cm and 6.30 cm, respectively.

4. Results and Discussions

4-1. Results of mesh size 1.26 cm

Figure 3 shows the correlation between the converged neutron currents estimated by MOC and that by finite difference approximation using D^{Conv}_i and D^{AGD}_i for all CMFD cells. The horizontal and vertical axes of Fig. 3 correspond to the first and negative of the second terms on the right side of Eq. (3), respectively. In the vicinity of the red dotted line, these terms cancel out each other and then $\tilde{D}^{COR}_{i+1/2} \approx 0$. The histogram of $|\tilde{D}^{COR}_{i+1/2}|$ is shown in Fig. 4.

Figures 3 and 4 show that the magnitudes of $\tilde{D}^{COR}_{i+1/2}$ are small for both diffusion coefficients. Moreover, MOC using either diffusion coefficient converged. These results suggest that the finite difference approximation formula of Eq. (1) is adequate for optically thin meshes.

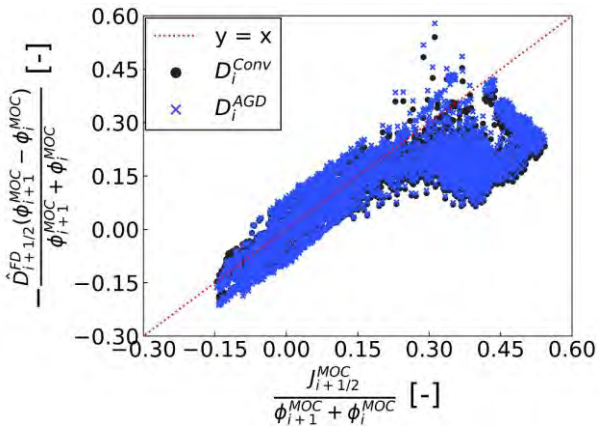

Fig. 3. Relation between the neutron currents obtained by MOC and finite difference diffusion approximation (mesh size 1.26 cm).

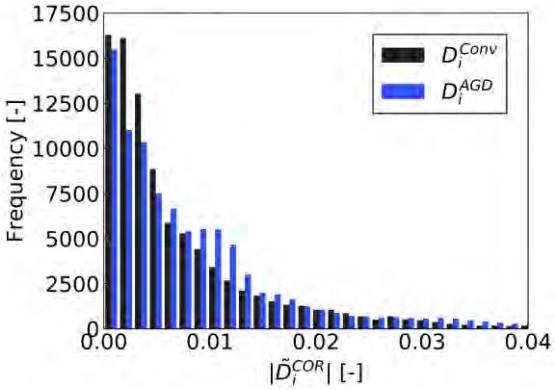

Fig. 4. The histogram of $\left|\tilde{D}_{i+1/2}^{COR}\right|$ for mesh size 1.26 cm.

4-2. Results of mesh size 6.30 cm

Figures 5 and 6 show the results for mesh size 6.30 cm in the same manner as Figs. 3 and 4. The magnitudes of $\tilde{D}_{i+1/2}^{COR}$ using either diffusion coefficient become larger than that for mesh size 1.26 cm. However, when D_i^{AGD} is used, the magnitude of $\tilde{D}_{i+1/2}^{COR}$ becomes smaller in comparison to D_i^{Conv}. Note that the MOC calculations using D_i^{Conv} and D_i^{AGD} diverges and converges, respectively.

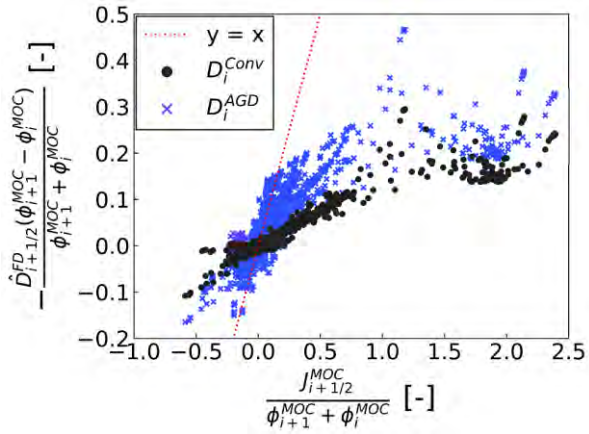

Fig. 5. Relation between the neutron currents obtained by MOC and finite difference diffusion approximation (mesh size 6.30 cm).

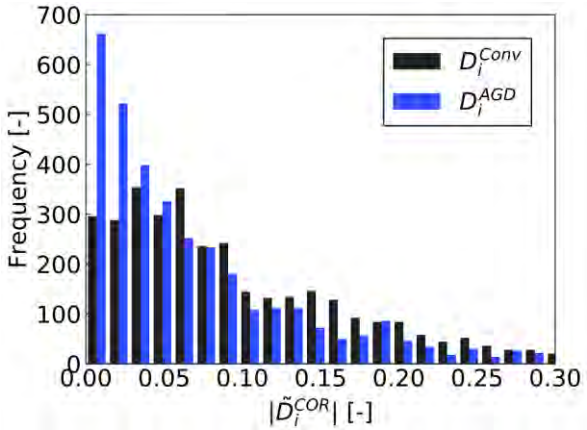

Fig. 6. The histogram of $\left|\tilde{D}_{i+1/2}^{COR}\right|$ for mesh size 6.30 cm.

The above results suggest that the magnitude of $\tilde{D}_{i+1/2}^{COR}$ becomes smaller when D_i^{AGD}, which shows no convergence issue, is used. Figure 5 suggests that further corrections on the diffusion coefficient are possible to make the magnitude of $\tilde{D}_{i+1/2}^{COR}$ smaller. Therefore, the diffusion coefficient D_i^*, which is calculated by Eq. (6), is considered. The correction value α, which is energy group independent value, is determined to minimize overall $\left|\tilde{D}_{i+1/2}^{COR}\right|$. Furthermore, Fig. 7 shows energy group dependent $\tilde{D}_{i+1/2}^{COR}$ in Fig. 5 for D_i^{AGD}. Figure 7 suggests that corrections on the diffusion coefficient would be energy group dependent to further minimize $\left|\tilde{D}_{i+1/2}^{COR}\right|$. Therefore, in addition to D_i^*, D_i^+, which has the group dependent correction term, is considered.

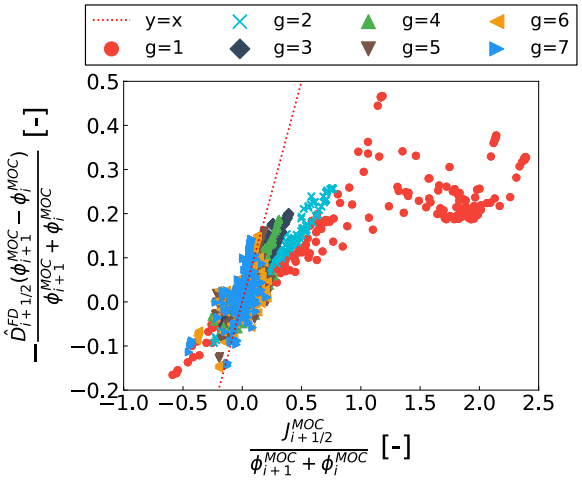

Fig. 7. Relation between the neutron currents obtained by MOC and finite difference diffusion approximation (D_i^{AGD}, group dependent, mesh size 6.30 cm).

The correction values α and α_g are determined by trial and error to minimize $\left|\tilde{D}_{i+1/2}^{COR}\right|$. As a result, $\alpha = 7.5$ and $\alpha_g = \{2.0, 1.0, 0.7, 0.5, 0.3, 0.2, 0.1\}$ are used. Figures 8 and 9 show the magnitudes of $\tilde{D}_{i+1/2}^{COR}$ using $D_i^{Conv}, D_i^{AGD}, D_i^*$ and D_i^+.

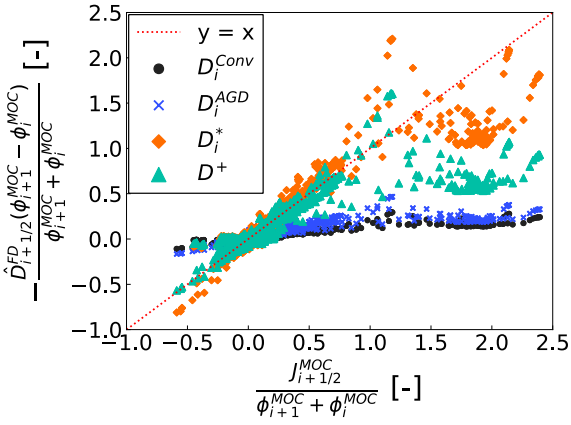

Fig. 8. Relation between the neutron currents obtained by MOC and finite difference diffusion approximation (various diffusion coefficients, mesh size 6.30 cm).

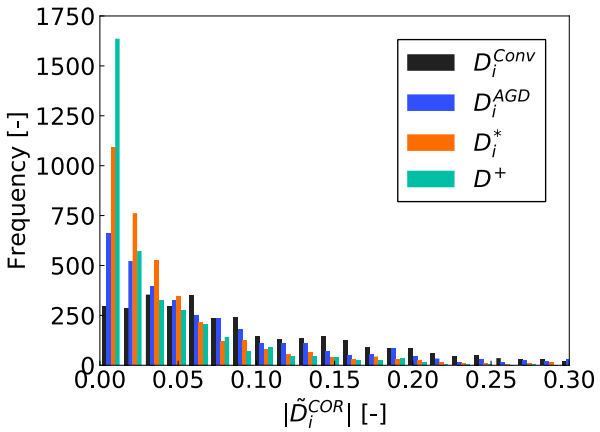

Fig. 9. The histogram of $\left|\tilde{D}_{i+1/2}^{COR}\right|$ using various diffusion coefficients.

The convergence performance for D_i^{AGD}, D_i^* and D_i^+ is shown in Figs. 10 and 11. Note that MOC using D_i^{Conv} diverges. Figures 10 and 11 indicate that no convergence improvement is observed for D_i^* and D_i^+. Namely, even if the correction term is further minimized, more improvement of convergence is not achieved. This suggests that the limitation of the current finite difference formula and prolongation process, in which scalar flux distribution inside a CMFD mesh is considered.

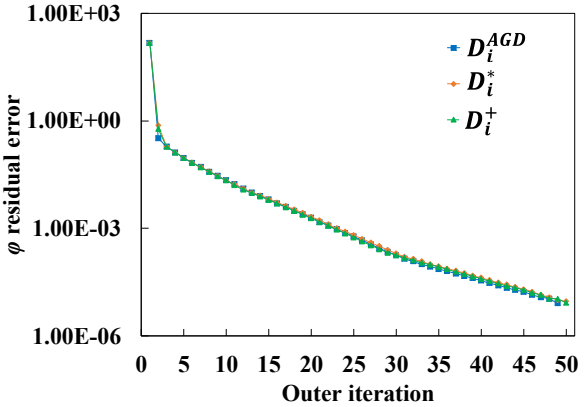

Fig. 10. The residual errors of ϕ.

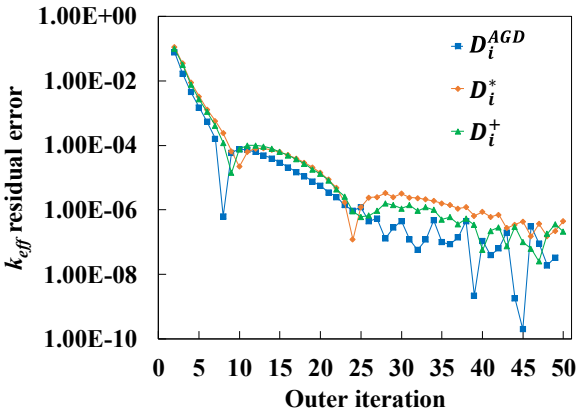

Fig. 11. The residual errors of k_{eff}.

5. Conclusions

In this study, impact of the diffusion coefficient and the correction term in the CMFD acceleration method were investigated to improve the convergence of CMFD. The magnitude of the correction term is small and the validity of the finite difference formula is confirmed for optically thin meshes. Contrary, when the optical mesh size becomes large, the correction term becomes larger and the convergence becomes worse. However, when the modified diffusion coefficient (AGD) which improves the stability of CMFD is used, the correction term becomes smaller and the calculation converges. Although the diffusion coefficient was further corrected to make the correction term smaller, the improvement of the convergence was not observed. These results suggest that the finite difference formula currently used in CMFD has the limitation and the improvement of the formula including reduction and prolongation would be necessary to improve the convergence performance.

References

1. Smith K, "Nodal Method Storage Reduction by Non-linear Iteration," *Trans. Am. Nucl. Soc.*, **44**, 265–266 (1983).
2. Smith K, Rhodes JD, "Full-core, 2-D, LWR Core Calculations with CASMO-4E," *Proc. PHYSOR 2002,* Seoul, South Korea, Oct. 7–10 (2002) (CD-ROM).
3. Joo HG, Cho JY, Kim KS, *et al.*, "Methods and Performance of a Three-dimensional Whole-Core Transport Code DeCART," *Proc. PHYSOR2004*, Chicago, Illinois, USA, Apr. 25–29 (2004) (CD-ROM).
4. Yamamoto A, "Generalized Coarse Mesh Rebalance Method for Acceleration of Neutron Transport Calculations," *Nucl. Sci. Eng.,* **151**, 274–282 (2005).
5. Jarrett M, Kochunas B, Zhu A, *et al.*, "Analysis of Stabilization Techniques for CMFD Acceleration of Neutron Transport Problems," *Nucl. Sci. Eng.,* **184**, 208–227 (2016).
6. Larsen E, "Infinite Medium Solutions to the Transport Equation, Sn Discretization Schemes, and the Diffusion Approximation," *Proc. M&C + SNA*, Salt Lake City, UT, USA, Sep. 9–13 (2001) (CD-ROM).
7. Yamamoto A, Endo T, Giho A, "Transport Consistent Diffusion Coefficient for CMFD Acceleration and Comparison of Convergence Properties," *J. Nucl. Sci. Technol.*, DOI:10.1080/00223131.2019.1618405 (2019).
8. Cho NZ, Lee GS, Park CJ, "Partial Current-based CMFD Acceleration of the 2D/1D Fusion Method for 3D Whole-core Transport Calculations," *Trans. Am. Nucl. Soc.*, **88**, 594–596 (2003).
9. Yamamoto A, Giho A, Kato Y, *et al.*, "GENESIS: a Three-dimensional Heterogeneous Transport Solver based on the Legendre Polynomial Expansion of Angular Flux Method," *Nucl. Sci. Eng.*, **186**, 1–22 (2017).

Application of Improved Tone's Method in STREAM for Fast Reactor Analysis

Xianan Du, Sooyoung Choi, Jiwon Choe, Woonghee Lee, and Deokjung Lee*

Ulsan National Institute of Science and Technology (UNIST)

50 UNIST-gil, Ulsan 44919, Republic of Korea

*Corresponding author: deokjung@unist.ac.kr

Abstract

In order to perform reactor core analysis with high accuracy, appropriate resonance treatment method plays a very important role within the whole calculation procedures. On the other hand, the fast reactor designs are the best choices to solve future energy problem. Therefore, the in-house code STREAM, which is initially developed for light water reactor calculation, is decided to upgrade for fast reactor analysis. Current work implements the Improved Tone's Method into the STREAM code to perform 2-D pin-cell/assembly calculation. Several verification tests show the accuracy of new STREAM code, with less than 50 pcm difference on k_{eff} value.

Key Words: **STREAM; Improved Tone's Method; Fast Reactor Analysis**

1. Introduction

In the previous work[1], the STREAM code was coupled with TULIP[2] code to perform fast reactor analysis. In that work, the Tone's method was used to calculate self-shielded cross sections. Due to the limitation of TULIP code, only 1-D geometry can be dealt with during the resonance calculation. An equivalent 1-D cylinder geometry should be used to generate self-shielded cross section for the 2-D assembly problem. This way works only if the assembly has the natural ring-wise characters. Therefore, it is necessary to have the 2-D resonance calculation capability in the STREAM code.

Compared with subgroup method or hyperfine-group method, the improved Tone's method attracts lots of attention in the recent decade due to its enough accuracy and efficiency[3-5]. In this paper, the improved Tone's method is implemented into the STREAM code. Considering the existed nuclear data library of TULIP code, these two codes are merged to perform 2-D fast reactor assembly calculation.

2. Methodology

To start with, the self-shielded cross sections of isotope r in the region i can be expressed as:

$$\sigma_{g,r,i} = \int_{\Delta E_g} \sigma_{r,i}(E)\phi_{r,i}(E)dE \Big/ \int_{\Delta E_g} \phi_{r,i}(E)dE \quad (1)$$

Based on the narrow resonance approximation, the neutron flux is approximately calculated by the total cross section and escape cross sections:

$$\phi_{r,i}(E) \approx \frac{1}{E}\frac{1}{\Sigma_{t,i}(E)+\Sigma_{e,g,r,i}} \quad (2)$$

where $\Sigma_{e,g,r,i}$ is escape cross sections for group g, isotope r and region i.

The escape cross section is calculated by using background cross section:

$$\Sigma_{e,g,r,i} = N_{r,i}\sigma^0_{t,g,r,i} - \sum_{k\neq r}\Sigma_{t,g,k,i} \quad (3)$$

where $\sigma^0_{t,g,r,i}$ is the background cross section and N is the nuclide density.

To determine the background cross sections, the collision probabilities and total cross sections can be used:

$$\sigma^0_{t,g,r,i} = \frac{\sum_j \sum_{k\neq r} P_{ji,g}\Sigma_{t,g,k,j}V_j}{\sum_j P_{ji,g}N_{r,j}V_j} \quad (4)$$

where $P_{ij,g}$ is the collision probability from region i to region j of group g. V is the volume.

The Eq. (4) comes from the original Tone's method[6]. In the 1-D problem, the collision probabilities are easy to obtain. However, it is quite time consumption to get collision probabilities in the 2-D or complex geometry.

According to the improved Tone's method, the background cross sections can be alternatively obtained with two fixed-source equations:

$$\begin{aligned}\Omega\cdot\nabla\psi_{1,g,r}(\mathbf{r},\Omega)+\Sigma_{t,g}(\mathbf{r})\psi_{1,g,r}(\mathbf{r},\Omega) &= \sum_{k\neq r}\Sigma_{t,g,k}(\mathbf{r}) \\ \Omega\cdot\nabla\psi_{2,g,r}(\mathbf{r},\Omega)+\Sigma_{t,g}(\mathbf{r})\psi_{2,g,r}(\mathbf{r},\Omega) &= N_r(\mathbf{r})\end{aligned} \quad (5)$$

And the background cross sections are determined by using the solution of Eq.(5):

$$\sigma^{0}_{t,g,r,i} = \frac{\int_{V_i} dV \int_{4\pi} d\Omega \psi_{1,g,r}(\mathbf{r},\Omega)}{\int_{V_i} dV \int_{4\pi} d\Omega \psi_{2,g,r}(\mathbf{r},\Omega)} = \frac{\phi_{1,g,r,i}}{\phi_{2,g,r,i}} \quad (6)$$

Figure 1 shows the flowchart of new STREAM code with improved Tone's method.

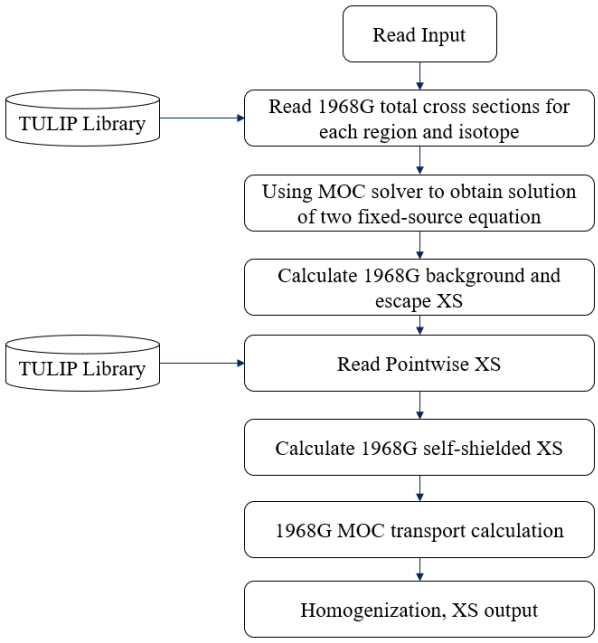

Figure 1 Flowchart of STREAM code using improved Tone's method

3. Verification Tests

3.1 Simplified Pin-cell Problem

For the initial test, a simplified rectangular fast reactor pin-cell calculation has been performed. Figure 2 shows the geometry information and Table 1 shows the specification of the problem.

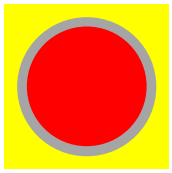

Figure 2 Simplified pin-cell problem

Table 1 Geometry and composition of simplified pin-cell problem

Region	Radius/Pitch, cm	Isotope	Nuclide Density, 10^{24} at/cm^3
Fuel	0.3236	U235	3.08220E-05
		U238	1.82440E-02
		Pu239	2.81470E-03
Cladding	0.3857	Cr52	8.68256E-03
		Fe56	6.39008E-02
Coolant	0.95186	Na23	2.22720E-02

At first, the 1968-group self-shielded cross sections are compared between TULIP and STREAM code. In TULIP code, the cross sections are prepared by 1-D equivalent cylinder geometry. Figures from Figure 3 to Figure 8 show the microscopic total cross sections and its difference of each nuclide. For a pin-cell problem, it does not have too much different between 1-D and 2-D resonance calculation. Therefore, for the generated cross sections set, the biggest relative differences are around 2.5%, and RMS of relative differences of each nuclide are 0.02%(U-5), 0.13%(U-8), 0.09%(Pu-9), 0.04%(Cr-52), 0.13%(Fe-56), 0.03%(Na-23).

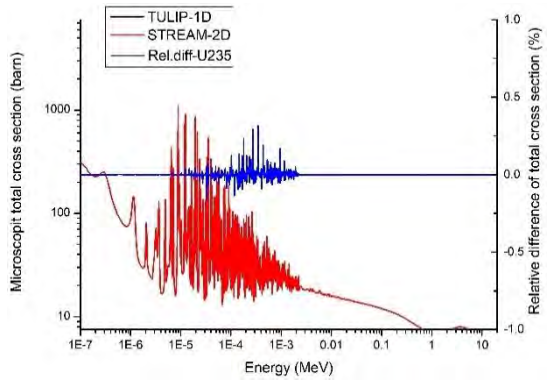

Figure 3 Microscopic total cross section of U-235 and its difference

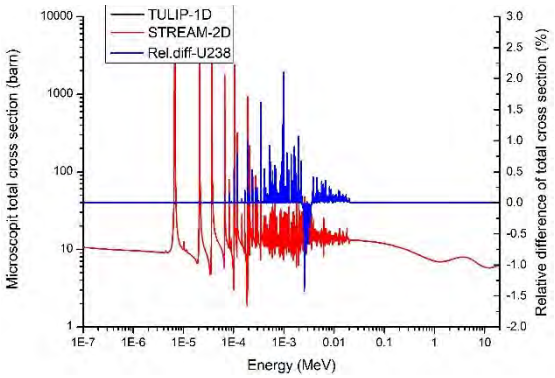

Figure 4 Microscopic total cross section of U-238 and its difference

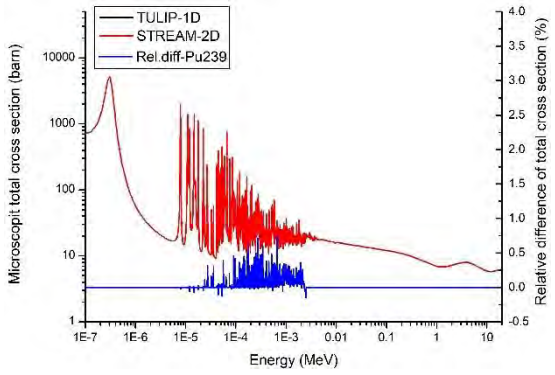

Figure 5 Microscopic total cross section of Pu-239 and its difference

The k_{inf} values are summarized in the Table 2. For the reference, the in-house MCS[7] Monte Carlo calculation was performed. In the calculation, P0, P1, and out-flow transport correction are used to take the anisotropic scattering into account. In the TULIP/STREAM

calculation, the 1968-group cross sections are prepared by TULIP code and STREAM performs the calculation with macroscopic cross sections.

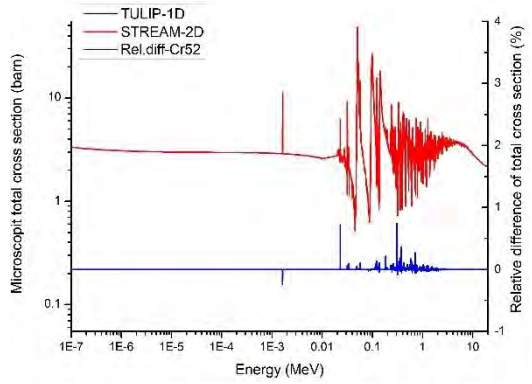

Figure 6 Microscopic total cross section of Cr-52 and its difference

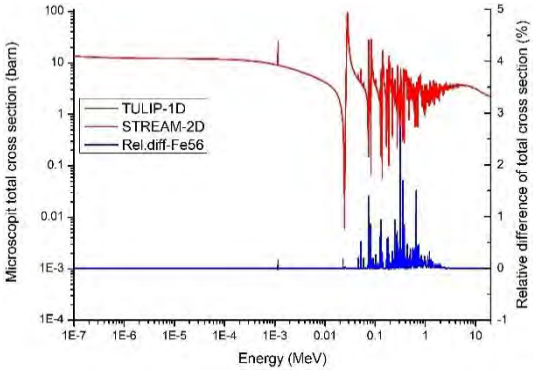

Figure 7 Microscopic total cross section of Fe-56 and its difference

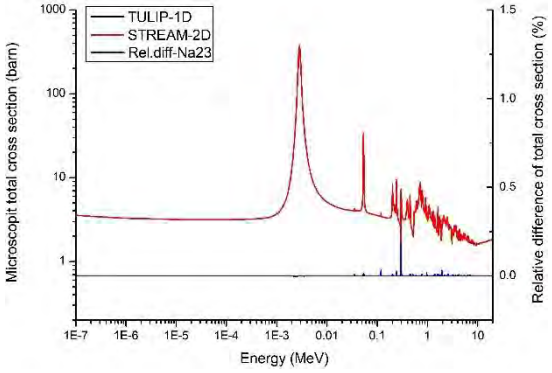

Figure 8 Microscopic total cross section of Na-23 and its difference

Table 2 Summary of k_{inf} *values of pin-cell problem*

Code	P_N Order	k_{inf}	Rel.diff, pcm
MCS		1.47705 ± 0.0005	
TULIP STREAM	P0	1.47648	-26
	TR	1.47638	-31
	P1	1.47646	-27
STREAM	P0	1.47768	28
	TR	1.47758	24
	P1	1.47766	27

As shown in the table, both TULIP/STREAM and STREAM directly calculation show good agreement compared with MCS reference solution. The relative differences are less than 30 pcm.

Based on the Eq.(6), the accuracy of cross sections depends on the accuracy of solution of two fixed-source problems. In order to see what happened when the loose convergence criteria is used, the STREAM calculations with different criteria (fsp-eps) were performed. The results are shown in Table 3. It indicates that the loose convergence criteria can be used without losing too much accuracy.

Table 3 Summary of k_{inf} *values of pin-cell problem with different convergence criteria*

Code	fsp-eps	k_{inf}	Rel.diff, pcm
MCS		1.47705 ± 0.0005	
STREAM	1e-4	1.47768	28
	1e-3	1.47764	27
	5e-3	1.47753	22
	1e-2	1.47762	26

3.2 Fast Reactor Assembly Problem

In this section, two sets of fast reactor assembly problem have been calculated. The specifications of first three cases are shown in Figure 9. The sodium is used as the coolant with metallic fuel pellet. The fuel pins with different enrichment are loaded in one assembly. The composition of each material is from MET-1000 core design, which is the 1000 MWth medium-size metallic benchmark core consisting of U-Zr fuel, HT-9 structure and, Sodium coolant [8].

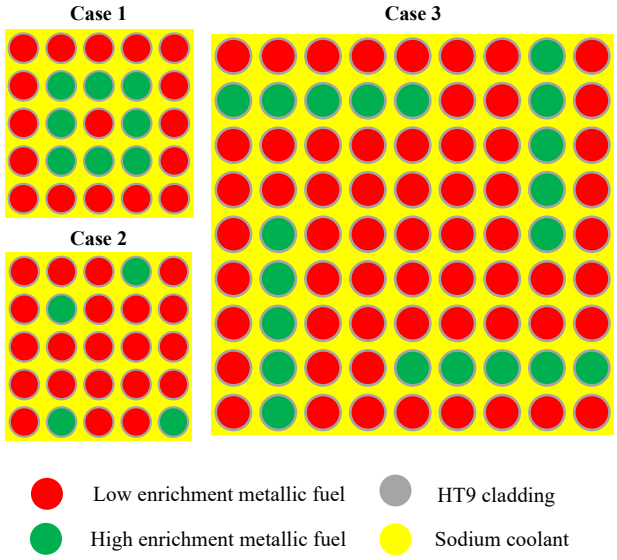

Figure 9 Specification of assembly problem, Case1~Case3

The second set of Case 4 and Case 5 is selected based on the PASCAR core inner/outer assembly. The specification of the problem can be found in the reference [1].

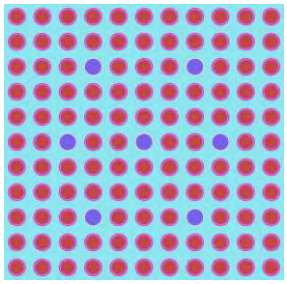

Figure 10 Specification of assembly problem, Case4 and Case5

Table 4 shows the k_{inf} results. In the calculation, the out-flow transport correction was applied for each case. For each case, the STREAM results still have good agreement compared with references. The largest relative difference is 34 pcm with negative sign. The difference does not change a lot when the problem has more fuel pins.

Table 4 Summary of k_{inf} values of assembly problem

Case	MCS	STREAM	Rel.diff, pcm
1	1.38880 ± 0.00010	1.38916	19
2	1.35624 ± 0.00010	1.35676	28
3	1.37392 ± 0.00010	1.37448	30
4	1.15252 ± 0.00008	1.15245	-5
5	1.32603 ± 0.00009	1.32543	-34

In the previous study, the 1-D equivalent cylinder geometry was used for rectangular assembly self-shielded cross sections' generation. For the Case 2 and Case 3, it is hard to use that geometry for the resonance calculation. To show the difference between 1-D and 2-D resonance treatment, the Case 4 was calculated again with TULIP 1-D resonance calculation module. The results are summarized in the Table 5. When the cross sections were prepared with 1-D equivalent geometry, the final k_{inf} value has -143 pcm difference compared with reference, which is acceptable. Compared with 1-D resonance calculation, the 2-D resonance calculation improves the final k_{inf} value around 138 pcm. That is to say, the assembly calculation with 2-D resonance treatment is necessary from the viewpoint of eigenvalue.

Table 5 Summary of k_{inf} values of assembly problem with different resonance calculation module

Code	k_{inf}	Rel.diff, pcm
MCS	1.15252 ± 0.00008	
TULIP/STREAM	1.15062	-143
STREAM	1.15245	-5

4. Discussions and Conclusions

Previously, the STREAM code is coupled with TULIP code for the fast reactor analysis. One limitation of the coupled code system is the resonance calculation needs to be done with 1-D equivalent geometry. In order to overcome this limitation, the improved Tone's method is implemented into the STREAM code in this study.

For the verifications, one pin-cell problem and several assembly problems have been calculated. Based on the numerical results, the improved Tone's method is successfully implemented into the STREAM code with reasonable accuracy. The loose convergence criteria can be used while solving two fixed-source equations. Compared with 1-D resonance calculation, the new STREAM code with 2-D resonance calculation obtains more accurate results. In the future, more verifications need to be done, especially for the hexagonal assembly.

Currently, there is no optimization in the resonance calculation. Therefore, the resonance calculation costs the same CPU times compared with MOC transport calculation. For example, Case 3 in Table 4, the resonance calculation took 903 seconds while MOC transport calculation took 806 seconds. In the future, several optimizations will be implemented for resonance calculation, such as OpenMP parallel calculation, selection of resonance nuclide.

Acknowledgements

This work was supported by the National Research Foundation of Korea (NRF) grant funded by the Korea government (MSIT). (No.NRF-2017M2A8A2018595)

References

1. X.N. Du, et al., Application of TULIP/STREAM code in 2-D Fast Reactor Core High-Fidelity Neutronic Analysis, Nucl. Eng. Tech, Accepted for publication, 2019. https://doi.org/10.1016/j.net.2019.06.010.
2. X.N. Du, et al., A hybrid method to generate few-group cross sections for fast reactor analysis, J. Nucl. Sci. Technol., 2018, 55(8):931-944.
3. C.H. Lee, et al., An Improved Resonance Self-shielding Method for Heterogeneous Fast Reactor Assembly and Core Calculations, M&C 2013, Sun Valley, Idaho, May 5-9, 2013.
4. H. Yu, T. ENDO, A. YAMAMOTO, Resonance Calculation for Large and Complicated Geometry Using Tone's Method by Incorporating the Method of Characteristics, Journal of Nuclear Science and Technology, 2011, 48(3): 330-336.
5. L. Mao, et al., A new Tone's method in APOLLO3® and its application to fast and thermal reactor calculations, Nucl. Eng. Tech, 2017, 49(6): 1269-1286.
6. T. Tone, A numerical study of heterogeneity effects in fast reactor critical assemblies, J. Nucl. Sci. Technol., 1975, 12(8): 467-481.
7. J.R. Jang, et al., Validation of UNIST Monte Carlo Code MCS for Criticality Safety Analysis of PWR Spent Fuel Pool and Storage Case, Annals of Nuclear Energy, 2018, 114:495-509.
8. OECD/NEA. Benchmark for neutronic analysis of sodium-cooled fast reactor cores with various fuel types and core sizes. France: OECD/NEA; 2016. (no. NEA/NSC/R(2015)9).

Application of the SuPer-Homogenization Method in Fast Reactor Analysis System SARAX

Linfang Wei, Youqi Zheng*, Bowen Xiao, Longfei Xu, Hongchun Wu
Xi'an Jiaotong University, No 28 Xianning West Road, Xi'an 710049, Shaanxi, China
*Corresponding author: yqzheng@mail.xjtu.edu.cn

Abstract

For better estimation of few-group cross-section considering heterogeneous effect during subassembly homogenization in fast reactor analysis, especially in the multi-region system, the traditional spatial SuPer-Homogenization (SPH) method was implemented in the few-group cross-section generation module, named TULIP, in the SARAX system to preserve the reaction rate conservation during spatial homogenization. Recently, the Energy-collapsing SuPer-Homogenization (ESPH) method was introduced in the new TULIP module to obtain the multigroup-fewgroup equivalence during group condensation. Using ESPH method, the infinite multiplication factor and the region-wise reaction rate of subassembly calculation were strictly conserved before and after energy collapsing. Besides, this paper also provides another way to generate few-group cross-section by using a whole core spectrum when condensing, in which the ESPH method was also used.

Key Words: **fast reactor, few-group cross-section, heterogeneous effect, SuPer-Homogenization, SARAX**

1. Introduction

Heterogeneous effect in fast reactor has become more and more significant along with the newly designed subassemblies nowadays [1-2]. For subassembly homogenization in fast reactor analysis, especially in the multi-region system, it is always essential to preserve the reaction rate conservation during the homogenization procedure. In early years, the SuPer-Homogenization (SPH) method [3] was applied to light water reactor (LWR) calculations, to preserve the reaction rates obtained from the subgroup calculations when transforming a multiband problem into a simple multigroup problem in heterogeneous cases by Hébert [4]. Nearly identical to the SPH method, the multigroup equivalence method was applied to the fine structure method in APOLLO3 code [5] without explicitly defining the SPH factors. This method is used to preserve the reference reaction rates obtained from the heterogeneous-homogeneous equivalence, which has been involved in the SARAX system [6].

In addition to this, researches show that during the generation of few-group cross-section, energy collapsing (or group condensing) procedure does not always preserve the reaction rates obtained from the multigroup calculations and few-group calculations in the multi-region system, which has been studied in the LWR calculations [7-8]. The same problem also occurs in fast reactor calculation. Therefore, the Energy-collapsing SuPer-Homogenization (ESPH) method was recently applied to the few-group cross-section generation module TULIP [9] in the SARAX system to preserve the multigroup - fewgroup equivalence. With this method, the infinite multiplication factor and the region-wise reaction rate conservation were strictly preserved. In order to account for the neutron leakage between different material regions, high order scattering matrices were also corrected using the ESPH method.

Different from the traditional two-step homogenization method in fast reactor analysis, another few-group cross-section generation method is proposed in this paper coupling with the newly-developed three-dimensional discrete ordinate transport code HYDRA [10]. By using a whole core spectrum provided by the S_N code when condensing, with the following ESPH correction, the effective multiplication factor and the reaction rates of respective materials in the reactor core are designed to be preserved.

2. Methodology

2.1 Subassembly homogenization with SPH method

The heterogeneous effect in resonance self-shielding was taken into account by region-wise escape cross-sections in original TULIP module. The one-dimensional transport solver was based on collision probability method (CPM) for slab and cylindrical geometries. For heterogeneous calculation models, the homogenization and group condensation processes were separated into two steps.

The first step was the spatial homogenization, with spatial SPH correction to proceed, in which the heterogeneous-homogeneous equivalence was made. The second step was the energy collapsing, with ESPH correction to proceed, in which the reaction rate conservation should be also kept to ensure the multigroup-fewgroup equivalence. The energy collapsing procedure was done by TULIP without whole core spectrum calculation, or done by S_N transport calculation code HYDRA. By computing two or three-dimensional spectrum of reactor core with approximately real model, HYDRA was expected to generate more accurate few-group constants considering neutron leakage between different types of subassembly precisely. Both flow paths were ended by a new method of ESPH correction, as shown in Figure 1.

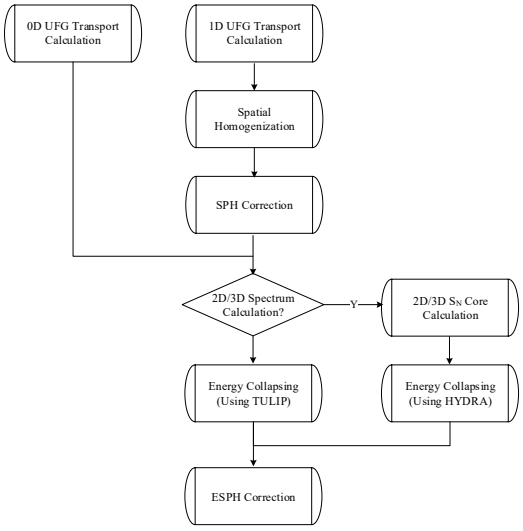

Fig. 1. The new computational flow chart of subassembly homogenization.

In the cases that final homogenized region number is more than one during spatial homogenization, e.g., a homogenization case of three regions with the first two regions merging into one, it is a typical multi-region case where the SPH method is used. According to the reaction rate conservation, it can be represented as:

$$\Sigma_{1,g}\phi_{1,g}V_1+\Sigma_{2,g}\phi_{2,g}V_2=\bar{\Sigma}_g\bar{\phi}_g(V_1+V_2) \tag{1}$$

Using the method proposed by Hébert [11], SPH factor was introduced in TULIP which is represented as:

$$\mu_g=\frac{\phi_{1,g}V_1+\phi_{2,g}V_2}{\bar{\phi}_g(V_1+V_2)} \tag{2}$$

In this work, the SPH factors were calculated for all homogenized regions.

Thus the corrected cross-section is represented as:

$$\bar{\Sigma}_g^*=\bar{\Sigma}_g\cdot\mu_g=\frac{\Sigma_{1,g}\phi_{1,g}V_1+\Sigma_{2,g}\phi_{2,g}V_2}{\phi_{1,g}V_1+\phi_{2,g}V_2}\cdot\frac{\phi_{1,g}V_1+\phi_{2,g}V_2}{\bar{\phi}_g(V_1+V_2)}=\frac{\Sigma_{1,g}\phi_{1,g}V_1+\Sigma_{2,g}\phi_{2,g}V_2}{\bar{\phi}_g(V_1+V_2)} \tag{3}$$

The conservation of reaction rate is always strictly enforced by iteration of μ_g and $\bar{\Sigma}_g^*$.

2.2 Energy collapsing with ESPH method

2.2.1. Energy collapsing using TULIP

Numerical results of fast reactor have shown that after group condensing, the k_{inf} results of few-group transport calculation was to some extent differ from that of multigroup transport calculation before condensing. The ever-present deviation indicated that energy collapsing would probably introduce inaccuracy of homogeneous parameters, particularly in the case that final homogenized region number larger than one, as in the heterogeneous super-subassembly models. This was because of the directly energy collapsing leading to non-conservation of reaction rates.

In order to enforce the reaction rate conservation while doing energy collapsing, the technique of ESPH was used in TULIP. Different from SPH, ESPH was applied within a broad group containing tens of fine groups. Detailed description can be found in the reference [12].

2.2.2. Energy collapsing using HYDRA

In order to consider the neutron leakage between different material regions in the whole core analysis, the S_N code HYDRA was used to provide the high order flux moment for group condensing. Recently, the group condensing function of HYDRA has been supplemented to generate few-group cross-sections, which are provided for core analysis in SARAX. However, there also remains the non-conservation of reaction rate before and after energy collapsing, thus the ESPH method was also applied. For different material regions in core calculation, the energy collapsing procedure (also the fine group structure being 1968 with the corresponding broad group structure being 33) can be represented as:

$$\bar{\Sigma}_{m,bg,bg\in 33}\bar{\phi}_{m,bg}=\sum_{g=g_1,g\in 1968}^{g_2}\Sigma_{m,g}\phi_{m,g} \tag{4}$$

The ESPH factor $\mu_{m,g}$ of material m in group g was defined as:

$$\mu_{m,g}=\frac{\sum_{g=g_1}^{g_2}\phi_{m,g}}{\bar{\phi}_{m,bg}} \tag{5}$$

Thus the few-group cross-section of material m was calculated as:

$$\bar{\Sigma}_{m,bg}^*=\bar{\Sigma}_{m,bg}\cdot\mu_{m,g}=\frac{\sum_{g=g_1}^{g_2}\Sigma_{m,g}\phi_{m,g}}{\sum_{g=g_1}^{g_2}\phi_{m,g}}\cdot\frac{\sum_{g=g_1}^{g_2}\phi_{m,g}}{\bar{\phi}_{m,bg}} \tag{6}$$

To ensure the convergence of iteration between $\mu_{m,g}$ and $\bar{\Sigma}_{m,bg}^*$, the constraint to $\mu_{m,g}$ was set as:

$$0.8<\mu_{m,g}<1.2 \tag{7}$$

If the calculated ESPH factor exceeded the limit, the boundary values were used. The convergence criterion of ESPH factor was

$$\sqrt{\frac{\sum_{g=1}^{G}[(\mu_{m,g}-\mu'_{m,g})/\mu'_{m,g}]^2}{G}}\le 1e^{-3} \tag{8}$$

The ESPH factors were updated by the iteration of Eq. (5), Eq. (6) and few-group P_N-consistent transport equation. For high order scattering matrices correction, the even-order and odd-order matrices were treated separately. The negative flux moments were replaced by their absolute values while condensing. The difference between ESPH method involved in HYDRA and in TULIP was that, the integrated flux normalization was managed according to the whole core spectrum in the ESPH correction involved in HYDRA. And because of the number of ESPH factors multiplied by material number, it took more iteration times for the ESPH convergence.

3. Numerical Results

3.1 Results of SPH and ESPH method in TULIP

In this section, the SPH and the ESPH method are respectively tested in separate procedures of TULIP using the flow path without 2D/3D spectrum calculation as presented in Figure 1. The verification test is a heterogeneous one-dimensional super-subassembly model constructed by inner control subassembly and outer fuel subassembly as designed in Figure 2.

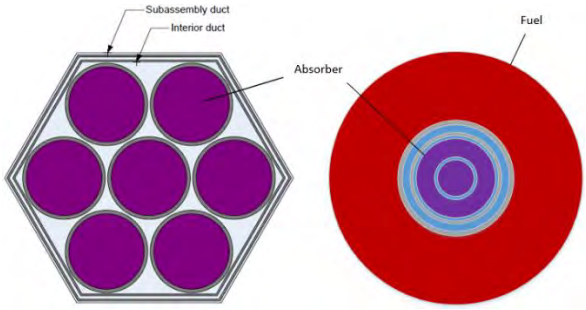

Fig. 2. Schematics of control subassembly [13] and equivalent super-subassembly model.

Table 1. k_{inf} results of super-subassembly calculation

Procedure	Reference	w/o Correction	w/ Correction	
			SPH	ESPH
Spatial homogenization	0.98822[a]	0.97143[b]	0.98827[c]	—
Energy collapsing	0.98827[c]	0.97431[d]	—	0.98808[e]

[a] Reference.
[b] Homogenized, w/o SPH, w/o condensation.
[c] Homogenized, w/ SPH, w/o condensation.
[d] Homogenized, w/ SPH, condensed, w/o ESPH.
[e] Homogenized, w/ SPH, condensed, w/ ESPH.

In this case, the final homogenized region number was 2 including one control subassembly region and one fuel subassembly region. The reference of spatial homogenization was from the heterogeneous multigroup transport calculation. It is presented in Table 1 that the error introduced by spatial homogenization is eliminated from -1749 pcm to 5 pcm by using the spatial SPH correction after homogenization. And in the second homogenization procedure of TULIP, the reference of energy collapsing was from the homogeneous multigroup transport calculation. It is also presented that the error introduced by energy collapsing is reduced from -1450 pcm to -19 pcm by using ESPH correction. The k_{inf} result of homogeneous few-group transport calculation agrees well with that of multigroup transport calculation.

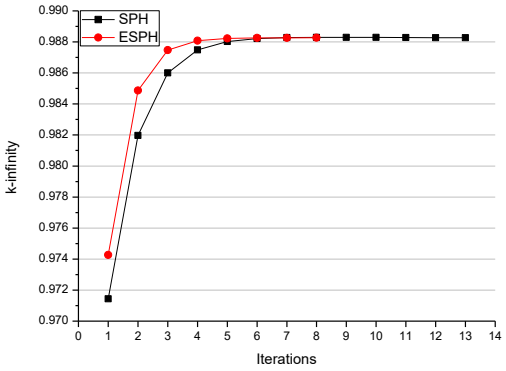

Fig. 3. k_{inf} convergence with SPH/ESPH iterations.

Figure 3 shows the convergence of k_{inf} with SPH/ESPH iterations. Compared to SPH iterations, it takes fewer iterations for ESPH to obtain a converged k_{inf} result of few-group transport calculation to the same convergence criterion.

In fact, the deviation of k_{inf} value is according to the deviation of reaction rate estimation. Application of SPH and ESPH correction respectively amends the homogenized cross section after spatial homogenization and after energy collapsing to more reasonable values. Therefore, the reaction rate conservation is virtually realized with these methods.

Table 2. Normalized total reaction rate using ESPH.

	Reference	w/o ESPH	Error/ %	w/ ESPH	Error/ %
Absorber region	0.11807	0.12314	4.29	0.11813	0.05
Fuel region	0.88193	0.87686	-0.57	0.88187	-0.01

Table 2 presents that energy collapsing without ESPH correction will cause overestimation of the total reaction rate in absorber region, which leads to k_{inf} smaller than the value it should be. After ESPH correction, the normalized reaction rates in both two regions are very closed to the reference.

3.2 Results of ESPH method in HYDRA

In this section, the ESPH method is tested using OECD/NEA SFR benchmarks [13], calculated by three-dimensional S_N transport calculation code HYDRA, with S_4P_1 approximation. The homogenized multigroup cross-

section was provided by TULIP. During the ESPH iterations, the averaged flux of each few group was kept, and the ESPH factors were calculated for all the materials.

Table 3. k_{eff} of SFR benchmarks using HYDRA.

Bench mark	1968-group reference	33-group w/o ESPH	Error / pcm	33-group w/ ESPH	Error /pcm
MET-1000	1.03026	1.02498	-528	1.03001	-25
MOX-3600	1.01151	1.00904	-247	1.01032	-119
MOX-1000	1.01791	1.01339	-452	1.01774	-17

Table 3 shows that the k_{eff} deviations between multigroup (1968) and few-group (33) calculation are significantly reduced with ESPH method. As the ESPH iteration times becomes larger, the error of few-group k_{eff} becomes smaller and finally leads to a converged value of core calculation. The remaining deviation between 1968-group calculation and converged 33-group calculation is due to the neutron current non-conservation during ESPH iterations for vacuum boundary conditions.

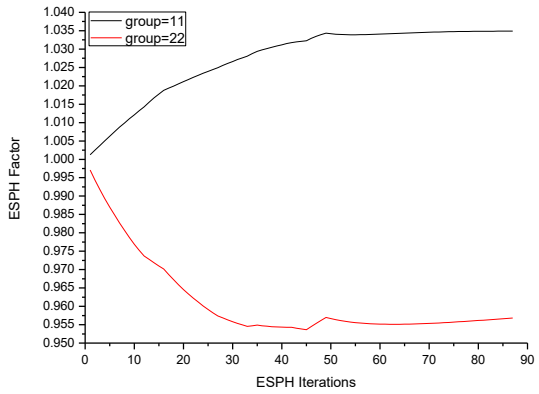

Fig. 4. ESPH factors of material 1.

Figure 4 shows the ESPH factor convergence of fuel material 1 of MET-1000 benchmark in 33-group transport calculation done by HYDRA. In different energy groups, the ESPH factor variation tendency can be opposite, but eventually converges to a fixed value.

4. Conclusions

This paper described the SuPer-Homogenization method implemented in the fast reactor analysis system SARAX. For subassembly calculation, the k_{inf} result was corrected to the true value, and more accurate homogenized few-group cross-sections were generated with this method. For the three-dimensional whole core calculation, the few-group k_{eff} result was much closer to the multigroup one, and the accuracy of normalized total reaction rates of fuel materials was improved, which were benefit from the utility of ESPH method during energy collapsing using the whole core spectrum. The numerical results indicate that with the new ESPH correction method, the accuracy of few-group cross-section generation in SARAX system has been significantly improved.

References

1. B. Faure, P. Archier, J-F. Vidal, et al., "Neutronic calculation of an axially heterogeneous ASTRID fuel assembly with APOLLO3: Analysis of biases and foreseen improvements," *Ann. Nucl. Energy.* **115**, p. 88–104 (2018).
2. M.G. Jarrett, E.R. Shemon, C.H. Lee, "Heterogeneous multigroup cross sections for fast reactor calculations with MC^2-3/Proteus," *Proc. PHYSOR 2016*, Sun Valley, ID, May 1-5 (2016).
3. A. Kavenoky. The SPH Homogenization Method, Proc. Specialists' Mtg. Homogenization Methods in Reactor Physics, International Atomic Energy Agency, Lugano, Switzerland, November 13-15, 1978, IAEA-TECDOC-231. International Atomic Energy Agency, p. 181 (1978).
4. A. Hébert, "Advances in the development of a subgroup method for the self-shielding of resonant isotopes in arbitrary geometries," *Nucl. Sci. Eng.* **126**(3), p. 245–263 (1997).
5. D. Schneider, et al., "APOLLO3: CEA/DEN deterministic multi-purpose code for reactor physics analysis," *Proc. PHYSOR 2016*, Sun Valley, ID, May 1-5 (2016).
6. Y. Zheng, X. Du, Z. Xu, et al., "SARAX: A new code for fast reactor analysis part I: Methods," *Nucl. Eng. Des.* **340**, p. 421–430 (2018).
7. N. Sugimura and A. Yamamoto, "Resonance Treatment Based on Ultra-fine-group Spectrum Calculation in the AEGIS Code," *J. Nucl. Sci. Technol.* **44**(7), p. 958–966 (2007).
8. H. Park, H.G. Joo, "Practical resolution of angle dependency of multigroup resonance cross sections using parametrized spectral superhomogenization factors," *Nucl. Eng. Technol.* **49**(6), p. 1287–1300 (2017).
9. X. Du, L. Cao, Y. Zheng, et al., "A hybrid method to generate few-group cross sections for fast reactor analysis," *J. Nucl. Sci. Technol.* **55**(8), p. 931–944 (2018).
10. L. Xu, L. Cao, Y. Zheng, et al., "Development of a new parallel S_N code for neutron-photon transport calculation in 3-D cylindrical geometry," *Progress in Nuclear Energy.* **94**, p. 1–21 (2017).
11. A. Hébert, "Applied Reactor Physics", Canada, Presses Internationales Polytechnique, p. 225 (2009).
12. L. Wei, Y. Zheng, H. Wu, "Improvement of few-group cross-section generation in fast reactor analysis system SARAX," *Ann. Nucl. Energy.* **132**, p. 149–160 (2019).
13. OECD/NEA, "Benchmark for neutronic analysis of sodium-cooled fast reactor cores with various fuel types and core sizes," NEA/NSC/R (2015)9.

Proceedings of the Reactor Physics Asia 2019 (RPHA19) Conference
Osaka, Japan, Dec. 2-3, 2019

Progress on Multi-physics Calculations of Nuclear Reactor Cores with the IGA method

W.F.G. van Rooijen[a,*]
[a]*Research Institute of Nuclear Engineering, University of Fukui*
〒914-0055 Fukui-ken Tsuruga-shi Kanawa-chō 1-3-33, JAPAN
[*]Corresponding author: rooijen@u-fukui.ac.jp

Abstract

A method is presented to solve the S_N neutron transport equation with Iso-Geometric Analysis (IGA). This method allows to solve the neutron transport equation on arbitrary geometrical domains. In the current work, a computer code has been developed to solve the multi-group S_N transport equations with IGA. The theory is being expanded to include diffusion theory and thermal conduction in a first approach to multiphysics calculations. The current computer code is actively being developed. Accuracy is good but calculation time is a weak point.

Key Words: **Iso-Geometric Analysis, S_N Neutron Transport Theory, Numerical Simulation, Diffusion Theory**

1. Introduction

The steady-state neutron transport equation (Boltzman-equation) is defined over three independent variable, i.e. space, direction of neutron movement, and neutron energy. In computer simulations, each of these independent variables must be discretized. Each discretization necessarily implies an approximation and becomes a source of uncertainty (error) in the calculation. Furthermore, in the particular case of the space variable, the conventional discretization methods are often limited to rather simple shapes, such as cylinders, sphere, and planes. In the current work, the so-called Iso-Geometric Analysis (IGA) is applied for the discretization of space. The IGA method allows to solve the neutron transport equation in arbitrary geometry without meshing or other discretization. With the IGA method, it is possible to analyze geometrical shapes which are (slightly) deformed, for example, due to thermal expansion. A calculation code has been developed to solve the multi-group SN transport equation as well as the neutron diffusion equation with the IGA method. In this manuscript theoretical background is given as well as some results of initial calculations.
In Section 2 an overview is given of the theory behind the IGA method, and in Section 3 the theory is given to apply IGA to the S_N neutron transport equation. In Section 4 detailed results are given, as well as an extension to diffusion theory and multiphysics calculations. Section 5 gives conclusions.

2. NURBS and Iso-Geometric Analysis

The introduction of IGA here is very limited. For more details, see reference [1]. For numerical analysis of arbitrary geometrical shapes, such as in Computer-Aided Design (CAD) systems, it is needed to represent arbitrary geometrical shapes as a (set of) mathematical equations. One theory for such a representation is based on so-called NURBS (Non-Uniform Rational B-Splines, [2]). In NURBS theory, one starts with a set of basis functions $N_{i,p}(u)$ of degree p and $= 1, \dots, I$, defined on a parameter space $0 \leq u \leq 1$. For each basis function $N_{i,p}(u)$ there is a corresponding point $\boldsymbol{P}_i$ in 3D space, called a "control point", and a weight, ω_i. A curve is defined as

$$\mathbf{C}(\mathrm{u}) = \frac{\sum_{i=0}^{I} \omega_i N_{i,p}(u) \boldsymbol{P}_i}{\sum_{j=0}^{I} \omega_j N_{j,p}(u)} \qquad (1)$$

Thus, as the parameter u goes from 0 to 1, the curve $\mathbf{C}(\mathrm{u})$ "interpolates" the control points resulting in a 3D curve. By the proper selection of the control points and weights, any desired curve can be defined. The theory can also be extended to 2D surfaces and 3D volumes.
The theory of NURBS also provides the following:

- A recursive definition of the basis functions which is easy to program and numerically stable.
- It is possible to determine the tangent vectors in each parameter direction and thus is it possible to determine the normal vector to a surface at any point.
- The NURBS basis functions have some features which make them attractive for application in the Finite Element Method (FEM), details in Ref. [1].

The Finite Element Method (FEM) is a general mathematical theory to solve Partial Differential Equations (PDE), such as the neutron transport equation. The PDE is defined on some geometrical domain Γ with corresponding boundary conditions. The basic approach of IGA is to use NURBS theory and the NURBS basis functions to define the geometrical domain Γ, and then also use those same NURBS basis functions in the FEM

solution of the PDE. Thus, the PDE can be solved on any arbitrary geometrical domain.

3. IGA, S_N transport, and diffusion theory

In the following, 2D geometry is assumed but the theory applies to 3D geometry as well. The simplest form of the transport equation is the following:

$$\hat{\boldsymbol{\Omega}} \cdot \boldsymbol{\nabla}\psi^g(\boldsymbol{r},\hat{\boldsymbol{\Omega}}) + \Sigma_t^g \psi^g = Q^g(\boldsymbol{r},\hat{\boldsymbol{\Omega}}) \qquad (2)$$

Where $\boldsymbol{r}$ indicates space, g indicates the energy group, $\hat{\boldsymbol{\Omega}}$ indicates neutron direction, Σ_t^g is the total cross section and Q^g is the neutron source; the equation is defined on a geometrical domain Γ, called a "patch". In general, a complete geometry is built-up of several patches in a so-called "multipatch geometry". In the S_N method, the variable of neutron direction $\hat{\boldsymbol{\Omega}}$ is discretized into a set $\hat{\boldsymbol{\Omega}}_k$ and Eq. (2) is solved for each $\hat{\boldsymbol{\Omega}}_k$ in the set. To obtain the form of the equation for use with the FEM, multiply the equation with an (arbitrary, but non-zero) weight function η, integrate over the patch Γ, and use the Gauss divergence theorem; furthermore, since neutrons travel in a straight line, the boundary of the domain can be divided into two parts, $\partial\Gamma^-$ where neutrons enter the domain (incoming boundary), and $\partial\Gamma^+$ where neutrons leave the domain (outgoing boundary). See also Fig. 1:

$$\hat{\boldsymbol{\Omega}}_k \cdot \int_{\partial\Gamma^+} \eta\psi\hat{\boldsymbol{n}}dl - \hat{\boldsymbol{\Omega}}_k \cdot \int_\Gamma \boldsymbol{\nabla}\eta\psi d\Gamma + \int_\Gamma \eta\Sigma_t\psi d\Gamma = \int_\Gamma \eta Q_k d\Gamma - \hat{\boldsymbol{\Omega}}_k \cdot \int_{\partial\Gamma^-} \eta\psi_{in}\hat{\boldsymbol{n}}dl \qquad (3)$$

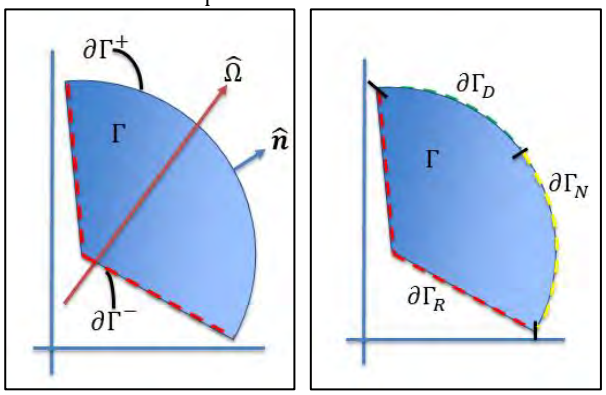

(a) (b)

Fig. 1. (a) Geometrical domain Γ for transport theory: neutron direction $\hat{\boldsymbol{\Omega}}$, incoming boundary $\partial\Gamma^-$, outgoing boundary $\partial\Gamma^+$ and normal vector $\hat{\boldsymbol{n}}$ are indicated. (b) Geometrical domain for diffusion calculations, with Dirichlet, Neumann, and Robin boundaries indicated as $\partial\Gamma_D$, $\partial\Gamma_N$ and $\partial\Gamma_R$

On the incoming boundary $\partial\Gamma^-$ the flux is known (boundary condition), and on the outgoing boundary $\partial\Gamma^+$ it is assumed that the flux is the same as the patch flux. The following step is to assume that the flux can be expanded into a set of basis functions, i.e. $\psi(\boldsymbol{r}) = \sum_{i=1}^{I} \alpha_i B_i(\boldsymbol{r})$, and to select a special weight function $\eta(\boldsymbol{r}) = \mathrm{B_j}(\boldsymbol{r})$:

$$\hat{\boldsymbol{\Omega}}_k \cdot \int_{\partial\Gamma^+} B_j(\boldsymbol{r}) \sum_{i=1}^{I} \alpha_i B_i(\boldsymbol{r})\, \hat{\boldsymbol{n}}dl - \hat{\boldsymbol{\Omega}}_\mathrm{k} \cdot \int_\Gamma \boldsymbol{\nabla}\mathrm{B_j}(\boldsymbol{r}) \sum_{i=1}^{I} \alpha_i B_i(\boldsymbol{r})\, d\Gamma + \int_\Gamma B_j(\boldsymbol{r})\Sigma_t \sum_{i=1}^{I} \alpha_i B_i(\boldsymbol{r})\, d\Gamma = \int_\Gamma B_j(\boldsymbol{r}) Q_k d\Gamma - \hat{\boldsymbol{\Omega}}_k \cdot \int_{\partial\Gamma^-} B_j(\boldsymbol{r})\psi_{in}\hat{\boldsymbol{n}}dl \qquad (4)$$

In the IGA method the NURBS basis functions which define the geometrical domain Γ are used also to expand the neutron flux. The basis functions are defined on the parameter space (u, v), thus the easiest option is to perform all the integrations of Eq. (4) in the parameter domain. This requires a coordinate transform, but that is precisely defined by the NURBS definition of the patch Γ; the NURBS theory also defines the normal vectors on the edges of the domain so that it becomes possible to determine the incoming and outgoing boundaries.

Eq. (4) is one equation, but there are I expansion coefficients for the flux, thus one needs I equations. This is achieved using the weight function: by selecting B_j, $j = 1, \ldots, I$ one obtains I equations. The entire problem can now be written in the form of a matrix multiplication, and the solution can be obtained by inversion of the matrix, for which many methods are available.

In the case of diffusion theory, the equation to solve is:

$$-\boldsymbol{\nabla} \cdot D\boldsymbol{\nabla}\phi^g(\boldsymbol{r}) + \Sigma_t^g \phi^g = Q^g(\boldsymbol{r}) \qquad (5)$$

Similar to the transport equation, multiply by a weight function and integrate over the patch. In the case of diffusion theory, one cannot make a distinction between *incoming* and *outgoing* boundaries, instead, the boundary is divided into 3 parts: (1) boundary with Dirichlet conditions $\partial\Gamma_D$ (flux is known on the boundary); (2) boundary with Neumann conditions $\partial\Gamma_N$ (derivative of the flux is known on the boundary) and (3), boundary with Robin conditions $\partial\Gamma_R$ (a superposition of Dirichlet and Neumann conditions). On $\partial\Gamma_D$, the flux is already known, thus that part of the boundary must not be included in the calculation. Assume that the only other boundary conditions are either perfect reflection (zero-derivative boundary condition) or perfect vacuum (i.e. $\boldsymbol{\nabla}\phi \cdot \hat{\boldsymbol{n}} = -\phi/\mathrm{d_{ex}}$, where $\mathrm{d_{ex}}$ is the extrapolation distance; this boundary condition is a special case of the Robin boundary condition). As before, expand the flux into basis functions $\phi(\boldsymbol{r}) = \sum_{i=1}^{I} \alpha_i B_i(\boldsymbol{r})$ and choose the weight function as $\eta(\boldsymbol{r}) = \mathrm{B_j}(\boldsymbol{r})$ to find:

$$D\sum_{i=1}^{I} \alpha_i \int_\Gamma \nabla B_j \cdot \nabla B_i d\Gamma + \beta D \sum_{i=1}^{I} \alpha_i \int_{\partial\Gamma_\mathrm{R}} B_j B_i dl + \Sigma_t \sum_{i=1}^{I} \alpha_i \int_\Gamma B_j B_i d\Gamma = \int_\Gamma B_j Q d\Gamma \qquad (6)$$

where β is a term due to the Robin-boundary conditions. As in the case of transport theory, choose the basis functions B_j with $j = 1, \ldots, I$ to make I equations for I unknowns. Again, all integrals are evaluated in the NURBS parameter domain, and the matrix inversion can be performed with any of the standard numerical techniques.

From a theoretical perspective, diffusion theory is inferior to transport theory. There are two reasons to include diffusion theory:

1. Diffusion theory can be used as a preconditioner for transport theory, i.e. diffusion theory can be used to find an approximate solution of the scalar flux which can be used as a starting guess for the transport theory solution
2. The neutron diffusion equation is the same as the equation for heat conduction, thus diffusion theory provides a way to include the calculation of temperature.

3.1 Some implementation details

There a few very important differences between the solutions for diffusion theory and transport theory. First of all, in diffusion theory the solution is calculated for all patches in the geometry at once, while for transport theory the solution proceeds on a patch-by-patch basis. In diffusion theory, the boundary condition on the boundary between patches is that the flux is continuous. This is implemented in practice by "merging" the basis functions across the boundary. Effectively, from the point of view of the calculation, the individual patches are "glued together" to form one big patch. This has an effect on the patch matrices in the calculation. The patch matrices in transport theory are quite dense, i.e. most of the elements of the matrix are not zero, whereas the matrices in diffusion theory can be very sparse. In the present work, for transport theory all matrices are stored as dense matrices and inverted with standard routines from BLAS [3] and LAPACK [4], whereas the matrices for diffusion theory are stored as sparse matrices and the inversion is performed with a special method for sparse matrices (SPARSKIT [5]).

4. Results

Application of the IGA method requires that one has a description of the geometrical domain in the form of NURBS. Currently the GeoPDEs package [6] is used. The GeoPDEs package is an IGA package for Matlab [7] and GNU Octave [8]. GeoPDEs has options to define 2D and 3D NURBS geometries.

4.1 Two-dimensional neutron transport

Calculations were first performed on PWR pin cell models, for which the C5G7 benchmark [9] was used. Calculations were performed for the four fuel types included in the benchmark, i.e. a UOX pin and three MOX pins (4.3%, 7.0%, 8.7%). Also a test geometry was defined with each of the four pins; the IGA mesh is shown in Fig. 2, and the results are shown in Table I.

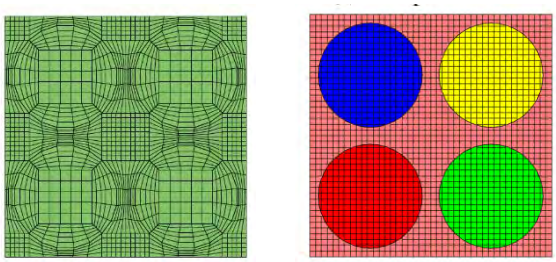

(a) (b)

Fig. 2. Example of the 4 pin geometry used for 2D calculations with the IGA code. (a): the IGA multipatch geometry, (b) the allocation of materials.

Table I: Results for 2D PWR pin cells of the C5G7 benchmark, and our own 4-pin model from Fig. 2.

	NEWT	IGA
UO2	1.323135	1.323086
MOX 4.3%	1.132954	1.130616
MOX 7.0%	1.156978	1.153789
MOX 8.7%	1.170037	1.166476
Four pin	1.18736	1.18544

Initial calculations showed that the calculation time of the IGA code was excessively long. To increase performance, an optimization of the patch order was implemented. As illustrated in Fig. 3, the direction $\hat{\boldsymbol{\Omega}}_k$ determines the "natural" order of the solution for the patches. The problem is thus to determine how neutrons "flow" from one patch to the next as a function of $\hat{\boldsymbol{\Omega}}_k$. This is really a problem of graph theory, and the GRAFPACK software [10] was used to find optimal solutions. The improvement of the calculation time is shown in Table II: calculation time was decreased by 60% - 75%.

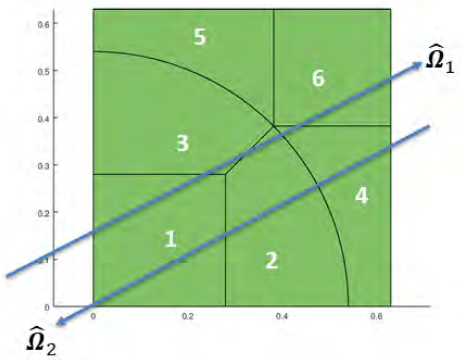

Fig. 3. A multipatch geometry and 2 directions $\hat{\boldsymbol{\Omega}}_1$ and $\hat{\boldsymbol{\Omega}}_2$. For $\hat{\boldsymbol{\Omega}}_1$, the solution should start in patch 1 and finish in 6, for $\hat{\boldsymbol{\Omega}}_2$ the order should be exactly opposite.

4.2 Three-dimensional neutron transport

Preliminary calculations were performed for 3D geometries as well. In particular, the Jezebel and Godiva

Table II. PWR pin cell, UOX fuel, calculation time (in seconds) before and after optimization of the sweep order.

GRAFPACK	S2	S8	S16
No	52.15	456.5	3170
Yes	14.51	178.9	1163

benchmarks were analyzed (anisotropic scatter is important in these benchmarks), as well as the Takeda-1 benchmark and a 3D system inspired by the Takeda-2 benchmark [11]. Results are given in Table III.

Table III: Results for 3D transport calculations with the IGA code, compared to 1D S_N transport (XSDRNPM), and Monte Carlo (KENO-VI)

	Jezebel-1	**Jezebel-2**	**Godiva-1**
XSDRNPM S_4P_0	1.08383	1.07335	1.11013
IGA S_4P_0	1.07242	1.06244	1.10373
XSDRNPM S_4P_5	0.99380	0.98222	1.02022
IGA S_4P_5	0.98093	0.96987	1.01232
Takeda benchmark, model 1: KUCA. S_8			
	Benchmark	IGA	KENO-VI
CR up	0.9766	0.97880	0.97750
CR down	0.9622	0.96361	0.96258
CR worth	0.0154	0.01518	0.01492
Takeda benchmark model 2 inspired. S_8			
	IGA, 2^{nd} degree	IGA, 4^{th} degree	KENO-VI
CR up	0.99147	0.99161	0.99042
CR down	0.95577	0.95647	0.95544
CR worth	0.0357	0.03514	0.03498

4.3 Diffusion theory.

The diffusion calculation is presently under development. At present, only one result can be presented, see Table IV. The UOX pin cell from the C5G7 benchmark was analyzed with diffusion theory and S_N transport theory. As can be seen, in comparison with S_4 calculations, the reduction of calculation time is about 2 orders of magnitude.

Table IV: Comparison of SN calculations and diffusion theory for a UOX PWR pin cell.

	k_∞	Time [s]
Diffusion	1.32599	4.40
S4	1.32314	466
S8	1.32407	1603

Code development is currently ongoing for diffusion theory, 3D calculations, and the calculation of heat conduction. Our final contribution will contain more results in these areas.

5. Conclusions and future outlook

The theory for the solution of the neutron transport equation with multigroup S_N theory and the IGA method was successfully derived and a computer code has been developed. The IGA method makes it possible to solve the neutron transport equation on arbitrary geometry, but there are a few aspects which require optimization, such as the sweeping order over the patches and even the sweeping order inside a patch. The current code includes anisotropic scatter and shows good accuracy but calculation time is clearly a problem. A diffusion version of the code was also developed and showed good accuracy.

Future developments are focusing on the following aspects:

- The multi-group theory requires self-shielded group cross sections. Research is currently ongoing to develop the necessary theory and numerical tools (submitted for presentation at the RPHA19 meeting)
- Multiphysics calculation taking into account heat conduction.
- The IGA method has many parameters, such as the degree of the basis functions, the support of the basis functions, etc. The optimal combination of these parameters is to be determined.
- At present, at least two reasons for the long calculation times have been found and remedies are being investigated.

References

1. J. Austin Cottrell, Thomas J.R. Hughes, and Yuri Bazilevs, *Isogeometric Analysis – Toward integration of CAD and FEA*, Wiley (2009)
2. Les Piegl and Wayne Tiller, *The NURBS Book*, Monographs in visual communication, Springer (1995)
3. BLAS, Basic Linear Algebra Subprograms, v3.8.0, http://www.netlib.org/blas/
4. LAPACK, Linear Algebra PACKage, v3.8.0, http://performance.netlib.org/lapack/
5. Y. Saad, "*SPARKSIT, a basic tool kit for sparse matrix computations, Version 2*", https://www-users.cs.umn.edu/~saad/software/SPARSKIT/
6. R. Vázquez, "*A new design for the implementation of isogeometric analysis in Octave and Matlab: GeoPDEs 3.0*", IMATI REPORT Series No. 16-02, CNR IMATI (2016)
7. https://www.mathworks.com/products/matlab.html
8. https://www.gnu.org/software/octave/
9. Benchmark on Deterministic Transport Calculations Without Spatial Homogenisation, A 2-D/3-D MOX Fuel Assembly Benchmark, OECD, NAE/NSC/DOC(2003)16
10. GRAFPACK Graph Computations, https://people.sc.fsu.edu/~jburkardt/f_src/grafpack/grafpack.html
11. Toshikazu Takeda and Hideaki Ikeda, "*3-D neutron transport benchmarks*", NEACRP-L-330, OECD-NEA (1991)

Proceedings of the Reactor Physics Asia 2019 (RPHA19) Conference
Osaka, Japan, Dec. 2-3, 2019

Research on a Method for Self-Shielding Calculations Based on IGA-Method

*Matthias Nezondet[a], W.F.G Van Rooijen[b]
[a]*University of Fukui, Graduate School of Engineering,*
3-9-1 Bunkyo, Fukui-shi, Fukui 910-8507, Japan
[b]*University of Fukui, Research Institute of Nuclear Engineering,*
1-3-33 Kanawa-cho, Tsuruga-shi, Fukui 914-0055, Japan

*E-mail : nmatth@u-fukui.ac.jp

Abstract

An innovative calculational method for neutron transport is described. This code uses a particular method to treat the spatial domain. This code allows to perform nuclear reactor physics evaluations for any arbitrary geometrical domains compared to conventional calculational methods that use commonly only ideal shapes (cylinders, spheres, plates,...) to describe the spatial domain. This new method is based on the Iso-Geometric Analysis. To treat the energy variable we use the Multi-group method, so it is essential to make self-shielding calculations to take into account the resonance phenomenon of cross sections to determine correctly and accurately the behavior of the core and the safety parameters. The self-shielding method that we use is based on a subgroup method developed by P.Ribon, known as method of the moments. This method replace the punctual micro cross sections by a density of probability that can be described by a quadrature set named probability table. It is also relevant to present this probability tables and the method to create them. From now, we have calculated our probability table and we will show their validity by making a comparison of the cross section calculated with the probability table and with an other method.

Key Words: **IGA-Method, Self-shielding, Cross sections, Sub-group method, Resonances, Probability table.**

1. Introduction

In conventional calculational methods for neutron transport, the spatial domain is often described based on "ideal" shapes. However, a nuclear reactor is not an ideal shape; for example, thermal expansion and/or mechanical stress deform the shape of the reactor. The effects of such spatial deformations can be large, but in conventional calculation methods such effects are often ignored or taken into account with correction factors. In recent years, in our lab we are developing a numerical method based on so-called Iso-Geometric Analysis (IGA) to simulate the transport of neutrons through arbitrary geometrical domains, which allows to perform simulations using the actual shape of the spatial domain [1]. In numerical simulation of nuclear reactor physics one problem occurs, the solution of the transport equation is linked to the treatment of the energy of the neutrons. The interaction between neutrons and atomic nuclei has so-called resonances, where the reaction rate can vary over several orders of magnitude in a narrow range of energy. The presence of resonances gives rise to the so-called self-shielding effect.

2. Iso-Geometric Analysis

In numerical simulations of nuclear reactor physics, the treatment of the spatial domain and the energy of the particles are directly related to each other. In recent years, a method to simulate the transport of neutrons through arbitrary spatial domains has been developed in our laboratory. To take into account every kind of shapes, our numerical code is based on the IGA which was firstly used in CAD design tools.

Previously in CAD software, the geometric shapes were delimited by curved surfaces described by NURBS (Non-Uniform Rational Basis Splines), function defined piecewise by polynomials. NURBS is a mathematical model used for generating and representing curves and surfaces. A NURBS curve is defined by its order, a set of weighted control points, and a knot vector. The order defines the number of nearby control points that influence any given point on the curve and set the order of the polynomials that represent the curves, the control points determine the shape of the curve by adjusting the weight of each point and the knot vector is a sequence of parameter values that determines

where and how the control points affect the curve. This method allows to represent every kind of curves and makes complex geometries.

On the other hands for finite element method (FEM), the geometric volumes are meshed, divided into polyhedrons (hexahedrons, cubes, tetrahedrons, prisms, ...). The way to describe the geometric shapes and the geometric volumes are different, so it is necessary to go through a conversion step: the meshing. The meshing of the geometrical domain is an approximation which has an impact on the accuracy of the calculation. To circumvent the issues related to the meshing, the IGA method has been improved [2, 3].

3. Self-shielding calculations

A basic topic in nuclear reactor analysis is the problem of self-shielding, which is due to the very fine energy structure of the nuclear cross sections. An adequate treatment of self-shielding is essential for the correct prediction of the safety parameters of a nuclear reactor (Doppler coefficient, void coefficient, etc). Self-shielding calculations commonly take into account only a few standard geometric shapes (plates, cylinders, spheres). Thus for IGA, it becomes necessary to calculate self-shielding in arbitrary geometry.

To resolve the transport equation of neutrons, it is often necessary to discretize the energy by using a certain number of groups (a dozen or hundreds groups). In that case, we need to take into account the resonant behavior of the cross sections because some group include many resonances that has an impact on the determination of the group cross sections. The goal of the self-shielding model is to calculate the multi-group self-shielded cross section $\sigma^g_{\rho,i}$ for any reaction ρ, in any group g and geometric zone i :

$$\sigma^g_{\rho,i} = \frac{\int_{u_{g-1}}^{u_g} \sigma_{\rho,i}(u)\Phi_i(u)du}{\int_{u_{g-1}}^{u_g} \Phi_i(u)du} = \frac{\langle \sigma_{\rho,i}\Phi_i \rangle^g}{\langle \Phi_i \rangle^g} \tag{1}$$

where

$u = ln(E_0/E) =$ lethargy
$\sigma_{\rho,i}(u) =$ microscopic cross section
$\Phi_i(u) =$ neutron flux

There are different methods for self-shielding calculations. The main ones are : method of equivalence, Stammlers method, Sub-group methods.

A lot of methods require a background cross section which is a function of the geometry. However most of these methods use simple shapes, but we need to use a method that does not rely on the assumption of simple geometrical domains. For our simulation code, we have decided to use the sub-group method because this method can be used for every geometric domain. Moreover, this method is compatible with any flux solution technique, more precisely with the discrete ordinates S_n theory that we use in our code based on IGA to resolve the transport equation.

4. Sub-group method and probability tables

4.1 Generalization of the sub-group method

The term of sub-group method was introduced in the 70s by Nikolaev [4]. All the different sub-group methods use the probability density of the microscopic cross section of the resonant isotopes. Indeed, the microscopic cross section can be defined by a function $\Pi(\sigma)$ so that $\Pi(\sigma)d\sigma$ is the probability for the microscopic cross section of the resonant isotope to have a value between σ and $\sigma + d\sigma$. This function $\Pi(\sigma)$, which is called probability density, is a positive function and this integral is equal to 1. A representation of the probability density function is shown on Fig.1.

With the definition of the probability density function it is possible to replace every Riemann integral with a σ dependent integrand by a Lebesgue integral :

$$\frac{1}{\Delta u_g} \int_{u_{g-1}}^{u_g} f[\sigma(u)]du = \int_{max(\sigma)}^{min(\sigma)} \Pi(\sigma) f(\sigma) d\sigma \tag{2}$$

If we look at Fig.1, the function $\Pi(\sigma)$ can be approximated by a series of δ-functions centered at discrete values σ_k and characterized by discrete weights w_k (the weights are positive and their sum is equal to 1) that represent the probability of the micro cross section to be equal to σ_k. Each value represents a discrete level that can be assimilated to a group inside the group g, hence the term of sub-group.

$$\Pi(\sigma) = \sum_{k=1}^{K} \delta(\sigma - \sigma_k) w_k \tag{3}$$

We substitute the Eq.(2) by the Eq.(3) and we obtain the following discretization :

$$\frac{1}{\Delta u_g} \int_{u_{g-1}}^{u_g} f[\sigma(u)]du = \sum_{k=1}^{K} w_k f(\sigma_k) \tag{4}$$

If we consider a heterogeneous system described in the S_n formalism, where the direction of movement is discretized into a set of directions $\hat{\Omega}_n$ and where a resonant isotope N^* is in a non-resonant background N^+, the transport equation is given by :

$$\hat{\Omega}_n \nabla \Phi^g(r, \hat{\Omega}_n) + [N^* \sigma_t(u) + N^+ \sigma_t^+] \Phi^g(r, u, \hat{\Omega}_n) = Q^g(r, \hat{\Omega}_n) \tag{5}$$

where $Q^g(r, \hat{\Omega}_n)$ is the source of neutrons that can be due to scattering neutrons, fission neutrons or neutrons from external source.

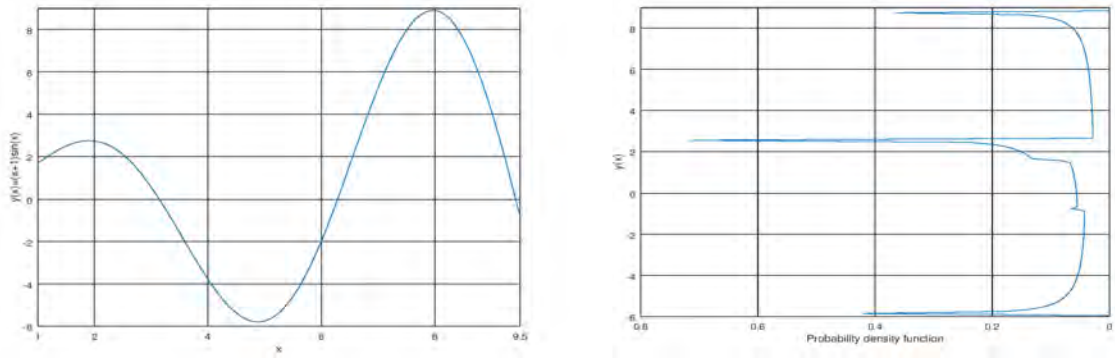

Fig.1. Representation of the probability density of the function $(x+1)sin(x)$

In the case we have a calculation code that is based on the S_n theory, it is possible to resolve the Eq.(5) and obtain the flux that will be a function of:

$$\Phi^g(r,\hat{\Omega}_n) = f[Q^g(r,\hat{\Omega}_n),\sigma_t(u)] \tag{6}$$

Since the flux is a quantity which depends on $\sigma_t(u)$,we can apply the sub-group method that we presented above and obtain the self-shielded cross section :

$$\sigma^g_{\rho,i} = \frac{\int_{u_{g-1}}^{u_g} \sigma_{\rho,i}(u)\Phi_i(u)du}{\int_{u_{g-1}}^{u_g} \Phi_i(u)du} = \frac{\sum_{k=1}^{K} \sigma_{\rho,k} f_k[Q^g(r,\hat{\Omega}_n),\sigma_{t,k}]}{\sum_{k=1}^{K} f_k[Q^g(r,\hat{\Omega}_n),\sigma_{t,k}]} \tag{7}$$

4.2 Moments method and mathematical probability tables

There are several subgroup methods. Their differences are about how to create the probability tables, which is the term to describe a quadrature set that represents a probability density. This term was introduced by Levitt [5]. In our case we will use a subgroup method that use mathematical probability tables. This method is a moments method which is based on Ribons method and more precisely on the Ribons extended self-shielding model proposed by Hebert and Coste. The moment approach allows to calculate the base points σ_k and the weights w_k simultaneously [6, 7, 8].

The first step of the method is to calculate the positive and negative moments M_l which are computed from the Riemann integrals of the microscopic cross-sections :

$$M_l = \frac{1}{\Delta u_g}\int_{u_{g-1}}^{u_g} \sigma(u)^l du \tag{8}$$

A K-order probability table is defined to preserve the 2K selected moments of Eq. (5) :

$$\sum_{k=1}^{K} w_k(\sigma_k)^l = M_l,\ 1-K \le l \le K \tag{9}$$

Using negative and positive moments allow to conserve a correct reaction rate at low and high values of the resonant cross sections. In the original Ribons method, they were no obligation for the choice of the different values of "l". The moments method is based on the Stieljes series and the Pade approximant. Considering the Stieljes function F(z) of the total cross-section moments, F(z) is defined as :

$$F(z) = \int_{min(\sigma)}^{max(\sigma)} \frac{(z\sigma)^{1-K}}{1-z\sigma} d\sigma = \sum_{l=1-K}^{K} z^l M_l + \mathbb{O}(z^{K+1}) \tag{10}$$

Then we use the Pade approximant to describe F(z) :

$$z^{K-1}F(z) = \sum_{l=0}^{2K-1} z^l M_{l-K+1} = \frac{\sum_{i=0}^{K-1} a_i z^i}{\sum_{j=0}^{K-1} b_j z^j + z^K} \tag{11}$$

Then by identification, we obtain the following linear system :

$$\begin{bmatrix} M_K & M_{K-1} & \cdots & M_1 \\ M_{K-1} & M_{K-2} & \cdots & M_0 \\ \vdots & \vdots & \ddots & \vdots \\ M_1 & M_0 & \cdots & M_{2-K} \end{bmatrix} \begin{bmatrix} b_0 \\ b_1 \\ \vdots \\ b_{K-1} \end{bmatrix} = - \begin{bmatrix} M_0 \\ M_{-1} \\ \vdots \\ M_{1-K} \end{bmatrix} \tag{12}$$

Resolving the Eq.(12) gives the coefficients b_k. Thanks to the property of the Pade approximant of a Stieljes series, the base point of the probability table σ_k are the roots of the following polynomial :

$$\prod_{k=1}^{K}(z-\sigma_k) = 1 + b_{K-1}z + \cdots + b_1 z^{K-1} + b_0 z^K \tag{13}$$

The second step is to calculate the corresponding weights w_k. They are chosen to preserve the moments of the total cross section :

$$M_l = \sum_{k=1}^{K} w_k \sigma_k^l \tag{14}$$

In our approach we have chosen to use a different set for the values of "l" compare to the set used in the Ribons extended method. The work of G. Chiba and H. Unesaki proved that preserving some values of the moments for $-1 \leq l \leq 0$ improve the accuracy of the probability tables description [9]. Eq.(15) gives the following linear system :

$$\begin{bmatrix} 1 & 1 & \cdots & 1 \\ \sigma_1^{-(K-1)^{-1}} & \sigma_2^{-(K-1)^{-1}} & \cdots & \sigma_K^{-(K-1)^{-1}} \\ \vdots & \vdots & \ddots & \vdots \\ \sigma_1^{-1} & \sigma_2^{-1} & \cdots & \sigma_K^{-1} \end{bmatrix} \begin{bmatrix} w_1 \\ w_2 \\ \vdots \\ w_K \end{bmatrix} = \begin{bmatrix} 1 \\ M_{-(K-1)^{-1}} \\ \vdots \\ M_{-1} \end{bmatrix} \quad (15)$$

Resolving this linear system gives us the weights w_k. The set $\{\sigma_k, w_k; k = 1, K\}$ is the probability table of the microscopic cross sections for the group g.

4.3 Verification of the Probability Table

Before using our probability table to perform calculation, we need to verify them by making a comparison between multi-group cross section calculated using the probability table and multi-group cross section using the Bondarenko self-shielding method.

For our example we calculated the multi-group fission cross section of Pu239 with the two methods for different values of dilution. On the Fig.2 we can see these cross sections.

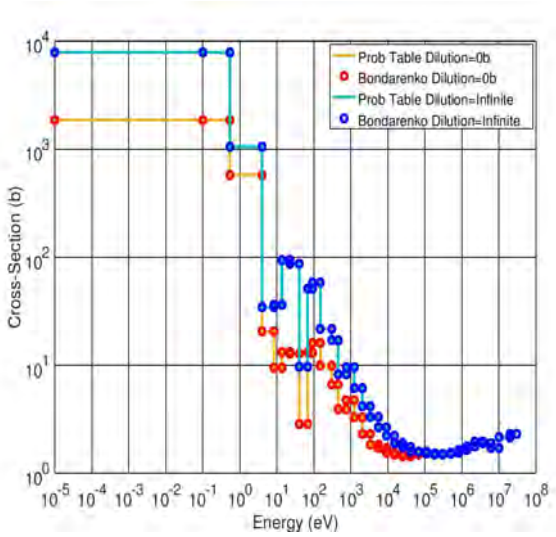

Fig.2. Multi-group fission cross section for Pu239

To see the real differences between the different type of cross section we also calculated the relative change. On the following table we can see the average and maximum error between the two different cross section for different values of dilution. As we can see, the results are good because the errors are less than 0.06703%.

Tab. 1. Errors between the two different cross section

Dilution (b)	Avg_err (%)	Max_err (%)
0	4.523e-2	6.703e-2
100	1.352e-3	2.319e-2
1.0e+4	1.219e-5	9.084e-5
1.0e+10	1.046e-5	6.6566e-5

5. Conclusion

We have started to improve this neutron transport code based on IGA method to take into account self-shielding effect. At the moment, we have found the self-shielding model, calculated and validated our probability table.

The next step is to code the sub-group method for "Sn" and perform calculations for a simple case. Then implement the method in our neutron calculation code based on IGA.

References

[1] W.F.G Rooijen and R. Horita. Three-dimensional "Sn" neutron transport calculations with iso-geometric analysis (IGA). Marrakech, Morocco, 17-19 September 2018. Proc. Int. Conf. PHYTRA4.

[2] Piegl L. and Tiller W. *The NURBS Book*. Springer, 1997.

[3] Hughues T.J.R. Austin Cottrell J. and Bazilevs Y. *Isogeometric Analysis : toward integration of CAD and FEA*. Wiley, 2012.

[4] Nikolaev M.N. Comments on the Probability Table Method. *Nucl. Sci. Eng.*, 61(286), 1976.

[5] Levitt L.B. The probability table metod for treating unresolved neutron resonances in monte carlo calculations. *Nucl. Sci. Eng.*, 49(450), 1972.

[6] Cullen D.E. Application of the Probability Table Method to Multigroup Calculations of Neutron Transport. *Nucl. Sci. Eng.*, 55(387), 1974.

[7] Ribon P. and Maillard J-M. Les Tables de Probabilite. Application au Traitement des Sections Efficaces pour la Neutronique. Technical report, Commisseriat l'Energie Atomique, 1986.

[8] Hebert A. The Ribon Extended Self-Shielding Model. *Nucl. Sci. Eng.*, 151(1-24), 2005.

[9] Chiba. G and Unesaki H. Improvement of Moment-Based Probability Table for Resonance Self-Shielding Calculation. *Annals of Nuclear Energy*, 33(1141-1146), 2006.

Proceedings of the Reactor Physics Asia 2019 (RPHA19) Conference
Osaka, Japan, Dec. 2-3, 2019

Study on Effective Cross Section of Pu Spot in MOX Fuel

Tatsuya Kawano[a,*], Satoshi Takeda[a], Takanori Kitada[a], Yasunori Ohoka[b], Shogo Matsuoka[b] and Hiroaki Nagano[b]

[a]*Osaka University, 1 Yamadaoka 1-chome Suita city Osaka Japan*

[b]*Nuclear Fuel Industories, Ltd., 950 Asashiro-Nishi 1-chome Kumatori-cho Sennan-gun Osaka Japan*

[*]Corresponding author: t-kawano@ne.see.eng.osaka-u.ac.jp

Abstract

It has been confirmed that Pu spot observes in MOX fuel pellet. In the study based on the deterministic method, it is necessary to calculate the appropriate effective cross section of Pu spot to evaluate the effect of Pu spot. Since the self-shielding effect of resonance varies depending on the particle size and the position in a fuel pellet, the effective cross section should be appropriately taken into account. Therefore, in this study, the influence of changing the particle position and particle size on the effective cross section of Pu spot was evaluated. The numerical results show that, in the case of calculation in the 107 group, the influence of changing the particle position and particle size on the effective cross section of Pu spot is mainly due to the effect of the resonance between 2 and 3 eV of Pu-242. Furthermore, it was also found the influence of changing the particle size is larger than that of the particle position.

Key Words: **Pu spot, self-shielding, resonance, effective cross section, reaction rate**

1. Introduction

It has been confirmed that Pu spot observes in MOX fuel production process. Recently, the importance of the double-heterogeneous model considering Pu spot for MOX fuel analysis has been emphasized [1], and it is necessary to calculate the effective cross section of Pu spot to evaluate the effect of Pu spot in the double-hete rogeneous model. These effective cross sections need to be calculated appropriately because self-shielding effect of resonance varies depending on the particle size and particle position in a fuel pellet. Therefore, in this study, the particle position and particle size were arranged to investigate the largest impact of changing them on the effective cross section, and the influence of changing the particle position and particle size on the effective cross section of Pu spot was evaluated.

2. Calculation Condition

In this study, in order to evaluate the effective cross section of particles in MOX fuel, the calculation of 107 groups for the pin cell model of a pressurized water reactor (PWR) is performed by integrated nuclear calculation code SRAC2006 [2]. The nuclear data library used in this study is JENDL-4.0 (Japanese evaluated nuclear data library) [3]. In order to evaluate the effect of the position on the effective cross section, the particles were arranged at the center and the edge in the fuel pellet. In addition, very large particle (400 μm) and small particle (50 μm) were used for the investigation of the effect of the particle size on the effective cross section. The reaction rate was calculated by GMVP [4] which is a General-purpose Monte Carlo code for neutron and photon transport calculation based on the multi-group method, and the influence of the reaction rate due to the change of effective cross section was confirmed. Furthermore, based on the result, it was confirmed which nuclide of Pu is mainly attributable to the effect. Figure 1 shows calculation geometry. Table I shows temperatures in each area. Table II shows the Pu enrichment of the matrix and Pu spot, the U-235 enrichment. Table III shows Pu isotope ratio in MOX fuel. Table IV shows calculation condition on GMVP. Figure 2 shows the calculation procedure. As shown in Fig. 2, effective cross sections in each area (Pu spot, matrix, cladding, moderator) were calculated by SRAC2006, then reaction rate was calculated by GMVP.

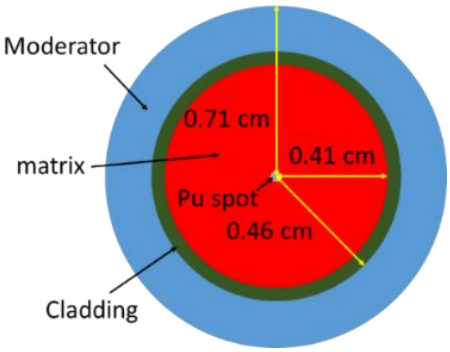

Fig. 1. Calculation geometry based on PWR pin-cell model

Table I. Temperatures in Each Area

	Fuel	Cladding	Moderator
temperature (K)	900	600	600

Table II. PuO_2 Content and U-235 Enrichment

	Matrix	Pu spot
PuO_2 content (PuO_2 / (PuO_2+UO_2))	1 wt %	100 wt %
U-235 enrichment (U-235 / U)	0.2 wt %	

Table III. Pu Isotope Ratio (wt %)

Pu-238	5
Pu-239	45
Pu-240	10
Pu-241	25
Pu-242	15

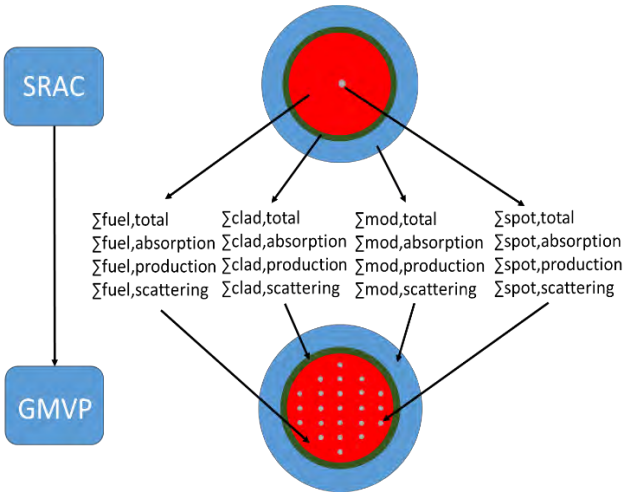

Fig. 2. Calculation procedure

Table IV. Calculation Condition of GMVP

Number of histories per batch	100000
Total number of batch	2050
Number of skip batch	50

3. Result and Discussion

3.1 Influence of changing the particle position on the effective cross section

Based on the calculation conditions given in Figs. 1, 2, and Tables I-III, the effective fission cross section and the effective capture cross section were calculated for the particle at the center and the edge in the fuel pellet. Figures 3 and 4 show the effective macroscopic fission and capture cross section. The relative differences shown in Figs. 3-5 were calculated by the comparison of the effective cross section at the edge in the fuel.

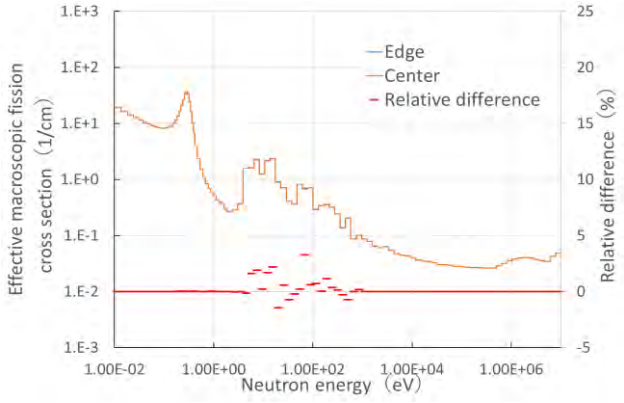

Fig. 3. Effect of position on effective macroscopic fission cross section

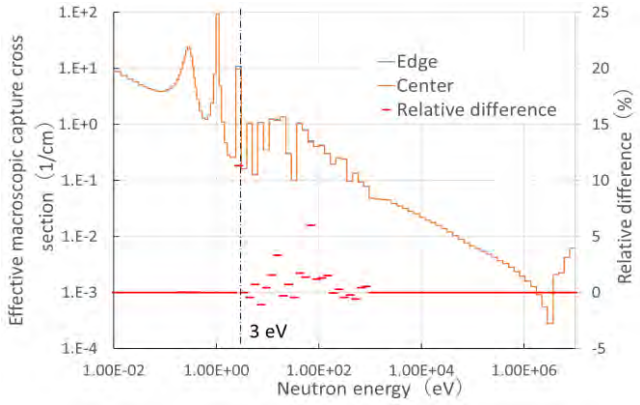

Fig. 4. Effect of position on effective macroscopic capture cross section

As shown in Figs. 3 and 4, the relative difference was mainly observed in the resonance energy region, and the largest relative difference was observed at resonance between 2 and 3 eV in the effective macroscopic capture cross section. Furthermore, based on the result, it was confirmed which nuclide of Pu is mainly attributable to the effect. The numerical results show that Pu242 is mainly attributable to the largest relative difference. Figure 5 shows effective macroscopic capture cross section of Pu-242. As shown in Fig. 5, it was found that the relative difference between 2 and 3 eV in effective cross section is due to Pu-242.

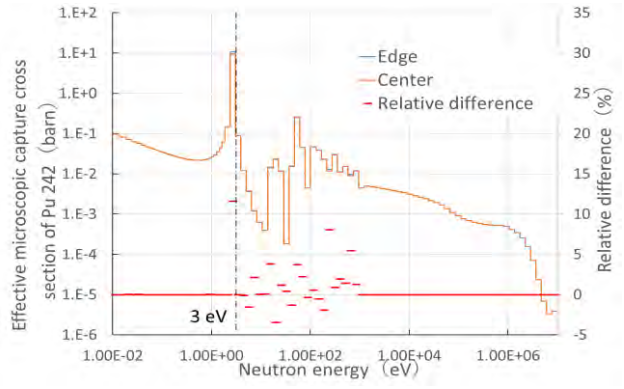

Fig. 5. Effect on effective macroscopic capture cross section of Pu-242 by change of the position

3.2 Influence of changing the particle size on the effective cross section

Based on the calculation conditions given Figs. 1, 2, and Tables I-III, effective fission cross section and effective capture cross section were calculated for large particle (400 μm) and small particle (50 μm). Figures 6 and 7 show the effective macroscopic fission and capture cross section, respectively. The relative differences shown in Figs. 6-8 were calculated by the comparison of the effective cross section of small particle (50 μm).

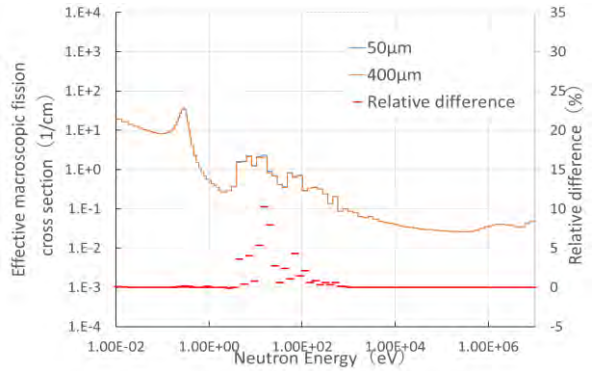

Fig. 6. Effect of particle size on effective macroscopic fission cross section

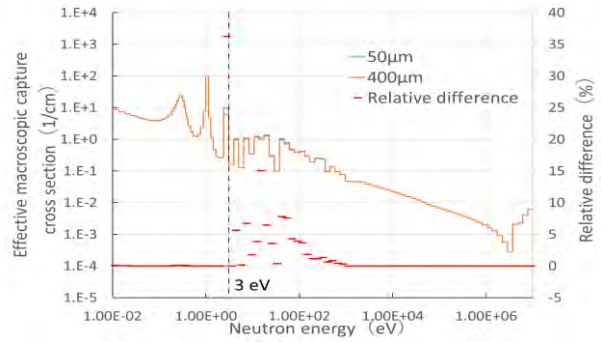

Fig. 7. Effect of particle size on effective macroscopic capture cross section

As shown in Figs. 6 and 7, the relative difference was mainly observed in the resonance energy region, and the largest relative difference was observed at resonance between 2 and 3 eV in the effective macroscopic capture cross section. Furthermore, based on the result, it was confirmed which nuclide of Pu is mainly attributable to the effect. The numerical results show that Pu242 is mainly attributable to the largest relative difference. Figure 8 shows the effective macroscopic capture cross section of Pu-242.

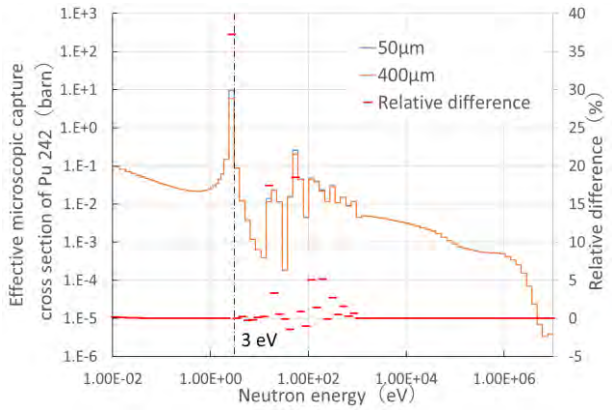

Fig. 8. Effect of particle size on effective macroscopic capture cross section of Pu-242

As shown in Fig. 8, it was found that the relative difference between 2 and 3 eV in effective cross section is due to Pu-242. Furthermore, it was also found that the change in particle size has a larger effect on the effective cross section than the change in position.

3.3 Influence of changing the particle size on the reaction rate

As mentioned in section 3.2, it was also found that the change in particle size has a larger effect on the effective cross section than the change in position. Therefore, the dependency of reaction rate on change particle size was described in this section. Based on the calculation conditions given Figs. 1, 2, and Tables I-IV, the macroscopic fission reaction rate and the macroscopic capture reaction rate were calculated by GMVP. Figures 9 and 10 show macroscopic fission reaction rate and macroscopic capture reaction rate, respectively. Figure 11 shows macroscopic capture reaction rate of Pu-242. The relative differences shown in Figs. 9-11 were calculated by the comparison of the effective cross section of small particle (50 μm). The reaction rates shown in Figs. 9-11 were calculated as reaction rates per production rate.

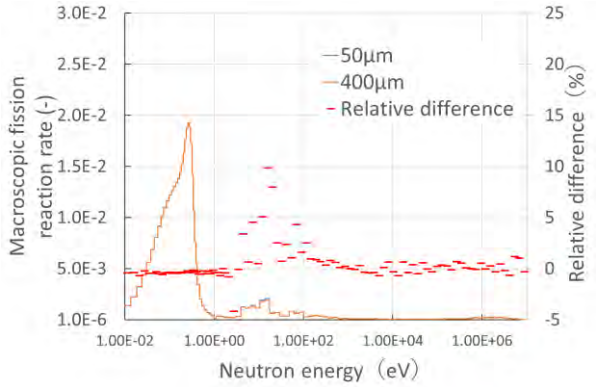

Fig. 9. Effect of particle size on macroscopic fission reaction rate

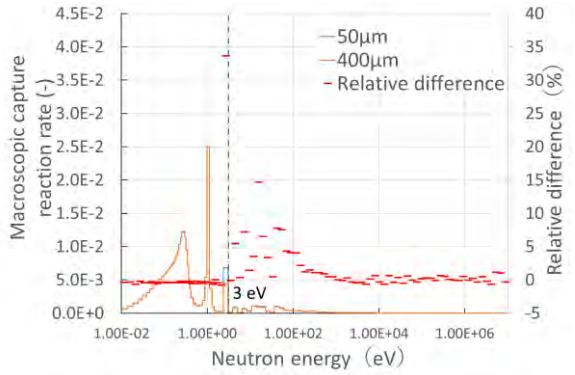

Fig. 10. Effect of particle size on macroscopic capture reaction rate

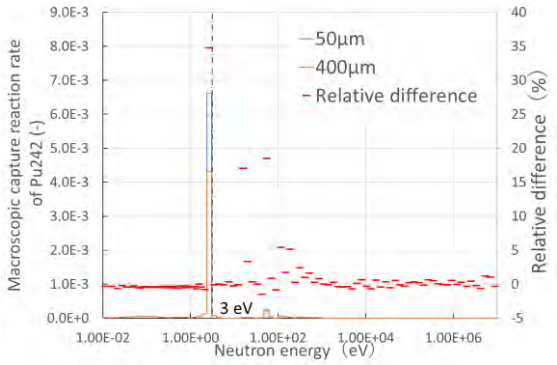

Fig. 11. Effect of particle size on macroscopic capture reaction rate of Pu-242

3.4 Discussion about energy group structure

As shown in Table V, in the 107-group structure, energy range between 2 and 3 eV is divided into about 2 groups. It is considered that the effect of the resonance of Pu-242 between 2 and 3 eV on the effective cross section can be decreased by increasing the division of energy range between 2 and 3 eV.

Table V. Energy Group Structure between 2 and 3 eV

Energy group number	Upper energy (eV)	Lower energy (eV)
61	3.0590	2.3820
62	2.3820	1.8550

4. Conclusion

In this study, in the case of calculation in the 107 group, the influence of changing the particle position and particle size on the effective cross section of the Pu spot is mainly due to the effect of the resonance between 2 and 3 eV of Pu-242. It was also found that the change in particle size has a larger effect on the effective cross section than the change in position. Furthermore, it is considered that the effect of the resonance between 2 and 3 eV of Pu−242 on the effective cross section can be decreased by increasing the division of energy range between 2 and 3 eV.

References

1. Reactor Integral Test Working Group, JENDL Committee, “Compilation of the Data Book on Light Water Reactor Benchmark to Develop the Next Version of JENDL– Utilization of Criticality Data in ICSBEP and IRPhEP Open Databases,” Japan Atomic Energy Agency (2017).
2. Okumura K, Kugo T, Kaneko K and Tsuchihashi K, “SRAC2006: A Comprehensive Neutronics Calculation Code System,” Japan Atomic Energy Agency (2007).
3. Shibata K, Iwamoto O, Nakagawa T, Iwamoto N, Ichihara A, Kunieda S, Chiba S, Furutaka K, Otuka N, Ohsawa T, Murata T, Matsunobu H, Zukeran A, Kamada S, and Katakura J, "JENDL-4.0: A New Library for Nuclear Science and Engineering," *J. Nucl. Sci. Technol.*, **48**, *1*, 1 (2011).
4. Nagaya Y, Okumura K, Sakurai T and Mori T, “MVP/GMVP Version 3: General Purpose Monte Carlo Codes for Neutron and Photon Transport Calculations Based on Continuous Energy and Multigroup Methods,” Japan Atomic Energy Agency (2017).

Modification of MOC for Considering Double Heterogeneity due to Pu Spots in MOX Fuel

Akifumi Ogawa[a*], Hikaru Yamaguchi[a], Satoshi Takeda[a], Takanori Kitada[a],
Yasunori Ohoka[b], Shogo Matsuoka[b] and Hiroaki Nagano[b]
[a]*Osaka University, 1 Yamadaoka 1-chome Suita city Osaka Japan*
[b]*Nuclear Fuel Industries, Ltd., 950 Asashiro-Nishi 1-chome Kumatori-cho Sennan-gun Osaka Japan*
[*]Corresponding author: a-ogawa@ne.see.eng.osaka-u.ac.jp

Abstract

The heterogeneity of Mixed Oxide (MOX) fuel due to Plutonium spots has impacts on criticality. In this study, a double heterogeneous model was introduced into OpenMOC by the model derived by R. Sanchez. The calculation result of modified OpenMOC was compared with that of GMVP. In the verification, the calculations were performed in pin-cell model. From the calculation results, the reactivity effect obtained by modified OpenMOC agrees with the results of GMVP within 0.1%Δk/kk′. Since the discrepancy comes from the difference between the lattice model used for GMVP and double heterogeneity model used for modified OpenMOC, it is confirmed that OpenMOC is properly modified for considering double heterogeneity due to Pu Spots.

Key Words: **Pu-spot, MOC, GMVP, Double-Heterogeneity**

1. Introduction

Plutonium (Pu) is produced through the operation of nuclear power plants. It is used as Mixed Oxide (MOX) fuel, but Pu spots exist in the Mixed Oxide (MOX) fuel pellets. It was found that the heterogeneity due to Pu spots has impacts on criticality in some systems [1]. The heterogeneous effects have been analyzed by Monte Carlo calculation. It can evaluate nuclear characteristics in detail, but Monte Carlo calculation results include the statistical error and the calculation cost is high compared to the deterministic method. Method Of Characteristics (MOC) is one of the deterministic method and the results don't include the statistical error. The double heterogeneous model for MOC has been derived by R. Sanchez [2-4], and Han Gyu Joo has derived analytic solution [5]. This model has been developed for the fuel compact of high-temperature gas-cooled reactor for considering. In this study, OpenMOC [6] is modified by applying the model in order to consider the heterogeneity due to Pu spots. As the verification, the results of modified OpenMOC is compared with that of GMVP.

2. Modification of OpenMOC

The calculation flow in the original OpenMOC code and the modified OpenMOC code are shown in Figs.1 and 2, respectively. Table I shows the newly added parameters for modification.

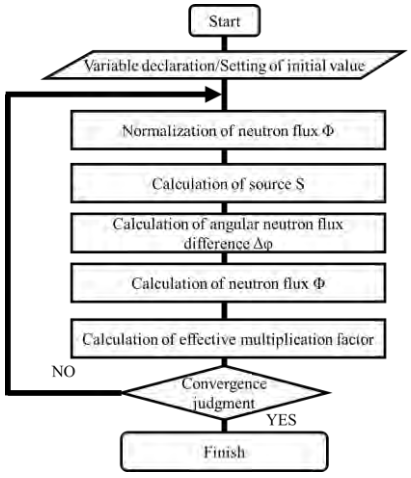

Fig. 1. Calculation flow of the original code

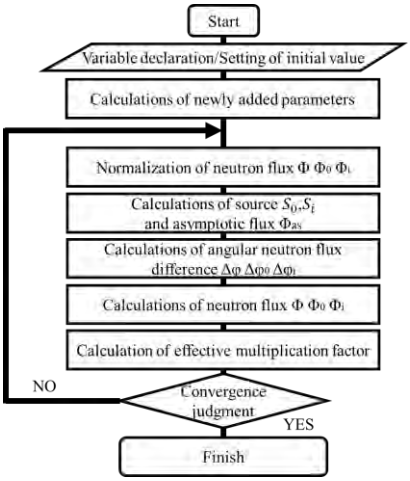

Fig. 2. Calculation flow of modified code

Table I. Newly Added Parameters for Modification

ϕ_0	Neutron flux in matrix
ϕ_i	Neutron flux in Pu spots
ϕ'	Average neutron flux
Σ_0	Cross section of matrix
Σ_i	Cross section of Pu spots
Σ	Homogenized cross section
E_i^g	Escape probability for neutrons generated in Pu spots to escape from the Pu spots without any collision
T_i^g	Transmission probability of neutron entering through surface of Pu spots
$\widehat{E_i^g}$	Reduced escape probability which corresponds to reduced cross section $(\Sigma_i - \Sigma)$
$\widehat{T_i^g}$	Transmission probability which corresponds to reduced cross section $(\Sigma_i - \Sigma)$
S_0	Source on matrix
S_i	Source on Pu spots
φ_{as}	Asymptotic flux
L_i	Pu spots diameter
p_0	Volume fraction of matrix
p_i	Volume fraction of Pu spots
$\tilde{\Sigma}$	Adjusted total cross section defined as $(\Sigma_0 + \frac{1}{p_0}\frac{p_i}{\bar{l}_i}(1 - T_i^g))$
Σ'	Adjusted total cross section defined as $(\Sigma_0 + \frac{1}{p_0}\frac{p_i}{\bar{l}_i}(1 - \widehat{T_i^g}))$
$\hat{\Sigma}$	Adjusted total cross section defined as $(p_0\Sigma_0 + p_i\Sigma_i\widehat{E_i^g})$
k_{eff}	Effective multiplication factor
χ	Fission neutron energy spectrum

The modifications of OpenMOC from the original to modified code are shown here.

i) Calculations of newly added parameters

The parameters E_i^g, T_i^g, $\widehat{E_i^g}$, and $\widehat{T_i^g}$ are calculated by the following formulas:

$$E_i^g = \frac{1}{\bar{l}_i}\int_0^{L_i} e^{-\Sigma_i y} \times \left(1 - \left(\frac{y}{L_i}\right)^2\right) dy, \quad (1)$$

$$T_i^g = \int_0^{L_i} e^{-\Sigma_i y}\frac{2}{{L_i}^2} y\, dy, \quad (2)$$

$$\widehat{E_i^g} = \int_0^{L_i} e^{-(\Sigma_i - \Sigma\prime)y} \left(1 - \left(\frac{y}{L_i}\right)^2\right) dy, \quad (3)$$

$$\widehat{T_i^g} = \int_0^{L_i} e^{-(\Sigma_i - \Sigma\prime)y}\frac{2}{{L_i}^2} y\, dy. \quad (4)$$

ii) Normalizations of neutron flux ϕ', ϕ_0, and ϕ_i

ϕ', ϕ_0 and ϕ_i are normalized based on the following formula:

$$\phi = \frac{\phi}{\Sigma\left((p_0 v\Sigma_0^F\phi_0 + p_i v\Sigma_i^F\phi_i) \times V\right) \times k_{eff}}. \quad (5)$$

iii) Calculations of sources S_0 and S_i

S_0, S_i, and φ_{as} are calculated by the following formulas:

$$S_0 = \frac{1}{4\pi}(\Sigma_{S,0}\phi_0 + \frac{\chi_0}{k_{eff}}\nu\Sigma_0^F\phi_0), \quad (6)$$

$$S_i = \frac{1}{4\pi}(\Sigma_{S,i}\phi_i + \frac{\chi_i}{k_{eff}}\nu\Sigma_i^F\phi_i), \quad (7)$$

$$\varphi_{as} = \frac{1}{\tilde{\Sigma}}\left(S_0 + \frac{p_i}{p_0}E_i^g S_i\right). \quad (8)$$

iv) Calculations of angular neutron flux differences $\Delta\varphi'$, $\Delta\varphi_0$ and $\Delta\varphi_i$

$\Delta\varphi'$, $\Delta\varphi_0$, and $\Delta\varphi_i$ are obtained by the following formulas using φ_{as}:

$$\Delta\varphi' = (\varphi_{as} - \varphi_{in}^0)\left(1 - e^{-\Sigma'x}\right)\frac{\hat{\Sigma}}{\Sigma'}, \quad (9)$$

$$\Delta\varphi_0 = (\varphi_{as} - \varphi_{in}^0)\left(1 - e^{-\Sigma'x}\right), \quad (10)$$

$$\Delta\varphi_i = (\varphi_{as} - \varphi_{in}^0)\left(1 - e^{-\Sigma'x}\right)\widehat{E_i^g}. \quad (11)$$

where, φ_{in}^0 is in-coming angular flux.

v) Calculations of neutron fluxes $\phi_0, \phi_i, and\ \phi'$

The neutron fluxes ϕ', ϕ_0, and ϕ_i are calculated by the following formulas by using S_0, S_i, φ_{as}, $\Delta\varphi'$, $\Delta\varphi_0$, and $\Delta\varphi_i$:

$$\phi_0 = \frac{4\pi}{\Sigma'}(\Sigma'\varphi_{as} + \frac{1}{A_n}\sum_{k\in A_n}\sum_{p=1}^{P}\omega_{m(k)}\omega_p\omega_k \sin\theta_k\Delta\varphi_0), \quad (12)$$

$$\phi_i = \frac{4\pi}{\Sigma'}(\Sigma'\varphi_{as}E_i^g + \left(1 - E_i^g\right)S_i + \frac{1}{A_n}\sum_{k\in A_n}\sum_{p=1}^{P}\omega_{m(k)}\omega_p\omega_k \sin\theta_k\Delta\varphi_i), \quad (13)$$

$$\phi' = \frac{4\pi}{\Sigma'}\left(\Sigma'\varphi_{as} + \frac{1}{A_n}\sum_{k\in A_n}\sum_{p=1}^{P}\omega_{m(k)}\omega_p\omega_k \sin\theta_k\Delta\varphi'\right). \quad (14)$$

3. Code verification

3.1 Calculation condition

This section shows the calculation condition of modified OpenMOC and the reference calculation obtained by GMVP [7]. The effective cross section was obtained by the collision probability method (PIJ) of SRAC2006 [8]. 107 energy groups structure is used. The fast neutron energy region is divided into 61 groups, and the thermal neutron energy region is divided into 46 groups. The fuel temperature is 900K and moderator temperature is 600K. JENDL-4.0 is used [9]. The verification was performed by changing the diameter of Pu spots. In the verification,

the Pu spots volume fraction is about 1% and the Pu enrichment of Pu spots is 100wt%. U-235 enrichment of the matrix is 0.2wt%. These calculations were performed under the conditions shown in Tables II and III. The total number of histories in GMVP calculation was 20 million excluding skipped histories.

Table II. Calculation Conditions on Modified OpenMOC

fuel temperature[K]	900
moderator temperature[K]	600
Pu spots diameter[μm]	100,200,400
Pu spots volume fraction	1%
number of polar angle (π) TY quadrature set	6
number of azimuth angle (2π)	32
length of path[cm]	0.01

Table III. Calculation Conditions on GMVP

Pu spot diameter[μm]	100,200,400
Pu spot volume fraction	approximately 1%
number of history	10000
number of batch without skipped batch	2000
skipped batch	50

Modified OpenMOC and GMVP calculations were performed in the pin-cell model. The geometry of pin-cell model is shown in Fig.3. In the GMVP calculation, Pu spots were treated by lattice model which assumes the spherical Pu spots is regularly arranged in the matrix. Note that the volume fraction of the Pu spots is not rigorously 1% in lattice model since the number of Pu spots in lattice model is integer value. Figures 4 and 5 show the overview of the lattice model for 100μm Pu spots and 400μm Pu spots, respectively. Table IV shows the diameter of the Pu spots, the number of Pu spots, and volume fraction of the Pu spots. Table V shows isotopic ratio of Pu.

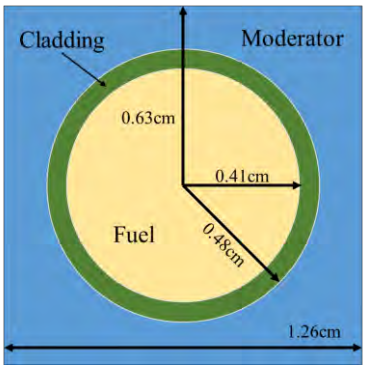

Fig. 3. Geometry of Pin-cell model

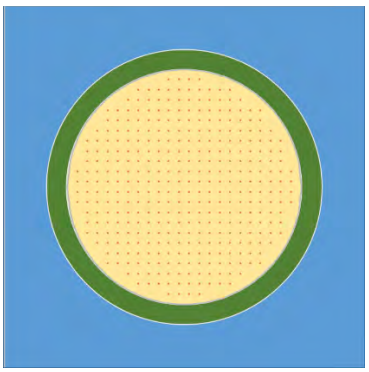

Fig. 4. Overview of lattice model for 100μm Pu spots

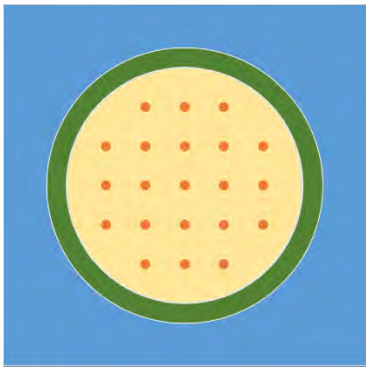

Fig. 5. Overview of lattice model for 400μm Pu spots

Table IV. Pu Spots Conditions

Pu spots diameter[μm]	number of Pu spots	volume fraction of Pu spots[%]
100	360	1.0012
200	86	0.9983
400	21	0.9750

Table V. Isotopic Ratio of Pu (wt%)

Pu-238	5
Pu-239	45
Pu-240	10
Pu-241	25
Pu-242	15

The heterogeneity reactivity effect is defined as the reactivity which is obtained by changing from the homogeneous model to heterogeneous model. The effect is defined as:

$$heterogeneity\ reactivity\ effect = \frac{1}{k_{(homogeneous\ model)}} - \frac{1}{k'_{(heterogeneous\ model)}}, \quad (15)$$

3.2 calculation results

Table VI and VII show the calculation result of modified OpenMOC and GMVP, respectively. Figure 6 shows the comparison of the heterogeneity reactivity effect between modified OpenMOC and GMVP.

Table VI. Result of Modified OpenMOC

	Pu spots diameter	infinite-multiplication factor	heterogeneity reactivity effect
homogenous model	-	1.185485	-
heterogeneous model	100μm	1.184218	-0.090%
	200μm	1.182571	-0.208%
	400μm	1.178735	-0.483%

Table VII. Result of GMVP

	Pu spots diameter	infinite-multiplication factor	statistical error (1σ)	heterogeneity reactivity effect	error(1σ)
homogenous model	-	1.18689	0.009%	-	-
heterogeneous model	100μm	1.18633	0.009%	-0.040%	0.011%
	200μm	1.18509	0.008%	-0.128%	0.011%
	400μm	1.18109	0.008%	-0.414%	0.010%

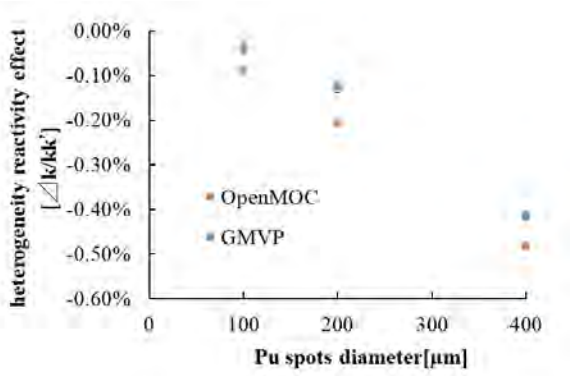

Fig. 6. Heterogeneity reactivity effect against Pu spots diameter

In both results of modified OpenMOC and GMVP, the heterogeneity reactivity effect is negatively increased with the increase of the Pu spots diameter. The magnitude of the heterogeneity reactivity effect obtained by modified OpenMOC is larger than the results of GMVP within 0.1 %Δk/kk′. The research by T. Yamamoto [10] also shows the magnitude of the heterogeneity effect obtained by the lattice model is smaller than that obtained by the random model. Although the statistical error of the heterogeneity effect is not negligible, the difference in the heterogeneity effect between the lattice model and random model is estimated about or less than the 0.05 %Δk/kk′. Therefore, it is considered that the difference in the heterogeneity effect between the results of GMVP and that of modified OpenMOC mainly comes from the difference between the lattice model and random model. From the calculation results, it is confirmed that OpenMOC is properly modified for considering double heterogeneity due to Pu spots in MOX Fuel. As the future research, more verification changing the Pu spots volume fractions is planned.

4. Conclusion

In this study, OpenMOC was modified in order to treat the double heterogeneity due to the Pu spots in MOX fuel. The modified OpenMOC was verified by the comparison with the calculation results obtained by GMVP. The results show that the heterogeneity reactivity effects obtained by modified OpenMOC and GMVP agree within 0.1%Δk/kk′ each other. The discrepancy is assumed to come mainly from the difference between the lattice model and random model, it is confirmed that OpenMOC is properly modified for considering double heterogeneity due to Pu spots.

References

1. Reactor Integral Test Working Group, JENDL Committee “Compilation of the Data Book on Light Water Reactor Benchmark,” Japan Atomic Energy Agency (2017).
2. Sanchez R, Pomraning GC, “A Statistical Analysis of the Double Heterogeneity Problem,” *Ann. Nucl. Energy.*, **18**, *7*, 371 (1991).
3. Sanchez R, Masiello E, “Treatment of the double heterogeneity with the method of characteristics,” *PHYSOR 2002*, October 7-10, (2002).
4. Sanchez R, “Renormalized treatment of the double heterogeneity with the method of characteristics,” *PHYSOR 2004*, April 25-29, (2004).
5. Joo HG, Park TK, “Derivation of Analytic Solution and MOC Calculation Procedure for Double Heterogeneity Treatment,” Seoul National University. SNURPL-SR-001 (2007).
6. William B, et.al “The Open MOC Method of Characteristics neutral particle transport code,” *Ann. Nucl. Energy*., **68**, 43 (2014).
7. Nagaya Y, Okumura K, Sakurai T, Mori T, “MVP/GMVP Version 3: General Purpose Monte Carlo Codes for Neutron and Photon Transport Calculations Based on Continuous Energy and Multigroup Methods,” JAEA-Data/Code 2016-018 Japan Atomic Energy Agency (2017).
8. Okumura K, Kugo T, Kaneko K, Tsuchihashi K, “SRAC2006: A Comprehensive Neutronics Calculation Code System,” Japan Atomic Energy Research Institute (2007).
9. Shibata K, Iwamoto O, Nakagawa T, Iwamoto N, Ichihara A, Kunieda S, Chiba S, Furutaka K, Otuka N, Ohsawa T, Murata T, Matsunobu H, Zukeran A, Kamada S, and Katakura J: “JENDL-4.0: A New Library for Nuclear Science and Engineering,” *J. Nucl. Sci. Technol*., **48** *1*, 1 (2011).
10. Yamamoto T, Sakai T, and Iwahashi D, “Effect of Pu-rich agglomerates in MOX fuel on reactivity analysis of light water reactor MOX core physics experiments,” *J. Nucl. Sci. Technol.,* **55**, *4*, 438 (2018).

Proceedings of the Reactor Physics Asia 2019 (RPHA19) Conference
Osaka, Japan, Dec. 2-3, 2019

Reactivity-Equivalent Physical Transformation for Homogenization Analysis of Double-Heterogeneous Fuel and Burnable Poison

Lou Lei[a], Yao Dong[a], Chai Xiaoming[a], Yu Yingrui[a] and Peng Xingjie[a,*]
[a] *National Key Laboratory of Science and Technology on Reactor System Design Technology, Nuclear Power Institute of China, No.328, Section 1, Changshun Avenue, Shuangliu, Chengdu, Sichuan, China*
[*]Corresponding author: loulei.necp@qq.com

Abstract

The traditional volumetric homogenization method on fuel and burnable poison with double heterogeneity will bring a certain calculation deviation. In the paper, from the DH(Double Heterogeneous) inequality criterion, the relationship between the calculation deviation of volumetric homogenization method and various factors on the dispersed particle-type fuel and burnable poison are analyzed. It is pointed out that for high enrichment or large size fuel particles and all types of burnable poisons, the traditional volumetric homogenization method will bring a certain calculation deviation. And then RPT(Reactivity-Equivalent Physical Transformation) method was used to treat dispersed particle-type fuel and burnable poison, the results show that the RPT method can be used to treat the dispersed particle-type fuel and burnable poison with relatively not too large absorption cross section which have double heterogeneity, and the calculation accuracy is similar to that of the grain model.

Key Words: **dispersed particle-type fuel burnable poison double-heterogeneity RPT method**

1. Introduction

Dispersed particle-type fuel[1] has been widely used in FCM(Fully Ceramic Micro-encapsulated Fuel) fuel and HTGRs(High Temperature Gas-cooled Reactors) fuel, and dispersed particle-type burnable poison has been more and more concerned because of its lasting and adjusting reactivity control ability. But the space self-shielding effect of the dispersed particle-type fuel and burnable poison will bring double heterogeneity which is the heterogeneity between dispersed fuel and matrix and the heterogeneity of fuel pin, clad and moderate in the cell level. The space self-shielding effect will make neutron flux in the center of fuel lower than that in the outer layer of the particle and that in the matrix, so the traditional pressurized water reactor calculation program with the traditional volumetric homogenization method will bring a certain calculation deviation. It's the challenge of double-heterogeneity for the calculation of dispersed particle-type fuel and burnable poison.

2. Homogenization Model

In order to better describe the random distribution of dispersed particles in the matrix, the Monte Carlo program RMC[2] was used to model the dispersed particles. For example, when 1000 UO_2 fuel particles with radius of 100μm are dispersed randomly in zirconium matrix, the distribution is shown in Fig. 1.

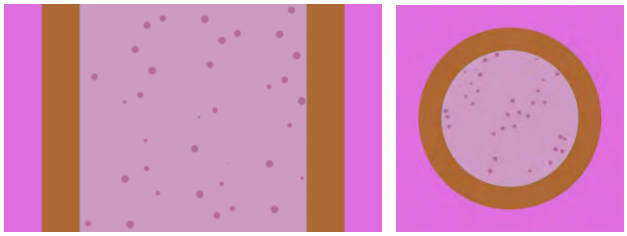

Side view Top view

Fig. 1. dispersed positions of 1000 fuel particles with the radius of 100μm

In order to compare the accuracy of the VHM(Volumetric Homogenization Model) and the GM(Grain Model), the following calculation case was constructed. With the parameters of Table 1, results of the VHM and the GM are compared in Fig. 2.

Table 1 Parameters of calculation case

Parameter	Value
Lattice pitch, cm	1.0
Pin radius, cm	0.6
Clad thickness, cm	0.1
Gas thickness between clad and pin, cm	0.0008
Pin height, cm	0.6

Dispersed particle radius, μm	100
Dispersed particle number, number	1000
UO_2 fuel enrichment, wt%	20.0

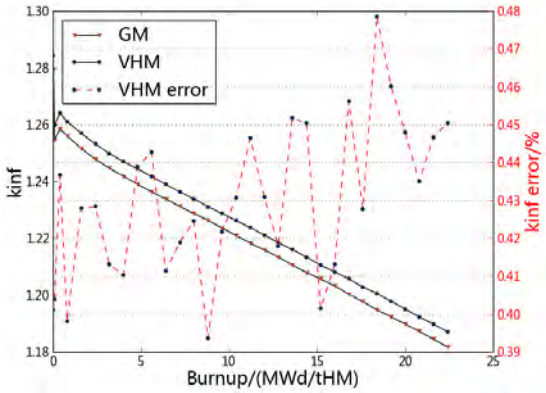

Fig. 2. Comparison of k_{inf} as function of burnup between the VHM and the GM

It can be observed from Fig. 2 that at the beginning of burnup k_{inf} of the VHM is larger than that of the GM, and as the burnup increases, relative deviation of the k_{inf} between the VHM and the GM is basically maintained at around 4‰~5‰. This relative deviation may increase with certain factors of the particle, and it may not meet the design requirements when the accuracy requirements are high. So it's necessary to analyze the deviation of the double heterogeneous dispersed fuel and study the appropriate method for neutronic calculation.

3. Deviation Analyze of Volumetric Homogenization Model

The traditional volumetric homogenization method underestimates the space self-shielding of the particles, and it's the cause of the deviation. There is a DH inequality criterion $|\Sigma_{matrix} - \Sigma_{grain}| \cdot d_{grain} > \varepsilon$, which can be used to determine if the space self-shielding of the particles need to be considered. In the above DH inequality criterion, Σ_{matrix} and Σ_{grain} are the macro cross section of the matrix and grain, d_{grain} is the diameter of the particle, and ε is the limit of optical length generally set to be 0.1 which means the flux deviation limit between the particles and the matrix is 10%.

According the above DH inequality criterion, the main influencing factors of the space self-shielding effect are the diameter of fuel particles and the fuel enrichment. So in the following the reactivity deviation between the VHM and GM will be analyzed.

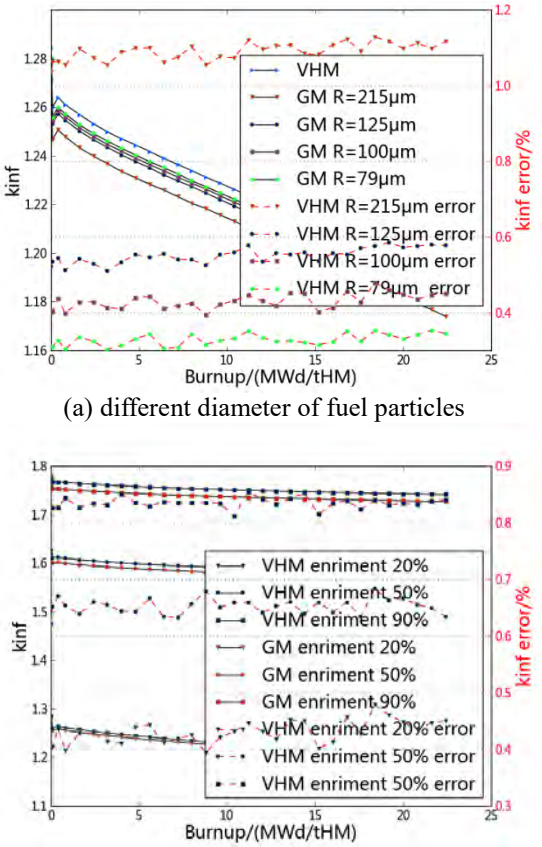

(a) different diameter of fuel particles

(b) different fuel enrichment

Fig. 3. Comparison of k_{inf} as function of burnup between the VHM and the GM with different diameter of fuel particles and different fuel enrichment

It can be observed from Fig. 3 that the reactivity deviation between the VHM and the GM is lower than 5‰ when the fuel enrichment is 20‰ and the diameter of fuel particles is less than 100μm. And the reactivity deviation is growing larger as the diameter of fuel particles or the fuel enrichment increases.

According the above results, the diameter of fuel particles and the fuel enrichment are the main influencing factors of the reactivity deviation. When the fuel enrichment or the diameter of fuel particles is relatively large, the traditional volumetric homogenization method will bring relatively large reactivity deviation, so it's necessary to study the computational model that can be applied to dispersed fuel and burnable poison.

4. RPT Model

4.1 RPT method introduction

For columnar and spherical geometry, the process of RPT[3](Reactivity-equivalent Physical Transformation) method can be found in Fig. 4. The first step is to compress all fuel particles in a smaller fuel zone, and the second step is to homogenize the fuel zone with volume weight. After the above two steps the traditional PWR p

rogram can be used to calculate the homogenized system . In RPT method, the diameter of the compressed fuel zo ne can be determined by ensuring the k_{inf} of system equal to the reference value which is obtained by a high fideli ty deterministic program or a Monte Carlo program.

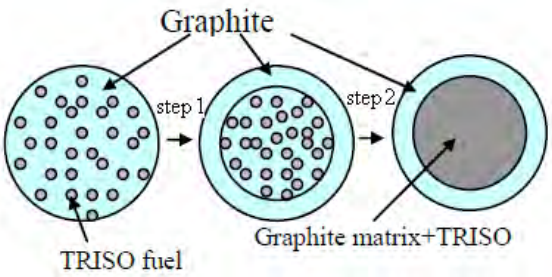

Fig. 4. The RPT Process

4.2 Numerical results

In order to get the radius of the compressed fuel zone in PRT method, an external script program was made to search the radius in which the k_{inf} of the system will be equal to that of RMC reference result, and then the burnup calculation was made to analyze the k_{inf} of system and other parameters change with burnup.

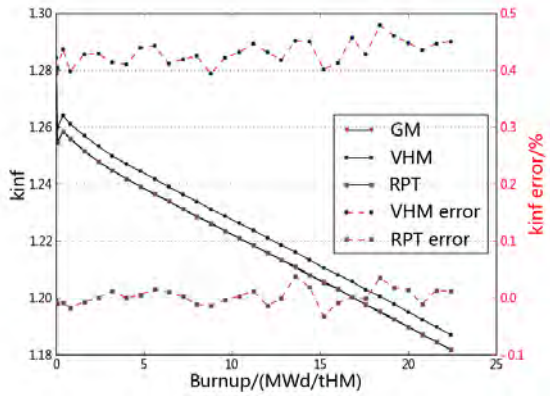

(a) k_{inf} of fuel enrichment 20%

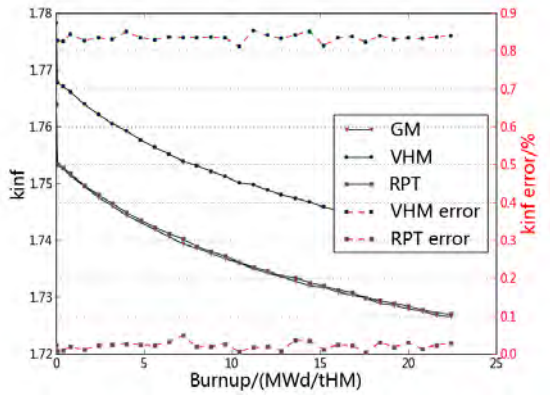

(b) k_{inf} of fuel enrichment 90%

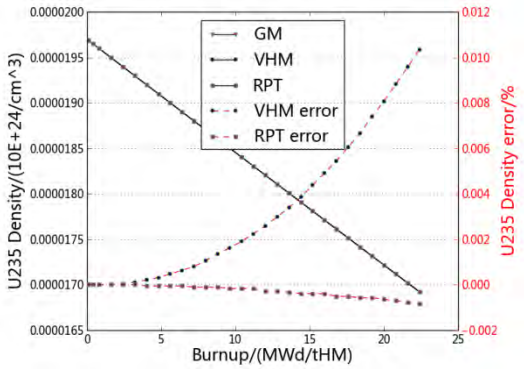

(c) ^{235}U nuclear density of fuel enrichment 20%

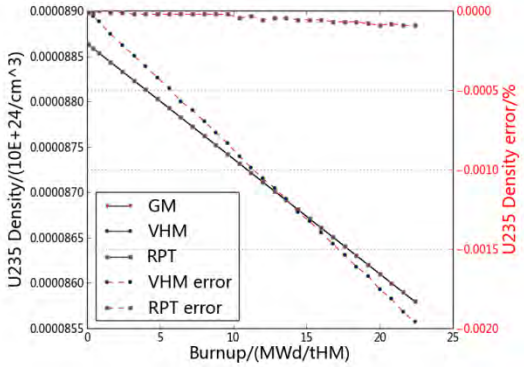

(d) ^{235}U nuclear density of fuel enrichment 90%

Fig. 5. k_{inf} and ^{235}U nuclide density as function of b urnup in cells with different enrichments and differe nt models

It can be observed from Fig. 5 that for dispersed fuel particles deviation of k_{inf} and ^{235}U nuclide density after RPT method keeps very small in the burnup life, which means RPT method can be used to calculate the neutronic parameters of dispersed fuel particles with double heterogeneity.

Because of the space self-shielding effect particle type burnable poison also need RPT method to treat the double heterogeneity. The reactivity deviation of different models as function of burnup shows in Fig. 6.

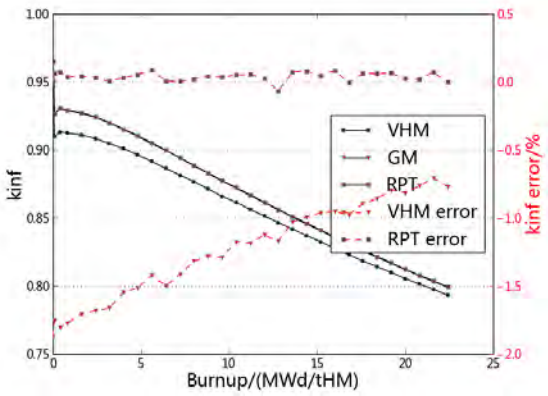

(a) AG

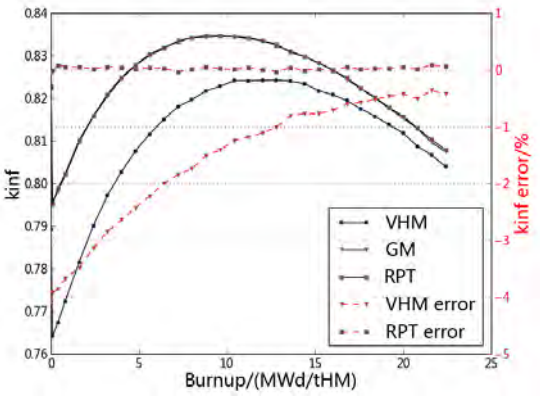

(b) HF

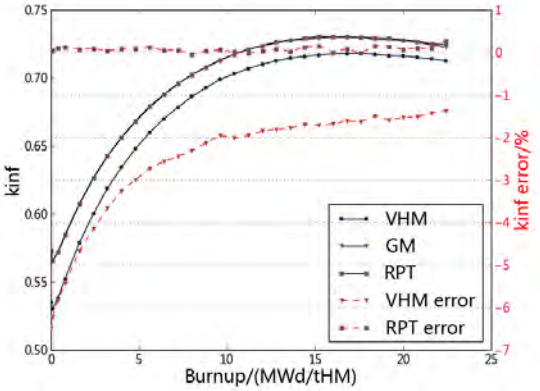

(c) Dy_2O_3

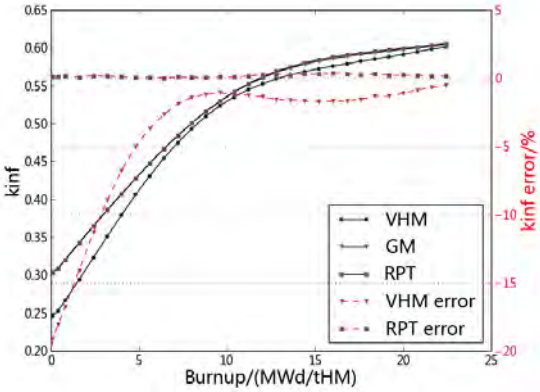

(d) Eu_2O_3

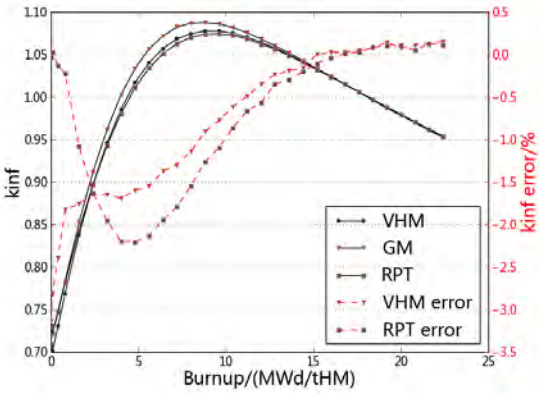

(e) B_4C

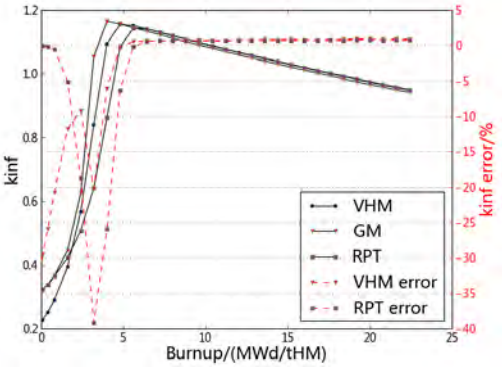

(f) Gd_2O_3

Fig. 6. k_{inf} as function of burnup in cells with differ ent burnable poison and different models

5. Conclusions

In this article, the calculation deviation of volumetric homogenization method and various factors on the dispersed particle-type fuel and burnable poison is analyzed. The research results shows that the enrichment of fuel particles, the size of fuel and burnable poison particles and the type of burnable poison are the main factors of double heterogeneity calculation. When these factors are relatively large, it will bring ineligible deviation. And then RPT method in the calculation of dispersed particle-type fuel and burnable poison shows that the RPT method can be used in the neutronic calculation of dispersed particle-type fuel and burnable poisons and the calculation deviation can be controlled within an acceptable range. For dispersed particles of burnable poison with large absorb cross section it's necessary to find a new method to solve the double heterogeneity.

Acknowledgements

This work is supported by the National Natural Scie nce Foundation of China (Approved number Nos.117 0051016).

References

[1] IAEA-TECDOC-1797, Accident Tolerant Fuel Concepts for Light Water Reactor, Proceedings of a Technical Meeting held at Oak Ridge National Labratories, United States of America, 13-16,October 2014.

[2] Shichang Liu, Ding She, Jin-gang Liang and Kan Wang，Random Geometry Capability in RMC Code and Applications to Stochastic Media Analysis，RPHA15,Jeju, Korea, Sept.16-18, 2015.

[3] Kim, Y., Kim, K., & Noh, J. Reactivity-Equivalent Physical Transformation for Homogenization of Double-Heterogeneous Fuels, Transactions of Korean Nuclear Society Autumn Meeting, Busan, Korea, October 27-28, 2005.

Proceedings of the Reactor Physics Asia 2019 (RPHA19) Conference
Osaka, Japan, Dec. 2-3, 2019

Prediction Analysis of ^{243}Am/^{235}U Fission Rate Ratio at KUCA Solid Moderator Core

Tadafumi Sano[a,*], Jun-ichi Hori[b] and Yoshiyuki Takahashi[b]
[a]*Kindai University Atomic Energy Research Institute,*
3-4-1, Kowakae, Higashi-Osaka, Osaka, 577-8502, Japan
[b]*Institute for Integrated Radiation and Nuclear Science, Kyoto University,*
2-1010, Asashiro-nishi, Kumatori-cho, Sennan-gun, 590-0494, Japan
[*]Corresponding author: t-sano@kindai.ac.jp

Abstract

We are planning new measurements of ^{243}Am/^{235}U fission rate ratio by using a back-to-back (BTB) fission chamber at two KUCA solid moderator core with difference neutron spectrums. The one core is named "EE1" which is one of typical experimental core at KUCA. Another core which named "EEG14" is newly construct for the present study. The "EEG14" core has hard neutron spectrum than EE1. In this study, prediction calculations of the criticalities and the fission rate ratio in the two KUCA cores. As the results, the k_{eff} of the EE1 is 1.00454±0.0139 % and that of the EEG14 is 1.00386±0.0144 % by using MVP3.0 with JENDL-4.0. The results of the fission rate ratio by using the JENDL-4.0 in the EE1 is 1.70E-2±1.86 %, the EEG14 is 5.75E-2. In addition, only the ^{243}Am cross sections were taken from JENDL-4.0, JENDL-3.3 and ENDF/B-VII.0 but the other nuclides were done from JENDL-4.0, to examine an impact of the difference of ^{243}Am cross section among these nuclear libraries to the fission rate ratio. As a result, the fission rate ratio with JENDL4.0 was about 10% larger than that of other libraries.

Key Words: **Minor Actinide, Fission Rate Ratio, Integral Experiment, KUCA, Back-to-back fission chamber**

1. Introduction

Accurate nuclear data of minor actinides (MAs) have important contribution for developments of nuclide transmutation technique, design of fuel cycle and disposal of high level radioactive waste (HLW). In order to verify evaluated nuclear data of MAs, a lot of integral experiments at various critical assemblies and research reactors were carried out. The measured integral neutronics characteristics were criticality, reactivity, sample reactivity worth, reaction rate distribution, reaction rate ratio and so on. The measurements of MAs (^{237}Np, ^{241}Am, ^{243}Am, ^{245}Cm and ^{246}Cm) reaction rate or reaction rate ratio were performed to obtain thermal neutron capture cross sections at various critical assembly and research reactor [1-3]. On the other hand, in order to perform the integral evaluation for the nuclear data libraries, ^{237}Np/^{235}U and ^{241}Am/^{235}U fission rate ratios by back-to-back (BTB) fission chamber and ^{237}Np/^{197}Au capture rate ratios has been obtained in the Kyoto University Critical Assembly (KUCA) [4-6].

^{243}Am is an important nuclide for the nuclear design and the design of HLW disposal, because ^{243}Am is a fertile nuclide of high-order minor actinides such as Cm. So, a lot of integral data for ^{243}Am capture cross section. However, there are few integral data of ^{243}Am fission cross section in thermal neutron system, because the fission cross section of ^{243}Am is very small compare to the capture cross section. Then, in order to enhance the integral data of ^{243}Am fission cross section, we are planning new measurements of ^{243}Am/^{235}U fission rate ratio by using the BTB fission chamber at the KUCA solid moderator core. The experiments will be performed with two cores which are soft and hard neutron spectrum cores. Then, in this study, prediction calculations of criticalities, neutron spectrum and ^{243}Am/^{235}U fission rate ratio in the two cores which are soft and hard spectrum cores are carried out.

The calculational models are explained at section II. In section III, the results of prediction calculations is described.

2. Calculational model

2.1 BTB fission chamber

Figure 1 shows a sample foil (^{235}U or ^{243}Am) with backing plate and a BTB fission chamber. The backing plate is made with titanium. The BTB fission chamber and the electrode is aluminum alloy (Al5052). The connector is made with cupper. A diameter of the foil is 20 mm. The backing plate has 30 mm diameter and 0.1 mm thickness. The distance from the sample deposit to electrode is 14 mm.

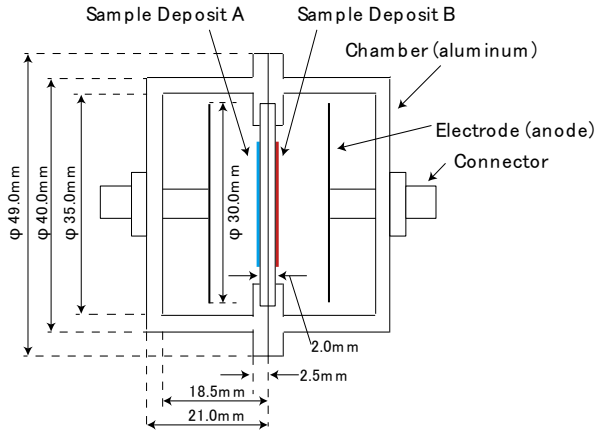

Fig. 1. BTB fission chamber.

2.2 Core Configuration

In KUCA, fuel and moderator plates in fuel element were set in a 1.5mm thickness aluminum sheath and all material plates have nominal cross section of 2” square. In this study, two cores with different neutron spectrum will be constructed. The one core is named EE1. The EE1 is one of typical experimental core at KUCA. The core configuration and the fuel element configuration are shown in Fig. 2. The fuel element is consisted of 60 unit cells and sandwiched by an upper and a lower polyethylene reflector. The upper and lower polyethylene reflector has 18” length. The unit cell has two enriched uranium (EU) plates of 1/16” thickness, one polyethylene plates of 1/8” thickness. The core is consist of 29 fuel element and one void tube with the BTB fission chamber.

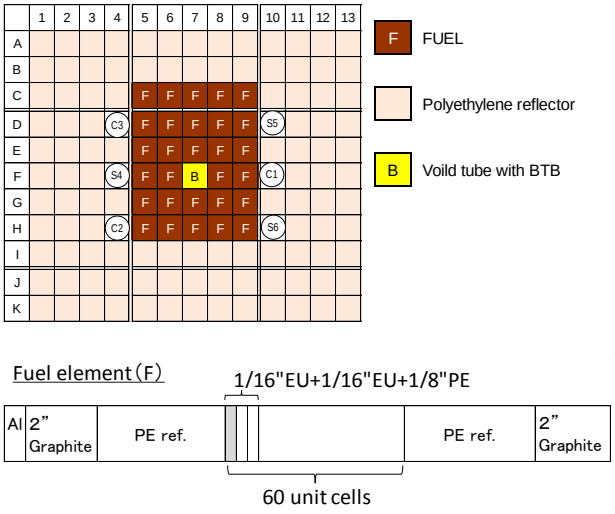

Fig. 2. Configurations of EE1 core and Fuel element (F).
(C : Control rod, S : Safety rod)

Another core is named EEG14 with hard neutron spectrum shown in Fig. 3. The EEG14 is newly set up for present study. The neutron spectrum in the core is more hardly than EE1. Then, the sensitivity of resonance fission in the core will be larger than EE1. The fuel element (F) is consisted of 41 unit cells and sandwiched by 2” bdellium and 16” polyethylene reflector. The unit cell has two 1/16” EU plates and one graphite plate of 1/4” thickness. The unit cell of driver fuel has one 1/16” EU plate and two 1/8” polyethylene plates. The driver fuel element (D) is consisted of 43 unit cells and sandwiched by 2” bdellium and 16” polyethylene reflector. The EEG14 is consisted of 24 fuels and 26 Driver fuels. In addition, the core are surrounded by graphite reflectors. The BTB fission chamber is set into “F-7”.

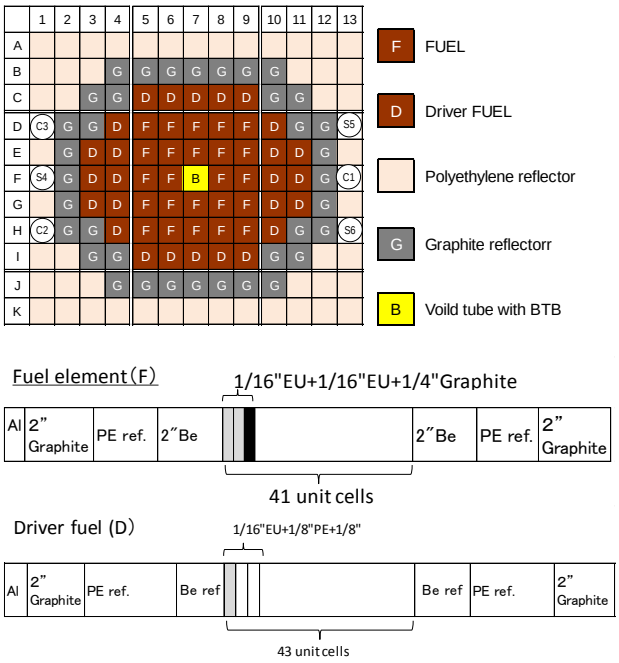

Fig. 3. Configurations of EEG14 core, Fuel element (F) and Driver fuel element (D).
(C : Control rod, S : Safety rod)

3. Prediction Analysis and Discussion

3.1 Criticality and Neutron Spectrum

In this sub-section, the criticalities and the neutron spectrum in the BTB fission chambers were calculated by the use of MVP3 [7] with JENDL-4.0 [8]. In particular、the criticality and the neutron spectrum of EEG14 is important. In the calculations, 300M neutron histories are generated to suppress the statistical error of k_{eff} to less than 0.03 % (1σ) because the typical experimental error for the k_{eff} is estimated to be about 0.03 %dk/k [9]. As the results, the k_{eff} of the EE1 (Fig.2) is 1.00454±0.0139 % and that of the EEG14 (Fig.3) is 1.00386±0.0144 %. As a result, it was confirmed that both cores reached criticality. Figure 4 shows the neutron spectrum in the BTB fission chamber. Here, a spectrum index is defined as follows;

$$\text{Spectrum Index} = \frac{\int_{1E-5\ eV}^{1.0\ eV} \phi \frac{dE}{E}}{\int_{1E-5\ eV}^{20\ MeV} \phi \frac{dE}{E}} . \quad (1)$$

The spectrum index at the position of the BTB fission chamber in EE1 core is 0.19. In the EEG15, the spectrum index at the position of the BTB fission chamber is 0.02.

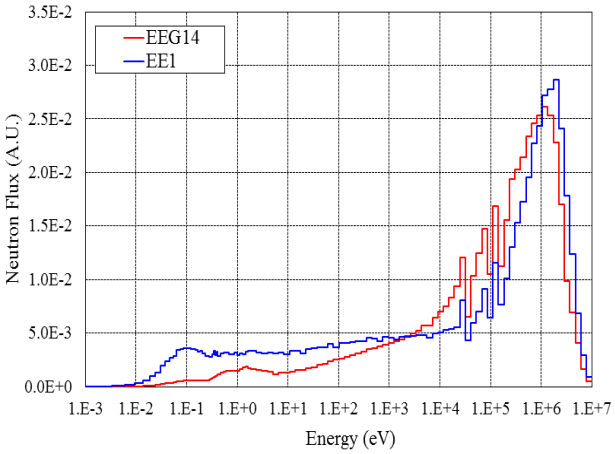

Fig. 3. Neutron spectrum in BTB fission chamber.

3.2 Fission Rate Ratio

The prediction analysis of the fission rate ratio are carried out by using MVP3 with JENDL-4.0, where only the ^{243}Am cross sections were taken from JENDL-4.0, JENDL-3.3 [10] and ENDF/B-VII.0 [11] but the other nuclides were done from JENDL-4.0, to examine an impact of the difference of ^{243}Am cross section among these nuclear libraries to the fission rate ratio. In the calculations, 1G neutron histories are generated to suppress the statistical error of fission rate ratio to less than 2.0 % (1σ) because the typical experimental error for the fission rate ratio is estimated to be about 2.0-2.3 % [9].

The results of the calculated fission rate ratio are shown in Table.1. From table 1, the fission rate ratio in EEG14 are about 3 times larger than EE1 because of the difference of neutron spectrum. Using the ^{243}Am cross section in JENDL-3.3 and ENDF/B-VII.0 from JENDL-4.0, the fission rate ratio in the EE1 is reduced about 3 %. In the EEG14, the reduction is 9 to 10 %.

Table 1. Calculated ^{243}Am/^{235}U fission rate ratio

	EE1	EEG14
JENDL-4.0	1.70E-2± 1.86 %	5.75E-2± 1.93 %
JENDL-3.3	1.66E-2± 1.88 %	5.23E-2± 1.94 %
ENDF/B-VII.0	1.65E-2± 1.86 %	5.20E-2± 1.94 %

Figure 4 and 5 shows the energy distribution of the fission rate ratio in the EE1 and the EEG14. From the both of figures, the ^{243}Am fission rate has a high sensitivity in a region of 2 MeV. In addition, the fission rate has sensitivities at resonance of 1.356 eV and 1.744 eV, respectively. ^{235}U fission rate in the EE1 are found to be dominant over the thermal region shown in Fig.7. In the EEG14, ^{235}U fission rate in the thermal energy region is decreased by hard neutron spectrum.

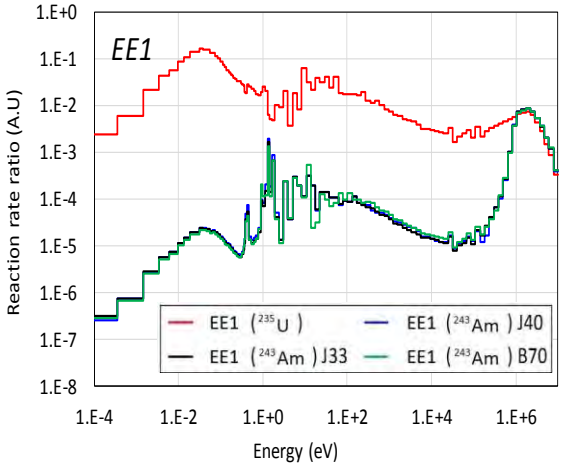

Fig. 4. Energy wise contribution of ^{243}Am and ^{235}U fission rate by MVP3 in EE1.

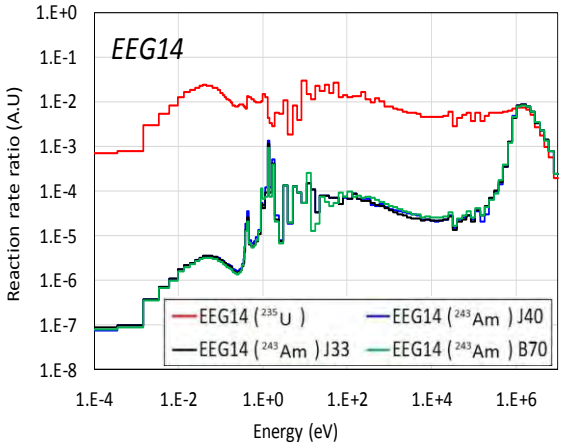

Fig. 5. Energy wise contribution of ^{243}Am and ^{235}U fission rate by MVP3 in EEG14.

5. Conclusion

For the purpose of enhancing the integral data to improve the accuracy of Am243 fission cross section, we are planning new measurements of ^{243}Am/^{235}U fission rate ratio by using the BTB fission chamber at the KUCA solid moderator core. The experimental cores were two cores which are soft and hard neutron spectrum cores. In this study, the prediction calculation of criticalities, neutron spectrum and ^{243}Am/^{235}U fission rate ratios were carried out.

1. Criticality and neutron spectrum

The multiplication factor of EE1 was 1.00454±0.01 39 % and that of the EEG14 is 1.00386±0.0144 %..

As the results, it was confirmed that both cores re ached criticality. The spectrum index of EE1 was 0.

19, and EEG14 was 0.02.

2. Fission rate ratio

The prediction calculation of ^{243}Am/^{235}U fission rate ratios in the EE1 and EEG14 were carried out. The ratio using by the JENDL-4.0 were 1.70E-2 ±1.86 % in the EE1 and the EEG14 was 5.75E-2±1.93 %.

Only the ^{243}Am cross sections were taken from JENDL-4.0, JENDL-3.3 and ENDF/B-VII.0 but the other nuclides were done from JENDL-4.0, to examine an impact of the difference of ^{243}Am cross section among these nuclear libraries to the fission rate ratio.

From the above results, it was found that ^{243}Am/^{235}U fission rate ratio depending on the neutron spectrum can be measured in KUCA solid moderator core.

Acknowledgements

The present work was performed as a joint research program of the KUCA at the Institute for Integrated Radiation and Nuclear Science, Kyoto University and supported by Kansai Genshiryoku Kondankai.

References

1. Kobayashi K, et al., “Measurements of Thermal Neutron Cross Section and Resonance Integral for 237Np (n, γ) 238Np Reaction,” *J. Nucl. Sci. and Technol.,* **31**, 1239 (1994).
2. Harada H, et al., “Measurement of Effective Capture Cross Section of 238Np for Thermal Neutrons,” *J. Nucl. Sci. and Technol.,* **41**, 1 (2004).
3. Ohta M, et al., “Measurement of Effective Capture Cross Section of Americium-243 for Thermal Neutrons,” *J. Nucl. Sci. and Technol.*, **43**, 1441 (2006).
4. Iwasaki T, et al., “Measurement and Analysis of Capture Reaction Rate of 237Np in Various Thermal Neutron Fields by Critical Assembly and Heavy Water Thermal Neutron Facility of Kyoto University,” *Nucl. Sci. Eng.,* **136**, 321 (2000).
5. Unesai H, et al., “Measurement ^{237}Np Fission Rate Ratio Relative to ^{235}U Fission Rate in Cores with Various Thermal Neutron Spectrum at the Kyoto University Critical Assembly,” *J. Nucl. Sci. Technol.,* **37**, 627 (2000).
6. Unesaki H, et al., “Measurement and Analysis of ^{241}Am Fission Rate Ratio Relative to ^{235}U Fission Rate in Thermal Neutron Systems Using Kyoto University Critical Assembly,” *J. Nucl. Sci. Technol.*, **38**, 600 (2001).
7. Nagaya Y, et al., “MVP/GMVP Version3: General purpose Monte Carlo codes for neutron and photon transport calculations based on continuous energy and multigroup methods,” JAEA-Data/Code 2016-018, JAEA (2016).
8. Shibata K, et al., “JENDL-4.0: A New Library for Nuclear Science and Engineering,” *J Nucl Sci Technol.,* **48**, 1 (2011).
9. Unesaki H, “Study on Verification of Nuclear Data for Nuclear Design of Next Generation Thermal Reactors,” dissertation, Kyoto University (2001).
10. Shibata K, et al., “Japanese Evaluated Nuclear Data Library Version 3 Revision-3: JENDL-3.3,” *J. Nucl. Sci. Technol.* **39**, 1125 (2006).
11. Chadwick MB, et al., “ENDF/B-VII.0: Next Generation Evaluated Nuclear Data Library for Nuclear Science and Technology,” *Nucl. Data Sheets*. **107**, 2931 (2006).

TS-02 Monte Carlo Methods and Applications

Proceedings of the Reactor Physics Asia 2019 (RPHA19) Conference
Osaka, Japan, Dec. 2-3, 2019

Effect of Neutron Absorber on Production of Plutonium238 for BWR Assembly

Hiroo Ohuchi[a,*], Satoshi Takeda[a] and Takanori Kitada[a]
[a]*Osaka University, Yamadaoka2-1, Suita, Osaka, Japan*
[*]Corresponding author: h-ohuchi@ne.see.eng.osaka-u.ac.jp

Abstract

The burnup calculations were performed for BWR assembly by using ^{162}Dy and Gd in order to evaluate the effect of the neutron absorber on the production of ^{238}Pu. From the results, it was found that ^{238}Pu production is decreased by the addition of ^{162}Dy, and is increased by the addition of Gd. By evaluating the capture rate which is related to ^{238}Pu production, it is confirmed that ^{162}Dy decreases ^{238}Pu production by reducing the capture rate of ^{236}U, and Gd increases ^{238}Pu production by increasing the capture rates of ^{235}U, ^{236}U, and ^{237}Np.

Key Words: **^{238}Pu, ^{162}Dy, Gd, BWR Assembly, Neutron capture reaction**

1. Introduction

Transuranic (TRU) nuclides produced by the use of nuclear reactor have high radiotoxicity for a long time. In order to reduce the radiotoxicity, the fast reactor and the accelerator driven systems have been studied. These innovative transmutation systems are very effective to reduce the radiotoxicity of the spent fuel. On the other hand, for the early reduction of radiotoxicity, a concept of FORSETI (Fuel cycle Of light water Reactor with Surplus Enriched uranium for TRU-production Inhibition) has been proposed[1]. In a feasibility study of FORSETI, Wada et al. showed that the potential radiotoxicity of the spent fuel is reduced by increasing the enrichment of uranium, and ^{238}Pu and ^{241}Pu have high potential radiotoxicity through 100 years after discharge. In addition, the high-enriched uranium fuel requires the burnable poison because of its high reactivity[2].

In the previous study[2], in order to decrease radiotoxicity of the spent fuel, neutron absorbers were added to the fuels. For BWR pin cell model, neutron absorbers were added to 10 wt% uranium fuels, and ^{162}Dy turned out to be effective for reducing the production of ^{238}Pu. It was found that the capture rate of ^{236}U is mainly occurred around 5.5 eV and the capture rate around 5.5 eV is reduced by adding ^{162}Dy, and ^{162}Dy reduces the capture rate of ^{236}U by their resonance around 5.5 eV. ^{238}Pu is produced in the burnup process ^{235}U → ^{236}U → ^{237}U → ^{237}Np → ^{238}Np → ^{238}Pu[3], therefore reducing the neutron capture reaction of ^{236}U results in reducing the production of ^{238}Pu.

In this study, the burnup calculation is performed for BWR assembly to evaluate the effect of the neutron absorber on the production of ^{238}Pu. Gd is generally used for the neutron absorber. Therefore, in addition to ^{162}Dy, Gd is used for BWR assembly.

2. Calculation Condition

For BWR assembly, burnup calculations were performed by two patterns. The first pattern is 9x9 assembly in which neutron absorbers are added to all fuel rods. The second pattern is 9x9 assembly in which neutron absorbers are added to several fuel rods. In the case of ^{162}Dy, burnup calculations are performed at both patterns. In the case of Gd, the calculations are performed at the former pattern. The calculation model is shown in Figures 1 and 2. 9x9 assembly has two water rods around the center of assembly.

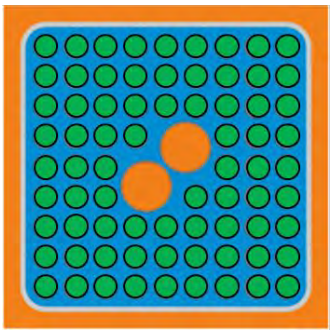

Fig. 1. 9x9 BWR assembly (neutron absorbers are added to all fuel rods)

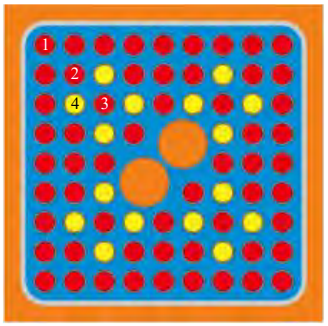

Fig. 2. 9x9 BWR assembly (neutron absorbers are added to several fuel rods)

Figure 1 shows 'green' fuel rods are 10 wt% uranium fuels without or with ^{162}Dy. Figure 2 shows 'Red' fuel rods are 10 wt% uranium fuels, and 'yellow' fuel rods are 10 wt% uranium fuels with neutron absorbers. The enrichment of uranium fuel rod was 10 wt%. The burnup calculations were performed in 4 cases. 10 wt% uranium fuels (case 1) in Figure 1. Gd-bearing 10 wt% uranium fuels (case 2) in Figure 2. ^{162}Dy-bearing 10 wt% uranium fuels at several positions (case 3) in Figure 2. ^{162}Dy-bearing 10 wt% uranium fuels at all positions (case 4) in Figure 1.

Burnup calculation was performed by MVP-BURN[4], and nuclear library was JENDL-4.0[5]. In the burnup calculation, the number of histories was 200,000 at each burnup step. The fuel region was annularly divided into 10 regions, and the volume of each subdivided region was the same. The number of burnup step was 40, and maximum burnup was set to 45.0 GWd/t.

3. Calculation Results and Discussion

Figure 3 shows the result of setting infinite multiplication factor at 22.5 GWd/t in order to determine the enrichment of adding neutron absorbers.

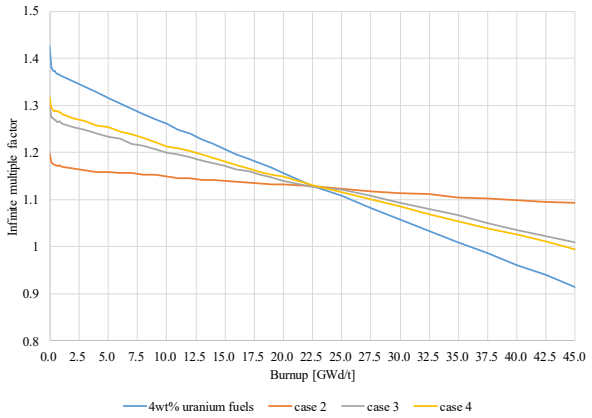

Fig. 3. Burnup dependence of multiplication factor

The amount of ^{162}Dy or Gd is adjusted so that the infinite multiplication factor for 10 wt% uranium fuels becomes equal to that for 4 wt% uranium fuels. The enrichment of case 2 was 12.65 %, that of case 3 was 18.65 %, and that of case 4 was 2.27 %. These values of the enrichment was set at 22.5 GWd/t. Table I. shows the average number density of ^{238}Pu at the 45.0 GWd/t and the relative difference from case 1.

Table I. Average Number Density of ^{238}Pu and Relative Difference

	Average production [10^{24}/cm^3]	Relative difference [%]
10wt% Uranium fuels (case 1)	2.062×10^{-4}	–
Gd-bearing 10wt% Uranium fuels (case 2)	2.538×10^{-4}	23.1%
^{162}Dy-bearing 10wt% Uranium fuels at several positions (case 3)	2.059×10^{-4}	-0.12%
^{162}Dy-bearing 10wt% Uranium fuels at all positions (case 3)	1.273×10^{-4}	-38.2%

For the production of ^{238}Pu in each case, the production of ^{238}Pu in case 2 is increased by 23.1 %, the production of ^{238}Pu in case 3 is decreased by 0.12 %, and the production of ^{238}Pu in case 4 is decreased by 38.2 %.

In Figure 2, selected four fuel rods were shown. Fuel rod number 1 is the farthest from the fuel rods with neutron absorbers. Fuel rod number 2 is next to the fuel rods with neutron absorbers. Fuel rod number 3 is surrounded by the 4 fuel rods with neutron absorbers. Fuel rod number 4 is the rod with neutron absorbers.

Figures 4-7 show the relationship between the burnup and the production of ^{238}Pu.

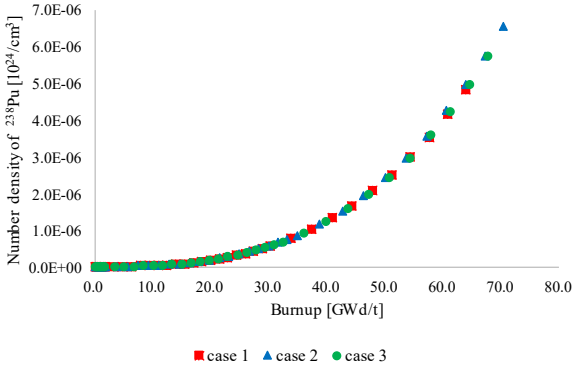

Fig. 4. Number density of ^{238}Pu at the fuel rod number 1

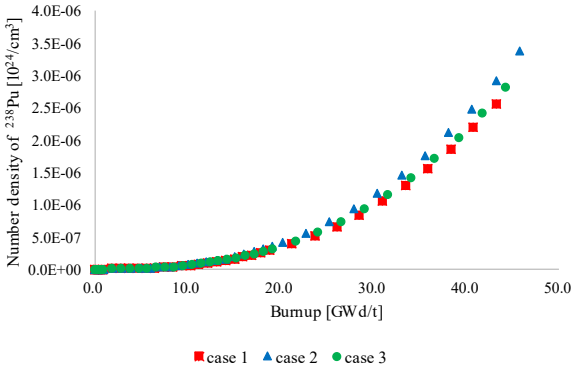

Fig. 5. Number density of ^{238}Pu at the fuel rod number 2

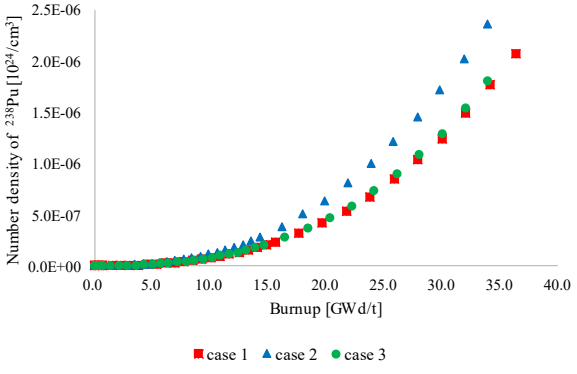

Fig. 6. Number density of ^{238}Pu at the fuel rod number 3

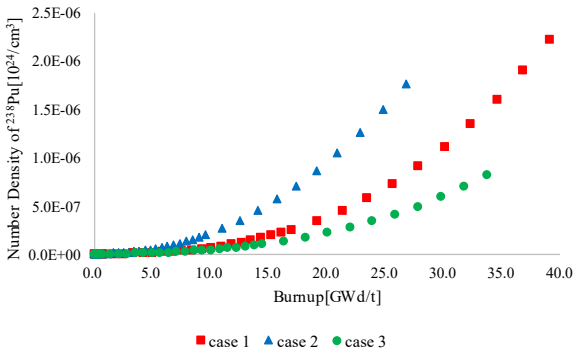

Fig. 7. Number density of ^{238}Pu at the fuel rod number 4

As shown in Figures 4-5, for the production of ^{238}Pu on burnup, the tendency of increasing the production of ^{238}Pu is almost the same. The addition of ^{162}Dy decreases the production of ^{238}Pu in case 3. In the fuel rod number 4, ^{238}Pu production obtained by case 2 is greatly increased.

Next, to investigate the difference of position where ^{162}Dy is added, the variation in burnup in case 3 and that in case 4 are compared. Figures 8 and 9 show burnup distributions at end of cycle. The unit of numerical value in Figures 8 and 9 is GWd/t. The standard deviations of the pin-wise burnup in Case 1, 2, 3, and 4 are respectively 7.14, 12.75, 9.91, and 7.75. The production of ^{238}Pu increases exponentially at high burnup. Therefore, even if the average burnup in assembly is same, ^{238}Pu production becomes large when the standard deviations of the pin-wise burnup is high. The standard deviations of the pin-wise burnup in case 3 is larger than that in case 4. Therefore, compared with case 4, the production of ^{238}Pu becomes large in case 3 from the difference of burnup distribution.

67.7	57.4	51.9	49.9	49.5	49.9	52.0	57.4	67.9
57.4	44.3	33.7	37.6	38.4	38.0	34.2	44.4	57.4
51.9	33.7	34.0	31.6	39.7	34.0	35.7	34.2	52.0
49.9	37.6	31.6	42.9			34.0	38.0	49.9
49.5	38.4	39.7				39.7	38.4	49.5
49.9	38.0	34.0			42.9	31.6	37.6	49.9
52.0	34.2	35.7	34.0	39.7	31.6	34.0	33.7	51.9
57.4	44.4	34.2	38.0	38.4	37.6	33.7	44.3	57.4
67.9	57.4	52.0	49.9	49.5	49.9	51.9	57.4	67.7

Fig. 8. Burnup distribution at 45 GWd/t in case 3

65.8	54.8	50.1	48.1	47.7	48.5	50.6	55.2	65.3
54.8	42.8	38.5	37.4	37.8	38.2	39.3	43.5	55.2
50.1	38.5	35.6	37.3	40.9	40.5	37.6	39.3	50.6
48.1	37.4	37.3	44.4			40.5	38.2	48.5
47.7	37.8	40.9				40.9	37.8	47.7
48.5	38.2	40.5			44.4	37.3	37.4	48.1
50.6	39.3	37.6	40.5	40.9	37.3	35.6	38.5	50.1
55.2	43.5	39.3	38.2	37.8	37.4	38.5	42.8	54.8
65.3	55.2	50.6	48.5	47.7	48.1	50.1	54.8	65.8

Fig. 9. Burnup distribution at 45 GWd/t in case 4

In case 2, as shown in Fig.7, the production of ^{238}Pu is different greatly between Gd-bearing and ^{162}Dy-bearing at the fuel rod number 4. To investigate the difference of ^{238}Pu production between case 2 and 3, energy distribution in terms of neutron spectrum is investigated. the neutron capture reaction of ^{235}U, ^{236}U, and ^{237}Np are evaluated at the fuel rod number 4. The capture rates are summarized in Table II. Neutron capture rates of ^{235}U, ^{236}U, and ^{237}Np are normalized by fission rate at each fuel rod. Table II shows the statistical error of neutron capture rates of ^{235}U, ^{236}U and ^{237}Np at the fuel rod number 4.

Table II. The Statistical Error of Neutron Capture Rates at the Fuel Rod Number 4

Neutron Capture Rates of ^{235}U	6.79 %
Neutron Capture Rates of ^{236}U	43.3 %
Neutron Capture Rates of ^{237}Np	9.71 %

Table III shows neutron capture rates of ^{235}U, ^{236}U, and ^{237}Np at fuel rod number 4.

Table III. Neutron Capture Rates of ^{235}U, ^{236}U, and ^{237}Np at the Fuel Rod Number 4

	Neutron Capture of ^{235}U	Neutron Capture of ^{236}U	Neutron Capture of ^{237}Np
case 1	7.00×10^{-2}	4.35×10^{-29}	1.47×10^{-28}
case 2	8.91×10^{-2}	1.39×10^{-28}	3.03×10^{-28}
case 3	7.44×10^{-2}	1.76×10^{-29}	1.89×10^{-28}
case2/case1	1.27	3.20	2.06
case3/case1	1.06	0.40	1.29

The relationship between neutron energy and neutron capture rate is shown in Figures10-12.

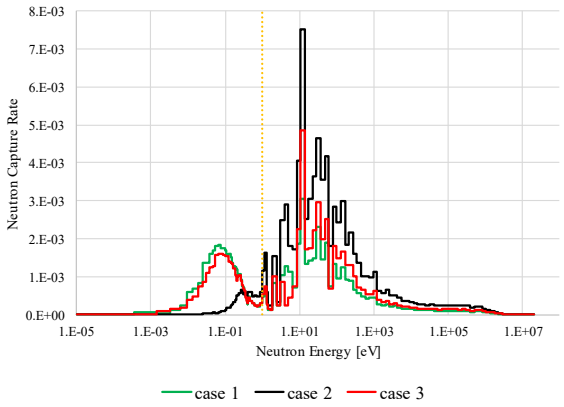

Fig.10. The energy distribution of neutron capture rate of ^{235}U at the fuel rod number 4

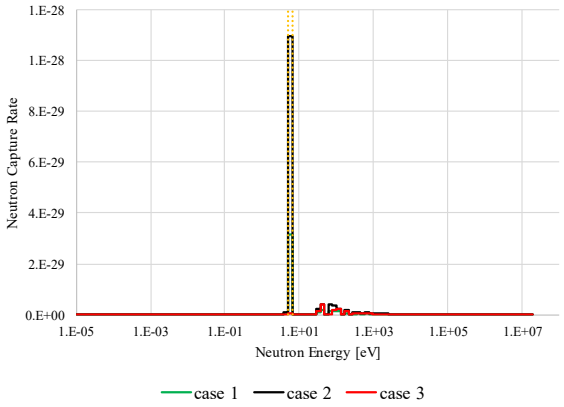

Fig.11. The energy distribution of neutron capture rate of ^{236}U at the fuel rod number 4

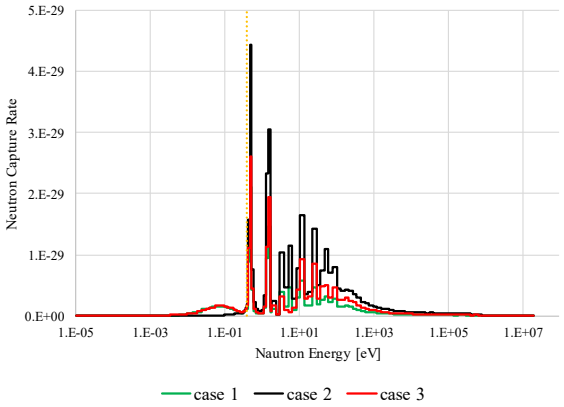

Fig.12. The energy distribution of neutron capture rate of ^{237}Np at the fuel rod number 4

In case 2, Figure 10 shows the neutron capture rate of ^{235}U is large in the energy region over 1 eV. Figure11 shows the capture cross section of Gd has the large neutron capture rate of ^{236}U in the energy region around 5.5 eV. Figure 12 shows that of Gd has that of ^{237}Np in the energy region over 1 eV. As a result, the reason for large capture rate of ^{235}U, ^{236}U, and ^{237}Np is the effect of increasing the proportion of neutrons more than 1 eV by adding Gd to fuel rods.

4. Summary

In the burnup calculation, ^{238}Pu production is evaluated for BWR assembly by adding Gd or ^{162}Dy to fuel rods. Compared with 10 wt% uranium fuels without neutron absorber, it was found that the addition of ^{162}Dy decreases ^{238}Pu production and that of Gd increases ^{238}Pu production. The addition of Gd increases ^{238}Pu production since Gd increases the capture rates of ^{235}U, ^{236}U, and ^{237}Np.

References

1. S. Wada, R. Kimura, S. Sakurai, K. Hiraiwa, K. Yoshioka, T. Sugita, “Reduced-radiotoxicity-production system by increasing initial and residual fuel enrichment,” Chengdu, China, Reactor Physics Asia (2017).
2. Takeda S, Kitada T. Study on suppression of TRU production by adding poison materials. Paper presented at: Pacific Basin Nuclear Conference (2018).
3. Satoshi Takeda, Takanori Kitada, Feasibility study on burnable absorber for FORSETI to reduce productions of Pu238 and Pu241, Journal of Nuclear Science and Technology, published online (DOI: 10.1080/00223131.2019.1659876) (2019).
4. Nagaya Y, Okumura K, Sakurai T, Mori T, “MVP/GMVP Version 3: General Purpose Monte Carlo Codes for Neutron and Photon Transport Calculations Based on Continuous Energy and Multigroup Methods,” JAEA-Data/Code 2016-018 Japan Atomic Energy Agency (2017).
5. Shibata K, Iwamoto O, Nakagawa T, Iwamoto N, Ichihara A, Kunieda S, Chiba S, Furutaka K, Otuka N, Ohsawa T, Murata T, Matsunobu H, Zukeran A, Kamada S, and Katakura J, “JENDL-4.0: A New Library for Nuclear Science and Engineering,” J. Nucl. Sci. Technol., 48 1, 1 (2011).

Study on the Optimization of Assembly Design of Single-Pass Supercritical Water-Cooled Fast Reactor

Liping HUANG[a,b], Zijing LIU[a,*] and Xiang WANG[b,*]

[a] *Department of Nuclear Science and Technology, University of South China, 421001, Hengyang, China*

[b]*College of Nuclear Science and Technology*, *Harbin Engineering University, 150001, Harbin, China*

[*]Zijing LIU: liuzijing1123@163.com, Xiang WANG: xiang.wang@hrbeu.edu.cn

Abstract

Supercritical water-cooled reactor (SCWR) is one of six types of Gen-IV reactors. Compared with conventional water-cooled reactor, current designs have shown a wider range of neutron spectrum and their corresponding core structure. This study, using MCNP4B to establish the neutron physics model, focused on the sensitivity of solid moderator, cladding material and fuel axial enrichment on the assemblies' characteristics in the fast spectrum single-pass SCWR (SCWRsf). It is found that reduced mass fraction of Pu isotope in the fuel brings more negative void reactivity coefficient, and adopting reasonable axial Pu enrichment stratification of fuel rods can improve the effective multiplication factor and reduce the axial power peaking factor. The reasonable thickness of solid moderator $ZrH_{1.7}$ layer can meet the negative void coefficient and flat the axial power distribution of the core.

Key Words: **Single-pass, SCWR, neutron physics; fuel assemblies**

1. Introduction

SCWR is the only water-cooled reactor among six Gen-IV nuclear energy systems. According to the features of reactor type and neutron energy spectrum, SCWR is classified in different ways[1]. For fast spectrum SCWR, it can be realized by supercritical water with low density and weak moderation under high temperature. Its advantages include high fuel efficiency, high power density and combustible actinides. However, the main technical challenges like the positive temperature coefficient, the complex design of the reactor core and fuel assemblies are also critical[2]. Besides, it is more difficult to select core-cladding materials.

SCWR (Fig. 1) has some designs in common with BWR and PWR, while the differences between is as well significant[3]. In the design of SCWR, the main circulation pump provides the driving pressure head, which enables the fluid to enter the reactor core through the main feed-water line. After nuclear heating, it becomes "supercritical steam" with high temperature and pressure (no phase transition), which enters the turbine through the main steam line. After that, the steam is further cooled in the condenser to liquid water, which returns to the main pump inlet and close the direct circulation loop.

At present, few countries have conducted researches on the fast spectrum SCWR. The most mature design is the one[4] has both two-pass (Fig. 2, a, b) and single-pass (Fig. 2, c) flow. Compared to two-pass design, the single-pass design simplifies the core structure. However, because the coolant density varies greatly along the axial direction, the core has extremely uneven axial power distribution and fluctuation during the cycle. This paper also carries out sensitivity analysis for this point.

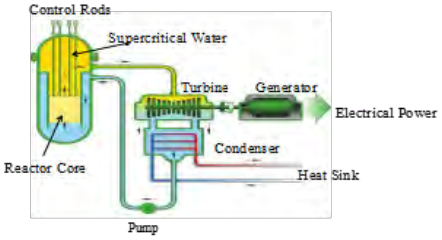

Fig. 1. Schematic diagram of SCWR system.

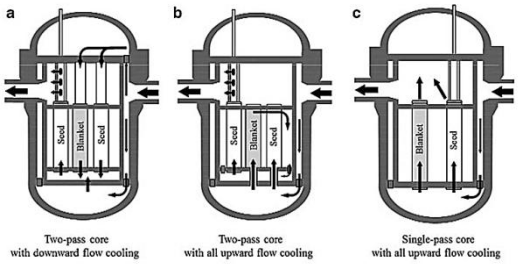

Fig. 2. Coolant flow schemes of Super FR.

2. Modelling of SCWRsf

2.1 Core Design Criteria

The design criteria of SCWRsf (SCWR with single-pass and fast spectrum) were adopted by previous studies [5]. (1) core power is 1000 MW. (2) the average core outlet temperature is above 500 ℃ to ensure the thermal efficiency of 44%. (3) the overall volume power density of the core is more than 100 W/cm^3 (including gas chamber and radial reflector). (4) in normal operation, the

maximum cladding surface temperature is lower than 650℃. (5) negative void reactivity is ensured. (6) under cold and hot operating conditions, the balance cycle and the new reactor core both have a sufficient shutdown margin of 1%.

2.2 Core Assembly design

The SCWRsf core is divided into two zones, namely, the seed and the blanket zone, filled with seed (SA) and blanket assemblies (BA), respectively. The design of the SA (Fig. 3) is similar to that of traditional fast reactor assembly, while that of the BA is slightly different as its function is to breed fertile material and to reduce the void coefficient (VC) of the core. Unlike SAs, BAs use a thick layer of ZrH (Fig. 4) rods as a solid moderator. ZrH moderated fast neutron produced from SAs, while fertile nuclides in BAs increase neutron absorption to provide negative void reactivity. Since ZrH fuel rods cause fuel peak between adjacent assemblies, the decorated stainless-steel rods (SS rods, Fig. 5) made of SUS304 are arranged to ease the peak. The entire core structure is shown in Fig. 6. The purple areas on the periphery represent water, the yellow areas represent the MOX fuel rods in SAs with six purple control rod guides evenly distributed in the middle, the dark-blue areas represent SS rods in BAs, the light-blue areas represent ZrH rods in BAs, and the pink areas represent the UO_2 fuel rods in BAs.

Some specific parameters of the assembly are shown in Table I, which refers to the design of professor Oka[6]. SAs use MOX fuel in the rod, while in BAs the upper part of the rod is depleted uranium, where ^{238}U absorbs neutrons and converts into ^{239}Pu. From the safety perspective, due to void effect, the resonance absorption of ^{238}U of neutrons from SAs makes VC more negative. The lower part uses MOX fuel to flat the power change.

The active zone of the assembly is divided into 10 sections in the axial direction. Different coolant densities are taken for upward flow positions of the coolant (Fig. 7, inlet 310℃, outlet 501.2℃). Two water reflection layers of 40 cm thick are located at both ends of the assembly, represent the chambers of the pressure vessel.

Table I. Design parameters of SA and BA

Assembly type	SA	BA
Types of fuel	MOX (2.4m)	Top: UO_2/1.8 m Bottom: MOX*/ 0.6 m
Fuel rod dia.	5.5 mm	
Fuel pellet dia.	4.65 mm	
Cladding mat/thickness	SUS304/0.4 mm	
Gap clearance	0.07 mm	
Fuel rod pinch	6.545 mm	
Number of fuel rods	978	547
Assembly pinch	21.76 cm	
Active length	240 cm	
Gas plenum length	40 cm	
Gas plenum location	Upper	
No. of CR guide tube	7	0
In. dia. of CR guide tube	13.8 mm	-
CR absorber/follower	B4C/ SUS304	-
No. of ZrH rods/thickness	0/-	270/19.64 mm
No. of SS rods top/bottom	0	210/480
ZrH/SS dia.	-	6.5 mm
Channel box thickness	3.0 mm	

*Pu isotopic 238/239/240/241/242 composition in wt%: 0.4/51.3/37.8/6.5/4.0.

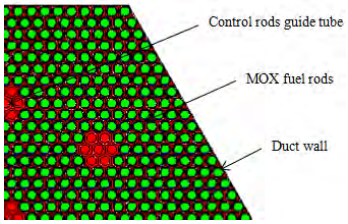

Fig. 3. Cross-sectional view of 1/4 SA.

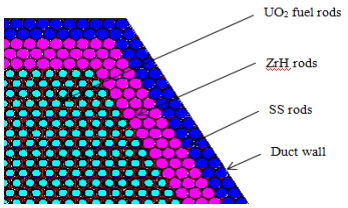

Fig. 4. Top cross-sectional view of 1/4 BA.

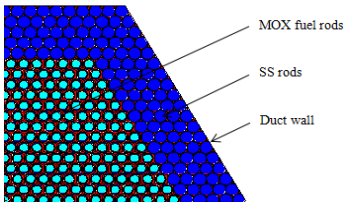

Fig.5. Bottom cross-sectional view of 1/4 BA.

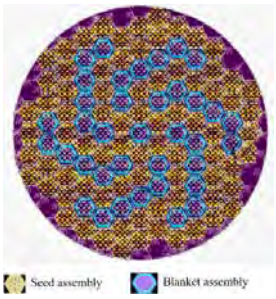

Fig. 6. In-core configuration in single-pass core design.

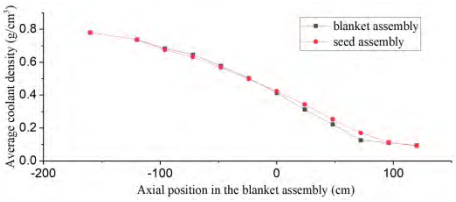

Fig. 7. Axial coolant density distributions in SA and BA.

3. Results

3.1 Steady-state assessment

The calculations are performed by MCNP4B with nuclear date library ENDF-b602[7]. The k_{eff} is 1.03933±0.00055 and the residual reactivity is 0.0378, which enables the core to breed as shown in the pink areas of Fig. 6.

The change of reactivity with the void fraction (ϕ, Fig. 8) shows that reactivity fluctuates significantly with the increase of ϕ. When the void fraction reaches 40%, the VC changes from negative to positive.

The void fraction is changed by changing the density of the coolant. If the coolant density decreases, the void fraction will increase. The most negative VC it can reach is -11.323 pcm/% as shown in Fig. 8, which results in negative feedback effect and thus maintains stable operation.

For a single assembly, the radial length is extremely small compared with the axial length, and the fuel rod arrangement is relatively dense, so the axial power change is not obvious. Therefore, this paper only focused on the axial power change. Axial power distributions of SA and BA (Fig. 9) are extremely uneven, and the power peak (PP) appears in the lower part of the assembly. This is because that the fission by Pu causes larger power output in the MOX fuel at the bottom. This helps to increase the coolant outlet temperature and helps to mitigate the later power change of BAs. During the operation, the PP shifts from bottom upwards in BAs. The power peaking factor (PPF) of SAs is 1.77 and that of BAs is 4.84, which is large and needs to be improved. Fig. 10 assesses the k_{eff} with ZrH thickness.

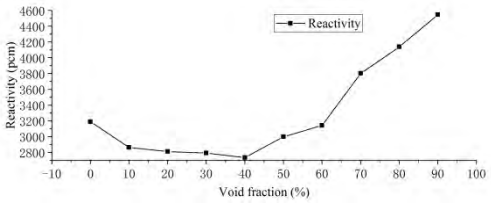

Fig. 8. Reactivity with ϕ.

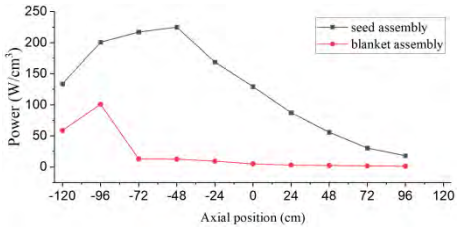

Fig. 9. Axial power distributions in SAs and BAs.

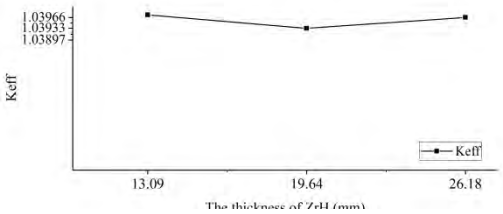

Fig. 10. k_{eff} with solid moderator layer thickness.

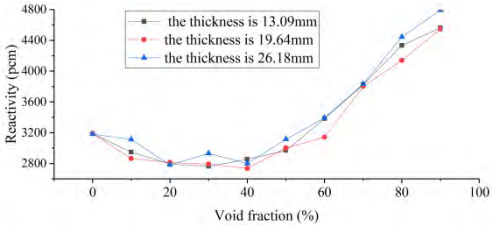

Fig. 11. Reactivity with ϕ, solid moderator thicknesses.

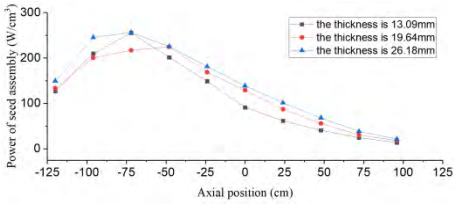

Fig. 12. Axial power of SA with moderator thicknesses.

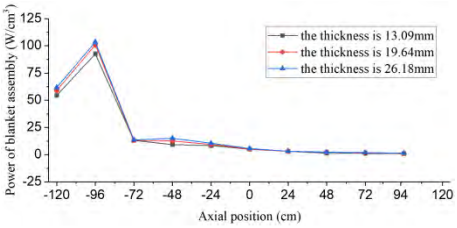

Fig. 13. Axial power of BA with moderator thicknesses.

3.2 Sensitivity of solid moderator thickness

The $ZrH_{1.7}$ solid moderator layer in BAs is applied due to its good thermal stability, strong moderation, high temperature and radiation resistance. It is also easy to be manufactured[6]. The reactivity (Fig. 11) and the k_{eff} (Fig. 14) change with ϕ, solid moderator thicknesses are studied. Axial power distributions of assemblies are in Fig. 12, 13.

Though the axial PPF is the smallest with a thickness of 13.09 mm, its VC which is more likely to be positive results in worse reactor safety. When the ZrH thickness increases, the axial PPF increases. Therefore, considering k_{eff}, VC and axial PPF, 19.635mm was selected as the optimal moderator layer thickness in this paper to ensure a negative VC and a small axial PPF with the k_{eff} greater than 1.

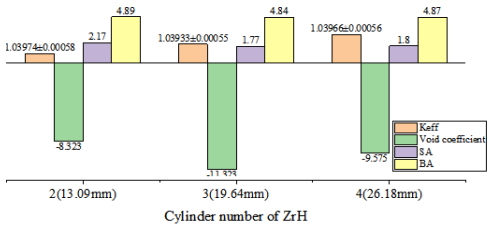

Fig. 14. k_{eff}, VC and axial PPF with ZrH thickness

3.3 Sensitivity of cladding materials

Supercritical water is irradiated and decomposed in the

core during the operation. The cladding materials should withstand large pressure and ultra-high temperature, resist strong corrosion and little hydrogen embrittlement. It is also necessary to have a small neutron absorption cross section as possible and to resist radiation damage. T91 and Zr-4 are selected to compare with SUS304 to study the impact of these materials on k_{eff}, VC and axial PPF.

The Composition of SUS304, T91, Zr-4 are shown in Table II~IV. The results are plotted in Fig. 15~18. It is clear that Zr-4 and T91 have larger k_{eff}, VCs and axial PPFs of SA. Therefore, SUS304 is more suitable as the cladding material here.

Table II. Composition of SUS304 (mass fraction)

C	Si	Cr	Mn	Ni	P	S
0.06	0.48	18.25	1.45	8.16	0.024	0.005

Table III. Composition of T91 (mass fraction)

C	Si	Nb	P	Mn
0.100	0.028	0.090	0.009	0.450
N	V	Mo	Cr	Ni
0.038	0.200	0.900	8.370	0.210

Table IV. Composition of Zr-4 (mass fraction)

C	Cr	Fe	Sn	Ni
0.002	0.100	0.200	1.500	0.007

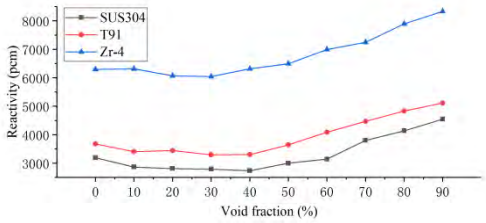

Fig. 15. Reactivity with ϕ and cladding materials.

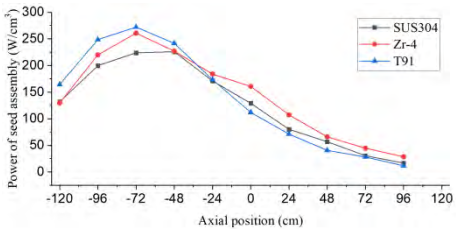

Fig.16. Axial power distribution of SA with materials.

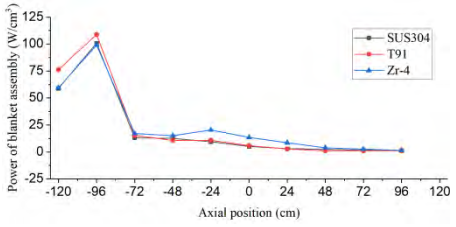

Fig. 17. Axial power distribution of BA with materials.

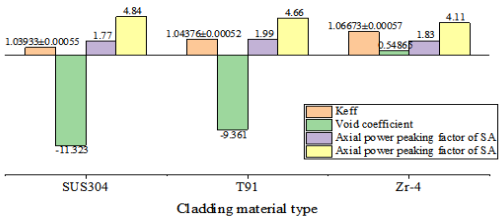

Fig. 18. k_{eff}, VC, axial PPF with cladding materials.

3.4 Optimization of axial enrichment of fuel rods

Based on the results, the axial power density distinguishes, and the PP appears at the bottom. To flat the axial power, Pu enrichment in SAs is stratified according to the axial PP position. The enrichment should be set to ensure negative VC and smaller axial PPF, and k_{eff} should be greater than 1. The enrichment of Pu was originally divided into two layers. On the basis of the original layer, the enrichment was divided into four layers, which reduced the enrichment at large power level, increased the enrichment at small power level. (Tab. V, average for 23.365%). The ZrH is 19.635 mm thick, and the cladding is SUS304.

The k_{eff} is 1.02298±0.00055, and the VC is -30.742 pcm/%. The reactivity with the ϕ is shown in Fig. 19 while the axial power distribution in Fig. 20. The comparison of parameters before and after optimization is shown in Table VI. The axial power distribution of the improved SAs is more uniform. The reactivity is slightly reduced after optimization, because the average Pu enrichment of fuel after optimization (23.365%) is slightly lower than before (23.4%). The VC is more negative, so the safety is improved.

Table V. Pu enrichment at axial positions of SAs

Axial position (cm)	Enrichment (%)
-120~-60	19.57
-60~-24	21.28
-24~24	25.48
24~120	27.16

Table VI. Comparison before and after optimization

Parameters	Before	After
Reactivity (K_{eff})	0.038 (1.03933)	0.023 (1.02298)
VC (pcm/%)	-11.323	-30.742
axial PPF of SA	1.770	1.427
axial PPF of BA	4.840	2.080

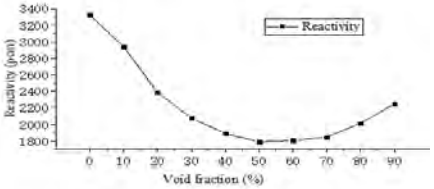

Fig. 19. Reactivity with ϕ after stratification

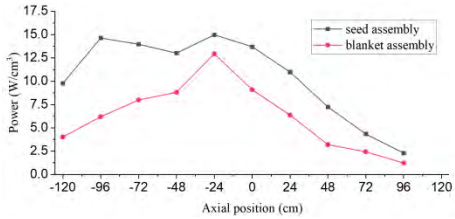

Fig. 20. Axial power distribution of assemblies after stratification

4. Summary

This paper refers to given assembly design of SCWRsf. Based on the given condition, a series of sensitivity calculations are carried out.

The optimal moderator layer thickness is 19.635 mm, when the VC is negative and the axial PPF is small. With the increase of the thickness of moderator layer, the k_{eff} increases, the VC tends to be negative, but the axial PPF increases.

The best cladding material is SUS304, which has better corrosion resistance and negative void reactivity in supercritical water compared with T91 and Zr-4.

By stratifying the axial enrichment of SAs, a relatively flat distribution of the axial power of the assembly can be achieved, and the axial PPF can be reduced to some extent.

References

1. Gabriel O. O., Alade A. M., Chad-Umoren Y. E., "Science and Technology of Supercritical Water Cooled Reactors: Review and Status," *Journal of Energy Technologies & Policy*, **15**, 4, p. 201, (2013).
2. Mukohara T., Koshizuka S. I., Oka Y., "Core design of a high-temperature fast reactor cooled by supercritical light water," *Annals of Nuclear Energy*, **26**, 16, p. 1423, (1999).
3. Oka Y., Koshizuku S., "Once-through Cycle Light Water Cooled Reactor Concept," *J. Nucl. Sci. Technol.*, **38**, 12, p. 1081, (2001).
4. Oka Y., Morooka S., *Reactor Design and Safety*, p. 21, Springer, Tokyo, Japan, (2014).
5. Oka Y., *Super Light Water Reactors and Super Fast Reactors,* p. 12, Springer, Tokyo, Japan, (2014).
6. Liu Q., Oka Y., "Single pass core design for a Super Fast Reactor Annals Nuclear Energy," *Annals of Nuclear Energy*, **80**, 10, p. 451, (2015).
7. X-5 Monte Carlo Team. "Mcnp4B general Monte Carlo N-particle transport code," LA-CP-03-0245, Los Alamos National Laboratory (2003).

Proceedings of the Reactor Physics Asia 2019 (RPHA19) Conference
Osaka, Japan, Dec. 2-3, 2019

Application of Direct Simulation Method for Neutron Space-Time Kinetics Based on RMC

Jian Lijun[a], Shang Xiaotong[a], Guo Xiaoyu[a], Wang Kan[a]
[a]*Department of engineering physics, Tsinghua university, Beijing*
[*]Corresponding author: wangkan@mail.tsinghua.edu.cn

Abstract

This paper studies the direct simulation method of neutron space-time kinetics, based on the RMC developed by Reactor Engineering Analysis Lab(REAL), Department of Engineering Physics, Tsinghua University. A comb sampling method that adjusts the neutron history numbers is developed to control the computational cost of the Monte Carlo algorithm, and is verified by the TRACY-r61 case. A method based on precursor forced decay and roulette is developed to reduce the variance of precursor simulation, and is verified by a single group point reactor model. The simulation process of absorption reaction and fission reaction was modified to smoothen the number of neutrons in each counting time box. Furthermore, after the critical calculation module is added, the code is verified by the case 16A. The results show that the simulation of the code reaches good precision.

Key Words: **Neutron space-time kinetics; direct simulation; RMC; comb sampling method; precursor forced decay**

1. Introduction

The numerical calculation methods of reactor can be divided into deterministic method and Monte Carlo method. In transient analysis of nuclear reactor, some people have studied the deterministic method to solve. But limited by the previous computational conditions, most of them used simplified transport model, such as diffusion theory [1]. Later, the method of using neutron transport equation was gradually developed, but in this case, the phase space needed to be stored after the geometric structure was very large. At present, an improved quasi-static method [2] is widely adopted, which holds that transient state is composed of the steady state at each moment, and the quasi-static method and Monte Carlo method are combined in the calculation. However, this method also has some limitations, such as kinetic parameters needed for time-related parts [3-4].

Direct simulation method is another idea of simulating transient problems. This method directly simulates transient problems through Monte Carlo and obtains a random process with exactly the same average result as the described problem. In principle, the accuracy can be controlled by statistical methods [5]. However, the consumption of computer resources is relatively large, but with the development of computers, the disadvantage becomes smaller. The work of this paper is based on the RMC [6] fixed source neutron start-up mode [7], which has the computational framework of direct simulation method.

2. Theoretical Model

2.1 comb sampling method

To control the change of neutron quantity in the transient process, comb sampling method [8-9] is added at the initial moment of each time interval.

The main idea of the comb method is to adjust the weight of neutrons to change the neutron quantity while keeping the total weight of neutrons unchanged. It is assumed that there are K particles before the execution of the comb method program, and the number of target particles after adjustment is M. Imagine that the original K particles are arranged in a row according to their weight widths, and the total length of this long row is the total weight W of K particles

$$\mathrm{W} = \sum_{k=1}^{K} w_k \tag{1}$$

The average weight of the original K particles is

$$w_{av} = \frac{W}{M} \tag{2}$$

It is considered that the weights of M particles after the comb method are equal. Therefore, the original K particles are rearranged into M particles.

The position of the first comb tooth is ξw_{av}, and ξ is random number between 0 and 1. The other comb teeth are arranged at equal intervals w_{av} with the previous one, so that the position of each comb tooth can be obtained

$$t_m = \xi \frac{W}{M} + (m-1)\frac{W}{M} \qquad m = 1, \cdots, M \tag{3}$$

Each particle on the tooth is reserved with weight w_{av} and continue simulation.

It is unbiased after the comb method, which can be proved mathematically. For a particle with the original

weight of w_k, the probability that a comb tooth falls within this weight range is

$$P_{hit,k} = \frac{w_k}{w_{av}} \quad (4)$$

The expectation that this particle can be retained aft er the comb method is

$$E_{conserved} = P_{hit,k} w_{av} = w_k \quad (5)$$

2.2 precursor forced decay

Compared with life-time prompt, the decay time of precursor can be very long, so some precursor will not decay in the calculative time interval, which will enlarge large variance. To solve this problem, the program uses the method of precursor forced decay, so that all precursor come into play. It is considered that each precursor is forced to yield a delayed neutron in each interval [10], so as to influent the neutron transport process, and the unbiasedness is kept by adjusting weight.

Setting the time interval small enough, it is that assumed that precursor yield uniformly at each time interval t_1 to $\mathrm{t}_1 + \Delta t$, the probability of decay is

$$\bar{p}(t) = \frac{1}{\Delta t} \quad (6)$$

To maintain the unbiased result, the weight of delayed neutrons is supposed to be exponential decay. The initial weight of precursor is set as w_c, and the weight of decay in the time interval is

$$w_d(t) = w_c \frac{p(t)}{\bar{p}(t)} = w_c \Delta t \sum_i f d_i \lambda_i e^{-\lambda_i (t - t_0)} \quad (7)$$

$$f d_i = \frac{\beta_i}{\beta} \quad (8)$$

$t_1 < \mathrm{t} \leq \mathrm{t}_1 + \Delta t$, β_i is the precursor share of precur sor group i and λ_i is the decay probability of precu rsor group i.

Average weight of delayed neutrons $w_{d,av}$ in this time interval is

$$w_{d,av} = \frac{1}{\Delta t} \int_{\mathrm{t}_1}^{\mathrm{t}_1 + \Delta t} w_d(t) dt \quad (9)$$

$$w_{d,av} = w_c \sum_i f d_i \left(e^{-\lambda_i (t_i - t_0)} - e^{-\lambda_i (\mathrm{t}_1 + \Delta t - t_0)} \right) \quad (10)$$

Similarly, the weight of the precursor w_{timed} also d ecreases exponentially

$$w_{timed} = w_c \left(1 - \int_{t_0}^{t} \sum_i f d_i \lambda_i e^{-\lambda_i (t - t_0)} dt \right) \quad (11)$$

$$w_{timed} = w_c \sum_i f d_i e^{-\lambda_i (t - t_0)} \quad (12)$$

To cancel the tracing of the inefficient precursor, the roulette is executed when the weight of the precursor w_{timed} is less than the threshold w_{surv}. The new weight w_{new} can be summarized as

$$w_{timed} = \begin{cases} 0 & \xi < w_{timed}/w_{surv} \\ w_{surv} & \xi > w_{timed}/w_{surv} \end{cases} \quad (13)$$

ξ is random number between 0 and 1.

2.3 adjustment of nuclear reaction simulation

The comb method regulates the quantity of neutrons totally and the comb method can only be used at the beginning or end of each time interval. However, due to the characteristics of the direct simulation method, the number of neutrons may vary greatly in each time interval. That's why the nuclear reaction process has also been adjusted.

The program uses implicit capture to deal with absorption reactions, rather than the direct simulation before. After sampling the type of reaction nucleus, implicit capture directly adjusts the weight of particle w_n to w_n'

$$w_n' = \left(1 - \frac{\sigma_a}{\sigma_t} \right) \times w_n \quad (14)$$

The program is inefficient when the weight is low, so when the new neutron weight w_n' is less than a certain threshold, a roulette process like equation (13) is carried out. In the program, the roulette lower threshold is set as

$$w_{min} = 0.2 \times \bar{w} \quad (15)$$

While $\bar{w}$ is the average neutron weight at the beginning of the initial time.

As for fission reactions, after sampling the number of fission neutrons in the original procedure, there is only one secondary neutron, whose weight is the number of fission neutrons sampled multiplies by the weight of the neutron before fission.

Correspondingly, when the neutron weight is extremely large, it is also divided by roulette. The upper threshold of roulette is set as

$$w_{min} = 4 \times \bar{w} \quad (16)$$

While $\bar{w}$ was introduced earlier.

3. Numerical Verification

We used TRACY-r61 of continuous energy to verify the correctness of the comb method and single group point reactor model to verify that the program of the precursor forced decay and modification of nuclear reaction simulation is correct. After adding the critical calculation module, we tested the 16A transient benchmark of one-dimensional two groups. The total weight of neutrons is selected as the output index, since it corresponds to neutron flux of the system.

3.1 TRACY-r61 neutronics benchmark

We test the comb method with r61 of TRACY experiment [11]. There is a uranyl nitrate solution in the shape of a hollow cylinder as fuel, surrounded by a cladding with air on the outside. With the result of the original program as a reference, the subcritical and instantaneous supercritical conditions are adopted for testing. The test items include three cases: no control of particle number, comb control of particle number to 4000 neutrons and comb control of particle number to 10000 neutrons. The test results are as follows

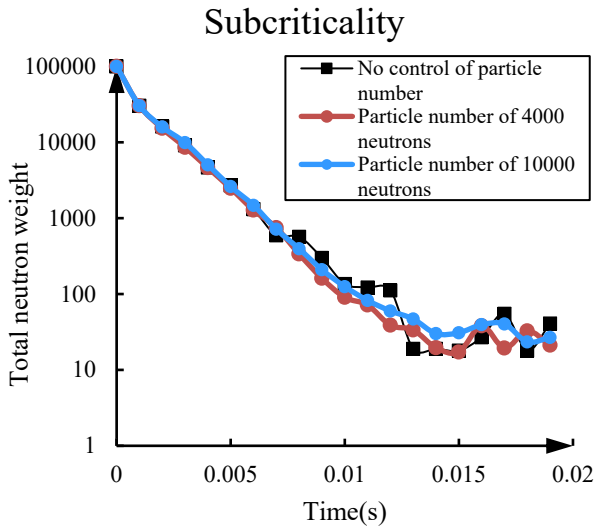

Fig. 1. Calculation results of r61 in subcritical state.

Table I. Single-core time of r61 in subcritical state

No control of particle number	Particle number of 4000 neutrons	Particle number of 10000 neutrons
1.55min	1.67min	3.02min

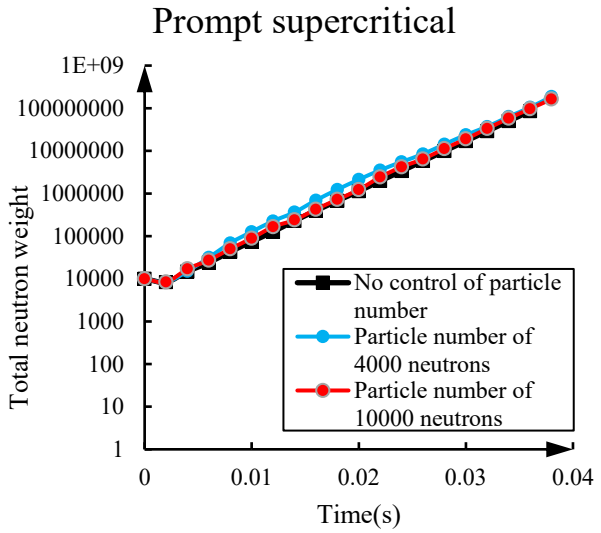

Fig. 2. Calculation results of r61 in prompt supercritical.

Table II. Single-core time of r61 in prompt supercritical

No control of particle number	Particle number of 4000 neutrons	Particle number of 10000 neutrons
Memory corruption	3.54min	8.29min

In subcritical state, the fluctuation of the total neutron weight decreases significantly after the addition of the comb method, which indicates that with the comb method, the procedure still maintains a certain amount of calculation. In prompt supercritical, under the premise of similar calculation results, the calculation time of the program is greatly shortened, indicating that the comb method balances the variance and calculation amount well. It is concluded that the comb method program makes it feasible to simulate the transient process directly.

3.2 a single group point reactor model

After the nuclear force decay and the modification of the nuclear reaction simulation, we use the simplest one group point reactor model to test. Taking the results of the point reactor program as reference, only the precursor forced decay and the precursor forced decay with modified nuclear reaction were tested in subcritical state. The controlled number of the comb method was 10000. The results are as follows.

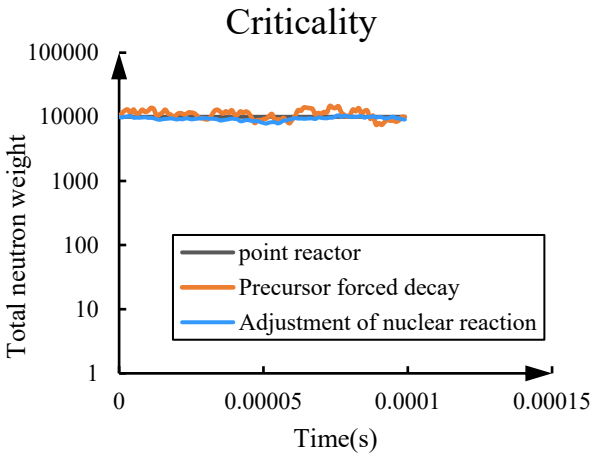

Fig. 3. Calculation results of a single-group point reactor model in subcritical state.

From the calculation results, we can see that after the forced decay of precursor, the calculation results are correct except that the volatility is relatively high. The volatility was reduced after adjusting for the nuclear reaction simulation.

3.3 16A neutronics benchmark

The transient process is considered to start from steady state. After adding the critical calculation module, the distribution of neutron and precursor in the initial steady state is obtained through the critical calculation, and then the subsequent simulation is carried out. Transient benchmark 16A [12] of one-dimensional two-group was tested in the critical condition(16A-0) and the prompt supercritical condition(16A-2). This model consists of seven uniform plates, which adjust the state of the system by changing the density of the fuel. The test results are as follows

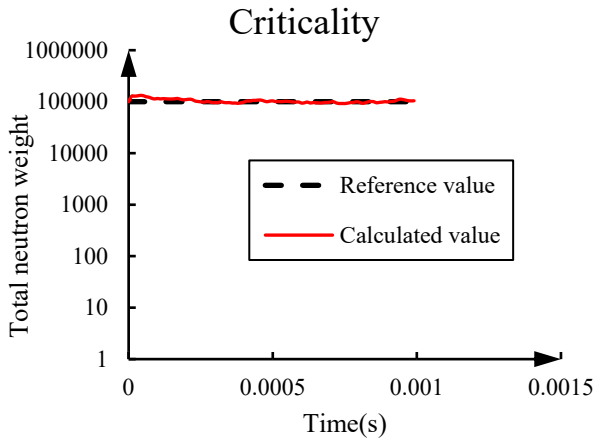

Fig. 4. Calculation results of 16A-0 in critical state.

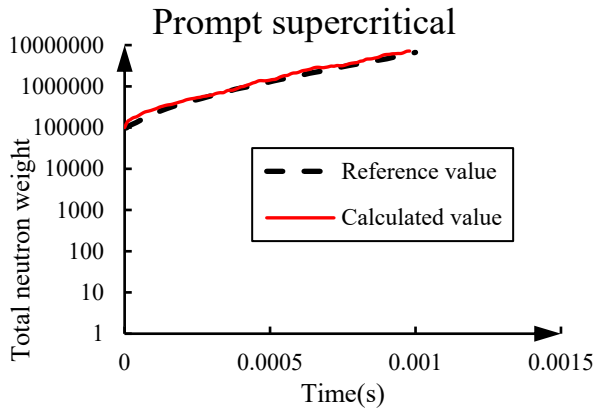

Fig. 5. Calculation results of 16A-0 in prompt supercritical.

It can be seen from the calculation results that the test results of critical and prompt supercritical agree well.

4. Conclusions

In this paper, based on RMC, we study several methods of direct simulation method for neutron space-time kinetics. Through the comb method and the modification of the nuclear reaction simulation, the fluctuation of the number of neutrons against time in the actual simulation is decreased. The forced decay method is adopted for the precursor, and the critical calculation module is added to obtain the initial steady state conditions. Finally, we used TRACY-r61, single group point reactor model and 16A to verify the correctness of the improved program. The results show that the algorithm can get the correct results and reduce the variance of the calculated results.

Acknowledgements

The work in this paper is supported by Science and Technology on Reactor System Design Technology Laboratory in China.

References

1. Boer, B., et al. “Validation of the DALTON-THERMIX code system with transient analyses of the HTR-10 and application to the PBMR”, Nuclear technology, 170.2, 306-321 (2010).
2. Kaplan, E. L. “Monte Carlo methods for equilibrium solutions in neutron multiplication”, UCRL-5275-T, Lawrence Radiation Lab (1958).
3. Carta, M., et al. “Calculation of the effective delayed neutron fraction by deterministic and Monte Carlo methods”, Science and Technology of Nuclear Installations, 2011 (2011).
4. Verboomen B., et al. “Monte Carlo calculation of the effective neutron generation time”, Annals of nuclear energy, 33.10, 911-916 (2006).
5. Sjenitzer B. L., “The dynamic Monte Carlo method for transient analysis of nuclear reactors”, Delft University of Technology (2013).
6. Wang K, et al. “Analysis of BEAVRS two-cycle benchmark using RMC based on full core detailed model”, Progress in Nuclear Energy, 98, 301-312 (2017).
7. Shang X. T., et al. “Burst waiting time simulation of CALIBAN pulse reactor with RMC”, ANS Transactions, (2017).
8. Booth T E. “A weight (charge) conserving importance-weighted comb for Monte Carlo”. LA-UR-96-0051; CONF-960415-10. Los Alamos National Lab., NM (United States) (1996).
9. Kuilman F, et al. “Implementing the combing method in the dynamic Monte Carlo”. Bachelor End Thesis, Faculteit Technische Natuurwetenschappen (2012).
10. Legrady D, et al. “Scouting the feasibility of Monte Carlo reactor dynamics simulations”. Proc. PHYSOR-2008, Interlaken, American Nuclear Society (2008).
11. Miyoshi, et al. “Inter-code Comparison Exercise for Criticality Excursion Analysis”, Benchmark Phase I: Pulse Mode Experiments with Uranyl Nitrate Solution in the TRACY and SILENE Facilities, NEA 6285 (2009).
12. Edgar C. A., “An adaptive Runge-Kutta-Fehlberg method for time-dependent discrete ordinate transport”, Georgia Institute of Technology (2015).

Proceedings of the Reactor Physics Asia 2019 (RPHA19) Conference
Osaka, Japan, Dec. 2-3, 2019

Core Design of a Molten Salt Reactor with Chloride Fuel

Masahiro Watanabe [a*], W.F.G. van Rooijen[b]
[a] *Graduate school of Engineering, University of Fukui, 3-9-1 Bunkyo, Fukui city, Fukui 910-8507 Japan*
[b] *Research Institute of Nuclear Engineering, University of Fukui, 1-3-33, Kanawa, Tsuruga city, Fukui 914-0055, Japan*
[*]Corresponding author: jn180101@u-fukui.ac.jp

Abstract

The disposal method of spent fuel is a problem all over the world. Minor actinide (MA) that has a long half-life and is the cause of the problem, it is considered that the method of MA reduction in the reactor due to depletion. In this study, basic reactor analysis for a simple cylindrical type of a small chloride molten salt reactor aimed at MA reduction is carried out using CSAS6 and TRITON in SCALE6. Criticality calculation and depletion calculation are performed, and the shape of the reactor and the changes in the K-effective due to the composition of the fuel salt, and the radio isotopes due to fuel depletion have been confirmed.

Key Words: **Molten salt reactor, Core design, Chloride fuel, Depletion calculation**

1. Introduction

Molten salt reactors were studied using fluoride at the Oak Ridge Laboratory in the United States from 1964 to 1969. At present, a reactor using molten chloride salt is considered, and since it is possible to make the fuel concentration higher than fluoride eutectic salt, it is considered to work as a fast reactor. It is expected to be usable for transmutation of MA. The aim of this study is to design a small reactor with a maximum thermal power of 50MW_{th}. Therefore, the reactor is designed as small as possible. The K-effective changes depending on the reactor system, dimensions, fuel temperature, and the composition and concentration of fuel and structural material. In this study, K-eff was calculated by changing fuel fraction, reflector thickness and fuel temperature. Furthermore, the depletion calculation was done changing the natural abundance of Li and Cl, and the concentration of Li-6 and Cl-35. In depletion calculation, the abundance of Li-6 and Cl-35 with large neutron absorption cross section in the fuel is changed, and the amount of H-3 produced and the Cl-36 with a long half-life are evaluated.

2. Parameter study of molten salt reactor with chloride fuel

In this study, when deciding the reactor system, K-eff and neutron calculation are evaluated using CSAS6 which is a module of SCALE6[1]. Besides depletion calculation is performed using the determined fuel radius and reflector thickness, and the influence of the abundance ratio of Li-6 and Cl-35 on the amount of H-3 and Cl-36 produced and the K-effective is confirmed. $PuCl_3$-KCl-LiCl is used for the fuel salt, the mole% of fuel salt is determined from the ternary phase diagram[2], considering the melting point and the concentration of Pu. SUS316 is used for the reflector. The fuel operating temperature is 500℃. The composition of the plutonium was calculated with TRITON in SCALE6 on the basis of a PWR fuel assembly model. The assumption was that the fresh fuel was 4.5% enriched UO2. The composition of the plutonium is shown in Table I, using the plutonium weight ratio in the spent fuel after 4 cycles in pressurized water reactor (PWR) operation. Fig. 1 shows the system of the reactor in this study. The fuel is represented in orange color and the reflector is blue color. It is considered that the core power density should be about 100 MWth/m^3. Thus, for a power of 50 MWth, the core volume must be 0.5 m^3. The core radius should be 43 cm and the core height 86 cm. The density of $PuCl_3$-KCl-LiCl[3] is calculated from equation 1 to 4. In molten salt reactor, the fuel flows and the temperature distribution is generated in the reactor. In this study, it was assumed that the temperature distribution was uniform, and ENDF/B-VII.1 is used.

$$\rho_{KCl} = 2.1359 - 5.831 \times 10^{-4}(273.15 + T), \quad (1)$$

$$\rho_{LiCl} = 1.8842 - 4.328 \times 10^{-4}(273.15 + T), \quad (2)$$

$$\rho_{PuCl_3} = 6.6252 - 1.522 \times 10^{-3}(273.15 + T), \quad (3)$$

$$\frac{1}{\rho_{calculated}} = \sum\left(\frac{w_i}{\rho_i}\right), \quad (4)$$

where
T : Temperature (℃).
w_i : Weight fraction of molten salt.
ρ_i : Density of molten salt (g/cm^3).

Table I. Plutonium abundance ratio in fuel salt

Nuclide	Plutonium abundance (%)
Pu-238	1.0
Pu-239	67.0
Pu-240	17.0
Pu-241	12.0
Pu-242	3.0

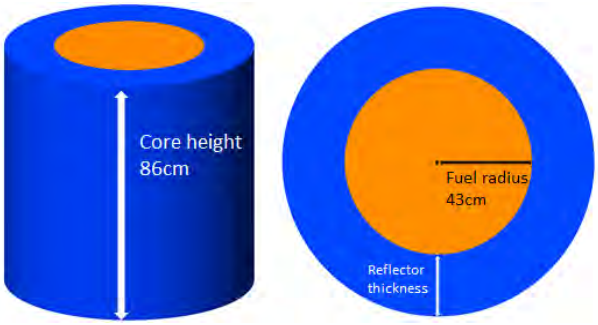

Fig. 1. Core geometry on this study (Fuel is orange color, Reflector is blue color, there are reflectors at the top and bottom of the core).

2.1 Core design by fuel fraction, reflector thickness and fuel temperature

In this section, the change in K-eff due to the fraction of fuel in the eutectic salt and reflector thickness. From the results, the thickness of the reflector and fraction of fuel are determined, and the change in K-eff is calculated due to the change in fuel temperature.

2.1.1 The k-eff by fraction of $PuCl_3$ and reflector thickness

In this study, k-eff was evaluated with CSAS6 (KENO-6), and it was determined fuel fraction and reflector thickness. The fuel fraction was increased from 10% and the reflector thickness was increased from 25 cm to 45 cm. Boundary condition is set as vacuum. In the KENO-6 calculations, the statistical error was smaller than 0.001. It can be seen that k-eff varies greatly depending on the fuel fraction, and k-eff does not change when the reflector thickness is 40 cm or more.

Since K-eff does not change greatly when the reflector is 40cm and 45cm, it is considered that the infinite thickness is at 40cm.

From the results of Fig. 2, the fuel fraction for which k-eff is about 1.1 was determined to be 17 mol%, the reflector thickness was determined to be 40 cm, and the parameters in this analysis are shown in Table II.

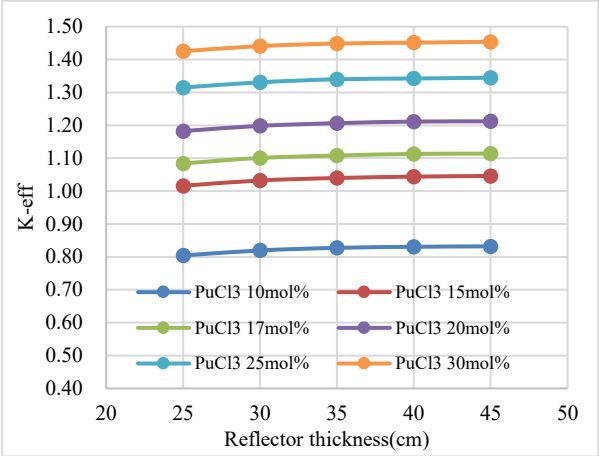

Fig. 2. The K-eff by different molar fraction of fuel and Reflector thickness.

Table II. Calculation conditions of Fuel, reflector and geometry

Parameters	Parameters	
Fuel	Composition	$PuCl_3$-KCl-LiCl (17-50-33 mole %)
	Temperature	500°C
	Density	2.6222g/cm^3 (500°C)
Reflector	Composition	Stainless steel 316
	Density	8.0300g/cm^3
Geometry	type	Cylinder
Boundary	type	Vacuum

2.1.2 The K-eff by fuel temperature

The K-eff is calculated by changing fuel temperature from 500 °C to 750°C every 50°C. Fig. 3 shows the K-eff by changing fuel temperature.

It can be seen that K-eff decreases almost linearly with temperature rise. It decreases approximately 0.008 every 50°C. The statistical error in KENO-6 is about 0.001. From the result of Fig.3, temperature reactivity coefficient is approximately -16×10^{-5} [Δk/k/°C].

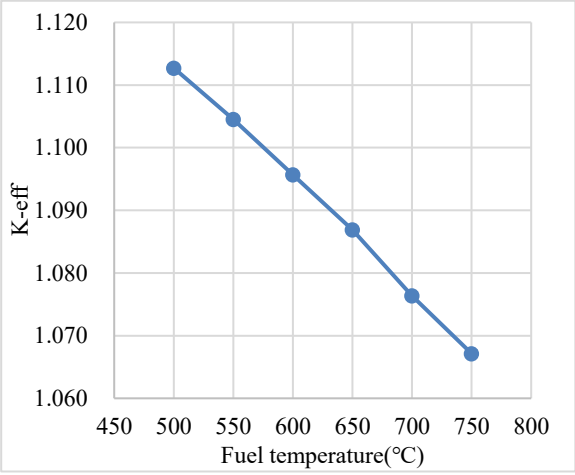

Fig. 3. The K-eff by fuel temperature

2.2 Depletion calculation

Li-6 has large cross section of (n,T) reaction that absorbs neutrons and emits H-3. Released H-3 is considered to affect the operation of the reactor due to gaseous H-3 as void reactivity and the released H-3 chemically reacts with chlorine to form hydrogen chloride. Hydrogen chloride may corrode the reactor vessel.

Cl-35 absorbs neutrons and Cl-36 is produced. Cl-36 has a long half-life that is approximately 301,000 years. The period at the time of landfill disposal may be long. Fig. 4 shows (n,γ) cross section of Cl-35 and Cl-37, it can be seen that the neutron absorption cross section of Cl-35 is larger than that of Cl-37. Therefore, it is necessary to consider the concentration of Li-6 and Cl-35.

Depletion calculations are performed with TRITON. The operation cycle is set as follows: the operation period is about 10 months, and the inspection period is 2 months, and calculated 4 cycles. It shows the cycle in Table III.

Table III. Cycle condition of depletion calculation

Cycle	Operation Time (day)	Inspection time (day)	Burnup (MWd/tHM)
1	300	60	5595
2	300	60	11813
3	300	60	18030
4	300	60	24247

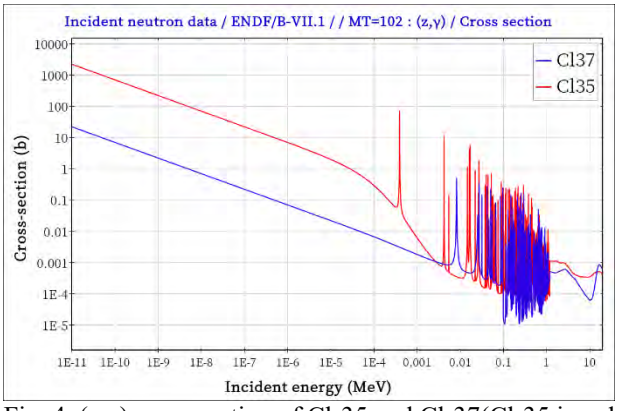

Fig. 4. (n,γ) cross section of Cl-35 and Cl-37(Cl-35 is red color, Cl-37 is blue color)

2.2.1 Depletion calculation of natural abundance of Li and Cl

Fig 5 shows produced Light elements by depletion. H-1, He-4, H-3, Ar-39, K-40 and Cl-36 are produced by depletion and activation reaction. H-1 is produced by proton emission reaction such as (n,p) reaction. He-4 is considered to be emitted of alpha decay of Pu and FP. Ar-39 is considered to be a product of (n,p) reaction of K-39. In the light elements, hydrogen is the most abundant, so there is a concern that it forms hydrogen chloride in the reactor and accelerates the corrosion of the structural material.

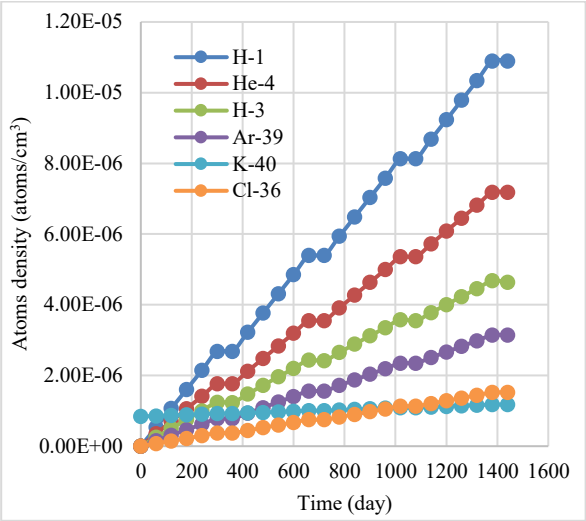

Fig.5. Produced Light elements by depletion.

2.2.2 Effect of concentration of Li-6

The concentration of Li-6 is changed to 0.01, 0.1, 1.0, 2.0, 4.0, 6.0, 7.59%, and calculated the influence of depletion of Li-6. The concentration of Cl-35 is natural abundance in this calculation.

Fig. 6 shows changes of the K-eff by concentration of Li-6. There is no significant change in K-eff at 0.01, and 0.1%. However there is a difference of K-eff about 0.044 between concentration of 0.1% and natural abundance. In each cases, K-eff decreases approximately 0.042 at the end of 4 cycles due to depletion.

Fig. 7 shows the result of changes of mass of H-3 by concentration of Li-6. It can be seen that as the concentration of Li-6 decreases, the production rate of H-3 decreases.

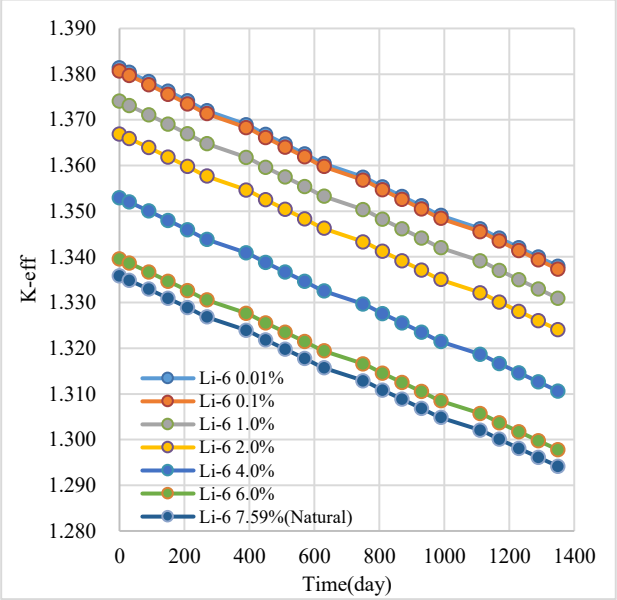

Fig. 6. K-eff by different concentration of Li-6 (Concentration of Cl-35 is natural abundance).

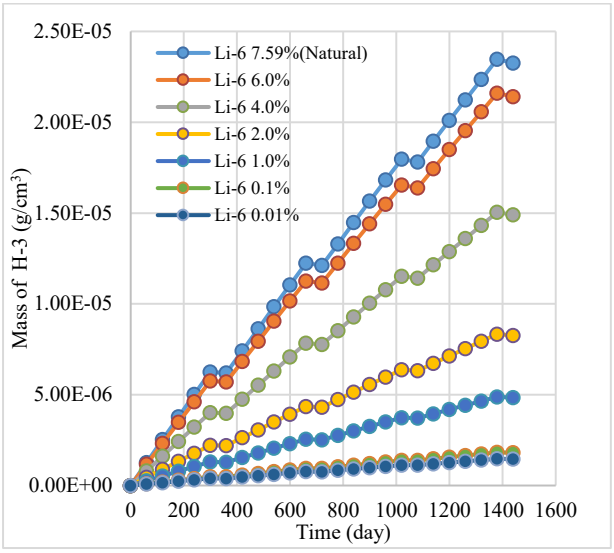

Fig.7. Mass of H-3 by different concentration of Li-6.

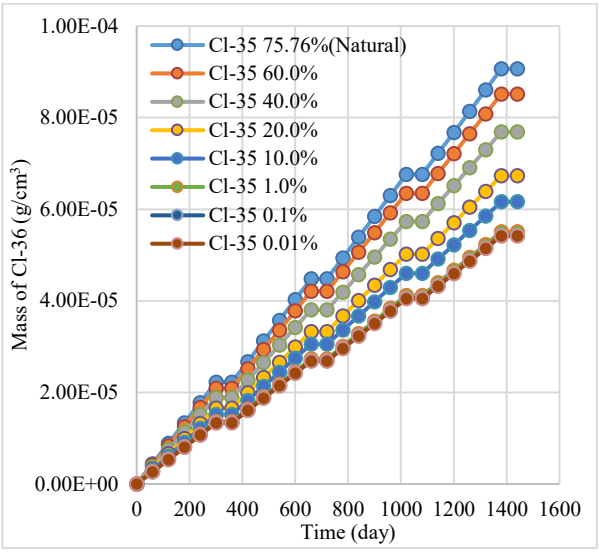

Fig.9. Mass of Cl-36 by different concentration of Cl-35.

2.2.3 Effect of concentration of Cl-35

In this simulation, the concentration of Cl-35 is changed to 0.01, 0.1, 1.0, 10, 20, 40, 60, 75.76% and calculated the influence of depletion of Cl-35. The concentration of Li-6 is natural abundance in this calculation. Fig. 8 shows changes of the K-eff by concentration of Cl-35. There is no significant change in K-eff at 0.01 and 0.1%. Comparing the case of 0.1% with the case of 75.76%, there is a difference of K-eff about 0.086. In each cases, K-eff decreases approximately 0.043 at the end of 4 cycles due to fuel depletion.

Fig. 9 shows the result of changes of mass of Cl-36 by different concentration of Cl-35. It can be seen that the produced amount of Cl-36 is almost the same value from the result of case of 0.01% to 1.0 %. From Fig. 9 it appears that there is not a large difference in the production of Cl-36, going from natural chlorine to enriched chlorine. However, the long-term effect on the radioactive waste due to Cl-36 has not yet been investigated.

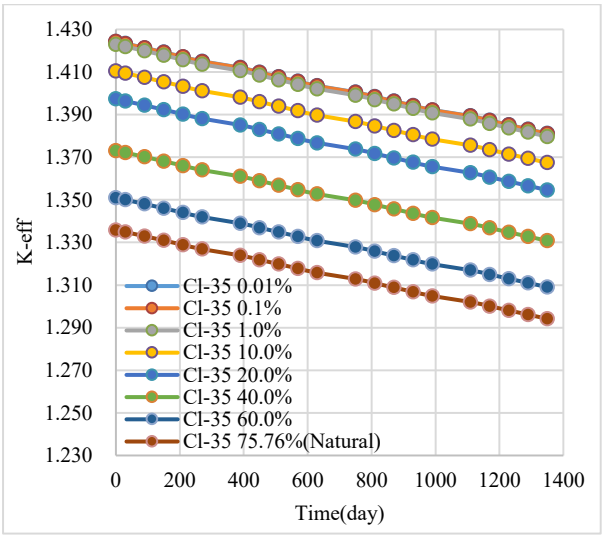

Fig. 8. The K-eff by different concentration of Cl-35 (Concentration of Li-6 is natural abundance).

3. Conclusions

It was found that effect of the fuel fraction and concentration of isotope in nuclear fuel at molten salt fast reactor with chloride salt.

In order to keep the value of K-eff above 1.00, it is necessary to keep the fuel fraction 15mol% or more, and infinite thickness of the reflector was found to be 40cm.

It was confirmed that the negative reactivity was added by the increase of the chloride fuel molten salt temperature. Temperature reactivity coefficient is approximately -16×10^{-5} [Δk/k/°C].

In depletion calculation, noble gases such as He and Ar are released by depletion and radioactivation. They can also affect the nuclear characteristics as void reactivity. Hydrogen and tritium react with chloride in the reactor. And it forms hydrogen chloride, which may corrode structural materials.

The changes in the concentration of Li-6 and Cl-35 have little effects on the amount of produced H-3 and Cl-36 during operation in 4 years. However, the concentrations of Li-6 and Cl-35 have a significant influence for K-eff, and need to be considered sufficiently.

References

1. B. T. Rearden and M. A. Jessee, Eds., SCALE Code System, ORNL/TM-2005/39, Version 6.2.3,Oak Ridge National Laboratory, Oak Ridge, Tennessee (2018)
2. Wentao Zhou, “Thermodynamic evaluation of LiCl-KCl-$PuCl_3$ system”, Journal of Alloys and Compounds 695 (2017) 2306-2313.
3. Robert D. Mariani, “Modeled salt density for nuclear material estimation in the treatment of spent nuclear fuel”, Journal of Nuclear Materials 404 (2010) 25-32.

Proceedings of the Reactor Physics Asia 2019 (RPHA19) Conference
Osaka, Japan, Dec. 2-3, 2019

Monte Carlo Based Analysis for CANDLE Burning Reactor

Hoang Hai Nguyen, Jun Nishiyama and Toru Obara*
Laboratory for Advanced Nuclear Energy, Institute of Innovative Research, Tokyo Institute of Technology, 2-12-1 N1-19, Ookayama, Meguro-ku, Tokyo, 152-8550 Japan
*Corresponding author: tobara@lane.iir.titech.ac.jp

Abstract

This study presents a Monte Carlo based analysis for CANDLE burning reactor. In this procedure, neutronic calculation was performed by MVP code with JENDL-4.0 library and burnup calculation was performed by MVP-BURN code with the detailed burnup chain. To simulate the fuel movement process, an auxiliary program was developed by Python language. To demonstrate the feasibility of this procedure, a trial calculation was performed for a reference core design. The results showed that this Monte Carlo based procedure was developed successfully.

Key Words: **CANDLE, Monte Carlo, MVP, MVP-BURN**

1. Introduction

CANDLE (Constant Axial Shape of Neutron Flux, Nuclide Densities and Power Profile During Life of Energy Production) burning concept was proposed by Sekimoto et al. [1]. Most of the studies of CANDLE reactor were performed by deterministic method. The most advantage of deterministic method is computational time. However, in deterministic method, several approximations must be used to obtained the group constants for several burnup stages. Therefore, it is difficult to improve the accuracy of results. On the other hand, in Monte Carlo method, the accuracy of results can be improved by increasing the number of neutron histories.

The purpose of this study is to develop a procedure to analyze the CANDLE burning by Monte Carlo based method to overcome the limitation of deterministic method.

2. Methodology

2.1 Procedure of CANDLE burning analysis by Monte Carlo method

The procedure of CANDLE burning analysis consists of the following steps. Firstly, the neutron transport calculation is performed by MVP code [2] with JENDL-4.0 nuclear data library. The microscopic reaction rates, obtained by neutron transport calculation, are transferred into MVP-BURN code [3] to solve the burnup calculation. After one fuel movement cycle (FMC), the fuel shuffling process is applied. In this process, spent fuel zones are removed from the core top and fresh fuel zones are loaded into core bottom. After this process, the new axial nuclide density distribution is established. To stimulate this process, an auxiliary code was developed by Python language.

By repeating this procedure, the core equilibrium condition can be achieved based on the convergence of the effective multiplication factor k_{eff}, neutron flux, power density and nuclide density distribution.

2.2 Reference core design

To demonstrate the feasibility of this procedure, a trial calculation was performed for a reference core design. In fuel pin design, the innermost layer is the cylindrical shaped fuel pellet. In this study, metallic uranium with the zirconium content of 10 % is used as fuel. The next layer in lead bismuth eutectic (LBE) bond. The ODS cladding layer covers the fuel and bond. The outermost layer is LBE coolant with hexagonal shape.

Table I. Core Design Parameters

Design parameters	**Value**
Thermal power [MWt]	200
Core height [cm]	220
Core radius [cm]	145
Reflector thickness [cm]	50
Fuel composition	U – 10 wt% Zr
Bond material	LBE
Cladding material	ODS
Coolant material	LBE
Reflector material	LBE
Fuel pin pitch [cm]	1.08
Cladding thickness [cm]	0.06
Bond thickness [cm]	0.06
Fuel pellet radius [cm]	0.39

The core design (figure 1 and table I) consists of 127 fuel

assemblies and each assembly is made from 397 fuel pins. In axial direction, the core is divided into 55 zones. In the initial core, the first 12 zones from the top to bottom are loaded with enriched uranium and the other zones are loaded with natural uranium.

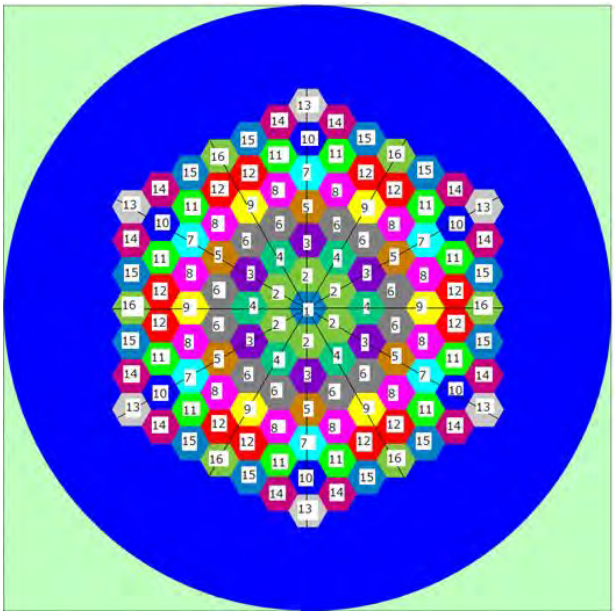

Fig. 1. Reference core layout

3. Results

To make the maximum uncertainty of calculated results less than 0.01%, 100,000 neutron histories per batch and 150 calculated batches were decided. In the burnup calculation, several calculations were performed with different burnup steps. These results show that with the burnup step less than 1250 days, there is no significant difference between results. Therefore, 1250 days was decided as the proper burnup step.

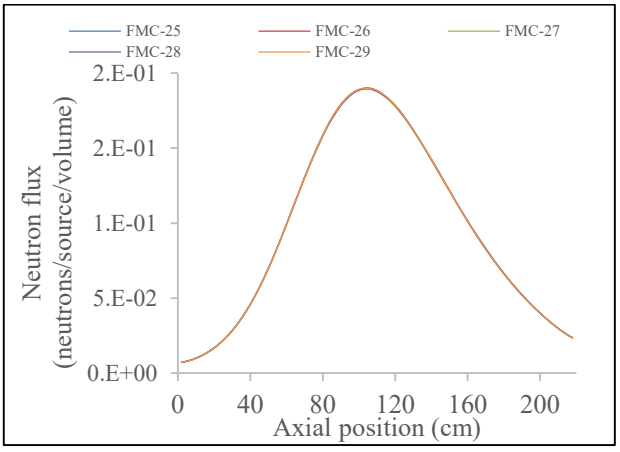

Fig. 2. Axial neutron flux distribution at each fuel movement cycle.

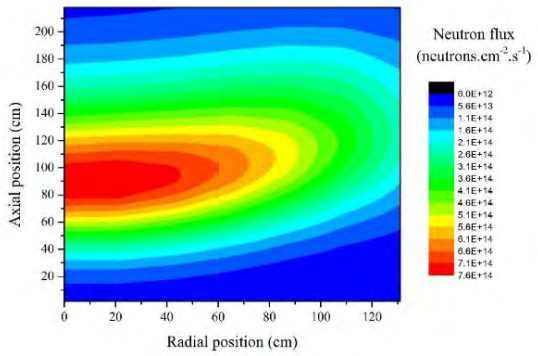

a) Beginning of cycle

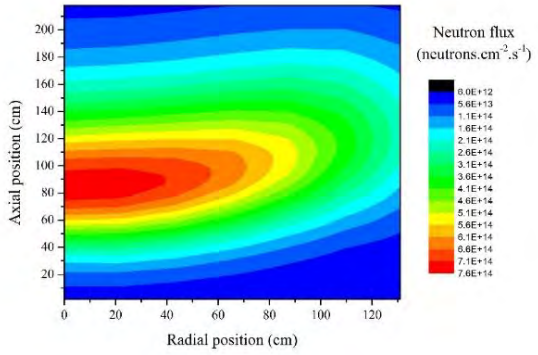

b) Middle of cycle

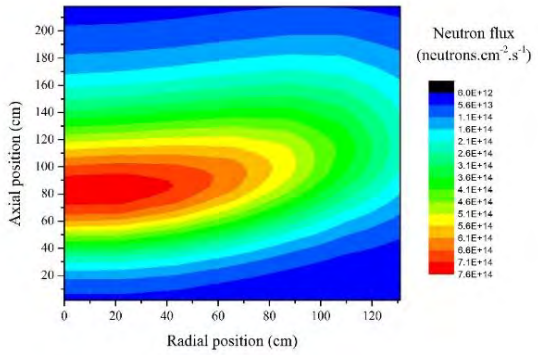

c) End of cycle

Fig. 3. Neutron flux profile in one fuel movement cycle.

In equilibrium condition, the k_{eff} at the beginning of cycle and at the end of cycle are 1.0172 and 1.0176, respectively.

Figure 2 shows the axial neutron flux profile for the different FMCs. It shows that the flux profile is converged to the equilibrium condition.

Figure 3 shows the flux profile from the beginning to the end of one FMC. In radial direction, the neutron flux at the core center reaches the highest value and decreases to core edge. In axial direction, the highest region of neutron flux is around the middle height. From the beginning to the end of one FMC, the flux moves from the top to bottom without changing the shape.

With the convergence of neutronic characteristics, such as neutron flux, to the equilibrium condition and the

movement of neutron flux from the top to the bottom of the core without changing the shape, it can be concluded that the CANDLE burning strategy has been developed successfully.

It is difficult to make the exactly similar geometry for comparison between deterministic method and Monte Carlo method. In deterministic method, the reactor core was simplified as cylindrical geometry. On the other hand, in Monte Carlo method, the hexagonal fuel pins were arranged in the hexagonal lattice to form the fuel assembly and the fuel assemblies were arranged in the hexagonal lattice to establish the reactor core However, the accuracy of Monte Carlo method has been widely accepted. Therefore, with the enough number of neutron histories, it can be expected that Monte Carlo method provide the better accuracy of results. In addition, for further detailed analysis, instead of deterministic method, Monte Carlo method can provide more information, such as the neutron leakage from the core.

4. Conclusions

In this study, a procedure for CANDLE burning analysis based on the Monte Carlo method was proposed to obtain the high accuracy of result. In this procedure, MVP code and MVP- BURN code were applied for neutron transport calculation and burnup calculation. To simulate the fuel movement process, an auxiliary code was developed by Python language. The results show that by repeating the fuel movement process, the equilibrium condition was achieved successfully. This means this Monte Carlo based procedure has been developed successfully.

References

1. SEKIMOTO H, RYU K, and YOSHIMURA Y, “CANDLE: The New Burnup Strategy”, *Nuclear Science and Engineering*, 139, p. 306 (2001).
2. NAGAYA Y et al., “MVP/GMVP II: General Purpose Monte Carlo Codes for Neutron and Photon Transport Calculations Based on Continuous Energy and Multigroup Methods”, JAERI 1348, Japan Atomic Energy Research Institute (2005).
3. OKUMURA K et al., “MVP-BURN: Burn-up Calculation Code Using a Continuous-energy Monte Carlo Code MVP”, Draft Report for JAEA-Data/Code, Japan Atomic Energy Agency (2005).

TS-03 Core Analysis Methods

Proceedings of the Reactor Physics Asia 2019 (RPHA19) Conference
Osaka, Japan, Dec. 2-3, 2019

Nuclear Waste Inventory Calculations from Fuel Cycle with Fast Reactors by a Reactor Physics Code System CBZ

Yu Kobayashi[a,*], Go Chiba[a]
[a]*Hokkaido University, Kita-13 Nishi-8, Sapporo, Japan*
[*]Corresponding author: esaking5884@eis.hokudai.ac.jp

Abstract

We investigate the effect of minor actinide recycling on nuclear wastes from fast reactors by using an updated version of a FRBurner module developed for fast reactor whole-core burn-up calculations in a code system CBZ.

The update of CBZ enables calculation of inventory of transuranic wastes composed of hulls and end-pieces, so calculations of decay heat of high-level wastes and transuranic wastes become possible. Decay heat of cobalt-60 from hulls and end-pieces is as large as decay heat of fission products. It is turned out that minor actinide recycling conditions and cooling time changes are not important for decay heat of transuranic wastes in comparison with that of high-level wastes.

Key Words: **fast reactor, fuel cycle, MA conversion, TRU wastes**

1. Introduction

When we utilize nuclear energy, we cannot avoid management of nuclear wastes. Nuclear wastes have to be managed for hundreds or thousands of years because of their decay heat (DH) and potential radiotoxicity. In order to properly and efficiently manage nuclear wastes, accurate evaluations of the inventory of radioactive nuclides such as fission products (FP) and minor actinide (MA) nuclides are necessary.

Some MA nuclides continue to emit DH for long period, so they increase the number of the waste units and required area of disposal sites because heat production of a waste unit is restricted. In addition, MA nuclides have potential radiotoxicity. From these reasons, reduction of the amount of MA nuclides is important.

MA nuclides can be converted to short-lived radioactive nuclides through burn-up in fast reactors. Thus, the nuclear fuel cycle with fast reactors is expected to reduce the area of disposal sites of the high-level wastes (HLW). However, the transuranic (TRU) wastes from the nuclear fuel cycle with fast reactors are generated but are not often considered. In this paper, the wastes only from hulls and end-pieces of fuel assemblies are called TRU wastes. Hulls and end-pieces of fuel assemblies include Co-59 as impurity and it is converted to the radioactive nuclide, Co-60, by capturing neutron during reactor operation [1]. The volume of TRU wastes is not small, so it is necessary to consider TRU wastes also when discussing about the nuclear wastes.

Moreover, the nuclear fuel cycle with fast rectors have many uncertainties, such as cooling time before reprocessing, operation time of fast reactors and so on. The fuel cycle with fast reactors is expected to reduce the amount of wastes, but the reduction amount would be dependent on these uncertainties. Therefore, we have to know how much the fuel cycle with fast reactors including uncertainties affects the amount of the nuclear wastes.

In order to carry out these calculations, we have implemented a new capability into a FRBurner module in a reactor physics code system CBZ. In the present work, some calculations are conducted with various conditions to demonstrate the effectiveness of the new capability. In the present work, the number of recycled MA nuclides is varied according to 4 cases for HLW first. All MA nuclides are recycled in case 1 and fewer MA nuclides are recycled in cases 2, 3 and 4 in sequence. Second, sensitivity study about recycling (separation) efficiency of MA nuclides in spent fuel reprocessing is carried out. Finally, the cooling time from the fuel discharging to reprocessing is changed for TRU wastes calculations. Four-, 10-, 25- and 50-year cooling are considered.

2. Implementation of Nuclear Waste Inventory Calculation Capability to CBZ/FRBurner

The FRBurner module has been developed to perform whole-core burn-up calculations for fast reactors in CBZ. On fuel assembly calculations, homogeneous or one-dimensional heterogeneous model can be adopted, and assembly-homogeneous (or homogenized) multi-group cross sections are used in subsequent whole-core calculations based on the transport or diffusion theory. A reactor core is modeled to the two-dimensional cylinder. More detailed information about FRBuener and results of its verification calculation are presented in a different paper in this conference [2]. In the present study, homogeneous assembly model and diffusion theory

module are used.

Generally, in fast reactor burn-up calculations, fission product nuclides are treated as simple pseudo nuclides, and explicit representations of important fission product nuclides in burn-up calculations are not introduced. On inventory calculations in nuclear waste, one-point fuel burn-up codes like ORIGEN are generally utilized. This procedure can roughly estimate inventory of nuclear wastes with reasonable computation time, but high accuracy cannot be expected because neutron flux energy spectrum is significantly dependent on spatial position in a fast reactor core and it is quite difficult to define unique one-group cross sections required for one-point burn-up calculations. To overcome this difficulty, a detailed burn-up chain consisting of 197 fission product nuclides can be used in whole-core burn-up calculations in FRBurner. In addition to that, activation calculations of Co-59 included in SUS cladding as an impurity material, which is important to quantify DH in TRU wastes, are also possible.

Whole-core burn-up calculations with FRBurner can provide nuclides inventory information included in discharged fuels, and using these information, we can calculate characteristics of HLW and TRU wastes. Decay heat of HLW and TRU wastes can be calculated by cooling calculation capability of a Burner module of CBZ, which uses rigorous burn-up chain model consisting of all the fission product nuclides defined in JENDL fission products yield data file-2011 (JENDL/FPY-2011) and Co-60.

3. Sample Calculation

The target reactor core is a large MOX-fuel high-internal conversion representative core provided in the final report on phase 2 of feasibility study on commercialized fast reactor cycle systems from Japan Atomic Energy Agency [3]. This is called JSFR-1500 and is a 1500 MWe sodium-cooled reactor. It's designed to achieve long operation term and high Pu generation ratio. This JSFR-1500 has two different core concepts, the transition-phase core and the equilibrium-phase core, and we consider the latter in the present calculation.

Decay heats of HLW and TRU wastes are shown in the following sub-sections.

In both calculations, burn-up calculations of JSFR-1500 are carried out with FRBurner and nuclide number densities of discharged fuel per one batch at an equilibrium cycle are obtained. Then 4-year cooling calculations are carried out with Burner, and nuclides number densities in HLW and TRU wastes generated from spent fuel reprocessing are calculated. Separation efficiency of MA nuclides is assumed 100%; all the recycled MA nuclides are included to the nuclear fuel and no recycled MA remains in HLW wastes. Time-dependent radioactivity and DH after reprocessing are calculated.

In spent fuel reprocessing, four cases with different conditions about recycled MA nuclides are considered; all MA nuclides are recycled in case 1, Cm remains in wastes in case 2, Cm and Am remain in case 3 and All MA nuclides (Cm, Am and Np) remain in wastes in case 4.

3.1 Decay heat of high-level waste

The total DH in HLW of each case is shown in Fig. 1. Reduction of the number of recycled MA nuclides increases DH of the wastes. DH of cases 3 and 4 are same, and this means that the contribution of Np recycling to reduction of wastes is negligible.

Component-wise DH of cases 1 and 2 are shown in Figs. 2 and 3. It represents the effect of recycling of Cm. In case 1, all MA nuclides are recycled, so DH of FP is identical with the total DH of wastes. In case 2, DH of heavy metals (HM) appears and be dominant around 300 years after reprocessing.

According to Fig. 3, at a time of reprocessing, DH of FP is dominant, but some years later, contribution of HM becomes large. Actually, the number of canisters is not affected by DH of HM since it is determined by DH of FP, but the interval of neighboring canisters at disposal site is dependent on DH of HM. That's why MA nuclides recycling reduce the area of disposal site.

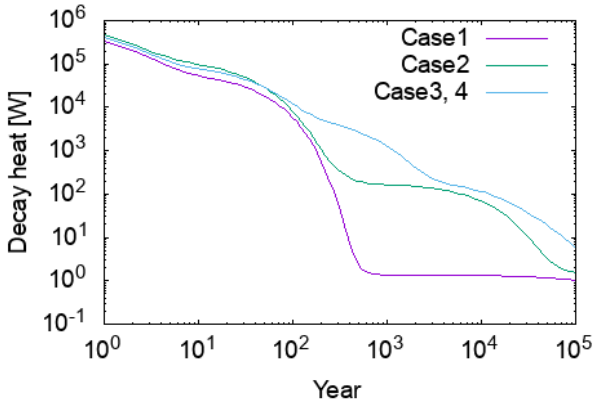

Fig. 1. The total decay heat of HLW

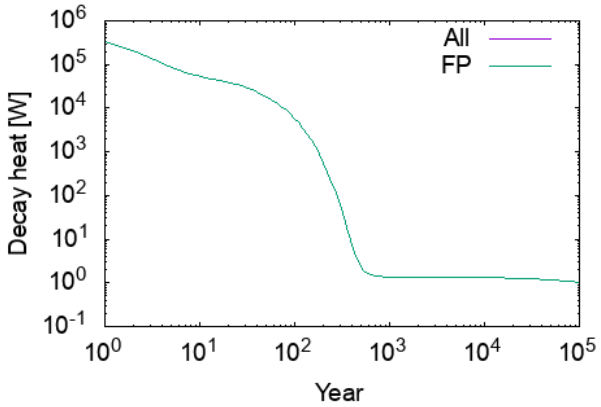

Fig. 2. Component-wise decay heat of HLW in case 1

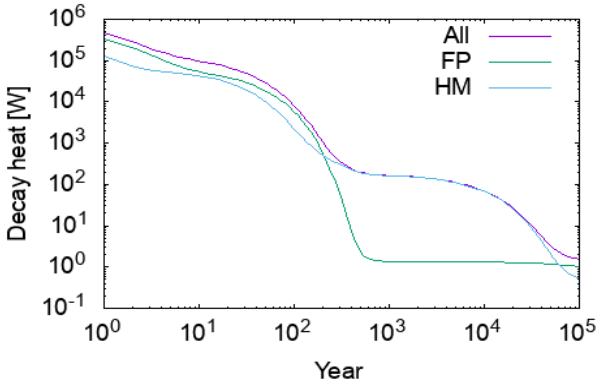

Fig. 3. Component-wise decay heat of HLW in case 2

Figure 4 shows element-wise DH in case 2. According to this figure, DH of Pu becomes larger than the others. It means that if Cm remains in HLW, the contribution of Pu becomes larger.

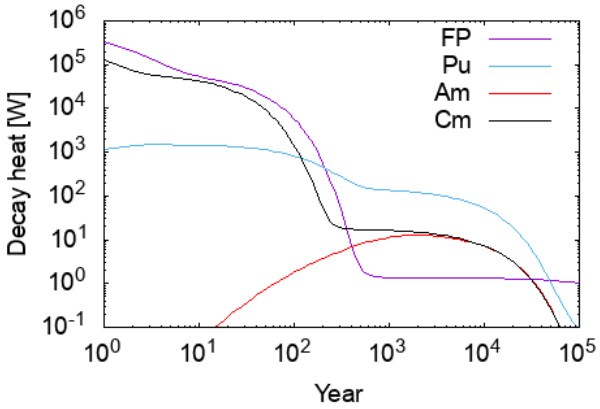

Fig. 4. Element-wise decay heat of HLW in case2

Next, let's see the effect of MA separation ratio change in spent fuel reprocessing. Total DH of HLW with separation rate of 99.9% is shown in Fig. 5. In this calculation, 0.1% of recycled MA is included in HLW.

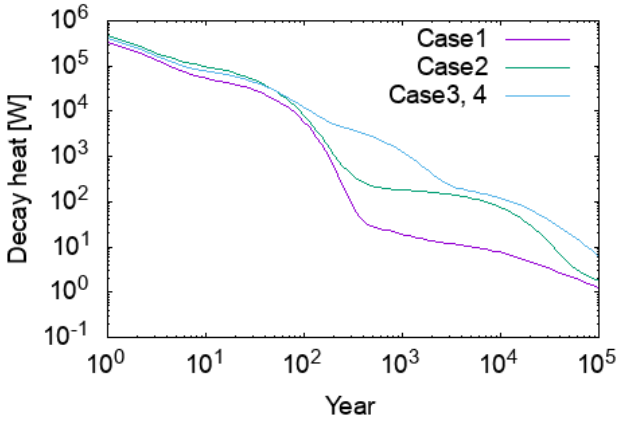

Fig. 5. The total decay heat of HLW
(separation ratio is 99.9%)

When separation ratio is 99.9%, only DH of case 1 increases from that with separation ratio of 100%. Because HM remain in other cases when separation ratio is 100%, the contribution of 0.01% of HM remaining in HLW is not significant. That's why the change appears only in case 1. Figure 6 shows DH of each nuclide of case 1 with 99.9% separation ratio. Decay heat of Cm and Pu become larger than that of FP when 400 years passed and soon DH of Pu becomes dominant.

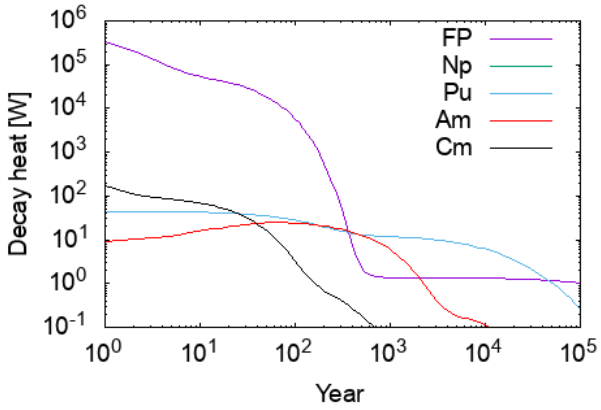

Fig. 6. Element-wise decay heat of HLW in case 1
(separation ratio is 99.9%)

3.2 TRU Wastes

Since detailed information about reprocessing of spent fuel from fast reactors is not available, it is assumed that condition of TRU waste generation in reprocessing in the present study is same as that of light water reactors. A few FP and HM in spent fuel attach to TRU wastes, and the attachment rate of FP and HM are assumed 0.3% and 0.2%, respectively [4]. Heavy metals are recycled under the same conditions adopted in sub-section 3.1.

Decay heat of Co-60 from hulls and end-pieces has become possible to be calculated by the updated FRBurner module. Decay heat of Co-60 is large as well as other FP and HM, so its contribution to volume of wastes is large.

Figure 7 shows DH of four cases. Few differences among four cases exist. When the number of recycled MA nuclides increases, the amount of MA nuclides in spent fuel increases, so DH of case 1 is the largest.

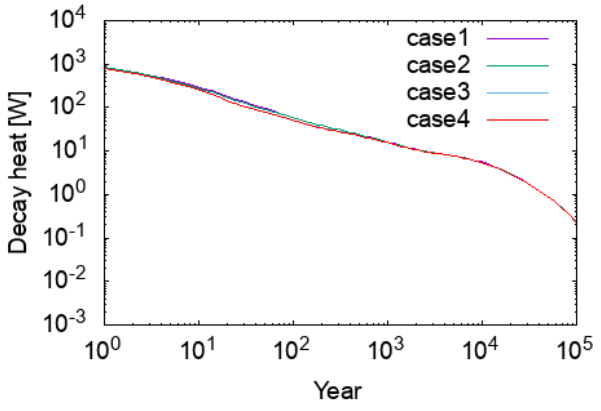

Fig. 7. The total decay heat of TRU wastes

Figure 8 shows the component-wise DH. At first, the DH of Co-60 is as large as DH of FP, and that's why considering Co-60 in TRU wastes are important. When tens of years passed, the DH of Co-60 decreases rapidly in comparison with the DH of FP.

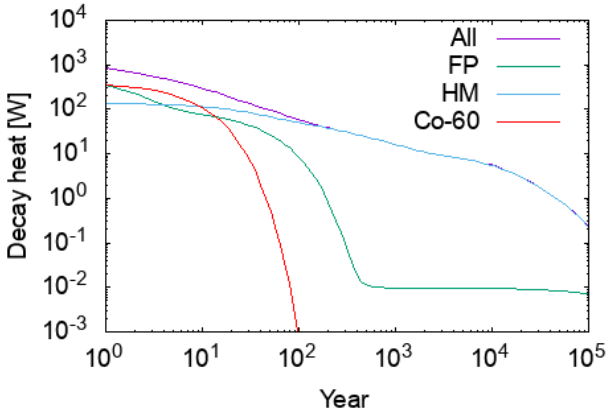

Fig. 8. Component-wise decay heat of TRU wastes in case 1

Finally, DH with various cooling time in case 2 is shown in Fig. 9. Here, cooling time means the time from fuel discharging to reprocessing. Four cases are calculated: 4-, 10-, 25- and 50-year cooling. The DH curves start at a year after reprocessing.

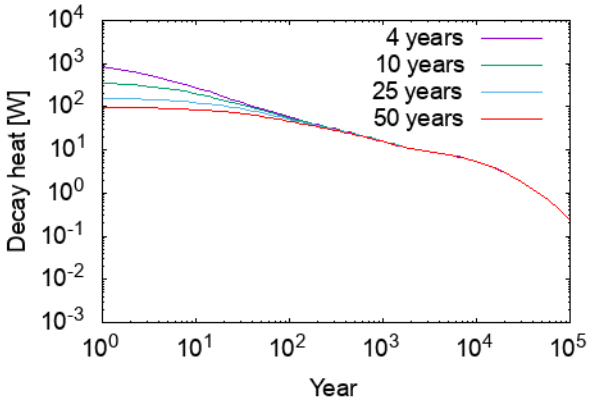

Fig. 9. The total decay heat of TRU wastes in case 2 with different cooling time

Long cooling time increases DH of HLW after the long-period disposal because Pu-241 is converted to Am-241 before reprocessing. In contrast, there are few changes in DH of TRU wastes because Pu-241 is not removed from TRU wastes when reprocessing.

The above results suggest that recycling conditions of MA nuclides and expanding cooling time are negligible when considering TRU wastes

4. Conclusion

We have investigated the effect of MA nuclides recycling on nuclear wastes from fast reactors by using the FRBurner module developed for fast reactors whole-core burn-up calculation in a code system CBZ. Four cases with different reprocessing conditions are considered for HLW and TRU wastes; no MA nuclides remains, Cm remains, Cm and Am remain and all MA nuclides remain in the HLW. By a comparison between the above two cases, the effect of Cm recycling has become clear. Curium recycling reduces DH around 100 years after reprocessing. If Cm remains in the wastes, the contribution of Pu is large.

The effect of changing separation ratio has been turned out. When separation ratio is not 100% but 99.9%, the DH of the case that all MA nuclides are recycled has increased to about ten times because FP do not initially exist in case 1, so the contribution of 0.1% of MA nuclides is large.

Update of CBZ has enabled calculation of inventory of TRU wastes. Decay heat of Co-60 from hulls and end-pieces is as large as DH of FP. Thus, TRU wastes should be considered when we use nuclear energy and manage the wastes from it. Minor actinide nuclides recycling conditions and cooling time changes are not important for DH of TRU wastes by comparison to it of HLW.

A calculation of DH of HLW and TRU wastes have become possible now. As a future study, we will consider impacts of uncertainties in various conditions on nuclear waste from nuclear fuel cycle with fast reactors.

Acknowledgements

Some of the results shown in the present paper are based on the research program conducted by the Radioactive Waste Management Funding and Research Center (RWMC), entitled "Study on the effects of advanced nuclear fuel cycle technology to the geological disposal concept". The authors are grateful to Dr. Hidekazu Asano and Dr. Masahiro Kawakubo of RWMC for their supports on the present work.

References

1. Hirano F, et al., "Thermal impact of geological disposal of hull and end piece wastes resulting from high-burn-up operation of LWR and introduction of MOX fuels into LWR," *J. Nucl. Sci. Technol.,* **46**, 443 (2009).
2. Fan J, Chiba G, "Verification of FRBurnermodule of CBZ code system based on OECD/NEA benchmark report," this conference.
3. Ohki S, et al., "FBR core concepts in the "FaCT" project in Japan," *Proc. PHYSOR 2008*, Interlaken, Switzerland, Sep. 14–19, 2008, (2008) (CD-ROM).
4. Hirano F, et al., "Burning of MOX fuels in LWRs; fuel history effects on thermal properties of hull and end piece wastes and the repository performance" *J. Nucl. Sci. Technol.*, **49**, 310 (2012).

Proceedings of the Reactor Physics Asia 2019 (RPHA19) Conference
Osaka, Japan, Dec. 2-3, 2019

Verification of FRBurner Module of CBZ Code System Based on OECD/NEA Benchmark Report

Junshuang Fan[a,*], Go Chiba[a]
[a]*Hokkaido University, Kita 13, Nishi 8, Sapporo, Japan*
[*]Corresponding author: fanjsh@eng.hokudai.ac.jp

Abstract

We verify the accuracy of our tools about sodium-cooled fast reactor calculation in this work by comparing results with the OECD/NEA benchmark report. Besides, we analyze the influences about transport theory, fuel assembly heterogeneity, and P_N-S_N condition on transport calculation on global parameters of core calculation. Maximum bias of k_{eff}, β_{eff}, $\Delta\rho_{void}$, and $\Delta\rho_{Doppler}$ are less than 0.80%, 3.2%, 8.9% and 9.0% respectively. Bias comparison shows our tool could provide reasonable results on sodium-cooled fast reactor cores with various types of fuel and sizes. Maximum value of transport theory correction effect for all cores on k_{eff}, β_{eff}, non-leakage and leakage component of $\Delta\rho_{void}$, $\Delta\rho_{void,}$ and $\Delta\rho_{Doppler}$ are around than 1.21%, 0.2%, 0.7%, 7.2%, 8.1% and 0.6% respectively. Transport correction effect indicates that it makes large differences in k_{eff} and $\Delta\rho_{void}$ calculations. Maximum heterogeneous correction effects of these parameters are around 0.67%, 0.6%, 10.1%, 0.6%, 13.4% and 8.9% respectively, which indicates it has large influence on k_{eff} and reactivity calculation. Independence between heterogeneous lattice model and transport theory calculation is observed. Besides, comparison between P1S4 and P3S8 shows negligible differences. Particularly, relative large transport correction effect occurs at k_{eff} and the leakage component of $\Delta\rho_{void}$ for MET-1000. This phenomenon is caused by a fact that neutron spectrum of the MET-1000 core is harder than the other cores. We also find transport theory correction effect will change with core size, fuel type and the number of energy groups.

Key Words : **fast reactor, burn-up calculation, verification, correction effect**

1. Introduction

We are going to develop our original fast reactor core concept in the near future and new module of our code system for fast reactor calculation has been developed. Consequently we choose one benchmark problem of OECD/NEA [1] as our reference to verify whether this new module could fit with various fuel types and core sizes or not.

This benchmark report provides four core concepts. Two of them are large size cores at 3600 MWe (MOX-3600, CAR-3600) and 2 of them are middle size cores at 1000 MWe (MOX-1000, MET-1000). Core name indicates the fuel type of each core ("CAR" means carbide fuel). Various institutions such as JAEA, ANL, CEA and so on, participated in this benchmark work and give their results based on different libraries, calculation theory, model, and energy group structure. This benchmark report indicates several points related to this work: (1) nuclear data library used has a large impact on the effective neutron multiplication factor k_{eff}; (2) cell and control rod models (heterogeneous vs. homogeneous) employed for lattice and whole core calculations also impact on k_{eff}, sodium void reactivity $\Delta\rho_{void}$, and control rod worth.

k_{eff}, effective delayed neutron fraction β_{eff}, $\Delta\rho_{void}$, Doppler reactivity $\Delta\rho_{Doppler}$ are compared with benchmark report. Particularly, we put different model/theory into account. We are able to quantify these effects consistently in our code system by doing this work.

2. Numerical Tools and Methods

A FRBurner module has been developed to perform whole-core burn-up calculations for fast reactors in CBZ, which is a general-purpose reactor physics code system developed by our laboratory.

On fuel assembly calculations, homogeneous or one-dimensional heterogeneous model can be adopted, and assembly-homogeneous (or homogenized) multi-group cross sections are used in subsequent whole-core calculations. In resonance self-shielding calculations, a 280-group library generated from the evaluated nuclear data files is used in the present work. A group structure of this 280-group library is generated from the 70-group structure adopted in the JAERI fast set-3 (JFS-3) [2], and each energy group in JFS-3 is divided into four groups with equal lethargy width. For heterogeneous model calculations, Tone's method [3] is

used to calculate background cross sections considering heterogeneity effect. Neutron transport calculations in heterogeneous assembly model are carried out with the collision probability method.

A reactor core is modeled to a two-dimensional cylinder. Neutron multiplication factor and neutron flux spatial and energy distributions are calculated by the diffusion or transport theory. In diffusion theory calculations, a finite volume method-based module, PLOS, is used. In transport theory calculations, a SNRZ module based on the diamond-differencing spatial discretization and discrete-ordinate angular discretization schemes is used. In SNRZ calculations, arbitrary number of the Legendre expansions for anisotropic scattering cross sections can be used. In nuclear fuel burn-up calculations, fission product nuclides are treated as simple pseudo nuclides. Sodium void and Doppler reactivity calculations and effective delayed neutron fraction calculations can be carried out also by the diffusion or transport theory, and reactivity is calculated by the perturbation theory.

In this benchmark, nuclides number density information at the beginning of cycle at the equilibrium state are provided for each of the four cores. With these number densities at BOC, users of this benchmark problem should perform nuclear fuel burn-up calculations to obtain number densities at the end of cycle (EOC). Hence comparisons at EOC should also include burn-up effects.

3. Bias Comparison

Different reference values are provided by the benchmark report but only four departments give results of all the fore cores result. To keep the consistency of reference value we choose results provided as CEA-1 (heterogeneous model, transport theory, JEFF-3.1.1-based library) as our reference. Figure 1-a and Figure 1-b show the biases between CBZ system and the references under heterogeneous lattice model with transport theory (P3-S8), which are consistent conditions with references.

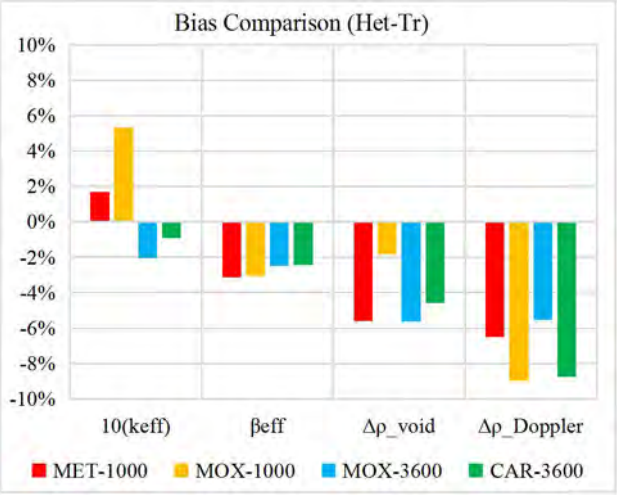

Fig. 1-a. Biases between CBZ and reference at BOC

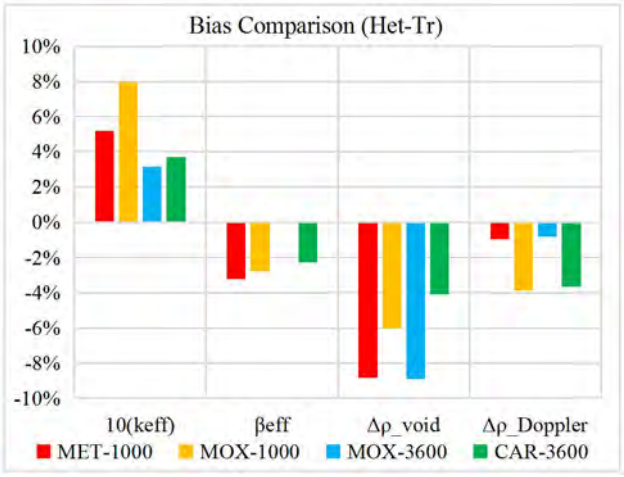

Fig. 1-b. Biases between CBZ and reference at EOC

In the CBZ calculations, we use JEFF-3.1.1-based library , the same as CEA-1. In Fig. 1-a and Fig. 1-b, biases on k_{eff} is multiplied by 10 for clear comparison.

For MET-1000, maximum biases of these parameters are around 0.52%, -3.2%, -8.8% and -6.5% respectively. Bias of EOC is also consistent with that of BOC.

For MOX-1000, maximum biases of these parameters are around 0.80%, -3.0%, -6.0% and -8.9% respectively. Bias of EOC is also consistent with that of BOC.

For MOX-3600, maximum biases of these parameters are around 0.32%, -2.5%, -8.9% and -5.5% respectively. Comparison of β_{eff} at EOC is not available because this reference has no data of β_{eff} at EOC.

For CAR-3600, maximum biases of CBZ are around 0.40%, -1.9%, -2.4% and -8.6%. Consistency between BOC and EOC is also obtained.

The above comparisons show us that CBZ could give reasonable results about burn-up calculations of sodium-cooled fast reactor with various types of fuel (metallic, MOX, carbide fuels) and different sizes. The maximum biases of our tool are less than 0.8% in k_{eff}, 4% in β_{eff}, 10% in two reactivities. The remaining bias would come from our 2-dimensional model in whole core calculation procedure whereas the reference applies 3-dimensional model.

4. Correction Effect

After the verification work is finished, we figure out the effect of heterogeneous lattice model and transport theory which are compared with homogeneous lattice model and diffusion theory.

Transport theory effect is compared under homogeneous and heterogeneous lattice models, as shown in Figure 2. Heterogeneous lattice model effect is compared under diffusion and transport theory (P3-S8), as shown in Figure 3. Effects on k_{eff} is multiplied by 10 for clear comparison for the both figures. Figure 2 and Figure 3 only show two correction effects at BOC because the effects at EOC are almost the same as BOC. In all figures, $\Delta\rho_{(N\text{-}Lk)}$ and $\Delta\rho_{(Lk)}$ mean non-leakage

component and leakage component of sodium void reactivity.

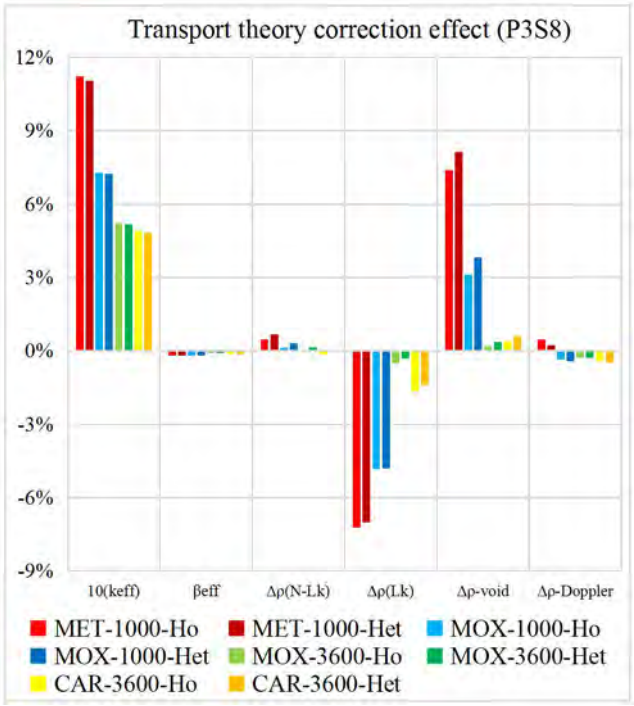

Fig. 2. Transport theory correction effect at BOC

Firstly, as shown in Figure 2, transport theory causes large increasing on k_{eff}, about 0.5%~1.2%. Reason of this increasing on k_{eff} is that diffusion theory overestimates neutron leakage. As a consequence, transport theory gives larger value of k_{eff}.

There almost no influences on β_{eff} and $\Delta\rho_{Doppler}$.

As for $\Delta\rho_{void}$, we decompose it into non-leakage component and leakage components. Non-leakage component includes yield, absorption, scattering and (n,2n) fractions. We can find that transport theory leads to a slight increasing on non-leakage component, but it has large negative effect on leakage component. The reason of negative effect on $\Delta\rho_{(N\text{-}Lk)}$ is that neutron leakage is overestimated with diffusion theory. Consequently, transport theory corrects this error and leakage component of sodium void reactivity will decrease with transport theory calculation.

Particularly, we could easily find that correction effect on k_{eff} and leakage component for the MET-1000 core is larger than the other cores. This is because metallic fuel core has harder neutron spectrum than the others. Another interesting thing is that we could observe obvious difference between large size core and middle size core. This phenomenon tells us transport theory calculation is important for small size systems because small size systems have larger neutron leakage.

Here we have to emphasize one important thing: transport theory correction effect will change with energy structure, i.e., transport theory effect in coarse-energy group and that in fine-energy group are different with each other, especially for k_{eff}. Thus result of Figure 2 is only suitable for 280-group library calculation.

Next, heterogeneous correction effect shows relatively large influence on non-leakage component of $\Delta\rho_{void}$ and $\Delta\rho_{Doppler}$. The maximum value on non-leakage component is around 10% which is indicated in the MOX-3600 case, and around 8.6% on Doppler reactivity for all the cores. The reason of large negative changes on non-leakage component of $\Delta\rho_{void}$ is yield component increasing with the decreasing in absorption and scattering components. Among them, yield component is negative effect, absorption and scattering components are positive effect. The dominant reason for negative reactivity increasing of yield component is homogenized macroscopic fission cross section decreasing. This is because in heterogeneous model, neutron flux level outside fuel region increases and the weight of neutron flux inside fuel region decreases when sodium void occurs, and macroscopic cross section is calculated by this weight of neutron. Finally, the net effect on non-leakage component of $\Delta\rho_{void}$ is negative.

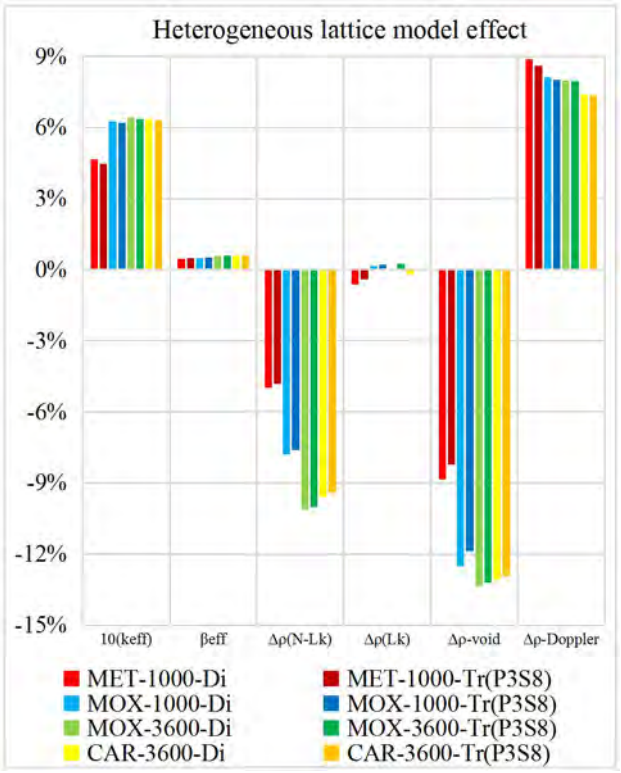

Fig. 3. Heterogeneous lattice model correction effect at BOC

The reason of large increasing on $\Delta\rho_{Doppler}$ in heterogeneous model is because the background cross section in heterogeneous model is smaller than it in homogeneous model. Since Doppler reactivity is mostly caused by U-238 resonance absorption and this absorption is related to background cross section.

Regarding k_{eff}, 0.47%~0.64% differences caused by heterogeneous effect is found. This is because energy self-shielding and spatial self-shielding effects. On the contrary, heterogeneous effect is not considerable for β_{eff}. Maximum value is around 0.7% which occurs in

MOX-3600 case.

Thirdly, we can easily observe that both effects show independence, i.e., transport effect under homogeneous model is consistent with it under heterogeneous model; heterogeneous effect under diffusion theory is consistent with it under transport theory.

5. P_N-S_N Effect

In transport theory we use P_N order and S_N order to control the degree of approximation of transport theory calculation. P_N is the maximum order of Legendre polynomials for anisotropic scattering cross section expansion. S_N is the order of discrete points in angle. In the present work, we use the level symmetric quadrature sets.

We compared the differences between P1-S4 and P3-S8, and the result is shown in Figure 4. Differences of k_{eff} are multiplied by 10 for clear comparison. Figure 4 only shows P_N-S_N effect at BOC because it is almost the same as EOC.

We could find that P3-S8 makes little difference to P1-S4. This means P1-S4 is enough for transport theory calculation because P3-S8 is quite time-consuming.

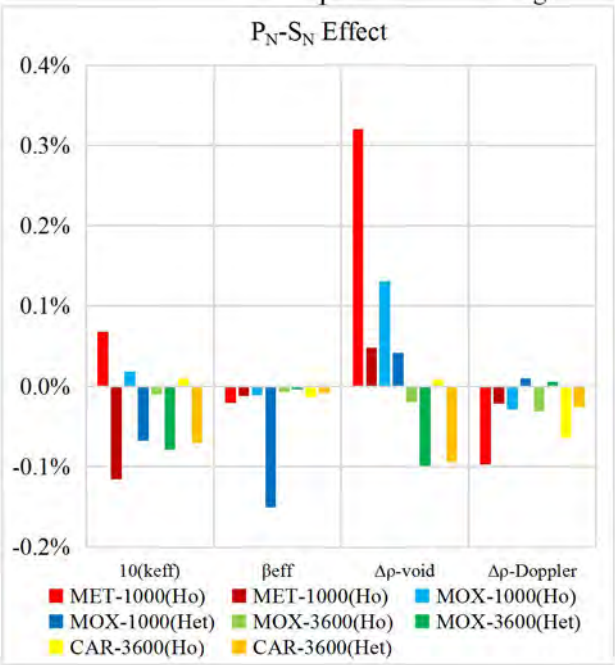

Fig. 4. P_N-S_N effect at BOC

6. Conclusion

In this work, we have verified the accuracy of our tools about fast reactor burn-up calculation. Totally, bias of all four cores for k_{eff}, β_{eff}, $\Delta\rho_{void}$, $\Delta\rho_{Doppler}$ are less than 0.80%, 3.2%, 8.9% and 9.0% respectively. This means new module for CBZ could provide acceptable result on sodium-cooled fast reactor with various types of fuel and sizes.

Secondly, we have quantified transport and heterogeneous correction effects for each core. Maximum value of transport theory correction effect for all four cores on k_{eff}, β_{eff}, non-leakage $\Delta\rho_{void}$, leakage $\Delta\rho_{void}$, $\Delta\rho_{void}$, and $\Delta\rho_{Doppler}$ are around 1.21%, 0.2%, 0.7%, 7.2%, 8.1% and 0.6% respectively. This result indicates that it makes large difference on k_{eff} and $\Delta\rho_{void}$. Maximum value of heterogeneous correction effect for all four cores on k_{eff}, β_{eff}, non-leakage $\Delta\rho_{void}$, leakage $\Delta\rho_{void}$, $\Delta\rho_{void}$, and $\Delta\rho_{Doppler}$ are around 0.67%, 0.6%, 10.1%, 0.6%, 13.4% and 8.9% respectively, and this result indicates it has large influence on k_{eff} and $\Delta\rho_{void}$ calculation. Besides, we have found that these two effects are independent with each other. Furthermore, we have observed transport theory correction effect relates to core size and fuel type.

Thirdly, P_N-S_N effect has been quantified, which is not estimated by benchmark report. Maximum difference between P3-S8 and P1-S4 of all four cores on k_{eff}, β_{eff}, $\Delta\rho_{void}$, $\Delta\rho_{Doppler}$ are around -0.12%, -0.02%, 0.32% and -0.1% respectively. The P_N-S_N effect shows negligible differences which means P1-S4 is better than P3-S8 due to P3-S8 is time-consuming.

Consequently, these three comparisons indicates we should apply heterogeneous lattice model with transport theory (P1-S4) calculation in our future work with CBZ code system.

References

1. "*Benchmark for Neutronic Analysis of Sodium cooled Fast Reactor Cores with Various Fuel Types and Core Sizes*", NEA/NSC/R(2015)9, OECD Nuclear Energy Agency (2016).
1. Takano H, Ishiguro Y, "Production and Benchmark Tests of Fast Reactor Group Constant Set JFS-3-J2," JAERI-M 82-135, Japan Atomic Energy Research Institute (1978).
2. Tone T, "A Numerical Study of Heterogeneity Effects in Fast Reactor Critical Assemblies," *J. Nucl. Sci. Technol.*, **12**, 467 (1975).

Proceedings of the Reactor Physics Asia 2019 (RPHA19) Conference
Osaka,Japan,Dec. 2-3, 2019

Development of aSteady-State Core Analysis Code System for VVER

Lulin Yu[a,*], Guohua Chen[a], Jiadong Bao[a], Lingfeng Wei[a], Zejun Liao[b], Shanghong Zhang[a]
[a]*NuStar Nuclear Power Technology Co., Ltd., Suite 1101,1698Yishan Road, Shanghai, China.*
[b]*Nuclear Power Operations Research Institute, Hangzhou, Zhejiang, China*
[*]Corresponding author:lulinyu@nustarnuclear.com

Abstract

Recently, a variant of NuStar's core analysis code system for western type PWR, has been developed in NuStar to satisfy the need of VVER applications. It is composed of NuStar's latest version of lattice code, ROBIN2, the variant of NuStar's 3D core code for hexagonal geometry, EGRET-H, and other components for cross section representation, high productivity and good user experience. This paper outlines the technical features of this new code system ORIENT-H, especially the features that are introduced recently. Verification and validation results of the code system are also briefly introduced.

Key Words: **Core Analysis, VVER, ORIENT-H, Code**

1. Introduction

As the major vendor-independent core analysis code developer and provider in mainland China, NuStar has been dedicating itself to satisfy the need coming from the ever-growing domestic nuclear power industry. Currently, NuStar's ROBIN/EGRET code system[1,2], which was designed for western type PWR, is being adopted by 11 operating units for reactor core operation support, independent reload design audit and advanced reactor physics test applications. To further serve the domestic clients, including utilities who are operating the Russian type VVER units, NuStar is independently developing a code system for VVER, since so far there is no domestically-developed vendor-independent code applicable to the operating 4 VVER-1000 units and the other 2 VVER-1200 units expected to be in operation in year 2026 and 2027.

Considering the fact that the original ROBIN/EGRET code system had been extensively verified and validated before it was licensed for production use, and its performance has been repeatedly recognized during its about 50 reactor-years of on-site application, the authors adopt as many modules/subroutines as possible from it when developing its variant for VVER. Therefore, in this paper, only these technical features/functions that are newly developed for VVER applications are emphasized. Section 2 outlines the key component codes for the system, while Section 3 introduces the verification and validation work so far has been performed and presents the preliminary results. Section 4 concludes the paper.

2. Component Code Development

The ORIENT-H system is developed by extensively employing today's technology not only existing in the area of reactor physics method and computation but also existing in the area of computer science and software engineering. It is a fruit of joint efforts by NuStar's reactor physicists and computer software engineers. The neutronics kernel of the system is composed of a 2D lattice code ROBIN2 and a 3D core code EGRET-H.

2.1 Lattice code ROBIN2

ROBIN2 is the latest version of NuStar's lattice code. Compared with its predecessor, one of the noticeable improvements of ROBIN2 is its applicability to complicated lattice geometries. In previous generation of ROBIN, there are only two types of geometry elements (i.e the box and the pin cell geometry) pre-defined in the codes, which limits the codes only applicable to typical western type PWR geometries and a small portion of BWR geometries. While for ROBIN2, since the idea of pre-defined geometry element is abandoned and the R-function method[3] is employed instead, its geometry applicability to complex fuel lattices significantly enhanced. As an example, Fig.1 illustrates three types of lattice geometries that ROBIN2 is applicable to.

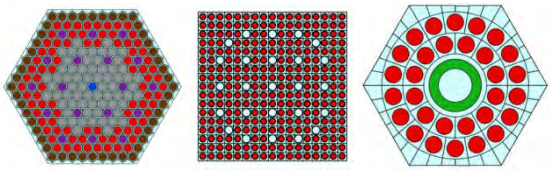

Fig.1 ROBIN2 applies both to regular and irregular lattice geometries.

Besides the above-mention enhancement in geometry applicability, there are also other enhancements adopted in ROBIN2 either to further improve the code's computational efficiency for transport calculation or to

improve its overall performance for industrial applications. For instance, while one set of space and angle discretization parameters are adopted for all the energy groups to perform MOC transport calculations in previous generation of ROBIN, discretization parameters change in ROBIN2 for different energy ranges as the neutron mean free path changes noticeably between fast neutron and thermal neutron.

In short, the main functionalities and features of ROBIN2 can be summarized as below:

1) Adopting R-function method to handle irregular geometry.
2) Rational approximation coupled with enhanced neutron current method[4] as its main resonance calculation method.
3) Pre-tabulated resonance interference factor table to account for the resonance interference effects among multiple resonance nuclides.
4) MOC [5,6] for transport calculation.
5) Assembly-based modular ray generation[7] and cyclic ray tracing for both square and hexagonal geometry.
6) Cell-based CMFD acceleration for both regular and irregular lattice geometry.
7) Smart azimuthal angle discretization scheme[8].
8) Different space and angle discretization scheme for different energy ranges.
9) Linear rate (LR) depletion method for normal fuel pins.
10) Logarithmic linear reaction rate (LLR) depletion method [9] for gadolinium-bearing fuel pins.

2.23D Core Code EGRET-H

EGRET[10] is NuStar's 3D core code for steady-state criticality and depletion calculation for western type PWR. As mentioned earlier, this code, as a key component for NuStar's core analysis code system, has so far been extensively verified and validated. With this code at hand, the key task to develop a variant for VVER is therefore to develop a 3D neutron diffusion problem solver that applies to hexagonal geometry.

To reuse modules/subroutines of EGRET as many as possible and also to minimize the code verification and validation efforts, the authors choose to employ Chao's conformal mapping method[11]to develop this diffusion problem solver.

2.2.1 Conformal Mapping

According to the conformal mapping theory, as illustrated in Fig.2, by introducing the Schwarz-christoffel mapping, a hexagon in complex *z*-plane can be mapped to a rectangle in another complex *w*-plane and the corresponding mapping function $g(u,v)$is defined as,

$$g(u,v)=\left|\frac{dz}{dw}\right|. \quad (1)$$

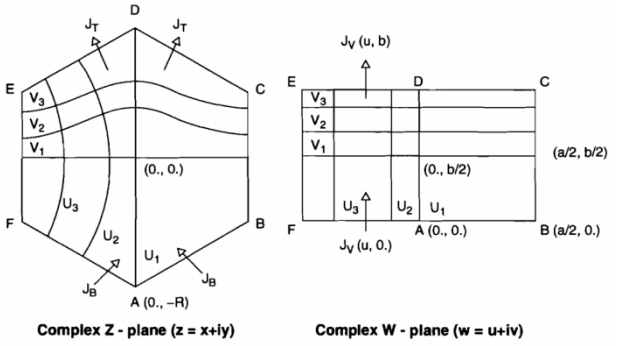

Fig. 2 Conformal mapping of a hexagon to a rectangle.

By applying this mapping, the original two-dimensional group-wise neutron diffusion equation defined in complex *z*-plane (as given in below),

$$-D(\frac{\partial^2}{\partial x^2}+\frac{\partial^2}{\partial y^2})\phi(x,y)+\Sigma_r\phi(x,y)=Q\ (x,y), \quad (2)$$

is now defined in complex *w*-plane and has a new form as follows,

$$-D(\frac{\partial^2}{\partial u^2}+\frac{\partial^2}{\partial v^2})\phi(u,v)+\Sigma_r g^2(u,v)\phi(u,v)=g^2(u,v)Q\ (u,v). \quad (3)$$

Compared against Eq.(2), the new form of Eq.(3) is very similar. The only difference is that the new form of equation has a non-uniform cross section within the rectangular node.

2.2.2 Semi-Analytical Nodal Solution

The method employed in EGRET to solve the 3D nodal diffusion problem is the so-called semi-analytical nodal method (SANM). By following the common practice of transverse integration technique and then approximately expanding the 1D nodal fluxes by a combination of analytical and polynomial base functions, one may solve the original 3D nodal diffusion problem iteratively. Enormous practical applications demonstrate that the method possesses an outstanding overall performance.

As for the hexagonal geometry case, as illustrated in Fig.2, for each radial direction perpendicular to a pair of surfaces, the hexagonal node can be mapped into a corresponding rectangle. Then by applying the transverse integration technique to Eq.(3) within the rectangle, one may obtain the following 1D equation, which is still quite similar to the form of the 1D equation solved by SANM in EGRET.

$$-D\frac{\partial^2}{\partial u^2}\varphi_u(u)+\Sigma_r\overline{g^2}(u)\varphi_u(u)=\overline{g^2}(u)Q_u(u)-L_u(u), \quad (4)$$

where

$$\varphi_u(u)=\frac{1}{a_v}\int_{-a_v/2}^{a_v/2}\phi(u,v)dv \quad (5)$$

$$\psi(u,v)=\frac{1}{a_z}\int_{-a_z/2}^{a_z/2}\phi(x,y,z)dz \quad (6)$$

$$\overline{g^2}(u)=\int_{-a_v/2}^{a_v/2}g^2(u,v)\phi(u,v)dv/\varphi(u) \quad (7)$$

$$L_u(u) = L_u^R(u) + \overline{g^2}(u) L_u^Z(u) \quad (8)$$

$$L_u^R(u) = \frac{1}{a_v} \int_{-a_v/2}^{a_v/2} -D \frac{\partial^2}{\partial v^2} \phi(u,v) dv \quad (9)$$

$$L_u^Z(u) = \frac{1}{a_z} \int_{-a_z/2}^{a_z/2} -D \frac{\partial^2}{\partial z^2} \phi(r) dz \quad (10)$$

Unlike the case of rectangle node, where only three coupled 1D equations are obtained after the application of transverse integration, one now obtains a coupled four integrated 1D equations, i.e. one from axial direction and the other three from radial directions perpendicular to three sets of surfaces of a hexagon. By some minor adaptation, the original EGRET SANM kernel can be used to solve this set of coupled 1D equations.

2.2.3 CIAMA technique

One noticeable feature of EGRET is that it adopts the innovative Channel-wise Intrinsic Axial Mesh Adaptation (CIAMA) technique[12] to practically eliminate the long-standing non-physical control rod cusping issue for the modern coarse-mesh nodal methods. Another advantage of this technique is that one may also explicitly represent the local effect caused by the fuel grid directly in the whole-core coarse-mesh nodal calculation. EGRET-H continues to employ this innovative technique unique to EGRET.

2.2.4 Intranode Representation

To capture the burnup gradient effect within a hexagonal node, the spatial variation of cross sections inside a hexagon is represented in EGRET-H. The diffusion coefficients are assumed to have negligible burnup gradient effect, while other cross sections are tracked with seven values per node, i.e. the values on the six hexagon surfaces and the node-averaged value. In SANM calculation, the effect of heterogeneous cross section is considered as an extra contribution to the neutron source.

2.3 System Integration

As an engineer-oriented software package, ORIENT-H is designed to encapsulate the process of the codes within two-steps framework, and provide a user-friendly interface, with a relatively gentle learning curve.

On the backend, besides the aforementioned lattice code ROBIN2 and 3D core nodal code EGRET-H, ORIENT-H relies on other components, including a database OASIS for storing modeling and calculation information, a management platform NYMPH for manipulating files and driving calculations, a cross section representation tool IDYLL for cross-section table pre-generation. With such an architecture, it simplifies the users' work and releases them from writing textual input card, which is tedious and prone error.

On the frontend, ORIENT-H adopts the techniques and tools from modern web development, to provide convenient interaction scheme without the need of installing a client application, i.e. a user can model a reactor, define a core loading scheme, specify a calculation task, and view the corresponding results with the help of a web browser.

3. Code Verification and Validation

Currently, verification and validation tests are being extensively performed for each component code and the ORIENT-H system as a whole. For verification purpose, emphases are directed to these modules that are newly developed or modified for VVER applications. Results obtained are compared either with internationally recognized benchmark results or with results obtained by other codes that are already verified or validated. While for validation purpose, as the first attempt, the calculation results for a VVER-1000 reactor are compared against the measurement data previously published in a proposal for an international benchmark problem.[13]

3.1 Validation Results for VVER-1000 Benchmark

The comparison of the critical boron concentrations for the first cycle is given in Fig. 3. While the corresponding comparison for axial offset (AO) is given in Fig.4. From these comparisons, one may notice that for most of the core depletion history, the ORIENT-H prediction results agree well with the measurement data. However, there are also some statuses that noticeably large discrepancies are observed. It is no doubt that the whole system and the problem modeling are still needed to be further tested, especially for these modules to perform TH feedback and to generate the homogenized parameters for the reactor baffle, the authors incline to the view that such large discrepancies are very likely to be caused by the inconformity of the core conditions between calculation and measurement. As shown in Fig.5, the operation history for the cycle is quite unstable, especially for the BOC and EOC period. Since any change in the reactor power and the insertion position of the control rod will inevitably result in the corresponding changes of the total xenon poison and its spatial distribution, and such changes always lag behind, the core conditions will never reach stable in the days after each change happens. Considering the fact that the measurement data is just provided once for a day, it is quite apprehensible that large discrepancies are apt to see for these days, since calculations are actually performed for core states that are noticeably different from these where the measurement is performed. The authors incline to believe that this fact could also account for the similar phenomenon that people see in results from other code systems[13].

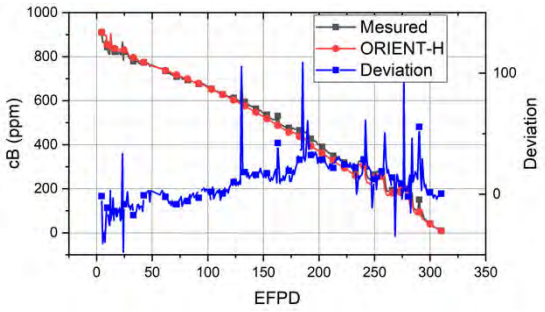

Fig. 3 Critical boron concentration of cycle 1.

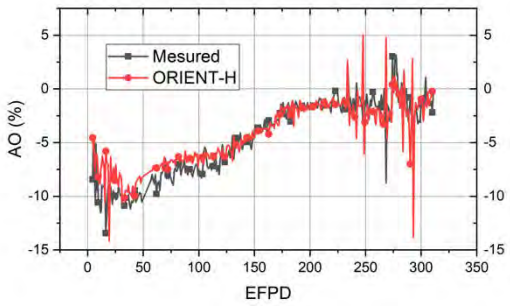

Fig. 4 Axial offset of cycle 1.

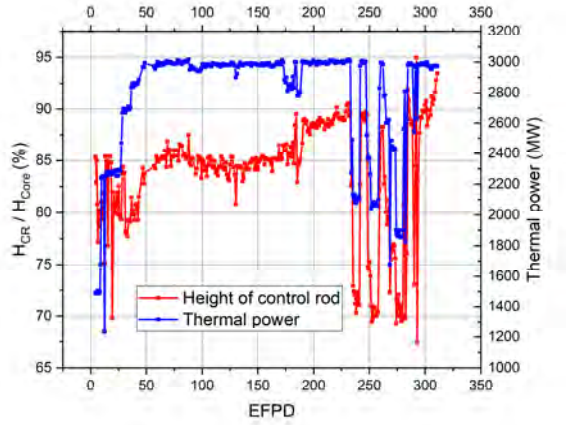

Fig. 5 Operation history of cycle 1.

4. Conclusions

A new variant of NuStar's core analysis code system has recently been developed for VVER application. It is mainly composed of NuStar's latest version of lattice code, ROBIN2 and the variant of NuStar's 3D core code for hexagonal geometry, EGRET-H. The first validation results obtained for the initial cycle of a VVER-1000 reactor has demonstrated that the development of the system is successful. Extensive validation against multiple units and multiple cycles are currently under way, and the results will be published in the near future.

Acknowledgements

The authors would like to express their sincere gratitude to Dr. Yung-An Chao for his kind help and invaluable discussions during this study.

Validation against the VVER-1000 benchmark was mainly undertaken by Mr. Lingfeng Wei during his internship in the company, who was then a graduate student of the Sino-French Institute for Nuclear Energy and Technology of Sun Yat-sen University.

References

1. Zhang SH et al., "Validation of NuStar's PWR Core Analysis System", *Proc PHYSOR2014*, Kyoto, Japan, Sept. 28-Oct. 3, 2014, American Nuclear Society (2014).
2. Zhang SH, "Current Status of NuStar's PWR Core Analysis Code System", *Proc RPHA15*, Jeju, Korea, Sept. 16-18, 2015.
3. Altiparmakov DV, Belicev P, "An Efficient Study of the R-function Method Applied as Solid Modeler for Monte Carlo Calculations". *Progress in Nuclear Energy*, 24, p77 (1990).
4. Yamamoto A, "Evaluation of Background Cross Section for Heterogeneous and Complicated Geometry by the Enhanced Neutron Current Method". *J. Nuclear Science and Technology*, v45, n12, p1287 (2008).
5. Askew R, "A Characteristics Formulation of the Neutron Transport Equation inComplicated Geometries." AEEW-M 1108 (1972).
6. Goldberg L et al., "The Method of Characteristics in General Geometry". *Trans. Am. Nucl. Soc.,* 73, 173 (1995).
7. Cho JY et al., "Whole Core Transport Calculation Employing Hexagonal Modular Ray Tracing and CMFD Formulation". *J Nuclear Science Technology*, 45, p.740-751(2008).
8. Yamamoto A et al., "Derivation of Optimum Polar Angle Quadrature Set for the Method of Characteristics Based on Approximation Error for the Bickley Function". *J Nuclear Science Technology*, 44, 129 (2007).
9. Carpenter DC et al., "The Log Linear Rate Constant Power Depletion Method". *Proc PHYSOR 2010*, Pittsburgh, Pennsylvania, May 9 - 14, 2010.
10. Zhang, SH, "The Multigroup Neutronics Model of NuStar's 3D Core Code EGRET", *Proc PHYSOR2014*, Kyoto, Japan, Sept. 28-Oct. 3, 2014, American Nuclear Society (2014).
11. ChaoYA et al., "Conformal Mapping and Hexagonal Nodal Methods". *Nuclear Science and Engineering*, 121, 202-225 (1995).
12. Lu D et al., "A Three-dimensional Nodal Method with Channel-wise Intrinsic Axial Mesh Adaptation", *Annals of Nuclear Energy*, 79, 152-157, 2015.
13. Lötsch T et al., "Corrections and Additions to the Proposal of a Benchmark for Core Burnup Calculations for a VVER-1000 Reactor", *Proc AER 2010*, Hanasaari, Espoo, Finland, Sept. 20–24, 2010.

Proceedings of the Reactor Physics Asia 2019 (RPHA19) Conference
Osaka, Japan, Dec. 2-3, 2019

BEAVRS Benchmark Evaluations with Studsvik CMS5 Code Package

Tamer Bahadir[a,*], Masatoshi Yamasaki[b]
[a]*Studsvik Scandpower, Inc, 10 Langley Rd, Suite 201, Newton, MA 02459, USA*
[b]*Studsvik Japan, Ltd, Rinku Gate Tower Bldg 1409, 1 Rinku Oraikita, Izumisano-city, Osaka, 598-0048 Japan*
[*]Corresponding author: tamer.bahadir@studsvik.com

Abstract

The MIT BEAVRS benchmark problem is evaluated using Studsvik's state-of-the-art in-core fuel management code package CMS5, which includes CASMO5 and SIMULATE5. The CMS5 calculated results for low-power physics tests (hot zero power critical boron, control rod worth and isothermal temperature coefficients) and full power operation (boron letdown and flux map reaction rate distributions) are compared to plant measured data provided in the benchmark specification. The CMS5 calculations are repeated with three different evaluated nuclear data libraries: ENDF/B-VII.1, ENDF/B-VIII.0 and JENDL-4.0. The CMS5 model predicts HZP critical boron concentration for all-rods-out conditions within 10 ppm for both Cycle-1and Cycle-2; the control rod worth is predicted with a difference of 0.7% ± 3.8%, where the maximum difference is less than 9%. For the core follow calculations at the hot full power condition, the average difference in predicting the critical boron concentration is less than 20 ppm. In addition, the radial and nodal reaction rate distributions are predicted with a mean difference of about 1.6 percent and 3.8 percent, respectively. No significant difference is observed in predicting measured plant parameters with different nuclear data libraries.

Key Words: **CMS5, CASMO5, SIMULATE5, BEAVRS benchmark**

1. Introduction

Studsvik's in-core fuel management code package CMS/CMS5, which includes lattice physics code CASMO4/5 [1] and 3D nodal code SIMULATE3/5 [2], has been widely used in the industry for LWR reactor analysis for more than 35 years. The initial lattice physics code, CASMO-3, and 3D nodal code, SIMULATE-3, developed in early 1980s were replaced with the state-of-the-art CASMO5 and SIMULATE5 codes in mid 2000s by taking advantage of today's modern computer resources to implement advanced physics and numerical models, as well as employing new nuclear data libraries. The CMS/CMS5 code package has been applied to approximately 200 reactors, analyzing more than a thousand cycles. It is proven to be accurate for typical LWR reactors. The CMS5 code package has recently been approved by the US NRC for generic application to Pressurized Water Reactors in the US [3].

The MIT BEAVRS reactor as defined in reference [4] contains information for the initial cycle 1 and the reloaded cycle 2 of a typical 4-loop Westinghouse reactor. The benchmark contains not only the detailed description of the reactor core, its fuel and other essential components, but also provides detailed measured data at hot-zero-power and at-power conditions. The benchmark was setup primarily for the verification and validation of high-fidelity tools that have coupled neutron transport, thermal-hydraulics, and fuel isotopic depletion models. Public availability of such detailed data makes this a valuable tool for validating any in-core fuel management code package. This work presents the results of such validation effort undertaken with the CMS5 code package.

2. CASMO5 and SIMULATE5 Overview

CASMO5 is a two-dimensional characteristics-based neutron and gamma transport theory lattice physics code with depletion capability. CASMO5 generates cross sections and discontinuity factors for both square lattice BWR/PWR and hexagonal lattice, VVER, diffusion theory 3-D nodal core analysis. CASMO5 includes many advancements both in physics modeling and capabilities, including updated neutron data libraries containing more than one thousand unique nuclides and materials, extended depletion chains solved with Chebyshev Rational Approximation Method (CRAM), refined 586 energy-group structure, quadratic gadolinium depletion, Characteristics-based Dancoff, and enhanced geometry modeling. Ref. [1] presents the details of CASMO5

capabilities and features.

SIMULATE5 is a three-dimensional multi-group analytical nodal diffusion code for both square and hexagonal geometries. It solves either the diffusion or optionally SP3 equation, which may become important for MOX cores. It employs a hybrid macroscopic/microscopic depletion model that tracks approximately 60 isotopes per node. It was designed from its inception to handle heterogeneities of modern fuel assemblies, both in the radial and axial directions, by using on-the-fly axial homogenization and a radial sub-mesh model. The embedded fuel temperature calculation is part of the new detailed thermal/hydraulic module. Ref. [2] presents the details of SIMULATE5 features.

3. BEAVRS Benchmark Problem

The MIT BEAVRS benchmark provides a detailed core and fuel description of the initial two cycles of a 4-loop Westinghouse reactor:

Cycle 1 contains 3 different fuel types with respect to U-235 enrichment (1.6%, 2.4% and 3.1.%) and 5 different configurations of PYREX® boron glass BP (Burnable Poison/Absorber pins) loaded.

Cycle 2 contains 129 shuffled assemblies from EOC-1, two different fresh fuel types with respect to U-235 enrichment and three different configurations of PYREX® boron glass BP (Burnable Poison/Absorber pins). For all shuffled fuel from cycle 1, the PYREX® boron glass BP has been withdrawn in cycle 2.

4. CMS5 BEAVRS Core Model

The core model of the BEAVRS benchmark is set up with the conventional two-step procedure: using cross-sections generated from 2D CASMO5 calculations in 3D SIMULATE5 calculations.

4.1 CASMO5 Fuel and Reflector Models

CASMO5 2D single assembly calculations, either in octant or full assembly geometry, are set up for all axial variation of the fuel within the active length. The variations in the axial regions include fuel with and without Burnable Poison (BP) or control rod as well as guide tubes with different dimensions, generally referred to as “DASHPOT” and “No DASHPOT” regions. The spacers in the active fuel zone are modeled as an additional delta cross-section dependency, generated from CASMO5 branch calculations, and are included in the SIMULATE5 library.

The initial cycle of the BEAVRS core contains asymmetric fuel assemblies with 6 and 15 BP pins loaded on core edges to flatten the power distribution. The CMS5 model makes use of a new model for building asymmetric assemblies by extracting the quarter assembly nodal data, in the linking code level, from the solution of the full-assembly CASMO5 calculations. The new model better captures the radial heterogeneity of the fuel assembly, both in nodal cross-sections/assembly discontinuity factors and pin form factors, compared to conventional methods, which use either a full- or quarter-assembly transport calculation run with periodic boundary conditions.

The cross-section library for the top and bottom reflectors are generated from conventional one-dimensional fuel and reflector CASMO5 calculations. The top and bottom reflector geometries account for all material compositions within the first 35 cm above the top and below the bottom of active fuel. The improved radial reflector model is employed for this benchmark problem [5]: Nine position-dependent radial reflector segments are generated from a multi-assembly CASMO5 calculation, as depicted for an octant core in Fig. 1.

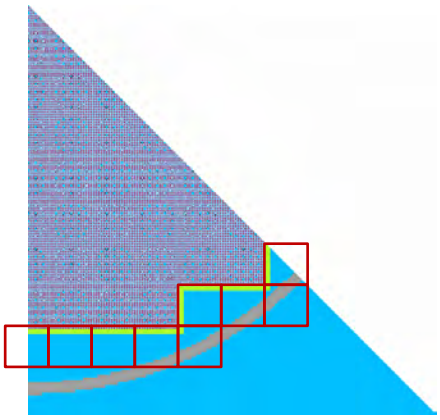

Fig. 1. CASMO5 multi-assembly geometry for generating position dependent radial reflector data.

CASMO5 calculations are performed using three different evaluated nuclear data libraries: ENDF/B-VII.1 (E7R1), ENDF/B-VIII.0 (E8R0) and JENDL-4.0 (J4). The E7R1 library is the default CASMO5 library. CASMO5 E8R0 library has been released recently in May 2019. The use of J4, Japanese Evaluated Neutron Data Library, is mostly limited to Japan.

All CASMO5 calculations are performed using the default calculational model options, using 19 energy groups in the 2D transport solution for fuel and 95 energy groups for reflector segments.

4.2 SIMULATE5 Core Model

SIMULATE5 core follow calculations are run in full core using 4 radial nodes per assembly and 24 uniformly spaced axial nodes. The diffusion calculations are performed in the default 4 energy groups. The sub-mesh model divides each quarter assembly into 5x5 sub-meshes. The microscopic depletion model tracks approximately 60 isotopes per node, and 5 actinides per sub-mesh, where the later captures intra-assembly burnup shape. The flux map evaluations are performed utilizing the benchmark provided, pre-processed (aligned and calibrated), measured reaction rate data files.

For the core follow calculations, the operating conditions are taken from the benchmark specification. The coolant inlet temperature of 560 K is assumed for the hot zero power calculations of both cycles.

5. Benchmark results

5.1 Zero-Power Physics Testing

The BEAVRS benchmark provides various zero-power physics test measurements: critical boron concentration, control rod bank worth, reactivity coefficients for cycle 1 and 2, and also one flux map taken in cycle 1 at 0.71% power, which is not included in this work. SIMULATE5 accuracy is presented in Table I.

Table I. Critical Boron Concentration at Zero Power

Rod Position	Meas. (ppm)	CMS5 - Measured		
		E7R1	E8R0	J4
Cycle 1				
ARO	975	-10	4	-4
D In	902	4	18	9
C, D In	810	1	14	7
A,B,C,D In	686	-7	4	-1
A,B,C,D,SE, SD,SC In	508	-15	-6	-9
Cycle 2				
ARO	1405	-9	-10	-7
C In	1273	26	25	29

The CMS5 critical boron concentration predictions for all rod configurations are in good agreement with the measurements. In Cycle 1 startup for all rods out (ARO) position, the CMS5 predictions are within 10 ppm against the measurement. In general, the E8R0 library gives slightly higher, 5-15 ppm, critical boron concentration compared to E7R1 and J4 libraries. The differences between the libraries disappear with Cycle 2 predictions where the maximum error is 10 ppm underprediction.

Table II shows the comparisons between SIMULATE5 control rod bank worth predictions and the measured values for a number of different bank configurations. The maximum error in Cycle 1 is approximately 8% encountered for the shutdown bank-SE. The E8R0 library results have slightly larger errors compared to the other two libraries. No inner or outer bank relation could be noted in the results presented.

Table II. Control Rod Bank Worth (pcm)

Rod Position	Rod Worth (pcm)	(1 - CMS5/Meas)%		
		E7R1	E8R0	J4
Cycle1				
D	788	-1.5	-1.9	-1.3
C	1203	0.9	1.5	0.6
B	1171	0.3	-0.2	1.6
A	548	3.2	6.0	1.8
SE	461	5.9	8.5	4.6
SD	772	0.6	0.5	0.6
SC	1099	-0.6	-1.0	-0.5
Cycle 2				
D	426	5.3	5.3	5.3
C	1014	-1.8	-2.2	-2.3
B	716	-7.0	-5.4	-5.6
A	420	-2.4	-4.5	-4.2
SE	438	-3.3	-4.3	-4.0
SD	305	6.2	7.3	7.3
SC	307	5.2	6.4	6.4
SB	781	-2.0	-1.6	-1.6
SA	326	3.0	4.7	4.7
Total	4733	5.3	5.3	5.3

Isothermal temperature coefficient (pcm/°F) predictions are given in Table III. The ITC predictions in both cycles are in excellent agreement vs the measurement. Note that the cycle 2 measured ITC is corrected to +1.71 pcm/°F [6], not -1.71 pcm/°F as reported in Ref. [4]. This would be corrected in newer revisions of the benchmark specification.

Table III. Isothermal Temperature Coefficient (pcm/°F)

Rod Position	ITC pcm/°F	CMS5-Measured		
		E7R1	E8R0	J4
Cycle 1				
ARO	-1.75	-0.43	0.01	-0.35
D In	-2.75	-0.63	-0.17	-0.55
C, D In	-8.01	-0.03	0.44	0.05
Cycle 2				
ARO	1.71	0.20	0.30	0.05

5.2 Hot Full Power (HFP) Boron Predictions

The core follow calculations are performed with a condensed number of state points compared to the operational logs provided in the benchmark. Sufficient detail is included such that the operating history (power, inlet temperature and control rod bank position) is accurately represented. The condensed Cycle 1 and Cycle 2 depletion decks contain 66 and 45 state points, respectively. Figures 2 and 3 present the measured and CMS5 predicted critical boron concentrations. The CMS5 predictions with different libraries are indistinguishable in these plots.

Except the initial 150 EFPD of Cycle 1, the CMS5 reactivity predictions are in good agreement vs the plant measurement. There is a notable difference (Calc - Meas) of around -33 ppm initially in the cycle (from around 25-125 EFPD). This coincides with a period of operation rarely at full power. One possible explanation for the difference is that the measured boron concertation was adjusted to nominal 100% power and ARO condition, as this is a common practice in some utilities. Unfortunately, no direct information on the conditions of these measurements is found in Ref [4].

In the exposure interval from 50-300 EFPD, comparing calculated boron with CMS5 E7R1 library versus the measured boron gives an average bias of -20 ppm. At the end of the cycle, the agreement is good and has an average difference of -16 ppm. In Cycle 2, the average bias between CMS5 E7R1 model prediction and the measurement is 22 ppm.

In general, all three nuclear data libraries yield similar reactivity and critical boron predictions at power. The higher reactivity observed with the E8R0 library at Cycle 1 startup quickly burns out after the first 100 EFPD operation. Overall, compared to the E7R1 library, the E8R0 library results in 3 and 6 ppm lower boron in Cycles

1 and 2 respectively; and the J4 library results in 6 ppm lower boron for the same cycles.

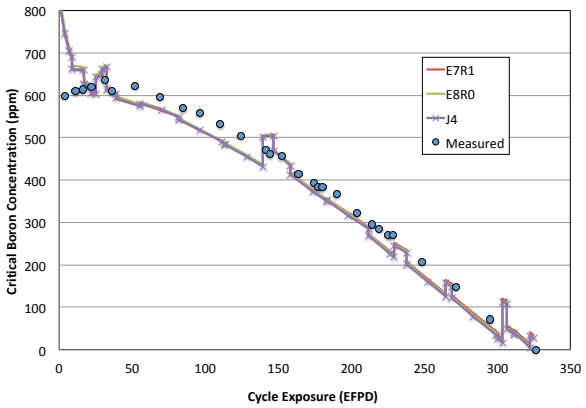

Fig. 2. Cycle 1 core follow boron.

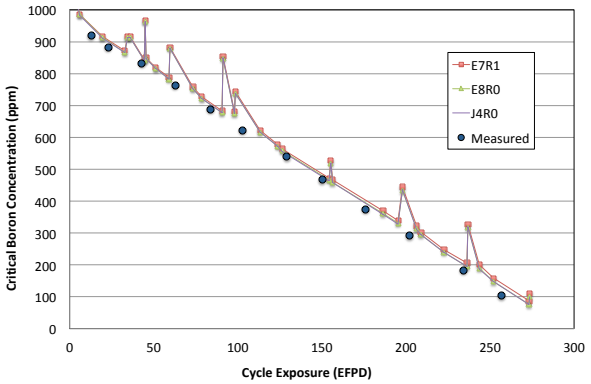

Fig. 3. Cycle 2 core follow boron.

5.3 Flux Map Comparisons

The 2D assembly and 3D nodal comparisons of the pre-processed measured and calculated detector reaction rates at the measured assembly locations are given in Fig.4 for Cycles 1 and 2 with the E7R1 model. The Cycle 1 flux map at low power on Day 7 (at 4% power) is excluded from comparisons. The results presented include all flux maps taken at low power as well as at hot full power. Table IV presents the flux map statistics, with three nuclear data libraries, for all flux maps and those taken above 95% power, separately.

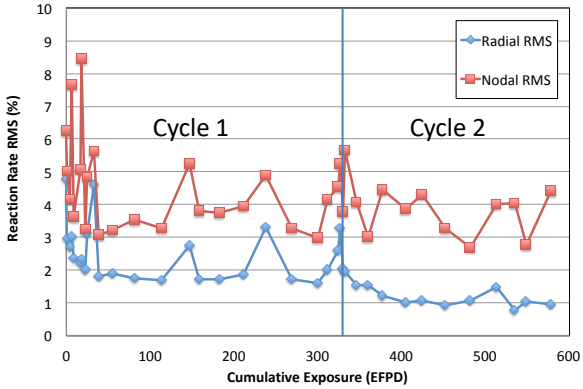

Fig. 4. Flux map assembly and nodal RMS with the E7R1 library.

Table IV. Flux Map Statistical Summary

Power	# of Maps	Assembly RMS (%)			Nodal RMS (%)		
		E7R1	E8R0	J4	E7R1	E8R0	J4
Cycle 1							
All	23	2.46	2.66	2.42	4.51	4.65	4.49
>95%	11	2.02	2.17	1.99	3.69	3.77	3.69
Cycle 2							
All	14	1.42	1.42	1.46	3.97	3.98	4.00
>95%	11	1.19	1.18	1.24	3.96	3.96	4.00

The noted RMS values, combined for 22 flux maps with power > 95%, show excellent predictions with the 2D radial below 2.1% and the 3D nodal below 4.0% for HFP conditions. The flux map statistics in general are insensitive (less than 0.2% difference) to the choice of the nuclear data library.

6. Conclusions

The MIT BEAVRS benchmark is evaluated with Studsvik's CMS5 code package using three different nuclear data libraries. The CMS5 calculated core parameters at zero and full power are in good agreement with the plant measurements: The boron predictions are within 30 ppm at zero power and less than 20 ppm at hot full power condition; the control rod worth is predicted with 0.7 ± 3.8% accuracy; the radial and nodal reaction rate distributions are predicted with a mean difference of about 1.6% and 3.8%, respectively. No significant difference is observed in predicting measured plant parameters with different nuclear data libraries.

Acknowledgment

The authors acknowledge the former Studsvik employee Magnus Kruners for his work constructing the initial BEAVRS core model with CMS5.

References

1. J. Rhodes, K. Smith and D. Lee, "CASMO5 Development and Applications," *Proc. in PHYSOR 2006*, Vancouver (2006).
2. T. Bahadir and S.-Ö. Lindahl, "Studsvik's Next Generation Nodal Code SIMULATE5," *Proc. in Advances in Nuclear Fuel Management IV*, Hilton Head Island, South Carolina, USA (2009).
3. B. Haugh, "Generic Application of the Studsvik Scandpower Core Management System to Pressurized Water Reactors," Studsvik Scandpower, Inc., SSP-14/P01-028-TR-NP-A (2017).
4. N. Horelik and B. Herman, "MIT Benchmark for Evaluation and Validation of Reactor Simulations (BEAVRS)", MIT Computational Reactor Physics Group, Rev. 2.0.2. (2018).
5. T. Bahadir, "Improved PWR Radial Reflector Modeling with SIMULATE5," *Proc. in Advances in Nuclear Fuel Management V*, Hilton Head Island, South Carolina, USA (2015)..
6. K. Smith, Personal e-mail communication, Sept 10, 2019.

Proceedings of the Reactor Physics Asia 2019 (RPHA19) Conference
Osaka, Japan, Dec. 2-3, 2019

An Improved Chebyshev Rational Approximation Method Base on Order Reduction of Krylov Subspace Method

Yuying HU[a], Qi LUO[b*], Dong YAO[a], Yingrui Yu[a], Hongkuan LIAO[a], Bingyan Zhou[a]
[a]*Science and Technology on Reactor System Design Technology Laboratory, Nuclear Power Institute of China, Chengdu, China*
[b]*Nuclear Power Institute of China, Chengdu, China*
[*]Corresponding author: 18200315798@sina.cn

Abstract

Burnup is an important part of physical calculation in reactors. The accuracy of results deeply influences critical physical characteristics of reactor such as the cycle length, reactivity and power distribution. Algorithm of solving burnup equations directly relates to the accuracy and efficiency of burnup calculation. In this study, an improved Chebyshev Rational Approximation Method, Combined algorithm, has been used to solve burnup equations. According to verification and analysis, comparing to CRAM, Combined algorithm has higher efficiency in large matrices. For the little burnup benchmark, the relative error could reach to 10^{-5}, worse than CRAM in calculation accuracy, but it basically meets the calculation requirements.

Key Words: **Burnup calculation, Combined algorithm, Improved CRAM, Benchmark verification**

1. Introduction

With the development of computer science and the improvement of nuclear technology, physical calculation of high accuracy and efficiency in reactors becomes more and more important. Using one-step method to complete physical design in cores becomes a trend. Thus, burnup algorithm needs to be improved. Nowadays, major methods to solve burnup equations contain Taylor series expansion, Chebyshev Rational Approximation Method (CRAM), Transmutation Trajectory Analysis (TTA) and others.

There are thousands of nuclides in the database, and the lives and cross section of nuclides differ greatly. Thus, compressed database has been used to improve calculation efficiency. The main idea of Krylov Subspace method is reducing the order of matrices to improve calculation efficiency[6]. The biggest character of CRAM is the computational stability[7]. Besides, results can always be carried out with CRAM even if the matrix is ill-conditioned. In this study, the idea of order reduction in Krylov Subspace has been used before solve burnup equations through CRAM, so that it improves the calculation efficiency while keeping the accuracy on an acceptable level.

2. Combined Algorithm

2.1 Order reduction in Krylov Subspace Method

In this method[1], the vector norm $\|\boldsymbol{N}\|_2$ was gained from initial nuclides density $\boldsymbol{N}$, and the first orthonormal basis $\boldsymbol{v}_1$ was built. According $\boldsymbol{v}_1$ and burnup matrix $\boldsymbol{A}_{n\times n}$, orthonormal basis matrix $\boldsymbol{V}=[\boldsymbol{v}_1,\boldsymbol{v}_2,\cdots,\boldsymbol{v}_m]$ could be built. With matrix $\boldsymbol{V}$ and $\boldsymbol{A}_{n\times n}$, matrix $\boldsymbol{H}_{m\times m}$ of reduced order could be gained. Thus, the initial exponential matrix calculation $\boldsymbol{N}e^{\boldsymbol{At}}$ has been changed to calculate $\|\boldsymbol{N}\|_2\boldsymbol{V}_m e^{-\boldsymbol{H}_m}e_1$, reaching the goal of reducing matrix scale and improving efficiency.

Re-orthogonalization Arnoldi method is used to generate the matrix of reduced-order, and orthonormal basis matrix $\boldsymbol{V}$ is generated by modified Gram-Schmidt orthogonalization algorithm. The details are shown as below.

(1) Calculating vector norm $\|\boldsymbol{N}\|_2$ according initial nuclides density $\boldsymbol{N}$;

(2) $\boldsymbol{v}_1=\boldsymbol{N}/\|\boldsymbol{N}\|_2$, $\boldsymbol{V}_{\mathrm{i},1}=\boldsymbol{v}_1$;

(3) Gaining orthonormal basis matrix $\boldsymbol{V}$:

for $j=1:m$
  $\boldsymbol{v}_{\mathrm{j}}[\mathrm{k}]=\boldsymbol{V}_{\mathrm{k,j}}$
  $\boldsymbol{w}=\boldsymbol{A}\times\boldsymbol{v}_{\mathrm{j}}$
  for $i=1:j$
    $\boldsymbol{v}_{\mathrm{i}}[\mathrm{k}]=\boldsymbol{V}_{\mathrm{k,i}}$

$\boldsymbol{Ht}_{\mathrm{i,j}} = \mathbf{w} \times \boldsymbol{v}_{\mathrm{i}}$
$\boldsymbol{w} = \boldsymbol{w} - \boldsymbol{Ht}_{\mathrm{i,j}} \times \boldsymbol{v}_{\mathrm{i}}$
end
for $i = 1{:}\,j$
$\mathrm{s} = \boldsymbol{w} \times \boldsymbol{v}_{\mathrm{i}}$
$\boldsymbol{w} = \boldsymbol{w} - \mathrm{s} \times \boldsymbol{v}_{\mathrm{i}}$
end
$\boldsymbol{V}_{\mathrm{k,j+1}} = \boldsymbol{w}_{\mathrm{k}} / \|\boldsymbol{w}\|_2$
end

(4) $\boldsymbol{H}_{\mathrm{m\times m}} = \boldsymbol{V}^{\mathrm{T}} \times \boldsymbol{Ht} \times \boldsymbol{V}$.

Through this method, original nth order matrix A has been translated to mth order matrix H. In the verification later, $\mathrm{m} = \mathrm{n}/4$.

2.2 Solve equations by Chebyshev Rational Approximation Method

After reducing burnup matrix order with Krylov subspace, new exponential matrix would be solved by CRAM[4], shown as follows.

$$\boldsymbol{N}_n = \alpha_0 \boldsymbol{N}_0 + 2\mathrm{Re}\left[\sum_{\mathrm{j}=1}^{\mathrm{k}/2} \alpha_{\mathrm{j}} (\boldsymbol{H}\mathrm{t} - \theta_{\mathrm{j}}\mathrm{I})^{-1}\right] \boldsymbol{N}_0 \qquad (1)$$

k is the order of CRAM, and the convergence accuracy of CRAM is $9.3^{-\mathrm{k}}$, calculation time increasing with k enlarging. α and θ are given parameters, depending on the calculation order. In the verification later, $\mathrm{k} = 16$.

3. Verification Analysis

The advantage of Krylov subspace method is improving efficiency through reducing matrix order. Efficiency of exponential matrix calculation could be held on a high level by using CRAM when calculating ill-conditioned matrix. Combined Algorithm combines the advantages of two methods to improve calculation efficiency with high accuracy. In this study, large scale matrices and IAEA little burnup benchmark has been verified.

3.1 Verification of large scale matrices

Compared with Krylov Subspace Method and CRAM, Combined Algorithm has better behavior in efficiency of large scale matrices calculation. In this study, different orders of matrices are generated with Matlab code[5], and verification has been done with these three methods.

Matrices orders range from 50~1500th. When using Krylov Subspace Method and Combined Algorithm, there is 1-substep, 5-substeps, 10-substeps and 20-substeps calculation in a single burnup step. Taylor Series Expansion was used to calculate matrix exponential in Krylov Subspace Method. The results are shown as below.

When calculating random matrices, the relative error of CRAM is about 10^{-12} and the same with Combined Algorithm, while the relative error of Krylov Subspace Method being 10^{-15}. However, when calculating ill-conditioned matrices such as Hilbert matrix, the accuracy of Krylov Subspace Method is quite low, and the max relative error reaches to 13%. As for CRAM, the relative error is still 10^{-12}, with 10^{-11} of Combined Algorithm. These two methods remain a level of high accuracy.

From Fig. 1, Combined Algorithm has high efficiency than Krylov Subspace Method when calculating in the same sub-steps. Compared with CRAM, Combined Algorithm behaves better with high order matrices even 20-substeps calculation.

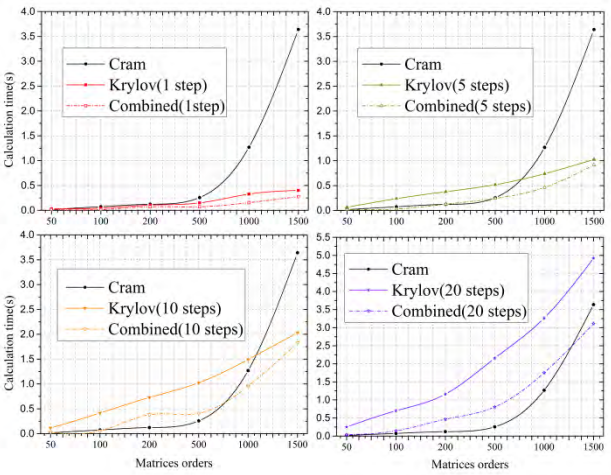

Fig. 1 Calculation time of random matrices

3.2 Verification of IAEA benchmark

In the burnup chains of this benchmark[3], there are 34 nuclides containing neutron capture, decay and generation of some important fission products. The burnup chains are shown in Fig. 2 Burnup time is 50 days, the initial density of ^{235}U and ^{238}U are 7.4003×10^{-5} g-atom and 6.9360×10^{-3} g-atom. The results are shown in Table I. The calculation results of TTA[2] have been used as reference value because there is no annular closed burnup chain.

From Table I, when the number of sub-steps is small, the accuracy of Combined Algorithm is not very high. However, the accuracy of 20-substeps calculation could reach to 10^{-3}, while 50-substeps reaching to 10^{-6}.

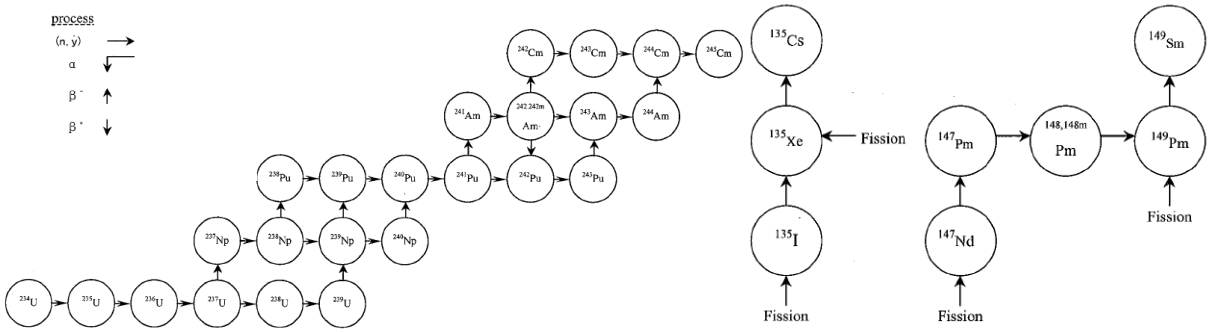

Fig. 2 Burnup chains of IAEA benchmark

4. Conclusions

According to the verification of large scale random matrices and IAEA benchmark, Combined Algorithm has higher efficiency than CRAM because of reducing orders before solve burnup equations. Some information is lost due to reducing the matrix order, so calculation accuracy of Combined Algorithm is lower than CRAM. However, calculation accuracy could be improved by choosing suitable burnup step. In the further work, algorithm optimization would become a key point, and accuracy of burnup could be improved by matrix reconstruction and other methods.

Reference

1. Cleve M., "Nineteen Dubious Way to Compute the Exponential of a Matrix, Twenty-five Years Later," *Society for Industrial and Applied Mathematics Review*, 45, 1 (2003).
2. Jerzy C, "General solution of Bateman equations for nuclear transmutations," *Annals of Nuclear Energy*, 33 (2006).
3. M. G, "Neutronic Depletion Benchmark Problems," *Trans. Am. Nucl. Soc,* 23 (1976).
4. Pusa M., "Rational Approximations to the Matrix Exponential in Burnup Calculations," *Nuclear Science and Engineering*, 169, 2 (2011).
5. Z Z, "Mastering MATLAB R2011a," Beijing University of Aeronautics and Astronautics Press, Beijing(2011).
6. Akio Y, Masahiro T, Naoki S. "Numerical Solution of Stiff Burnup Equation with Short Half Lived Nuclides by the Krylov Subspace Method," *Journal of Nuclear Science and Technology*, 44, 2(2007).
7. Songqian T, Feng X, Yi T, Shuping W. "Analysis of Complex Nuclide Chain Equation Calculation Based on Different Method," *Nuclear Power Engineering*, 37, 1(2016).

Table I. Results of CRAM and Combined Algorithm

nuclide	TTA g-atom	CRAM g-atom	Relative error	Combined(20) g-atom	Relative error	Combined(50) g-atom	Relative error
^{234}U	0	0	0	0	0	0	0
^{235}U	5.833942×10^{-5}	5.833939×10^{-5}	-5.77×10^{-7}	5.833882×10^{-5}	-1.02×10^{-5}	5.833942×10^{-5}	-4.41×10^{-10}
^{236}U	2.860583×10^{-6}	2.860583×10^{-6}	-1.58×10^{-7}	2.860563×10^{-6}	-6.93×10^{-6}	2.860583×10^{-6}	1.88×10^{-9}
^{237}U	2.061026×10^{-8}	2.061026×10^{-8}	-1.01×10^{-7}	2.061034×10^{-8}	3.92×10^{-6}	2.061026×10^{-8}	3.05×10^{-9}
^{238}U	6.919236×10^{-3}	6.919233×10^{-3}	-4.88×10^{-7}	6.919169×10^{-3}	-9.75×10^{-6}	6.919236×10^{-3}	-1.56×10^{-10}
^{239}U	7.183703×10^{-9}	7.183700×10^{-9}	-4.88×10^{-7}	7.183617×10^{-9}	-1.20×10^{-5}	7.183703×10^{-9}	-1.96×10^{-10}
^{237}Np	4.508447×10^{-8}	4.508447×10^{-8}	-1.57×10^{-8}	4.508197×10^{-8}	-5.55×10^{-5}	4.508447×10^{-8}	-3.89×10^{-8}
^{238}Np	3.248943×10^{-10}	3.248943×10^{-10}	-6.01×10^{-9}	3.248732×10^{-10}	-6.50×10^{-5}	3.248943×10^{-10}	-4.51×10^{-8}
^{239}Np	1.029451×10^{-6}	1.029451×10^{-6}	-4.56×10^{-7}	1.029441×10^{-6}	-9.80×10^{-6}	1.029451×10^{-6}	-2.30×10^{-10}
^{240}Np	1.322940×10^{-11}	1.322940×10^{-11}	-4.56×10^{-7}	1.326491×10^{-11}	2.68×10^{-3}	1.322940×10^{-11}	-4.12×10^{-9}
^{238}Pu	1.472831×10^{-9}	1.472831×10^{-9}	3.08×10^{-8}	1.471592×10^{-9}	-8.41×10^{-4}	1.472831×10^{-9}	-5.83×10^{-7}
^{239}Pu	1.057469×10^{-5}	1.057469×10^{-5}	-1.49×10^{-7}	1.057456×10^{-5}	-1.18×10^{-5}	1.057469×10^{-5}	5.57×10^{-10}
^{240}Pu	9.959276×10^{-7}	9.959276×10^{-7}	-5.41×10^{-8}	9.959928×10^{-7}	6.54×10^{-5}	9.959277×10^{-7}	3.10×10^{-8}
^{241}Pu	3.342055×10^{-7}	3.342055×10^{-7}	8.61×10^{-10}	3.341756×10^{-7}	-8.93×10^{-5}	3.342055×10^{-7}	-2.83×10^{-8}
^{242}Pu	1.636514×10^{-8}	1.636514×10^{-8}	3.48×10^{-8}	1.634770×10^{-8}	-1.07×10^{-3}	1.636512×10^{-8}	-7.34×10^{-7}
^{243}Pu	1.362797×10^{-11}	1.362797×10^{-11}	3.56×10^{-8}	1.289188×10^{-11}	-5.40×10^{-2}	1.362796×10^{-11}	-7.50×10^{-7}
^{241}Am	5.864330×10^{-10}	5.864330×10^{-10}	3.34×10^{-8}	5.859058×10^{-10}	-8.99×10^{-4}	5.864327×10^{-10}	-5.72×10^{-7}
^{242}Am	6.172483×10^{-12}	6.172483×10^{-12}	3.52×10^{-8}	6.166452×10^{-12}	-9.77×10^{-4}	6.172479×10^{-12}	-6.25×10^{-7}
^{242m}Am	5.048715×10^{-12}	5.048715×10^{-12}	5.05×10^{-8}	5.038860×10^{-12}	-1.95×10^{-3}	5.048708×10^{-12}	-1.42×10^{-6}
^{243}Am	4.568499×10^{-10}	4.568500×10^{-10}	5.78×10^{-8}	4.561127×10^{-10}	-1.61×10^{-3}	4.568486×10^{-10}	-2.85×10^{-6}
^{244}Am	6.377320×10^{-14}	6.377321×10^{-14}	5.31×10^{-8}	6.238801×10^{-14}	-2.17×10^{-2}	6.377297×10^{-14}	-3.58×10^{-6}
^{242}Cm	5.499801×10^{-11}	5.499801×10^{-11}	4.99×10^{-8}	5.481788×10^{-11}	-3.28×10^{-3}	5.499785×10^{-11}	-2.92×10^{-6}
^{243}Cm	1.153872×10^{-13}	1.153871×10^{-13}	-2.30×10^{-7}	1.146019×10^{-13}	-6.81×10^{-3}	1.153863×10^{-13}	-7.75×10^{-6}
^{244}Cm	2.068299×10^{-11}	2.068299×10^{-11}	5.47×10^{-8}	2.053931×10^{-11}	-6.95×10^{-3}	2.068283×10^{-11}	-7.69×10^{-6}
^{245}Cm	2.434189×10^{-13}	2.434188×10^{-13}	-3.04×10^{-7}	2.405039×10^{-13}	-1.20×10^{-2}	2.434152×10^{-13}	-1.50×10^{-5}
^{135}I	8.827566×10^{-9}	8.827563×10^{-9}	-4.23×10^{-7}	8.824156×10^{-9}	-3.86×10^{-4}	8.827566×10^{-9}	-3.94×10^{-10}
^{135}Xe	9.147625×10^{-10}	9.147621×10^{-10}	-4.24×10^{-7}	9.144409×10^{-10}	-3.52×10^{-4}	9.147625×10^{-10}	-4.48×10^{-10}
^{147}Nd	1.211571×10^{-7}	1.211571×10^{-7}	-2.84×10^{-7}	1.211490×10^{-7}	-6.72×10^{-5}	1.211571×10^{-7}	-1.16×10^{-8}
^{147}Pm	2.018147×10^{-7}	2.018146×10^{-7}	-9.31×10^{-8}	2.018217×10^{-7}	3.48×10^{-5}	2.018147×10^{-7}	1.10×10^{-8}
^{148}Pm	4.570362×10^{-9}	4.570362×10^{-9}	-7.32×10^{-8}	4.570592×10^{-9}	5.03×10^{-5}	4.570363×10^{-9}	1.43×10^{-8}
^{148m}Pm	3.867448×10^{-9}	3.867448×10^{-9}	-7.42×10^{-8}	3.867638×10^{-9}	4.92×10^{-5}	3.867448×10^{-9}	1.41×10^{-8}
^{149}Pm	1.996828×10^{-8}	1.996827×10^{-8}	-3.08×10^{-7}	1.996855×10^{-8}	1.39×10^{-5}	1.996828×10^{-8}	5.46×10^{-9}
^{149}Sm	1.197771×10^{-8}	1.197770×10^{-8}	-2.92×10^{-7}	1.197792×10^{-8}	1.78×10^{-5}	1.197771×10^{-8}	6.23×10^{-9}
FP	1.452279×10^{-5}	1.452279×10^{-5}	-1.39×10^{-7}	1.452262×10^{-5}	-1.14×10^{-5}	1.452279×10^{-5}	-2.73×10^{-9}

Proceedings of the Reactor Physics Asia 2019 (RPHA19) Conference
Osaka, Japan, Dec. 2-3, 2019

Improvement of Optimally-Weighted Predictor-Corrector Method for Nuclear Fuel Burnup Calculations

Jumpei Sasuga[a,*], Go Chiba[a], Yasunori Ohoka[b], Kento Yamamoto[b] and Hiroaki Nagano[b]
[a]*Hokkaido University, Kita 13 Nishi 8, Sapporo, Hokkaido, Japan*
[b]*Nuclear Fuel Industries, Ltd., 950 Asashiro-Nishi 1-chome Kumatori-cho, Sennan-gun, Osaka, Japan*
[*]Corresponding author: qazxcvbnm@eis.hokudai.ac.jp

Abstract

A new algorithm to determine a proper weight in the optimally-weighted predictor-corrector (OWPC) method is proposed. This concept is based on problem simplification in which the proper weight can be easily obtained. Verification calculations are performed for three different PWR fuel assemblies including burnable absorber. The new OWPC method shows better performance than the original PC method and the projected PC method.

Key Words: **burnup calculation, burnable poison, predictor-corrector method**

1. Introduction

Generally, fuel assemblies of Light Water Reactors (LWRs) contain burnable absorbers such as gadolinium (Gd). Since impact of this burnable absorber on reactor physics property drastically changes even during small time period, accurate numerical scheme for time discretization is required. The predictor-corrector (PC) method [1] has been well known as one of the accurate schemes, but further improvement of the numerical scheme has been attempted and proposed by many researchers so far [2-4]. Okumura and Chiba have proposed improved methods based on the PC method: a Weighted Predictor-Corrector (WPC) method which introduces weight to the PC method and an Optimally-Weighted Predictor-Corrector (OWPC) method which introduces an algorithm to obtain proper weight automatically in WPC [5]. During our recent works, however, we have found that the original OWPC method does not work well in certain conditions. In addition, there still be a free parameter which should be determined by users in the original OWPC method. Under these circumstances, we propose a new OWPC method which does not contain any users-defining parameters and is applicable for various condition.

2. Theory

First, let us consider the original PC method. We use the PC method in burnup calculations for neutron absorbing nuclides. In the PC method, we calculate number density (ND) at the end of time step N_p using the reaction rate at the beginning of time step R_p. This procedure is called *a predictor calculation*. Next, we obtain the reaction rate at the end of time step R_c from N_p. Then, using R_c, we again calculate ND at the end of the step, and it is denoted to as N_c. This is referred to as a *corrector calculation*. With those two NDs, N_p and N_c, we finally calculate ND at the end of time step N as follows:

$$N = \frac{N_p + N_c}{2}. \tag{1}$$

We have another choise to calculate N as follows [5]:

$$N = \exp\left(\frac{\ln N_p + \ln N_c}{2}\right). \tag{2}$$

This is based on simple averaging of reaction rate and linear dependence of reaction rate with time is implicitly assumed in this definition.

In case of calculation for ND of neutron absorbers, there is a systematic error when we use the PC method since the following two approximations are introduced in the PC method.

One is the approximation about reaction rates in the corrector calculation R_c. This is calculated from N_p, but this is not the true value of ND at the end of time step. This ND, N_p, is calculated from the predictor calculations in which reaction rates are assumed constant during the time step. Reaction rate of neutron absorbing materials should increase during time step because of neutron energy spectrum softening, so ND at the end of time step should be smaller than N_p and reaction rate at the end of time step should be larger than R_c.

Another one is the approximation introduced at the final step in the procedure. As mentioned above, averaging of final ND using Eq. (2) is based on the assumption that neutron absorber reaction rate changes linearly with time.

In order to improve accuracy of the PC method,

Okumura and Chiba have proposed new advanced methods based on the original PC method: the WPC and OWPC methods [5]. Instead of Eq. (2), the following equation is used in the WPC method:

$$N = \exp\{(1-\omega)\ln N_p + \omega \ln N_c\}. \quad (3)$$

We introduce a weight ω to obtain more accurate ND at the end of time step than the PC method. In the original OWPC method, an algorithm to determine ω has been proposed, but recently we have found that it does not work well in certain conditions, so we propose a new algorithm to determine ω for the OWPC method as follows.

Let us consider that ND of neutron absorbing materials such as Gd-155 and -157 changes mainly due to absorbing neutrons. In our study, we use the following simplified model. This model assumes that ND of these neutron absorbing nuclides changes as the following simple differential equation:

$$\frac{dN(t)}{dt} = -R(t)N(t). \quad (4)$$

It means that ND of this nuclide decreases by only neutron absorption. Yamamoto has numerically presented that reaction rate of Gd-155 and -157 decrease linearly with ND of themselves [3]. Since we calculate N_p and R_c during the procedure of the PC method, we can determine $\frac{dR}{dN}$ from (N_0, R_p) and (N_p, R_c) where N_0 is the ND at the beginning of time step. By assuming a linear dependence of R on N, we can easily obtain accurate numerical result of ND at the end of time step, N_r, in this simple model represented by Eq. (4) with fine time mesh divisions. From N_r, we can obtain corresponding reaction rate R_r as follows:

$$N_r = N_0 \exp(-R_r \Delta t). \quad (5)$$

At the same time, calculation based on the PC method is carried out in the same simple model, and the reaction rate $\tilde{R}_c$ is calculated. Using R_r, R_p and $\tilde{R}_c$, a proper weight ω for the OWPC method can be defined as

$$\omega = \frac{(R_r - R_p)}{(\tilde{R}_c - R_p)}. \quad (6)$$

Using this ω, we can obtain ND at end of the time step in the original problem from Eq. (3). In the present paper, this method is referred to as the OWPC method.

Note that the concept of this new OWPC method is quite similar to the quadratic depletion model proposed by Lee. [4]

3. Test Problems and Numerical Procedure

3.1 Brief description of numerical methods of CBZ

All the calculations are carried out with a module named MulticellBurner in a deterministic reactor physics code system CBZ which is under development at Hokkaido University. 107-group self-shielded cross sections are calculated based on the advanced Bondarenko model from a 107-group CBZLIB generated from JENDL-4.0 [6]. Lattice effect is taken into account by the Dancoff factor method. Neutron transport equation of multicell problems is solved by a module MEC based on the method of characteristics. Scattering anisotropy is taken into account by the P0 transport approximation. With neutron flux and self-shielded cross sections, fuel burnup calculations are carried out. A simplified burnup chain consisting of 138 fission products is used and burnup equation is solved by the matrix exponential method. The matrix exponential is numerically calculated by the mini-max polynomial approximation method. This nuclear fuel burnup calculation capability of CBZ has been well verified in the previous work [5].

3.2 Test problem

Numerical calculations are curried out for three PWR fuel assemblies. One of them is shown in Fig.1 called as the Okumura problem [5] in the present paper. This contains burnable poison rods composed of 9.6 wt% Gd_2O_3 and UO_2 whose uranium-235 enrichment is 2.6 wt%. Geometrical configuration of this burnable poison rod is same as that of the UO_2 rod. In addition, 25 guide tubes, in which water is filled inside of cladding whose inner and outer radii are 0.569 cm and 0.61 cm, are also located. Total thermal power of 5.75523×10^{-2} MW per unit height in cm is assumed. Temperature of fuel, cladding and moderator are 900, 600, 591 K, respectably. The other two PWR fuel assemblies are the 2O and 2P problems in the VERA depletion benchmark model [7]. Gadolinium concentration of a gadolinium pins in these assemblies is 5 wt%.

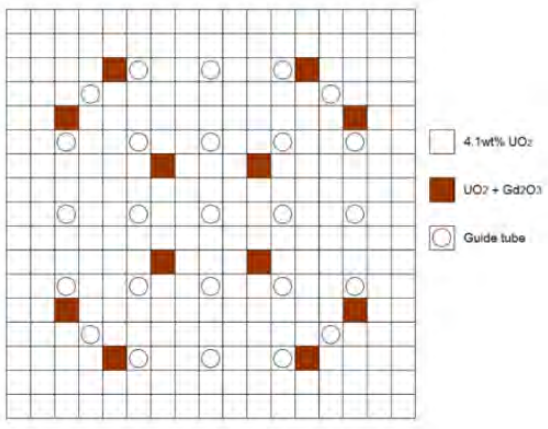

Fig. 1. Geometric configuration of the Okumura problem

We compare infinite neutron multiplication factor k_{inf} to test our method. References of k_{inf} are calculated using the conventional PC method with 0.055 GWd/t burnup

step. The PC method is generally considered effective during Gd depletion, so we adopt our proposed method only in the condition of $\frac{N_0-N_p}{N_0} > 0.01$.

3.3 Numerical procedure

We calculate ND by the OWPC method as the following:

1. Carry out a one-step burnup calculation with the original PC method and obtain the parameters about nuclide i (i=155,157): N_0^i, R_p^i, N_p^i and R_c^i.

2. We assume relation between microscopic absorbing reaction rate and ND of themselves linearly in each time step and $\frac{dR^i}{dN^i}$ is obtained as follows:

$$\frac{dR^i}{dN^i} = \frac{R_p^i - R_c^i}{N_0^i - N_p^i}. \quad (7)$$

3. With the parameters, N_0^i, R_p^i, $\frac{dR^i}{dN^i}$ and Δt, a simplified model presented as Eq. (4) is prepared and N_r^i is numerically calculated. In addition, we calculate $\tilde{R}_c^i$ in the simplified model also.

4. From Eq. (6), a proper weight ω is calculated, and then N^i is obtained from Eq. (3).

4. Numerical Results

Differences in k_{inf} obtained by the PC method and the OWPC method against the references are shown in Figs. 2 to 4. The OWPC method shows better performance than the original PC method and Projected Predictor-Corrector method (PPC method) whose time step width is equal to that of the OWPC method. The PPC method modifies reaction rate at the end of time step. However, the other approximation remains in the PPC method. On the other hand, our OWPC method does not introduce these approximations. Therefore, the PPC method performs better than the PC method but inferior to the OWPC method. Notably, the OWPC method shows good performance in the 2O and 2P fuel assemblies. Gadolinium concentration of these two assemblies is less than that of the Okumura problem. When the large amount of Gd is included, thermal neutron absorption is enhanced, and neutron flux energy spectrum becomes hard. In such cases, contributions of other reaction except the thermal neutron absorption become large. In the OWPC method, we assume that ND of Gd changes mainly due to neutron absorption. That is why the OWPC method shows poor performance in the Okumura problem in comparison with the 2O and 2P fuel assemblies.

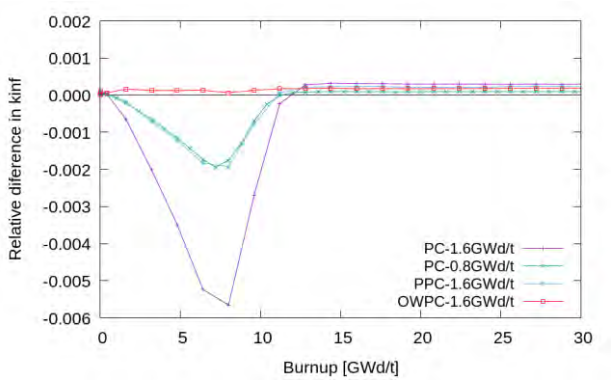

Fig. 2. Errors of k_{inf} in the VERA/2O problem

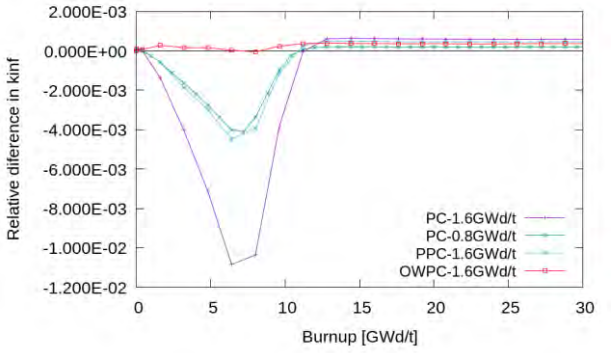

Fig. 3. Errors of k_{inf} in the VERA/2P problem

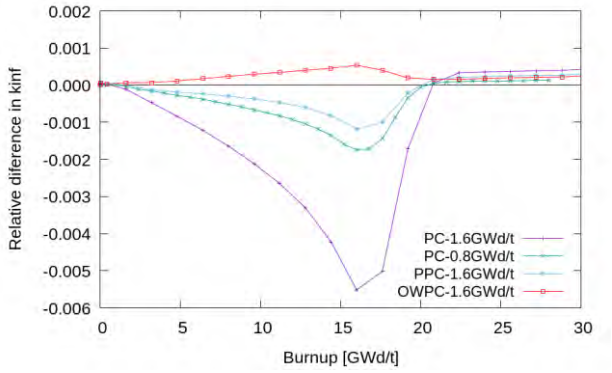

Fig. 4. Errors of k_{inf} in the Okumura problem

We assume that the microscopic reaction rate is proportional to the ND for each isotope: Gd-155 reaction rate with ND of Gd-155 and Gd-157 reaction rate with ND of Gd-157. This is because ND of Gd influences neutron spectrum. Since neutron absorbing cross section of Gd-157 is larger than that of Gd-155, Gd-157 burns out earlier than Gd-155. A comparison of macroscopic absorption reaction rates is shown in Fig. 5. This figure suggests that Gd-155 absorption becomes dominant after the burnout of Gd-157. Therefore, we should use correlation between microscopic reaction rate of Gd-157 and ND of Gd-155 in such situations. Based on this observation, we can say that during the period when Gd-155 absorption is dominant, we should use correlation

between ND of Gd-155 and microscopic reaction rate of Gd-157. We judge a timing when the isotope which burn up mainly changes by comparing depletion quantity of these two isotopes. In the case that ND of Gd-157 decreases more than that of Gd-155, we use original correlation of the OWPC method. On the other hand, in the case that Gd-155 decreases more than Gd-157, instead of $\frac{dR^{157}}{dN^{157}}$, we use the correlation as follows:

$$\frac{dR^{157}}{dN^{155}} = \frac{R_p^{157} - R_c^{157}}{N_0^{155} - N_p^{155}}. \quad (9)$$

We call this method in which we change correlation as an OWPC-MIX method.

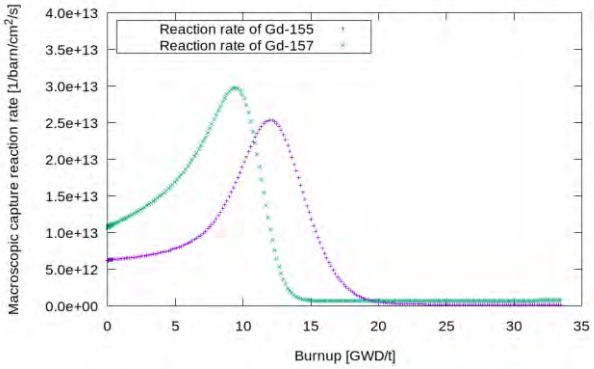

Fig. 5. Macroscopic reaction rates of gadolinium isotopes

Result of the OWPC-MIX method in the VERA/2O problem is shown in Fig. 6. Using the OWPC-MIX method, the calculation accuracy is not affected, and similar results are obtained in the other two assemblies. The isotope effect of the correlation between ND and reaction rate is not important in these problems.

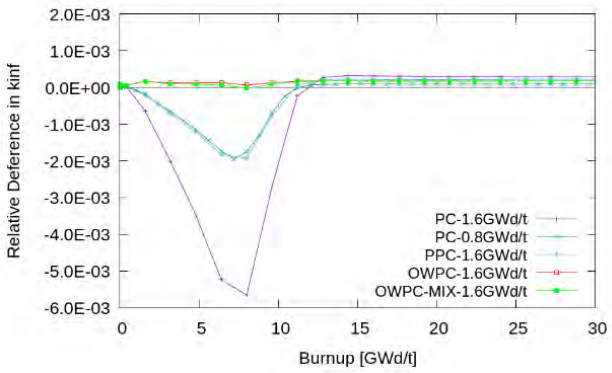

Fig. 6. Errors of k_{inf} in the VERA/2O problem

5. Conclusion

A new algorithm to determine a proper weight in the optimally-weighted predictor-corrector method has been proposed. This concept is based on problem simplification in which proper weight can be easily obtained. Verification calculation has been performed for three PWR fuel assemblies including Gd_2O_3. Better performance of the OWPC method over the original PC method and the PPC method has been demonstrated. In addition, we have examined which correlation is better to improve calculation accuracy.

References

1. Stamm'er RJJ, et al., *Methods of Steady-State Reactor Physics in Nuclear Design*, Academic Press (1983).
2. Yamamoto M, "Coarse Time-Step Integration Method for Burnup Calculation of LWR Lattice Containing Gadoninium-Poisoned Rods," *J. Nucl. Sci. Technol.,* **22**, 1 (1985).
3. Yamamoto A, Tatsumi M, Sugimura N, "Projected Predictor-Corrector Method for Capability for LWR Fuel Assembly in Reactor Physics Burnup Calculation," *Nucl. Sci. Eng.,* **163**, 144 (2009).
4. Lee DJ, Rhodes J, Smith K, "Quadratic Depletion Model for Gadolinium Isotopes in CASMO-5," *Proc. Int. Conf. Adv. Nucl. Fuel Management, ANFM 2009,* Hilton Head Island, SC, April 12-15, 2009 (2009).
5. Okumura S, Chiba G, "Development of Nuclear Fuel Depletion Calculation for LWR Fuel Assembly in Reactor Physics Code System CBZ," *Proc. of Reactor Physics Asia 2017, RPHA17,* Chengdu, China, August 24-25, 2017 (2017).
6. Shibata K, Iwamoto O, Nakagawa T, Iwamoto N, Ichihara A, Kunieda S, Chiba S, Furukawa K, Otuka N, Ohsawa T, Murata T, Matsunobu H, Zukaran A, Kameda S, Katakura J, "JENDL-4.0: A new library for nuclear science and technology," *J. Nucl. Sci. Technol.*, **48**, 1 (2011).
7. Kim KS, "Specification for the VERA Depletion Benchmark Suite," CASL-X-2015-1014-000, Oak Ridge National Laboratory (2015).

Proceedings of the Reactor Physics Asia 2019 (RPHA19) Conference
Osaka, Japan, Dec. 2-3, 2019

Robustness of the GPS Functions in Pinwise Neutronics Analysis of PWRs

Hwanyeal Yu[a] and Yonghee Kim[a,*]
[a]*Dept. of Nuclear and Quantum Eng., KAIST, 291 Daehak-ro Yuseong-gu, Daejeon, Korea, 34141*
[*]Corresponding author: yongheekim@kaist.ac.kr

Abstract

The generalized equivalence theory (GET) plus superhomogenization (SPH) [GET Plus SPH (GPS)] method, which is a new leakage correction method has been investigated to demonstrate its applicability to PWR cores with different conditions. In the GPS method, the pin-wise cross section (XS)-dependent SPH factors are parameterized as a function of normalized leakage information, i.e., current-to-flux ratio (CFR). In this paper, the given GPS functions, which are pre-determined at BOC HFP condition have been applied to two different conditions (HZP and CZP). Both UOX-loaded and partially MOX-loaded small PWR cores are analyzed using given HFP GPS functions to investigate the temperature dependency of the GPS method. The two-dimensional method of characteristics (MOC)-based DeCART2D code is used for both lattice and reference core calculation in this work. The GPS method is implemented to an in-house nodal expansion method (NEM)-based pin-wise diffusion code with the hybrid CMFD (HCMFD) algorithm. Based on the comprehensive result of this work, it is concluded that the GPS method has minor temperature dependency.

Key Words: **Pin-by-pin core analysis, Leakage correction, GPS method**

1. Introduction

The conventional two-step core analysis is based on the homogenized parameters obtained by the heterogeneous transport calculation with the all-reflective boundary condition. Consequently, the homogenized group constants (GCs) are always subjected to an inherent spatial homogenization error due to the loss of information and the unphysical boundary condition.

Recently, a new leakage correction method, called GET plus SPH (GPS) method was proposed to overcome this unavoidable error of conventional two-step core analysis. As a combination of generalized equivalence theory (GET) [1] and super-homogenization method (SPH) [2], the modified SPH concept was introduced to correct the pin-wise cross section (XS) of conventional GET-based two-step core analysis. The feasibility of the GPS method was demonstrated in the previous studies [3,4].

In this paper, the applicability of the GPS method to different temperature conditions (including density change of coolant) is investigated. Both UOX-loaded and partially MOX-loaded small PWR cores with three different conditions were considered: Hot Full Power (HFP), Hot Zero Power (HZP), Cold Zero Power (CZP). These small PWR cores were analysis with given GPS functions, which are pre-determined at HFP condition (hereafter called HFP-GPS function) in previous studies [3,4]. A 2-D method of characteristics (MOC) based lattice code, DeCART2D [5] was used for the reference cores and lattice calculations. The GPS method is implemented to an in-house pin-wise diffusion solver with the hybrid CMFD (HCMFD) algorithm [6].

2. The GPS Methodologies

In the GPS method, a modified SPH factor, called XS-dependent SPH factor is introduced to correct the pin-wise XSs of the conventional two-step core analyses

$$SPH_{\alpha,g} = SPH_g \times \frac{\Sigma^{ref}_{\alpha,g}}{\Sigma^{SA}_{\alpha,g}} = \frac{\Sigma^{corrected}_{\alpha,g}}{\Sigma^{SA}_{\alpha,g}}, \quad (\,)$$

where g is the group index, α denotes reaction type, $\Sigma^{ref}_{\alpha,g}$ is the reference pin-wise XS, $\Sigma^{SA}_{\alpha,g}$ is the pin-wise XS obtained from the 2-D lattice calculation, and SPHg is the standard SPH factor.

The XS-dependent SPH factor is parameterized as a function of pin-wise leakage information, current-to-flux ratio (CFR), defined as in Eq. (2):

$$CFR_g = \frac{\sum_s J^s_g}{\phi_g}, \quad (2)$$

where g is the group index, s is the surface index, J^s_g is the outward net current on a surface, and ϕ_g is the pin-wise volume-averaged flux.

In the GPS method, the change of both XS-dependent SPH factor and CFR are defined as:

$$\Delta SPH_{\alpha,g} = SPH_{\alpha,g} - SPH^{SA}_{\alpha,g}, \quad (3)$$

$$\Delta CFR_g = CFR_g - CFR_g^{SA}, \quad (4)$$

where $SPH_{\alpha,g}^{SA}$ and CFR_g^{SA} are the pin-wise XS-dependent SPH factor and CFR from the infinite lattice calculation, respectively.

The changes in the pin-wise XS-dependent SPH factors and their initial values from the lattice calculation are functionalized by the change of pin-wise two-group CFR for reaction α and group g ('F' for fast group and 'T' for thermal group)

$$\Delta SPH_{\alpha,F} = a_{1,\alpha,F}\Delta CFR_F + a_{2,\alpha,F}\Delta CFR_T + a_{3,\alpha,F}, \quad (5)$$

$$\Delta SPH_{\alpha,T} = a_{1,\alpha,T}\Delta CFR_F + a_{2,\alpha,T}\Delta CFR_T + a_{3,\alpha,T}, \quad (6)$$

where $a_{1,\alpha,g}$, $a_{2,\alpha,g}$, and $a_{3,\alpha,g}$ are coefficients.

3. Numerical Results and Discussions

To investigate temperature dependency of the GPS method, a small PWR [3] in Fig. 1 and a partially MOX-loaded PWR (KAIST 1A benchmark) [4,7] in Fig. 2 were considered. The FA designs are same as the one of Ref. 3 and 4. For the consistency, the baffle-reflector regions are also treated with pin-wise GCs. The pin-wise GCs of baffle-reflector are determined by same processes with Ref. 3.

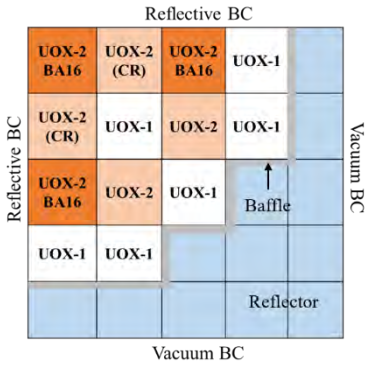

Fig.) . Configuration of the small PWR benchmark

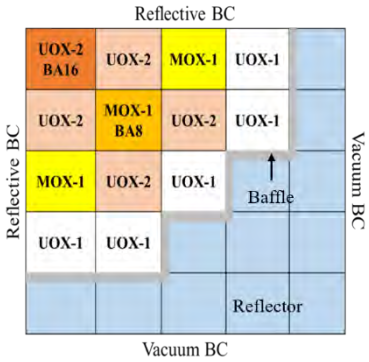

Fig. 2. Configuration of the KAIST) A benchmark

The HFP and CZP conditions of both small PWRs are the same as the one of Ref 7. For HZP condition, the average temperatures of coolant, cladding, and fuel are 570 K (0.7295 g/cm^3), 630 K, and 900 K, respectively. For CZP condition, all temperatures are assumed to be 300 K () .0 g/cm^3). In case of HZP condition, temperatures were set to be 555 K (0.7603 g/cm^3 for coolant density) for all with an assumption of conventional temperature difference (30 K) between core inlet and outlet temperature.

To investigate the temperature dependency of the GPS method, the HFP-GPS functions from previous studies [3,4] were used to analyze small PWR cores of HZP and CZP condition. To focus on temperature dependency of the GPS function only, the pin-wise two-group constants used for each condition are determined from corresponding condition. Similar with the pin-wise group constants, the $SPH_{\alpha,g}^{SA}$ and CFR_g^{SA} in Eqs. (3) and (4) are also set to be values from corresponding conditions.

3.1 UOX-loaded small PWR

Table 1 shows summaries of an UOX-loaded small PWR with different conditions. It is clearly shown that, in HZP and CZP conditions, the GPS correction by HFP-GPS functions can provides similar accuracy in terms of eigenvalue and pin-power as shown in Table 1 and Figs. 3 to 5. It is understandable since the change of XS-dependent SPH factor is parameterized with the change of CFR information and temperature effect is already taken into account by the pin-wise group constants. Therefore, the temperature effect on GPS functions is minor.

Table) . Summaries of UOX-loaded small PWR

Condition	k-eff	Δρ [pcm]	Pin-power % error Max (RMS)
HFP condition			
Ref. DeCARD2D	1.112455	-	-
Standard two-step*	1.113307	68.81	-2.95 (0.82)
GPS	1.112681	18.28	1.64 (0.21)
HZP condition			
Ref. DeCARD2D	1.123510	-	-
Standard two-step*	1.124351	66.55	-2.98 (0.87)
GPS	1.123737	17.97	1.38 (0.22)
CZP condition			
Ref. DeCARD2D	1.139892	-	-
Standard two-step*	1.140636	57.24	3.02 (0.95)
GPS	1.140155	20.21	1.70 (0.33)

* GET-based two-step core analysis

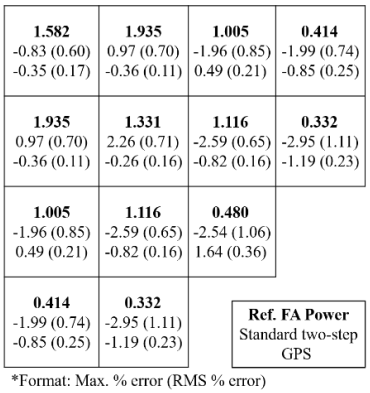

*Format: Max. % error (RMS % error)

Fig. 3. FA-wise maximum and RMS pin-power %error distribution (HFP condition)

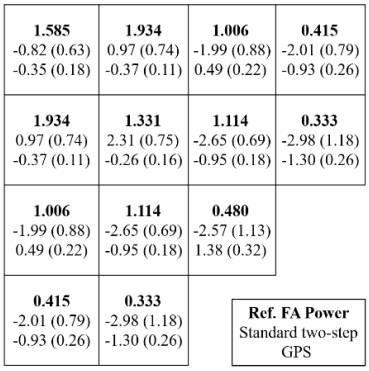

Fig. 4. FA-wise maximum and RMS pin-power %error distribution (HZP condition)

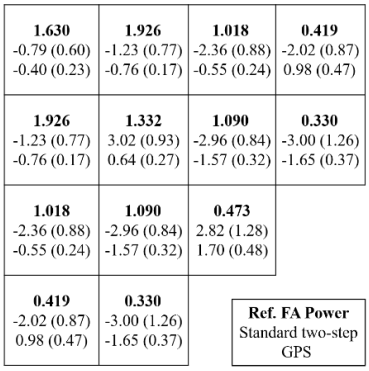

Fig. 5. FA-wise maximum and RMS pin-power %error distribution (CZP condition)

3.2 Rodded UOX-loaded small PWR

A rodded UOX-loaded small PWR was also considered. In this study, only two rodded FAs are located in inner core regions as shown in Fig. 1. As shown in Table 2 and Figs 6 to 8, the GPS correction by HFP-GPS functions effectively improved the accuracy of the pin-by-pin core analyses with different conditions. Although the maximum error in CZP condition is still significant, the normalized pin-power of corresponding pin is relatively low, 0.115.

Table 2. Summaries of rodded UOX-loaded small PWR

Condition	k-eff	Δρ [pcm]	Pin-power % error Max (RMS)
HFP condition			
Ref. DeCARD2D	1.014952	-	-
Standard two-step	1.016220	122.97	-4.15 (1.14)
GPS	1.014905	-4.57	-1.57 (0.59)
HZP condition			
Ref. DeCARD2D	1.025144	-	-
Standard two-step	1.026401	119.45	-4.21 (1.20)
GPS	1.025096	-4.56	-1.89 (0.66)
CZP condition			
Ref. DeCARD2D	1.042166	-	-
Standard two-step	1.043337	107.67	-4.98 (1.29)
GPS	1.042374	19.14	-3.36 (0.67)

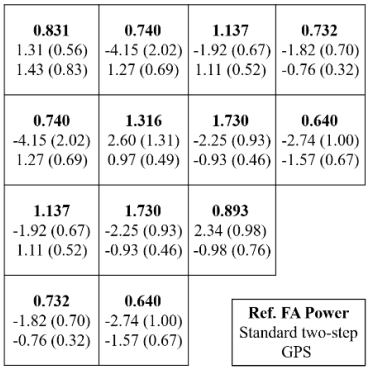

Fig. 6. FA-wise maximum and RMS pin-power %error distribution (HFP condition)

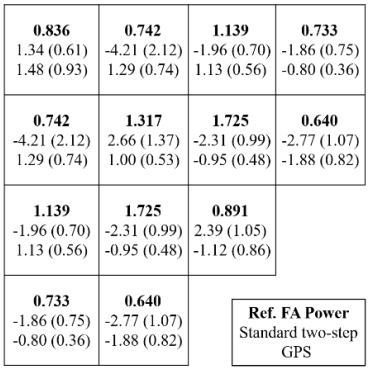

Fig. 7. FA-wise maximum and RMS pin-power %error distribution (HZP condition)

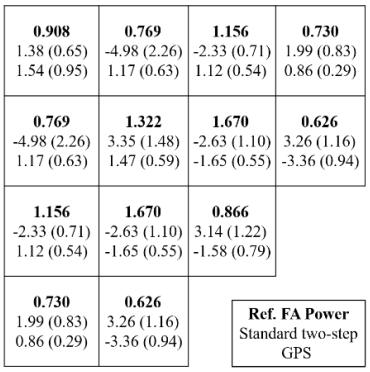

Fig. 8. FA-wise maximum and RMS pin-power %error distribution (CZP condition)

3.3 Partially MOX-loaded small PWR

Table 3 shows summaries of a partially MOX-loaded small PWR with different conditions. Figures 9 to 11 show the FA-wise maximum and RMS pin-power %error distribution of each condition. As expected, even if different GPS functions are applied in terms of temperature condition, the GPS corrections improve accuracy of pin-by-pin core analysis.

Table 3. Summaries of partially MOX-loaded PWR

Condition	k-eff	Δρ [pcm]	Pin-power % error Max (RMS)
HFP condition			
Ref. DeCARD2D	1.116271	-	-
Standard two-step	1.118000	138.57	3.94 (1.15)
GPS	1.116599	26.30	-1.78 (0.34)
HZP condition			
Ref. DeCARD2D	1.127773	-	-
Standard two-step	1.129454	132.00	3.89 (1.19)
GPS	1.128095	25.32	-1.90 (0.36)
CZP condition			
Ref. DeCARD2D	1.140499	-	-
Standard two-step	1.142178	128.92	4.13 (1.22)
GPS	1.141020	40.03	-2.18 (0.43)

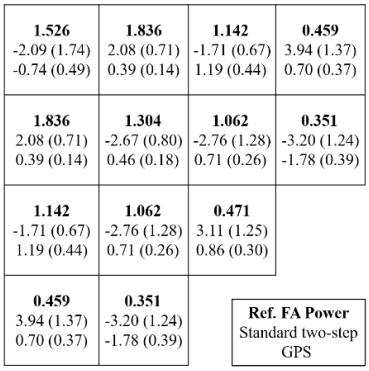

*Format: Max. % error (RMS % error)

Fig. 9. FA-wise maximum and RMS pin-power %error distribution (HFP condition)

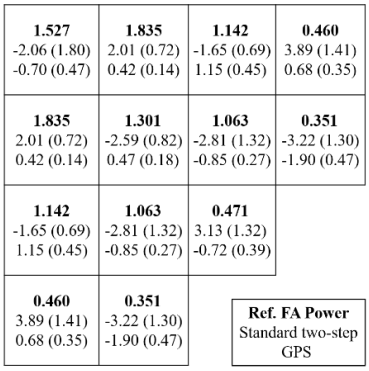

*Format: Max. % error (RMS % error)

Fig.)0 . FA-wise maximum and RMS pin-power %error distribution (HZP condition)

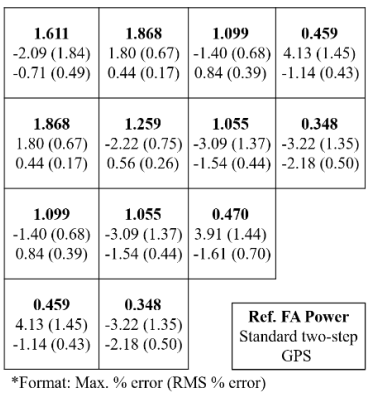

*Format: Max. % error (RMS % error)

Fig.)) . FA-wise maximum and RMS pin-power %error distribution (CZP condition)

It is noted that, in rodded and partially MOX-loaded cores there are slightly higher errors of CZP condition compared with HZP and HFP condition. It is expected that it is caused by huge temperature difference and difficulty of problem itself. Fortunately, the impact is minor and the accuracy is acceptable.

4. Conclusions

In this paper, the applicability of the GPS functions to different temperature conditions was investigated. Both UOX-loaded and partially MOX-loaded small PWR cores with three different conditions, HFP, HZP, and CZP were analyzed with given GPS functions obtained from HFP conditions. Based on the implementation of given GPS correction on the different temperature conditions, it can be concluded that the GPS method has minor temperature dependency since the change of XS-dependent SPH factor is parameterized by the change of CFR information in the GPS functionalization. The temperature effect will be considered by the pin-wise group constants from TH-coupling.

Acknowledgements

This work was supported by the National Research Foundation of Korea (NRF) Grant funded by the Korean Government (MSIP) (NRF-20) 6R) A5A) 0) 39) 9)

References

1. K. S. Smith, “Assembly Homogenization Techniques for Light Water Reactor Analysis,” *Progress in Nuclear Energy*, 17, 303, 1986.
2. A. Hebert, “A Consistent Technique for the Pin-by-Pin Homogenization of a Pressurized Water Reactor Assembly”, *Nucl. Sci. Eng.*, 113, 227, 1993.
3. H. Yu, W. Kim, and Y. Kim, “A Leakage Correction with SPH Factors for Two-group Constants in GET-based Pin-by-Pin Reactor Analyses”, *Annals of Nuclear Energy*, Vol. 129, p. 30-50, July, 2019.
4. H. Yu, J. Kim, and Y. Kim, “Pinwise Diffusion Solution of Partially MOX-loaded PWRs with the GPS (GET PLUS SPH) Method”, Nuclear Science and Engineering, online published, June, 2019
5. J. Y. Cho, DeCART2D v) .) User’s Manual, KAERI/UM-40/2016, 2016
6. S. Song, H. Yu, and Y. Kim, “One-node and two-node hybrid coarse-mesh finite difference algorithm for efficient pin-by-pin core calculation”, *Nuclear Engineering and Technology*, Vol. 50, Issue 3, 327-339, 2018
7. N. Z. Cho, “Benchmark Problem) A: MOX Fuel-Loaded Small PWR Core (MOX Fuel with Zoning)”, KAIST/NuratT, http://nurapt.kaist.ac.kr/benchmark, June 23 (2000)

Proceedings of the Reactor Physics Asia 2019 (RPHA19) Conference
Osaka, Japan, Dec. 2-3, 2019

APEC-corrected NEM Analysis of the VERA Core

Seongdong Jang[a], Kyunghoon Lee[b] and Yonghee Kim[a,*]
[a]*Korea Advanced Institute of Science and Technology, 291, Daehak-ro, Yuseong-gu, Daejeon, 34141, Korea*
[b]*Korea Atomic Energy Research Institute, 111, Daedeok-daero 989beon-gil, Yuseong-gu, Daejeon, 34057, Korea*
[*]Corresponding author: yongheekim@kaist.ac.kr

Abstract

The limitation of the conventional two-step method for the modern reactor physics analysis is quite obvious due to the lack of leakage information. To overcome its genetic limitation caused by unphysical boundary condition at the single assembly lattice calculation, the albedo-corrected parameterized equivalence constants (APEC) method has been proposed. The main idea of this APEC method is to construct linear APEC functions taking into account normalized leakage information and then use it during NEM calculation. The APEC functions were set up in terms of the current-to-flux ratio, spectral index and flux ratio to consider leakage information. The purpose of this study is to verify the impact of the APEC-corrected NEM analysis by solving 2-D VERA core benchmarked problem at the 0 MWD/MTU burnup. All of the single assembly lattice and color-set was calculated by DeCART2D code and NEM nodal analysis with APEC method was conducted by in-house NEM nodal code. The results showed that the solution of the APEC-corrected NEM analysis can be improved in terms of the multiplication factor and relative power error. It is concluded that the APEC method is a one of the improved methodology to assist the conventional two-step method.

Key Words: **APEC Method, VERA Core, In-situ Leakage Correction**

1. Introduction

The conventional two-step method based on the generalized equivalence theory (GET) is the one of the corner-stone in the modern reactor physics analysis. The main idea of the GET is that the equivalence can be applied into the homogeneous diffusion nodal analysis by preserving the reaction rate of the heterogeneous transport analysis via homogenized group constants (HGCs) and discontinuity factors (DFs). The actual application to the conventional two-step method is through the single assembly lattice calculation to obtain the HGCs, which are also called flux weighted constants (FWCs), and assembly DFs (ADFs). However, some errors of the multiplication factor and power distribution are occurred due to its limit by neighboring effects so the neighbor- and spectrum-irrelevant leakage correction are mainly used.

Recently, the albedo-corrected parameterized equivalence constants (APEC) method was developed to correct all of the lattice-based HGCs and DFs during nodal analysis. It was showed that the HGCs and DFs can be updated as an in-situ correction method during the nodal analysis through the APEC functions taking into account normalized leakage parameters such as a current-to-flux ratio (CFR) and flux ratio (FR). In this study, the effect of the APEC-corrected NEM analysis is discussed by solving 2-D VERA core.

2. APEC Leakage-corrected Two-step Method

The main principle of the APEC leakage-corrected method is that the HGCs and DFs are corrected by APEC functions which are predetermined by the color-set calculation. It is possible to obtain all of the coefficients of the APEC functions, which can consider the actual leakage information based on their lattice-wise HGCs and ADFs, by multiple linear regression using the results of the additional color-set model. In this study, to focus on the effect of the APEC functions for the fuel assembly (FA), the reference HGCs and DFs, which were obtained from the whole core transport calculation, were used for the reflector region. All of the single assembly lattice and color-set model was calculated by DeCART2D code and the homogeneous diffusion NEM nodal calculation based on APEC method was analyzed by in-house NEM nodal code.

The philosophy of the APEC methodology is based on conventional two-step method as follows: 1) obtaining the single assembly-wise HGCs and ADFs by lattice calculation, 2) constructing APEC function by determining all of coefficients in terms of leakage parameter via additional color-set calculation including the results of the lattice calculation and 3) applying the in-situ correction of the HGCs and DFs through the updated leakage parameters in the iteration of nodal calculation.

2.1 APEC functions for the HGCs

To do the in-situ correction of the HGCs during NEM nodal calculation, the APEC cross section (XS) functions are set up in terms of node- and group-wise CFRs. As shown in Eq. (1), the HGCs based on the single assembly HGCs can be corrected through the updated △XS terms. The APEC XS functions are defined as △XS for each energy group as shown in Eq. (2) and (3), respectively.

$$\Sigma_{x,g} = \Sigma_{x,g}^{SA} + \Delta\Sigma_{x,g} \quad (1),$$

$$\Delta\Sigma_{x,F} = a_{x,F}\frac{\sum \bar{J}_F^s}{\sum \hat{\phi}_F^s} + b_{x,F}\frac{\sum \bar{J}_T^s}{\sum \hat{\phi}_T^s} + c_{x,F} \quad (2),$$

$$\Delta\Sigma_{x,T} = a_{x,T}\frac{\sum \bar{J}_T^s}{\sum \hat{\phi}_T^s} + b_{x,T}\left(\frac{\sum \bar{J}_T^s}{\sum \hat{\phi}_T^s}\right)^2 + c_{x,T} \quad (3),$$

where, Σ^{SA} : single assembly HGC,
F : fast group, T : thermal group,
$\bar{J}^s$: surface current, $\hat{\phi}^s$: surface flux, $\bar{\phi}^{avg}$: average flux,

$$c_{x,G}\begin{cases} = 0 & \text{for interior FA} \\ \neq 0 & \text{for peripheral FA} \end{cases}.$$

Note that the constant terms are designated depending on the position of the FA. Using the node-wise CFR parameters calculated by color-set calculation, the coefficients can be determined. Then, these coefficients can do the in-situ update of the △XS by node-wise CFRs determined by NEM calculation during its iteration.

2.2 APEC functions for the DFs

In case of the APEC DF functions, improved model is considered as follows:

$$DF_g = ADF_g + \Delta DF_g \quad (4),$$

$$\Delta DF_g = a_{g,1}\frac{\bar{\phi}_g^{Avg}}{\hat{\phi}_g^s} + a_{g,2}\frac{\bar{J}_g^s}{\hat{\phi}_g^s} + a_{g,3}\frac{\sum \bar{J}_g^s}{\sum \hat{\phi}_g^s} + c_g \quad (5).$$

It was demonstrated that surface-wise leakage parameters, such as FR and CFR, can improve the accuracy of the DF even for partially MOX-loaded PWRs. The generalized procedure to obtain all of the coefficients of APEC DF functions is as follows: 1) classification by FA types, 2) (optional) classification by surface directions, 3) (optional) filtering by adjacent FA types, and 4) generation of APEC DF functions. In this study, optional surface-wise APEC DF functions are considered for the peripheral FA which is mark by (*) with the name of the FA type as shown in Fig. 3.

3. Numerical Results

To verify the APEC-corrected NEM analysis, 2-D VERA core was analyzed as a benchmark problem. The core and FA configuration are as shown in Fig. 1.

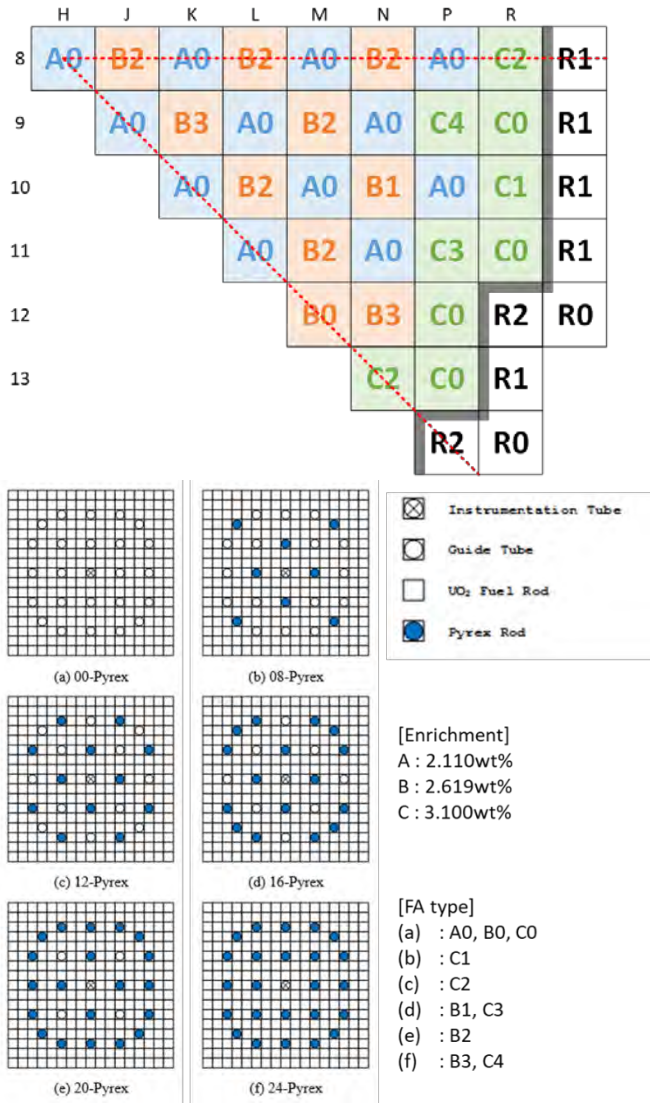

Fig. 1. 2-D VERA core and fuel assembly configuration.

The color-set was calculated based on the list of them and their models as shown in Table I and Fig.2, respectively.

Table I. List of Color-set Calculations

Color-set Model	Combination of FAs
Checkerboard	(A0,B0), (A0,B1), (A0,B2), (A0,B3), (A0,C0), (A0,C1), (A0,C2), (A0,C3), (A0,C4), (B0,B3), (B0,C0), (B0,C4), (B1,B3), (B1,C0), (B1,C4), (B2,B3), (B2,C0), (B2,C4), (B3,C0), (B3,C1), (B3,C2), (B3,C3), (B3,C4), (C0,C1), (C0,C2), (C0,C3), (C0,C4), (C1,C4), (C2,C4), (C3,C4)
Flat baffle	(A0,C0), (C0,C0), (C4,C0), (A0,C1), (C1,C1), (C4,C1), (A0,C2), (C2,C2), (C4,C2)
L-shape type 1	(C0,C0), (C0,C4)
L-shape type 2	(C0,B0,B3), (C0,C4,A0), (C0,A0,B1), (C0,A0,B2), (C0,A0,C3)

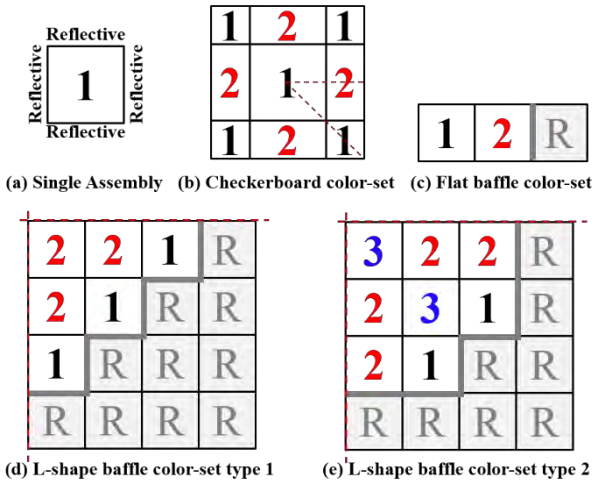

Fig. 2. Color-set models for the APEC XS and DF.

In this study, the sensitivity test of the APEC DF constant term in Eq. (5) was conducted. Only for the APEC DF functions, they were categorized depending on the existence of the constant term as follows: 1) APEC-a (w/o constant) and 2) APEC-b (w/ constant).

Table II. Results for VERA 2-D Core

XS	DF	k_{eff}	Δρ (pcm)	RMS (%)	Max. (%)
DeCART2D		1.162661			
FWC	ADF	1.161181	-109.59	1.988	5.954
APEC	ADF	1.162309	-26.04	0.456	2.091
APEC	APEC-a	1.162415	-18.20	0.121	0.473
APEC	APEC-b	1.162667	0.43	0.306	0.677

The results showed that APEC XS and APEC DF functions can improve the results in terms of the multiplication factor and relative power error as shown in Table II. Although the results of the conventional two-step method using FWC XS and ADF could be significantly improved by applying only in-situ APEC XS update with conventional ADF, it was still not good enough to overcome the limit of the conventional two-step method. It was noted that introduced in-situ APEC DF correction can enhance the results when in-situ APEC XS correction is also applied simultaneously. It can be interpreted that this APEC DF correction can overcome the limit which is occurred when APEC XS correction is only used.

Note that the constant term in the APEC DF functions may affect to the multiplication factor because it is integrated parameter of the whole core. Depending on their power distribution, the multiplication factor may be sensitive due to the error cancellation. Therefore, it might be hard to say which APEC DF function is better than the other in point of view of the multiplication factor. In terms of the relative power error, both of the APEC DF function can improve the results compared to those of the conventional two-step method. Regarding the sensitivity of the constant term in the APEC DF function, the results of the APEC-a (w/o constant) are better than those of APEC-b (w/ constant) in terms of the relative power error.

A0	B2	A0	B2	A0	B2	A0	C2
1.29	**1.13**	**1.26**	**1.14**	**1.27**	**1.06**	**1.03**	**0.68**
-2.07	-4.20	-1.67	-3.33	-0.48	-2.16	0.81	0.52
-0.78	-0.40	-0.64	-0.29	-0.57	-0.05	-0.12	0.06
-0.22	-0.11	-0.19	-0.01	-0.06	0.00	-0.15	-0.47
0.22	-0.51	0.25	-0.45	0.38	-0.45	0.24	-0.34

	A0	B3	A0	B2	A0	C4	C0*
	1.26	**1.06**	**1.28**	**1.13**	**1.21**	**0.95**	**0.78**
	-1.90	-4.58	-0.93	-2.48	0.33	-1.73	1.97
	-0.67	-0.57	-0.59	-0.13	-0.37	0.11	-0.15
	-0.22	-0.09	-0.10	0.11	-0.03	0.07	-0.03
	0.32	-0.20	0.37	-0.35	0.26	-0.20	-0.09

		A0	B2	A0	B1	A0	C1*
		1.26	**1.14**	**1.27**	**1.12**	**1.03**	**0.68**
		-1.09	-2.68	0.27	-0.68	2.02	2.62
		-0.56	-0.20	-0.49	0.19	0.12	0.82
		-0.13	0.05	-0.03	0.06	0.04	0.06
		0.45	-0.31	0.31	-0.09	0.32	0.44

			A0	B2	A0	C3*	C0*
			1.27	**1.08**	**1.11**	**0.89**	**0.55**
			0.32	-0.93	2.12	1.97	4.23
			-0.43	0.09	0.05	1.03	0.85
			0.00	0.18	-0.07	0.03	0.00
			0.68	-0.43	0.32	-0.06	0.22

				B0	B3	C0*
				1.22	**0.76**	**0.77**
				2.29	1.22	4.99
				-0.05	0.79	1.15
				0.42	0.14	0.03
				0.01	-0.62	-0.59

FA Type					C2*	C0*
DeCART2D					**0.71**	**0.50**
FWC / ADF (%)					4.87	5.95
APEC XS/ ADF (%)					2.09	1.17
APEC XS/ APEC-a DF (%)					0.43	-0.12
APEC XS/ APEC-b DF (%)					0.13	-0.26

Fig. 3. Power distribution of VERA 2-D core

The reference power distribution of the VERA core, the results of the conventional two-step method and the results of the in-situ APEC correction were calculated as shown in Fig. 3. The results showed that the relative error of the power distribution from the conventional two-step method can be reduced to around zero by applying APEC correction. Specifically, the maximum and minimum relative error of the conventional two-step method, (5.95, -4.58), could be reduced to (2.09, -0.78) respectively, when only APEC XS correction was applied. In case of in-situ APEC XS and DF correction, these maximum and minimum values could be improved to (0.43, -0.47) by APEC-a (w/o constant), and (0.68, -0.62) by APEC-b (w/ constant).

Table III. Relative RMS Error of the HGCs

RMS Error (%)	FWC	APEC XS / APEC-a DF	APEC XS / APEC-b DF
D_1	1.45E-01	6.60E-02	6.59E-02
Σ_{a1}	4.85E-03	1.06E-03	1.30E-03
$\upsilon\Sigma_{f1}$	1.78E-03	6.22E-04	7.77E-04
$\Sigma_{s1\rightarrow2}$	2.05E-02	3.31E-03	4.06E-03
D_2	2.73E-01	9.23E-03	2.68E-02
Σ_{a2}	5.79E-02	1.61E-03	4.63E-03
$\upsilon\Sigma_{f2}$	1.21E-01	3.08E-03	1.04E-02
$\Sigma_{s2\rightarrow1}$	6.53E-04	1.76E-05	5.75E-05

The results of Table III showed the comparison of HGCs RMS error based on those of reference. The FWC

indicates the HGCs calculated by lattice calculation and the APEC XS means the converged HGCs in in-situ APEC corrected nodal calculation. It is noted that the HGCs could be converged different values depending on the APEC DF function because the leakage parameters might be differently updated depending on their APEC function.

The results showed that all of the HGCs converged by APEC correction could be improved compared to those of conventional two-step method.

Table IV. Relative RMS Error of the DFs

RMS Error (%)	ADF	APEC-a	APEC-b
Fast Group	0.794	0.369	0.462
Thermal Group	1.821	0.665	1.245

Similar to Table III, the relative RMS error of the DFs compared to the reference are arranged in Table IV. The results showed that the converged APEC DF values are improved compared to ADFs which are determined by lattice calculation. Especially for APEC-a (w/o constant) function, the thermal group DFs were significantly improved compared to those of APEC-b (w/ constant) function.

4. Conclusions

The APEC-corrected NEM analysis has been successfully verified by solving the 2-D VERA core benchmark problem. It is demonstrated that the in-situ APEC leakage correction method can improve the results in terms of the multiplication factor and relative power error, when both of the HGCs and DFs are corrected simultaneously.

Acknowledgements

This work was supported by the National Research Foundation of Korea (NRF) Grant funded by the Korean Government (MSIP) (NRF-2016R1A5A1013919)

References

1. K. Lee, W. Kim and Y. Kim, “Improved Nodal Equivalence with Leakage-corrected Cross Sections and Discontinuity Factors for PWR Depletion Analysis,” *Nucl. Eng. Tech.*, **51**, *5*, (2019).
2. W. Kim, W. Heo and Y. Kim, “Improvement of Nodal Accuracy by Using Albedo-Corrected Parameterized Equivalence Constants,” *Nucl. Sci. Eng.*, **188**, 207 (2017).
3. W. Kim, K. Lee and Y. Kim, “Functionalization of the Discontinuity Factor in the Albedo-corrected Parameterized Equivalence Constants (APEC) Method,” *Nucl. Sci. Eng.*, **192**, 1 (2018).
4. J. Y. Cho, et al., “DeCART2D v1.0 Methodology Manual,” KAERI/TR-5283/2013, Korea Atomic Energy Research Institute (2013).
5. A. T. Godfrey, “VERA Core Physics Benchmark Progression Problem Specifications, Revision 4,” CASL-U-2012-0131-004, Oak Ridge National Laboratory (2014).
6. S. Jang, and Y. Kim “Improved Discontinuity Factor Modeling for the in-situ APEC Leakage Correction in Nodal Analysis,” Transactions of ANS Winter, November 17-21, Washington, D.C., 2019

Proceedings of the Reactor Physics Asia 2019 (RPHA19) Conference
Osaka, Japan, Dec. 2-3, 2019

Discontinuity Factor: A Discontinuity Condition for Angular Flux?

Akio Yamamoto[a*], Tomohiro Endo[a]
[a]*Nagoya Unversity, Furo-cho, Chikusa-ku, Nagoya, Japan*
[*]Corresponding author: a-yamamoto@energy.nagoya-u.ac.jp

Abstract

The discontinuity factor (DF) has been considered as a discontinuity condition for scalar flux, partial current, or angular flux. However, DF can be also considered as a partial reflective condition at a region interface and is consistent with the refractive index used in optics. The unphysical interpretation regarding to DF, e.g., loss or production of neutrons at an interface, can be avoided through this new insight.

Key Words: **Discontinuity factor, scalar flux, partial current, angular flux, refractive index**

1. Introduction

The discontinuity factor (DF) is a well-known concept in the reactor analysis field and is widely used [1]-[3]. The use of DF greatly reduces the homogenization error in the advanced nodal method and is a key technology of its success.

The application area of DF has become wider and it is currently applied not only to reduce homogenization errors but also to reduce spatial and angular discretization errors in diffusion and transport calculations.

Though there is no doubt on its usefulness, its concept is somewhat strange since application of DF makes partial current or angular flux discontinuous, i.e., "stream" of neutrons becomes discontinuous. We usually accept this inconsistency by excusing that the scalar flux/partial current/angular fluxes appeared in homogenized (or energy collapsed) calculations are not "physical" quantities thus they can be discontinuous at an interface.

In the present summary, another interpretation of DF that can avoid the above inconsistency is described [4].

2. Theory

There are various ways to apply DF. In this summary, the continuous condition is applied to the odd-parity angular fluxes (or flux moments) while the discontinuous condition is allowed for even-parity angular fluxes (or flux moments).

Firstly, let us consider the diffusion theory. In this case, the following interface condition is used:

$$\begin{aligned} f_L\phi_L &= f_R\phi_R, \\ J_L^{net} &= J_R^{net}, \end{aligned} \tag{1}$$

where

f_L and f_R : DFs for the left and the right region surfaces, respectively,

ϕ_L and ϕ_R : scalar fluxes at the left and the right region surfaces, respectively,

J_L^{net} and J_R^{net} : net currents at the left and the right region surfaces, respectively.

By applying the relationship between the partial currents and scalar flux in the diffusion theory, the following relation for partial currents are obtained at the interface (Fig.1):

$$\begin{aligned} J_R^{in} &= \frac{2f_L}{f_L+f_R}J_L^{out} + \frac{f_L-f_R}{f_L+f_R}J_R^{out}, \\ J_L^{in} &= \frac{2f_R}{f_L+f_R}J_R^{out} + \frac{f_R-f_L}{f_L+f_R}J_L^{out}, \end{aligned} \tag{2}$$

where

J_L^{in} and J_L^{out}: incoming and outgoing partial currents at the left region surface,

J_R^{in} and J_R^{out}: incoming and outgoing partial currents at the right region surface.

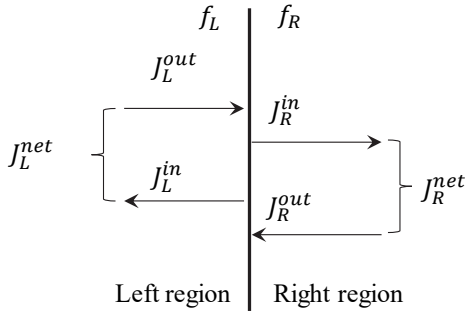

Fig 1. Relationship among partial and net currents

Equation (2) indicates that the partial currents are discontinuous at the interface while the net neutron current is continuous:

$$J_L^{net} = J_L^{out} - J_L^{in} = J_R^{in} - J_R^{out} = J_R^{net}. \tag{3}$$

Next, we consider the transport equation in the Pn form. In this case, the discussion for the diffusion theory can be extended straightforward manner, i.e., the scalar flux and the net current are considered as the even and odd angular flux moments, respectively.

Thirdly, the transport equation for even-parity angular flux is considered. In this case, the following interface

condition is applied:

$$f_L^e(\mathbf{\Omega})\psi_L^e(\mathbf{\Omega}) = f_R^e(\mathbf{\Omega})\psi_R^e(\mathbf{\Omega}),$$
$$\psi_L^o(\mathbf{\Omega}) = \psi_R^o(\mathbf{\Omega}), \tag{4}$$

where

$f_L^e(\mathbf{\Omega})$ and $f_R^e(\mathbf{\Omega})$: DFs for even-parity angular flux at the left and the right surfaces for direction $\mathbf{\Omega}$, and $f_L^e(\mathbf{\Omega}) = f_L^e(-\mathbf{\Omega})$, $f_R^e(\mathbf{\Omega}) = f_R^e(-\mathbf{\Omega})$.

$\psi_L^e(\mathbf{\Omega})$ and $\psi_R^e(\mathbf{\Omega})$: even-parity angular fluxes at the left and the right surfaces for direction $\mathbf{\Omega}$,

$\psi_L^o(\mathbf{\Omega})$ and $\psi_R^o(\mathbf{\Omega})$: odd-parity angular fluxes at the left and the right surfaces for direction $\mathbf{\Omega}$.

The even and odd parity angular fluxes are defined by:

$$\psi_L^e(\mathbf{\Omega}) = \frac{\psi_L(\mathbf{\Omega}) + \psi_L(-\mathbf{\Omega})}{2},$$
$$\psi_L^o(\mathbf{\Omega}) = \frac{\psi_L(\mathbf{\Omega}) - \psi_L(-\mathbf{\Omega})}{2},$$
$$\psi_R^e(\mathbf{\Omega}) = \frac{\psi_R(\mathbf{\Omega}) + \psi_R(-\mathbf{\Omega})}{2},$$
$$\psi_R^o(\mathbf{\Omega}) = \frac{\psi_R(\mathbf{\Omega}) - \psi_R(-\mathbf{\Omega})}{2}, \tag{5}$$

where $\psi_L(\mathbf{\Omega})$ and $\psi_R(\mathbf{\Omega})$ are the angular flux at the left and the right surfaces for direction $\mathbf{\Omega}$, respectively.

By inserting Eq.(5) into Eq.(4), the following relations are obtained:

$$\psi_R(\mathbf{\Omega}) = \frac{2f_L^e(\mathbf{\Omega})}{f_L^e(\mathbf{\Omega}) + f_R^e(\mathbf{\Omega})}\psi_L(\mathbf{\Omega}) + \frac{f_L^e(\mathbf{\Omega}) - f_R^e(\mathbf{\Omega})}{f_L^e(\mathbf{\Omega}) + f_R^e(\mathbf{\Omega})}\psi_R(-\mathbf{\Omega}),$$
$$\psi_L(-\mathbf{\Omega}) = \frac{2f_R^e(\mathbf{\Omega})}{f_L^e(\mathbf{\Omega}) + f_R^e(\mathbf{\Omega})}\psi_R(-\mathbf{\Omega}) + \frac{f_R^e(\mathbf{\Omega}) - f_L^e(\mathbf{\Omega})}{f_L^e(\mathbf{\Omega}) + f_R^e(\mathbf{\Omega})}\psi_L(\mathbf{\Omega}). \tag{6}$$

3. Discussion

By applying the discontinuity condition for the scalar flux and even-parity angular flux, the partial current and the angular flux become discontinuous as shown in Eqs.(2) and (6) except for DFs for the left and right regions are identical. The partial current and angular flux represent a stream of neutrons for a particular direction. Therefore, Eqs. (2) and (6) indicate that the stream of neutrons is discontinuous at an interface when DFs of the left and right regions are different. In this case, neutrons look like disappeared or produced at an interface. Apparently, neutrons are not disappeared or produced at the interface thus the above interpretation is unphysical.

However, if Eqs. (2) and (6) are carefully observed, they can be also considered as the transmission and the reflection of partial current or angular flux at an interface. For example, the transmission and the reflection coefficients for the partial current or angular flux going from left to right are expressed as:

$$\text{Transmission coefficient for partial current: } \frac{2f_L}{f_L + f_R},$$
$$\text{Reflection coefficient for partial current: } \frac{f_R - f_L}{f_L + f_R}. \tag{7}$$

$$\text{Transmittion coefficient for angular flux: } \frac{2f_L^e(\mathbf{\Omega})}{f_L^e(\mathbf{\Omega}) + f_R^e(\mathbf{\Omega})},$$
$$\text{Reflection coefficient for angular flux: } \frac{f_R^e(\mathbf{\Omega}) - f_L^e(\mathbf{\Omega})}{f_L^e(\mathbf{\Omega}) + f_R^e(\mathbf{\Omega})}. \tag{8}$$

Summation of the transmission and the reflection coefficients are 1 as derived from Eqs.(7) and (8).

The above interpretation (the transmission and reflection) is more natural and intuitive. Namely, when different regions having different DFs are adjacent, stream of neutrons (partial current or angular flux) are partially reflected at the interface. On the other hand, when the adjacent regions have identical DF, no partial reflection occurs and all neutrons are transmitted to adjacent region. It should be noted that the reflection considered in this discussion is different from physical one. In physical reflection, flight direction of a neutron changes at the surface of reflection. However, in the reflection described in Eq.(6), a neutron entering an interface reflected to the opposite of entering direction regardless of the entering angle to the interface.

It is worthwhile to see the relation with the optics. In the case of light, the amplitude of the transmitted and reflected lights are described by:

$$A_t = \frac{2n_L}{n_L + n_R}A,$$
$$A_r = \frac{n_R - n_L}{n_L + n_R}A, \tag{9}$$

where

n_L and n_R: refractive indexes for the left and the right materials,

A, A_t, and A_r: amplitude of entering, transmitted, and reflected lights.

Interestingly, there is a clear relationship between Eqs.(8) and (9). The DF in Eq.(8) correspond to the refractive indexes in optics in Eq. (9). The light entering to different material is partly reflected and the rest is transmitted. No reflection occurs when the same materials (or materials having the identical refractive indexes) are adjacent. This is an excellent analogy for the neutron transport with DF. When different materials are adjacent, part of the entering neutrons are "reflected" and the rests are transmitted. For example, Eq.(2) indicates that J_R^{in} is a summation of the transmitted partial current from the left region and the reflected partial current from the right region. As a result, we see the discontinuity of partial current or the angular flux, which is an analogy of the behavior of light.

When $f_R < f_L$, the coefficients for the "reflection" term $(f_R - f_L)/(f_L + f_R)$ and the transmission term $(2f_L)/(f_L + f_R)$ in Eq.(2) become negative and greater than 1, respectively. In this case, the transmitted partial current or the angular flux is "amplified". In order to preserve the neutron balance at the interface, the reflected partial current or the angular flux becomes negative.

The DF has been considered as a discontinuous condition for scalar flux, partial current, or angular flux. However, when the present discussion is taken into account, the DF can be considered as the partial reflective boundary condition at the material interface. In the most

simple and coarse case, a partial reflective boundary condition for partial current is considered that reproduce the reference reaction rate in a region. As a more detail condition, a partial reflective boundary condition can be considered for face average angular flux or angular flux on a ray trace. Spatial and angular resolution of partial reflective boundary condition can be adjusted by the purpose. The advantage of the present approach is that the neutron balance at interfaces is always preserved.

In summary, no unphysical interpretation is necessary by adopting this concept and it can be applied to diffusion or transport theory with flexibility.

4. Conclusions

In the present summary, a new interpretation of DF is described. The DF can be understood through the analogy of optics, i.e., partial reflection and transmission of light at a material interface. By adopting this concept, an unphysical interpretation that requires artificial loss and production of neutrons at an interface is no more necessary.

Acknowledgments

The author sincerely thanks Dr. Yung-An Chao for his advice and insightful comments on this topic.

References

1. Koebke K., “A New Approach to Homogenization and Group Condensation,” Proceedings of IAEA Technical Committee Meeting on Homogenization Methods in Reactor Physics, Lugano, Switzerland, (1978).
2. Smith K. S., “Assembly Homogenization Techniques for Light Water Reactor Analysis,” Prog. Nucl. Energy, 17, 303 (1986).
3. Sanchez R., “Assembly Homogenization Techniques for Core Calculations,” Prog. Nucl. Energy, 51, 14 (2009).
4. Yamamoto A, Endo T, “A New Interpretation of Discontinuity Factor,” *Nucl. Sci. Eng*., (2019). https://doi.org/10.1080/00295639.2019.1579514

Proceedings of the Reactor Physics Asia 2019 (RPHA19) Conference
Osaka, Japan, Dec. 2-3, 2019

Calculation of Higher Eigen-modes of the Forward and Adjoint Neutron Diffusion Equations Using IRAM Algorithm Based on Domain Decomposition

Wenbin Wu[a*], Yingrui Yu[a], Qi Luo[a], Dong Yao[a], Qing Li[a], and Xiaoming Chai[a]
[a]*Science and Technology on Reactor System Design Technology Laboratory, Nuclear Power Institute of China*
NO. 328 Section 1 Changshun Ave, Shuangliu District, Chengdu, Sichuan Province, China 610213
[*]Corresponding author: wenbinwu@126.com

Abstract

The higher eigen-modes of the forward and adjoint neutron diffusion equations are widely used in several application perspectives for engineering purpose, such as the power distribution reconstruction, the stability analysis, and generalized perturbation theory (GPT) based sensitivity and uncertainty analysis. In this study, the higher eigen-modes of both the forward and adjoint neutron diffusion equations are calculated using implicitly restarted Arnoldi method (IRAM) based on domain decomposition parallelism and the multi-group multi-domain coupled PGMRES algorithm. A multi-dimensional LWR diffusion problem is solved for verification. Numerical results demonstrate that the forward equation and the adjoint equation have the same eigenvalue spectrum, and the obtained higher order eigen-vectors follow the orthogonality relationship. The numerical results agree well with the anticipated theory analysis.

Key Words: **Neutron diffusion equation, Forward and adjoint equations, IRAM algorithm, PGMRES algorithm, Higher eigen-modes, Orthogonality.**

1. Introduction

The neutron diffusion equation is usually represented as a generalized eigenvalue problem, of which the fundamental solution is the effective multiplication factor of a fission system, i.e. k_{eff}, and the flux distribution. For this diffusion eigenvalue system, the higher eigen-modes could be computed for theory analysis and some engineering applications in the aspects of the power distribution reconstruction [1], the transient analysis [2], the stability analysis [3], and the loading pattern optimization [4].

The adjoint (in contrary to forward) neutron diffusion equation is also a generalized eigenvalue problem, of which the fundamental solution, known as the adjoint neutron flux, has the physical meaning of neutron importance. The adjoint neutron flux is widely used in the perturbation theory [5] and the sensitivity and uncertainty (SU) analysis. Similar as the forward neutron diffusion equation, the higher eigen-modes of the adjoint equation could also be computed, which have potential value in high-order perturbation theory and generalized SU analysis [6].

In this study, the IRAM [7] algorithm is employed for the calculation of the higher eigen-modes of both the forward and adjoint neutron diffusion equations based on domain decomposition and the multi-group multi-domain coupled PGMRES algorithm.

2. Methodologies

2.1 The forward and adjoint diffusion equations

The neutron diffusion equation is derived based on the Fick's law, which introduces a heuristic relation between the neutron current and the gradient of the neutron flux [8]. The multi-group form of the forward neutron diffusion equation is

$$-\boldsymbol{\nabla}\cdot D_g(\boldsymbol{r})\nabla\phi_g(\boldsymbol{r})+\Sigma_{rg}(\boldsymbol{r})\phi_g(\boldsymbol{r})=Q_g(\boldsymbol{r}), \qquad (1)$$

where

$$Q_g(\boldsymbol{r})=Q_{sg}(\boldsymbol{r})+Q_{fg}(\boldsymbol{r}),$$

$$Q_{sg}(\boldsymbol{r})=\sum_{\substack{h=1\\h\neq g}}^{G}\Sigma_{g\leftarrow h}(\boldsymbol{r})\phi_h(\boldsymbol{r}),$$

$$Q_{fg}(\boldsymbol{r})=\frac{\chi_g(\boldsymbol{r})}{k}\sum_{h=1}^{G}\upsilon\Sigma_{fh}(\boldsymbol{r})\phi_h(\boldsymbol{r}).$$

The symbols have their usual physical meanings consistent with the definitions in literature [8]. The static neutron diffusion equation is a generalized eigenvalue problem, of which the fundamental solution corresponds to the k_{eff} and the neutron flux.

The multi-group form of the adjoint neutron diffusion equation is represented as

$$-\nabla \cdot D_g(\boldsymbol{r})\nabla\phi_g^*(\boldsymbol{r}) + \Sigma_{rg}(\boldsymbol{r})\phi_g^*(\boldsymbol{r}) = Q_g^*(\boldsymbol{r}), \quad (2)$$

where

$\phi_g^*(\boldsymbol{r})$ = adjoint flux,

$$Q_g^*(\boldsymbol{r}) = Q_{sg}^*(\boldsymbol{r}) + Q_{fg}^*(\boldsymbol{r}),$$

$$Q_{sg}^*(\boldsymbol{r}) = \sum_{\substack{h=1 \\ h\neq g}}^{G} \Sigma_{h\leftarrow g}(\boldsymbol{r})\phi_h^*(\boldsymbol{r}),$$

$$Q_{fg}^*(\boldsymbol{r}) = \frac{\upsilon\Sigma_{fg}(\boldsymbol{r})}{k}\sum_{h=1}^{G}\chi_h(\boldsymbol{r})\phi_h^*(\boldsymbol{r}).$$

As we can see from equations (1)(2), the adjoint form is straightforwardly obtained by permuting primary and secondary group indices of the forward form. The adjoint equation could be solved in the same method with the forward equation by properly manipulating the energy groups.

2.2 Discretization of the neutron diffusion equations

It is usually impossible to analytically solve the diffusion equations. Hence, discretization methods such as the finite difference and the finite element are employed to transform the algebraic operator into a matrix operator in order to solve numerically.

In this study, the mesh centered finite difference method is employed to discretize the neutron diffusion equation, as depicted in Fig. 1. The balance relation of the diffusion equation is represented by the neutron currents of all six surfaces as

$$\sum_{\upsilon\epsilon(x,y,z)} \frac{J_{\upsilon+,g}^{i,j,k} - J_{\upsilon-,g}^{i,j,k}}{\Delta\upsilon^{i,j,k}} + \Sigma_{r,g}^{i,j,k}\phi_g^{i,j,k} - Q_{sg}^{i,j,k} = Q_{fg}^{i,j,k}, \quad (3)$$

where

$$J_{x+,g}^{i,j,k} = D_{eff,x+,g}^{i,j,k}\left(\phi_g^{i+1,j,k} - \phi_g^{i,j,k}\right),$$

$$D_{eff,x+,g}^{i,j,k} = \frac{-2D_g^{i,j,k}D_g^{i+1,j,k}}{\Delta x^{i+1,j,k}D_g^{i,j,k} + \Delta x^{i,j,k}D_g^{i+1,j,k}}.$$

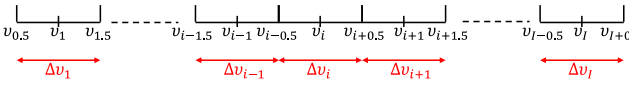

Fig. 1 Illustration of mesh centered finite difference discretization method

Equation (3) is the fundamental equation of the discretized diffusion equation. By moving the scattering source term to the left side, the diffusion equation is re-arranged as

$$\boldsymbol{L\phi} = \frac{1}{k}\boldsymbol{F\phi} \;\; or \;\; \boldsymbol{L^{-1}F\phi} = k\boldsymbol{\phi}, \quad (4)$$

where

$\boldsymbol{\phi}$ = scalar flux vector,
$\boldsymbol{L}$ = loss operator,
$\boldsymbol{F}$ = multiplicative operator.

Generally, the diffusion equation is computed with the power iteration method in the form of inner-outer iteration. In this study, IRAM algorithm serves as the eigenvalue solver and the multi-group multi-domain coupled PGMRES algorithm serves as the linear solver. These two algorithms will be described in detail in the following sections.

2.3 The multi-group multi-domain coupled PGMRES algorithm

For either the power iteration method or the IRAM algorithm, it is necessary to solve the linear system $\boldsymbol{Lx} = \boldsymbol{F\phi}$ also known as the fixed source problem (FSP). There exist many advanced algorithms widely used in the reactor physics community, such as the GMRES algorithm [9].

GMRES is one of the famous Krylov sub-space methods (in contrary to the stationary iterative methods), which employs orthogonalization based Arnoldi process. For the Arnoldi process, several orthogonalization techniques such as classical Gram-Schmidt, modified Gram-Schmidt, and Householder transformations could be adopted. All these techniques need the operation of matrix-vector multiplication $\boldsymbol{y} = \boldsymbol{Lx}$. GMRES algorithm is implemented in many excellent numerical libraries, such as Intel MKL and PETSc, which provide convenient reverse communication interface. Only the matrix-vector multiplication operator should be provided to the GMRES interface. In this study, domain decomposition parallelism is applied. Hence, PGMRES, the parallel version of the GMRES algorithm is used.

In this study, the PGMRES algorithm is from the PETSc library [10]. PETSc supports the matrix-free methods, which require no explicit storage of the matrix. However, users should define routines representing operations of the implicit matrix on a vector.

Specific to the discretized multi-group and domain-decomposed diffusion equation, the input vector of the multiplication operation includes the fluxes of all groups in all sub-domains, and the results vector is obtained by substitute the fluxes to the left hand side of equation (3). Each sub-domain is assigned to a MPI process, which stores only the fluxes of meshes within the individual

sub-domain. Since the multiplication operation needs fluxes of neighbors, message passing is applied for fluxes transferring, which happens primarily in the multiplication operation.

The fluxes of all groups in all sub-domains are solved simultaneously by the PGMRES algorithm. Thus, this is called the multi-group multi-domain coupled PGMRES algorithm.

2.4 The application of IRAM for higher eigen-modes

IRAM is an efficient and robust Krylov subspace iterative method to calculate part or all of the higher eigen-modes simultaneously. As with most Krylov subspace iterative methods, only the matrix-vector multiplication operator should be provided to the IRAM interface to complete the Arnoldi process. For equation (4), the matrix-vector multiplication is written as

$$\boldsymbol{y} = \boldsymbol{L^{-1}F\phi}, \tag{5}$$

where $\boldsymbol{\phi}$ is the input vector and $\boldsymbol{y}$ is the result vector.

Inversion of a large matrix is often unacceptable. Hence, it's transformed into the FSP (6), which is solved by the multi-group multi-domain coupled PGMRES algorithm proposed above.

$$\boldsymbol{Ly} = \boldsymbol{F\phi}, \tag{6}$$

The IRAM implementation in the ARPACK library is widely used. Similarly as the PETSc library, the ARPACK library wrapped in the SLEPc library [11] provides a reverse communication interface. It simplifies the IRAM implementation into practical applications because the IRAM solver can simply be wrapped around the existing FSP module without explicitly constructing the matrix $\boldsymbol{L^{-1}F}$.

2.5 The theory analysis of forward and adjoint higher eigen-modes

The forward and adjoint forms of the diffusion equation are represented as

$$\boldsymbol{L\phi} = \frac{1}{k}\boldsymbol{F\phi}, \tag{7}$$

$$\boldsymbol{L^*\phi^*} = \frac{1}{k^*}\boldsymbol{F^*\phi^*}. \tag{8}$$

By multiplying equation (7) with $\boldsymbol{\phi^*}$ and equation (8) with $\boldsymbol{\phi}$, and integrating both equations over phase space, equation (7)(8) are re-written as

$$\langle \boldsymbol{L\phi}, \boldsymbol{\phi^*} \rangle = \frac{1}{k}\langle \boldsymbol{F\phi}, \boldsymbol{\phi^*} \rangle, \tag{9}$$

$$\langle \boldsymbol{L^*\phi^*}, \boldsymbol{\phi} \rangle = \frac{1}{k^*}\langle \boldsymbol{F^*\phi^*}, \boldsymbol{\phi} \rangle. \tag{10}$$

Applying the definition of adjoint operators and subtracting equation (9) from (10) results in

$$\left(\frac{1}{k} - \frac{1}{k^*}\right)\langle \boldsymbol{F\phi}, \boldsymbol{\phi^*} \rangle = \boldsymbol{0}. \tag{11}$$

Therefore, the orthogonality relationship for the forward and adjoint higher eigen-modes is expressed as

$$\langle \boldsymbol{F\phi}_m, \boldsymbol{\phi}_n^* \rangle = \boldsymbol{0} \;\; for \;\; m \neq n, \tag{12}$$

$$\text{and } k_m = k_n^*; \;\; \langle \boldsymbol{F\phi}_m, \boldsymbol{\phi}_n^* \rangle \neq \boldsymbol{0} \;\; for \;\; m = n. \tag{13}$$

3. Numerical results

In this study, two Krylov subspace iterative methods are employed: IRAM for eigenvalue problems along with PGMRES for linear systems. The PGMRES implementation is from the PETSc library, and the IRAM implementation is from the SLEPc library, which wraps around the ARPACK and PARPACK libraries and makes use of PETSc data structures. According to the methodologies above, the ParaFiDi (Parallel Finite Difference) code based on domain decomposition is developed using MPI (Message Passing Interface).

3.1 The benchmark description and computing parameters

A multi-dimensional LWR diffusion problem [12] is solved to demonstrate the capability of ParaFiDi for the calculation of higher eigen-modes of forward and adjoint neutron diffusion equations. It is a 3D 2-group 1/4 symmetric diffusion problem with the size of 170cm×170cm×380cm. Details of this problem is originally from reference [12].

The mesh size employed for the finite difference discretization is 1.25cm×1.25cm×2.5cm in the xyz directions, leading to about 3 millions of meshes. The stopping criteria are set to be 10^{-5} for PGMRES and 10^{-6} for IRAM. The platform where ParaFiDi runs is a cluster with Intel SandBridge E5-2670 CPU linked by Infinite band network. 320 CPU cores are used, and the total elapsed time is around 1100 seconds for 500 orders of eigen-modes.

3.2 Accuracy of the fundamental solution

Since the fundamental solution corresponds to the k_{eff} and neutron flux, it's compared with the benchmark results. k_{eff} by ParaFiDi is 1.02904, which shows 1 pcm error with the reference. The maximum error of assembly power is -0.94% located at the outer part of the core. This implies the fundamental solution has good accuracy.

3.3 The eigenvalue spectrum

500 order eigenvalues of both the forward and adjoint equations along with their relative differences are plotted in Fig. 2, which shows that the relative differences are within 5 pcm. This implies the forward and adjoint equation have the same spectrum, which is consistent with the adjoint theory.

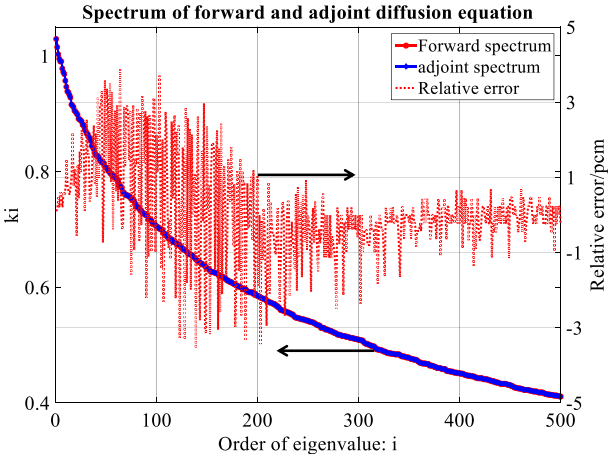

Fig. 2 Eigenvalues of both the forward and adjoint equations along with their relative differences

3.4 The orthogonality relationship

The angle of a forward eigenvector and an adjoint eigenvector is defined as

$$\theta_{mn} = cos^{-1}\frac{\langle \boldsymbol{F}\boldsymbol{\phi}_m, \boldsymbol{\phi}_n^* \rangle}{\|\boldsymbol{\phi}_m\|\|\boldsymbol{\phi}_n^*\|}, for\ \ m \neq n. \qquad (14)$$

The results of MAX, AVG, RMS are separately 1.25, 6.25×10^{-5}, 8.30×10^{-6} in degree (90 means absolute orthogonality), which implies the orthogonality relationship for the forward and adjoint higher eigen-vectors are well satisfied, being consistent with the theory.

6. Conclusions

In this study, the higher eigen-modes of the forward and adjoint neutron diffusion equations are calculated using IRAM along with the multi-group multi-domain coupled PGMRES algorithm based on domain decomposition. The ParaFiDi code is developed accordingly and a multi-dimensional LWR diffusion problem is solved to verify ParaFiDi. Numerical results demonstrate that the fundamental solution agrees well with the reference results, the forward and adjoint equation have the same spectrum, and the forward and adjoint higher eigenvectors follow the orthogonality relationship. The ParaFiDi results are consistent with the anticipated theory analysis.

Future work will include employing pre-conditioner for the IRAM and PGMRES algorithms, and making use of these higher eigen-modes in GPT based SU analysis.

Acknowledgements

This work is supported by the Exploring Grant of Nuclear Power Institute of China under the file No. JJXM-TSJJ-15-12-01.

References

1 C. Wang, H. Wu, L. Cao, et al. "On-Line Reconstruction of in-Core Power Distribution by Harmonics Expansion Method," *Nucl Eng Des*. **241**(8), pp. 3042-3050 (2011).
2 Z. R. de Lima, F. C. Da Silva, A. C. M. Alvim. "A Modal Multidimensional Kinetics Method Using Pseudo-Harmonics," *Ann Nucl Energy*. **36**(6), pp. 752-759 (2009).
3 F. Zinzani, C. Demazière, C. Sunde. "Calculation of the Eigenfunctions of the Two-Group Neutron Diffusion Equation and Application to Modal Decomposition of Bwr Instabilities," *Ann Nucl Energy*. **35**(11), pp. 2109-2125 (2008).
4 X. Zhaodong. Study On the Improvement of Low-Order Harmonies Expansion Method. Beijing: China Institute of Atomic EnergyNuclear Science and Engineering, 2007.
5 E. E. Lewls, J. R. W. F. Mlller. Computational Methods of Neutron Transport. La Grange Park, lliinois USA: American Nuclear Society, 1993.
6 S. Carney, F. Brown, B. Kiedrowski, et al. "Theory and Applications of the Fission Matrix Method for Continuous-Energy Monte Carlo," *Ann Nucl Energy*. **73**, pp. 423-431 (2014).
7 Y. Saad. Numerical Methods for Large Eigenvalue Problems. Halsted Press, 1992.
8 A. Hébert. *Multigroup Neutron Transport and Diffusion Computations* Handbook of Nuclear Engineering. Springer, 2010:874.
9 Y. Saad. Iterative Methods for Sparse Linear Systems. Society for Industrial and Applied Mathematics, 2003.
10 S. Balay, J. Brown, K. Buschelman, et al. ”Petsc Users Manual (Revision 3.4)”Argonne National Laboratory（2013）.
11 C. Campos, J. E. Roman, E. Romero, et al. ”Slepc Users Manual: Scalable Library for Eigenvalue Problem Computations (Revision 3.4)”Universidad Politecnica de Valencia, Spain（2013）.
12 A. C. Center. ”Benchmark Problem Book”, ANL-7416. Computational Benchmark Problems Committee of the Mathematics and Computation Division of the American Nuclear Society（1977）.

Proceedings of the Reactor Physics Asia 2019 (RPHA19) Conference
Osaka, Japan, Dec. 2-3, 2019

Performance of the RSE (Resonance calculation using energy Spectral Expansion) Method for Heterogeneous Pin-cell Geometry

Ryoichi Kondo[a,*], Tomohiro Endo[a], Akio Yamamoto[a], Satoshi Takeda[b],
Hiroki Koike[c], Kazuya Yamaji[c] and Daisuke Sato[c]
[a]*Nagoya University, Furo-cho, Chikusa-ku, Nagoya-shi, Aichi, 464-8603, Japan*
[b] *Osaka University, 2-1 Yamadaoka, Suita-shi, Osaka, Japan, 565-087*
[c] *Mitsubishi Heavy Industries, Ltd., 1-1-1 Wadasaki-Cho, Hyogo-ku, Kobe, Japan, 652-8585*
[*]Corresponding author: r-kondo@fermi.energy.nagoya-u.ac.jp

Abstract

A Resonance calculation using energy Spectral Expansion (RSE) method has been applied to a heterogeneous pin cell geometry and its validity is confirmed through comparison with the ultra-fine group calculation. The RSE method utilizes expansion of angular flux by orthogonal basis on continuous energy. The singular value decomposition (SVD) and the low-rank approximation (LRA) are used to construct the orthogonal basis from ultra-fine group spectrum calculations in the homogeneous geometry. The calculation results show the validity of the present method.

Key Words: **Resonance calculation, effective cross section, reduced order model, low-rank approximation, singular value decomposition**

1. Introduction

Various resonance calculation methods have been developed so far, *e.g.*, the equivalence, the sub-group, and the ultra-fine group methods [1]. These methods have advantages and disadvantages from the viewpoints of computational efficiency. Since the most accurate method is the ultra-fine group method, it would be suitable for high-fidelity core simulations. However, its application to a large geometry is still limited from the viewpoint of computational time.

The RSE method has been recently proposed by the authors as an alternative resonance calculation method [2]. In this approach, continuous (pointwise) neutron energy spectra in heterogeneous regions are expanded by orthogonal basis on continuous energy. The singular value decomposition (SVD) and the low-rank approximation (LRA) [3][4] are used to construct orthogonal basis on continuous energy from the calculation results of ultra-fine group spectrum in homogeneous geometry for typical materials and background cross sections.

In principle, the proposed method has several advantages over conventional methods. For example, accuracy is not dominated by the number of resonances in a group and the resonance interference can be explicitly considered.

In the present summary, the RSE method is applied to a heterogeneous geometry and its accuracy is verified through comparisons with the reference results obtained by the ultra-fine group calculation in a heterogeneous geometry.

2. Theory

The transport equation assuming isotropic scattering and neutron sources is:

$$\mathbf{\Omega}\cdot\nabla\Psi(\mathbf{r},\mathbf{\Omega},E)+\Sigma_t(\mathbf{r},E)\Psi(\mathbf{r},\mathbf{\Omega},E)=\frac{1}{4\pi}Q(\mathbf{r},E). \quad (1)$$

Consider a multi-group energy range (energy range for multi-group g, $1\le g\le \mathrm{G}$):

$$\mathbf{\Omega}\cdot\nabla\Psi(\mathbf{r},\mathbf{\Omega},E_g)+\Sigma_t(\mathbf{r},E_g)\Psi(\mathbf{r},\mathbf{\Omega},E_g)=\frac{1}{4\pi}Q(\mathbf{r},E_g). \quad (2)$$

Angular flux, scalar flux, and neutron source are expanded by the orthogonal bases on energy:

$$\Psi(\mathbf{r},\mathbf{\Omega},E_g)=\sum_{i=1}^{N}f_{i,g}(E_g)\Psi_{i,g}(\mathbf{r},\mathbf{\Omega}), \quad (3)$$

$$\phi(\mathbf{r},E_g)=\sum_{i=1}^{N}f_{i,g}(E_g)\phi_{i,g}(\mathbf{r}), \quad (4)$$

$$Q(\mathbf{r},E_g)=\sum_{i=1}^{N}f_{i,g}(E_g)Q_{i,g}(\mathbf{r}), \quad (5)$$

where the orthogonal property of the bases is:

$$\int_{\Delta E_g}f_{i,g}(E_g)f_{j,g}(E_g)dE_g=\delta_{ij}. \quad (6)$$

By substituting Eqs.(3)–(5) into Eq.(2), and multiplying $f_{n,g}(E_g)$ to the both sides of Eq.(2) and performing energy integration for ΔE_g, we have:

$$\boldsymbol{\Omega}\cdot\nabla\Psi_{n,g}(\mathbf{r},\boldsymbol{\Omega})+\sum_{i=1}^{N}\Sigma_{t,g,n,i}(\mathbf{r})\Psi_{i,g}(\mathbf{r},\boldsymbol{\Omega}) = \frac{1}{4\pi}Q_{n,g}(\mathbf{r}), \quad (7)$$

where

$$\Sigma_{t,g,n,i}(\mathbf{r})=\int_{\Delta E_g} f_{n,g}(E_g)\Sigma_t(\mathbf{r},E_g)f_{i,g}(E_g)dE_g \ . \quad (8)$$

In the RSE method, Eq.(7) is solved with the cross sections defined by Eq.(8). Note that the neutron source in Eq.(7) is directly obtained by an ultra-fine group calculation in heterogeneous geometry in this study. Treatment of the scattering source will be one of the future tasks.

One of the key points of the RSE method is the selection of orthogonal basis. In principle, any complete orthogonal basis can be used for energy spectra [5]–[9]. However, if an inappropriate basis is used, the number of expansions to achieve sufficient accuracy will increase, which makes the present method inefficient.

In order to make efficient orthogonal basis that well reproduces various neutron spectra in heterogeneous regions, SVD, LRA, and ultra-fine group calculations in homogeneous geometry with various background cross sections are used in this study. Namely, neutron spectra in each region in a heterogeneous geometry are expressed by the orthogonal basis obtained in a homogeneous geometry. This process is called reduced order modeling (ROM) [10].

3. Calculations

The following calculation flow is used in the present study:

(1) Perform ultra-fine group slowing down calculations in homogeneous geometry with various background cross sections. The slowing down calculations are carried out for materials (e.g., UO_2) appeared in the heterogeneous geometry. Background cross sections are chosen to cover from the fully shielded (very small background cross section) to the fully diluted (very large background cross section) conditions.
(2) Repeat Step (1) for materials used in the calculation geometry.
(3) Collect ultra-fine group spectra obtained by Step (2) and perform SVD and LRA for each multi-group.
(4) Generate $\Sigma_{t,g,n,i}$ using Eq.(8).
(5) Perform MOC transport calculation using Eq.(7). Note that, the direct numerical solution using the matrix exponential is adopted in this study.
(6) Once $\Psi_{i,g}$ is obtained in Step (5), ultra-fine group angular flux is reconstructed by Eq.(3).
(7) Effective microscopic cross sections for each energy group are generated by angular flux obtained in Step (6) and continuous energy microscopic cross sections.
(8) The ultra-fine group slowing down calculation is carried out in the heterogeneous geometry using the conventional MOC to obtain the reference solution.
(9) Effective cross section obtained in Step (7) is compared with the reference obtained in Step (8).

The four cases shown in Table I are considered. Note that these four cases are chosen to investigate the impact of NR approximation on orthogonal basis and slowing down source. For example, the NR approximation is generally used for slowing down source calculation in the sub-group method. A pin cell geometry shown in Fig.1 is used in the present study. The fuel pellet is divided into two annular regions in order to verify the variation of neutron spectra and effective cross sections due to the spatial self-shielding effect. Number densities of fuel and coolant are summarized in Table II and the temperature of all material is 600 K.

Table I. Calculation cases

Case	Spectra used for orthogonal basis	Slowing down source in Eq.(7)
1	SLD1	SLD2
2	SLD1	NR2
3	NR1	SLD2
4	NR1	NR2

SLD1: Obtained by ultra-fine group slowing down calculation in homogeneous geometry
SLD2: Obtained by ultra-fine group slowing down calculation in heterogeneous geometry
NR1: Obtained by ultra-fine group calculation in homogeneous geometry using the NR approximation
NR2: Obtained by the NR approximation

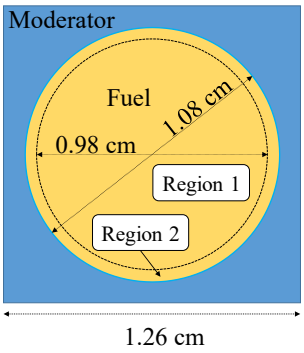

Fig. 1. Pin cell geometry

Table II. Number densities

Material	Nuclide	Density [1/barn/cm]
Fuel (UO_2)	U235	1.1e-3
	U238	2.1e-2
	O16	4.4e-2
Moderator (H_2O)	H1	4.7e-2
	O16	2.35e-2

For the pointwise cross sections used in the present method, the ACE formatted cross sections, which are generated by the FRENDY code [11] using JENDL-4.0 [12], is applied. The GENESIS code [13] is used as the MOC transport solver for the ultra-fine group calculation

in the pin cell geometry with the following calculation conditions:
-Number of polar angles: 6 for π using the TY quadrature set [14]
-Number of azimuthal angles: 32 for 2π
-Ray trace width: 0.05 cm
-Convergence criterion for scalar flux: 10^{-5}

The energy group structure for ultra-fine group calculation is shown in Table III. The XMAS 172 group structure is adopted for multi-group.

Table III. Energy group structure for ultra-fine group calculation

Upper energy boundary [eV]	Number of divisions (Equal division for lethargy)
20,000,000	10,000
52,475	56,000
9118.8	12,000
4307.4	12,000
961.12	8,000
130.07	12,000
0.32242	10,000

Lower energy boundary: 0.00001 eV

A maximum number of the orthogonal bases is 11 on the present calculation since the background cross sections for UO_2 and H_2O are 10^{10}-10^{1} barn (10 points) and 10^{10} barn (1 point), respectively.

4. Results

Relative errors of the effective microscopic total cross sections of U235 and U238 in the energy range including major resolved resonance (1 eV – 1000 eV) are shown in Figs. 2-5. The relative error is defined by (Present – Reference)/Reference. The number of bases is fixed to 11 in these figures to observe the effects of the NR approximation in orthogonal bases and neutron source on the calculation results.

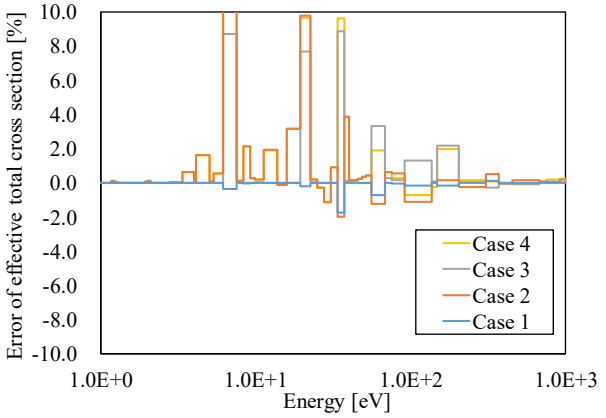

Fig. 2. Error of U235 effective total cross section in 172 XMAS energy group structure (Region 1, inner region of pellet).

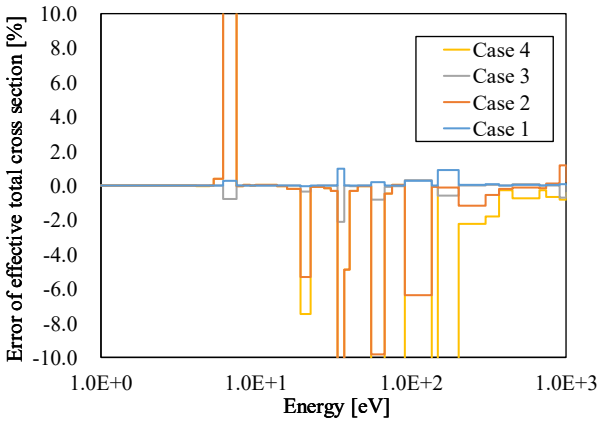

Fig. 3. Error of U238 effective total cross section in 172 XMAS energy group structure (Region 1, inner region of pellet).

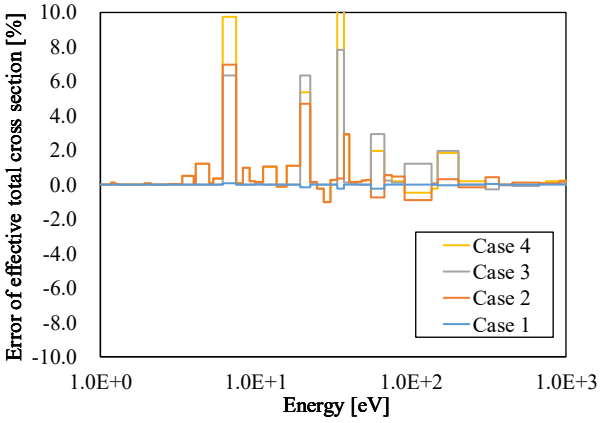

Fig. 4. Error of U235 effective total cross section in 172 XMAS energy group structure (Region 2, outer region of pellet).

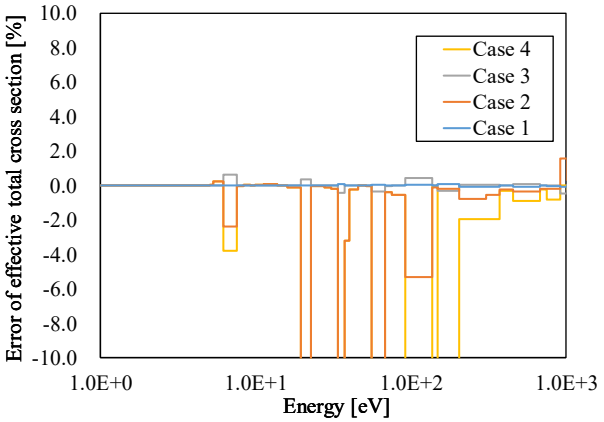

Fig. 5. Error of U238 effective total cross section in 172 XMAS energy group structure (Region 2, outer region of pellet).

Figures 2-5 indicate that the RSE method for Case 1, in which NR approximation is not used, well reproduces the reference effective cross section. When the NR approximation is applied to the neutron source, the

accuracy of the RSE method decreases. This result suggests that consideration of fine energy dependence of scattering neutron source would be necessary.

Next, the impact of the number of bases used in the RSE method is discussed. The relation between the number of orthogonal bases and the accuracy of the effective cross section for group 88 in the XMAS 172 group structure, in which a large resonance of U238 exists, is investigated. Figure 6 indicates that errors are almost converged to small value at five orthogonal bases. The values of error in Region 1 are slightly larger than those in Region 2. The slight differences come from the approximation in the present study, i.e., the neutron spectra in heterogeneous geometry is expanded by those in homogeneous geometry.

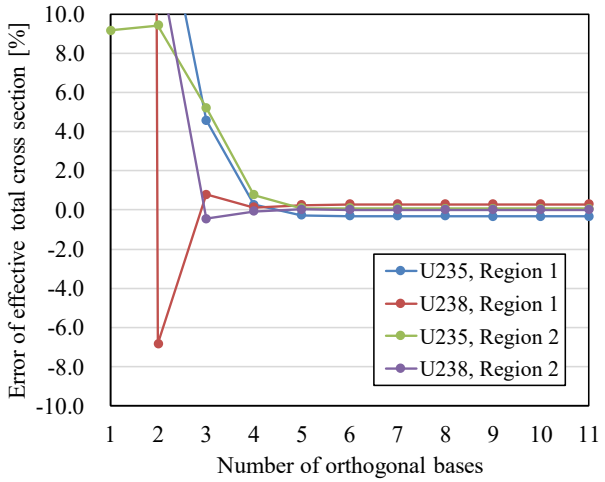

Fig. 6. Comparison of effective total cross section for various number of orthogonal bases in group 88.

5. Conclusions

The Resonance calculation based on energy Spectral Expansion (RSE) is applied to a pin cell geometry and its accuracy is verified through comparison with the results by the ultra-fine group MOC calculation. Impact of the generation method of the orthogonal bases and the neutron source treatment is quantified through the benchmark calculation.

Though the results obtained by the present study is promising, the following issues will be addressed: 1) treatment of scattering source, 2) generation method of orthogonal basis, 3) application to more complicated conditions including multi-cell geometry with different fuel compositions/temperatures 4) efficient numerical calculations for matrix exponential 5) computational cost of the proposed method.

References

1. Cacuci DG ed., *Handbook of Nuclear Engineering, Chap.9, Lattice Physics Computations*, Springer, ISBN 978-0-387-98150-5, (2010).
2. Yamamoto A et al., "A Resonance Calculation Method using Energy Expansion Bases based on a Reduced Order Model," *Proc. M&C2019*, Portland, Oregon, Aug.25–29, (2019).
3. Matsushita M, Endo T, Yamamoto A, Kitao T, "Development of Reduced Order Model of Severe Accident Analysis Code for Probabilistic Safety Margin Analysis," *Proc. PHYSOR2018*, Cancun, Mexico, Apr. 22–Apr. 26, 2018 (2018). [USB].
4. Reed R, Roberts J, "Enhancements to the Discrete Generalized Multigroup Method," *Trans. Am. Nucl. Soc*., **120**, 475 (2019).
5. Rahnema F, Douglass S, Forget B, "Generalized Energy Condensation Theory," *Nucl. Sci. Eng*., **160**, 41 (2008).
6. Zhu L, Forget B, "A Discrete Generalized Multigroup Energy Expansion Theory," *Nucl. Sci. Eng.*, **166**, 239 (2010).
7. Le Tellier R, Fournier D, Ruggieri JM, "A Wavelet-Based Finite Element Method for the Self-Shielding Issue in Neutron Transport." *Nucl. Sci. Eng*., **163**, 34 (2009).
8. Yang W, Wu H, Zheng Y, Cao L, "Application of Wavelets Scaling Function Expansion Method in Resonance Self-Shielding Calculation," *Ann. Nucl. Energy*, **37**, 653 (2010).
9. Rooijen W, "Feasibility of Wavelet Expansion Method to Treat the Energy Variable," *Proc. PHYSOR2012*, Knoxville, TN, Apr. 15–20, 2012 (2012). [USB-DRIVE]
10. Abdel-Khalik HS, *Feasibility Study of an Integrated Framework for Characterization of Uncertainties with Application to CANDU Steady State and Transient Reactor Physics Simulation*, Canadian Nuclear Safety Commission, Canada (2015).
11. Tada K, Nagaya Y, Kunieda S, Suyama K, Fukahori T, "Development and Verification of A New Nuclear Data Processing System FRENDY," *J. Nucl. Sci. Technol*., **54**, 806 (2017).
12. Shibata K et al., "JENDL-4.0: A New Library for Nuclear Science and Engineering," *J. Nucl. Sci. Technol.* **48**, 1–30 (2011).
13. Yamamoto A, Giho A, Kato Y, Endo T, "GENESIS – A Three-dimensional Heterogeneous Transport Solver based on the Legendre Polynomial Expansion of Angular Flux Method," *Nucl. Sci. Eng*., **186**, 1 (2017).
14. Yamamoto A, Tabuchi M, Sugimura N, Ushio T, Mori M, "Derivation of Optimum Polar Angle Quadrature Set for the Method of Characteristics Based on Approximation Error of the Bickley Function," *J. Nucl. Sci. Technol*., **44**, 129 (2007).

Proceedings of the Reactor Physics Asia 2019 (RPHA19) Conference
Osaka, Japan, Dec. 2-3, 2019

Application of Singular Value Decomposition and Low Rank Approximation for Compression of Macroscopic and Microscopic Cross Section Table for Core Calculations

Masato Yamamoto[a*], Tomohiro Endo[a], Akio Yamamoto[a]
[a]*Nagoya University: Furo-cho, Chikusa-ku, Nagoya, 464-8603, Japan*
[*]Corresponding author: m-yamamoto@fermi.energy.nagoya-u.ac.jp

Abstract

The singular value decomposition and the low-rank approximation are applied to reduce size of macroscopic and microscopic cross sections of heterogeneous material regions obtained from a typical lattice physics calculation considering various state points including burnup and branches. The impact of the compression is investigated by calculating the effective multiplication factor and scalar flux of heterogeneous regions using the reference (original) and compressed cross sections. In this study, approximately 99% reduction in cross section table size is achieve while suppressing the error of the effective multiplication factor due to compression of cross section below 0.1%.

Key Words: **macroscopic cross section, microscopic cross section, dimensionality reduction, singular value decomposition, low-rank approximation, heterogeneous assembly calculation, heterogeneous core calculation**

1. Introduction

In the current core analysis, an assembly calculation is carried out and then assembly average, pin average, or material average multi-group macroscopic and microscopic cross sections are edited. These multi-group cross sections are generally pre-tabulated and later used for successive core simulations.

In the today's state-of-art core analysis, space, and energy resolutions are increased, and such simulations naturally require spatially and energetically detailed macroscopic and microscopic cross sections. Therefore, the data size of these cross sections also increases as the spatial or energetic resolution becomes higher.

Spatial and energetic resolutions of core analysis tend to continuously increase. Thus the development of an efficient reduction method of a cross section table size is desirable. In the previous study [1], the dimensionality reduction technique using the singular value decomposition and the low-rank approximation is used for cell-averaged macroscopic cross sections.

Though the dimensionality reduction technique was applied to multi-group macroscopic cross sections of homogenized pin-cell in the previous study, a high fidelity core analysis will require macroscopic and microscopic cross sections for heterogeneous material regions. In addition, the data size of microscopic cross sections is proportional to as the number of nuclides considered in a core calculation. Therefore, the reduction of not only macroscopic cross sections but also microscopic cross sections in each material region is necessary. In this study, 16-group macroscopic and microscopic cross sections in heterogeneous material regions obtained by a typical lattice physics calculation are considered and they are compressed by the singular value decomposition and the low-rank approximation. The impact of the compression on the effective multiplication factor and scalar flux is investigated in single assembly geometry using the compressed and the original cross section data.

2. Theory for Cross Section Compression

A single assembly calculation using a typical case matrix is performed to generate multi-group macroscopic and microscopic cross sections for heterogeneous material regions. The cross sections in the fuel region are considered in this study, and the cross section matrix $\mathbf{A}$ is generated. Note that moderator and cladding cross sections are not discussed in the present paper since their variations are not very large.

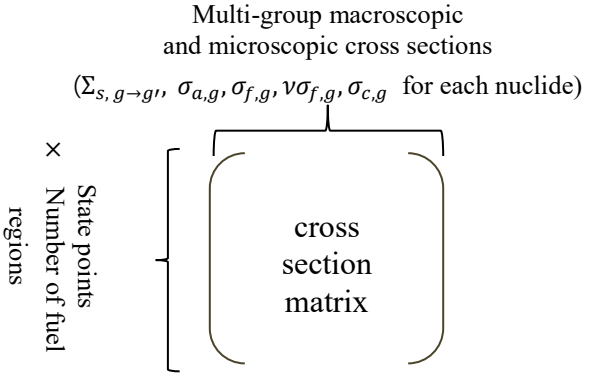

Fig. 1. Generated cross section matrix.

In the matrix $\mathbf{A}$, the cross sections for each fuel

region at each burnup, fuel temperature, moderator temperature, boron concentration, and void fraction are arranged as rows. Then, if a pellet region in a fuel rod is annularly divided, the cross sections of the divided regions are arranged in different rows. When the number of state points and fuel cells are I and J, respectively, and the fuel region in a pellet is divided to K regions, there are I × J × K rows in the matrix. The types of cross sections considered in this study are macroscopic scattering cross section $\Sigma_{s,g\to g'}$ and microscopic cross sections $\sigma_{a,g}, \sigma_{f,g}, \nu\sigma_{f,g}, \sigma_{c,g}$ for each nuclides, which are arranged as columns. When the number of energy groups and the number of nuclides are N and M, respectively, there are $N^2 + 4NM$ columns in the matrix (the number of $\Sigma_{s,g\to g'}$ is N^2, and that of microscopic cross sections is 4 reaction types × N groups × M nuclides = 4NM). The matrix $\mathbf{A}$ has m (= I × J × K) rows and n (= N^2 + 4NM) columns.

The singular value decomposition [2] is applied to $\mathbf{A}$ (here $m > n$ is assumed) as shown in Eqs. (1) – (4).

$$\mathbf{A} = \mathbf{U}\boldsymbol{\Sigma}\mathbf{V}^{\mathbf{T}} \tag{1}$$

$$\boldsymbol{\Sigma} = \begin{pmatrix} S_1 & 0 & \cdots & 0 \\ 0 & S_2 & & \vdots \\ \vdots & 0 & \ddots & 0 \\ \vdots & \vdots & 0 & S_n \\ \vdots & \vdots & \vdots & 0 \\ \vdots & \vdots & \vdots & \vdots \\ 0 & 0 & 0 & 0 \end{pmatrix} \tag{2}$$

$$\mathbf{U} = \begin{pmatrix} u_{11} & \cdots & u_{1m} \\ \vdots & \ddots & \vdots \\ u_{m1} & \cdots & u_{mm} \end{pmatrix} \tag{3}$$

$$\mathbf{V} = \begin{pmatrix} v_{11} & \cdots & v_{1n} \\ \vdots & \ddots & \vdots \\ v_{n1} & \cdots & v_{nn} \end{pmatrix} \tag{4}$$

$\mathbf{U}$ of Eq. (3) and $\mathbf{V}$ of Eq. (4) are unitary matrixes composed by the left and the right singular vectors, respectively. The diagonal components of $\boldsymbol{\Sigma}$ in Eq. (2) are the singular values. By singular value decomposition, n singular values of $S_1, \cdots, S_n$ are obtained. The low-rank approximation is performed by neglecting the small singular values $(S_{k+1}, \cdots, S_n)$ as shown in Eq. (5).

$$\boldsymbol{\Sigma}' = \begin{pmatrix} S_1 & 0 & \cdots & \cdots & 0 \\ 0 & \ddots & & & \vdots \\ \vdots & 0 & S_k & & \\ & \vdots & 0 & \ddots & 0 \\ & & \vdots & 0 & S_n \\ & & & \vdots & 0 \\ \vdots & \vdots & \vdots & \vdots & \vdots \\ 0 & 0 & 0 & 0 & 0 \end{pmatrix} \approx \begin{pmatrix} S_1 & \cdots & 0 \\ \vdots & \ddots & \vdots \\ 0 & \cdots & S_k \end{pmatrix} \tag{5}$$

As the result, the left singular vector $\mathbf{U}$ and the right singular vector $\mathbf{V}$ can also be approximated as Eqs. (6) and (7).

$$\mathbf{U}' = \begin{pmatrix} u_{11} & \cdots & u_{1k} \\ \vdots & \ddots & \vdots \\ u_{m1} & \cdots & u_{mk} \end{pmatrix} \tag{6}$$

$$\mathbf{V}' = \begin{pmatrix} v_{11} & \cdots & v_{1k} \\ \vdots & \ddots & \vdots \\ v_{n1} & \cdots & v_{nk} \end{pmatrix} \tag{7}$$

Storage of $\boldsymbol{\Sigma}'$ is not necessary when it is multiplied to the left (or right) singular vector as shown Eq. (8).

$$\mathbf{U}'\boldsymbol{\Sigma}' = \begin{pmatrix} S_1 u_{11} & \cdots & S_k u_{1k} \\ \vdots & \ddots & \vdots \\ S_1 u_{m1} & \cdots & S_k u_{mk} \end{pmatrix} \tag{8}$$

By multiplying $\mathbf{U}'$, $\boldsymbol{\Sigma}'$ and $\mathbf{V}'$, a reconstructed cross section matrix $\mathbf{A}'$ is obtained as shown Eq. (9).

$$\mathbf{A}' = \mathbf{U}'\boldsymbol{\Sigma}'\mathbf{V}'^{\mathbf{T}} \tag{9}$$

The number of the singular values adopted in $\boldsymbol{\Sigma}'$ can be changed from 1 to n, and $\mathbf{A}'$ can be calculated in each case. Apparently, a smaller number of the adopted singular values results in the smaller size of the cross section set while the reconstruction accuracy decreases.

Macroscopic cross sections except for the scattering are reconstructed by Eq. (10).

$$\Sigma_x = \sum_i N_i \sigma_{x,i}, \tag{10}$$

where

N_i : nuclide number density of nuclide i,

$\sigma_{x,i}$: microscopic cross section of nuclide i of reaction x. Note that energy group index is omitted.

The computing time for the reconstruction is negligibly short compared to that of an assembly or core calculation.

3. Calculation Condition

In this study, a heterogeneous single assembly calculation was performed using AEGIS [3] for the 17 × 17 PWR fuel assembly (^{235}U enrichment: 4.8 wt %) shown in Fig. 2 considering the burnup and branch points.

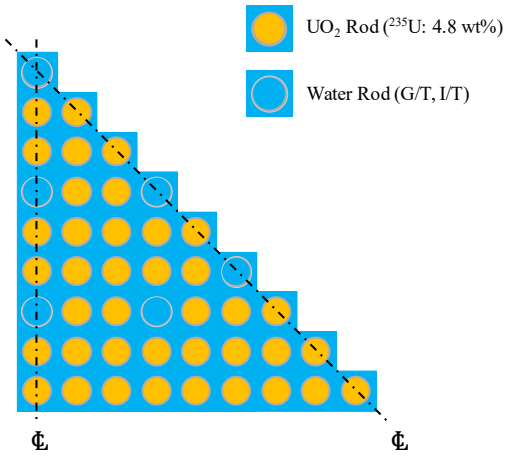

Fig. 2. 17×17 UO_2 fuel assembly for PWR.

Then, 189 state points for various burnup, fuel temperatures, moderator temperatures, boron

concentrations, and void fractions whose ranges are shown in Table I, are considered. The 16-group microscopic cross sections, nuclide number density for each nuclide, and macroscopic scattering cross section are edited for each material region in fuel rods, guide thimbles (G/T), or an instrumentation thimble (I/T). The material regions of a fuel cell are shown in Fig. 3 and the geometry is shown in Table II. Note that the total number of cells is 45 (39 fuel rods and 6 water rods) considering octant symmetry.

Table I. Range of state point parameters

Parameters	Value (or State)
Burnup [MWd/kg]	0.1 – 70
Temperature of Fuel [K]	556 or 900
Temperature of Moderator [K]	556 – 596
Boron Concentration [ppm]	0 – 2400
Void Fraction [%]	0 – 80
Control Rod	No

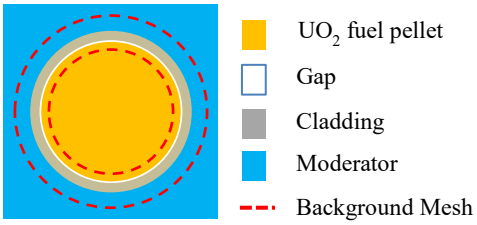

Fig. 3. Material regions in a fuel cell.

Table II. Geometry of a square cell (cell pitch: 1.26 cm)

Materials	Radius [cm]
Fuel Pellet (inner)	0.3663
Fuel Pellet (outer)	0.3663 – 0.4095
Gap	0.4095 – 0.4180
Cladding	0.4180 – 0.4750
Moderator (inner)	0.4750 – 0.5647
Moderator (outer)	0.5647 – Boundary

Among the cross sections edited for each material region, we focused on those of fuel regions to generate the cross section matrix. There are 221 nuclides in a fuel region and the number of the cross sections for a region is 14400 (number of $\Sigma_{s,g\to g'}$ is $16 \times 16 = 256$, and those of $\sigma_{a,g}$, $\sigma_{f,g}$, $\nu\sigma_{f,g}$, $\sigma_{c,g}$ are $4 \times 16 \times 221 = 14144$, thus $256 + 14144 = 14400$). The fuel pellet region is divided into two and cross sections for these regions are arranged in different rows. Therefore, the generated matrix has 14742 rows (= 39 cells × 2 regions × 189 state points) and 14400 columns, and has 14400 singular values.

Singular value decomposition was performed for this matrix using the `numpy.linalg.svd` function of the Python's numerical calculation library NumPy [4]. The singular values were truncated from 14400 using the low-rank approximation and the cross section matrix was reconstructed using the reduced singular vectors and singular values. The reconstructed macroscopic cross section Σ_x required for a heterogeneous assembly analysis is calculated by Eq. (10) using the nuclide number densities calculated by AEGIS and the reconstructed microscopic cross sections. Transport calculations in heterogeneous assembly geometry were performed by GENESIS [5] using the reconstructed and the original macroscopic cross sections to estimate the error of k_{eff} and scalar flux due to compression of the cross sections.

4. Numerical Results

The singular values obtained by the singular value decomposition are shown in Fig. 4.

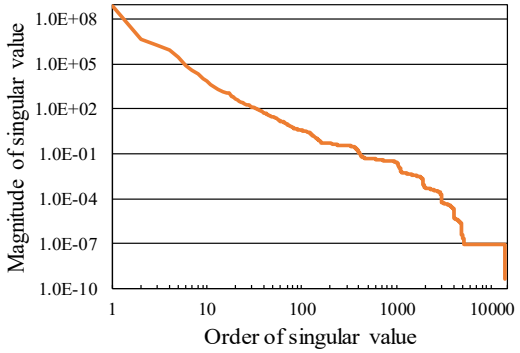

Fig. 4. The magnitude of singular values.

The maximum error of k_{eff} is defined by the maximum relative error among all state points. The maximum and the root mean square (RMS) errors of k_{eff} are shown in Fig. 5. Note that error of scalar fluxes will be shown in the presentation.

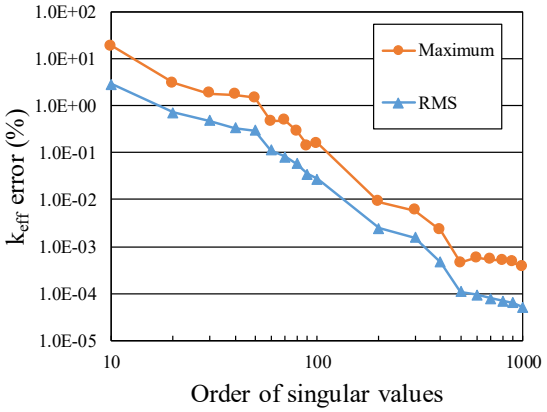

Fig. 5. The maximum and RMS errors of k_{eff} using the reconstructed cross sections (from 10 to 1000 singular values).

RMS error of k_{eff} is calculated by Eq. (11).

$$\Delta k_{eff,RMS} = \sqrt{\frac{\sum_i^{N_{state}} \left(\frac{k_{eff,reconst,i} - k_{eff,original,i}}{k_{eff,original,i}} \right)^2}{N_{state}}} \quad (11)$$

where

N_{state} : number of state points,

$k_{eff,original,i}$: k_{eff} in the i-th state point calculated from the original cross sections,

$k_{eff,reconst,i}$: k_{eff} in the i-th state point calculated from the reconstructed cross sections.

In Fig. 5, the maximum error of k_{eff} is approximately 0.1% when the number of adopted singular values is 100. When 100 singular values are adopted, 14742 × 14400 cross section matrix is compressed into 14742 × 100 left singular vector (multiplied by singular values) and 14400 × 100 right singular vector, which means 98.6% reduction of the original cross section data $\left(= 1 - \frac{14742 \times 100 + 14400 \times 100}{14742 \times 14400}\right)$.

5. Conclusions

Reduction of cross section table size including macroscopic and microscopic cross sections is investigated by applying the singular value decomposition and the low-rank approximation. Among the material-wise cross sections obtained by a lattice physics calculation, those of fuel pellet are considered in this study. The impact of dimensionality reduction is investigated with a comparison of the assembly calculations using the reconstructed and original cross sections. In this study, approximately 99% reduction in cross section table size is achieved while suppressing the error of k_{eff} below 0.1%.

Application of the present method to other lattice types is one of the future studies. Furthermore, development of the tabulation method using dimensionality reduced cross sections is considered from the viewpoint of the applicability of the present method for actual core calculations.

Acknowledgments

The authors sincerely thanks to Dr. Masato Tabuchi of Nuclear Engineering Ltd. for his technical support. The cross section data used in this study were obtained during the internship in NEL.

References

1. Yamamoto M, Endo T, Yamamoto A, "Reduction of Cross Section Table Size for Core Analysis using Dimensionality Reduction Technique," *Trans. Am. Nucl. Soc.*, **119**, 1226 (2018) (USB).
2. Golub G, Van Loan C, *Matrix Computations 3rd ed.*, Chapter 2, Johns Hopkins University Press, Baltimore, Maryland (1996).
3. Yamamoto A, Endo T, Tabuchi M, *et al.*, "AEGIS: An Advanced Lattice Physics Code for Light Water Reactor Analyses," *Nucl. Eng. Technol.*, **42**, *5*, 500 (2010).
4. "Scipy.org," https://docs.scipy.org/doc/numpy/reference/generated/numpy.linalg.svd.html (access: 2019/06/07).
5. Yamamoto A, Giho A, Kato Y, *et al.*, "GENESIS: A Three-Dimensional Heterogeneous Transport Solver Based on the Legendre Polynomial Expansion of Angular Flux Method," *Nucl. Sci. Eng.*, **186**, *1*, 1 (2017).

Proceedings of the Reactor Physics Asia 2019 (RPHA19) Conference
Osaka, Japan, Dec. 2-3, 2019

Compression of the Multi-Physics Simulation Output Data Using Principle Component Analysis

Alexey Cherezov[a], Jinsu Park[a], Hanjoo Kim[a], Nur Syazwani Mohd Ali[b] and Deokjng Lee[a,*]
[a]*Ulsan National Institute of Science and Technology, 50 UNIST-gil, Eonyang-eup, Ulju-gun, Ulsan*
[b]*University of Technology, Malaysia, Skudai, Johor, 81310*
[*]Corresponding author: deokjung@unist.ac.kr

Abstract

High-fidelity multi-physics reactor core simulation includes the pin-by-pin neutronics, thermal-hydraulics, thermal-mechanics and fuel performance physical models. Every run of a high-fidelity code consumes a lot of computation time, memory and usually requires an expansive multi-core computational cluster. All output data is to be saved for further analysis if one does not want to repeat the expansive calculations. The memory amount of high-fidelity output data can be too large, e.g. in the case of uncertainty analysis. Therefore, the data compression algorithms are needed for reduction of the memory without accuracy loose. In this paper we suggest such algorithm based on Principle Component Analysis (PCA) adopted for multi-physics data.

Key Words: **Multiphysics, Compression, PCA, RIA**

1. Introduction

The continuous evolution of reactor core numerical methods and computer technologies has approached the high-fidelity neutron transport simulation with pin-by-pin resolution [1,2]. The further improvement of the nuclear reactor simulation requires the tight coupling of neutronics, coolant thermal-hydraulics, fuel rod thermal-mechanics and other physical models.

This work is devoted to the coupled multi-physics code designed for multi-physics and hypothetical accident analysis of pressurized water reactor (PWR) cores. The code provides the pin-by-pin nodal diffusion neutronics, coolant thermal-hydraulic, one-dimensional thermal-mechanics of pellet and cladding, fuel performance. The code is considered to be used for PWR uncertainty analysis. However, every single run of the code produces large amount of output data. In order to reduce the memory size the data compression algorithms based on Principle Component Analysis (PCA) and sparse matrix representation has been developed.

The paper is organized as follow. Section 2 is devoted to the multi-physics code physical models and coupling algorithm description. Section 3.1 briefly explains the PCA method. In section 3.2 we discuss the residual matrix and sparse matrix representation approaches. Section 3.3 is about the compression rate analysis. In section 3.4 we present the step-by-step description of the compression algorithm. Section 4 presents the calculation results.

2. Multi-Physics Code

The multi-physics code has been developed at UNIST Core Lab. for steady-state and transient simulation of PWR cores. It consists of three program modules for calculation of: 1) reactor core neutron field and isotope number density; 2) coolant thermal-hydraulics; 3) fuel rod thermal-mechanics and fuel performance. Below we describe each of these modules.

RAST-K [1] is a neutron diffusion nodal code with pin-power reconstruction designed for the steady-state and transport calculation of the pressurized water reactor cores with rectangular assemblies. The code utilizes the two-group cross-section library calculated by a lattice code.

CTF [2] is a thermal-hydraulic code that uses the subchannel modeling approach for light water reactor simulation. The code uses a two-fluid, three-field modeling approach and was originally developed by Pacific Northwest Laboratory.

FRAPTRAN [3,4] is a fuel performance code designed to perform the transient and hypothetical accidents simulation of light-water reactor fuel rods. The phenomena modeled by the code include heat conduction, fuel and cladding mechanical deformation, cladding oxidation, fission gas release and fuel rod gas pressure.

FRAPCON is a fuel performance code designed to calculate the steady-state response of light-water reactor fuel rods during long term burnup. The numerical methods and modeled phenomena of the code are similar with FRAPTRAN. Both codes were developed by Pacific Northwest National Laboratory and are used for

certification of the light-water core designs.

In order to use the FRAPCON and FRAPTRAN fuel performance codes for the time integration with a tight coupling, the Fuel Rod Analysis Program Interface FRAPI has been developed. FRAPI runs a fuel performance code and updates a fuel rod state at the each time step with respect to the data transferred by an external code. Also FRAPI restarts the previous fuel rod state when within time step iteration is repeated.

3. Methodology

3.1 Principle Component Analysis

The data compression method under consideration is based on the Principle Component Analysis (PCA) [5]. PCA is the statistical method that processes the linear correlations of a vector set and produces the optimal basis vectors such that the variance of truncation error is minimal. This concept is well-known and it is widely used for many applications of reactor physics [6-11]. Therefore, here we explain only the main idea of the method.

Let's consider (*n*, *N*)-matrix **X** having *n* rows and *N* columns. In our application *n* is a number of time steps and *N* is a total number of spatial nodes. The total number of spatial nodes is equal to a number of fuel rods by a number of axial nodes. We assume that $n << N$ and that the mean vector of rows of **X** is equal to zero.

Let's approximate data **X** by an orthonormal set of *m* basis vectors. The basis vectors forms (*m*,*N*)-matrix which we denote as **Y**. The truncation error is the difference between original vectors **X** and a linear combination of basis vectors, i.e.

$$\mathbf{X} - \mathbf{C} \times \mathbf{Y}.$$

Matrix **C** is a (*n*,*m*)-matrix of approximation coefficients. Here and further the symbol × denotes the matrix dot product, while · denotes the tensor product. The minimum value of the truncation error is observed if vectors $\mathbf{C} \times \mathbf{Y}$ are the orthogonal projection of vectors **X** onto the linear subspace formed by **Y**. Therefore, the approximation coefficients are

$$\mathbf{C} = \mathbf{X} \times \mathbf{Y}^T.$$

Now let's consider the variance of the truncation error and find the optimum basis vectors of **Y**. Remember, that the basis vectors are normalized such that $\mathbf{Y}\mathbf{Y}^T = \mathbf{I}$. The variance V_m depends on a number *m* of basis functions and it is calculated as follow

$$n \cdot V_m^2 = trace\ [\ (\mathbf{X} - \mathbf{C} \times \mathbf{Y})^{\mathrm{T}} \times (\mathbf{X} - \mathbf{C} \times \mathbf{Y})\ ]$$

We denote **I** is an identity matrix, $\mathbf{P} = \mathbf{Y}^{\mathrm{T}} \times \mathbf{Y}$ is a projection matrix and $\mathbf{M} = \mathbf{X}^{\mathbf{T}} \times \mathbf{X}$ is a covariance matrix. All these matrices have the shape (*N*,*N*). Then the previous equation is transformed in the form

$$n \cdot V_m^2 = trace\ [\ (\mathbf{I} - \mathbf{P}) \times \mathbf{M}\ ].$$

The trace of a matrix is the sum of its eigenvalues. Projector $\mathbf{I} - \mathbf{P}$ is orthogonal, therefore spectrum of matrix $(\mathbf{I} - \mathbf{P}) \times \mathbf{M}$ is a subset of the spectrum of matrix **M**. In order to minimize the variance matrix **P** should be a projector on any eigensubspace of **M**. Therefore, basis vectors of **Y** called principle components are the eigenvectors of matrix **M** and the minimal variance is the sum of eigenvalues σ_i of **M**, i.e.

$$n \cdot V_m^2 = \sigma_{m+1} + \sigma_{m+2} + \ldots + \sigma_n.$$

Obviously, the principle components should belong to the largest eigenvalues of covariance matrix **M**. Solution of the eigenvalue problem is conducted by the Singular Value Decomposition (SVD) algorithms. It is worth to note that PCA is efficient for the high correlated data. Otherwise the truncation error, especially in the maximum norm, is huge.

3.2 Residual Matrix and Sparse Representation

The ouput data of multiphysics simulation contains many variables distributed in time and space, such as linear power, fuel temperature, cladding stress and strain etc. Although these variables can be processed as a large data set, we begin our research from the independent compression of each variable and looking forward a more general approach in future works. In additional, this approach is beneficial from the computational point of view since the covariance matrix rank is not too large and computational cost of SVD algorithm is reasonable.

Consider multi-physics variable *u* and (*n*, *N*)-array **U** which contains the corresponding numerical simulation data. One can turn **U** into a centered data set **X** and calculate *m* principle components such that the resulting truncation error satisfies to a given tolerance. However, these direct approach does not show enough well results due to few features of the considered distributions:

1) presence of large variations over time and space;
2) weak spatial correlation of some locations.

The first problem is fixed by a proper normalization of data **U**. Introduce (*n*,)-vector **A** which is the sum of *N* columns of data **U**. Vector **A** depends on the time step and represents the magnitude of variable *u*,

$$A_i = U_{i1} + \ldots + U_{iN} \qquad (1)$$

Along with the magnitude vector we introduce the (*N*,)-vector **B** that catches the average shape of variable *u* over a time,

$$B_j = (U_{1j} / A_1 + \ldots + U_{nj} / A_n) / n \qquad (2)$$

Finally, we normalize and center the given data set **U** as follow

$$X_{ij} = U_{ij} / (\delta + A_i B_j) - 1. \qquad (3)$$

The absolute tolerance δ is used here in order to prevent the division by zero. One can easily confirm that $X_{1j} + \ldots + X_{nj} = 0$ with the accuracy δ.

As we noted above, PCA is able to approximate well only the high-correlated data. However, for example, some locations in a power distribution can be not correlated due to the different position of control rods. Therefore, along with PCA another approach is needed for catch and save the uncorrelated part. Here we use the residual matrix **Z** which is the simple difference between the original data set **X** and its PCA approximation. Thus the approximation formula of original data **U** is

$$\mathbf{U} = \mathbf{A} \times \mathbf{B} \times (\mathbf{I} + \mathbf{C} \times \mathbf{Y} + \mathbf{Z}) \qquad (4)$$

It should be noted, that this representation is accurate if there is not any assumptions about matrix **Z**. However, we assume the most elements of the residual matrix are close to zero. Therefore, the small elements of **Z** are filtered in order to the essential remaining part can be stored in the sparse format.

3.3 Compression Rate

A compression algorithm is designed to minimize the memory costs of data. Let us evaluate the memory costs required according to formula 4. Assume that the memory of a float number is 8 bytes and the memory of an integer number is 4 bytes. Then the memory size of the original data **U** is

$$S_U = 8 \cdot n \cdot N .$$

As mentioned above, residual matrix **Z** is represented in the sparse format. If the number of non-zero elements is $K << n \cdot N$ then $16 \cdot K$ bytes is needed to store the three arrays for represent the residual matrix in the coordinate format: *a*) data array ($8 \cdot K$ bytes); b) column coordinates ($4 \cdot K$ bytes) and c) row coordinates ($4 \cdot K$ bytes). The total memory size of approximation 4 is

$$S_m = 8 \cdot (m \cdot N + n \cdot m + n + N + 2 \cdot K_m). \qquad (5)$$

The more principle components *m* is employed, the less number K_m of non-zero elements is needed in **Z**. However, because *m* and *K* have the different multipliers in formula 5, there is an optimal number of principle components m^* for which S_m takes a minimal value.

For further numerical estimations we define the compression rate as a ratio between the memory of the original and compressed data,

$$R = 100\% \; S_{m^*} / S_U$$

3.4 Compression Algorithm

The compression algorithm consists of few steps depicted in Fig.1. The input arguments are data **U**, relative tolerance ε, absolute tolerance δ and a maximum number of principle components $M < min(n,N)$. Initial number of principle components $m = 0$. Then algorithm makes the next steps:

1. Calculate the magnitude vector **A**
2. Calculate the average shape function **B**
3. Normalize and center original data **U**
4. Calculate first *M* principle components by PCA
5. Calculate approximation coefficients **C**
6. Calculate residual matrix **Z** for *m* principle components
7. Eliminate the close to zero elements from the residual matrix according to the rule $|z_{ij}| < \varepsilon$ and count the number of remaining non-zero elements *K*
8. Estimate memory size S_m by formula 5. If $S_{m-1} < S_m$ go to step 6 with $m := m + 1$, otherwise exit from the cycle.

The algorithm output are vectors **A** and **B**, dense matrices **Y** and **C**, sparse residual matrix **Z**.

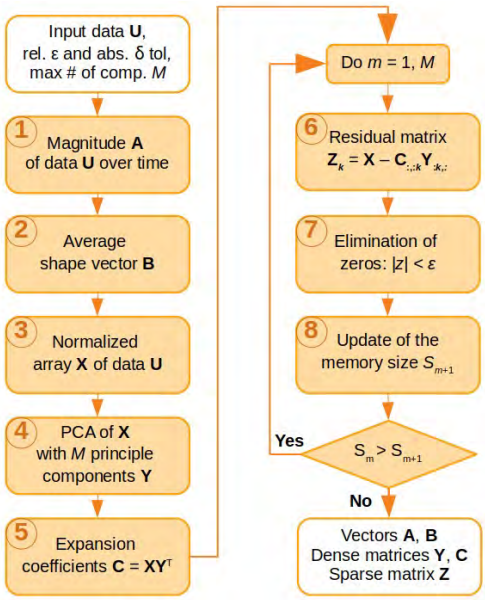

Fig.1. Flowchart of the data compression algorithm

4. Numerical Results

The compression algorithm has been tested for the output data file obtained by simulation of the control rod ejection accident in pressurized water reactor core OPR-1000. The fresh core of first cycle is considered. The initial total power is 1 MW.

OPR-1000 core consists of 177 square assemblies arranged as depicted in Fig.2. Each assembly contains 5 guide tubes and 236 fuel rods placed in 16x16 lattice. Sizes of a fuel assembly and a fuel rod are shown in Fig.3. Number of axial layers in the fuel performance and thermal-hydraulic models is set to 10. At the initial state all control rods of 1 – 6 groups are located at the bottom position while the groups 7, 8 and 9 are fully ejected out of the core. From 100 ms to 200 ms the control rods are gradually ejected from the core until the upper limit.

For demonstration of the compression algorithm we present the case with three ejected control rods placed as depicted in Fig.2. In this case the inserted reactivity is about 1.2 $. It causes a large power pulse suppressed by increase of the fuel temperature and Doppler effect. Power distribution at the pick of the pulse shown in Fig.4. The simulation is performed using time step 10 ms and total number of made time steps is 50. Therefore, the shape of the data to be compressed is n = 50 rows and N = 16·16·236·10 columns. We demand the compression of data with a small loose of accuracy withing tolerance $\delta = 10^{-3}$.

In the considered example the compression rate of linear power distribution is about 30% only. That is because the power strictly depends on the control rod position and many components are needed for an accurate approximation in the region from 100 and 200 ms. However, the other parameters are approximated much better that is shown in Table I. Mostly one or two components is enough for achieve the accuracy 0.1%, while the fraction of non-zero elements in the residual matrix is about 1%.

The compression algorithm has been applied for various configurations of ejected control rods, initial power levels, number of axial nodes and time step sizes. Some of the compression results are presented in Table II. Refining of the axial and time mesh does not lead to the principle component increase. However, the size of the principle components depends on the number of axial nodes. Therefore, the compression rate drops twice for the twice decreased time step size, while keeps the same if the number of axial steps increases.

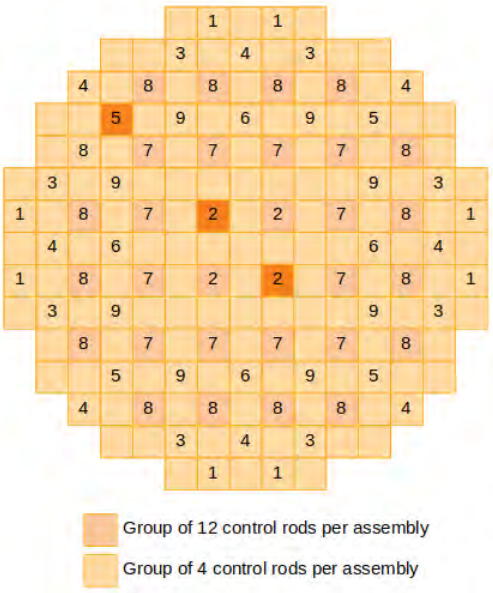

Fig.2. Control rods groups of OPR-1000 reactor core. Ejecting groups are colored by orange.

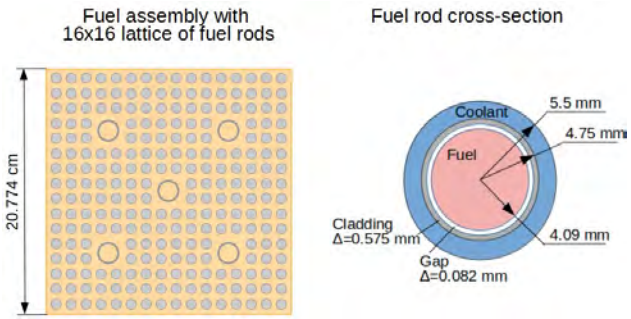

Fig.3. Fuel assembly and fuel rod geometry and sizes.

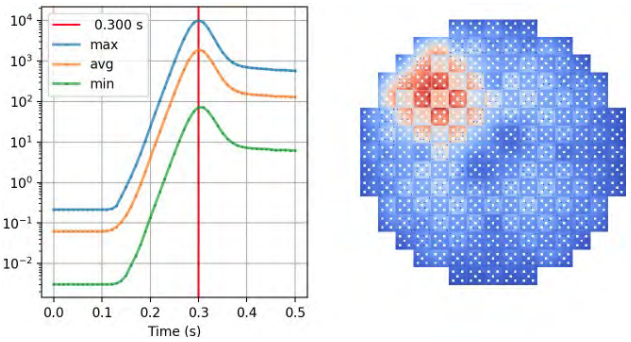

Fig.4. Linear power pulse (*W/cm*) and shape function at the middle height of reactor core

TABLE I. Compression Rate of Multiphysics Parameters

Parameter	Units	m	R, %	Max. rel. error, %
Cladding temperature	*K*	1	4	0.1
Cladding hoop stress	*MPa*	1	4	0.2
Pellet hoop strain	%	2	6	0.0
Coolant temperature	*K*	1	4	0.0
Gap thickness	*μm*	1	4	0.1
Fuel enthalpy	*cal/g*	1	4	0.1
Gap HTC	$W/(K \cdot m^2)$	1	6	0.2
Linear power	*W/cm*	13	30	1.3
Pellet temp.	*K*	2	6	0.1

TABLE II. Compression Rate of Multiphysics Simulation Output Data Files

#	Nz	Δt, *ms*	Size, GB		R, %
			Original	Compressed	
1	5	5	4.3	0.14	3
2	5	10	2.2	0.14	6
3	10	5	8.7	0.26	3
4	10	10	4.4	0.29	6

6. Conclusions

The multiphysics pin-by-pin code for steady-state and transient simulation has been developed at UNIST. The multiphysics code is based on the coolant thermal-hydraulic code CTF, fuel performance code FRAPTRAN and neutron nodal diffusion code RAST-K. The code is supposed to be used for uncertainty analysis of PWR using sampling approach. The result of the sampling is large number of output data files that have to be stored in hardware for further processing. These files require a lot of memory, therefore the storage and proper compression of the multiphysics data becomes the important problem.

The developed data compression algorithm is designed to decrease the memory costs of transient multiphysics output data. The algorithm is based on decomposition of data on high and low correlated parts. The high correlated part is approximated by PCA, while the low correlated part is saved in a sparse format.

The compression algorithm has been applied to the control rods ejection accident of OPR-1000 core simulated by the developed multiphysics code. It has been shown that the data can be compressed up to 3-6 % of initial size of data. The relative error of the compressed data is less than 1%.

Although the developed algorithm demonstrates enough well results, the further improvement is suggested:

1. Use one set of principle components which is common for all multi-physics variables in order to improve the compression rate
2. Take into account the correlations of assembly shapes for further compression rate improvement
3. Develop a recurrent algorithm for on-the-fly data compression in order to save a memory during calculation

Acknowledgements

This research was partially supported by the project (L17S018000) by Korea Hydro & Nuclear Power Co. Ltd. This work was partially supported by the National Research Foundation of Korea (NRF) grant funded by the Korea government (MSIT) (No. NRF-2019R1C1C1010063).

References

1. F. Khoshahva, M. Park et al. Vanadium, rhodium, silver and cobalt self-powered neutron detector calculations by RAST-K v2.0. Annals of Nuclear Energy, vol. 111, pp. 644-659, 2018
2. K.J. Geelhood, W.G. Luscher, and J.M. Cuta. FRAPTRAN-2.0: A Computer Code for the Transient Analysis of Oxide Fuel Rods. PNNL-19400, Vol. 1, rev.1, Pacifc Northwest National Laboratory, Richland, WA, 2016
3. K.J. Geelhood and W.G. Luscher. FRAPTRAN-2.0: Intenral Assessment. PNNL-19400, Vol. 2 Rev. 2, Pacifc Northwest National Laboratory, Richland, WA, 2016
4. M.J. Thurgood et al. COBRA-TF Development. In 8th Water Reactor Safety Information Meeting, 1980.
5. A. Gorban et al. Principle Manifolds for Data Visualization and Dimension Reduction. Springer-Verlag Berlin Heidelberg, 2008
6. A. SARTORI, A. CAMMI, and L. LUZZI, “A Multi-Physics Reduced Order Model for the Analysis of theLead Fast Reactor Single Channel,”Annals of NuclearEnergy,87, 198–208 (2016).
7. Buchan, A., Calloo, A., Goffin, M., Dargaville, S., Fang, F., Pain, C., Navon, I., 2015. A POD reduced order model for resolving angular direction in neutron/photon transport problems. J. Comput. Phys. 296, 138.
8. Pasetto, D., Ferronato, M., Putti, M., 2017. A reduced order model-based preconditioner for the efficient solution of transient diffusion equations. Int. J. Numer. Meth. Eng. 109, 1159.
9. Semenov, A., Shchukin, N., Ryabov, N., 2007. Using of the reduction order model for the reconstruction of the power distribution by the lateral ionization chambers. J. Nucl. Eng. 4, 47
10. A. YANKOV, “Analysis of Reactor Simulation Using Surrogate Model,” Ph.D. thesis, University of Michigan (2015).
11. M. Matsushita, T. Endo, A. Yamamoto, T. Kitao, "Development of Reduced Order Model of Severe Accident Analysis Code for Probabilistic Safety Margin Analysis," Proc. PHYSOR2018, Cancun, Mexico, Apr. 22- Apr. 26, 2018, (2018).

Proceedings of the Reactor Physics Asia 2019 (RPHA19) Conference
Osaka, Japan, Dec. 2-3, 2019

Refinement of Convolutional Neural Network for Neutronic Design Parameter Prediction of a Loading Pattern

Hyunbin Jang[a], Ho Cheol Shin[b], Hyun Chul Lee[a*]
[a]*School of Mechanical Engineering, Pusan National University, 2, Busandaehak-ro 63beon-gil, Geumjeong-gu, Busan, 46241, Korea*
[b]*Core and Fuel Analysis Group, Korea Hydro and Nuclear Power Central Research Institute (KHNP-CRI), Daejeon, Korea*
[*]Corresponding author: hyunchul.lee@pusan.ac.kr

Abstract

The computational cost of numerical analysis codes for optimizing the loading pattern is expensive. Therefore, in the previous study, the convolutional neural network was selected as the deep learning algorithm to replace the numerical analysis codes in order to quickly find the optimal loading pattern. Furthermore, in this study, we improved the prediction model of peaking factor and cycle length by applying internal structure modification, the normalization and regularization. The improved model predicts the reactor design parameters well within a small error range compared with the reference numerical code.

Key Words: **Loading pattern optimization, Deep learning, Convolutional neural network, Reactor design parameter**

1. Introduction

Optimization for the loading pattern of the reactor core is to find the most economical loading pattern among all the various cases that satisfy the safety limit. To obtain an optimal loading pattern, all loading patterns must be computed as numerical analysis codes. However, despite improved computer performance, it takes a lot of computation time to find optimized loading patterns. If the reactor design parameters can be predicted with low computational cost, the optimized loading pattern can be found faster than the numerical methods.

In the previous study, a comparison of prediction performance between Convolutional Neural Network (CNN) and Deep Neural Network (DNN) was performed [1]. As a result of the comparison, CNN algorithm showed higher performance in both the peaking factor and the cycle length.

In this study, internal structure modification of the CNN algorithm was performed to improve prediction accuracy. Also, normalization and regularization were applied to the peaking factor and the cycle length prediction algorithm. Furthermore, sensitivity tests based on the depth of the prediction models were performed to further improve the prediction accuracy.

2. Review of Previous Works

The development of an artificial neural network (ANN) algorithm to find the optimal loading pattern was performed to replace the numerical analysis codes. A deep learning algorithm was used to predict the peaking factor and the cycle length because it can be used for learning by extracting more complex and nonlinear features using multiple hidden layers.

2.1 Automatic generation of training data

A system for generating training data was established to obtain a large amount of training data. The training data was automatically generated by the system using the STREAM / RAST-K 2.0 [2-4] code system and updated with the big data. The STEAM code is a neutron transport analysis code for Light Water Reactor (LWR) core calculation and developed at Ulsan National Institute of Science and Technology (UNIST) and the RAST-K 2.0 code is a diffusion nodal code for Pressurized Water Reactor (PWR) core analysis developed by UNIST.

2.2 Selection of deep learning algorithm

The CNN algorithm was adopted to preserve spatial information and to consider the effects of surrounding assemblies. The comparison of prediction performance between the DNN which is the basic algorithm of deep learning and the CNN was performed. As a result of the comparison, the CNN showed better performance than the DNN, but it was necessary to improve prediction performance. Table I and Table II summarize the peaking factor and the cycle length prediction errors of the DNN and CNN.

Table I. Prediction error of the peaking factor using DNN and CNN

Algorithm	Prediction error	
	RMS (%)	Max (%)
DNN	9.28	60.91
CNN	1.74	13.81

Table II. Prediction error of the cycle length using DNN and CNN

Algorithm	Prediction error	
	RMS (%)	Max (%)
DNN	1.06	3.98
CNN	1.07	2.12

3. Improvement of Prediction Accuracy

In the previous study, the CNN was adopted as the deep learning method to replace numerical analysis codes in loading pattern optimization. Furthermore, in this study, internal structural modification of the CNN, normalization and regularization were applied to improve prediction performance [5].

3.1 Normalization and regularization

Normalization of input data is a technique of machine learning used when the scale of input data is different. The normalization means normalizing the data dimensions to the same scale. Applying the normalization leads to more stable and faster learning. In this study, Min-Max scaling is applied and normalized data can be obtained as:

$$x_{norm} = \frac{x_{data} - x_{min}}{x_{max} - x_{min}}, \quad (1)$$

Where,

x_{data}= original value,
x_{max} = maximum value in data,
x_{mim} = minimum value in data.

The input data size is 8x8 of the quarter core size and the input parameters are fuel enrichment, BP fraction, number of BP pins, and assembly burnup. Fig. 1 shows a example of input data.

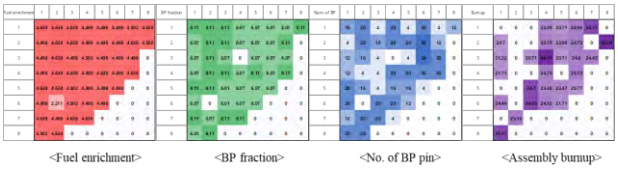

Fig. 1. Example of input data

Overfitting refers to the problem of poor performance in test data because it is learned too closely fit to limited training data. In this study, the L2 regularization was applied to improve the performance by preventing overfitting. It is the most common regularization method that prevents overfitting resulting from large weighting parameters. The new loss function L' is implemented by adding a regularization term to the general loss function L.

$$L' = L + \frac{\lambda}{2m}\sum_{i=1}^{m}\omega_i^2, \quad (2)$$

Where,

λ = regularization parameter,
ω = weighting parameter.

In the gradient descent parameter update, using the l2 regularization reduces all weight values.

3.2 Internal structure modification of CNN

In order to increase the prediction performance of the peaking factor, learning was performed by increasing the weight layer depth like VGG NET [6]. Also, the max pooling layer was removed to prevent loss of assembly information. Therefore, the training data size is fixed to 8x8. Fig. 2 shows the internal structure of the prediction models, where model 1 is the configuration used in the previous study and model 2 is the modified configuration through sensitivity test in this study.

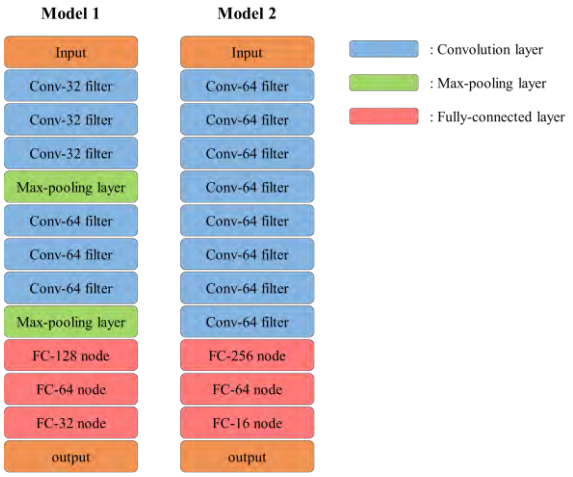

Fig. 2. Internal structures of the prediction models

4. Results and Discussion

In this section, the prediction performance of the improved model is evaluated. The normalization and the L2 regularization were applied to both the peaking factor and the cycle length prediction models. Since the cycle length prediction model showed sufficient prediction accuracy, the sensitivity test through internal structure modification was performed only for the peaking factor prediction model. The overall structure of the prediction model is shown in Fig. 2. In addition, 3x3 convolution filter, about 42,000 training data, and 6,000 test data were used equally in all models. The prediction models were implemented using the TensorFlow library [7].

4.1 Training Result of Peaking Factor

In this content, the performance of the improved peaking factor prediction model is evaluated. The performance of model 1 and 2 using normalization and L2 regularization (M1NR and M2NR) are compared with the results of the previous study (M1). Fig. 3 shows the process of the prediction error convergence according to the training step using test data. Fig. 4~6 show the training results of peaking factor using M1, M1NR, and M2NR.

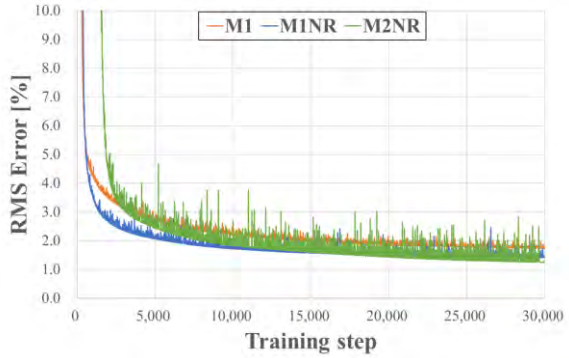

Fig. 3. Convergence process for peaking factor prediction

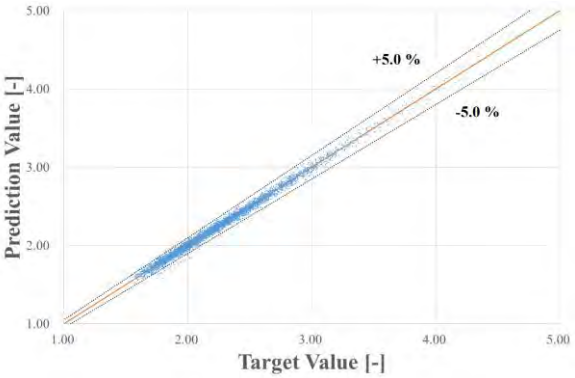

Fig. 4. Training result of peaking factor using M1

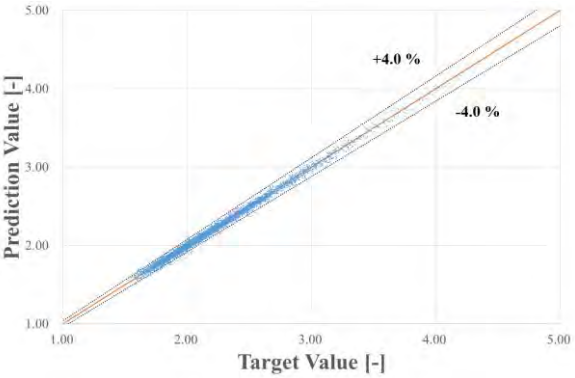

Fig. 5. Training result of peaking factor using M1NR

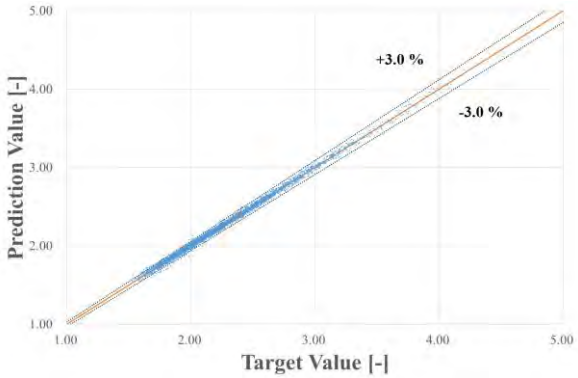

Fig. 6. Training result of peaking factor using M2NR

As the results of training using the M1, 98.7% of the test data is predicted within 5% error range. With M1NR, 98.5% of the test data is predicted within 4% error range, and with M2NR, 98.3% of the test data is predicted within 3% error range. The results show that the M2NR has the best performance in peaking factor prediction. Table III summarizes the peaking factor prediction errors.

Table III. Prediction error of peaking factor

Model	Prediction error	
	RMS (%)	Max (%)
M1	1.74	13.81
M1NR	1.42	8.41
M2NR	1.14	6.92

4.2 Training Result of Cycle Length

In this content, the performance of M1, M1NR and M2NR in cycle length prediction were compared. Fig. 7 shows the process of the prediction error convergence according to the training step using test data. Fig. 8~10 show the training results of the cycle length using M1, M1NR and M2NR.

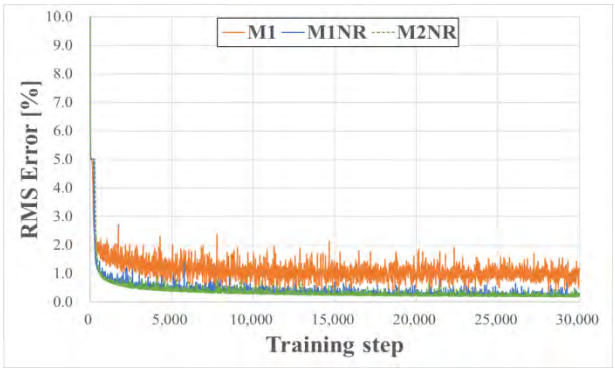

Fig. 7. Convergence process for cycle length prediction

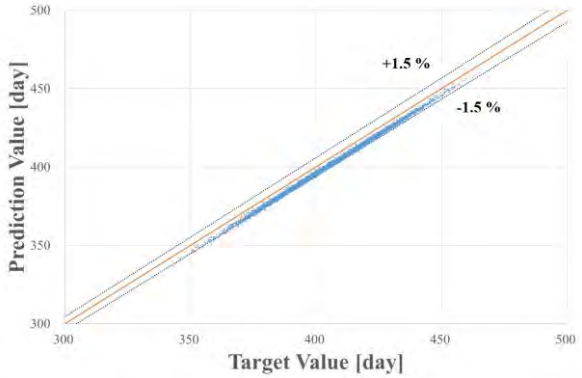

Fig. 8. Training result of cycle length using M1

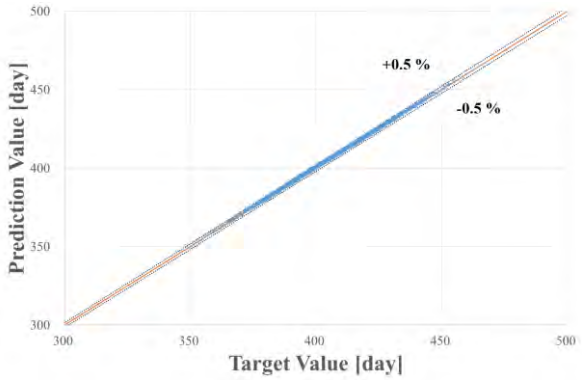

Fig. 9. Training result of cycle length using M1NR

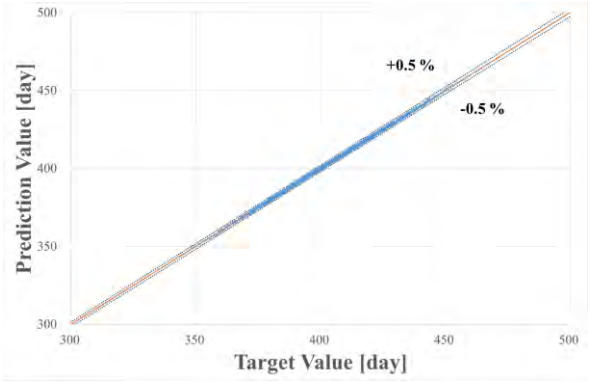

Fig. 10. Training result of cycle length using M2NR

As the results of training using the M1, 96.9% of the test data is predicted within 1.5% error range. With M1NR, 95.6% of the test data is predicted within 0.5% error range, and with M2NR, 99.0% of the test data is predicted within 0.5% error range. The results show that the M2NR has the higher performance in cycle length prediction. Table IV summarizes the cycle length prediction errors.

Table IV. Prediction error of cycle length

Model	Prediction error	
	RMS (%)	Max (%)
M1	1.07	2.12
M1NR	0.26	1.44
M2NR	0.18	1.96

5. Conclusions

In this study, we successfully applied the internal structure modification, the normalization and the regularization as a way to improve the prediction performance. As a result of the model improvement, the prediction performance was improved in both the peaking factor and the cycle length. In particular, the cycle length prediction model has sufficient prediction accuracy, while the peaking factor prediction model still needs improvement.

Therefore, the peaking factor prediction model needs to improve the performance through additional sensitivity test for the weight layer depth and the number of filters. Furthermore, we will also develop the prediction models of other parameters such as power distribution and MTC as future work.

Acknowledgements

This research was supported by the project (Development of Artificial Intelligence Technology for Multi-Cycle Core Design Based on Machine Learning) by Korea Hydro & Nuclear Power Co. Ltd.

References

1. H. Jang, et al, “Prediction of Pressurized Water Reactor Core Design Parameters Using Artificial Neural Network for Loading Pattern Optimization,” Korea Nuclear Society Jeju, Korea, May 22-24 (2019).
2. S. Choi, et al, “Resonance Treatment using Pin-Based Pointwise Energy Slowing-Down Method,” Journal of Computational Physics, **330**, pp.134 (2017).
3. J. Choe, et al, “Verification and validation of STREAM/RAST-K for PWR analysis,” Nuclear Engineering and Technology, **51**, *2*, pp.356 (2019).
4. F. Khoshahval, et al, “Vanadium, rhodium, silver and cobalt self-powered neutron detector calculations by RAST-K v2.0,” Annals of Nuclear Energy, **111**, pp.644 (2018).
5. Karpathy, et al, "Cs231n convolutional neural networks for visual recognition," Neural networks, 1 (2016).
6. K. Simonyan, et al, “Very deep convolutional networks for large-scale image recognition,” arXiv preprint arXiv:1409.1556.
7. M. Abadi, et al., “TensorFlow: A System for Large-scale Machine Learning,” *Proceeding of the 12th USENIX conference on Operating Systems Design and Implementation*, Savannah, Nov. 2-4, pp.265, GA (2016).

Proceedings of the Reactor Physics Asia 2019 (RPHA19) Conference
Osaka, Japan, Dec. 2-3, 2019

Experimental Validation for the Pin-wise Isotope Prediction Methodology

Minjae Lee, Taeyang Noh and Myung Hyun Kim*
Kyung Hee University, 1732 Deogyeong-daero, Giheung-gu, Yongin-si, Gyeonggi-do, Republic of Korea, 17104
*Corresponding author: mhkim@khu.ac.kr

Abstract

Detail and reliable isotope assessment of spent nuclear fuels is an essential task for criticality analysis, shielding design, decay heat cooling analysis and others in the application for storage, transport and disposal. Because of time limitation and data processing issues, material assay has been evaluated in the unit of assembly. A mathematical methodology to predict pin-wise isotope inventory was developed and used for the reutilization of spent fuel pins in PWR. In this paper, validation of this method is done by comparing with experimental data published by OECD/NEA. Validation was carried out by comparing with experimental data for three reactor cases. Because quite a few data are available from experiment, calculation results were compared only for a few fuel pins in an assembly. For the most of major isotopes which has large impact, it was found that error to the experimental data is less than 5%. However, in case of minor isotopes with small number density and low importance to criticality, error exceeds over 5%, while they are within an error band of 30%. Importance of each isotope to the criticality was measured by an index of importance; as ratio of isotope contribution to total absorption or fission rates. It was found that all isotopes showing large error over 5% have very low importance compared with major isotopes. In case of short half-life fission products, calculation was overestimated because of fast radioactive decay and unknown cooling time of spent fuels. Overall estimation results are reasonably good within an acceptable range.

Key Words: **Validation, Pin-wise, Isotope prediction, Experimental data**

1. Introduction

Management of spent nuclear fuels has been studied in order to reduce safety margin related to many applications such as reprocessing, interim storage, cask transportation and final disposal. Technical assessments for criticality analysis, shielding design, decay heat evaluations need time-dependent data of detail isotopic concentrations in all spent fuel pins. However, it has been out of scope of core designer to treat all kinds of isotopes in all fuel pins. Modern core design methodologies based on nodal methods gave big benefits in saving of computational time and memory. However, detail pin-wise information has been lost during book keeping for spent fuel management. Therefore, available data for all spent fuels are not complete. Most of isotopic inventory data are managed as assembly-averaged data and number of isotopes traced are limited to a certain number.

A mathematical methodology to predict pin-wise isotope inventory was developed and used for the reutilization of spent fuel pins in PWR [1, 2]. Pin-wise isotope prediction is done by three stages. First stage is to predict pin-wise burnup distribution by simulating core calculation with historical information about spent fuel assemblies. Second step is the production of database as many tables of isotope number densities vs. pin burnup. Last stage is to match the pin information to the proper table and interpolate to assess the fuel pin composition. We may establish many different model options depending on the level of depth and width of treatment.

In this study, validation of mathematical model has been tried. A numerical benchmark may be the easiest way to be achieved in a near future. Monte Carlo simulation for all spent fuel pins in a full-sized reactor model cannot be solved for all kinds of isotopes and for a long period of fuel depletion history. A simplified numerical benchmark problem can be developed as a future work scope. In the other stream, experimental assessment is available for a limited number of isotopes. Recently experimental assessment results for a few fuel pins from many PWR and BWR cores were published. OECD/NEA organized an international collaboration team to assess the spent fuel compositions and published two documents [3, 4]. In this paper, simulation of assembly-wise depletion was performed and predicted isotopic compositions were compared with OECD/NEA experimental data.

2. Analysis method

2.1 Pin-wise isotope prediction methodology

Pin-wise isotope prediction methodology consists of three stages. Figure 1 shows the pin-wise isotope prediction methodology procedure. First stage is to predict the pin-wise burnup distribution through core calculation and reconstruction techniques. Core calculation was done by DeCART2D and MASTER code package which was developed by Korea Atomic Energy Research Institute (KAERI) [5, 6]. Group constant and form function library is produced by DeCART2D and HELIOS 47group library. Then, core calculation is done by MASTER with group constant and form function library, and pin-wise burnup distribution was forecasted by using reconstruction method.

Second stage is production of isotope number density tables as a function of burnup through assembly calculation by using DeCART2D. In this stage, grouping of fuel pins inside of an assembly is an essential work to reduce the number of tables. Isotope number density tables are classified along with fuel pin types and loaded place within assembly. Fuel pins in the center of assembly and near the water hole have a characteristic to deplete faster than other pins while fuel pins located in edge of assembly fuel pin is depleted slowly. Through this way, isotope number density tables between 3 and 6 is produced in accordance with assembly loading pattern. Last Step is to predict isotope composition by usual interpolation technique using prepared group of tables and predicted burnup information.

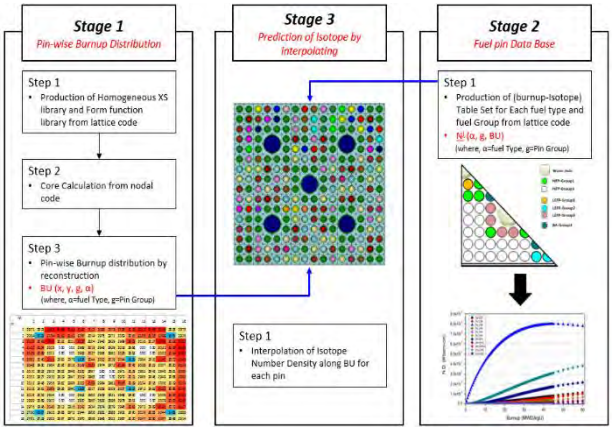

Fig. 1. Pin-wise isotope prediction methodology scheme

2.2 OECD/NEA experimental data

In this study, OECD/NEA experimental data is used for validating pin-wise isotope prediction methodology. These experimental data are managed by OECD/NEA for the purpose of burnup credit license and many types of reactor are included in this package. Since methodology was developed only for Pressurized Water Reactor (PWR) cores, selection of data set for comparison was limited to PWR cores.

Table I. OECD/NEA Measurement Data List

Reactor	Assembly	Pin	Sample Name	Burnup (GWd/tU)	Cooling Time (d)
Takahama Unit 3	NT3G23	SF95	2	24.35	841
			3	35.42	
			4	36.69	
			5	30.4	
		SF96	2	16.44	1051
			3	28.2	
			4	28.91	
			5	24.19	
	NT3G24	SF97	2	30.73	1358
			3	42.16	
			4	47.03	
			5	47.25	
			6	40.79	
Calvert Cliffs Unit 1	D047	MKP 109	CC	37.12	4656
			LL	27.35	
			P	44.34	
	D101	MLA 098	BB	26.62	1824
			JJ	18.68	
			P	33.17	
Ohi Unit 1&2	G13	N13	91E07	52.434	No data
	17G	C5	89G01	21.465	No data
			89G03	28.717	
		F4	89G08	30.172	
			89G10	38.496	
		O13	89G05	25.137	

** Cooling time means the days from shutdown to the measured day*

Because detailed core configuration is not described, core calculation is not able. Instead of output of core calculation, measured burnup is used. The burnup calculated by the MASTER code is assumed to be same to the burnup in Table I. Finally, number density is calculated by the DeCART2D code. Cooling time is not considered in this step, because the number of isotopes are not enough in spite of complex decay chain.

2.3 Evaluation procedure

Results were checked by using the ratio of calculated value to experimental data (i.e., C/E ratio). In this study, acceptable error was defined to 5% for major isotopes and 30% for insignificant isotopes which have negligible amount or affect negligible in terms of criticality. Amount of isotope is evaluated by number density and impact on criticality is assessed by cross section. Impact is evaluated by ratio of isotope contribution to total absorption, which is named "importance" in this paper. The importance is defined as the followings and they are evaluated by MCNP6 where ENDF-VII.1 is used as nuclear library data. In order to suggest trustworthy results, relative error was set under 50pcm. Also, cycle is divided into 50 inactive cycle and 100 active cycle that each cycle has 50000 neutron histories.

$$\text{Importance} = \begin{cases} \dfrac{\Sigma_{f,N^i}^{pin}}{\Sigma_{a,total}^{pin}}, (for\ \ fissile\ \ material) \\ \dfrac{\Sigma_{f,N^i}^{pin}}{\Sigma_{a,total}^{pin}}, (for\ \ fertile\ \ and\ \ fission\ \ product) \end{cases}$$

3. Results

3.1 Takahama Unit 3

Results of takahama unit 3 is shown in Fig. 2 and Fig. 3. Isotope distribution along error band is listed in Table II. Error under 5% means to predict suitably. Evaluation for number density and importance is conducted for isotope above 5% error. In below figures, the boundaries of 5% and 30% errors are represented by the red line and blue line, respectively.

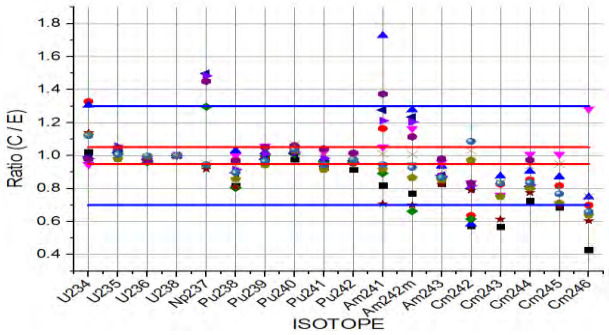

Fig. 2. C/E ratio – Takahama Unit 3 (actinide)

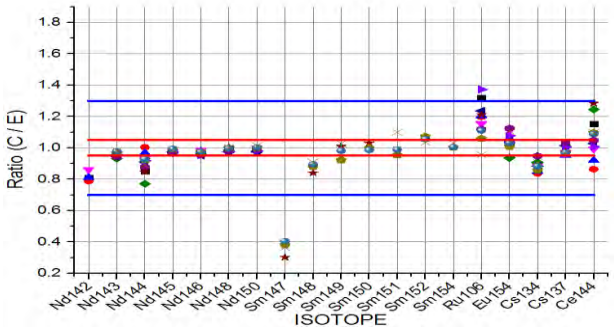

Fig. 3. C/E ratio – Takahama Unit 3 (fission product)

Table II. Isotope List according to Relative Error

Relative Error	Isotope
Under 5%	^{235}U, ^{236}U, ^{238}U, ^{239}Pu, 240Pu, ^{241}Pu, ^{242}Pu, ^{143}Nd, ^{145}Nd, ^{146}Nd, ^{148}Nd, ^{150}Nd, ^{149}Sm, ^{150}Sm, ^{151}Sm, ^{152}Sm, ^{154}Sm, ^{137}Cs
From 5% to 30%	^{234}U, ^{238}Pu, ^{241}Am, ^{242m}Am, ^{243}Am, ^{244}Cm, ^{245}Cm, ^{142}Nd, ^{144}Nd, ^{148}Sm, ^{154}Eu, ^{134}Cs, ^{144}Ce
Above 30%	^{237}Nd, ^{242}Cm, ^{243}Cm, ^{147}Sm, ^{106}Ru, ^{125}Sb

Evaluation of number density was performed on 50GWd/tU burnup. Number density is shown in Table III. Except for ^{144}Nd and ^{144}Ce, isotopes have small number density. Therefore, these isotopes are accepted up to 30% error. However, there are much number density for ^{144}Nd and ^{144}Ce, so importance evaluation has to be done. Table IV shows importance for criticality. While ^{144}Nd and ^{144}Ce have a large number of number density, importance is low because of low XS. Therefore, 30% error is permitted for ^{144}Nd and ^{144}Ce.

Table III. Fuel Pin Number Density – 50GWd/tU

	Isotope	Number Density		Isotope	Number Density
1	U238	2.1430E-02	21	Pu238	7.4531E-06
2	U235	1.8755E-04	22	Sm152	5.0241E-06
3	Pu239	1.4265E-04	23	U235	4.8103E-06
4	U236	1.3013E-04	24	Am243	4.2682E-06
5	Cs137	7.0714E-05	25	Sm147	3.8790E-06
6	Pu240	6.5680E-05	26	Cm244	1.9880E-06
7	Nd144	5.8388E-05	27	Sm154	1.9858E-06
8	Pu241	4.1129E-05	28	Eu154	1.5008E-06
9	Nd143	4.0688E-05	29	Nd142	1.3353E-06
10	Nd146	3.8602E-05	30	Am241	1.2836E-06
11	Nd145	3.5367E-05	31	Sb125	8.1856E-07
12	Nd148	2.0039E-05	32	Sm151	5.7244E-07
13	Pu242	1.9741E-05	33	Cm242	5.6097E-07
14	Np237	1.5468E-05	34	Sm149	1.4852E-07
15	Ce144	1.5419E-05	35	Cm245	1.3374E-07
16	Sm150	1.5346E-05	36	Am242m	2.9900E-08
17	Ru106	1.1559E-05	37	Cm243	1.9222E-08
18	Nd150	9.6805E-06	38	Cm246	1.4228E-08
19	Sm148	8.3964E-06			
20	Cs134	8.3225E-06			

Table IV. Importance for Criticality – 50GWd/tU

	Isotope	Number Density		Isotope	Number Density
1	U238	2.6333E-01	21	U234	1.0486E-03
2	Pu239	1.5645E-01	22	Cm244	4.5129E-04
3	U235	8.1254E-02	23	Nd144	2.7590E-04
4	Pu240	7.6283E-02	24	Cm245	2.3868E-04
5	Pu241	5.0495E-02	25	Am242m	2.2667E-04
6	Nd143	1.1440E-02	26	Nd148	1.4737E-04
7	U236	9.6123E-03	27	Sm148	1.3824E-04
8	Pu242	6.6572E-03	28	Nd146	9.6285E-05
9	Np237	6.2807E-03	29	Nd150	6.5580E-05
10	Sm149	6.2133E-03	30	Cm242	4.5848E-05
11	Sm152	5.1523E-03	31	Sm154	3.8387E-05
12	Sm151	4.3474E-03	32	Cs137	2.6230E-05
13	Eu154	3.8636E-03	33	Ce144	2.4606E-05
14	Nd145	3.6388E-03	34	Nd142	2.3695E-05
15	Am243	3.0888E-03	35	Sb125	2.1928E-05
16	Pu238	2.2487E-03	36	Cm243	2.1789E-05
17	Sm150	2.1295E-03	37	Ru106	1.2698E-05
18	Am241	1.6682E-03	38	Cm246	7.9081E-07
19	Cs134	1.2551E-03			
20	Sm147	1.1605E-03			

3.2 Calvert Cliffs Unit 1 and Ohi Unit 1&2

Calvert Cliffs Unit 1 and Ohi Unit 1&2 also apply same method for evaluation. Results of Calvert Cliffs and Ohi is shown in Fig. 4, 5 and 6. ^{237}Nd, ^{242}Cm and ^{243}Cm is matched well in Calvert Cliffs and Ohi reactor while error is large in Takahama reactor.

However, some isotopes are overestimated. These isotopes are listed in Table V. In case of ^{241}Pu, it is overestimated a little bit for Calvert Cliffs Unit 1. But this isotope is estimated very accurately in other cases. There are no reasons to be overestimated, without decay-out. We guess that workers had experiment with too long cooling time in the Calvert Cliffs reactors, therefore short-lived isotopes were decayed out. Half-life of ^{241}Pu and ^{155}Eu are 14.3 years and 4.75 years, respectively. On the other hand, calculated value are results at the time of discharged point without any cooling time because there are no data of

cooling time in the referred documents. Five isotopes may be overestimated for the same reasons in case of Ohi Unit 1&2. Half-life of ^{154}Eu, ^{125}Sb, ^{134}Cs, ^{106}Ru and ^{144}Ce are 8.6 years, 2.76 years, 2.07 years, 371.8 days and 284.9 days, respectively. These are the shortest value in case of Ohi Unit 1&2.

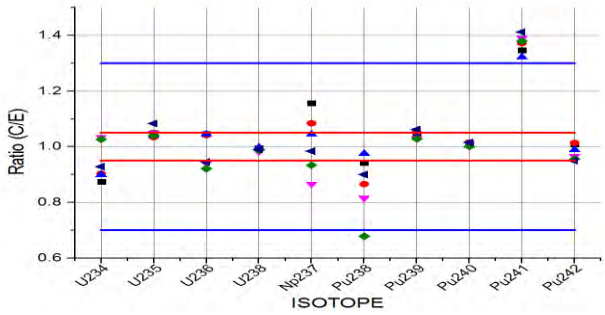

Fig. 4. C/E ratio – Calvert Cliffs Unit 1 (actinide)

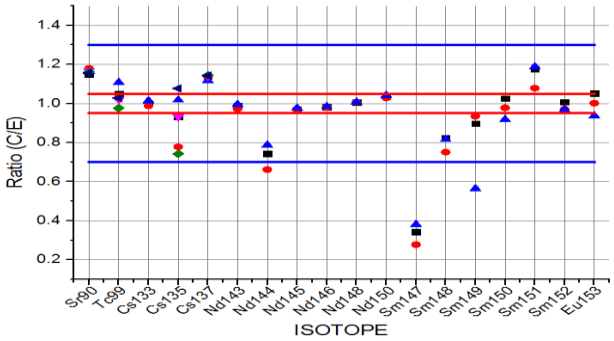

Fig. 5. C/E ratio – Calvert Cliffs Unit 1 (fission product)

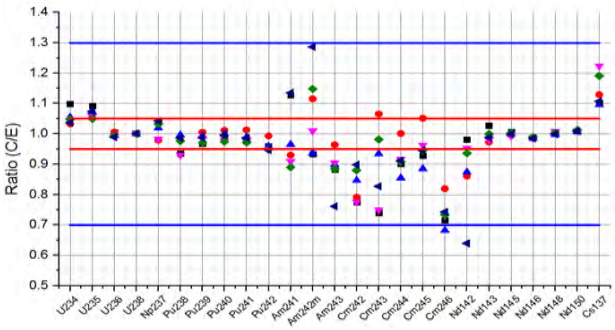

Fig. 6. C/E ratio – Ohi Unit 1&2 (all isotopes)

Table V. Overestimated Isotopes (C/E ratio)

Calvert Cliffs Unit 1						
Isotope	MKP109 CC	MKP109 LL	MKP109 P	MLA098 BB	MLA098 JJ	MLA098 P
Pu241	1.347	1.372	1.323	1.391	1.380	1.413
Eu155	2.618	2.607	2.422	-	-	-
Ohi Unit 1&2						
Isotope	N13 91E07	C5 89G01	C5 89G03	F4 89G10	F4 89G08	O13 89G05
Eu154	1.727	1.545	1.635	1.887	1.894	1.604
Sb125	8.020	7.497	7.100	8.758	8.876	7.600
Cs134	5.419	5.128	4.864	5.485	5.280	4.897
Ru106	36.036	31.488	28.657	34.144	31.255	28.589
Ce144	109.996	88.012	86.157	94.216	81.858	81.806

4. Conclusions

In this paper, validation of pin-wise isotope prediction was tried by comparing with OECD/NEA experimental data. Twenty-five assay sample in three reactors were used for validation. Objective error for major isotopes was set as 5% and 30% error was permitted for minor isotopes with small amount and low importance to criticality. Isotope's amount is evaluated by number density and importance is assessed by ratio of isotope's reaction rate to fuel pin total reaction rate. Based on these results, most isotopes satisfy the objective error. However, there were overestimated isotopes which did not satisfied the objective error. These isotopes have relatively short half-life. It can cause the radioactive decay during cooling time and it will be studied in the future.

Acknowledgements

This work was supported by Korea Hydro & Nuclear Power Company, LTD (Project No. 2017-Tech-12).

References

1. Aung T.D. and M.H. Kim, "Investigation into Fuel Pin Reshuffling Options in PWR In-core Fuel Management for Enhancement of Efficient Use of Nuclear Fuel", *Nucl. Eng. Des.*, 273, 332, (2014).
2. Z. Zafar, Y.S. Park and M.H. Kim, "Evaluation of the reutilization of used nuclear fuel in a PWR core without reprocessing", *Nucl. Eng. Tech.*, 2, 51, 345-355, (2018).
3. ALEJANO.C, et al., Spent Nuclear Fuel Assay Data for Isotopic Validation, NEA/NSC/WPNCS/DOC (2011)5, Nuclear Science Committee, Working party on Nuclear Criticality Safety (WPNCS), Expert Group on Assay Data of Spent Nuclear Fuel (EGADSNF), OECD/NEA, Jun. (2011).
4. P.Ortego, et al., Evaluation Guide for the Evaluated Spent Fuel Nuclear Fuel Assay Data Base, NEA/NSC/R(2015)8, Nuclear Science Committee, Working party on Nuclear Criticality Safety (WPNCS), Expert Group on Assay Data of Spent Nuclear Fuel (EGADSNF), OECD/NEA, Feb. (2016).
5. B.O. Cho, H.G. Joo, J.Y. Cho and S.Q. Zee, "MASTER-3.0: Multi-purpose Analyzer for Static and Transient Effects of Reactors", KAERI/TR-2061/2002, Korea Atomic Energy Research Institute, (2002).
6. J.Y. Cho, J.C. Lee, K.H. Lee, S.Y. Park, H.J. Park, H.Y. Kim, K.Y. Kim, H.J. Jung, J.S. Song, S.Q. Zee, C.K. Jo and H.C. Lee, "DeCART2D v1.0 User`s Manual", KAERI/TR-5116/2013, Korea Atomic Energy Research Institute, (2013).

Proceedings of the Reactor Physics Asia 2019 (RPHA19) Conference
Osaka, Japan, Dec. 2-3, 2019

The Neutron Streaming Correction Method in the Homogenization of Pebble-bed HTGR Reflector

Yutong Wen*, Ding She, Lei Shi and Jing Zhao
Institute of Nuclear And New Energy Technology, Tsinghua University
Tsinghua University, Haidian, Beijing, China
wenyt17@mails.tsinghua.edu.cn

Abstract

In pebble bed high temperature gas-cooled reactors (HTGRs), the graphite reflector generally contains void regions including control rod channels, absorber ball channels and coolant channels. However, reactor physics design of HTGR based on deterministic codes usually models the reactor by two dimensional r-z coordinate system, which means the regions must be homogenized in azimuthal direction. PANGU is a modern computer code for pebble-bed HTGR physics analyses and fuel cycle simulations. This paper demonstrates a new method, for the homogenization of the reflector, implemented in PANGU code. The new method, taking into account the neutron streaming effect, can improve the accuracy of neutronics calculation.

Key Words: **HTGR, PANGU code, void regions, neutron streaming, homogenization**

1. Introduction

In HTGR physics analysis deterministic code such as VSOP [1] and PANGU [2], the reactor is usually modelled in two dimensional r-z coordinate system, assuming that the model is azimuthally uniform. While, in high temperature gas-cooled reactors (HTRGs), the graphite reflector generally contains certain void regions, such as control rod channels, absorber ball channels and coolant channels, which have azimuthal dependence. It is required that the regions containing void channels must be homogenized in the azimuthal direction. The most convenient method is to treat the regions by volumetric homogenization. However, because of the neutron streaming effect of voided region, the volumetric homogenization will bring about remarkable deviation.

In this paper, a new method for homogenization is introduced. In this method, the equivalent diffusion coefficient will be calculated to take into account the neutron streaming effect. The method has been implemented in PANGU code.

The remainder of the paper is organized as follows. In Section 2, the general correction method for neutron streaming in HTGR has been introduced. The new method is described in Section 3. In Section 4, the numerical tests of HTR-10 and HTR-PM are demonstrated, and the conclusion remarks are provided in Section 5.

2. Neutron streaming effect correction in HTGR

In the regions, which contains void space, neutrons can stream through the void space, increasing the migration length. The simple volumetric homogenization can lead to the underestimation of the neutron transport, resulting in less neutron leakage out of the region [3]. In pebble bed HTGR, neutron streaming effect is remarkable in pebble bed. To treat the streaming effect in pebble bed, the general method is to calculate the spatially homogenized diffusion coefficient, using streaming effect correction factor of diffusion coefficient, as is proposed by Behrens (1949) [4]

$$D_{\mathrm{hom}} = C_{str}\, \bar{D}_{\mathrm{vol}} \qquad (1)$$

D_{hom} is the homogenized diffusion coefficient. The formula of C_{str} can be referred in Reference [4]. D_{vol} is the volume-averaged diffusion coefficient.

$$D_{\mathrm{vol}} = \frac{1}{3\sum_{tr,vol}} \qquad (2)$$

Where $\sum_{tr,vol}$ is the volume-averaged transport cross-section.

Lieberoth etc (1980) proposed a new formula for

the correction factor C_{str}, on basis of Behrens' work, which can be referred in Reference [5] The formula is of general validity in various HTGR physics analysis codes [6][7]. The HTGR graphite reflector also contains void regions. However, the spatial distribution and geometry shape of the void regions, as well as the neutron's anisotropy are all distinctly different from that in pebble bed. Therefore the correction factor of pebble bed can not be applied to the reflector. But the streaming correction of pebble bed provides the idea that, the streaming effect can be taken into account by adjusting the spatially homogenized diffusion coefficient.

3. Description of the method

The homogenized diffusion coefficient is calculated by the following:

$$D_{\text{hom}} = \frac{1}{3\bar{\Sigma}_{tr}} \tag{3}$$

Where $\bar{\Sigma}_{tr}$ is the spatially homogenized transport cross-section. The simplest way to obtain $\bar{\Sigma}_{tr}$ is by volume-averaging as eq (2). However, In general, it is calculated by following some equivalence principles. Reference [8] suggests a method to obtain homogenized cross-sections, which approximates the neutron's transmission behavior, from a simplified physics model. This method follows the equivalence principle that the transmission probability of the region is preserved. This method is designed for the spatial homogenization of fuel grains in HTGR fuel elements. The idea of the method is applied in this work to calculate the $\bar{\Sigma}_{tr}$.

In the HTGR reflector, there are various void channels, which vary distinctly in geometry shape. For the sake of simplicity and convenience, a simplified transmission model is established. As is shown in Figure 1. The void region is supposed to be located at the center of a square in circle form (or infinite length cylinder), surrounded by the reflector material. The area of the circle is the mean value of the cross sectional areas of all void channels, and the side length of the square is determined by the following:

$$L = \sqrt{\frac{\pi}{f}} R \tag{4}$$

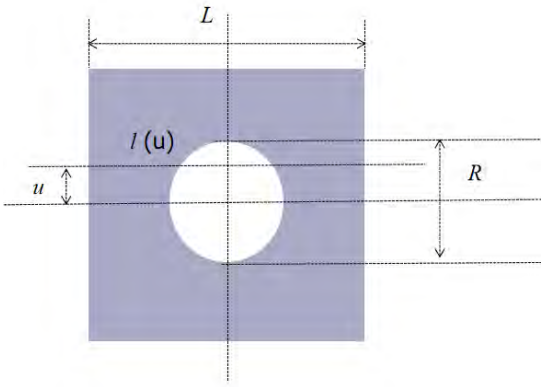

Fig. 1. The transmission model of the reflector

Where L is the side length of the square. f is the void fraction. R is the radius of the void circle. The model assumes that a parallel neutron beam transverses the square. The penetrating probability p can be calculated by:

$$p = \frac{2}{L}\int_0^{\frac{L}{2}} du \cdot e^{-\Sigma_{tr} l(u)} \tag{5}$$

And $l(u)$ is the length of the neutron trajectory in reflector material.

$$l(u) = \begin{cases} L - 2\sqrt{R^2 - u^2} & \text{u < R} \\ L & \text{u >= R} \end{cases} \tag{6}$$

The integration in Eq (5) is solved numerically. Then, it is assumed that the square is filled with homogeneous media. Importantly, this work assumes that the homogenization procedure preserves the penetration probability. The penetration probability of the homogenized square is

$$p = e^{-\bar{\Sigma}_{tr} L} \tag{7}$$

Fig. 2. The spatial homogenization, by preserving the penetration probability

To preserve the penetration probability, the equivalent transport cross section is calculated as:

$$\bar{\Sigma}_{tr} = -\frac{\ln p}{L} \tag{8}$$

The homogenized diffusion coefficient is calculated by Eq (3).

4. Numerical Validation

4.1 Description of Test Cases

The method for homogenized diffusion coefficient has been implemented in PANGU code. In order to validate the method for homogenized diffusion coefficient calculation, The calculation models of HTR-10 and HTR-PM are tested. The calculation results of keff is compared with that by MCNP.

The HTR-10 is a test modular pebble bed HTGR, designed and constructed by Tsinghua University's Institute of Nuclear Energy Technology (INET) . The horizontal cross sectional view of HTR-10 is shown in Fig.3 (a). As is shown in Fig 3 (b), the annular regions containing void channels are homogenized in the azimuthal direction, for the 2D physics calculation by PANGU.

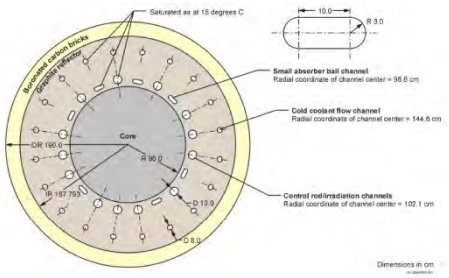

(a) The 3D high-fidelity model of HTR-10

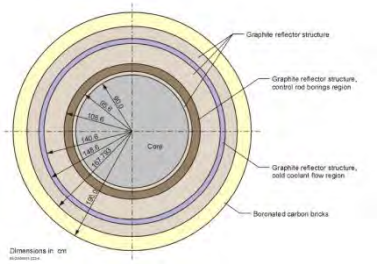

(b) The simplified 2D model of HTR-10 [9]

Fig. 3. The horizontal cross sectional view of HTR-10

There are two annular zones requiring homogenization. The inner annular zone contains 13 control rods channels and the 7 absorber ball channels. And the outer annular zone contains 20 coolant flow channels. The detailed design parameters of HTR-10 can be found in Reference [10].

The two annular zones are separately calculated by transmission model, to obtain the homogenized transport cross sections $\bar{\Sigma}_{tr}$. The radius of the void circle R in Eq(4) is determined by the mean value of the cross sectional areas of all void channels in the annular zone.

HTR-PM is a modular pebble bed HTGR demonstration power plant, approved as part of the National Major Science and Technology Project in China. The distribution of the void channels in HTR-PM is similar with that in HTR-10, and the design parameters can be found in Reference [11].

4.2. Calculation Results and Analysis

4.2.1 HTR-10

Due to the fact that PANGU is a deterministic code, quite different from Monte Carlo code in neutronics calculation. It is necessary to evaluate the inherent difference between the two codes. The deviation caused by the void channels must be removed at first. Hence, the annular zones containing void regions are firstly treated by volumetric homogenization, as is shown in Fig 3 (b). The 2D model is calculated by MCNP and PANGU. The results of the keff are given in Table I. It can be concluded that, without the void regions, the neutronics calculation results of PANGU code agrees well with the MCNP code.

Table I. Calculation results of HTR-10 (without void channels) by PANGU and MCNP

code	keff	Error(pcm)
MCNP	1.22225	
PANGU	1.22119	-106

The calculation results of HTR-10 are demonstrated in Tab II. It can be found that, without correction, the keff calculated by PANGU code is higher than that by MCNP code by more than 1000 pcm. While, after the streaming correction, the deviation decreases remarkably.

Table II. Calculation results of keff for HTR-10 model by PANGU and MCNP

code	keff	Error(pcm)
MCNP(3D high fidelity)	1.21071	
PANGU(2D ,without correction)	1.22119	1048
PANGU(2D)	1.21026	-45

4.2.2 HTR-PM

Table III demonstrates the test results of keff for HTR-PM. Similar with the results of HTR-10, the streaming correction significantly reduces the difference between the calculation results of the MCNP 3D model and PANGU 2D model.

Table III. Calculation results of keff for HTR-PM model by PANGU and MCNP

code	keff	Error(pcm)
MCNP(3D high fidelity)	1.24337	
PANGU(2D,without correction)	1.25498	1161
PANGU(2D)	1.24575	238

4.2.3 Analysis

From the results of HTR-10 and HTR-PM, it can be found that the results of calculation by PANGU, with streaming correction, agrees well with that by MCNP, which illustrates that streaming effect can be taken into account by calculating the homogenized diffusion coefficient, thus reducing the deviation caused by the homogenization from 3D model to 2D model.

5.Conclusion

In this work, a method is proposed to treat the neutron streaming effect in the homogenization of HTGR reflector, which contains void channels, by calculating the equivalent homogenized diffusion coefficients. In this method, a simplified physics model is proposed to approximate the regions containing void channels. The homogenization follows the rule that, the neutron penetrating probability should be preserved. The method has been implemented in PANGU code. The numerical results of a simplified HTGR model agree well with Monte Carlo 3D high-fidelity solutions. It can be concluded that the method effectively improve the accuracy of PANGU 2D neutronics calculation.

References

1. E. TEUCHERT et al., “V.S.O.P. (’94) Computer Code System for Reactor Physics and Fuel Cycle Simulation,” Juel-2897, Institut für Sicherheitsforschung und Reaktortechnik (1994).
2. Ding She et,PANGU code for pebble-bed HTGR reactor physics and fuel cycle simulations,Annals of Nuclear Energy,Volume 126,2019
3. Auwerda G J , Kloosterman J L , Lathouwers D , et al. Effects of random pebble distribution on the multiplication factor in HTR pebble bed reactors[J]. Annals of Nuclear Energy, 2010, 37(8):1056-1066.
4. Behrens D J . The Effect of Holes in a Reacting Material on the Passage of Neutrons[J]. Proceedings of the Physical Society, 2002, 62(10):607.
5. Lieberoth J , Stojadinovi? A . Neutron Streaming in Pebble Beds[J]. Nuclear Science and Engineering, 1980, 76(3):336-344.
6. Gougar H D . The Application of the PEBBED Code Suite to the PBMR-400 Coupled Code Benchmark - FY 2006 Annual Report[J]. Office of Scientific & Technical Information Technical Reports, 2006.
7. Bernnat W , Feltes W . Models for reactor physics calculations for HTR pebble bed modular reactors[J]. Nuclear Engineering and Design, 2003, 222(2-3):331-347.
8. She D , Liu Z , Shi L . An Equivalent Homogenization Method for Treating the Stochastic Media[J]. Nuclear Science & Engineering the Journal of the American Nuclear Society, 2017, 185(2):351-360.
9. Terry W K , Kim S S , Montierth L M , et al. Evaluation of the HTR-10 Reactor as a Benchmark for Physics Code QA[J]. Office of Scientific & Technical Information Technical Reports, 2006.
10. Evaluation of high temperature gas cooled reactor performance: Benchmark analysis related to initial testing of the HTTR and HTR-10, IAEA-TECDOC-1382, International Atomic Energy Agency, Vienna 2003.
11. Zhang Z , Wu Z , Sun Y , et al. Design aspects of the Chinese modular high-temperature gas-cooled reactor HTR-PM[J]. Nuclear Engineering and Design, 2006, 236(5-6):485-490.

Proceedings of the Reactor Physics Asia 2019 (RPHA19) Conference
Osaka, Japan, Dec. 2-3, 2019

Application of Neutron Balance Analysis in Enhancing the Temperature Reactivity Feedback of Gas-cooled Fast Reactor

Ce Zhang[a], Youqi Zheng[a,*] and Linfang Wei[a]
[a] *School of Nuclear Science and Technology, Xi'an Jiaotong University, Xi'an 710049, China*
[*]Corresponding author: yqzheng@mail.xjtu.edu.cn

Abstract

In recent years, more gas-cooled fast reactor are designed for various applications. However, for all kinds of gas coolant, the temperature reactivity feedback is generally very small, which will cause safety problem in the transients. Out of this consideration, the optimization methods for enhancing the negative feedback are investigated. A series of gas-cooled fast reactor core designs are calculated by the SARAX (System for Advanced Reactor Analysis at Xi'an Jiaotong University) code system. To further study the influence factors of temperature reactivity feedback, the neutron balance method is applied. Reactivity decomposition based on neutron balance method is available for the quantitative analysis of reactivity change. On the basis of neutron balance, the coolant expansion reactivity can be decomposed into the contribution from reaction-types, nuclides, or energy-groups. The decomposition results support that the optimization measures are effective.

Key Words: **reactivity feedback, neutron balance, core design, GFR**

1. Introduction

Since GFR was listed as one of the six generation IV reactors, the application and performance of gas coolant in nuclear reactors have been developed greatly. The Helium, the He-Xe mixed gas and so on have been investigated a lot.

However, all kinds of gas-cooled fast reactors have potential problems in the transients. Because of its small density and cross-sections, the coolant provides little reactivity feedback, while it has much weaker heat transfer capacity than water or liquid metal. Thus, it's required to take a special design to enhance the temperature feedback of the reactor to improve the safety performance.

This paper describes the works on enhancing the temperature reactivity feedback of a medium size gas-cooled fast reactor. Two methods are tried. One is to use the moderator material to adjust the neutron spectrum, which aims to enhance the Doppler feedback. The other is to enhance the leakage of the core, which aims to make the coolant expansion feedback larger. To guide the tests, the neutron balance method is applied in the analysis, which quantitatively supports the enhancing approaches.

2. Reactivity temperature feedback analysis

The feedback of PWR mainly comes from Doppler Effect of fuel and the feedback of the influence of coolant density on the neutron slowing ability with change of temperature. The difference of coolant temperature between the inlet and outlet of PWR core is mostly 30℃, which leads to small overall temperature rise of the core material. However, this difference of gas cooled fast reactor core is 150~200℃. In addition to the feedback brought by fuel Doppler Effect and coolant expansion effect, the expansion effect of core material should also be considered.

The Doppler Effect mainly comes from the change of neutron absorption capacity of heavy nuclides in the core. When the temperature increases, the height of the resonance peak of the nuclide decreases and the width becomes wider, and the total resonance absorption capacity will become stronger, which will cause the absorption cross section of the neutron to become larger and the total reactivity of the system to become smaller.

The coolant expansion feedback mainly comes from the change of neutron slowing ability caused by the change of coolant density and the influence of the decrease of density on the neutron leakage of reactor. The specific contribution of gas coolant expansion feedback has not been studied quantitatively. It can refer to two main reasons for the density change of water in PWR. First, the absorption of neutrons by the coolant decreases when the density changes, while the thermal neutron utilization coefficient of fuel increases, leading to the increase of reactivity. Second, as the density changes, the coolant slow down less neutrons, which increases the number of epithermal neutrons, and thus the resonance absorption of the fuel increases, making the reactivity decrease. Therefore, only appropriate

water-uranium ratio can make the coolant void feedback negative [1]. Different from PWR, the reaction cross-section of gas coolant with neutrons is much smaller than that of water, and the absorption of neutrons is much smaller. The influence of the neutron moderation and leakage in the reactor core needs to be further analyzed in combination with specific reactor cores.

The expansion effect of structure materials is considered by referring to sodium-cooled fast reactor, which is mainly divided into axial expansion of fuel, radial expansion of cladding and assembly wall, and expansion of grid plate under the core. The feedback effect of axial expansion of fuel mainly comes from the reduction of reactivity caused by the decrease of nuclear density of fuel and the increase of reactivity caused by axial elongation of fuel. The radial expansion feedback effect of cladding and component wall is mainly due to the reduction of coolant caused by volume expansion of cladding and component wall, which further influences the reactivity. The influence of expansion of the lower grid plate on reactivity is increased by increasing the spacing of components and increasing coolant and core leakage.

In our research, the reactivity temperature feedback is composed of Doppler Effect, coolant expansion reactivity and the expansion effect of structural materials. The structure materials used in the nuclear reactor are all tested by engineering application. It's not wise to optimize the reactivity feedback in terms of materials selection. In consequence, our optimization focuses on the Doppler Effect and coolant expansion reactivity.

3. Neutron balance method

It can be known from the above qualitative analysis that we can enhance the Doppler Effect by softening neutron energy spectrum and reduce coolant expansion reactivity by increasing core neutron leakage. But the traditional way can only provide qualitative judgment. Neutron balance method is able to help analyze reactivity feedback of core design quantitatively.

The neutron balance method can be used for detailed reactivity decompositions in terms of different reaction-types, nuclides or energy groups [2]. Reference to the method of decompositions of void reactivity in the sodium-cooled fast reactor, we take a similar way to analyze the Doppler Effect and the coolant expansion of gas-cooled fast reactor core.

In the core, the steady-state neutron transport equation can be shown as below:

$$\begin{aligned}&\Omega\cdot\nabla\psi(r,E,\Omega)+\Sigma_t(r,E)\psi(r,E,\Omega)\\&=\frac{\chi(E)}{4\pi k_{eff}}\iint\nu\Sigma_f(r,E')\psi(r,E',\Omega')dE'd\Omega'\\&+\iint\Sigma_s(r;E',\Omega'\to E,\Omega)\psi(r,E',\Omega')dE'd\Omega'\end{aligned}\tag{1}$$

If Eq. (1) is integrated over space and energy in a specific region, we can obtain neutron balance equation:

$$\begin{aligned}&\iiint\Omega\cdot\nabla\psi(r,E,\Omega)dEd\Omega dV\\&+\iiint\Sigma_A(r,E)\psi(r,E,\Omega)dEd\Omega dV\\&=\frac{1}{k_{eff}}\iiint\nu\Sigma_f(r,E')\psi(r,E',\Omega')dE'd\Omega'dV\end{aligned}\tag{2}$$

The transport solver of SARAX uses the SN node method based on arbitrary triangular mesh. Calculation mesh can be shown like Fig. 1

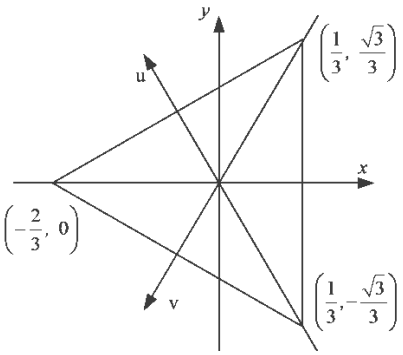

Fig. 1. Triangular calculation mesh.

The single-group steady-state neutron transport equation in m-th discrete direction in the mesh is:

$$\begin{aligned}&2\mu_x^m\bar{\psi}_x^m+2\mu_u^m\bar{\psi}_u^m+2\mu_v^m\bar{\psi}_v^m+\\&+\frac{\xi^m}{h_z}\left(\bar{\psi}_{z+}^m-\bar{\psi}_{z-}^m\right)+\Sigma_t\bar{\psi}^m=\bar{Q}\end{aligned}\tag{3}$$

Where m is the number of energy group, μ_x, μ_u, μ_v and ξ are the quadrature for the three triangular surfaces and z axis, $\bar{\psi}_x$, $\bar{\psi}_x$ and $\bar{\psi}_x$ are the three surfaces flux, $\bar{\psi}_{z+}$ and $\bar{\psi}_{z-}$ are the nodal top and bottom surface flux, h_z is the nodal height, $\bar{\psi}$ is the nodal average flux. Σ_t is total cross section and $\bar{Q}$ is the neutron generation term.

Integrate Eq. (3) over space and energy like Eq. (2). It can lead to the discrete neutron balance equation:

$$\begin{aligned}&\int\sum_{m=1}^{M}w_m\left(2\mu_x^m\bar{\psi}_x^m+2\mu_u^m\bar{\psi}_u^m+2\mu_v^m\bar{\psi}_v^m\right)dV\\&+\int\sum_{m=1}^{M}w_m\frac{\xi^m}{h_z}\left(\bar{\psi}_{z+}^m-\bar{\psi}_{z-}^m\right)dV+\int\sum_{m=1}^{M}w_m\Sigma_A\bar{\psi}^m dV\\&=\frac{1}{k_{eff}}\int\sum_{m=1}^{M}\upsilon\Sigma_f w_m\bar{\psi}^m dV\end{aligned}\tag{4}$$

Where w_m is the weight coefficient in each discrete direction, and meets that $\sum_{m=1}^{M}w_m=1$.

The Eq. (4) is the form of neutron balance used in SARAX. The first integral term represents radial leakage (Lr), the second is axial leakage (La), the third is

absorption (A , it can be decomposed into capture C and fission F). And the right of Eq. (4) is neutron production (P). We simplify this equation and replace k_{eff} into reactivity ρ :

$$\rho = 1 - \frac{L + C + F}{P} \tag{5}$$

When the reactivity changes, it's approximately believed that the neutron reaction rates are independent of each other, and that the change of reactivity is linear with the change of the disturbance quantity of each reaction rate. We can get that:

$$\begin{aligned} \Delta\rho &= \left(\frac{\partial\rho}{\partial L}\right)\Delta L + \left(\frac{\partial\rho}{\partial C}\right)\Delta C + \left(\frac{\partial\rho}{\partial F}\right)\Delta F + \left(\frac{\partial\rho}{\partial P}\right)\Delta P \\ &= -\frac{L'-L}{P} - \frac{C'-C}{P} - \frac{F'-F}{P} + \frac{P'-P}{k_{eff}P} \\ &= \Delta\rho_L + \Delta\rho_C + \Delta\rho_F + \Delta\rho_P \end{aligned} \tag{6}$$

Eq. (6) is the result of decomposition reactivity based on neutron balance method. The changes of reactivity are decomposed into different reaction type. According Eq. (4), when we integrate the reaction rates by singe energy or nuclide, it can be decomposed into every energy group or every nuclide. In consideration of that neutron leakage is weakly correlated with nuclide, and that fission reaction and neutron production can't be optimized by choosing nuclides, we only take the decomposition into capture reaction of each nuclide. These can be expressed as Eq. (7) and Eq. (8).

$$\Delta\rho = \Delta\rho_{g1} + \Delta\rho_{g2} + \cdots + \Delta\rho_{G-1} + \Delta\rho_G \tag{7}$$

$$\Delta\rho_C = \frac{\Delta C_{U-235}}{P} + \frac{\Delta C_{U-238}}{P} + \cdots + \frac{\Delta C_{C-12}}{P} + \frac{\Delta C_{O-16}}{P} \tag{8}$$

4. Core design and numerical result

A medium size gas-cooled fast reactor core is analyzed in this paper. Some special designs are proposed to enhance the temperature reactivity feedback. There are two main optimization measures. One is that $ZrH_{1.7}$ material layer is added in the process of assembly design. The other is increasing the neutron leakage by special core layout.

4.1 Fuel assembly design

The fuel assembly design is shown in Fig. 2. The flat-to-flat distance is 8.50 cm, thickness of assembly wall is 0.2 cm, and there is coolant in a thickness of 0.1 cm between assemblies. So the center distance of assemblies is 8.60 cm. And in the fuel region, there are 6 rings or 91 rods in total. There is a ZrH1.7 layer thick outside the fuel region. It can slow down the neutrons, enhancing the Doppler Effect [3].

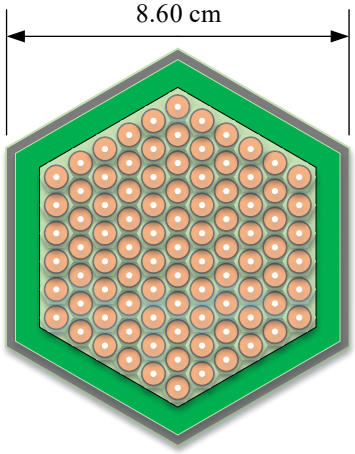

Fig.2. Fuel assembly design diagram.

4.2 Core layout

The core layout is shown in Fig. 3. In order to obtain large neuron leakage rate, it adopts a complex geometry layout. The active region of inner fuel assemblies is divided into three layers by two blanket layer axially. And blanket assemblies are also arranged radially.

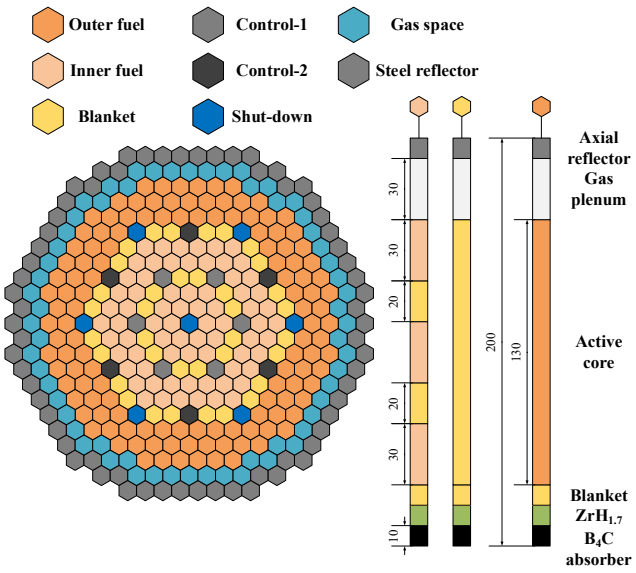

Fig. 3. Layout of gas-cooled core design

The depleted uranium blanket is expected to absorb neutrons to increase leakage rate, and then enhance the coolant expansion reactivity [4]. The radial gas space is designed to improve the radial leakage [5]. When the temperature of core increases, the density of the gas in this space decreases. So that more neutrons can run out of the active core.

4.3 Numerical results of the design

The isothermal coefficient is calculated by SARAX in a critical condition. The coolant expansion reactivity is obtained when coolant density decreased by 1%. The

Doppler Effect is calculated at 600K and 900K of fuel temperature. The structure expansions reactivity changes are all calculated in the condition of expansion 1%. That the respective reactivity divides by the corresponding temperature will reach the isothermal coefficient.

As we can see in Table I given below, the comparison between a normal gas-cooled core and optimized one. The optimization measures greatly enhanced Doppler Effect, while coolant expansion reactivity and the structure expansion gets smaller. The $ZrH_{1.7}$ material slows down neutrons, that decreases the neutron free path, enhancing the Doppler Effect as well as letting the leakage down. The blanket in the core absorb neutrons and increase the leakage on the opposite. The sum reactivity feedback is enhanced by the optimization measures.

Table I. Isothermal coefficient of the core

Reactivity feedback	Normal /pcm·K^{-1}	Optimization /pcm·K^{-1}
Coolant expansion	-1.884	-1.072
Doppler	-0.219	-2.478
Fuel axial expansion	-0.378	-0.168
Cladding and wall radial expansion	0.098	0.006
Grid expansion	-1.066	-0.394
Sum	-3.449	-4.11

The coolant expansion reactivity decomposition in reaction-type and nuclide are given in Table II and Table III, in energy-group shown in Fig. 4. As it can be seen, the main components are radial leakage and capture reaction. Table III lists a part of nuclides contribution on the capture. It mainly consists of the U-238 and structure materials element such as Fe, Ni and so on. As for the energy-group decomposition, it's basically negative in all group and closely related to neutron flux.

Table II. Coolant expansion reactivity decomposition in reaction-type

Reaction-types	Value/pcm
Radial leakage	-2.743
Axial leakage	-0.902
Capture	-2.809
Fission	-0.448
Production	-0.833
Sum	-6.842

Table II. Capture reaction decomposition in nuclide

Nuclides	Value/pcm
U-235	1.227
U-238	-1.044
Fe	-0.498
Ni	-0.427
...	...
Sum	-2.809

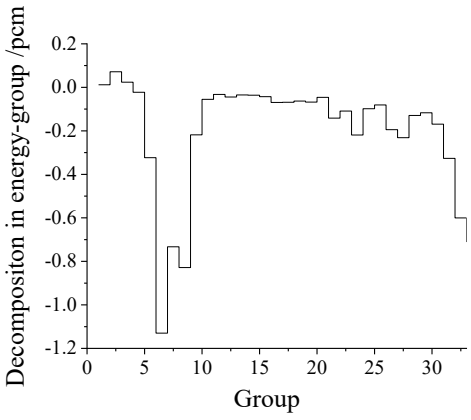

Fig. 4 Coolant expansion reactivity decomposition in energy group

5. Conclusions

This paper describes the work on the enhancing the temperature reactivity feedback of a medium size gas-cooled fast reactor. This paper quantitatively analyzes the physical reasons, develops reactivity decomposition based on neutron balance method, and calculates the numerical results. The results show that the two optimization measures are effective to enhance the temperature reactivity feedback, which are supported by the results in the neutron balance analysis.

Acknowledgements

This work is supported partly by the National Natural Science Foundation of China (Approved Number: 11775170 and 11735011).

References

1. Wu HC, Cao Lz, Zheng YQ, et al, *Nuclear reactor physics*, 104-107, Atomic Energy Press, Beijing, (2014).
2. Sun K, Krepel J, Mikityuk K, et al, "Void reactivity decomposition for the Sodium-cooled Fast Reactor in equilibrium fuel cycle," *Annals of Nuclear Energy*, **(38)**, 1645-1657, (2011).
3. Yoo J, "Three-Dimensional Core Design of Large Scale Supercritical Light Water-Cooled Fast Reactor," The University of Tokyo, Tokyo, (2006).
4. Beck T, Blanc V, Escleine JM, et al, "Conceptual design of ASTRID fuel sub-assemblies," *Nuclear Engineering and Design*, **(315)**, 51-60, (2017).
5. Michael AP, "Thermal hydraulics design of a 2400MWth Direct supercritical CO2-cooled fast reactor," Thesis of Massachusetts Institute of Technology, (2006).

Proceedings of the Reactor Physics Asia 2019 (RPHA19) Conference
Osaka, Japan, Dec. 2-3, 2019

Innovative Design Concepts of Burnable Poison Rods for PWR

Aiman Dandi and Myung Hyun Kim*
Kyung Hee University, 1732 Deogyeong-daero, Giheung-gu, Yongin-si, Gyeonggi-do, Korea, 17104
*mhkim@khu.ac.kr

Abstract

The Burnable Poisons (BPs) are the main players to hold-down the initial excess reactivity and to control the power peaking for Pressurized Water Reactors (PWRs). Even though all conventional BPs have some drawbacks, they satisfy the design requirements for 18-month cycle PWR. On the other hand, these conventional BPs cannot meet the design requirements for a longer operation cycle PWR cores. In this paper two BP design concepts are presented: Matryoshka Doll Burnable Poison (MDBP) for Westinghouse (WH) fuel assembly and Burnable poison Attached to Guide tube (BAG) for Combustion Engineering (CE) fuel assembly. The MDBP consists of two tubes inside each other and covered with clad. The outer tube contains of natural boron and the inner tube contains of erbium as absorber materials. While, the BAG is a 4 thin wires that contain of natural boron as absorber material and attached to the guide tubes in the outer corners. The assembly calculations of the two new designs were performed by DeCART2D code and compared with the conventional BPs results. These results show that the MDBP can hold-down the initial excess reactivity as much as Gad and stronger than any other conventional BPs. Even though BAG+Erbia case contains much lower Erbia pins than in Erbia case, both cases reduce the initial excess reactivity to the same level. The new designs can control the excess reactivity much longer than any other conventional BPs. Also, they show reasonable values of power peaking factor and moderator temperature coefficient (MTC).

Key Words: **Burnable Poison, PWR, Innovative Design Concept**

1. Introduction

The Burnable Poison (BP) is the main feature to maintain operating Pressurized Water Reactor (PWR) core within the design constraints of average excess reactivity level, power peaking and moderator temperature coefficient (MTC). There are different conventional BP designs that are compatible with 18-month cycle PWR regardless each BP design flaws. These flaws become more effective when operate PWR longer than 18 months due to the requirement of large number of conventional BP pins to hold-down the unavoidable higher excess reactivity into appropriate level. This leads to a failure to meet the design constraints of PWR core operation [1, 2]. Based on that, inventing a new BP design with good properties that allows PWR core to operate longer cycle than 18 months within the design constraints is essential.

In the presented study, an attempt was done to invent two new BP designs for both standard fuel assembly types: Westinghouse (WH) fuel assembly and Combustion Engineering (CE) fuel assembly. Only assembly calculations were performed by DeCART-2D code [3]. The obtained results were compared with the conventional BP results in terms of k-infinite letdown curve, power peaking and MTC.

2. Designing Tools and Reference Design

In this study, DeCART-2D code is used to perform the assembly calculations. The reference designs used here are 17×17 WH and 16×16 CE fuel assembly types as shown in Figs. 1 and 2. Table I shows design parameters of the two reference designs [4,5]. The direct increase method of fuel enrichment is adopted in order to simulate a long cycle operation PWR core [6,7]. Consequently, only fuel enrichment is increased to 6.96w/o for normal fuel rod and 4.10w/o for zoning fuel rod with keeping the other design parameters as the same as in both reference designs.

3. Innovative Design Concepts

To design BP suitable for long operation cycle, some conditions should be considered. These conditions are: the BP should be able to hold-down the initial excess reactivity to an adequate level; the consumption rate of absorber material should be as flat as possible; and at End-Of-Cycle (EOC), the residual reactivity penalty should be as small as possible [8].

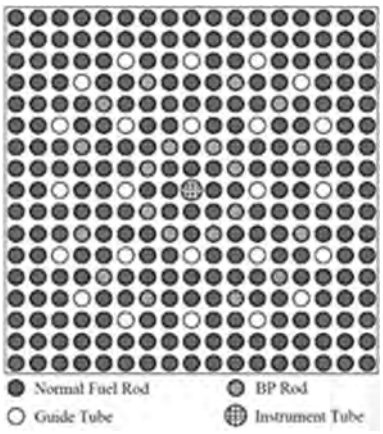

Fig. 1. Standard WH fuel assembly type.

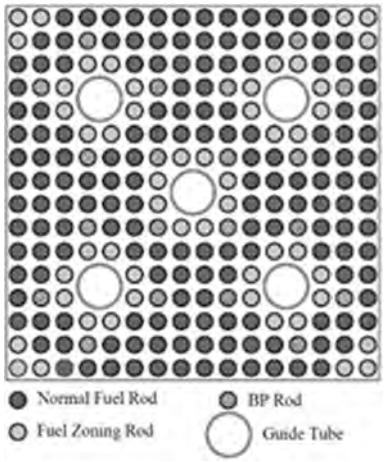

Fig. 2. Standard CE fuel assembly type.

Table I. WH and CE Fuel Assembly Design Parameters

Design Parameter	WH	CE
Fuel Rod Array	17×17	16×16
Number of Fuel Rods	264	236
Active Fuel Length	365.76	381
Number of Guide Tube (GT)	24	4
Number of Instrumentation tube	1	1
Fuel Assembly Length (cm)	406.3	452.8
Fuel Assembly Pitch (cm)	21.5040	20.7772
Fuel Rod Length (cm)	388.1	409.4
Cell Pitch (cm)	1.260	1.285
Fuel Diameter (cm)	0.8192	0.8192
Cladding material	ZIRLO	ZIRLO
Cladding I.D. (cm)	0.8357	0.8357
Cladding O.D. (cm)	0.95	0.95
GT material	ZIRLO	ZIRLO
GT I.D. (cm)	1.008	2.286
GT O.D. (cm)	1.224	2.4892

The two BP design concepts are: 'Matryoshka Doll Burnable Poison' (MDBP) for WH fuel assembly and Burnable poison Attached to Guide tube (BAG) for CE fuel assembly. Figure 3 shows the structure of MDBP which comprises of two tubes inside each other and covered with clad. The inner tube consists of ZIRLO mixed homogeneously with 40w/o of Er_2O_3 and the outer tube made of Al_2O_3-B_4C. This design is loaded in the GTs without control rod. The design structure can be changed to three tubes or more and use different absorber material with different concentration, depend on the required performance. For example the expected performance of this design is to have a good ability to hold-down the initial excess reactivity, the burnup rate of absorber material is slow and to induce the MTC toward more negative value due to the resonant behavior of erbium at the epithermal range (~0.5 eV) [9], which is suitable for longer operation cycle and high burnup fuel as targeted in this study.

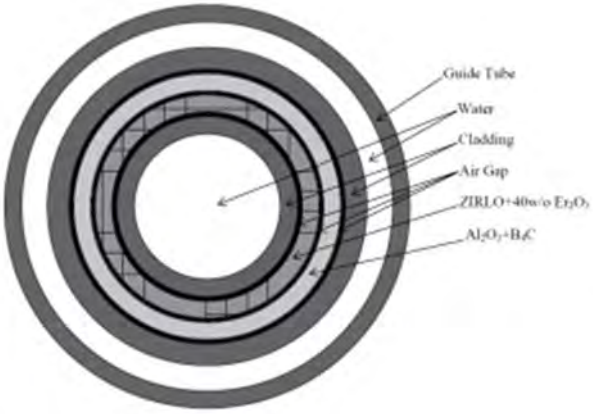

Fig. 3. MDBP design for WH fuel assembly type.

BAG design is based on a simple idea; in the outside corners of each GT there are some spaces that can accommodate small amount of absorber material [10]. Therefore, in this study Al_2O_3-B_4C made as a thin wire (radius ≈ 0.235 cm) and welded at the outside of the GT at the free spaces as shown in Figs. 4 and 5. Similar to MDBP design, the absorber material in BAG design also can be changed to any absorber material with any concentrations. This design has small amount of absorber martial which is not enough to reduce the initial excess reactivity to the needed level by itself, but due to its good characteristics, it can give support to any conventional BP design and improve their performance to be suitable for PWR core design with any operation cycle, i.e., 18 months operation cycle or longer.

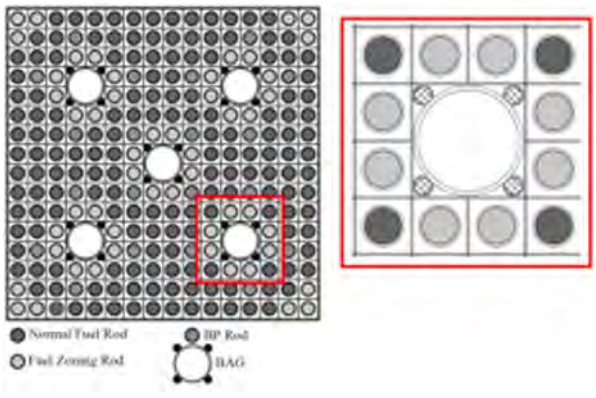

Fig. 4. Standard CE fuel assembly type with BAG design.

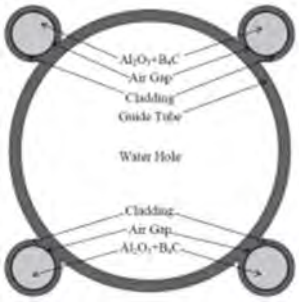

Fig. 5. BAG design for CE fuel assembly type.

MDBP and BAG designs are considered as a discrete BP which they are not mixed within the fuel thus does not displace the fissile material, and does not reduce the thermal conductivity of the fuel. Furthermore, these designs are easy to manufacture, during manufacturing no need for a radiological regulated facility and during the refueling time they can be removed from the core to avoid the effect of any undestroyed high absorption cross section isotopes on the next cycles.

In the next section, MDBP and BAG designs are compared with the conventional BP designs: Wet Annular Burnable Absorber (WABA), Gadolinia (Gad), Erbia and Integral Fuel Burnable Absorber (IFBA) in terms of k-infinite, power peaking and MTC. Also, a combined case of BAG+Erbia is added to the comparison as an example to show the benefit of combining BAG design with any of the conventional BP design. In WH design, each case of WABA, Gad and MDBP consist of 24 pins. Moreover, Erbia and IFBA consist of 96 pins loaded in the fuel assembly. In CE design, BAG and Gad cases consist of 20 pins of BP. Further, IFBA and Erbia cases consist of 112 and 132 pins of BP respectively. On the other hand, the combination of BAG and Erbia case consists of 20 wires of BAG and 64 pins of Erbia. In both designs, 8.0w/o of Gd_2O_3 is mixed with 2.5w/o of UO_2 and 2.0w/o of Er_2O_3 is mixed with fully enriched UO_2. Lastly, the boron in WABA, MDBP and BAG cases is natural boron with concentration of 10.96w/o.

4. Calculation Results

Fig. 6 shows the k-infinite versus burnup (MWD/kgHM) for WH fuel assembly type of No BP, 24WABA, 24Gad, 96Erbia, 96IFBA and 24MDBP cases. At the Beginning-Of-Life (BOL) 24MDBP and 24Gad cases have the strongest ability among all cases to hold-down the initial excess reactivity by 12,500 pcm and 12,890 pcm respectively. At the burnup step of 25 MWD/kgHM all the cases lost their ability to hold-down the excess reactivity except 24MDBP case which it can hold-down the excess reactivity effectively until the burnup step of 36 MWD/kgHM. Since one of the tubes in MDBP design contains Erbia, thus some of undestroyed high neutron absorption cross section isotopes cause high residual reactivity penalty at End-Of-Life (EOL) [9] which is about 1,162 pcm. This value is similar to the value of Erbia case but it is much lower than the value of Gad case by about 1,638 pcm. On the other hand, 24WABA and 96IFBA cases have the lowest residual reactivity penalty which is less than 300 pcm for each.

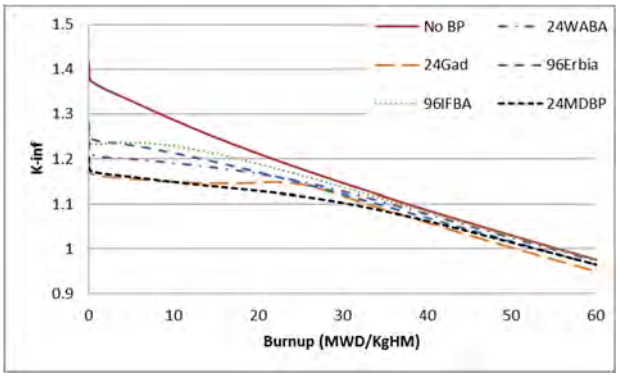

Fig. 6. Comparison of excess reactivity for WH fuel assembly type.

Fig. 7 shows the k-infinite versus burnup (MWD/kgHM) for CE fuel assembly type of No BP, Erbia, Gad, IFBA, BAG and BAG+Erbia cases. At the BOL all cases have almost the same effect on holding-down the initial excess reactivity except the BAG case has the lowest value which is about 6,404 pcm. This is due to the fact that BAG design can contain only small amount of absorber material in few locations. However, this value is more than half of the other cases values which means the combination of BAG with any conventional BP designs can reduce the number of this conventional BP pins by half to achieve the same effect on holding-down the initial excess reactivity. For instance, the combination of 20 wires of BAG with 64 pins of Erbia can hold-down the initial excess reactivity as the same as 132 pins of Erbia. This reduction of Erbia pins can be reflected positively on the residual reactivity penalty. At the burnup step of 21 MWD/kgHM, all cases lost their ability to hold-down the excess reactivity except Erbia and BAG+Erbia cases which can hold-down the excess reactivity effectively much longer. The residual reactivity penalty at the EOL of BAG+Erbia case is 468 pcm which is much lower than the values of Gad and Erbia cases by about 2,066 pcm and 798 pcm respectively. The other cases of IFBA and BAG have the lowest value of this penalty among all cases.

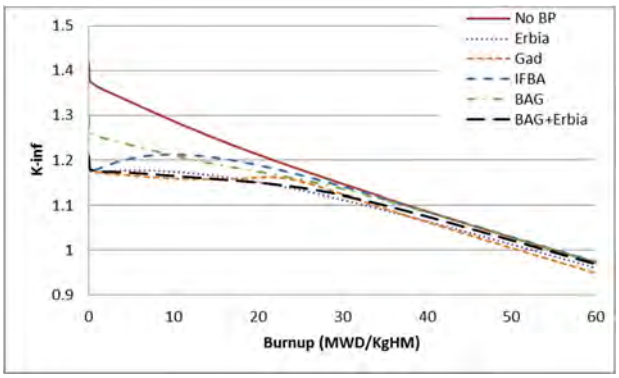

Fig. 7. Comparison of excess reactivity for CE fuel assembly type.

Fig. 8 illustrates the power peaking factor in 2-D assembly geometry versus burnup (MWD/kgHM) of the

same cases for WH fuel assembly type. At BOL the power peaking factor of 24MDBP case is higher than all cases except 24Gad case. Around the burnup step of 25 MWD/kgHM the values of all cases become very close to each other except 24Gad case which is much higher.

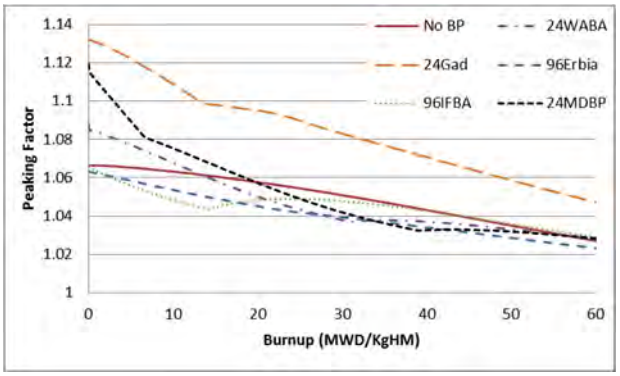

Fig. 8. Comparison of power peaking factor in 2-D assembly geometry for WH fuel assembly type.

Fig. 9 demonstrates the power peaking factor in 2-D assembly geometry versus burnup (MWD/kgHM) of the same cases for CE fuel assembly type. Gad case has the highest power peaking factor among all cases throughout the burnup. At the BOL the power peaking factor of BAG case is little bit higher than the other cases. Around the burnup step of 13 MWD/kgHM, the values of all cases except Gad case become very close to each other until the EOL. Generally, the highest power peaking factor of Gad cases in both fuel assembly types is due to the low content of U^{235} with high concentration of gadolinium in Gad pins [9].

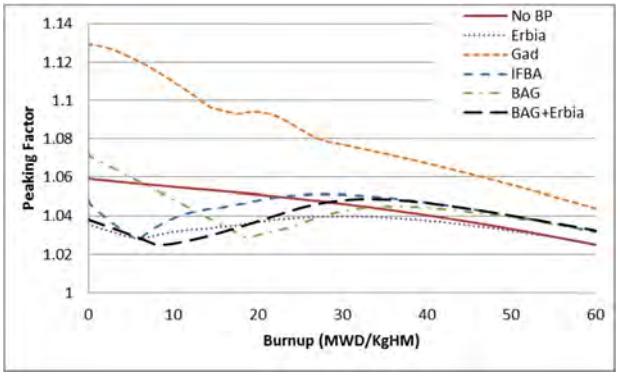

Fig. 9. Comparison of power peaking factor in 2-D assembly geometry for CE fuel assembly type.

Fig. 10 shows the MTC (pcm/C°) versus burnup (MWD/kgHM) of the same cases for WH fuel assembly type. At the BOL, 24MDBP and 96Erbia cases have almost the same MTC values which are the most negative values among all cases. At the burnup step of 20 MWD/kgHM until the EOL, the values of 24MDBP case become more negative than the values of 96Erbia case.

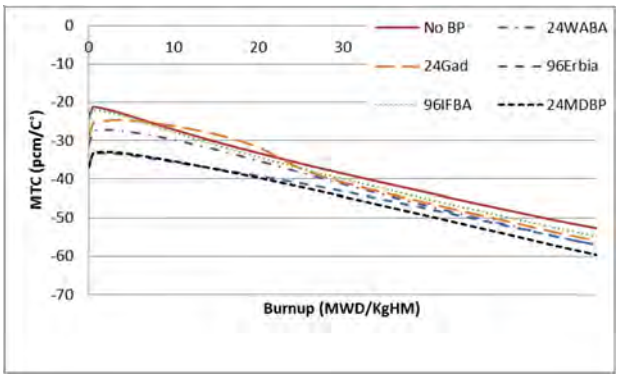

Fig. 10. Comparison of MTC for WH fuel assembly type.

Fig. 11 demonstrates the MTC (pcm/C°) versus burnup (MWD/kgHM) of the same cases for WH fuel assembly type. At the BOL Erbia and BAG+Erbia cases have the most negative MTC values among all cases with the values of -42.28 pcm/C° and -37.18 pcm/C° respectively. Around the burnup step of 50 MWD/kgHM, the values of these two cases become almost the same values until the EOL.

Worth mentioning, for the power peaking factor and MTC values any design satisfy the design limitations is acceptable. The values of power peaking factor and MTC no need to be very low.

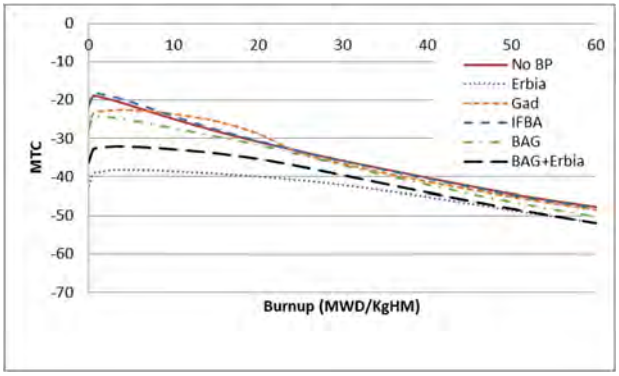

Fig. 11. Comparison of MTC for CE fuel assembly type.

5. Conclusions

Matryoshka Doll Burnable Poison (MDBP) and Burnable poison Attached to Guide tube (BAG) are new design concepts that can be optimized to be suitable for any cycle operation length for PWR core.

DeCART2D code was used in this study as a design tool to perform assembly calculations for WH and CE fuel assembly types. The obtained results of these two new BP concepts were compared with the results of conventional BP designs regarding k-infinite, MTC and power peaking factor.

24MDBP and BAG+Erbia cases reduced the initial excess reactivity by about 43%. Also, they have the ability to hold-down the excess reactivity for a longer time than any other cases. Both cases provide a very good MTC values due to the presence of erbium in both designs. BAG+Erbia case provides good power peaking factor and low residual reactivity penalty. On the other hand, the

power peaking factor and residual reactivity penalty values of 24MDBP case are reasonable.

Although 24MDBP and BAG+Erbia cases in this study are designed to be suitable for long operating cycle and high burnup fuel, both designs have a degree of freedom to be adjusted to satisfy any cycle length by using appropriate absorber material.

This study is prelaminar study therefore more investigation is needed.

References

[1] J. Secker, J. Brown, Westinghouse PWR Burnable Absorber Evolution and Usage, in: 2010 ANS Winter Meeting, Las Vegas, NV, USA, Nov. 7-11, (2010).
[2] Jeffery A. Brown, Ho Q. Lam, Hybrid IFBA Gad Assembly Designs for Long PWR Cycles, in: 2017 Water Reactor Fuel Performance Meeting, Ramada Plaza Jeju, Jeju Island, Korea, Sep. 10-14, (2017).
[3] J.Y. Cho, J.C. Lee, K.H. Lee, S.Y. Park, H.J. Park, H.Y. Kim, K.Y. Kim, H.J. Jung, J.S. Song, S.Q. Zee, C.K. Jo, H.C. Lee, DeCART2D v1.0 User's Manual, KAERI/TR-5116/2013, Korea Atomic Energy Research Institute (2013).
[4] Young Kim Jang, Kyeong Lak Jeon. (2010). In-reactor Irradiation Performances of Advanced Fuels, ACE7™, for Westinghouse Type Nuclear Power Plants, Transactions of the Korean Society of Mechanical Engineers Spring Meeting, 5, pp. 343-344, (2010).
[5] Kyu-Tae Kim, Young-Ki Jang, Jae-Ik Kim, In-Reactor Performance of an Advanced PWR Fuel, PLUS7, for OPR1000s in Korea, Journal of Nuclear Science and Technology, 45:8 (2008) 836-849.
[6] Aiman Dandi, MinJae Lee, Myung Hyun Kim, Soon Ki Kim, Sang Rin Shon, Combination of Burnable Poison Pins for 24 months Cycle PWR Reload Core, in: 2018 Transactions of the Korean Nuclear Society Spring Meeting, Jeju, Korea, May 17-18, (2018).
[7] MinJae Lee, Aiman Dandi, Myung Hyun Kim, Soon Ki Kim, Sang Rin Shon, The Combinational Use of Burnable Poison Pins for 24 Months Cycle PWR, in: 2018 Transactions of the American Nuclear Society Summer Meeting, Philadelphia, Pennsylvania, USA, June 17–21, (2018).
[8] J. Choe, H.C. Shin, D. Lee, New burnable absorber for long-cycle low boron operation of PWRs, Ann. Nucl. Energy 88, pp. 272-279, (2016).
[9] F. Franceschini, B. Petrovic, Fuel with advavced burnable absorbers design for the IRIS reactor core: combined erbia and IFBA, Ann. Nucl. Energy 36, pp.1201-1207, (2009).
[10] H. Yu, M.-S. Yahya, Y. Kim, A Reduced-Boron OPR1000 Core Based on the BigT Burnable Absorber, Nuclear Engineering and Technology (2016).

Proceedings of the Reactor Physics Asia 2019 (RPHA19) Conference
Osaka, Japan, Dec. 2-3, 2019

Research on Core Design of Pebble Bed Advanced High Temperature Reactor

Wang Lianjie[a], Sun Wei[a], Xia Bangyang[a], Zou Yang[b], Yan Rui[b]
[a]*Science and Technology on Reactor System Design Technology Laboratory, Nuclear Power Institute of China, Chengdu, China;*
[b]*Shanghai Institute of Applied Physics, Chinese Academy of Sciences, Shanghai, 201800, China*[*]

Abstract

We find that evacuating molten salt and injecting poison into coolant both can be used as the auxiliary system of the second shutdown system in Pebble Bed Advanced High Temperature Reactor (PB-AHTR). Compared with injecting poison into coolant, the effect of evacuating molten salt on the core is smaller and more beneficial to the engineering realization. Compared to one time charging scheme, batch charging scheme can ensure that a small core excess reactivity in whole life-time which is easier to be controlled, but more complex to operation. In one time charging scheme, the second shutdown system gains enough fast shutdown margin by increasing the number of second control rod, instead of reducing the stack height of core activity. In this study, A PB-AHTR core with burn-up life-time of 100 equivalent full power days (EFPDs) is proposed. The shutdown margins of both the first shutdown system and the second shutdown system meet the design requirements.

Key Words: **Pebble Bed Advanced High Temperature Reactor, Second s hutdown system, Evacuating molten salt, Core design**

1. Introduction

In 2002, based on the consideration of sustainability, economy and safety, reliability and nuclear non-proliferation, the International Symposium on Fourth Generation Nuclear Reactors screened out six fourth generation nuclear reactors from more than 100 types of reactors [1]: Molten Salt Reactor (MSR), Gas-cooled Fast Reactor (GFR), Lead-cooled Fast Reactor (LFR), Sodium-cooled Fast Reactor (SFR), Super Critical Water-cooled Reactor (SCWR), Very-High Temperature Reactor (VHTR). The pebble bed advanced high temperature reactor (PB-AHTR) is a combination of molten salt reactor and very-high temperature reactor. It is an advanced high temperature reactor using molten salt as coolant. It has five characteristics: molten salt cooling, coated granular fuel and passive cooling safety system, supercritical water energy circulation system and conventional island design. Due to the inheritance of many advantages and technical foundations of the existing cores, the PB-AHTR fully meets the requirements of the fourth generation nuclear reactor core. Moreover, the commercial application of the PB-AHTR is also highly feasible under the conditions of current technical foundation.

Studies on the core design of the PB-AHTR have been carried out. The key parameters of core design ar e studied, and then the preferred design concept of the PB-AHTR core is proposed.

2. Calculation Code

This study uses the MCNP code [2] and the ORIGEN code [3]. The MCNP code is a computer code developed by the Los Alamos National Laboratory for transport calculation based on the Monte Carlo method. It can handle the movement of neutrons, protons and photons in various media and give corresponding results. It has been widely used in various aspects such as reactor physics and radiation protection.

The ORIGEN code is a code system developed by the Oak Ridge National Laboratory for radionuclide ignition, decay calculation, and radioactive material processing. The ORIGEN code is primarily used for fuel consumption calculations, as well as flux-to-power conversion calculations. ORIGEN provides various databases for different reactor types, different fuel combinations and different fuel burn depths, which can be selected by users according to actual needs [3].

A large number of open literatures have applied MCNP code and the ORIGEN code to investigate the design of pebble bed reactors [4-6].

3. Research on key parameters of core design

3.1 Overall parameters of core

In this paper, the thermal power of the reactor is designed as 10 MWt, the coolant is 2LiF-BeF_2 molten

salt, and the spherical fuel element is undertaken as same as the high temperature gas cooled reactor used. It contains TRISO coated particulate fuel and graphite base. The diameter of the fuel sphere is 6.0 cm, the fuel is UO_2 with ^{235}U enrichment of 17.0 wt%, and the uranium loading amount of per fuel sphere is 7.0 g.

The pebble bed advanced high temperature reactor core consists of a core active zone and a graphite reflective layer (Fig. 1). The upper part of the active area is placed a fuel pebble, the lower part settles a graphite pebble, the remaining space is filled with molten salt, and the gap between the pebbles forms a random irregular flow path for the molten salt coolant. The coolant takes heat generated by fission away from bottom to top. As a neutron reflecting material, the graphite reflective layer constructs an active area of the upper and lower circular table and the middle column, and accommodates special channels such as neutron source and shutdown system. The positions of 16 control rods are shown in Fig. 1. The core active zone is surrounded by the core's graphite member forming as upper and lower circular tables and a middle cylindrical region. The cylinder height is 180.0 cm.

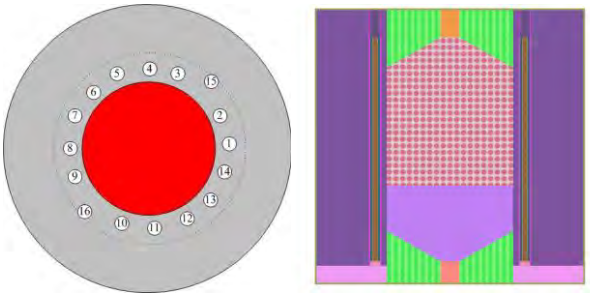

a. Core Cross Section b. Core Longitudinal Section

Fig.1 Schematic Diagram of PB-AHTR Core

3.2 Calculation Model

The fuel pebble TRISO particle geometry model uses the same structure as the actual TRISO grain which means a fuel core with addition of four coating layers. The TRISO particles are filled in the fuel sphere using a simple cubic equivalent simulation of TRISO particles [4-5] (Fig. 2).

According to the literature research, the duty cycle of the fuel sphere in the core is about 60 % [6-8] that can be modeled by body-centered cubic repeating cell [6]. In this paper, a 60% duty cycle body-centered cubic repeating cell model is used, and the graphite pebbles at the bottom of the core are arranged in the same way.

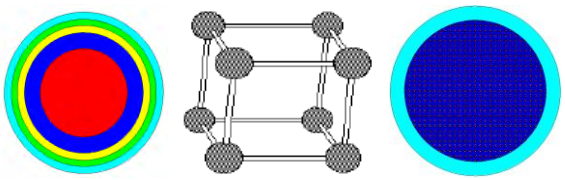

a) TRISO b) TRISO Rule Packing c) Profile of Fuel Sphere

Fig.2 Schematic Diagram of TRISO Particle and Packing Equivalence

3.3 Research on the design of the second shutdown system

The fuel ball of pebble bed advanced high-temperature reactor core is arranged in a cross arrangement, hence the control rod can only be arranged in the outer reflection layer of the active area that greatly reduces the value of control rod. Due to the limitation of peripheral position, only 16 B_4C control rods are arranged so far, and the total value of these 16 control rods is also small. If 16 control rods are divided into two parts, one for the first shutdown system and another for the second shutdown system, while meeting the safe margin, the initial residual reactivity of the core is small, that seriously affects the core life. In order to increase the options and diversity of the scheme, it considers to conduct an analysis of other possible alternative auxiliary shutdown methods for the second shutdown system for design reference, including: evacuation of molten salt and addition of soluble poisons.

(1) Evacuate Molten Salt

In the calculation and analysis, the core active zone is loaded to the lower end plane of the cylinder. In order to prevent the pebble bed from gradually sinking and being out of shape when the molten salt is emptied, the graphite ball (diameter is 6 cm) is loaded into the fuel pebbles located at the bottom of active zone Of the 16 control rods, 2 (2 and 9 in Figure 1a) control rods serve as the second shutdown system control rods for fast shutdown.

Table I shows the Keff values after inserting the second shutdown rods at different burn-up and normal cold state equilibrium Xenon (the first set of control rods is at the critical rod position). As can be seen from Table I, the maximum Keff value is 0.99728 after the core is inserted into the second set of shutdown rods. It can be seen that when the first set of control rods is stuck in the power operation critical rod position, the second set of shutdown rods can bring the reactor into the cold shutdown state. As the xenon is reduced, the Keff value of the core at the cold state without xenon is greater than 1 (Table I). In order to avoid the reactor core returning to criticality, it is necessary to start the molten salt system before the xenon poison disappears.

Table I Keff value of core after inserting second sets of shutdown rods

Burn-up EFPD	Keff Value (Cold State With Equilibrium Xenon)	Keff Vaulue (Cold State Without Xenon)
0.0	0.99728(0.00041*)	0.99728(0.00041)
2.0	0.99325(0.00040)	1.01754 (0.00040)
100.0	0.98822(0.00039)	1.01369(0.00043)
150.0	0.98729(0.00043)	1.01199(0.00041)

Note: * is the statistical error of the Monte Carlo code

Table II Keff value of core after evacuating molten salt (cold state without xenon)

Burn-up/EFPD	Keff Value
0.0	0.84777(0.00043)
2.0	0.88951(0.00045)
100.0	0.91448(0.00046)
150.0	0.92906(0.00042)

After the core has been shut down by the second set of shutdown rods, Table II gives the Keff value of the core after the molten salt is emptied at the cold state without xenon in the core at different burn-up states. It can be seen from Table III that after the core is shut down by the second set of shutdown rods, the molten salt evacuation system can ensure that reactor maintaining a cold shutdown state before the core returns to critical due to the xenon poison consumption.

(2)Add Soluble Poison

The injection of poison into coolant is also a common means of shutdown, so that a neutron poison salt which is soluble and compatible with the molten salt can be injected as a shutdown means. The calculation conditions are the same as venting molten salt.

Table III shows the Keff value of the core when injected into the Li-6 solution at the cold state without xenon in different burn-up. It can be seen from Table III that after the core is shut down by the second set of shutdown rods, the injection of Li-6 solution can ensure that the reactor maintains a cold shutdown state before the core returns to critical due to xenon poison consumption.

Table III Keff value of core after injecting Li-6

Burn-up/EFPD	Condition 1①	Condition 2②
0	0.96833（0.00042）	0.95085（0.00040）
2	0.98709（0.00041）	0.97038（0.00041）
100	0.98322（0.00041）	0.96507（0.00042）
150	0.98131（0.00041）	0.96363（0.00039）

Note: ①Li-6 accounts for 0.05% of the mass of the coolant; ②Li-6 accounts for 0.08% of the mass of the coolant.

3.3 Research on core fuel loadage design

When the core active zone is loaded to the lower end plane of the cylinder, 2 rods of the second set is inserted while the first set of control rods at the critical rod position. It can be seen from Table 2 that the core's Keff of the initial is 0.99728 whilst the quick shutdown margin is small. In order to solve this problem, there are two methods: ①reducing the height of the core active zone; ②while meeting the requirements of the first shutdown system, distributing some control rods of the first set of shutdown systems to the second set of shutdown systems.

(1) Reducing the height of the core active zone

Table IV shows the Keff value of the core under various operating conditions when the core loading height of the active zone is 150 cm. It can be seen from Table IV that even if the height of the core active zone is lowered, in case of the second set of shutdown systems only maintains two control rods, the Keff value will be 0.99212 and the margin is small, too. The reason is mainly because of the second set of shutdown system control rods are inserted at the critical rod position of the first set of shutdown system control rods to achieve rapid shutdown, and total value of these two rods is basically unchanged. Even if the height of active area is reduced, the shutdown margin of the second shutdown system is also small.

Table IV Keff value of core under different working conditions when the core height is 150 cm and the second shutdown system has two control rods

Conditions	Keff Value
Withdraw All Control Rods	1.05974（0.00039）
Two rods of the second set of shutdown system（The position is 2, 9 in Figure 1） are both insered （Cold State With Equilibrium Xenon）	0.99212（0.00040）
All control rods of the first set of shutdown system are all inserted （Cold State）	0.95400（0.00041）

(2) Increase the number of control rods in the second set of shutdown systems

The Keff values of the cores under various working conditions when the core loading height of the active zone is 150, 160 and 165 cm are calculated. When the three rods of the second set of shutdown systems are all inserted, the shutdown margin meets the requirements (Keff < 0.99 when the second set of control rods is inserted).

4. Preferred core design

Compared with the core injecting poisonous molten salt, the method of evacuating the molten salt is more practical, because after the core is injected with poison, the core will be contaminated, and the entire reactor is scrapped. In order to meet the requirements of the first set and the second set of shutdown systems at the same time, the final core loading height of the active zone is 160 cm, and the second set of shutdown system has 3 rods(the position is 2, 7, 10 in Figure 1) all inserted.

4.1 numerical result

At the beginning of the life whilst the core is at cold state and control rods are all withdrawn, Keff value is 1.07762, and will be 0.96603 while control rods are all

inserted; The cold shutdown depth is -3516 pcm (1 pcm=10^{-5}).

Table V shows the Keff values when the second set of shutdown rods are inserted under different burn-up while the core is at cold state with equilibrium xenon (the first set of control rods are at the critical rod position). It can be seen from Table V that the maximum Keff value is 0.98438 after the second set of shutdown system is inserted. It can be seen that when the control rods of the first set of shutdown system are stuck at the power operation critical rod position, the control rods of the second set of shutdown system can bring the reactor into the cold shutdown state.

After inserting the control rods of the second set of shutdown system to achieve shutdown, in order to avoid the reactor core returning to criticality, it is necessary to start the molten salt evacuation system before the xenon poison disappears. Table VI shows the Keff value of the core by evacuating molten salt at cold state without xenon in different burn-up. It can be seen from Table VI that after shutdown by inserting the control rods of the second shutdown system, the molten salt evacuation system can ensure that the reactor maintains a cold shutdown state if it is started before the reactor return to criticality for xenon poison reducing. Among which, the maximum Keff value after evacuating molten salt in different burn-up is 0.90725 (corresponding to the cold shutdown depth is -1023 pcm), which meets the design requirements.

Table V Keff value of core when the second control rods inserting (cold state with equilibrium xenon)

Burn-up/EFPD	Keff Value
0.0	0.98438(0.00042)
2.0	0.97900(0.00040)
50.0	0.97628(0.00040)
100.0	0.97469(0.00040)

Table VI Keff value of Core after evacuating Molten Salt (Cold State without Xenon)

Burn-up/EFPD	Keff Value
0.0	0.84305(0.00044)
2.0	0.88201(0.00045)
50.0	0.89643(0.00042)
100.0	0.90725(0.00045)

5. Conclusion

This paper investigates and conducts a series of studies on the set of second shutdown systems and core fuel loading of PB-AHTR. It has been found that venting molten salt and injecting poison into the coolant can be used as an auxiliary system for the second shutdown system of the core. However, the effect of evacuating molten salt on the core is smaller than that of the core injected with poisonous molten salt and more practical. It is impossible to make the second shutdown system have sufficient rapid shutdown margin by reducing the height of the core active zone. Unlikely, it is possible to do so by increasing the number of control rods in the second shutdown system. Based on the above research, the optimal core design scheme of 10 MW PB-AHTR is proposed. The scheme has a burn-up life reaching 100 EFPD. The first shutdown system has a cold shutdown depth of -3516 pcm whilst the second shutdown system has a cold shutdown depth of -10223 pcm. This design has a sufficient cold shutdown depth to meet design requirements.

References

1. “US DOE Nuclear Energy Research Advisory Committee and the Generation IV International Forum,” A Technology Roadmap for Generation IV Nuclear Energy Systems, GIF-002-00 (2002).
2. J.F. Briesmeister, “MCNP – A General Monte Carlo N-Particle Transport Code,” Los Alamos National Laboratory (1997).
3. A.G. Croff, “A User’s Manual for ORIGEN2 Computer Code,”USA：Oak Ridge National Laboratory (1980).
4. M.Q. Huda, T. Obara, “Development and testing of analytical models for the pebble bed type HTRs,” Annals of Nuclear Energy, 35 (2008).
5. Volkan Seker，Uner Colak, “HTR-10 full core first criticality analysis with MCNP,” Nuclear Engineering and Design, 222(2003).
6. G.J.Auwerda, J.L.Kloosterman, D. Lathouwers, T.H.J.J. van der Hagen. “Effects of random pebble distribution on the multiplication factor in HTR pebble bed reactors,” Annals of Nuclear Energy, 37(2010).
7. Yixiang Gan, Marc Kamlaha, Jorg Reimanna, “Computer simulation of packing structure in pebble beds,” Fusion Engineering and Design, 85(2010).
8. Joerg Reimanna, Ali Abou-Senaa, Rainer Nippenb, Paul Tafforeauc, “Pebble bed packing in prismatic containers,” Fusion Engineering and Design, 88(2013).

TS-04 Reactor Kinetics

Proceedings of the Reactor Physics Asia 2019 (RPHA19) Conference
Osaka, Japan, Dec. 2-3, 2019

C5G7-TD Benchmark Analysis using Multigrid Amplitude Function Method

Kosuke TSUJITA[a*], Tomohiro ENDO[b], and Akio YAMAMOTO[b]
[a]*Nuclear Engineering, Ltd., 1-3-7 Tosabori, Nishi-ku, Osaka, Japan*
[b]*Nagoya University, Furo-cho, Chikusa-ku, Nagoya, Japan*
[*]Corresponding author: ktsujita@neltd.co.jp

Abstract

C5G7-TD 2D benchmark analysis is performed using the linear source approximation and the multigrid amplitude function (MAF) method. Through the sensitivity analysis for neutron flight direction, spatial mesh division, and time step size, spatially and temporally fine kinetic calculations are carried out for the TD1 perturbation condition of the C5G7-TD benchmark problem. The initial eigenvalue and the core power transitions are compared with that of MCNP and MPACT codes respectively and they are in good agreement.

Key Words: **method of characteristics, multigrid amplitude function method, linear source approximation, C5G7-TD benchmark problem**

1. Introduction

Time-dependent transport calculations without spatial homogenization are one of the most challenging topics since the computational cost of the method of characteristics (MOC) [1] in large heterogeneous geometry is still expensive. Thus, various efficient numerical methods for solving the time-dependent transport equation is developed to improve the computational efficiency of the time-dependent transport calculations. Especially, the multigrid amplitude function (MAF) method [2] archives high computational efficiency with the minimum degradation of the accuracy by using the coarse mesh and fine time step diffusion calculation. However, since the flat source assumption is employed in the previous study [3], a large number of flux regions are required in strongly heterogeneous geometry to obtain fine calculation results, e.g., the C5G7-TD benchmark problem [4].

In this study, C5G7-TD 2D benchmark analysis using the MAF method with the linear source approximation [5] is carried out to provide spatially and temporally fine solution. In the present summary, the theoretical basis of the MAF method with the linear source approximation is described in section 2. The calculation results of the TD1 perturbation condition are described in section 3. Finally concluding remarks are summarized in section 4.

2. Multigrid Amplitude Function Method with Linear Source Approximation

In this section, the theoretical basis of the MAF method with the linear source approximation is described. The time-dependent transport equations are written as:

$$\frac{1}{\mathrm{v}_g}\frac{\partial \psi_g}{\partial t} = -\Omega\cdot\nabla\psi_g - \Sigma_{t,g}\psi_g + Q_g, \qquad (1)$$

$$Q_g = \frac{1}{4\pi}\left\{\begin{array}{l}\chi_{p,g}(1-\beta)\sum_{g'}\nu\Sigma_{f,g'}\phi_{g'} \\ +\sum_{g'}\Sigma_{s,g'\to g}\phi_{g'} + \sum_j \chi_{d,j,g}\lambda_j C_j\end{array}\right\}, \qquad (2)$$

$$\frac{\partial C_j}{\partial t} = \beta_j\sum_{g'}\nu\Sigma_{f,g'}\phi_{g'} - \lambda_j C_j\,, \qquad (3)$$

where,

Ω : the unit vector in the direction of flying neutron,
ψ : angular flux, ϕ : scalar flux,
χ : fission spectrum, Σ : cross section,
C : precursor density, λ : decay constant,
β : delayed neutron fraction, v : neutron velocity,

g, *j*, *p*, and *d* are the subscript for neutron energy group, delayed precursor group, prompt and delayed neutrons, respectively. An approximation for the temporal derivative of the angular flux is necessary to perform the kinetic calculation using MOC within practical memory requirement. Since the previous study revealed that the isotropic approximation for the temporal derivative of the angular flux has a negligible impact for the accuracy [6], thus Eq.(1) is approximated as:

$$\frac{1}{4\pi}\frac{1}{\mathrm{v}_g}\frac{\partial \phi_g}{\partial t} = -\Omega\cdot\nabla\psi_g - \Sigma_{t,g}\psi_g + Q_g, \qquad (4)$$

Discretizing the neutron flight direction and space for Eq. (4), the balance equation along a neutron path line is described as:

$$\frac{1}{4\pi}\frac{1}{\mathrm{v}_{g,r}}\frac{\partial \phi_{g,m,k,i}(s,t)}{\partial t} = -\frac{\partial \psi_{g,m,k,i}(s,t)}{\partial s} - \Sigma_{t,g,r}\psi_{g,m,k,i}(s,t) + Q_{g,m,k,i}(s,t)\,, \qquad (5)$$

where,

s : coordinate along the neutron flight direction.
m : neutron flight direction,
k : sequential number of the path line,
i : segment, r : flux region,

and Fig. 1 shows their definitions.

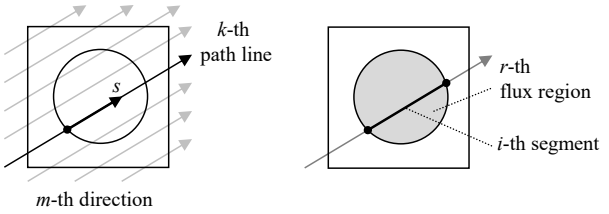

Fig. 1. Flight direction, path line, segment, flux region

In the present study, the linear source approximation [5] is employed to reduce the spatial discretization error, i.e., the scalar flux is described as:

$$\phi_{g,m,k,i}(s,t) = \phi_{g,r}(t) + x_{m,k,i}(s)\phi^{x}_{g,r}(t) + y_{m,k,i}(s)\phi^{y}_{g,r}(t), \tag{6}$$

where, $x_{m,k,i}(s)$ and $y_{m,k,i}(s)$ are the local coordinates whose origin is the geometrical centroid of the flux region [5], and thus the neutron source is described as a linear function of the track distance. The 1st order coefficients of the scalar flux, $\phi^{x}_{g,r}$ and $\phi^{y}_{g,r}$, represent the local shape of the scalar flux distribution inside the flux region and their temporal derivative are considered to be small. Therefore, the 0th order coefficient of the scalar flux is factorized as a product of the shape and amplitude functions:

$$\phi_{g,r}(t) \equiv \varphi_{g,r}(t)P_{g,I}(t)\,, \tag{7}$$

where $\varphi_{g,r}(t)$ denotes the shape function that represents the strong and weak dependences for space and time, respectively. On the other hand, the amplitude function $P_{g,I}(t)$, which is defined as Eq. (8), represents the weak and strong dependences for time and space, respectively.

$$P_{g,I}(t) \equiv \sum_{r\in I} \frac{\phi_{g,r}(t)}{\mathrm{v}_{g,r}} V_r, \tag{8}$$

where I and V_r represent the coarse mesh which includes the flux region r and the volume of the flux region, respectively. Using the Eq. (7) and assuming the temporal derivative of 1st order coefficients of the scalar flux as zero, the temporal derivative of the scalar flux is approximated as:

$$\frac{\partial \phi_{g,m,k,i}(s,t)}{\partial t} \approx \frac{d\phi_{g,r}(t)}{dt} = \frac{d\varphi_{g,r}(t)}{dt}P_{g,I}(t) + \phi_{g,r}(t)\omega_{g,I}(t)\,, \tag{9}$$

where $\omega_{g,I}(t)$ is the space- and energy-dependent dynamic frequency defined as:

$$\omega_{g,I}(t) \equiv \frac{1}{P_{g,I}(t)}\frac{dP_{g,I}(t)}{dt}. \tag{10}$$

Substituting Eq. (9) into Eq. (5) and solving it for the temporal derivative of the shape function,

$$\frac{1}{4\pi}\frac{1}{\mathrm{v}_{g,r}}\frac{d\varphi_{g,r}(t)}{dt} = \frac{1}{P_{g,I}(t)}\left(R_{g,m,k,i}(s,t) - \frac{1}{4\pi}\frac{\omega_{g,I}(t)}{\mathrm{v}_{g,r}}\phi_{g,r}(t)\right), \tag{11}$$

$$R_{g,m,k,i}(s,t) = -\frac{\partial \psi_{g,m,k,i}(s,t)}{\partial s} - \Sigma_{t,g,r}\psi_{g,m,k,i}(s,t) + Q_{g,m,k,i}(s,t)\,. \tag{12}$$

Employing the fully implicit method for the temporal derivative of the shape function,

$$\frac{1}{4\pi}\frac{1}{\mathrm{v}_{g,r}}\frac{\varphi_{g,r}(t_{n+1}) - \varphi_{g,r}(t_n)}{\Delta t_{shape}} = \frac{R_{g,m,k,i}(s,t_{n+1}) - \frac{\phi_{g,r}(t_{n+1})}{4\pi}\frac{\omega_{g,I}(t_{n+1})}{\mathrm{v}_{g,r}}}{P_{g,I}(t_{n+1})}, \tag{13}$$

where n and Δt_{shape} denote time step and time step size for the shape function, respectively. Since the shape function weakly depends on time, a coarse time step can be used for the temporal discretization. Multiplying the $P_{g,I}(t_{n+1})$ for both sides, the balance equation for the angular flux and thus the scalar flux is obtained as:

$$\frac{\partial \psi_{g,m,k,i}(s,t_{n+1})}{\partial s} + \Sigma_{t,g,r}\psi_{g,m,k,i}(s,t_{n+1}) = Q_{g,m,k,i}(s,t_{n+1}) + \frac{1}{4\pi}\frac{\phi_{g,r}(t_n)}{\mathrm{v}_{g,r}\Delta t_{shape}}\frac{P_{g,I}(t_{n+1})}{P_{g,I}(t_n)} - \frac{\phi_{g,r}(t_{n+1})}{4\pi \mathrm{v}_{g,r}}\left(\omega_{g,I}(t_{n+1}) + \frac{1}{\Delta t_{shape}}\right). \tag{14}$$

In the MAF method, the fine temporal dependence is captured in Eq. (14) by the amplitude function and the dynamic frequency. In order to calculate them, the time-dependent coarse mesh finite difference (TCMFD) method [2] is employed in the present study.

In the TCMFD method, both sides of Eq. (4) are integrated for total solid angle and spatially averaged within each coarse mesh I. The balance equation is written as:

$$\frac{1}{\mathrm{v}^{CM}_{g,I}}\frac{d\phi^{CM}_{g,I}(t)}{dt} = -L_{g,I}(t) - \Sigma^{CM}_{r,g,I}(t)\phi^{CM}_{g,I}(t) + Q^{CM}_{g,I}(t), \tag{15}$$

$$L_{g,I}(t) = \sum_{x,y}\frac{J^{CM}_{g,I+1/2}(t) - J^{CM}_{g,I-1/2}(t)}{\Delta h_I}, \tag{16}$$

where J^{CM}_{g} and Δh_I represent the neutron current at the coarse mesh surface and the width of the coarse mesh in x- or y-direction, respectively. To obtain the consistent neutron current between the TCMFD and MOC calculations, the correction term for the neutron current is employed in the TCMFD calculation [3]. Employing the theta method, Eq. (15) is written as

$$L_{g,I}(t) + \hat{\Sigma}^{CM}_{r,g,I}(t_{N+1})\phi^{CM}_{g,I}(t_{N+1}) = Q^{CM}_{g,I}(t_{N+1}) + \frac{\phi^{CM}_{g,I}(t_N)}{\theta \mathrm{v}^{CM}_{g,I}\Delta t_{amp}} + \frac{1-\theta}{\theta}R^{CM}_{g}(t_N), \tag{17}$$

$$\hat{\Sigma}^{CM}_{r,g,I}(t_{N+1}) = \Sigma^{CM}_{r,g,I}(t_{N+1}) + \frac{1}{\theta \mathrm{v}^{CM}_{g,I}\Delta t_{amp}}, \tag{18}$$

$$R^{CM}_{g}(t) = -L_{g,I}(t) - \Sigma^{CM}_{r,g,I}(t)\phi^{CM}_{g,I}(t) + Q^{CM}_{g,I}(t), \tag{19}$$

where θ, N, and Δt_{amp} denote the weighting parameter in the theta method, the time step, and the time step size for the TCMFD calculation, respectively.

Note that Eq. (17) should be solved with finer time step size than that of shape function from $t = t_n$ to $t = t_{n+1}$ because the amplitude function and the dynamic frequency are calculated by the scalar flux in the coarse mesh as follows:

$$P_{g,I}(t) = \sum_{r\in I}\frac{\phi_{g,r}(t)}{\mathrm{v}_{g,r}}V_r = \frac{\phi^{CM}_{g,I}(t)}{\mathrm{v}^{CM}_{g,I}}V_I\,, \tag{20}$$

$$\omega_{g,I}(t) = \frac{1}{P_{g,I}(t)}\frac{dP_{g,I}(t)}{dt} = \frac{1}{\phi^{CM}_{g,I}(t)}\frac{d\phi^{CM}_{g,I}(t)}{dt}, \tag{21}$$

The TCMFD calculation and the transport calculation using MOC are iterated until the neutron flux at $t = t_{n+1}$ in fine geometry sufficiently converges.

3. C5G7-TD Benchmark Analysis

The C5G7-TD benchmark problem [4] consists of two UO_2 and MOX PWR heterogeneous fuel assemblies surrounded by water reflectors. The cross sections for seven energy groups and the delayed neutron parameters for 8 precursor groups specified in the benchmark problem are used in the present calculations.

3.1 Sensitivity analysis for the initial condition

To confirm sufficient divisions for neutron flight directions and spatial meshes, a sensitivity analysis for the azimuthal angle division, ray separation, and flux region division is carried out. Table I shows the case matrix of the present sensitivity analysis. Figure 2 shows the flux region structure used in the present calculations.

Table I. Calculation condition for the neutron flight directions and spatial meshes

Case	Ref.	Case 1	Case 2	Case 3	Case 4
N_{azim}	128	128	128	64	128
N_{pol}	3	3	3	3	3
Δ_{path}	0.01	0.01	0.01	0.01	0.02
FR	Fig. 2(a)	Fig. 2(b)	Fig. 2(c)	Fig. 2(b)	Fig. 2(b)

* N_{azim} : azimuthal angle division for 2π using cyclic quadrature set,
N_{pol} : polar angle division for $\pi/2$ using Tabuchi-Yamamoto optimum quadrature set,
Δ_{path} : ray separation (cm),
FR : flux region division.

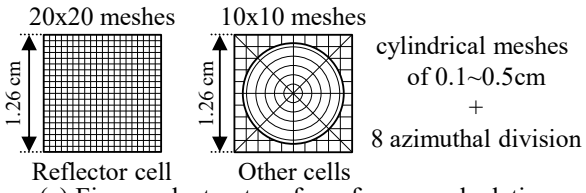

(a) Fine mesh structure for reference calculation

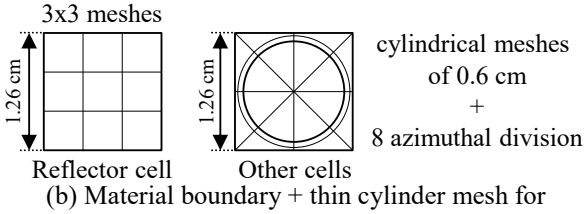

(b) Material boundary + thin cylinder mesh for moderator + octant division, 3x3 meshes for reflector

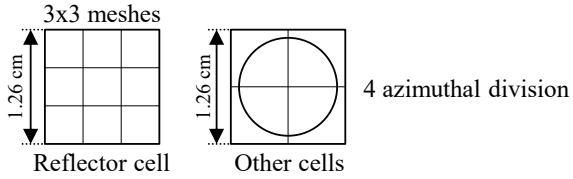

(c) Material boundary + quarter division, 3x3 meshes for reflectors

Fig. 2. Flux region divisions

Table II shows the initial eigenvalue, maximum and minimum pin power for each test case. In Table II, core-averaged pin power is normalized as 1.0.

Table II. Sensitivity for azimuthal angle division, ray separation, and flux region division

Case	Ref.	Case 1	Case 2	Case 3	Case 4
N_{azim}	128	128	128	64	128
Δ_{path}	0.01	0.01	0.01	0.01	0.02
FR	Fig. 2(a)	Fig. 2(b)	Fig. 2(c)	Fig. 2(b)	Fig. 2(b)
k_{eff}	1.18649	1.18651 (+2pcm)	1.18657 (+7pcm)	1.18638 (-9pcm)	1.18669 (+17pcm)
P_{max}	2.500	2.500	2.500	2.501	2.499
P_{min}	0.232	0.232	0.232	0.232	0.232
RMS	-	0.007%	0.030%	0.010%	0.050%

P_{max} : Maximum pin power (-),
P_{min} : Minimum pin power (-),
RMS : Root mean square difference with respect to the resference solution (Case : Ref.).

As shown in Table II, small discretization error remains in the case of the azimuthal angle division = 64 and the ray separation = 0.02 cm. The flux region division is sufficiently fine in the case of Fig. 2(b). The present result is also in good agreement with the MCNP5's initial k_{eff} solution, which is provided as 1.18646±0.07%.

3.2 Sensitivity analysis for the time step size

A sensitivity analysis for the time step size is carried out for the TD1 perturbation condition of the C5G7-TD benchmark problem [4] using the MAF method. Table III shows the case matrix of the present sensitivity analysis. The weighting parameter θ in the theta method was 1.0 for all calculations (the fully implicit method).

Table III. Calculation conditions for the time step

Case	Ref.	Case 1	Case 2
N_{azim}	128	128	128
N_{pol}	3	3	3
Δ_{path}	0.01	0.01	0.01
FR	Fig. 2(b)	Fig. 2(b)	Fig. 2(b)
Δt_{shape}	1000 msec	1000 msec	1000 msec
Δt_{amp}	1 msec	10 msec	100 msec

The reference core power transition, which is shown in Fig. 3, is calculated with Δt_{amp} = 1 msec.

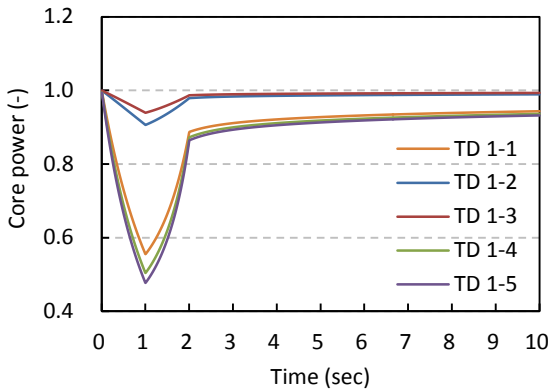

Fig. 3. Reference core power transition for TD1 perturbation

The accuracy of the core power transitions with respect to the reference solution is evaluated for Δt_{amp} = 10 msec and Δt_{amp} = 100 msec, respectively. Figure 4 shows the relative difference of the core power, which is calculated as:

$$\left(P - P_{ref}\right)/P_{ref} \times 100\ (\%)\ , \quad (P: core\ power, ref: reference\ solution). \qquad (22)$$

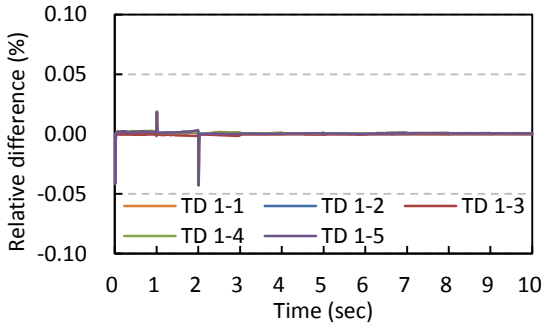

(a) Δt_{amp} = 10 msec

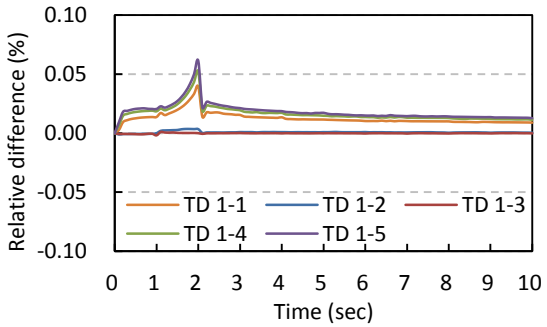

(b) Δt_{amp} = 100 msec

Fig. 4. Relative difference of the core power comparing to the reference solution

As shown in Fig. 4, the temporal discretization error is sufficiently reduced at Δt_{amp} = 10 msec for all test problems. Table IV shows a summary of the core power transitions in the present study.

Table IV. Summary of the core power transition*

Time (sec)	TD 1-1	TD 1-2	TD 1-3	TD 1-4	TD 1-5
0.0	1.00000	1.00000	1.00000	1.00000	1.00000
0.5	0.73048	0.95381	0.97044	0.68931	0.66629
1.0	0.55530	0.90639	0.93938	0.50412	0.47713
1.5	0.66388	0.93674	0.95945	0.61909	0.59455
2.0	0.88531	0.97872	0.98654	0.87035	0.86202
2.5	0.90237	0.98180	0.98846	0.88975	0.88275
3.0	0.91104	0.98339	0.98946	0.89955	0.89318
4.0	0.92115	0.98525	0.99062	0.91098	0.90534
6.0	0.93205	0.98723	0.99186	0.92329	0.91843
8.0	0.93868	0.98844	0.99261	0.93078	0.92639
10.0	0.94336	0.98928	0.99312	0.93607	0.93202

* calculation results of Δt_{amp} = 1 msec

3.3 Verification

To verify the present calculation results, a comparison of the core power transition with the other calculation code is carried out. Figure 5 shows the relative difference of the core power between the present study and the MPACT code [7] and they are in good agreement, where the relative difference is calculated as:

$$\left(P_{present\ study} - P_{MPACT}\right)/P_{MPACT} \times 100\ (\%)\ . \qquad (23)$$

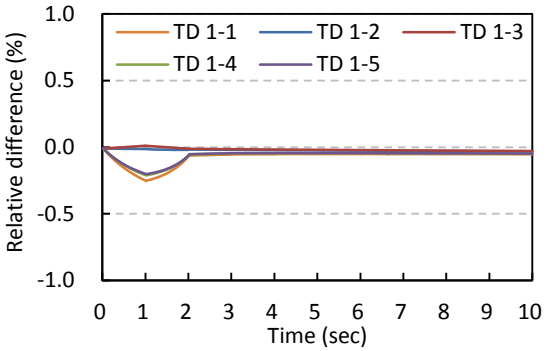

Fig. 5. Comparison of the core power transition with the MPACT code

5. Conclusions

Analysis of the C5G7-TD 2D benchmark is carried out by MOC using the linear source approximation and the MAF method. In the present summary, sensitivity analyses for neutron flight directions, spatial mesh structures, and the time step size are carried out and spatially and temporally fine transitions are obtained. The initial eigenvalue and the core power transitions for TD1 perturbation conditions were compared with those of the MCNP and MPACT code, respectively. They are in good agreement. The more detailed pin-wise comparison will be carried out in the future study.

References

1. Halsall MJ, *CACTUS, A Characteristics Solution to the Neutron Transport Equation in Complicated Geometries*, UKAEA, Winfrith (1980).
2. Ban Y, Endo T, Yamamoto A, "A Unified Approach for Numerical Calculation of Space-dependent Kinetic Equation," *J. Nucl. Sci. Technol.* **49**, 496 (2012).
3. Tsujita K, Endo T, Yamamoto A, "Application of the Multigrid Amplitude Function Method for Time-dependent Transport Equation using MOC," *Proc. M&C 2013*, Sun Valley, Idaho, May 5–9, 2013, American Nuclear Society (2013) (CD-ROM).
4. Boyarinov VF, Fomichenko PA, Hou JJ, *et al.*, "Deterministic Time-dependent Neutron Transport Benchmark without Spatial Homogenization (C5G7-TD)," OECD Nuclear Energy Agency (2017).
5. Ferrer R, Rhodes J, "Linear Source Approximation in CASMO5," *Proc. PHYSOR 2012*, Knoxville, Tennessee, Apr. 15–20, 2012, American Nuclear Society (2012) (CD-ROM).
6. Tsujita K, Endo T, Yamamoto A, *et al.*, "Higher Order Treatment on Temporal Derivative of Angular Flux for Time-dependent MOC," *Proc. M&C 2013*, Sun Valley, Idaho, USA, May 5–9 (2013) (CD-ROM).
7. Shen Q, Wang Y, Jabaay D, *et al*, "Transient analysis of C5G7-TD benchmark with MPACT," *Ann. Nucl. Energy*, **125**, 107 (2019).

Proceedings of the Reactor Physics Asia 2019 (RPHA19) Conference
Osaka, Japan, Dec. 2-3, 2019

FAST (Floating Absorber for Safety at Transient) for the Improved Safety of MOX-loaded Sodium-cooled Fast Reactors

Chihyung Kim and Yonghee Kim*
Dept. of Nuclear & Quantum Engineering, KAIST, 291 Daehak-ro, Yuseong-gu, Daejeon 34141, South Korea
*Corresponding author: yongheekim@kaist.ac.kr

Abstract

This paper presents passive safety device called FAST (Floating Absorber for Safety at Transient) for the improved inherent safety of sodium-cooled fast reactors (SFR). FAST is designed to cause negative reactivity feedback against coolant temperature rise compensating the positive reactivity induced by positive coolant temperature reactivity feedback. This study investigates the transient response of FAST in MOX-loaded SFR considering three ATWS (Anticipated Transient Without Scram) scenarios, which are ULOF (Unprotected Loss of Flow), ULOHS (Unprotected Loss of Heat Sink) and UTOP (Unprotected Transient Overpower). The ATWS simulations are performed with an in-house computer code taking into account all possible reactivity feedback components including the FAST movement and core expansion coefficients, and EOL (End-Of-Life) condition of the core with most positive CTC (Coolant Temperature Coefficient) is considered for the conservative analysis. Temperatures of core components and reactor power are considered as main factors of interest and it is confirmed that consequence of ULOF, ULOHS and UTOP in a MOX-loaded SFR core can be noticeably mitigated by the application of FAST device.

Key Words: **SFR, passive safety device, FAST, coolant temperature coeff icient, ATWS**

1. Introduction

Floating absorber for safety at transient (FAST) is a passive safety device for sodium-cooled fast reactors, which inserts negative reactivity in case of coolant temperature rise or coolant voiding [1]. Previous study showed that FAST in metallic fuel-loaded breed-and-burn sodium-cooled fast reactor (B&BR) core effectively works to compensate the coolant temperature feedback induced positive reactivity by inserting the negative reactivity in case of coolant temperature rise [2]. However, feasibility of FAST in metallic fuel-loaded B&BR with moving active core cannot represent the feasibility of FAST in oxide fuel-loaded SFR or burner-type SFR. In this regard, this study investigates the feasibility of FAST in MOX-loaded burner-type SFR core. The response of FAST at transient in advanced burner reactor (ABR) developed by ANL (Argonne National Laboratory) [3] is analyzed. In-house thermal hydraulics coupled point kinetics based transient code are used for the analysis.

2. Description of the FAST

FAST apparently has the same geometry as the fuel rod, but it does not contain the fuel inside as shown in Fig 1.

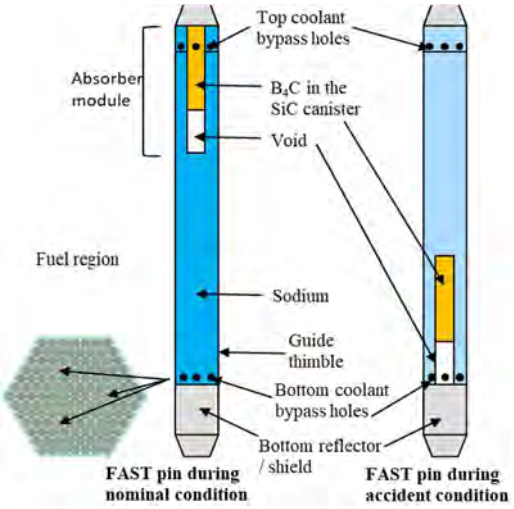

Fig. 1. Concept of FAST

The inside of the FAST is filled with coolant and the neutron absorber module is located in the coolant. The axial position of the absorber module is determined by the balance of buoyancy and gravity. There are several holes at the top and bottom of the FAST pin to allow the inflow and outflow of the coolant. The absorber module consists of the absorber and void canister to adjust the magnitude of buoyancy force. The absorber part is B_4C enclosed in a

SiC/SiC composite cladding and void part is filled with noble air. SiC/SiC composite is helium permeable so that the helium produced by (n,α) reaction of B-10 can be vented out through the cladding to release the internal pressure [4]. It is noteworthy that void part and absorber part are not attached to each other to increase the freedom of drop path in case of fuel pin or assembly bowing. One can also consider the separation of absorber part of absorber module in several pieces.

3. Reference Core: Advanced Burner Reactor

1000 MWth advanced burner reactor (ABR) core developed by ANL (Argonne National Laboratory) [3] is chosen as a reference core for the analysis of FAST behavior during the transient. Reactivity feedback coefficients of the reference core listed in Table I are used for the reactivity feedback during the transient.

Table I. Reactivity feedback coefficients of ABR

Reactivity feedback coefficients	Value
Fuel temperature (pcm/K)	-0.372
Coolant temperature (pcm/K)	0.496
Axial expansion (pcm/K)	-0.930
Radial expansion (pcm/K)	-0.155

4. Methodologies for FAST Behavior Analysis

4.1 Heat transfer model

Assuming radial temperature distribution of coolant is flat, heat transfer by the coolant flow can be modeled by 1-D time-dependent energy and mass conservation in the axial direction:

$$\rho c_{p_{coolant}} \frac{\partial T_{coolant}}{\partial t} + \rho c_{p_{coolant}} v_{coolant} \frac{\partial T_{coolant}}{\partial z} = q''' \quad (1)$$

$$\frac{\partial \rho_{coolant}}{\partial t} + v_{coolant} \frac{\partial \rho_{coolant}}{\partial z} + \rho_{coolant} \frac{\partial v_{coolant}}{\partial z} = 0 \quad (2)$$

In Eqs. (1) and (2), $\rho_{coolant}$ and $T_{coolant}$ are density and temperature of the coolant, respectively, and $v_{coolant}$ is velocity of the coolant flow. $c_{p,coolant}$ means the specific heat of coolant and it is assumed to be a constant since it is almost constant between 600 K and 900 K [5]. The heat source term for each axial node in the fuel region is calculated by considering the axial power distribution. A chopped cosine shape is assumed for the axial power distribution as shown in Fig. 2. It is assumed that the power distribution does not change during the transient since power distribution hardly changes in fast reactors.

Heat transfer in the fuel pin and FAST pin is treated as a radial 1-D heat conduction in cylindrical coordinate since axial heat conduction in the fuel rod is negligible compared to the radial heat conduction:

$$\rho c_p \frac{\partial T}{\partial t} = \frac{1}{r} \frac{\partial}{\partial r} \left(kr \frac{\partial T}{\partial r} \right) + q''' \quad (3)$$

Eq. (3) is solved by typical finite difference method using coolant temperature as a boundary condition.

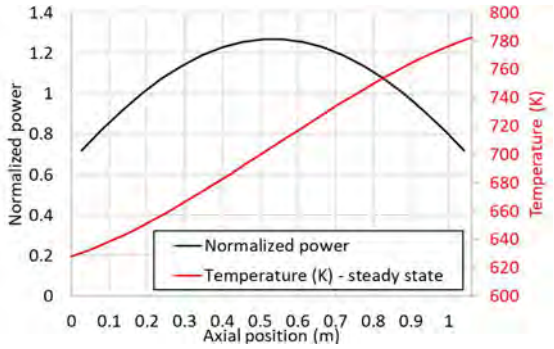

Fig. 2. Axial power profile of reference core

4.2 FAST movement model

Assuming that the fluid is incompressible, irrotational and fully developed, velocity field of coolant surrounding the absorber module ($V_{coolant}$) in FAST pin can be derived by Navier-Stokes equation in cylindrical coordinate [6].

$$\frac{d(\rho V_{coolant}(r))}{dt} = -r\frac{dp}{dz} + \mu \frac{d}{dr}\left\{ r\left(\frac{dV_{coolant}(r)}{dr} \right) \right\} \quad (4)$$

$$B.C.:\ V_{coolant}(r_{FAST}) = V_{FAST},\ V_{coolant}(r_{pin}) = 0$$

The equations for forces acting on FAST are tabulated in Table II.

TABLE II. Mathematical formulation of forces acting on FAST

Force type	Equation
Gravity	$F_g = \rho_{FAST} Volume_{FAST} g$
Buoyancy	$F_b = \int_V \rho_{coolant}(z)\, g dV$
Drag	$F_D = \int \mu \frac{dV_{coolant}}{dr} dA_{FAST\_side}$
Pressure	$F_p = \Delta p \times A_{FAST\_front}$

4.3 Point kinetics model

The standard point kinetics model is considered to simulate the change of reactivity in accordance with the temperature change of core components and insertion of the FAST. The point kinetics equation is solved by the simple finite difference method and the reactivity change is calculated by the equation (5).

$$\rho(t) = \rho_0 + \alpha_f \Delta T_f + \alpha_c \Delta T_c + \Delta\rho_{ex} + \Delta\rho_{FAST} \quad (5)$$

4.4 Reference FAST design

Detailed design parameters of reference FAST used for the transient analysis are listed in Table III.

Table III. Reference FAST design parameters

Design parameters	Value
Absorber height, cm	60
Void height, cm	20
Absorber module average density, g/cc	0.832
Absorber module radius, cm	0.20
FAST pin radius (inner/outer), cm	0.3215 / 0.3775

It should be noted this feasibility study considers arbitrarily determined design parameters of reference

FAST to be physically feasible. Maximum reactivity worth of FAST can be controlled by adjusting the enrichment of B_4C in absorber module and maximum reactivity of 1$ is considered for this study. Analyses in Ref. 2 showed that FAST reactivity worth of 1$ can be easily achieved by installing 3~4 FAST pins in each assembly. Position-wise reactivity worth of FAST absorber module is shown in Fig. 3 and it is determined assuming typical S-shape curve similar to that of the reactivity worth of control rods. At nominal state, void part of absorber module is fully sank in active core region, while absorber part is floating above the active core as shown in Fig. 3 to avoid the positive reactivity insertion by void insertion at transient and to minimize the reactivity perturbation by FAST at nominal state.

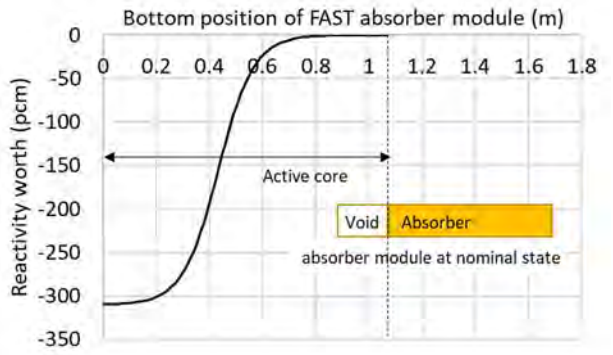

Fig. 3. Position-wise reactivity worth of FAST

5. Transient Response with the FAST Device

Three representative anticipated transient without scram (ATWS) scenarios are considered. All the transient events are triggered in an initially steady state.

In the ULOF scenario, failure of all the coolant pumps in the primary system is assumed. During the ULOF transient, coolant mass flow rate decreases with pump halving time of 5 seconds and 5% natural circulation is considered. Inlet coolant temperature of the core is assumed to remain unchanged during the ULOF.

In the ULOHS scenario, a complete loss of heat removal capacity in intermediate heat exchangers (IHXs) is considered and it is assumed that IHX heat removal capacity decreases from 100% to 0.0% over 20 seconds. It should be noted that the flow rate of the coolant in the primary circuit does not change during the ULOHS.

The UTOP scenario in this study assumes 50 seconds of external reactivity insertion with a ramp rate of 0.02 $/sec, while keeping the nominal coolant flow rate. Two heat removal scenarios in the IHX are considered for the simulation of UTOP: constant temperature drop in IHX and constant core inlet coolant temperature. The constant temperature drop in IHX scenario assumes that the amount of heat removal in IHX is always the same as the nominal full power. In the case of the constant inlet temperature scenario, core inlet coolant temperature is always kept the same as in the nominal condition, regardless of core outlet temperature.

Failure limit of the fuel is assumed to be 3000 K, which is slightly lower than the melting point of typical UO_2. The coolant boiling point of 1,150 K at 1 bar is considered to be a failure limit for the coolant in this work. However, the transient simulations are not interrupted even when temperatures of the core components reach the failure limit due to difficulties and uncertainties in modelling the fuel melting and coolant boiling.

5.1 Unprotected loss of flow (ULOF)

Figure 4 compares the transition of core power and maximum temperature of fuel and coolant with and without FAST. The power and the temperatures of fuel and coolant decreased sharply in the presence of FAST. One can note in Fig. 4 that FAST can prevent the coolant boiling that happens in case without FAST and it is clearly shown that FAST effectively mitigates the temperature rise of core components during the ULOF.

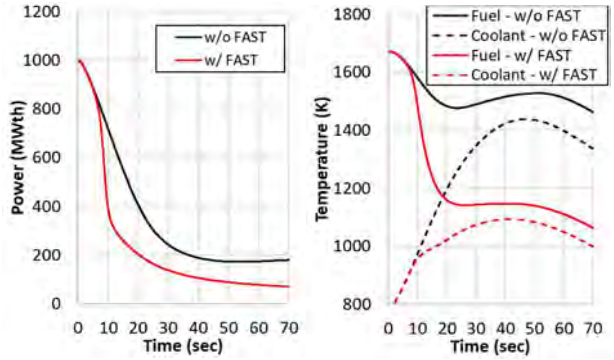

Fig. 4. Time evolution of the core power in ULOF

5.2 Unprotected loss of heat sink (ULOHS)

Figure 5 compares the transient progress of with and without FAST in ULOHS scenario.

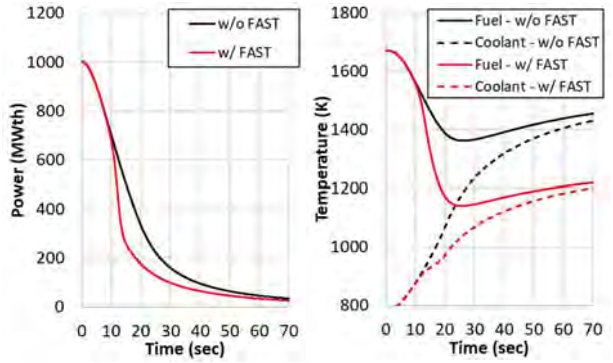

Fig. 5. Time evolution of temperature in ULOHS

In the presence of FAST, power decrease at ULOHS is more rapid and therefore, the temperature rise of the core components is much less than that without FAST. The reference core with FAST quickly shutdown and the temperatures of core components quickly converge to the equilibrium during the ULOHS as shown in Fig 5.

5.3 Unprotected transient overpower (UTOP)

Simulation results for the hypothetical UTOP case are shown in Figs. 6 and 7. In the absence of FAST, the power of the core increases sharply due to positive external reactivity insertion. On the other hand, the reactor power at the initial stage of UTOP is effectively suppressed by the FAST device and the core can survive the serious UTOP transient much longer with FAST with any IHX models.

However, oscillatory behavior of power and temperature due to refloating of FAST is observed in case with FAST. Although previous study showed that low reactivity worth of FAST is better to minimize the oscillation during the UTOP [2], it is difficult to make any concrete conclusions about the performances of FAST due to the highly uncertain IHX models. Consequently, a reliable reactor system model with a practical IHX model is necessary for a more accurate simulation of the UTOP scenario.

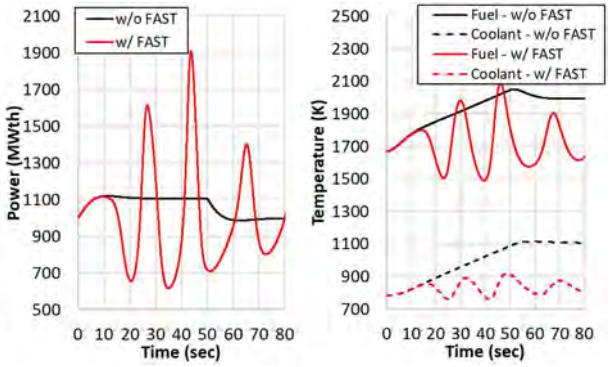

Fig. 6. Temperature change during the UTOP with constant temperature drop in IHX model

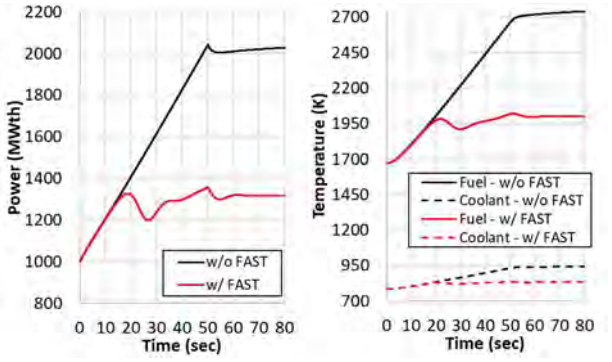

Fig. 7. Temperature change during the UTOP with constant inlet temperature IHX model

6. Conclusions

The transient analysis using a neutronics-thermal hydraulics coupled model showed that the FAST device can effectively prevent early failure of a MOX-fueled SFR core during the hypothetical ULOF, ULOHS and UTOP scenarios. In the case of the ULOF and ULOHS transients, a long-term safety is shown to be almost achievable with the aid of FAST. On the other hand, it is confirmed that the current FAST design is prone to a noticeable oscillation in case of external reactivity insertion during the UTOP case, in spite of very successful mitigation of power increase at the early stage of UTOP.

For more practical performance evaluation of FAST, it is necessary to analyze the ATWS transients by using accurate system code in the future.

Acknowledgements

This work was supported by the National Research Foundation of Korea Grant funded by the Korean government NRF-2016R1A5A1013919.

References

1. Donny Hartanto, Chihyung Kim, and Yonghee Kim, "A Comparative Physics Study for an Innovative Sodium-Cooled Fast Reactor (iSFR)," *International Journal of Energy Research*, Vol. 42, Issue 1, January (2018).
2. Chihyung Kim, "Passive Safety Device to Improve Coolant Temperature Coefficient of Reactivity for Sodium-cooled Fast Reactors," PhD Dissertation, KAIST (2019).
3. Cahalan, James E. et al. "Advanced Burner Reactor 1000MWth Reference Concept," ANL-AFCI-202, Argonne National Laboratory (2007).
4. Y. Katoh, et al., "Mechanical Properties of Chemically Vapor-Infiltrated Silicon Carbide Structural Composites with Thin Carbon Interphases for Fusion and Advanced Fission Applications," *Materials Transactions* 46 (3), 527-535 (2005).
5. Fink, J. K. and L. Leibowitz., "Thermodynamic and transport properties of sodium liquid and vapor," ANL/RE-95/2, Argonne National Laboratory (1995)
6. Khalil, M. F., Kassab, S. Z., Adam, I. G., & Samaha, M. "Laminar flow in concentric annulus with a moving core," *12th International Water Technology Conference*, IWTC12 (2008).

Proceedings of the Reactor Physics Asia 2019 (RPHA19) Conference
Osaka, Japan, Dec. 2-3, 2019

A Comparative Study on the IQS (Improved Quasi-Static) and PCQS (Predictor Corrector Quasi-Static) Methods

Tae-suk Oh[a], Yunseok Chung[a], and Yonghee Kim[a,*]
[a]*Dept. of Nuclear and Quantum Eng., KAIST, 291 Daehak-ro Yuseong-gu, Daejeon, Korea, 34141*
[*]Corresponding author: yongheekim@kaist.ac.kr

Abstract

In order to acquire the space-time solution of neutron balance equation with in a tolerable computational burden, factorization of flux into the product of two functions, which are namely '*amplitude'* and '*shape'* is widely utilized. The shape function varies in a longer time-scale than the amplitude, which makes the implementation of different time steps viable. In this paper, IQS (Improved Quasi-Static) and PCQS (Predictor Corrector Quasi-Static) method s have been employed, which contains Point Kinetic Equations (PKE), to solve a transient problem in a 1D-1group slab reactor. The new method to harness physical quantities of Kinetic Equation to attain the variation of amplitude is implemented along with the conventional approach. It has been shown that the proposed method more aptly reflects the physical perturbation.

Key Words: **Transient problem, IQS, PCQS, Point Kinetic Equations**

1. Introduction

Being able to investigate the behavior of the reactor subjected to various perturbations is important while designing or performing safety analysis of the nuclear power plants. However, directly solving the time-dependent neutron balance equation to acquire space-time solution imposes unaffordable computation burden. In order to circumvent such a situation, the quasi-static (QS) approach which factorizes the neutron flux had been devised and is widely used [1, 2].

Recently, the QS method had been revisited that illustrates the algorithms of Improved Quasi-Static (IQS) and Predictor Corrector Quasi-Static (PCQS) methods [3]. Both methods were implemented to ascertain the response of a one-dimensional slab reactor having localized perturbation in the multiplication properties.

In this paper, both IQS and PCQS methods are briefly introduced along with the key-concept of factorization approach. The authors also propose an improved concept to estimate the kinetic parameters for PCQS method which alleviates errors originating from the factorization. A numerical test on a one-dimensional one-group slab reactor diffusion problem was performed for two different perturbation scenarios (step-reactivity and ramp-up reactivity insertions) to validate the applicability of the aforementioned methods.

2. Quasi-Static Approach of a Time-Dependent Neutron Balance Equation

The quasi-static approach hinges on the factorization of neutron flux into the product of amplitude function $p(t)$ and shape function $\psi(\boldsymbol{r}, E, t)$.

$$\phi(\mathbf{r},E,t) = p(t)\psi(\mathbf{r},E,t)\,, \tag{1}$$

which is not an approximation but instead requires additional equation for being unique

$$\begin{aligned}\left\langle \psi_0^{\,*}, \frac{1}{v}\psi \right\rangle &:= \iint \psi_0^{\,*}(\mathbf{r},E)\frac{1}{v}\psi(\mathbf{r},E,t)d\mathbf{r}dE \\ &= c \equiv \left\langle \psi_0^{\,*}, \frac{1}{v}\phi_0 \right\rangle\end{aligned}\,. \tag{2}$$

Time-dependent neutron balance equation can be expressed as

$$\begin{aligned}&\frac{1}{v}\frac{\partial\phi}{\partial t} = (\mathbf{F}_p - \mathbf{M})\phi(\mathbf{r},\mathrm{E},\mathrm{t}) + \mathbf{S_d}[\phi(\mathbf{r},\mathrm{E},\mathrm{t})] + \mathbf{S}_{ext}(\mathbf{r},\mathrm{E},\mathrm{t}), \\ &\mathbf{S_d}[\phi(\mathbf{r},\mathrm{E},\mathrm{t})] = \sum_k \lambda_k \chi_{dk}(\mathrm{E})\mathrm{C}_k(\mathbf{r},t)\end{aligned}\,, \tag{3}$$

where ϕ and C_k denote energy-time dependent neutron flux and delayed neutron precursor concentrations. The operator $\mathbf{F}_p - \mathbf{M}$ denotes the time-dependent operator that includes prompt fission, absorption, scattering, and streaming. $\mathbf{S_d}$ and $\mathbf{S_{ext}}$ indicate the contribution from delayed neutrons and external source respectively. The balance for precursor concentration is expressed as

$$\frac{\partial C_k}{\partial t} = -\lambda_k \chi_{dk}(\mathrm{E})\mathrm{C}_k(\mathbf{r},t) + \int_0^\infty dE' \nu_{dk}\Sigma_f(\mathbf{r},E',t)\phi(\mathbf{r},E',t),\,. \tag{4}$$

$k =$ the number of considered precursor groups

For one-dimensional one-group problem, eqs (3) and (4) reduces into

$$\frac{1}{v}\frac{\partial \phi}{\partial t} = (\mathbf{F}_p - \mathbf{M})\phi(\mathbf{r},\mathrm{t}) + \mathbf{S_d}[\phi(\mathbf{r},\mathrm{t})], \quad \mathbf{S_d}[\phi(\mathbf{r},\mathrm{t})] = \sum_k \lambda_k \mathrm{C}_k(\mathbf{r},t) \quad (5)$$

$$\frac{\partial C_k}{\partial t} = -\lambda_k \mathrm{C}_k(\mathbf{r},t) + \nu_{dk}\Sigma_f(\mathbf{r},t)\phi(\mathbf{r},t)\,, \quad (6)$$

while neglecting the contribution from external source. Taking eq (1) into account, the balance equation can be expressed as

$$(\mathbf{F}_p - \mathbf{M})\psi(\mathbf{r},E,t) + \frac{1}{p(t)}\mathbf{S_d}[p(t')\psi(\mathbf{r},\mathrm{E},\mathrm{t}')] = \frac{\dot{p}}{vp}\psi(\mathbf{r},E,t) + \frac{1}{v}\frac{\partial\psi(\mathbf{r},E,t)}{\partial t}\,, \quad (7)$$

where $\dot{p}$ denotes the time derivative of power. The evolution of amplitude can be treated via exact-point kinetic equation (EPK)

$$\frac{dp}{dt} = \frac{\rho(t)-\beta(t)}{\Lambda(t)}p(t) + \frac{1}{\Lambda_0}\sum_k \lambda_k \xi_k(t)\,,$$
$$\frac{d\xi_k}{dt} = -\lambda_k\xi_k(t) + \frac{F(t)}{F_0}\beta_k(t)p(t)\,, \quad (8)$$

where each parameter can be calculated as

$$F(t) = \langle \psi_0^*, \mathbf{F}\psi\rangle,$$
$$\Lambda(t) = {}^{c}\!/_{F(t)},$$
$$\beta_k(t) = \frac{1}{F(t)}\langle \psi_0^*, \mathbf{F}_{dk}\psi\rangle,$$
$$\xi_k(t) = \frac{1}{F_0}\langle \psi_0^*, C_k(\mathbf{r},t)\rangle,$$
$$\rho(t) = \frac{1}{F(t)}\langle \psi_0^*, [\Delta\mathbf{F} - \Delta\mathbf{M}]\psi\rangle\,. \quad (9)$$

Notation ψ_0^* indicates the adjoint flux (shape) which is conventionally employed as a weighting factor.

From the reasonable conjecture that the shape of the flux varies much slower than its amplitude, different time-steps are implemented while numerically solving eqs (7) and (8) which is the key idea of QS approach. It is worthwhile to underline that p and $\dot{p}$ from eq (8) is subsumed while deducing the shape $\psi(\boldsymbol{r},t)$ from eq (7), and the (updated) shape is then used to acquire EPK parameters by eq (9).

2.1 Improved Quasi-Static (IQS)

IQS method can be achieved by the following steps, which requires iteration(s) to satisfy the convergence of the shape function.

[1] Calculate EPK parameters (9) using current shape function $\psi(\boldsymbol{r},t)$.
[2] Solve EPK for micro-step δt until $t+\Delta t$ to acquire p and $\dot{p}$ at $t+\Delta t$.
[3] Calculate the shape function at $t+\Delta t$ with eq (7).
[4] Calculate the normalized difference $\varepsilon_\psi = \frac{\left|<\phi_0^*, \frac{1}{v}\psi> - c\right|}{c}$, and normalize the updated shape function to c.
[5] Repeat 1-4 until ε_ψ becomes smaller than certain value. Note that EPK parameters must be re-evaluated using the updated shape function

2.2 Predictor Corrector Quasi-Static (PCQS)

PCQS method directly solves the neutron balance equation rather than employing eq (7) for macro-step Δt. After acquiring the updated flux and precursor information, EPK parameters are evaluated and used for solving eq (8) for micro-step δt.

[1] Solve eq (3) to acquire flux and precursor concentration at $t+\Delta$t. Such solutions are denoted as $\tilde{\phi}(\boldsymbol{r},t)$ and $\tilde{C}_k(\boldsymbol{r},t)$.
[2] Calculate $z = \left\langle \psi_0^*, \frac{1}{v}\psi \right\rangle / c$ to obtain the shape function $\psi(\boldsymbol{r},\Delta t) := \frac{1}{z}\tilde{\phi}(\boldsymbol{r},\Delta t)$ where $c := <\phi_0^*, \frac{1}{v}\phi_0>$
[3] Evaluate the EPK parameters using eq (9) and solve eq (8) until $t+\Delta$t to obtain $p(t+\Delta t)$.
[4] Correct the flux and precursor concentrations.

$$\phi(\mathbf{r},E,t+\Delta) = p(t+\Delta t)\psi(\mathbf{r},E,t+\Delta t)\,,$$
$$C_k(\mathbf{r},\mathrm{t}+\Delta\mathrm{t}) = \frac{1}{1+\lambda_k\Delta t}C_k(\mathbf{r},\mathrm{t}) + \frac{\beta_k\Delta t}{1+\lambda_k\Delta t}\int \nu\Sigma_f\phi(\mathbf{r},E,t+\Delta t)dE'\,. \quad (10)$$

3. Numerical Results and Discussion

To investigate the reliability of IQS and PCQS methods, a one-dimensional one-group 1 [m] slab reactor subjected to localized perturbation (ranging from 20 [cm] to 30 [cm]) in the absorption cross section was considered. The perturbation was given at $t = 2.0\,[s]$ in two different ways: Case (1) step-transition, and Case (2) ramp-up transition for 1 [s]. The micro-step was fixed to 0.1 [ms] throughout the simulation. The detailed physical information regarding the problem is depicted in Table 1

Table 1. Summary of Physical Information

1D 1Group Slab Reactor	
Σ_a	0.066 [1/cm]
$\nu\Sigma_f$	0.070 [#/cm]
D	0.9 [cm]
v_0	300,000 [cm/sec]
Slab Length	100 [cm]
${}^{\delta\Sigma_a}\!/_{\Sigma_a}$	$\pm$5%

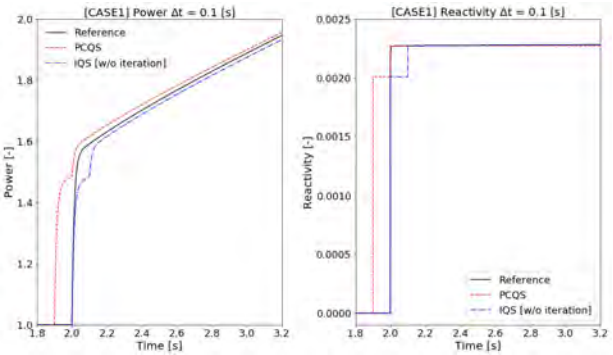

Fig. 1. Power and reactivity from IQS and PCQS for step-transition.

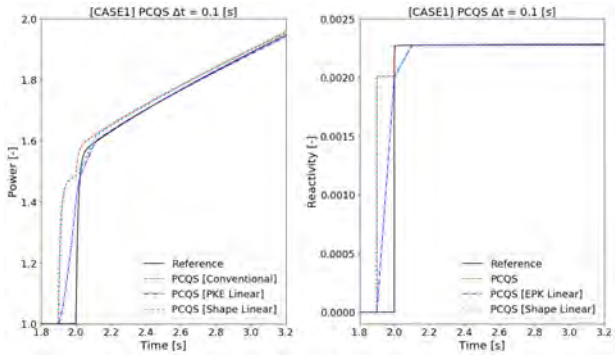

Fig. 3. Power and reactivity from linear interpolation PCQS for step-transition.

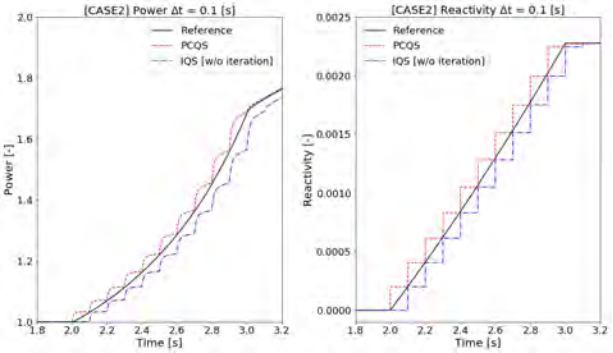

Fig. 2. Power and reactivity from IQS and PCQS for ramp-up transition.

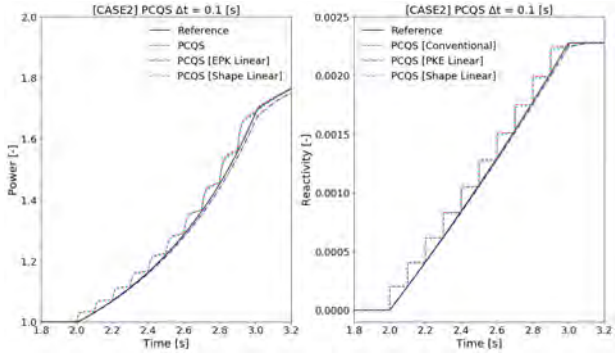

Fig. 4. Power and reactivity from linear interpolation PCQS for ramp-up transition.

Calculated power and reactivity evolution via IQS and PCQS after the onset of transitions are shown in Fig. 1 and Fig. 2. For obtaining IQS solution, lenient convergence criterion was imposed in order to minimize the computation burden originating from the iterative procedure. Such treatment renders the IQS method to be consistent with the PCQS method in terms of non-iterative attribute. It can be seen that reference solution, which was obtained by solving eq (3) within a fine time-step, is preceded by PCQS solution whereas the IQS solution tends to lag with respect to the reference for both cases. Such behavior originates from the usage of updated shape function for PCQS and initial shape for IQS while deducing the EPK parameters. Furthermore, since the EPK parameters are assumed to be constant within a macro-step Δt, saw-tooth like evolution of power was observed.

3.1 Linearization Approaches to PCQS method

The saw-tooth like evolution can induce a significant error in the calculated power when the calculation is performed with a large time-step. To overcome such a problem, the authors liberated the constraint of having constant EPK parameters while solving eq (8). Based on the PCQS approach, after acquiring the updated EPK parameters which hinge on the updated shape, either EPK parameters or shape can be linearly interpolated for each micro-step. Then the exact point kinetic equation can be solved from such parameters.

Fig. 3 and 4 depicts the time evolution of power and reactivity after the perturbation estimated by PCQS (red-dashed), PCQS with linear EPK interpolation (blue-dashed dot), and PCQS with linear shape interpolation (cyan-dotted) after step and ramp-up transient respectively.

There was no noticeable difference between the shape interpolated result and the conventional PCQS result except for the foremost macro-step after the onset of step-transition as shown in Fig. 3. This implies that the shape does not vary substantially except for severely abrupt perturbation, i.e., step-transition. For ramp-up transient, it can be seen that power and reactivity obtained from linear interpolation of EPK adequately resembles the reference solution since change in the absorption cross section varies linearly.

3.2 Consideration of Different Macro-Steps

The magnitude of macro-step contributes to both computational burden and accuracy. For more realistic problems, e.g., three-dimensional multigroup whole core problem, solving the space-time dependent equation for shape (or flux) demands majority of the computational resources than solving exact point kinetic equation. Furthermore, since the variation of power within a macro-step is estimated through point kinetic equation, one can conclude that having larger macro-step is beneficial in terms of computation time; however, a drawback from the perspective of accuracy.

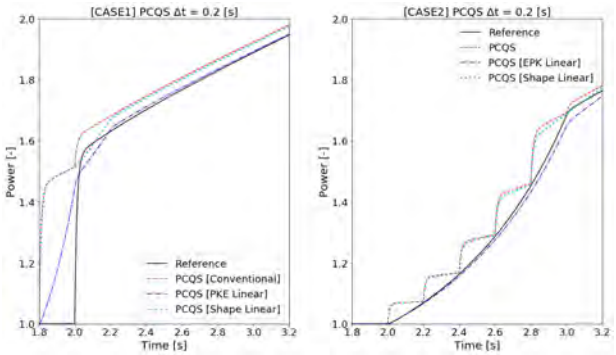

Fig. 5. Power evolution for step and ramp-up transient for macro-step of 0.2 [s]

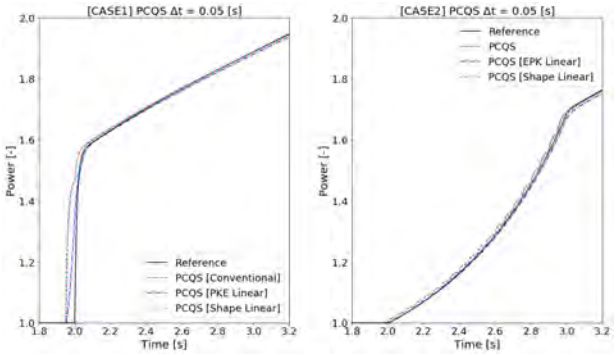

Fig. 6. Power evolution for step and ramp-up transient for macro-step of 0.05 [s]

Fig. 5 depicts the estimated power evolution for macro-step of 0.2 [s] for both step and ramp-up transient cases. Compared to macro-step of 0.1 [s] results, which are shown in Fig. 3 and 4, the calculated solution deviates further from the reference. Fig. 6 shows the result obtained for macro-step of 0.05 [s]. The saw-tooth like evolution feature from the original PCQS and linear-shape interpolated PCQS dwindles as macro-step increases which implies that having shorter macro-step increases the accuracy. Required computational time for each case is tabulated in Table 2. Considering both the computational time and accuracy of the solution, one can conclude that PCQS with linear EPK interpolation is the most suitable method among the proposed methods.

4. Conclusions

In this paper, IQS and PCQS methods were implemented to solve space-time dependent neutron balance equation for one-dimensional one-group slab reactor subjected to localized perturbation. Due to the usage of initial and updated shape while attaining EPK parameters, which do not vary during EPK calculations, the IQS tends to lag and PCQS tends to be ahead of the reference solution respectively. Furthermore, both methods become unreliable in terms of power when the macro-step increases.

To surmount such defects, the authors proposed a new method to harness EPK parameters for each micro-step by employing either linear interpolation of EPK parameters or the shape.

Table 2. Summary of computational time

Method	Δt [s]	Computational Time [s]
Case 1. Step-Transition		
Reference	0.0001	141.445
IQS [w/o iteration]	0.1	2.454
PCQS	0.2	2.542
PCQS [EPK Linear]	0.2	2.670
PCQS [Shape Linear]	0.2	7.856
PCQS	0.1	2.593
PCQS [EPK Linear]	0.1	2.670
PCQS [Shape Linear]	0.1	7.749
PCQS	0.05	2.980
PCQS [EPK Linear]	0.05	3.081
PCQS [Shape Linear]	0.05	7.938

Method	Δt [s]	Computational Time [s]
Case 2. Ramp-up Transition		
Reference	0.0001	147.542
IQS [w/o iteration]	0.1	2.433
PCQS	0.2	2.515
PCQS [EPK Linear]	0.2	2.613
PCQS [Shape Linear]	0.2	7.710
PCQS	0.1	2.595
PCQS [EPK Linear]	0.1	2.819
PCQS [Shape Linear]	0.1	7.985
PCQS	0.05	3.001
PCQS [EPK Linear]	0.05	3.074
PCQS [Shape Linear]	0.05	8.464

It has been shown that implementation of PCQS method aided with interpolation of kinetic parameters results in the most physically acceptable solution. Consideration of higher order interpolation along with the adaptive time-step scheme will be pursued in the future.

Acknowledgements

This work was supported by the National Research Foundation of Korea (NRF) Grant funded by the Korean Government (MSIP) (NRF-2016R1A5A1013919)

References

1. A. F. Henry & N. J. Curlee (1958), "Verification of a Method for Treating Neutron Space-Time Problems", *Nuclear Science and Engineering*, 4:6, 727-744.
2. K. O. Ott & D. A. Meneley (1969), "Accuracy of the Quasistatic Treatment of Spatial Reactor Kinetics", *Nuclear Science and Engineering*, 36:3, 402-411.
3. Sandura Dulla *et al.,* "The quasi-static method revisited", *Progress in Nuclear Energy*, 50 (2008) 908-920

Proceedings of the Reactor Physics Asia 2019 (RPHA19) Conference
Osaka, Japan, Dec. 2-3, 2019

Point Kinetics Analysis for Source-jerk Experiment at AGN-201K

Seulki Lim[a], Hyung Jin Shim[a*], Myung-Hyun Kim[b]

a Nucl. Eng. Dept., Seoul National University, 1 Gwanak-ro, Gwanak-gu, Seoul 08826, Korea

b Nucl. Eng. Dept., Kyung Hee University 1732, Deogyeong-daero, Giheung-gu, Yongin-si, Gyeonggi-do 17104, Korea

[s*]Corresponding author: shimhj@snu.ac.kr

Abstract

Point kinetics analysis is a widely used for performing analyses of dynamic phenomena. However, it is based on kinetics theory developed for critical reactor studies, and thus its applicability to subcritical systems is subject to investigation. In this paper, we conducted point kinetics analysis on source-jerk experiment at AGN-201K reactor, Kyung Hee University. And the point kinetics analysis results are compared with experiment data.

Key Words: **point kinetics analysis, subcritical system, source-jerk**

1. Introduction

Point kinetics analysis is a widely used for performing analyses of dynamic phenomena.

It has been extensively applied for the transient design analysis of existing reactors and forms the basis of many transient analysis computational codes. However, it is based on kinetics theory developed for critical reactor studies and thus its applicability to subcritical systems is subject to investigation. [1] Thus, in this paper, we conducted point kinetics analysis on source-jerk experiments at AGN-201K [2,3] reactor in subcritical state. The main objectives of this study is to confirm the change of the detector signal according to the initial location of the source, and to compare the result of the point kinetics analysis with the experimental result that changes subcriticality.

2. Source jerk experiments

2.1 AGN-201K reactor

The experiment was conducted with AGN-201K reactor at Kyung Hee University. The AGN-201K reactor has been operated for research and education since 1982. AGN-201K consists of polyethylene disks embedding 19.5 wt. % enriched UO2 particles, control rods, graphite reflector, lead and water shields. [4]

The AGN-201K reactor has four control rods –two safety rods (SR 1 and SR 2), one coarse rod (CR), and one fine rod (FR) – which can be inserted by 16 cm from the bottom of the fuel disk 9 in a total flight length of 24cm within vertical control element tubes. The reactor operator can insert negative reactivity by withdrawing the control rods. The composition of control rods is the same as the fuel disks. The thicknesses of its cladding and control element tube made of aluminum are 0.25 cm and 0.25 cm, respectively. The FR contains 2.5 g of 235U with the inner diameter of 2 cm. Then AGN-201K becomes to have the total 235U amount of 690g in the fuel disks and the control rods.

2.2 Source jerk experiment

The experiment goal is to measure the detector signal that appears when removing the source from the subcritical reactor that contains the neutron source. In this experiment, we used Ra-Be neutron source

Before the experiments, we conducted a task of finding the critical state control rod position of this reactor and as a result, this reactor's critical state control rod position is FR 15.56cm, CR 20.67cm, SR 23cm.

The experiment is conducted in two stage. First, put a neutron source into the subcritical state reactor and wait 150 seconds for the detector signal to stabilize. Second, inserted neutron source quickly removes at 151 seconds and detector signal measured up to 300 seconds. In this experiment, Helium-3 detector was used to measure the count rate.

Figure 1. shows the planar configuration of AGN-201K used in the experiment and Table I. shows details of the experiments that we conducted

.

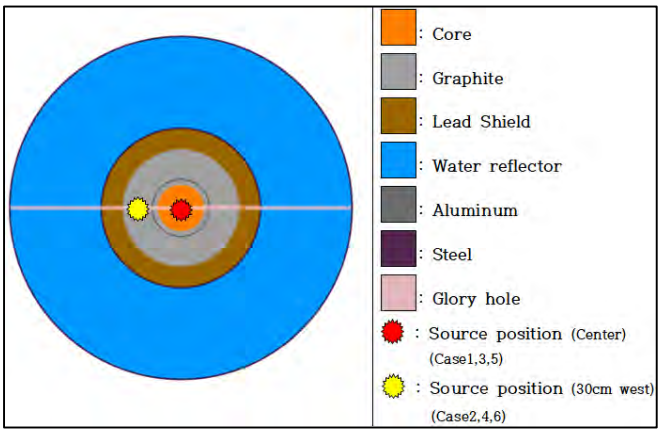

Fig. 1. Planar Configuration of experiment

Table I. Experiment conditions

Case	Control Rod Position			Source position	Initial count rate
	Fine rod	Coarse rod	Safety rod		
1	0cm	10cm	23cm	Center	5,610
2				30cm west	1,066
3		0cm	23cm	Center	4,378
4				30cm west	753
5			0cm	Center	1,571
6				30cm west	338

2.3 Experiment result

Figures 2.–4. show result of source jerk experiment.

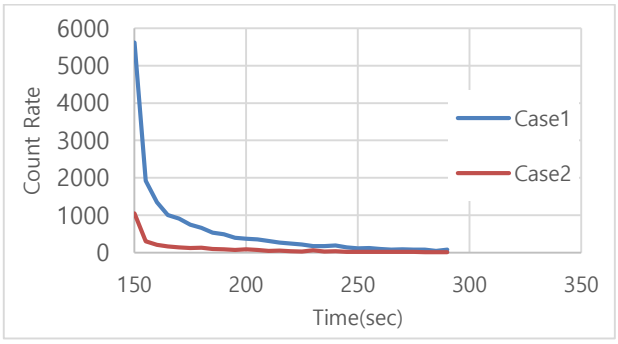

Fig. 2. Experiment result (Case 1,2)

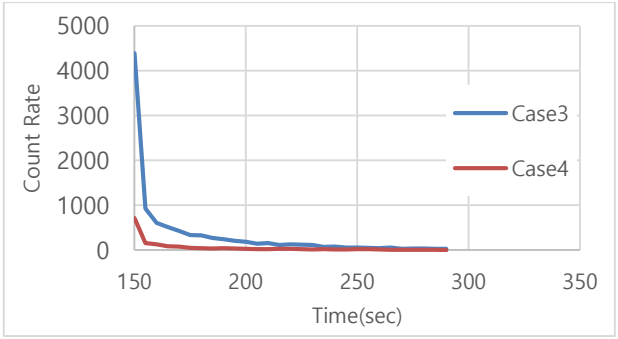

Fig. 3. Experiment result (Case 3,4)

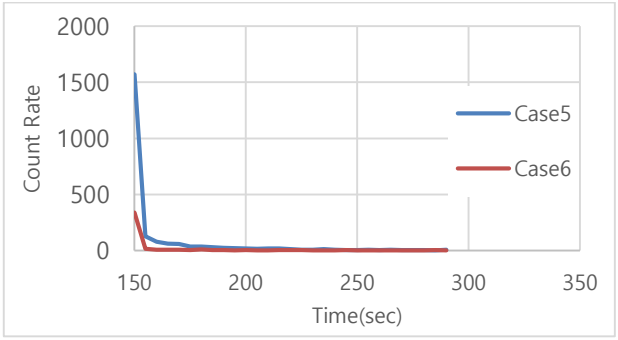

Fig. 4. Experiment result (Case 5,6)

The signal after 150 seconds was measured every 5 seconds. It was showed that the count rate drops rapidly as soon as the neutron source was removed.

3. Point kinetics analysis for source-jerk experiment

3.1 Point kinetics analysis for experiments.

To conduct point kinetics analysis for this experiments, we should obtain initial reactivity and kinetics parameter. To get initial reactivity and kinetics parameter, the McCARD[6] eigenvalue calculations are performed with 1,000,000 histories per cycle on 50 inactive and 400 active cycles using the continuous-energy cross section libraries produced from ENDF/B-VII.1 and thermal scattering libraries, for water, graphite, and polyethylene.

Table II. shows the k_{eff} and initial reactivity that calculated by McCARD. We get initial reactivity as the relative difference between experiment case and critical state. Table III. shows kinetics parameters that calculated by McCARD.

Table II. McCARD calculation of k_{eff} and reactivity

	$k_{\mathrm{eff\,(S/D)}}$	Reactivity $(1/k_{\mathrm{critical}} - 1/k_{\mathrm{experiment}})$
Case 1,2	1.00383 (0.00004)	-720 pcm
Case 3,4	1.00028 (0.00004)	-1,074 pcm
Case 5,6	0.97824 (0.00004)	-3,326 pcm
Critical state	1.01114 (0.00005)	-

Table III. McCARD calculation of Kinetics Parameters

Kinetics parameter	Case 1,2	Case 3,4	Case 5,6
$\beta_{i,eff}$ (S/D)	0.00757 (0.00283)	0.00761 (0.00278)	0.00760 (0.00284)
β_1 (S/D)	0.00026 (0.01454)	0.00028 (0.01473)	0.00027 (0.01575)
β_2 (S/D)	0.00139 (0.00641)	0.00137 (0.00657)	0.00138 (0.00684)
β_3 (S/D)	0.00131 (0.00660)	0.00133 (0.00670)	0.00132 (0.00669)
β_4 (S/D)	0.00291 (0.00450)	0.00291 (0.00455)	0.00290 (0.00457)
β_5 (S/D)	0.00120 (0.00727)	0.00122 (0.00684)	0.00122 (0.00726)
β_6 (S/D)	0.00050 (0.01118)	0.00051 (0.01073)	0.00051 (0.01128)
(S/D)	0.00007 (0.00069)	0.00007 (0.00064)	0.00008 (0.00068)

3.2 Comparison between experiment and numerical result

Figure 5.-7. show comparisons between point kinetics analyses and experiments.

The figures showed that even when the experiment was carried out by changing the position of the neutron source with the same rod position, the dropping rate was not significantly different. And it showed that the point kinetics analyses are quite in accordance with experiments that carried out in a subcritical state.

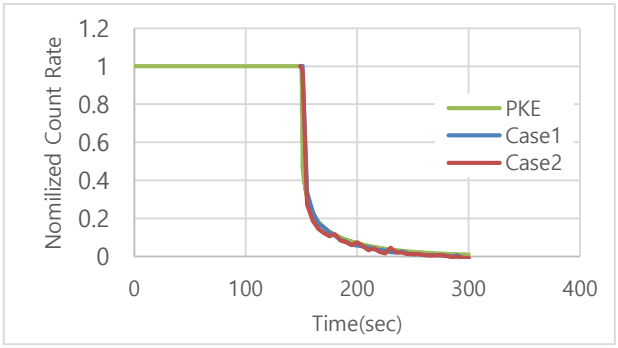

Fig. 5. Comparison between point kinetics analysis and experiment (Case 1,2)

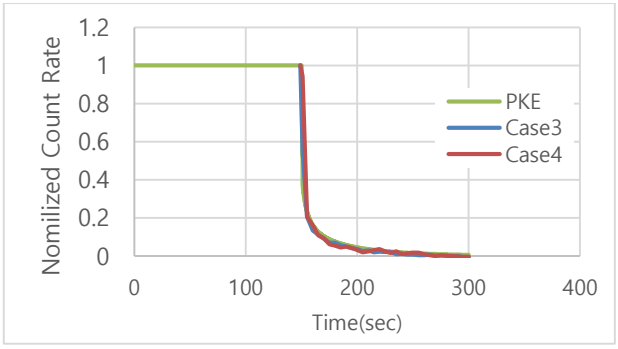

Fig. 6. Comparison between point kinetics analysis and experiment (Case 3,4)

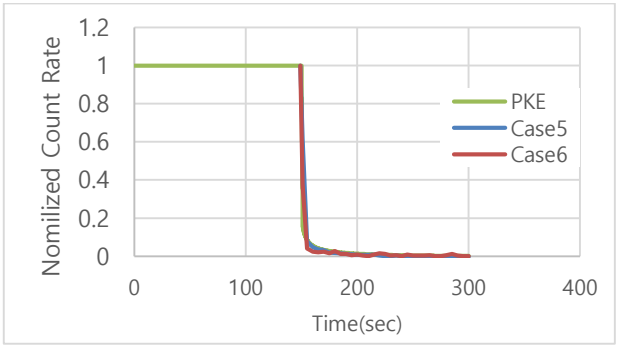

Fig. 7. Comparison between point kinetics analysis and experiment (Case 5,6)

4. Conclusion

It was confirmed that there was no significant difference in the dropping rate seven when the source jerk experiment was conducted with different neutron source positions. And although this experiments were conducted in subcritical state, the point kinetics analyses for the source jerk experiments are quite in accordance with experiments data. The reason seems to be that the experimental reactor subcriticality is slightly smaller than 1.0 and it is not deep enough.

For the future work, point kinetics analysis of the source trip experiment will be carried at KUCA with deep subcriticality condition.

References

1. Eriksson M, Cahalan JE, Yang WS. On the Performance of Point Kinetics for the Analysis of Accelerator-Driven Systems. Nucl. Sci. Eng. (2005)
2. M. H. Kim, Research & Educational Reactor AGN-201K, Reactor Research & Education Center, Kyung Hee University, (2018).
3. M. H. Kim, Utilization of AGN-201K for Education and Research in Korea. No. INIS-BE--11N0031. (2011).
4. Kyoseong Song., McCARD Analysis for AGN-201K Reactor Physics Experiments, Seoul National University, Korea nuclear society (2018)
5. H. J. Shim et al., McCARD for Neutronics Design and Analysis of Research Reactor Cores, Seoul National University, Annals of Nuclear Energy, 82, pp.45-53, (2015).

TS-05 Reactor Physics Experiments

A Subcriticality Measurement of AGN-201K Reactor using the Rossi-α Method

Sungho Moon, Jong Hoon Kim, Myung Hyun Kim and Ser Gi Hong*
Kyung Hee University, Department of Nuclear Engineering
1732 Deogyeong-daero, Giheung-gu, Yongin, Gyeonggi-do, 17104 - Korea
*Corresponding author: sergihong@khu.ac.kr

Abstract

A continuous subcriticality monitoring using ex-core detectors signal can provide operational margin with respect to criticality of nuclear reactors. The Rossi-α method which is one of the most popular noise analysis methods estimates the prompt neutron decay constant(α) by using the probability representing auto-correlation of the detector signals in time and it can be used in estimating k_{eff} with kinetic parameters. In this study, subcriticality measurement using the Rossi-α method is performed at AGN-201K. The results show that the subcriticality for several control rod positions can be estimated within ~330 pcm Δk.

Key Words: **Subcriticality, Rossi-α method, Noise analysis method, AGN -201K**

1. Introduction

Most nuclear facilities are designed to have conservative subcritical margin to accidentally uncontrolled neutron multiplications. Therefore, an accurate real-time measurement of subcriticality can provide a helpful way to guarantee the safe operation of nuclear facilities. Noise analysis methods have been studied for a long time for this purpose. The most noise analysis methods have the same basis that the properties of a subcritical system can be determined by measuring fluctuations in the fission chain processes. The fluctuations in fission chain processes are dependent on the stochastic nature of chain reactions. The Rossi-α method is one of the popular noise analysis methods. In this work, subcriticality experiment is performed with the Rossi-α method for checking its suitability at AGN-201K which is unique zero-power research and training reactor in our country.

2. Theory and Method for Rossi-α Method

2.1 Review of Rossi-α method

An understanding of the distinction between correlated neutron pairs which are derived from same neutron ancestor and uncorrelated neutron pairs is essential to the comprehension of how the Rossi-α method was developed. Fig. 1 provides a random branching process of neutron in the view point of correlated and uncorrelated neutron pairs. The left hand fission event represents the relationship of correlated fission neutrons between A and B. On the other hand, the event C describes the uncorrelated event with the event A or B. The probability that a neutron is counted at time t_0=0 can be defined as follows :

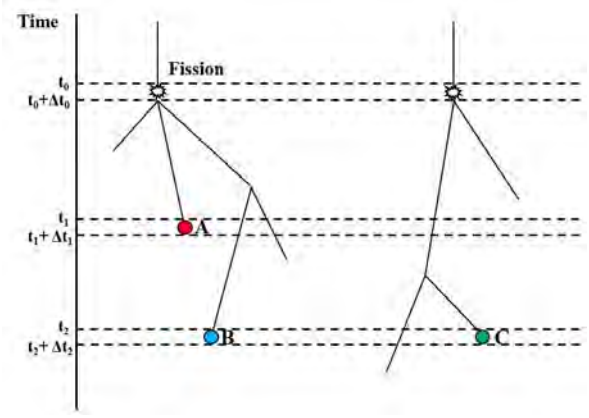

Fig. 1. Random branching process of fission neutron

$$p_0(t_0)dt_0 = Fdt_0, \tag{1}$$

where F is the average fission rate. The probability of detecting correlated neutron detection event near time t_1 and t_2 (i.e., the probability that the neutrons generated from a fission reaction at t_0 are detected at t_1+dt_1 and dt_2 respectively) are given by

$$\begin{aligned} p_1(t_1)dt_1 &= \varepsilon \nu_p \upsilon \Sigma_f e^{-\alpha(t_1-t_0)}dt_1 \\ p_2(t_2)dt_2 &= \varepsilon(\nu_p - 1)\upsilon \Sigma_f e^{-\alpha(t_2-t_0)}dt_2 \end{aligned}, \tag{2}$$

where ε is the detector efficiency and ν_p is the average number of prompt neutrons generated by one fission, υ is the neutron velocity, and Σ_f is the macroscopic fission cross section. It is noted that the ν term has been modified to $(\nu-1)$ to account for the neutron lost at t_1 to the fission chain. Therefore, the total probability of detecting two chain-related counts initiated by a fission at time t_0 can be

derived as follows :

$$p_c(t_1,t_2)dt_1dt_2 = \int_{-\infty}^{t_1} p(t_1)dt_1 p(t_2)dt_2 F dt_0 = F\varepsilon^2 \frac{D_v k_p^2}{2(1-k_p)\Lambda} e^{-\alpha(t_2-t_1)} dt_1 dt_2 \quad , \qquad (3)$$

where D_v is the Diven's factor considering an average of the number of prompt neutrons emitted, k_p is the prompt critical, and Λ is the neutron generation time. The probability of detecting two random uncorrelated events which are not derived from same ancestor can be seen in Eq. (4)

$$p_r(t_1,t_2)dt_1dt_2 = F^2\varepsilon^2 dt_1 dt_2 \,, \qquad (4)$$

The final total probability of detecting two neutron counts is obtained by summing the correlated and uncorrelated event probabilities, which is given by

$$p(t_1,t_2)dt_1dt_2 = F\varepsilon^2 \left(F + \frac{D_v k_p^2}{2(1-k_p)\Lambda} e^{-\alpha(t_2-t_1)} \right) dt_1 dt_2 \,. \qquad (5)$$

It is shown that a correlation between two detecting points decreases exponentially with the form of Eq. (5) as their time difference increases. This method can determine the prompt neutron decay constant (α) by considering the auto-correlation of the detector signals in time using Eq. (6), which is supposed to be equivalent to Eq. (5) theoretically.

$$P(\tau) = P(k\Delta t) = \frac{1}{N-k} \sum_{i=1}^{N-k} C(i)C(i+k) \,, \qquad (6)$$

where τ is the time interval between two detecting time points (=t_2-t_1), N is the total number of time bins, and C is the detector counts in a given time bin. By using the following least square fitting of the Rossi probability which is equivalent with Eq. (5) versus the gate time τ, α can be obtained [1, 2] :

$$Fitting\ \ Curve = A + Be^{-\alpha\tau} \,, \qquad (7)$$

After the determination of the prompt neutron decay constant (α), the effective multiplication factor can be calculated using Eq. (8) derived from point kinetics equation [3] as follows :

$$k_{eff} = \frac{1}{1-\beta+\alpha\Lambda} \,. \qquad (8)$$

2.2 Subcriticality Measurement System (SMS)

In this study, a time-series data of neutron counts within a fine unit gate time of 10μsec is acquired using the Subcriticality Measurement System (SMS) which was developed by Korea Electric Power Research Institute (KEPRI) for measuring the ex-core detector signal from commercial PWR to get the condition of large subcriticality [4]. Since the neutron generation time (Λ) of AGN-201K is estimated about 50~60 μsec, the shorter gate time can acquire more detailed information for estimating the α value [4]. Therefore, in this work, the unit gate time is set to 10 μsec. Due to this measuring system, the neutron counts in a few seconds provide a large number of count data for a huge number of time bins. Fig. 2 shows the measured neutron counts during 0.1 seconds containing 10,000-time bin data using 10 μsec unit gate time.

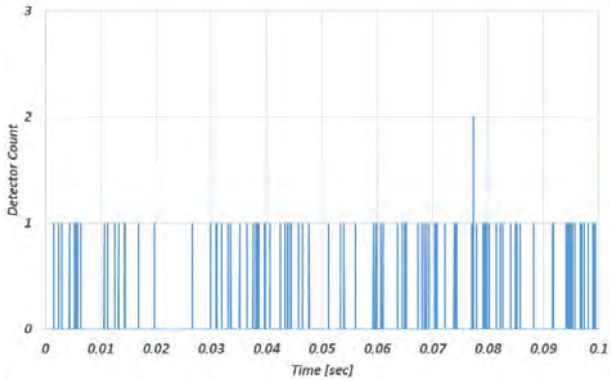

Fig. 2. Time-series data of neutron counts by using SMS for 0.1 sec

3. Description of AGN-201K and Subcritical States

3.1 AGN-201K

AGN-201K which is a zero-power reactor for educational and research purposes is polyethylene-moderated and graphite-reflected reactor [5]. The fuel material is a homogeneous mixture of UO_2 and polyethylene. As shown in Fig. 3, the fuel is comprised of 10 disks with 12.8 cm radius and 25 cm active core height [6]. Uranium enrichment of the fuel is about 19.5 wt%. The active core is surrounded by 25 cm thick graphite reflector followed by a 10 cm thick lead gamma shield. For fast neutron shielding, the outside of the core tank is filled with water of ~47.5 cm thickness [6]. The control rods which have the same composition as the fuel material consist of two Safety Rods (SR), one Coarse Rod (Cr), one Fine Rod (FR). During operation, reactor power is controlled by CR and FR [5]. In particular, external Ra-Be source located in the left-upper beam port supplies neutrons with an intensity of 10 mCi. A He-3 ex-core detector is located in right-lower beam port.

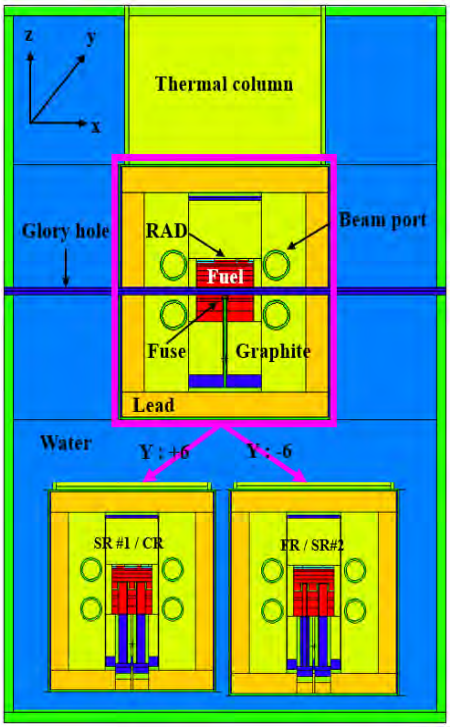

Fig. 3. Axial configuration of AGN-201K modelled with MCNP6

3.2 Subcritical states

We considered five different subcritical states corresponding to five different control rod configurations to apply the Rossi-α method. Table I describes the control rod positions and the k_{eff} values and kinetic parameters estimated with MCNP6 for the specified five subcritical states [7]. Estimation of subcriticality depends heavily on the kinetic parameters such as effective delayed neutron fraction (β) and neutron generation time (Λ). In order to minimize the statistical error of k_{eff} and kinetic parameters, the MCNP6 criticality calculations are performed with 100 inactive and 5,000 active cycles of 100,000 histories, which give the standard deviation of k_{eff} less than 3 pcm with ENDF/B-VII.1 neutron cross-section library. As shown in Table I, the SCR1 state has the highest subcriticality of 1,236 pcm Δk.

4. Results and Discussion

A series of neutron counts was obtained for the five subcritical conditions by using SMS with a unit gate time of 10 μsec during 4~5 minutes. The number of time bins considered was 25 million counts (i.e., 25,000,000τ, τ=10 μsec). For curve fitting, the length of gate time was up to 0.05 sec (i.e., 5,000τ). Table II shows the results of subcriticality measurements using Rossi-α method. The α-PKE values in Table II represent the ideal value giving the reference k_{eff} values using the given kinetic parameters in Table I. In other words, the α-PKE value can be obtained by Eq. (8). As shown in Table II, the Rossi-α method using the whole data gives good agreements in k_{eff} within 330 pcm Δk for all the cases.

Table II. The results of Rossi-α method

Condition	k_{eff}	α-PKE	k-est	α-est
SCR1	*0.98764*	*358.95*	0.99086	300.00
			[a] -322.46	[b] 58.95
SCR2	*0.99668*	*200.53*	0.99889	159.92
			-220.62	40.62
SCR3	*0.99737*	*186.03*	0.99939	148.77
			-201.57	37.26
SCR4	*0.99811*	*175.53*	0.99982	143.68
			-171.40	31.86
SCR5	*0.99885*	*162.60*	1.00031	135.56
			-145.92	27.04

[a] [(k_{eff}) – (k-est)] (pcm Δk)
[b] [(α-PKE) – (α-est)] (1/s)

Figs. 4 to 8 show the illustration of Rossi-α method with curve fitting. It is noted that the more subcritical condition has a larger dispersion as the time increase.

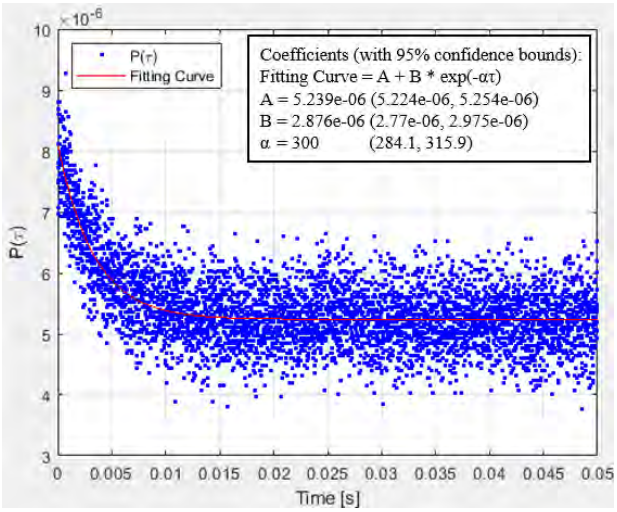

Fig. 4. Rossi-α fitting curve for SCR1

Table I. Calculated reference multiplication factor and kinetic parameters for considered control rod position

Condition	k_{eff}	σ (pcm)	β-eff	Λ (μsec)	Inserted rod position (cm)			
					SR#1	SR#2	CR	FR
SCR1	0.98764	3	0.00755	55.89873	23.07	23.44	0	12.56
SCR2	0.99668	3	0.00761	54.55938	23.07	23.44	17.25	12.56
SCR3	0.99737	3	0.00746	54.27638	23.07	23.44	18.25	12.56
SCR4	0.99811	3	0.00757	53.91283	23.07	23.44	19.25	12.56
SCR5	0.99885	3	0.00763	54.00546	23.07	23.44	20.25	12.56

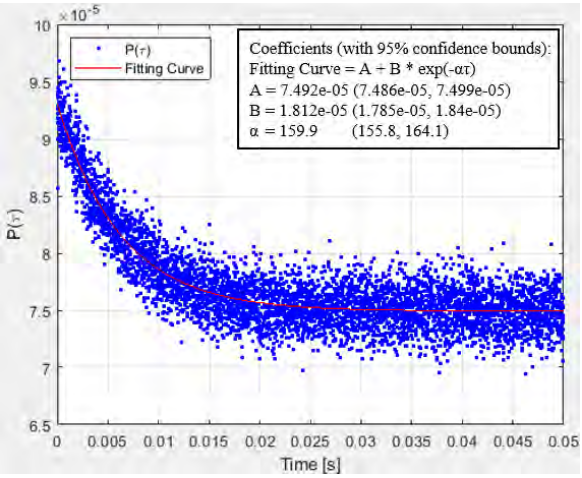

Fig. 5. Rossi-α fitting curve for SCR2

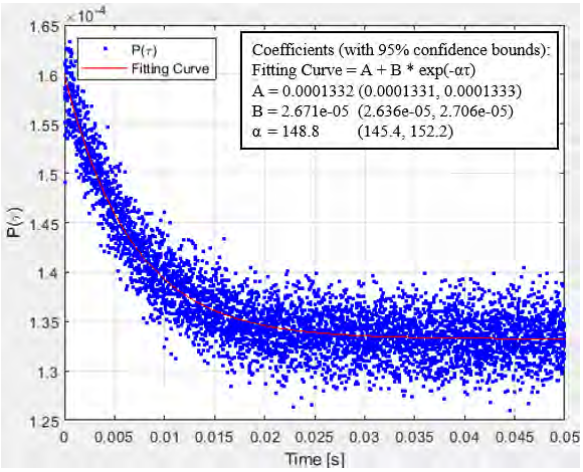

Fig. 6. Rossi-α fitting curve for SCR3

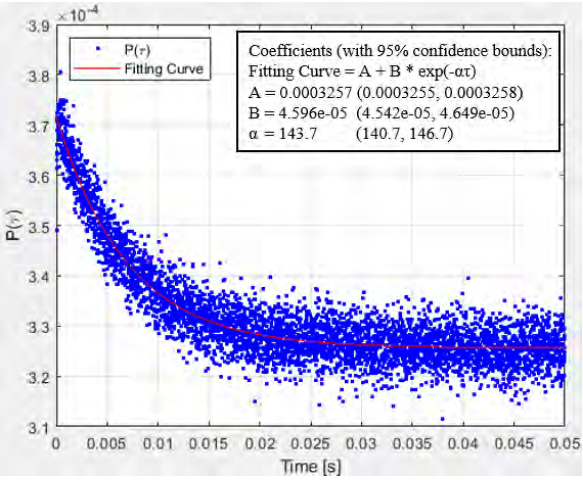

Fig. 7. Rossi-α fitting curve for SCR4

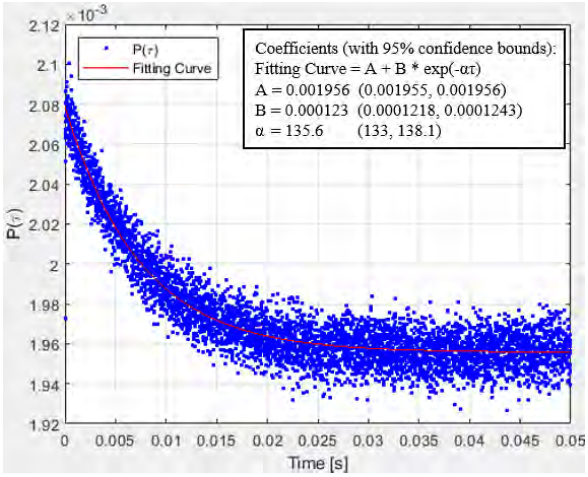

Fig. 8. Rossi-α fitting curve for SCR5

5. Conclusions

In this work, Rossi-α method using auto-correlation of detector signals was performed for subcriticality measurements for AGN-201K. From the results of application to the considered five subcritical states, it was shown that the Rossi-α method estimated the subcriticalities within 330 pcm Δk.

Acknowledgements

This work was supported by the National research Foundation of Korea(NRF) grant funded by the Korean government (MSIP : Ministry of Science, ICT and Future Planning) (No.2017M2B2B1072806). We would like to thank for Dr. Eun Kee Lee and Mr. Ho Cheol Shin at CRI (Central Research Institute) of KHNP (Korea Hydro and Nuclear Power) Company and Prof. Deokjung Lee at UNIST (Ulsan National Institute of Science and Technology).

References

1. Uhrig. R.E., *Random noise techniques in nuclear reactor systems*, p. 60, The Ronald Press Company, New York (1970).
2. Mckenzie G.E., "Modern Rossi Alpha Measurements," University of Illinois (2014).
3. Kong C, et al., "Stability improvement of noise analysis method in the case of random noise contamination for subcriticality measurements," *Annals of Nuclear Energy*., **71**, p. 245-253 (2014).
4. Lee E.K., et al., "Experimental determination of subcriticality at subcritical PWRs in Korea," *Annals of Nuclear Energy*., **37**, p. 1601-1608 (2010).
5. Kim M.H., et al., "KHU AGN-201K technical Specification," Kyung Hee University (2014).
6. Gorham M., "Evaluation of the AGN-201 Reactor at Idaho State University," NEA/NSC/DOC(2006)1, Idaho National Laboratory (2006).
7. Goorley J.T., et al., "MCNP6™ USER'S MANUAL Version 1.0," LA-CP-13-00634, Los Alamos National Laboratory (2013).

Proceedings of the Reactor Physics Asia 2019 (RPHA19) Conference
Osaka, Japan, Dec. 2-3, 2019

Feynman-α Method Experiment Using a Random Selection Method for AGN-201K

Jong Hoon Kim, Sung Ho Moon, Ser Gi Hong and Myung Hyun Kim*
Kyung Hee University, Department of Nuclear Engineering
1732 Deogyeong-daero, Giheung-gu, Yongin si Gyeonggi-do, Republic of Korea, 17104
* mhkim@khu.ac.kr

Abstract

In this study, Feynman-α experiment was conducted on AGN-201K research reactor of Kyung Hee University, Korea. A sufficient number of data is required to use the Feynman-α method. For this purpose, the experiment was conducted with a device designed by Korea Electric Power Research Institute (KEPRI) using 10 μsec as the gate time. To calculate the criticality, the time swap method and the random selection method were used as the experimental data processing method. The time-swap method is called "Bunching technique" and is one of the widely used methods in the Feynman-α experiment. The Random selecting method is a method in which several Y values are calculated at the same gate time by randomly setting the start point of data selection from experimental data and the interval between gate time and gate time. In order to compare the experiment data, the k-value was calculated using MCNP6 and estimated through the control rod worth. The criticality, the delayed neutron fraction and neutron generation time were calculated using the MCNP6 under the same conditions as in the experiment, and the criticality was estimated using the control rod worth obtained from the compensation method by comparing the control rod position between the critical state of experiment and each experiments. As a result, the differences of the criticality between estimation from rod worth, MCNP6 results and the methods are within 300pcm.

Key Words: **Noise analysis method, Feynman-α method, sub-criticality, AGN-201K,**

1. Introduction

1.1 Purpose

In this study, we carried out noise analysis experiment on AGN-201K, a research reactor of Kyung Hee University, Korea. Feynman-α method, widely used as one of the noise analysis methods, was used in this experiment.

AGN-201K is a small reactor with a total height of 280 cm and a diameter of 198 cm. Because of its small size, there is a lot of noise being measured on the detector. In this respect, the Feynman-α method, one of the noise analysis methods to be applied, is highly worthy of experimentation. Therefore, in this study, we applied the Feynman-alpha method using the data obtained through AGN-201K and compared it with the MCNP calculation results.

From the data obtained by the experiment, the k value can be calculated through the Feynman-α method. For the comparison, we used the MCNP6 to calculate the criticality, the delayed neutron fraction and neutron generation time. We also used the estimated criticality through the compensation method which is the control rod worth measuring method for the comparison.

1.2 Description of AGN-201K

AGN-201K research reactor in Korea is very safe reactor because of the limited excess reactivity and the strong negative temperature feedback coefficient. The reactor core tank is sealed with the aluminum of 2mm thickness to keep the fission gas and its diameter is 32.2cm, height is 76cm. The reactor core is surrounded by the reflector of the high-density graphite with 20cm thickness. The gamma shield surrounding the reflector is the lead of 10cm thickness.

The reactor tank is comprised of core tank, reflector, lead shielding, control rod, Glory-Hole and Access Ports. There is a movable thermal column on the top of the reactor tank and reactor tank which is surrounded by the light waters (about 1,000 gallon) of 55cm thickness except bottom part. AGN-201K has four control rods, one fine control rod, one coarse control rod, and two safety control rods.

There are a total of six detectors in the reactor. It has 3 He-3 detectors, 3 BF3 ionization chambers, and 1 Fission chamber. Experiments were conducted using a He-3 detector, one of the portable detectors.

2. Experiment Using Feynman- α method

2.1 Feynman-α method

Feynman-α method is a method of calculating the criticality using the mean and variance ratio of the number of neutrons detected in regular intervals (Gate time). The significant equation can be represented as [1] :

$$\frac{\overline{Z^2}-\bar{Z}^2}{\bar{Z}} \cong 1+\frac{\varepsilon D_v(1-\beta)^2}{(\beta-\rho)^2}\left[1-\frac{1-e^{-\alpha t}}{\alpha t}\right] = 1+a\left[1-\frac{1-e^{-\alpha t}}{\alpha t}\right] = 1+Y \quad (1)$$

where Z is the count rate detected over time t, D_v is Diven Factor, β is the delayed neutron fraction and ρ is the reactivity. The effective multiplication factor can be calculated as:

$$k_{eff} = \frac{1}{1-\beta+\alpha\Lambda} \quad (2)$$

where α is the prompt decay constant, Λ is the neutron generation time. The effective multiplication factor can be calculated by substituting the prompt decay constant obtained from Eq. (1).

2.2 Description of the experiment process

Noise analysis is a method of determining the criticality by analyzing the noise of detector signal under a sub-critical state. Therefore, this has the advantage of not requiring a lot of other equipment. Generally, when applying the Feynman-alpha method, there should be sufficient measurement data to ensure statistical significance by increasing the gate time and sufficient number of measurements.

In order to obtain enough measurement data, Korea Electric Power Research Institute (KEPRI) developed a measuring device with a minimum gate time of 10 μsec. In this study, sub-criticality measurement experiment was performed using this measuring device [2].

The Feynman-alpha method experiment was conducted using a He-3 detector while changing the position of the Coarse Rod. The initial state of the reactor was critical at 20.25 cm for the position of the Coarse Rod.

The experiment data were acquired by measuring the minimum gate time at 10 μsec for about 5 minutes. In the process of the experiment, the coarse control rod positions for data measurements were changed to 19.5 cm, 18.5 cm, 17.5 cm, and 0 cm, and the data were collected for 5 minutes in the same process. The data format consists of a set of neutrons counts, measured in 10 μsec continuously, in time and neutron numbers. That is, the data consists of about 30,000,000 bundles, assuming a measurement time of about five minutes.

As a result, sufficient data were obtained to apply the Feynman-alpha method. In addition, the obtained data can be selectively used according to the purpose. In the selected data, a graph was drawn using the ratio of the average and the number of neutrons measured per gate time. Using the right-hand side of Eq.(1), the appropriate alpha value was obtained by least squares fitting method. We proceeded to calculate the criticality by substituting the delayed neutron fraction and neutron regeneration time in Eq (2).

3. Data selection

The data obtained from the experiment consists of a bundle of neutron numbers measured within 10 μsec of continuous time as mentioned above. In this study, we proceeded in two ways to select the data from the experimental data for using the Feynman-α method.

For the first time, data selection was performed using a method called "Bunching-technique (Time swap)" [2, 3, 4]. This method is a widely known method for using the Feynman- α method to obtain the number of data bundles obtained from experimental data even in data selection of different conditions.

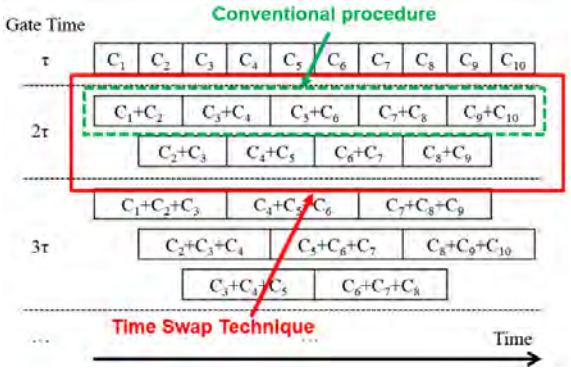

Fig. 1. Schematic view of the time-swap technique

The second method is a continuous random selecting method. As shown in Fig. 2, this method sets the gate time and randomly sets the interval time and the initial time between the gate times to have several Y values at the same gate time. The initial time is an arbitrary time from 0 second to 1 second, and the interval time is from 0 second to 0.01 second. In this method, the Y value has a total of 10 different values through different initial time and interval time for each gate time, and the alpha value is calculated using this values.

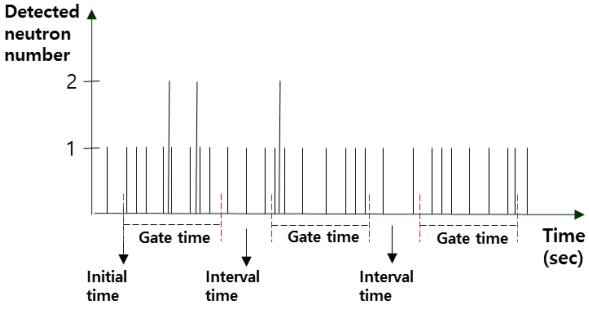

Fig. 2. Schematic view of Random selecting method

4. Results

4.1 Criticality Estimation with Control rod calibration curve

To compare the criticality calculated by the Feynman-α method, we use the data obtained from the control rod worth measurement experiment to calculate the criticality according to the control rod position in the above five experiments. KHU Research Reactor

By design, the control rods are the same in configuration and only differ in size. Since the control rod worth is known through the experiment, the coarse control rod is estimated through the fine control rod in order to calculate the criticality according to the reactor state. The fine control rod was measured using the compensation method, one of the control rod worth measurement experiments. Experiments were conducted using DDRCS (Direct Digital Reactivity Computer System) to obtain the integral rod worth of fine control rod. Integral rod worth of the coarse control rod was calculated using the control rod design value (CR: 1250pcm, FR: 310pcm) [5]. This can be seen in Figure 3 below.

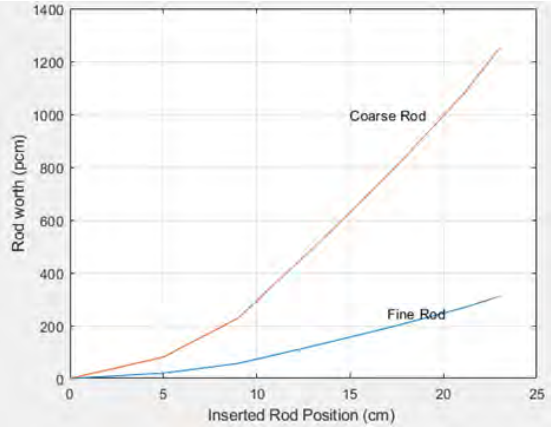

Fig. 3. Integral rod worth of Coarse rod and Fine rod

4.2 Criticality Calculation with MCNP6

As shown in Figure 4, we calculated the criticality by MCNP6 based on the structure of AGN-201K described in Section 1. The k_{eff} values and kinetic parameters were calculated according to the positions of the control rods in each experiment and summarized in the Table 1 [6].

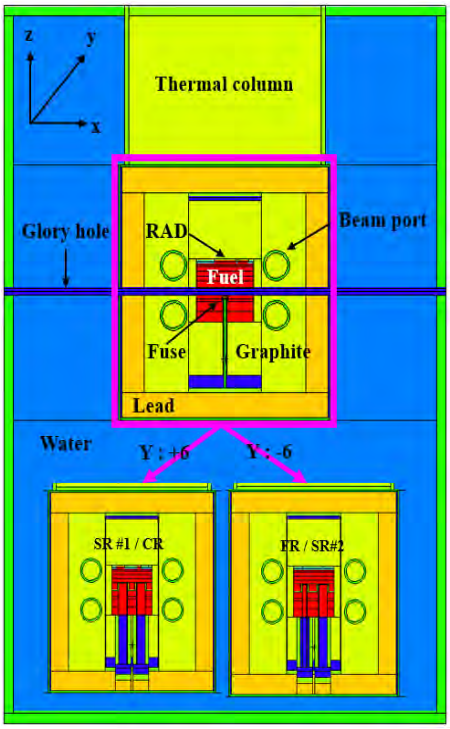

Fig. 4. Axial configuration of AGN-201K modelled with MCNP6

Table I. Calculated reference multiplication factor and kinetic parameters for considered control rod position

Experiment Order	Inserted rod position (cm)				β-eff	Λ (μsec)	σ (pcm)	k_{eff}
	SR#1	SR#2	CR	FR				
1	23.07	23.44	20.25	12.56	0.00763	54.00546	3	**0.99885**
2	23.07	23.44	19.25	12.56	0.00757	53.91283	3	**0.99811**
3	23.07	23.44	18.25	12.56	0.00746	54.27638	3	**0.99737**
4	23.07	23.44	17.25	12.56	0.00761	54.55938	3	**0.99668**
5	23.07	23.44	0	12.56	0.00755	55.89873	3	**0.98764**

Table Ⅱ. Difference of the multiplication factor between Estimation value from Rod worth and Each method.

Order	Estimation by Rod worth		Time swap method			Random selecting method		
	α-value	k_{eff} (A)	α-value	k_{eff} (B)	A-B (pcm)	α-value	k_{eff} (C)	A-C (pcm)
1	152.577	0.99939	123.400	1.00097	**-158**	125.386	1.00086	**-147**
2	163.374	0.99876	137.271	1.00017	**-141**	138.229	1.00012	**-135**
3	178.534	0.99778	147.517	0.99945	**-168**	145.770	0.99955	**-177**
4	194.432	0.99701	156.462	0.99907	**-206**	149.009	0.99948	**-247**
5	333.328	0.98904	278.044	0.99207	**-303**	216.601	0.99546	**-642**

Table Ⅲ. Difference of the multiplication factor between Calculated value using MCNP6 and Each method.

Order	MCNP6		Time swap method			Random selecting method		
	α-value	k_{eff} (A)	α-value	k_{eff} (B)	A-B (pcm)	α-value	k_{eff} (C)	A-C (pcm)
1	162.601	0.99885	123.400	1.00097	**-212**	125.386	1.00086	**-201**
2	175.535	0.99811	137.271	1.00017	**-206**	138.229	1.00012	**-201**
3	186.028	0.99737	147.517	0.99945	**-208**	145.770	0.99955	**-218**
4	200.535	0.99668	156.462	0.99907	**-239**	149.009	0.99948	**-280**
5	358.947	0.98764	278.044	0.99207	**-443**	216.601	0.99546	**-782**

4.3 Comparison of Multiplication factor

We compared the criticality obtained from the experiment using the Feynman- α method and Time swap method between the estimated criticality using the control rod and calculated criticality using MCNP6. TableⅡ shows difference of the criticality between estimated value from Rod worth and each method. TableⅢ shows difference of the multiplication factor between calculated value using MCNP6 and each method.

As a result of the comparison, the calculation errors of the two methods are within the range of 300pcm until the criticality reaches 0.98. However, we could see that the difference of the criticality was large in the experiments where the coarse control rod was all rod out state. Below Figure 4,5 shows Feynman- α curve of Time swap and Random selecting method.

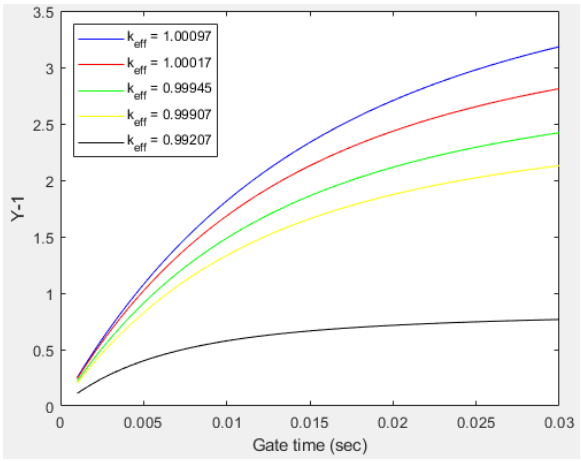

Fig. 4. Feynman- α curve of Time swap method

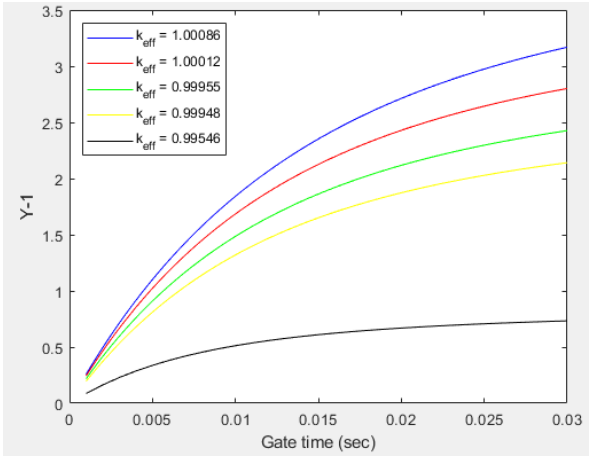

Fig. 5. Feynman- α curve of Random selecting method

5. Conclusions

The Feynman- α experiment to measure sub-criticality in the Research reactor AGN-201K of Kyung Hee University, Korea was carried out.

The data was collected using a device with a minimum gate time of 10 μsec, which was used by KEPRI, and the code was programmed to select the desired data to obtain the sub-criticality.

In order to verify the calculated criticality, we used the control rod worth of the reactor to estimate the criticality under the same experimental conditions. Also MCNP6 is used to verify the calculated multiplication factor obtained by each method.

As a result, it can be confirmed in that the differences of the criticality of the two methods were relatively small for forth experiment, but difference of criticality in the last experiment in which coarse rod (CR) is all out state was large. Since the experiments in the intermediate range have not been carried out, further experiments will be carried out.

Acknowledgements

This work was supported by the National Research Foundation of Korea(NRF) grant funded by the Korean government (Ministry of Science and ICT) (2017M2B2B1072803)

References

1. Juan Blazquez, Remarks on kinetics parameters of a sub-critical reactor for nuclear waste incieraation, NEA, 2001 pp826-829.
2. Lee E.K., et al., "Experimental determination of subcriticality at subcritical PWRs in Korea," *Annals of Nuclear Energy*., **37**, p. 1601-1608 (2010)
3. Misawa T., et al., "Measurement of Prompt Neutron Decay Constant and Large Subcriticality by the Feynman-α Method," *Nuclear Science and Engineering*., **104**, p. 53-65 (1990)
4. Okuda R., et al., "An improved Feynman-α analysis with a moving-bunching technique," *Journal of Nuclear Science and Technology*., **53**, *10*, p. 1647-1652 (2016).
5. KHU AGN-201K Technical Specification", Kyung Hee University, 2014.
6. Goorley J.T., et al., "MCNP6™ USER'S MANUAL Version 1.0," LA-CP-13-00634, Los Alamos National Laboratory (2013).

Proceedings of the Reactor Physics Asia 2019 (RPHA19) Conference
Osaka, Japan, Dec. 2-3, 2019

Education on Reactor Physics and Fuel Cycle using Experimental Facilities of the Nuclear Industry

Kenichi Yoshioka*, Tsukasa Sugita, Satoshi Wada, Rei Kimura, Yu Yamashita, Hironori Kumanomido, Tadaharu Masuyama, Masahide Akiyama, Haruo Miyadera and Kouji Hiraiwa
Toshiba Energy Systems & Solutions Corporation, 4-1 Ukishima-cho, Kawasaki-ku, Kawasaki, Japan
*Corresponding author: kenichi.yoshioka@toshiba.co.jp

Abstract

Education programs using experimental facilities of Toshiba Energy Systems & Solutions are being conducted for college students. The reactor physics & fuel cycle education course is one of the programs. There are experimental items such as a critical experiment with a critical assembly, a moderation experiment with a neutron source, gamma-ray measurement of a fuel rod, and a chemical separation experiment employing ion exchange resin. Students study the basic theory of a nuclear reaction, power plants, and the fuel cycle through these experimental items. This education has been conducted for over 10 years. More than 400 students have received the education. Some of the students currently work in the nuclear industry.

Key Words: **Reactor physics, fuel cycle, education, critical assembly, moderation, gamma-ray measurement, chemical separation**

1. Introduction

Reactor physics is one of the most important educational themes concerning the utilization of nuclear energy. However, many students experience difficulty in studying reactor physics because neutron transport theory is complex and hard to visualize. On the other hand, the fuel cycle is also important. In particular, the disposal of radioactive waste is a critical issue with an important bearing on the continuing use of nuclear energy. Many students may not understand how to dispose of radioactive waste safely and be skeptical about the utilization of nuclear energy.

Experiments can be effective for understanding complex concepts. There are some experimental facilities in the nuclear industry. These facilities are also attractive for use in the education of college students who are studying nuclear engineering.

Education programs using experimental facilities of Toshiba Energy Systems & Solutions are being conducted for college students [1]-[2]. The reactor physics & fuel cycle education course is one of the programs.

The reactor physics & fuel cycle education course consists of a critical experiment with a critical assembly, a moderation experiment with a neutron source, gamma-ray measurement of a fuel rod, a chemical separation experiment with ion exchange resin, etc.

Target students are technical college students, undergraduate students and graduate students. The period of the education course is about 1 week. Educational items are adjusted in light of the level of the students' knowledge. For students unfamiliar with nuclear energy, the basic theory of nuclear engineering can be covered in lectures prior to the course.

This paper introduces the outline of the reactor physics & fuel cycle education course.

2. Critical Experiment

Toshiba Nuclear Critical Assembly (NCA) is a slightly enriched, uranium-fueled, light-water-moderated critical assembly. NCA was utilized to validate an LWR nuclear design methodology and to develop a new fuel design concept [3]-[5]. Figure 1 shows the overview of the NCA core. Operators directly handle fuel rods to set up an experimental core because the activity of the fuel rods is low.

Figure 2 shows the concept of NCA. Reactivity is controlled by adjusting the water level. The maximum power of NCA is 200 W. The critical experiment to measure critical mass is mostly conducted at less than 1 W. Figure 3 shows the vertical cross section of NCA. The fuel rod of NCA consists of UO2 pellets of 10 mm diameter and aluminum cladding. The active length of the fuel rod is 1500 mm.

Figure 4 is an example of a critical approach by a student. Students also view the experimental core directly as shown in Fig.4. Reactivity measurements with the period method and neutron flux distribution measurements have been conducted for education.

The control panel of NCA shown in Fig.4 is used for the education on safety systems in nuclear power plants, such as "fail safe" or "interlock".

NCA has already shut down. Although this experimental item is not conducted as of 2019, inverse

multiplication plots using historical data and education using the control panel continues to be conducted.

3. Neutron Moderation and Fission Measurement

The concept of moderation is important for understanding fission and the chain reaction. A moderation and fission experiment is conducted with a standard neutron source, polyethylene blocks, a He-3 neutron detector, cadmium sheets, and fuel rods. Figure 5 shows an example of an experimental setup conceived and implemented by a student. In particular, this experiment helps students who are not majoring in nuclear engineering to understand the basic theory of nuclear power.

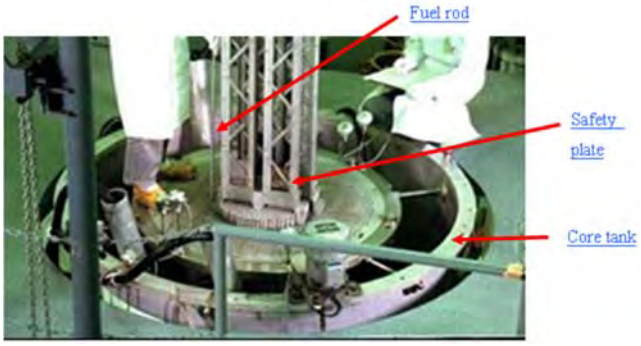

Fig 1. NCA core

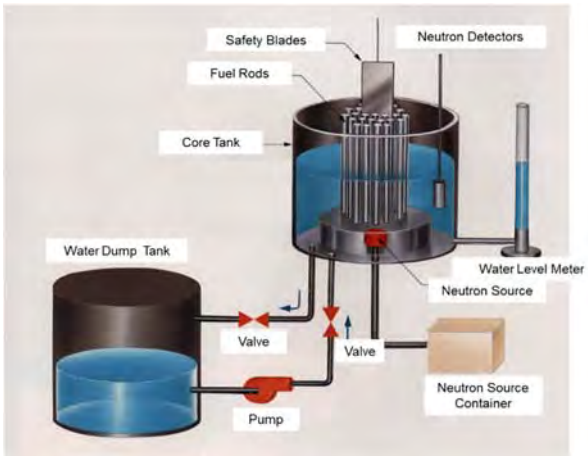

Fig 2. Concept of NCA

4. Gamma-ray Measurement of Fuel Rods

The NCA facility possesses a variety of fuel rods such as fuel rods with 1wt% to 4.9wt% enrichment and gadolinia-bearing fuel rods. Gamma rays emitted from U-235 and U-238 in the fuel rods are measured with a Ge detector. Students speculate on the difference of enrichment or uranium inventory in the fuel rods in light of the measurements. Even a slight amount of Cs-137 can be detected. The gamma-ray intensity of Cs-137 is proportional to total fission in a fuel rod. Students study the concept of burnup and the difference of power between a critical assembly and a commercial plant.

Figure 6 shows an example of fuel rod measurement with a Ge detector and gamma-ray spectrum.

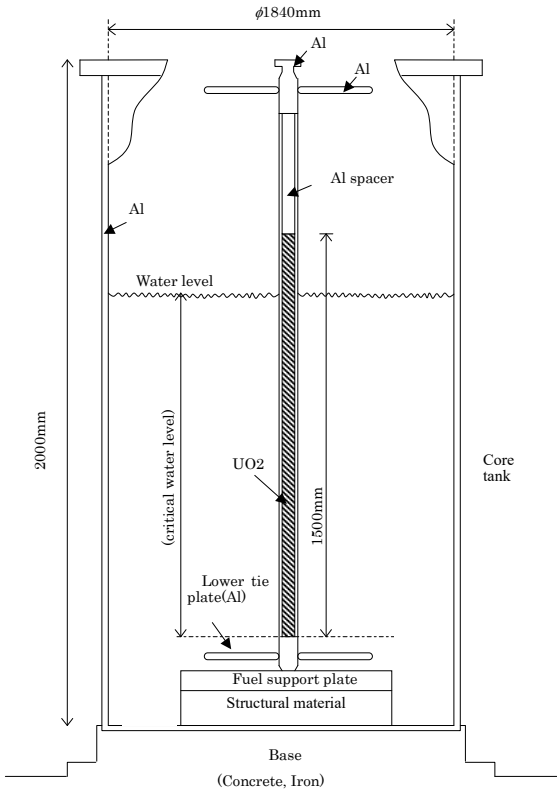

Fig 3. Vertical cross section of NCA

Fig 4. Critical approach by a student

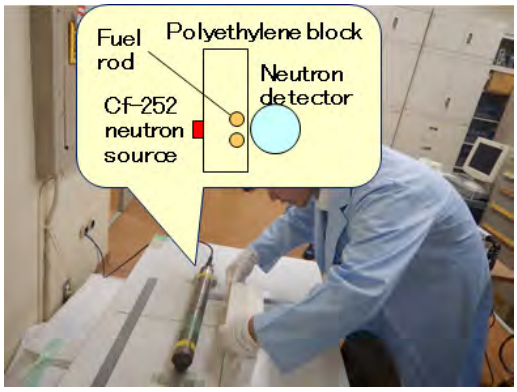

Fig 5. Moderation and fission measurement

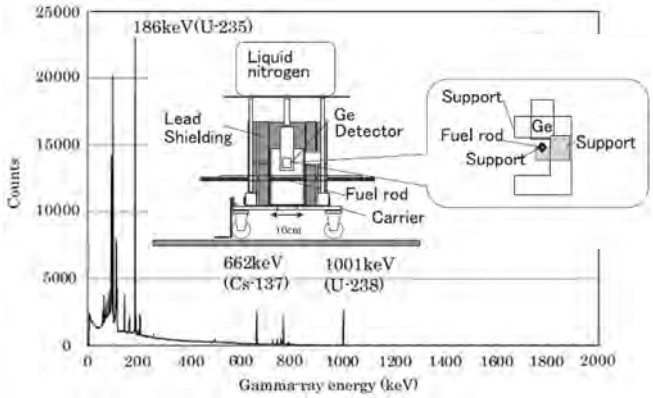

Fig.6 Gamma-ray measurement of a fuel rod

5. Chemical Separation Experiment

The disposal of radioactive waste is one of the important technical issues concerning the sustainable utilization of nuclear energy. As well as studying reactor physics, learning how to treat radioactive waste helps students understand the concept of the nuclear fuel cycle. Chemical separation is an essential technique for reducing radioactive waste.

Unsealed radioactive isotopes of Co-60 and Cs-137 are used. These isotopes are separated by a chemical separation technique employing an ion exchange resin.

Figure 7 shows an example of the chemical separation experiment.

6. Number of Participants

This reactor physics education has been conducted for over 10 years. Figure 8 shows the trend of the number of participants. More than 400 students have received the education. Some students currently work in the nuclear industry.

Fig.7 Chemical separation experiment

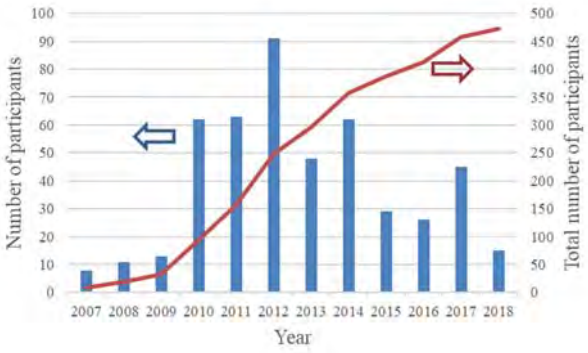

Fig.8 Trend of the number of participants

7. Conclusions

Reactor physics education using experimental facilities of Toshiba Energy Systems & Solutions is being conducted. Experimental items have contributed to the education of college students. Reactor physics education is becoming increasingly important for maintaining human resources in the field of nuclear energy.

8. Future Plan

Although NCA has already shut down, we intend to improve the education course using the equipment available and to continue conducting these education programs in order to develop human resource for the nuclear industry.

Acknowledgement

These education programs have been conducted as a subsidy project of the Ministry of Education, Culture, Sports, Science and Technology (MEXT) of Japan.

References

1. Hiraiwa K, et al., “Education programs for students and graduate students with experimental facilities for nuclear energy in Toshiba,” *PHYSOR 2014(Only presentation), Kyoto, Japan, Sep 28-Oct 3, 2014.*
2. Ito R, et al., “Approach to Light-Water Reactor Safety Education,” *ICONE2017 (Only presentation)*, Shanghai, China, July 2-6, 2017.
3. Kurosawa F, Sekiguchi Y and Yokoyama T, “Critical experiments in a BWR lattice using NAIG critical assembly,” Toshiba review (1972).
4. Umano T, et al., “Critical experiments simulating the operating conditions of PWRs in the Toshiba NCA Facility,” *Proc. ICAPP09,* Tokyo, Japan, May 10-14, 2009.
5. Yoshioka K, et al., “Critical experiments for BWR fuel assemblies with cluster of gadolinia rods,” *Proc. PHYSOR 2014*, Kyoto, Japan, Sep 28-Oct 3, 2014.

TS-06 Nuclear Data and Evaluation

Proceedings of the Reactor Physics Asia 2019 (RPHA19) Conference
Osaka, Japan, Dec. 2-3, 2019

Treatment of R-matrix Limited Formula in FRENDY

Kenichi Tada[a*] and Satoshi Kunieda[a]
[a]*Japan Atomic Energy Agency, Shirakata 2-4, Tokai-mura, Naka-gun, Ibaraki 319-1195, Japan*

[*]Corresponding author: tada.kenichi@jaea.go.jp

Abstract

The R-matrix limited formula is formatted by the current nuclear data format and it is adopted some nuclei in the latest evaluated nuclear data library. Since the processing of the R-matrix limited formula is significantly different to the other resonance formulae, it is difficult to treat this formula without large modification of the nuclear data processing code. In this study, we implemented one of the R-matrix code AMUR to treat this formula in FRENDY. The processing results of FRENDY are compared to those of NJOY2016 to verify FRENDY. The comparison results indicate that FRENDY appropriately treat the R-matrix limited formula with similar computational time.

Key Words: **FRENDY, AMUR, R-matrix limited formula, nuclear data processing**

1. Introduction

Nuclear data processing is an important interface between evaluated nuclear data library and neutronics transport codes. The neutronics transport codes cannot directly treat an evaluated nuclear data library and these codes require a cross-section data library which is generated by the nuclear data processing code as shown in Fig. 1.

Japan Atomic Energy Agency (JAEA) has developed a new nuclear data processing code FRENDY (FRom Evaluated Nuclear Data librarY to any application) and released FRENDY version 1 [1]. FRENDY version 1 can generate the cross-section library for a continuous energy Monte Carlo calculation codes. The many processes, e.g., resonance reconstruction, Doppler broadening, generation of the probability table, are required to generate cross section library. We have been improved the processing method of FRENDY [2]. In this study, we focused on the expansion of the resonance reconstruction.

The R-matrix limited formula is one of the resonance formula for the resolved resonance region. The current nuclear data format, i.e., the ENDF-6 format [3], prepares five resonance formulae in the resolved resonance region. The Single- and Multi- Level Breit Wigner (SLBW) [4] and the Reich-Moore (RM) resonance formulae [5] are mainly adopted in the current evaluated nuclear data library. The R-matrix limited formula is more rigorous formula than SLBW and RM formulae. Currently, this formula is adopted in ^{35}Cl, ^{40}Ca, ^{54}Fe, ^{57}Fe, ^{63}Cu, and ^{65}Cu from ENDF/B-VIII.0 [6] and ^{63}Cu and ^{65}Cu from JEFF-3.3 [7].

The processing of the R-matrix limited formula is significantly different to the other resonance formulae. For example, the conventional resonance formulae only treat the total, elastic scattering, fission, and radiative capture cross sections. The R-matrix limited formula can treat other reactions and the differential cross-sections, i.e., angular and energy distribution of the secondary particle. Therefore, the large modification is required to treat the R-matrix limited formula in the nuclear data processing code.

JAEA has developed AMUR (A Multi-channel R-matrix code) in order to evaluate the cross-section and covariance for the light-mass nuclei, e.g., ^{16}O [8]. AMUR

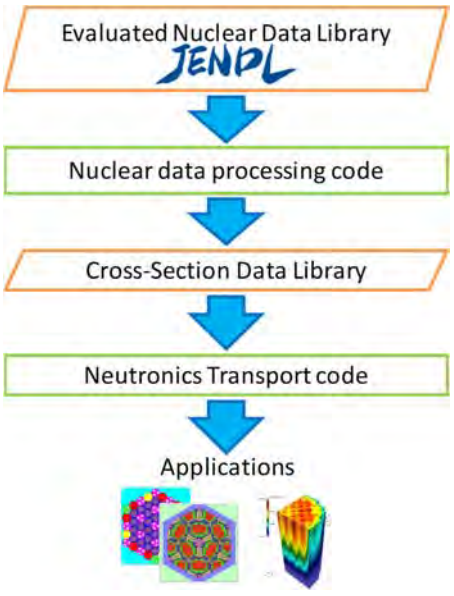

Fig.1. Calculation flow from evaluated nuclear data library to nuclear calculation.

is a multi-level and multi-channel R-matrix code based on the Wigner and Eisenbud formalism [9] with RM approximation [5] for the radiative neutron capture channels Since AMUR can treat the cross-sections and the differential cross-sections, we implemented AMUR to treat the R-matrix limited formula in FRENDY.

This paper shows the overview of nuclear data processing code FRENDY and verification of the R-matrix limited formula calculation function using AMUR. To verify FRENDY, we compared the processing results of FRENDY to those of NJOY2016 [10] which is the conventional nuclear data processing code.

2. Overview of FRENDY and AMUR

2.1 Overview of FRENDY

FRENDY is developed in order to process JENDL [11] which is the evaluated nuclear data library developed in JAEA [1]. The current version of FRENDY can generate ACE (A Compact ENDF) formatted files for continuous energy Monte Carlo calculation codes such as MCNP [12] and PHITS [13]. It uses the same processing method as NJOY because the implementation of the conventional method is an important step to develop the new code.

FRENDY is written in the object-oriented language C++ so as to enhance maintainability, modularity, portability and flexibility. FRENDY is developed not only to process nuclear data libraries but also to implement the FRENDY modules to other calculation codes. Users can easily use many functions e.g., reading, writing, and processing the nuclear data library, in their own codes.

The system structure of FRENDY is shown in Fig. 2. The modules with solid-lined shapes have been already implemented, while the ones with dashed-lines shapes have not been developed yet. In this study, we focus on the improvement the "ResonanceReconstructor" module to treat the R-matrix limited formula.

The current version of FRENDY only treats the ENDF-6 format. Recently, the introduction of the new nuclear data format GNDS (Generalized Nuclear Data Structure) has been considered [14]. This format uses XML format and it is quite different from the current ENDF-6 format. The difference of the nuclear data format has no large impact on the processing since FRENDY converts the nuclear data format from each nuclear data format to "NuclearDataObject". FRENDY can treat such a new nuclear data format when parser, writer and converter modules are implemented.

FRENDY accepts two types of input formats. One is the NJOY compatible format and the other is the original input format [15]. The original input format requires only a processing mode and the file name of an evaluated nuclear data library at minimum. Therefore, everyone can process the nuclear data library without expert knowledge of the nuclear data processing.

2.2 Overview of AMUR

AMUR is developed in order to evaluate the cross-section and covariance for the light-mass nuclei [8]. Values of the resonance parameters are estimated from the experimental cross-sections with the generalized least-square method. This code is also designed to take account of the experimental resolution, renormalization and so on to obtain reasonable resonance parameters as much as possible.

AMUR is also prepared the cross-section calculation function using the resonance parameter in the ENDF-6 format. We implemented this function to processing of the R-matrix limited formula in FRENDY.

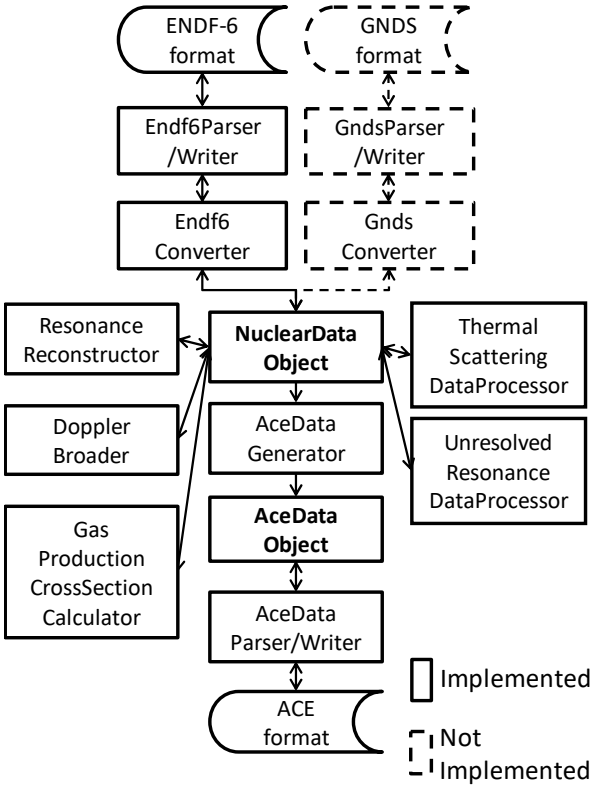

Fig. 2. The system structure of FRENDY.

3. Verification of FRENDY

The processing results of FRENDY are compared to those of NJOY2016 [10] to verify calculation of R-matrix limited formula. The all nuclei which use R-matrix limited formula in ENDF/B-VIII.0 and JEFF-3.3 are used for comparison.

The processing results of FRENDY and NJOY2016 and its comparison for ^{35}Cl from ENDF/B-VIII.0 are shown in Figs. 3-7. As shown in Figs. 3-7, the difference is only found in the discontinuity region where the boundary of the resolved and unresolved resonance regions. Since the difference is only found in small energy region and the maximum relative difference is less than a few percent, this difference has not impact on the neutronics calculations. As shown in Figs. 3-7, the difference in the other region is so small. These results indicate that the processing results of FRENDY show good agreement with those of NJOY2016.

The R-matrix limited formula can treat not only total,

elastic scattering, fission, and radiative capture cross sections but also other reactions. ^{35}Cl from ENDF/B-VIII.0 has resonance parameter for (n, p_0) cross section. As shown in Fig. 6, the relative differences of the (n, p_0) cross section is similar to those of other reactions. This result indicate that FRENDY appropriately treat the all reaction prepared in the R-matrix limited formula.

^{35}Cl from ENDF/B-VIII.0 prepares the (n, p) cross section. The (n, p) cross section is the total proton production cross section, i.e., the sum of (n, p_n) cross section. The (n, p) cross section must be modified when the (n, p_0) cross section is calculated. As shown in Fig. 7, FRENDY appropriately treat the total proton production cross section.

Other nuclei which use R-matrix limited formula in ENDF/B-VIII.0 and JEFF-3.3 are also show similar difference. These results indicate that FRENDY appropriately calculate the R-matrix limited formula.

The processing time of FRENDY is also compared to that of NJOY2016. Table I shows the comparison of the processing time and the energy grid number. As shown in Table I, the processing time of FRENDY is similar to that of NJOY2016 in many nuclei. However, FRENDY requires long computational time to process ^{40}Ca and ^{57}Fe from ENDF/B-VIII.0. The energy grid number of FRENDY is similar to that of NJOY. Therefore, the difference of energy grid number is not cause of the long processing time. The improvement of the processing time of these nuclei is now undergoing.

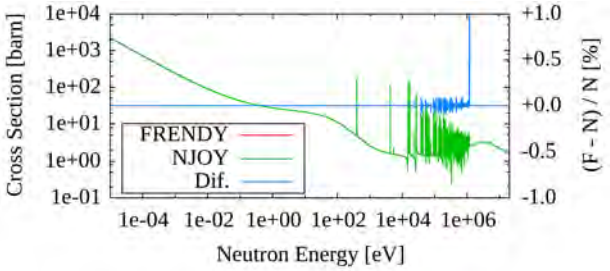

Fig. 3. The comparison of the total cross section for ^{35}Cl from ENDF/B-VIII.0.

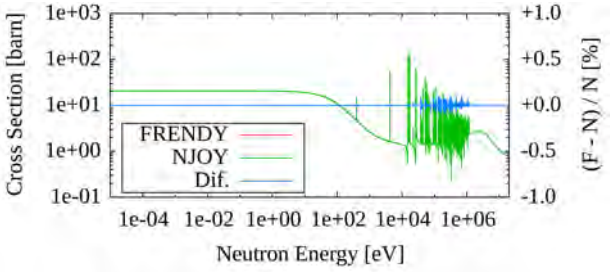

Fig. 4. The comparison of the elastic scattering cross section for ^{35}Cl from ENDF/B-VIII.0.

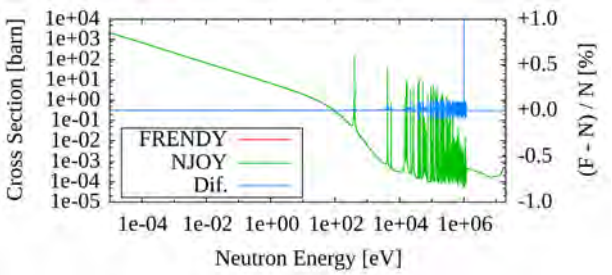

Fig. 5. The comparison of the radiative capture cross section for ^{35}Cl from ENDF/B-VIII.0.

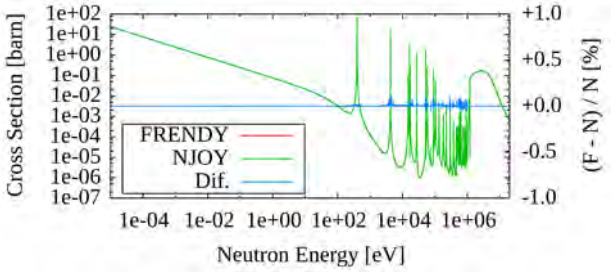

Fig. 6. The comparison of the (n, p_0) cross section for ^{35}Cl from ENDF/B-VIII.0.

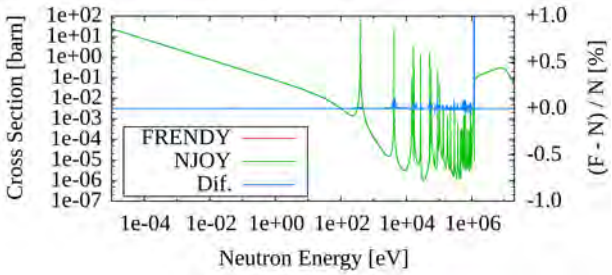

Fig. 7. The comparison of the (n, p) cross section for ^{35}Cl from ENDF/B-VIII.0.

Table I. Comparison of the processing time and energy grid number.

		Calculation time			Energy grid	
		FRENDY	NJOY	F/N	FRENDY	NJOY
B80	^{35}Cl	63.4	49.7	1.3	22,844	22,656
	^{40}Ca	221.2	19.9	11.1	27,861	28,376
	^{54}Fe	13.2	23.8	0.6	49,311	43,038
	^{57}Fe	41.3	6.8	6.1	16,993	16,380
	^{63}Cu	17.9	26.0	0.7	54,931	43,582
	^{65}Cu	13.6	19.5	0.7	44,502	35,794
F33	^{63}Cu	41.2	57.4	0.7	90,334	93,973
	^{65}Cu	35.6	44.9	0.8	105,670	81,380

4. Conclusions and future works

The processing of R-matrix limited formula is implemented in FRENDY. AMUR is used to process the R-matrix limited formula.

The processing results of FRENDY are compared to

those of NJOY2016 to verify FRENDY. The processing results of FRENDY show good agreement with those of NJOY2016. This result indicate that FRENDY appropriately process the R-matrix limited formula. The processing time of FRENDY is similar to that of NJOY in many nuclei.

The current version of FRENDY only calculate the cross-sections. The R-matrix limited formula can treat not only the cross-section but also the differential cross-sections, i.e., angular and energy distribution of the secondary particle. The calculation function of the differential cross-sections are developed in the near future.

References

1. Tada K., Nagaya Y., Kunieda S., et al., "Development and verification of a new nuclear data processing system FRENDY," *J. Nucl. Sci. Technol.*, **54**, 806 (2017).
2. Tada K., "Improvement of Probability Table Generation Using Ladder Method for a New Nuclear Data Processing System FRENDY," *Proc. PHYSOR 2018*, Cancun, Mexico, Apr. 22–26, 2018, American Nuclear Society (2018).
3. Trkov A., Herman M., Brown, D. A., "ENDF-6 Formats Manual," *BNL-203218-2018-INRE*, Brookhaven National Laboratory (2018).
4. Breit G., Wigner E., "Capture of Slow Neutrons," *Phys. Rev.*, **49**, 519 (1936).
5. Reich C. W., Moore M. S., "Multilevel Formula for the Fission Process," *Phys. Rev.*, **111**, 929 (1958).
6. Brown D. A., Chadwick M. B., Capote R., et al., "ENDF/B-VIII.0: The 8th Major Release of the Nuclear Reaction Data Library with CIELO-project Cross Sections, New Standards and Thermal Scattering Data," *Nucl. Data Sheets*, **148**, 1 (2018).
7. Cabellos .O, Alvarez-Velarde F., Angelone C. J., et al., "Benchmarking and Validation Activities within JEFF Project," *EPJ Web of Conf.*, **146**, 06004 (2017).
8. Kunieda S., "Status of the R-matrix Code AMUR toward a consistent cross-section evaluation and covariance analysis for the light nuclei," *EPJ Web of Conf.*, **146**, 12029 (2017).
9. Wigner E. P., Eisenbud L., "Higher Angular Momenta and Long Range Interaction in Resonance Reactions," *Phys. Rev.*, **72**, 29 (1947).
10. MacFarlane R. E. and Kahler A. C., "The NJOY Nuclear data Processing System Version 2016," *LA-UR-17-20093*, Los Alamos National Laboratory (2017).
11. Shibata K., Iwamoto O., Nakagawa T. et al., "JENDL-4.0: A New Library for Nuclear Science and Engineering," *J. Nucl. Sci. Technol.*, **48**, 1 (2011).
12. X-5 Monte Carlo Team, "MCNP – A General Monte Carlo N-Particle Transport Code, Version 5," *LA-UR-03-1987*, Los Alamos National Laboratory (2003).
13. Sato T., Iwamoto Y., Hashimoto S., et al., "Features of Particle and Heavy Ion Transport code System (PHITS) version 3.02," *J. Nucl. Sci. Technol.*, **55**, 684 (2018).
14. Mattoon C. M., Beck B. R., Patel N. R., et al., "Generalized Nuclear Data: A New Structure (with Supporting Infrastructure) for Handling Nuclear Data," *Nucl. Data Sheets*, **113**, 3145 (2012).
15. Tada K., Kunieda S., Nagaya Y., "Nuclear Data Processing Code FRENDY Version 1," *JAEA-Data/Code 2018-014*, Japan Atomic Energy Agency (2019).

Proceedings of the Reactor Physics Asia 2019 (RPHA19) Conference
Osaka, Japan, Dec. 2-3, 2019

Validation of new Fission Yield by Analysis of Post-Irradiation Examination

Atsuya Iso[a,*], Satoshi Takeda[a] and Takanori Kitada[a]
[a]*Osaka University, Yamadaoka2-1, Suita, Osaka, Japan*
[*]Corresponding author: a-iso@ne.see.eng.osaka-u.ac.jp

Abstract

Fission yield is an important physical quantity to evaluate the amount of fission products after irradiation. Tokyo Institute of Technology (Tokyo Tech) newly evaluated fission yield. It is necessary to confirm the validity of the fission yield evaluated by Tokyo Tech because the fission yield is expected to be included in the next Japanese Evaluated Nuclear Data Library (JENDL). In this study, the analysis of post-irradiation examination using JENDL FP Fission Yields Data File 2011 (FPY-2011) and new fission yield was performed. The integrated burnup calculation code system SWAT4.0 was used for the analysis. BM5 sample of the Swiss Beznau-1 PWR was used in this study. It was found that the C/E values using new fission yield for Sm151, Sm152, and Eu151 are improved more than 10 %. The improvement of the C/E value of Sm151, Sm152 and Eu151 mainly come from the updating fission yield of Pu241.

Key Words: **Fission yield, FPY-2011, analysis of post-irradiation examination, SWAT4.0**

1. Introduction

Fission yield is an important physical quantity to evaluate fission products after irradiation. The fission yield used in Japanese Evaluated Nuclear Data Library (JENDL) employs ENDF/B data. The fission yield has recently been evaluated in Japan based on the various theories. Tokyo Institute of Technology (Tokyo Tech) newly evaluated fission yield [1]. It is necessary to confirm the validity of the new fission yield because this fission yield is expected to be included in the next JENDL. In this study, the analysis of Post-Irradiation Examination (PIE) using the fission yield evaluated by Tokyo Tech and JENDL FP Fission Yields Data File 2011 (FPY-2011) [2] that is the latest fission yield data in Japan was performed and validation of new fission yield was checked.

2. Calculation Condition

The burn-up calculation was performed by SWAT4.0 [3] using two data of FPY-2011 and the fission yield evaluated by Tokyo Tech, and the calculation results is compared with the experimental value. The continuous energy Monte Carlo code MVP version 3 was used as a neutron transportation solver. JENDL-4.0 was used in the MVP calculation. In the analysis, the fission yield of ORLIBJ40 [4] was replaced by using FPY-2011 and the fission yield evaluated by Tokyo Tech. Fission yields of Th232, U233, U235, U238, Pu238, Pu241, Cm245, and Cf249 are used because ORLIBJ40 has fission yields of these 8 fissile nuclides. The PIE data of ARIANE program was used [5]. In the ARIANE program, target core is Swiss Beznau-1 PWR. BM5 sample measured by Studiecentrum voor Kernenergie-Centre d'étude de l'Energie Nucléaire (SCK.CEN) was analyzed. The sample was chosen because its measurement error is relatively small among samples. BM5 sample was obtained from M308 assembly and this assembly has a diagonal symmetry. Burnup periods were separated by about 60 days, and the final burnup was about 56.6GWd/t with the consideration of the cooling time between irradiation cycles. Figure 1 shows the position of BM5 sample in M308 assembly and Table I summarizes initial composition of BM5 sample. Table II shows calculation condition of MVP.

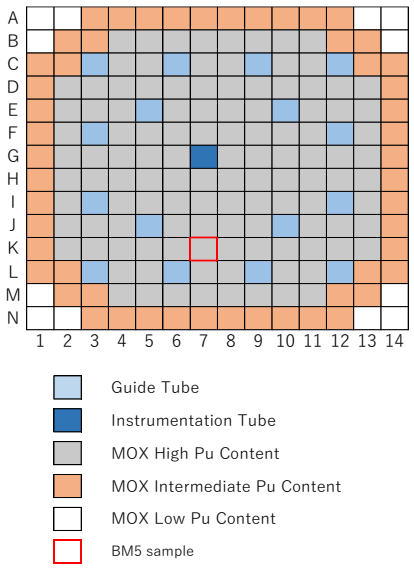

Fig. 1. Position of the sample obtained from the fuel assembly

Table I. Initial Composition of BM5 Sample

Nuclides	Composition (wt%)	Nuclides	Composition (wt%)
U234	0.002	Pu240	1.287
U235	0.218	Pu241	0.364
U238	94.232	Pu242	0.147
Pu238	0.033	Am241	0.051
Pu239	3.666		

Table II. Calculation Condition of MVP

Number of History per Batch	5000
Total Number of Batch	220
Number of Skip Batch	20

3. Calculation Results

Based on the calculation condition mentioned in previous chapter, burn-up calculation was carried out for the fuel assembly. Figures 2 and 3 show C/E values of the amount of actinides and fission products. Error bar in figs 2 and 3 shows experimental error and this confidence level is 95 %.

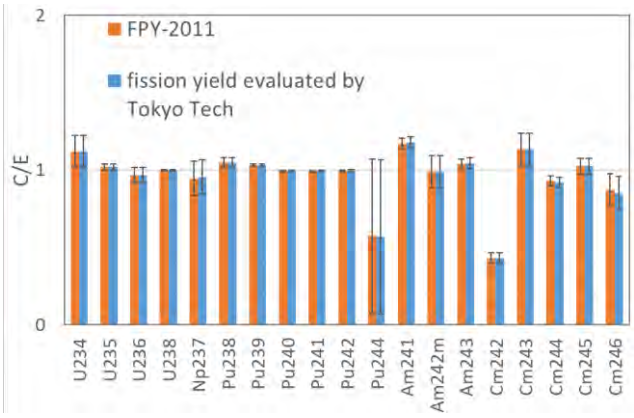

Fig. 2. C/E values of actinides

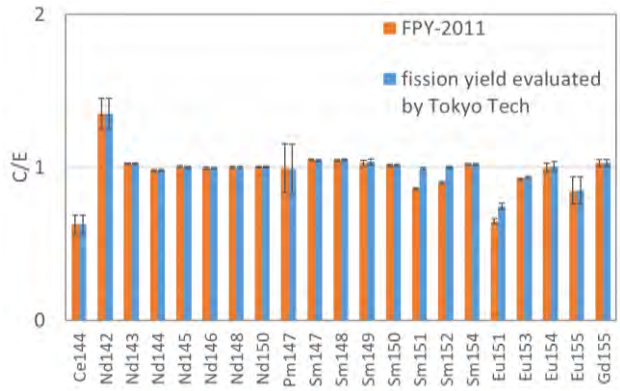

Fig. 3. C/E values of fission products

The results of actinides and fission products for FPY-2011 and fission yield evaluated by Tokyo Tech are almost the same as shown in figs 2 and 3. The results of the fission products with mass number 90 to 137 are also nearly the same for two fission yields. The C/E values using the fission yield evaluated by Tokyo Tech are improved over 10 % for Sm151, Sm152, and Eu151. These nuclides are known for nuclides that those absorption cross sections are not negligible and affect the criticality as described in reference [6]. It was found that the fission yields of Sm151, Sm152, and Eu151 are improved in the fission yield evaluated by Tokyo Tech compared to FPY-2011.

4. Discussion

The reason for the improvement of the results of Sm151, Sm152, and Eu151 is considered in this chapter. Table III shows the amounts of productions of Sm151, Sm152, and Eu151 and the relative differences between the results of FPY-2011 and the new fission yield evaluated by Tokyo Tech.

Table III. Amounts of Production and Relative Differences between two Fission Yields

Nuclides	FPY-2011 ① (g/tU)	Fission Yield evaluated by Tokyo Tech ② (g/tU)	Relative Differences (②/①-1)(%)
Sm151	23.60	27.15	15.1
Sm152	177.82	198.27	11.5
Eu151	0.63	0.72	15.1

Figure 4 shows relative differences in productions of Sm151, Sm152, and Eu151 when the yield of U235, U238, Pu239, or Pu241 is changed from FPY-2011 to new fission yield. It was found that fission yield of Pu241 mainly affects the production of Sm151, Sm152, and Eu151. As an example, the fission yield of Sm151 and its parent nuclides produced from Pu241 was shown in Table IV. The relative difference between the fission yields for Ce151 is more than 700% and their differences affect the improvement of the C/E value. Therefore, relative differences shown in Table III mainly come from the difference of the fission yield of Pu241.

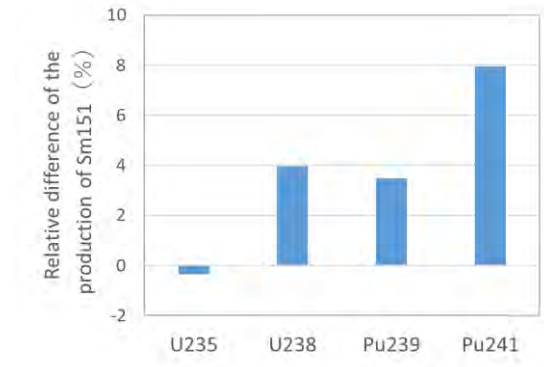

(a) Sm151

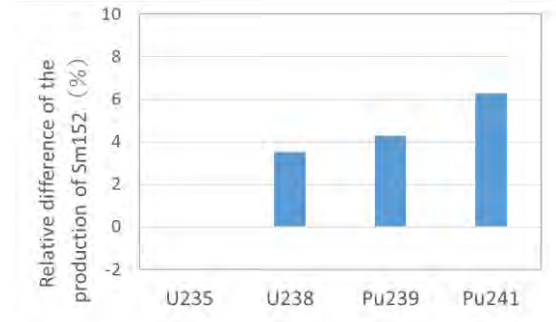

(b) Sm152

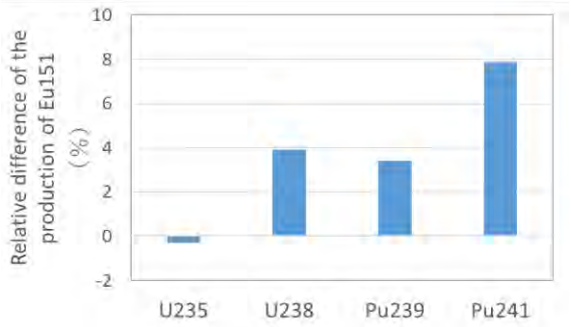

(c) Eu151

Fig.4. Relative differences in production of Sm151, Sm152, and Eu151 when yield of U235, U238, Pu239, or Pu241 is changed from FPY-2011 to new fission yield

Table IV. Comparison between FPY-2011 and fission yield evaluated by Tokyo Tech

	FPY-2011 ① (%)	Fission Yield evaluated by Tokyo Tech ② (%)	Relative Differences (②/①-1)(%)
La151	8.10E-03	1.09E-02	34.9
Ce151	3.63E-02	3.04E-01	737.5
Pr151	5.15E-01	5.31E-01	3.2
Nd151	8.80E-02	6.68E-02	-24.1
Sm151	2.58E-07	1.34E-07	-47.9

5. Conclusion

The results for FPY-2011 and fission yield evaluated by Tokyo Institute of Technology are almost the same. As for Sm151, Sm152, and, Eu151, compared to FPY-2011, it was found that the C/E values are improved over 10 % by using the fission yield evaluated by Tokyo Tech. The improvement of the C/E value of Sm151, Sm152, and Eu151 is mainly due to the update of the fission yield of Pu241.

References

1. Tsubakihara K et al. To be submitted to JNST; S. Chiba, private communication.
2. Katakura J, "JENDL FP Decay Data File 2011 and Fission Yields Data File 2011," JAEA-Data/Code 2011-025, Japan Atomic Energy Agency (2011).
3. Kashima T, Suyama K and Takada T, "SWAT4.0 - The Integrated Burnup Code System Driving Continuous Energy Monte Carlo Codes MVP, MCNP and Deterministic Calculation Code SRAC," JAEA-Data/Code 2014-028, Japan Atomic Energy Agency (2014).
4. Okumura K, Sugino K, Kojima K, Jin T, Okamoto T, and Katakura J, "A Set of ORIGEN2 Cross Section Libraries Based on JENDL-4.0: ORLIBJ40," JAEA-Data/Code 2012-032, Japan Atomic Energy Agency (2012).
5. Primm R, "ARIANE International Programme Final Report," ORNL/SUB/97-XSV750-1, Oak Ridge National Laboratory (2003).
6. Parks C, DeHart M, and Wagner J, "Review and Prioritization of Technical Issues Related to Burnup Credit for LWR Fuel," NUREG/CR-6665, ORNL/TM-1999/303, Oak Ridge National Laboratory (2000).

Proceedings of the Reactor Physics Asia 2019 (RPHA19) Conference
Osaka, Japan, Dec. 2-3, 2019

Continuous Thermal Neutron Scattering Data Processing Capability in RMC Code

ZHENG Lei[a *], WANG Kan[a] , WANG Wei[a]
[a]*Department of Engineering Physics, Tsinghua University, 1st Qinghuayuan, Haidian District,Beijing, China*
[*]Corresponding author: zl17@mails.tsinghua.edu.cn

Abstract

A new continuous representation of the ACE format thermal neutron scattering data was released in 2007, this representation gives more accurate description for the secondary neutron energies, but was not widely known. In this paper, the continuous representation was introduced and compared with the traditional discrete one, the continuous thermal neutron scattering data processing capability was also developed in RMC code. The capability was validated by a set of benchmarks, of the 63 testing cases, only 2 cases show difference a bit more than 3σ for the discrete representation and the continuous representation. Results show that a change from the traditional discrete representation to the continuous one does not produce noticeable changes for the eigenvalues when calculating critical experiments.

Key Words: **Continuous Thermal Neutron Scattering Data, RMC, Benchmarks, ENDF/B-VIII.0**

1. Introduction

In the thermal energy range (<10eV), neutron scattering events can occur resulting in a gain or loss in energy from interaction with the target material. Meanwhile, the neutron scattering data is affected by the chemical binding of the target to other nuclides in a material or crystalline structure effects. All these effects complicate the physics of the scattering process and the calculation of the scattering data. To provide high fidelity Monte Carlo neutronics calculations for thermal reactors, A Compact ENDF (ACE) format thermal neutron scattering data processed through NJOY [1] is always used.

Since the thermal scattering data is complicated, large amount of computer memory is need to store all the detailed thermal neutron scattering information, a discrete representation of the secondary neutron spectrum and angular distribution has been used since the early 1980s due to the limited storage capabilities of computers [2]. The use of the discrete representation does not produce noticeable effects in integral calculations such as k_{eff} eigenvalues [3], but can produce unphysical phenomena [4] and noticeable deficiencies for differential calculations [5].

A new continuous ACE representation of the thermal neutron scattering data was firstly created by Los Alamos National Laboratory in 2007 and implemented in MCNP in 2008 [6].This representation has been available online since 2007, but was not widely known. In 2012 [7] and 2014 [8], continuous ACE representation of thermal neutron scattering data was released subsequently based on ENDF/B-VII.0 and ENDF/B-VII.1 libraries. In the lasted ENDF/B-VIII.0 [9], only the continuous ACE representation of the thermal neutron scattering data was provided by Los Alamos National Laboratory (LANL). It is therefore necessary to use the more physical and rigorous thermal neutron scattering data representation for the high fidelity neutronics calculation. This paper introduces the new continuous representation briefly, the implementation of the continuous thermal neutron scattering data processing capability in Reactor Monte Carlo code RMC [10], and the verification & validation results.

2. Continuous Thermal Neutron Scattering Data

From the traditional discrete representation of thermal neutron scattering data, the secondary neutron is limited to discrete energies and angles, which is not the real case for the scattering kernel. While the continuous representation allows users to process the secondary neutron energies in a continuous manner, with a memory storage consumption increasing of ~10 times larger than the previous discrete one [7].

In order to obtain the continuous representation thermal neutron scattering data, the *aceth* module in NJOY has been modified to convert the secondary energy distributions from *thermr* into probability density functions (PDFs) and cumulative density functions (CDFs) form, PDFs and CDFs are packed into the big inelastic array of the ACE format thermal scattering data [3]. The continuous representation contains a table of incident energies, a table of inelastic cross sections, a table of pointers to the start of each distributions, a table of the number of points in each distribution and the secondary energy and angle distributions. Detailed formats and data

blocks of the discrete and continuous representation for the inelastic thermal scattering data are given in Fig. 1. It can be noted that two extra data blocks as well as PDFs/CDFs for secondary energy distributions are added to the continuous representation.

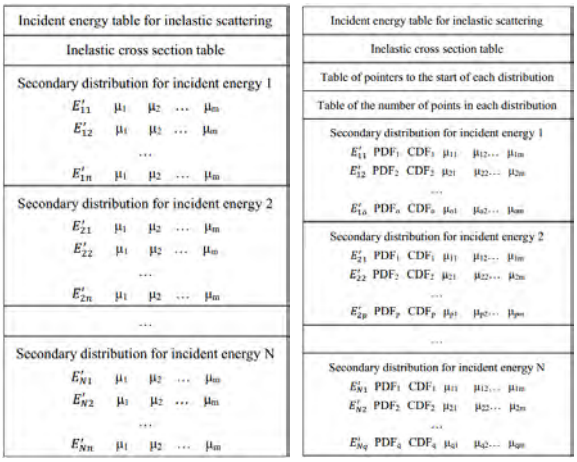

Fig. 1 Discrete (left) and continuous (right) represen tation for inelastic thermal scattering data.

To obtain the continuous ACE representation thermal neutron scattering data, the weighting option (iwt flag) in card 9 of the ACER module should be set to 2 (tabulated) when using NJOY to process the thermal neutron scattering data.

3. Implementation of Continuous Thermal Neutron Scattering Data Processing Capability

In the thermal energy range, neutrons will scatter coherently or incoherently with target atoms depending on the material. Inelastic scattering is important for all thermal materials, coherent elastic scattering is of great importance for powdered crystalline materials, and incoherent elastic scattering is significant for partially ordered materials such as polyethylene [11].Each thermal material will have inelastic scattering and may have either coherent or incoherent scattering, but not both.

The continuous thermal neutron scattering data processing capability was developed in RMC code. For a given incident energy, the treatment starts with the sampling of scattering type depending on the cross sections of elastic scattering and inelastic scattering, then the closest energy in the incident energy table is matched, the cumulative distribution function data is searched for the random sample, the PDFs and CDFs are used to calculate the outgoing energy. Outgoing angle is then sampled and calculated to the outgoing energy. Next, the outgoing energy is projected up or down to correspond to the actual incident energy. The projection scheme is much faster than the real interpolation of incident energies, but still produces relatively accurate results since the incident energy points are enough [3]. The calculation steps are shown as below:

(1) Sample the scattering type for incident energy, σ_{inel} and σ_{el} are the inelastic cross section and the elastic cross section, ξ_1 is the random number.

$$\xi_1 < \frac{\sigma_{inel}}{\sigma_{inel}+\sigma_{el}} \tag{1}$$

(2) Search the location of the incident energy E_{in} in the energy table, and calculate the energy fraction r . E_i and E_{i+1} are the energy grids in the incident energy table.

$$\begin{aligned} &E_i < E_{in} < E_{i+1} \\ &E_{in} = E_i + r\left(E_{i+1} - E_i\right) \end{aligned} \tag{2}$$

(3) Chose the closest energy as the "incident energy", if $r > 0.5$, E_i is chosen as the "incident energy", otherwise, E_{i+1} is chosen.

(4) Sample random number ξ_2 , search CDFs to determine the outgoing energy grid, $c_{l,k}$ and $c_{l,k+1}$ are the CDFs corresponding to the incident energy.

$$c_{l,k} < \xi_2 < c_{l,k+1} \tag{3}$$

(5) Calculate the outgoing energy E' and the interpolation fraction ri for outgoing angle. $E_{l,k}$ and $E_{l,k+1}$ are the sampled outgoing energy grids corresponding to ξ_2, $p_{l,k}$ and $p_{l,k+1}$ are the PDFs .

$$E' = E_{l,k} + \frac{\left|\sqrt{p_{l,k}^2 + 2\left(\xi_2 - c_{l,k}\right)\frac{p_{l,k+1}-p_{l,k}}{E_{l,k+1}-E_{l,k}}} - p_{l,k}\right|}{\frac{p_{l,k+1}-p_{l,k}}{E_{l,k+1}-E_{l,k}}} \tag{4}$$

$$ri = \frac{E' - E_{l,k}}{E_{l,k+1} - E_{l,k+1}} \tag{5}$$

(6) Sample random number ξ_3 , and search the outgoing angle grid. *NIL* is the inelastic dimensioning parameter.

$$j = \mathrm{int}\left[\left(NIL-1\right) * \xi_3\right] \tag{6}$$

(7) Calculate the outgoing angle μ_{out} , $\mu_{l,k,j}$ is the outgoing angle grid corresponding to the outgoing energy.

$$\mu_{out} = \mu_{l,k,j} + ri*(\mu_{l,k+1,j} - \mu_{l,k,j}) + d*(2\xi_4 - 1) \tag{7}$$

$$d = \min\left[d_1, d_2\right] \tag{8}$$

$$d_1 = \frac{(\mu_{l,k,j} - \mu_{l,k,j-1}) + ri*\left[\left(\mu_{l,k+1,j} - \mu_{l,k+1,j-1}\right) + \left(\mu_{l,k,j-1} - \mu_{l,k,j}\right)\right]}{2} \tag{9}$$

$$d_2 = \frac{(\mu_{l,k,j+1} - \mu_{l,k,j}) + ri*\left[\left(\mu_{l,k+1,j+1} - \mu_{l,k+1,j}\right) + \left(\mu_{l,k,j} - \mu_{l,k,j+1}\right)\right]}{2} \tag{10}$$

(8) Project the outgoing energy, and calculate the secondary energy. The down projection and up projection schemes are given in Eq. (11) and (12).

$$E_{out} = \begin{cases} E' * \dfrac{2E_{in} - E_i}{E_i}, E' > 0.5E_i \\ E' + E_{in} - E_i, E' \le 0.5E_i \end{cases} \tag{11}$$

$$E_{out} = \begin{cases} E' * \dfrac{2E_{in} - E_{i+1}}{E_{i+1}}, E' > 0.5E_{i+1} \\ E' + E_{in} - E_{i+1}, E' \le 0.5E_{i+1} \end{cases} \tag{12}$$

4. Verification and Validation

To evaluate the validity of the continuous thermal neutron scattering capability and the effects of the discrete and continuous representation, a set of 63 benchmarks from the International Handbook of Evaluated Criticality Safety Benchmark Experiments (ICSBEP) [12] was selected. The suite is divided into five categories depending on the major fissile material, the neutron spectrum can be divided into fast spectrum, intermediate spectrum and thermal spectrum according to its contribution to fission rate. General information for the suite is given in Table I.

Table I. General information for the validation suite.

Fissile material	Number of benchmarks			
	Fast	intermediate	Thermal	Total
^{233}U	2	1	6	9
HEU	7	4	5	16
IEU	1	0	1	2
LEU	0	0	19	19
Pu	7	1	9	17
Total	17	6	40	63

Thermal materials covers light water, 10%-porosity graphite [13], beryllium oxide, polyethylene, and beryllium metal. The latest thermal neutron scattering data library and neutron data library from ENDF/B-VIII.0 were employed, version 2016.20 [14] of NJOY was used to produce the ACE format neutron data and discrete representation thermal neutron scattering data, the number of exit energy grids for the discrete representation is 64. The continuous representation thermal scattering data was taken from LANL.

The 63 benchmarks using the continuous representation and discrete representation data were run with RMC code, version 2.5.7. All cases were run in the criticality mode, using 100 inactive cycles, 700 additional active cycles, and 30000 neutrons per cycle. Uncertainties of k-effective were less than 20pcm for all cases.

5. Results

Results of the calculated k_{eff} values are given in Table II. to VI. K_{eff} values of the discrete representation and the continuous representation agreed within statistics for most cases: 40 of 63 cases showed difference not more than 1σ, 49 of 63 cases showed difference not more than 2σ, with 9 cases differed by more than 3σ.

Detailed examination is conducted for cases: hmf9-2, lct8-2, lct8-5, lct8-7, lct8-11, pmf21-1, pst9-3a, pst18-9. It is observed that uncertainties of these cases are near but a bit smaller than 15pcm, in the final comparsion, these uncertainties are treated as 10pcm because of rounding, resulting in the overestimated deviation. 3 of these 7 cases showed difference less than 2σ, 4 of these 7 cases differed by less than 3σ using the real uncertainties. Finally, only 2 of 63 cases differed by a bit more than 3σ using the real uncertainties, which is not noticeable.

Table II. ^{233}U benchmark results

Case name	Thermal material	Experiment keff	Continuous keff	Discrete keff	Δkeff
umf5-1	Be	1.0000(30)	0.9975(1)	0.9976(1)	0.0001 (1)
umf5-2	Be	1.0000(30)	0.9977(2)	0.9972(2)	0.0005 (3)
usi1-1	H_2O/poly	1.0000(83)	0.9872(2)	0.9872(2)	0.0000 (3)
ust1-1	H_2O/poly	1.0000(31)	1.0011(1)	1.0012(1)	0.0001 (1)
ust1-2	H_2O/poly	1.0005(33)	1.0010(1)	1.0009(1)	0.0001 (1)
ust1-3	H_2O/poly	1.0006(33)	1.0006(1)	1.0007(1)	0.0001 (1)
ust1-4	Be/H2O	0.9998(33)	1.0006(1)	1.0006(1)	0.0000 (1)
ust1-5	H_2O	0.9999(33)	1.0001(1)	1.0001(1)	0.0000 (1)
ust-8	H_2O	1.0006(29)	1.0012(1)	1.0011(1)	0.0001 (1)

Table III. HEU benchmark results

Case name	Thermal material	Experiment keff	Continuous keff	Discrete keff	Δkeff
hmf4-1	H_2O	1.0020(10)	1.0056(2)	1.0052(2)	0.0004 (3)
hmf4-2	H_2O	0.9985(10)	1.0014(2)	1.0013(2)	0.0004 (3)
hmf9-2	BeO	0.9992(15)	0.9956(1)	0.9953(1)	0.0003 (1)
hmf-11	Poly	0.9989(15)	0.9984(2)	0.9982(1)	0.0002 (3)
hmf19-2	Grph	1.0000(28)	1.0006(1)	1.0006(1)	0.0000 (1)
hmf20-2	Poly	1.0000(28)	1.0004(1)	1.0004(1)	0.0000 (1)
hmf26-11	Poly	1.0000(38)	1.0014(2)	1.0018(2)	0.0004 (3)
hmi6-1	Grph	0.9977(8)	0.9989(2)	0.9988(2)	0.0001 (3)
hmi6-2	Grph	1.0001(8)	1.0026(2)	1.0024(2)	0.0002 (3)
hmi6-3	Grph	1.0015(9)	1.0043(2)	1.0042(2)	0.0004 (3)
hmi6-4	Grph	1.0016(8)	1.0062(2)	1.0060(2)	0.0002 (3)
hst13-1	H_2O	1.0012(26)	0.9982(1)	0.9983(1)	0.0001 (1)
hst13-2	H_2O	1.0007(36)	0.9977(1)	0.9978(1)	0.0001 (1)
hst13-3	H_2O	1.0009(36)	0.9946(1)	0.9947(1)	0.0001 (1)
hst13-4	H_2O	1.0003(36)	0.9962(1)	0.9962(1)	0.0000 (1)
hst32	H_2O	1.0015(26)	0.9994(1)	0.9994(1)	0.0000 (1)

Table IV. IEU benchmark results

Case name	Thermal material	Experiment keff	Continuous keff	Discrete keff	Δ keff
imf4-2	Grph	1.0000(30)	1.0049(1)	1.0049 (1)	0.0000 (1)
ict2-3	H_2O	1.0017(44)	1.0063(2)	1.0068 (2)	0.0005 (3)

Table V. LEU benchmark results

Case name	Thermal material	Experiment keff	Continuous keff	Discrete keff	Δkeff
lst2-1	H_2O	1.0004(26)	0.9997(1)	0.9996(1)	0.0001 (1)
lst2-2	H_2O	1.0003(32)	0.9956(1)	0.9954(1)	0.0002 (1)
lst7-14	H_2O	0.9961(9)	0.9955(1)	0.9953(1)	0.0002 (1)
lst7-30	H_2O	0.9973(9)	0.9978(1)	0.9977(1)	0.0001 (1)
lst7-32	H_2O	0.9985(10)	0.9965(1)	0.9966(1)	0.0001 (1)
lst7-36	H_2O	0.9988(11)	1.0165(1)	1.0167(1)	0.0002 (1)
lst6-49	H_2O	0.9983(11)	0.9977(1)	0.9977(1)	0.0000

					(1)
lct8-1	H_2O	1.0007(16)	1.0026(1)	1.0033(1)	0.0007 (1)
lct8-2	H_2O	1.0007(16)	1.0031(1)	1.0034(1)	0.0003 (1)
lct8-5	H_2O	1.0007(16)	1.0019(1)	1.0023(1)	0.0004 (1)
lct8-7	H_2O	1.0007(16)	1.0013(1)	1.0018(1)	0.0005 (1)
lct8-8	H_2O	1.0007(16)	1.0008(1)	1.0015(1)	0.0007 (1)
lct8-11	H_2O	1.0007(16)	1.0034(1)	1.0039(1)	0.0005 (1)
mct2-pnl30	H2O	1.0024(60)	1.0005(2)	1.0005(2)	0.0000 (3)
mct2-pnl31	H2O	1.0009(47)	1.0015(2)	1.0023(2)	0.0008 (3)
mct2-pnl32	H2O	1.0042(31)	1.0014(2)	1.0013(2)	0.0001 (3)
mct2-pnl33	H2O	1.0024(24)	1.0058(2)	1.0059(2)	0.0001 (3)
mct2-pnl34	H2O	1.0038(25)	1.0023(1)	1.0024(2)	0.0001 (3)
mct2-pnl35	H2O	1.0029(27)	1.0054(1)	1.0056(2)	0.0002 (3)

Table VI. Pu benchmark results

Case name	Thermal material	Experiment keff	Continuous keff	Discrete keff	Δkeff
pmf11	H_2O	1.0000(10)	1.0011(2)	1.0012(2)	0.0001 (3)
pmf18	Be	1.0000(30)	0.9985(1)	0.9984(1)	0.0001 (1)
pmf19	Be	0.9992(15)	1.0001(1)	0.9999(1)	0.0002 (1)
pmf21-1	Be	1.0000(26)	1.0042(1)	1.0038(1)	0.0004 (1)
pmf21-2	BeO	1.0000(26)	0.9929(1)	0.9928(1)	0.0001 (1)
pmf23-2	Grph	1.0000(20)	0.9986(1)	0.9986(1)	0.0000 (1)
pmf24-2	Poly	1.0000(20)	1.0014(1)	1.0015(1)	0.0001 (1)
pci1	Grph	1.0000(11)	1.0092(1)	1.0093(1)	0.0001 (1)
pst9-3a	H_2O	1.0000(33)	1.0129(1)	1.0126(1)	0.0003 (1)
pst11-16-1	H_2O	1.0000(52)	1.0028(2)	1.0028(2)	0.0000 (1)
pst11-16-5	H_2O	1.0000(52)	0.9993(2)	0.9993(2)	0.0000 (1)
pst11-18-1	H_2O	1.0000(52)	0.9871(2)	0.9873(2)	0.0002 (3)
pst11-18-6	H_2O	1.0000(52)	0.9930(2)	0.9931(2)	0.0001 (3)
pst18-9	H_2O	1.0000(34)	0.9998(1)	0.9995(1)	0.0003 (1)
pst21-1	H_2O	1.0000(32)	0.9981(2)	0.9980(2)	0.0001 (3)
pst21-3	H_2O	1.0000(65)	1.0005(2)	1.0001(2)	0.0004 (3)
pst34-1	H_2O	1.0000(62)	0.9968(2)	0.9962(2)	0.0006 (3)

6. Conclusions

The continuous ACE representation of the thermal neutron scattering data was introduced in this paper, the processing capability was also implemented in the Reactor Monte Carlo code RMC. Of the 63 testing cases, only 2 cases show difference a bit larger than 3σ for the discrete representation and the continuous representation. Results show that a change from the traditional discrete representation to the continuous one does not produce noticeable changes for the eigenvalues when calculating critical experiments.

Acknowledgements

This work was supported by the Science Challenge Project, No. TZ2018001.

References

1. Macfarlane RE, and Kahler AC, “Methods for Processing ENDF/B-VII with NJOY,” *Nucl. Data Sheets*, **111**, *12,* 2739 (2010).
2. MacFarlane RE, “A discussion of the MCNP Thermal Scattering Model,” (March 22 2005).
3. Pavlou AT, Brown FB, Martin WR, et al, “Comparison of discrete and continuous thermal neutron scattering treatments in MCNP5,” *Proc. PHYSOR 2012*, LaGrange Park, IL, April 15–20, 2012, American Nuclear Society (2012).
4. Conlin JL, Parsons DK, Brown FB, et al, “Continunous S(α,β) Capability in MCNP,” *Proc. ANS Annual Meeting 2012*, Chicago, IL June 24–28, 2012.
5. Cullen DE, Hansen LF, Lent EM, et al, “Thermal Scattering Law Data: Implementation and Testing using the Monte Carlo neutron transport codes COG, MCNP and TART,” UCRL-ID-153656, Los Alamos National Laboratory (2003).
6. Booth TE, Brown FB, Bull JS, et al, “MCNP5 1.50 Release Notes,” LS-UR-08-2300, Los Alamos National Laboratory (2008).
7. Parsons DK and Conlin JL, “Release of Continuous Representation for S(α,β) ACE Data,” LA-UR-12-00800, Los Alamos National Laboratory (2012).
8. Parsons DK and Conlin JL, “Release of Continuous Representation for S(α,β) ACE Data,” LA-UR-14-21878, Los Alamos National Laboratory (2014).
9. Brown DA, Chadwick MB, Capote R, et al, “ENDF/B-VIII.0: The 8th, Major Release of the Nuclear Reaction Data Library with CIELO-project Cross Sections, New Standards and Thermal Scattering Data,” *Nucl. Data Sheets*, **148**, 1 (2018).
10. Wang K, Li Z, She D, et al, "RMC – A Monte Carlo code for reactor core analysis." *Ann. Nucl. Energy*, **82**, 121 (2015).
11. Trkov A, Herman M, Brown DA, et al, “ENDF-6 Formats Manual: Data Formats and Procedures for the Evaluated Nuclear Data Files ENDF/B-VI, ENDF/B-VII and ENDF/B-VIII”, BNL-203218-2018-INRE, Cross Sections Evaluation Working Group (2018).
12. OECD-NEA "The International Criticality Safety Benchmark Evaluation Project." NEA/NSC/DOC (95)03, OECD Nuclear Energy Agency (2011).
13. Parsons DK, “NJOY Processing of ENDF/B VIII.0 Thermal Scattering Files,” LA-UR-18-25096, Group XCP-5, Los Alamos National Laboratory (2018).
14. Macfarlane RE, Muir DW, Boicourt RM, et al, "The NJOY Nuclear Data Processing System, Version 2016," LA-UR-17-20093, Los Alamos National Laboratory (2017).

Proceedings of the Reactor Physics Asia 2019 (RPHA19) Conference
Osaka, Japan, Dec. 2-3, 2019

Thermal neutron scattering data generation function in the nuclear data processing code NECP-Atlas

Yongqiang Tang[a], Tiejun Zu[a,*], Siyu Yi[a], Jialong Xu[a], Liangzhi Cao[a] and Jin Yang [b]
[a]*School of Nuclear Science and Technology, Xi'an Jiaotong University, Xi'an, Shaanxi 710049, China*
[b]*College of Urban and Environmental Sciences, Hunan University of Technology, ZhuZhou, Hunan 412007, China*
[*]Corresponding author: tiejun@xjtu.edu.cn (T. Zu)

Abstract

A new module called sab_calc was implemented into NECP-Atlas, a nuclear data processing code developed at Xi'an Jiaotong University in China, to evaluate the thermal neutron scattering law (TSL), which describes the thermal scattering from bound moderators. Coupling this new module and thermal scattering cross section calculation module, NECP-Atlas can provide accurate thermal scattering cross section for various moderators used in nuclear reactors. In this paper, ZrH_2 was selected as an example to illustrate the function to generate thermal scattering laws and cross sections in NECP-Atlas. The Finite Difference Method (FDM) was applied to calculate crystal force constants, which is transferred to a lattice dynamics code Phonopy to calculate phonon density of states (DOS), which is the basis to evaluate TSL data. The five isotopes of Zr in ε-phase ZrH_2 were treated individually, then a new ACE format library using the evaluated ZrH_2 TSL data in this work was generated. Six benchmarks from International Criticality Safety Benchmark Evaluation Project (ICSBEP) with ZrH_x (x=1.9) moderator were calculated using the Monte Carlo code, and the numerical results show that ε-phase ZrH_2 can provide more precious thermal scattering cross section than the approximated ZrH_x in ENDF/B VIII.0.

Key Words: **NECP-Atlas, Thermal neutron scattering, First-principles calculations, ENDF/B VIII.0**

1. Introduction

The performance of thermal neutron driven reactors physics calculating is limited by the accuracy of the thermal scattering cross sections. In thermal energy region, the wavelengths of neutrons are similar to the interatomic distances in matter, so the neutron scattering behavior in the energy region of atomic thermal motion is fundamentally different from high energy regions. And neutron energies are similar to those of excitations in matter, therefore, interactions between neutrons and materials will excite or deexcite the system's energy states[1]. The TSL data is used to describe the thermal scattering from bound moderators in thermal energy region. The TSL of several materials are given in the evaluated nuclear data file (ENDF). For these materials, the thermal scattering cross sections are evaluated directly using the TSL data. While, for the materials without TSL data, the free gas model is used to evaluate the thermal scattering cross sections, which will introduce large errors. Therefore, a numerical method is applied to calculate the TSL data based on the first principle, such as the LERPR module in NJOY.

The nuclear data processing code NECP-Atlas is newly developed to establish a platform to carry out deeper researches on nuclear data processing methods. All the different types of TSL and free gas model can be processed by therm_clac module in NECP-Atlas, and point-wise cross sections can be transformed into ACE library by ace_outp module as described by Zu et al. [2]. However, NECP-Atlas didn't have the function to calculate the TSL data based on the first-principle calculations. In this work, a new module called sab_calc was implemented in NECP-Atlas to provide accurate thermal scattering data for the materials without TSL data in ENDF.

In this work, the zirconium hydride (ZrH_2) moderator was selected as the example to illustrate the function to generate thermal scattering data in NECP-Atlas. Six benchmark experiments with the ZrH_2 were analyzed and evaluated to verify the precision of the thermal neutron scattering data. The calculated results were compared with the benchmark results and experimental results.

2. Theory of Thermal Scattering Cross Section

From Born scattering theory and Femi's Golden rule, the double differential scattering cross section can be derived

as:

$$\sigma(E \to E', \mu) = \frac{1}{2k_B T}\sqrt{\frac{E'}{E}}\left(\sigma_{coh} S(\alpha,\beta) + \sigma_{inc} S_s(\alpha,\beta)\right) \quad (1)$$

where

$$\alpha = \frac{E' + E - 2\mu\sqrt{E'E}}{Ak_B T}$$

$$\beta = \frac{E' - E}{k_B T}$$

The first term in Eq. (1) is coherent scattering in which neutron waves scattered from different particles interface with each other. The second term is incoherent scattering, where there are no interference effects between waves scattered by different particles. Using incoherent approximation, the coherent and incoherent inelastic can be considered as a whole part, and formulas are listed as follow.

Inelastic scattering:

$$\sigma(E \to E', \mu) = \frac{\sigma_b}{2k_B T}\sqrt{\frac{E'}{E}} S_s(\alpha,\beta) \quad (2)$$

$$\sigma_b = \sigma_{inc} + \sigma_{coh} \quad (3)$$

S_s is the asymmetric form of the scattering law:

$$S_s(\alpha,\beta) = \frac{1}{2\pi}\int_{-\infty}^{\infty} e^{i\beta\hat{t}} e^{-\gamma(\hat{t})} d\hat{t} \quad (4)$$

where $\hat{t}$ is time in units of $\hbar / k_B T$, and the second exponential can be expanded as a Taylor series known as phonon expansion,

$$e^{-\gamma(\hat{t})} = e^{-\alpha\lambda}\sum_{n=0}^{\infty}\frac{1}{n!}\left[\alpha\int_{-\infty}^{\infty}\frac{\rho(\beta)}{2\beta\sinh(\beta/2)} e^{-\beta/2} e^{-i\beta\hat{t}} d\beta\right]^n \quad (5)$$

As seen, the PDOS $\rho(\beta)$ is the important needed input to calculate the scattering law.

Incoherent elastic scattering (the same in all directions):

$$\sigma(E \to E') = \frac{\sigma_b}{2}\left\{\frac{1 - e^{-4wE}}{2wE}\right\} \quad (6)$$

where the Debye-Waller integral w is computed from the PDOS as

$$w = \int_{-\infty}^{\infty}\frac{\rho(\beta)}{2k_B T\beta\sinh(\beta/2)} e^{-\beta/2} d\beta \quad (7)$$

The above equations calculating the thermal scattering law are newly implemented in NECP-Atlas as a new module called sab_calc.

3. Results

In this work, ZrH_2 (ε-phase) was selected as an example material to explain the workflow of producing the thermal scattering cross sections. Six benchmarks from the ICSBEP handbook were used to verify the thermal cross sections.

In ENDF/B VIII.0, the crystal structure of ZrH_x is approximated to a face-centered cubic structure based on a central-force lattice dynamics model [3]. Generally, zirconium hydride has several lattice structures dependent on the hydrogen content. In this work, the approximation in ENDF/B thermal scattering library was removed, and the pure face centered tetragonal ε-phase ZrH_2 was investigated. Also, the five isotopes of Zr were treated individually, because of their different atomic mass ratios and bound scattering cross sections.

3.1 Crystal Structure of ZrH2

Through systematically investigation on the structure of Zr hydrides ZrH_x (x =0.5, 1.5, 2)[4], ZrH_2 (ε-phase) is Fluorite-like structured and crystallizes in the tetragonal *I4/mmm* space group. Thus, *I4/mmm* (c/a=1.25) structure is taken into consideration.

The structure of the ZrH_2 unit cell is shown in Fig. 1 with the Zr atoms colored green and the H atoms colored blue. The structure has the constants a=b=3.54186 Å and c= 4.45270 Å, c/a = 1.257, which agree well with the previous calculation by Zhu et al[4]. a=b=3.538 Å, c=4.406 Å, c/a=1.25.

The calculations of the structural properties in this study were carried with the Vienna ab initio simulation package [5,6]based on Finite Difference Method (FDM) with plane-wave basis sets and the Projector augmented wave (PAW) pseudopotential. The generalized gradient approximation (GGA) of Perdew-Burker-Ernzerhof (PBE) functional has been applied to evaluate exchange-correlation functions.

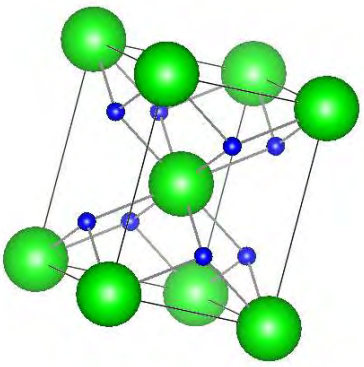

Fig. 1. The ZrH2 unit cell

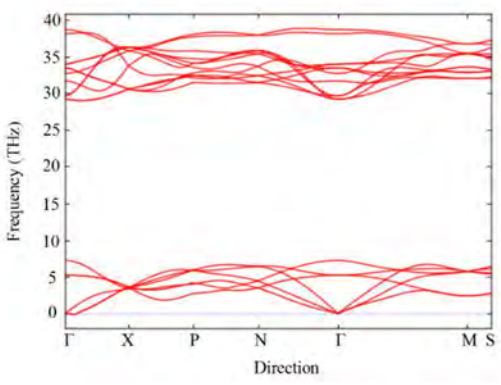

Fig. 2 Ab initio calculated ZrH_2 dispersion relations

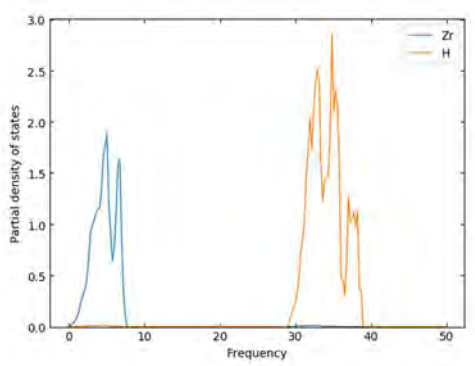

Fig. 3 Calculated partial phonon DOS of ZrH_2

Fig. 2 shows the dispersion relations along the highest symmetry points of the first reduced Brillouin zone, calculated by the Phonopy package[7]. Fig. 3 shows the partial phonon frequency distributions for H in ZrH_2 and Zr in ZrH_2. This is consistent with the work of Zhu et al[4].

3.2 Thermal Scattering Cross section

In ENDF/B VIII.0, Zr in ZrH_x was treated as a natural nuclide. Generally, natural zirconium is formed of five isotopes: Zr-90, Zr-91, Zr-92, Zr-94 and Zr-96. Table I shows abundance and neutron scattering cross sections of zirconium and their isotopes. Besides the calculated partial phonon DOS, atomic mass ratios and atom scattering cross sections are important inputs to calculate TSLs using the sab_module in NECP-Atlas. Therefore, in this work, there five isotopes were treated individually.
Fig. 4 shows inelastic scattering cross section of Zr-90, Zr-91, Zr-92, Zr-94 and Zr-95 at 300K generated by therm_calc module in NECP-Atlas. Fig. 5 shows elastic scattering cross section of Zr-90, Zr-91, Zr-92, Zr-94 and Zr-95 at 300K generated by therm_calc module in NECP-Atlas. Fig. 6 shows scattering cross section of the crystal models for H in ZrH2 at 300K generated by NECP-Atlas. Fig.7 shows the differences of HinZrH2 thermal scattering cross sections between ENDF/B-VIII.0 TSL and NECP-Atlas TSL in this work. The inelastic scattering cross section generated by NECP-Atlas TSL shows higher values at energy rangy of 0.002~0.1eV.

Table I. abundance and neutron scattering cross sections of zirconium and their isotopes[8]

	abundance	Coh xs[a] /barn	Inc xs[b] /barn	Scatt xs[c] barn
Zr	---	6.44	0.02	6.46
Zr-90	51.45%	5.1	0	5.1
Zr-91	11.22%	9.5	0.15	9.7
Zr-92	17.15%	6.9	0	6.9
Zr-94	17.38%	8.4	0	8.4
Zr-96	2.80%	3.8	0	3.8

notes
a bound coherent scattering cross section
b bound incoherent scattering cross section
c total bound scattering cross section

3.3 Verifications with ICSBEP benchmark calculation

HEU-COMP-MIXED-003 benchmark experiment[9], with highly enriched fuel (approximately 96% U-235), zirconium hydride moderator and beryllium reflector, was calculated using ACE format libraries prepared by NECP-Atlas. The Beryllium, Beryllium Oxide and HinH2O thermal scattering libraries were generated by NECP-Atlas, using the PDOS and atoms site position provided by ENDF/B-VIII.0.The atomic densities of the main materials

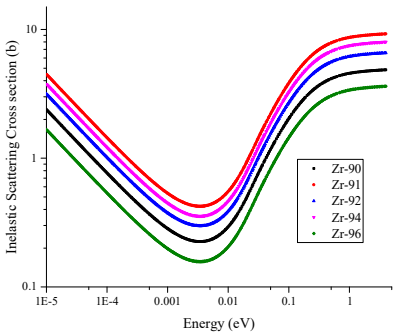

Fig. 4 Inelastic scattering cross section of Zr-90, Zr-91, Zr-92, Zr-94 and Zr-95 at 300K

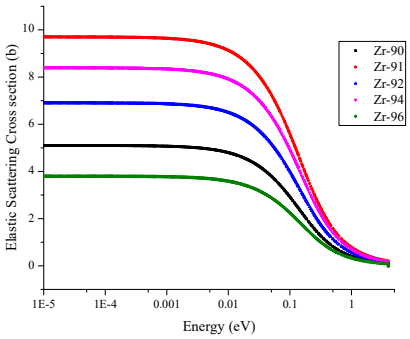

Fig. 5 Elastic scattering cross section of Zr-90, Zr-91, Zr-92, Zr-94 and Zr-95 at 300K

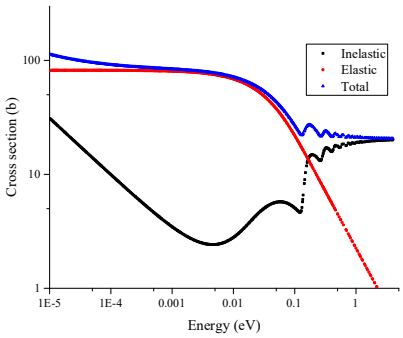

Fig. 6 Thermal scattering cross section of the crystal models for H in ZrH_2 at 300K

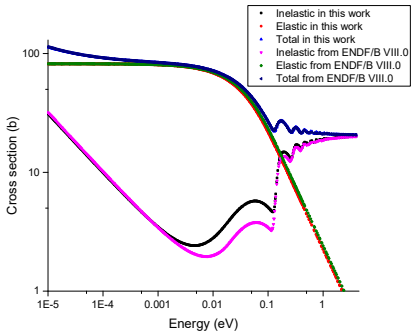

Fig. 7 A comparison of HinZrH2 thermal scattering cross sections between the ENDF/B-VIII.0 TSL and NECP-Atlas TSL in this work

can be easily found in ICSBEP handbook. The ratio of H and total Zr atomic density is about 1.9, which is consistent with pre-calculated ε-phase zirconium hydride. Table II shows experimental, benchmark and calculated k_{eff} by MCNP using different libraries. Compared to the ZrH_x TSL from ENDF/B VIII.0, the evaluated ZrH_2 TSL in this work performed about 100 pcm closer to experiment values, while TSL from ENDF/B VIII.0 shows a better results in benchmark hcm003_05. The last two columns show that Zr in ZrH_2 treated with as five isotopes performed a slight improvement compared to Zr treated as a natural nuclide.

Table II Experimental, benchmark and calculated k_{eff} using different libraries.

	experiment	ENDF/B VIII.0-TSL Zr-nat[a]	Atlas-TSL Zr-nat[b]	Atlas-TSL Zr-iso[c]
hcm003_01	1.00000	0.99834(8)	0.99974(8)	0.99980(8)
hcm003_02	1.00000	0.99905(8)	1.00028(8)	1.00017(8)
hcm003_03	1.00000	0.99898(8)	1.00011(9)	1.00028(8)
hcm003_04	1.00000	0.99885(8)	1.00033(8)	1.00035(8)
hcm003_05	1.00000	0.99989(8)	1.00114(8)	1.00109(8)
hcm003_06	1.00000	0.99886(8)	1.00026(8)	1.00026(8)

notes

a. Zr in ZrH_x was treated as a natural nuclide. Zr TSL in ENDF/B VIII.0 was used.
b. Zr in ZrH_2 was treated as a natural nuclide. Zr TSL generated in this work was used.
c. Zr in ZrH_2 was treated as five isotopes. Zr TSL generated in this work was used.

4. Conclusions

A new module sab_calc was implemented in NECP-Atlas to generate thermal scattering library. Starting from first-principles calculations, the complete generation workflow of thermal scattering laws and cross sections was investigated. ZrH2 (ε-phase) was selected as an example material to validate the workflow of thermal cross sections generation. Zr in ZrH_2 was separated to five isotopes. The numerical results of benchmark experiment from ICSBEP handbook shows a higher accuracy thermal scattering library of ZrH_2 was developed. The reason is that for zirconium hydride with the ratio of H and total Zr atomic density around 2, the lattice structure should be pure face centered tetragonal ε-phase. The workflow of providing thermal neutron scattering data based on NECP-Atlas is workable, and more validation will be done in the future.

Acknowledgements

This research was supported by National Natural Science Foundation of China (No. 11605128)

References

1. BUCKNALL D, *Introduction to the Theory of Thermal Neutron Scattering, 3rd edn., by G.L. Squires*, 3rd ed., in Contemporary Physics **53** 6, 3rd ed., Cambridge University Press (2012).
2. ZU T et al., "NECP-Atlas: A new nuclear data processing code," *Ann. Nucl. Energy* **123**, 153, Elsevier Ltd (2019).
3. MACFARLANE R, "New Thermal Neutron Scattering Files for ENDF/B-VI Release 2" (1994).
4. ZHU X et al., "Structure and thermodynamic properties of zirconium hydrides by structure search method and first principles calculations," *Comput. Mater. Sci.* **150** April, 77, Elsevier (2018).
5. KRESSE G, FURTHMÜLLER J, "Efficiency of ab-initio total energy calculations for metals and semiconductors using a plane-wave basis set," *Comput. Mater. Sci.* **6** 1, 15, Elsevier (1996).
6. KRESSE G, FURTHMÜLLER J, "Efficient iterative schemes for ab initio total-energy calculations using a plane-wave basis set," *Phys. Rev. B* **54** 16, 11169, American Physical Society (1996).
7. TOGO A, OBA F, TANAKA I, "First-principles calculations of the ferroelastic transition between rutile-type and CaCl2-typ SiO2 at high pressures," *Phys. rev. B* **78** 13, 134106 (2008).
8. SEARS V, "Neutron scattering lengths and cross sections," *Neutron News* **3**, 26 (1992).
9. OECD-NEA, "International Criticality Safety Benchmark Evaluation Project" (2014).

Proceedings of the Reactor Physics Asia 2019 (RPHA19) Conference
Osaka, Japan, Dec. 2-3, 2019

Quantification of Effectiveness of Integral Data Using Active Sub-Space in Nuclear Data Testing

Daichi Imazato[a*], Go Chiba[a]
[a]*Hokkaido University, Kita-13 Nishi-8, Sapporo, Japan*
[*]Corresponding author: daiti@eis.hokudai.ac.jp

Abstract

We develop a quantification method of effectiveness of a set of integral data for verification of nuclear data. This study uses the singular value decomposition, the orthogonal projection and the concept of active sub-space. By using the proposed method, we can quantify the independency of a set of integral data and the possibility of verification of individual nuclear data by a set of integral data. In this study, we consider fictitious homogeneous spherical critical assemblies: bare assemblies and water-reflected assemblies, and the proposed method is tested against these assemblies. Through numerical calculations it is found that the proposed method is promissing.

Key Words: **nuclear data, integral data, sensitivities, singular value decomposition, active sub-space, orthogonal projection**

1. Introduction

Nuclear data values are evaluated by using results of theoretical calculations and nuclear data experiments, and integral data experiments are used for verification and updating of evaluated nuclear data. True values of nuclear data can be theoretically obtained from integral data if the number of independent integral data is larger than the number of nuclear data. This is not realistic because the number of nuclear data is generally much larger than the number of integral data. However, there is a possibility that some of nuclear data can be independently verified by using integral data. Therefore, it is important to quantify the effectiveness of a set of integral data for verifying individual nuclear data. Also, various different integral data can be obtained by changing the experimental condition, but there should be dependencies among the different integral data because of similarity of experiment condition, material composition, and so on. Consequently, it is also important to quantify the independency of each integral data in a set of integral data.

In this study, we propose a method to quantify how much individual nuclear data can be verified with a set of integral data, and how much each of integral data are dependent on each other. These are attained by using mathematical techniques, such as the singular value decomposition (SVD), the orthogonal projection [1] and the concept of active sub-space (ASS) [2].

2. Theory and Numerical Procedure

2.1 Singular value decomposition

Let us consider m-column vectors $\vec{a}_i$ and the number of them is n. In such a case, a matrix $A_{m\times n}$ consisting of these vectors is defined as

$$A_{m\times n} = (\vec{a}_1 \quad \vec{a}_2 \quad \cdots \quad \vec{a}_n). \tag{1}$$

This matrix can be transformed by SVD as

$$A_{m\times n} = U_{m\times m} D_{m\times n} (V_{n\times n})^T, \tag{2}$$

where the superscript T is for the matrix transposition. When we assume $n<m$, $D_{m\times n}$ can be presented as

$$D_{m\times n} = \begin{pmatrix} \sigma_1 & 0 & 0 & \cdots & 0 & \cdots & 0 \\ 0 & \sigma_2 & 0 & \cdots & 0 & \cdots & 0 \\ & 0 & \sigma_3 & \cdots & 0 & \cdots & 0 \\ & & 0 & \ddots & 0 & & 0 \\ \vdots & & & 0 & \sigma_s & 0 & 0 \\ & & & & & \ddots & 0 \\ 0 & \cdots & & & \cdots & 0 & \sigma_n \\ & & & & & & 0 \\ \vdots & \vdots & \vdots & \vdots & \vdots & \vdots & \vdots \\ 0 & \cdots & & & & \cdots & 0 \end{pmatrix}, \tag{3}$$

where σ_i are singular values arranged by descending order. The matrices $U_{m\times m}$ and $V_{n\times n}$ are the unitary matrices and presented as

$$U_{m\times m} = (\vec{u}_1 \quad \vec{u}_2 \quad \cdots \quad \vec{u}_s \quad \cdots \quad \vec{u}_m), \tag{4}$$

$$V_{n\times n} = (\vec{v}_1 \quad \vec{v}_2 \quad \cdots \quad \vec{v}_s \quad \cdots \quad \vec{v}_n). \tag{5}$$

Then, the sets of $\vec{u}_i$ and $\vec{v}_i$ are the orthonormal basis components of the m-dimensional and the n−dimensional sub-spaces, respectively, so

$$UU^T = U^T U = I, \tag{6}$$

$$VV^T = V^T V = I, \tag{7}$$

where I is the unit matrix.

Let us consider a m-dimensional vector $\vec{r}$, which is described as a linear combination of $\vec{a}_i$. This vector $\vec{r}$

can be expressed as

$$\vec{r} = \begin{pmatrix} r_1 \\ r_2 \\ \vdots \\ r_m \end{pmatrix} = (\vec{a}_1 \quad \vec{a}_2 \quad \cdots \quad \vec{a}_n) \begin{pmatrix} r_1' \\ r_2' \\ \vdots \\ r_n' \end{pmatrix} = \sum \vec{a}_i r_i' = A_{m\times n}\overrightarrow{r'}. \tag{8}$$

If the matrix $A_{m\times n}$ is decomposed as Eq. (2), Eq. (8) can be written as

$$\vec{r} = U_{m\times m}D_{m\times n}(V_{n\times n})^T\overrightarrow{r'} = \sum_{i=1}^{n}\left(\sigma_i \vec{v}_i^T\overrightarrow{r'}\right)\vec{u}_i. \tag{9}$$

If the singular values σ_i $(i > s)$ are extremely small, Eq. (9) can be transformed to

$$\vec{r} = \sum_{i=1}^{s}\left(\sigma_i \vec{v}_i^T\overrightarrow{r'}\right)\vec{u}_i. \tag{10}$$

This shows that an arbitrary vector represented as a linear combination $\vec{a}_i$ can be described by a linear combination of $\vec{u}_i$; orthogonal basis of a space spanned by $\vec{a}_i$ is $\vec{u}_i$.

In this study, the matrix $A_{m\times n}$ is constructed by a set of vectors, and SVD is adopted to obtain the orthonormal basis vectors $\vec{u}_i$. These vectors are used for the subsequent orthogonal projection and the quantification methods of the effectiveness of a set of integral data.

2.2 Orthogonal projection

Let us consider a vector $\vec{a}$ in a *M*-dimensional space, and this vector is orthogonally projected to a *N*-dimensional ($N< M$) sub-space.

In the case of M=3 and N=2, $\vec{a}$ is expressed as

$$\vec{a} = b_1\overrightarrow{u_1} + b_2\overrightarrow{u_2} + b_3\overrightarrow{u_3}, \tag{11}$$

where $\overrightarrow{u_l}$ is the orthonormal basis of the *M*-dimensional space. Equation (11) can be transformed to

$$\vec{a} = (\overrightarrow{u_1} \quad \overrightarrow{u_2} \quad \overrightarrow{u_3}) \cdot \begin{pmatrix} b_1 \\ b_2 \\ b_3 \end{pmatrix} = U\vec{b}, \tag{12}$$

where U is the unitary matrix. By multiplying by U^T, Eq. (12) is transformed to the following equation:

$$\vec{b} = U^T\vec{a}. \tag{13}$$

An orthogonally-projected-two-dimensional vector $\vec{c}$ of $\vec{a}$ is written as

$$\vec{c} = b_1\overrightarrow{u_1} + b_2\overrightarrow{u_2}, \tag{14}$$

and this equation can be transformed as follows:

$$\vec{c} = \left(\overrightarrow{u_1}^T \cdot \vec{a}\right)\overrightarrow{u_1} + \left(\overrightarrow{u_2}^T \cdot \vec{a}\right)\overrightarrow{u_2} = U'U'^T\vec{a}, \tag{15}$$

where $U' = (\overrightarrow{u_1} \quad \overrightarrow{u_2})$ This means that the orthogonal projection can be performed by multiplying the orthonormal basis matrix of the sub-space to be projected, and its transposition to the objective vector.

Based on the above, the orthogonal projection of the objective data on the sub-space of the data set is expressed as

$$P_{U'} = U'_{N\times N}(U'_{N\times N})^T, \tag{16}$$

where $U'_{N\times N}$ is the orthonormal basis matrix which spans the sub-space of the data set. Multiplying $P_{U'}$ to a vector enables us to know how much this vector can be presented by this sub-space. If this vector is a column unit vector $\overrightarrow{e_j}$ in which the j-th entry is unity, the following equation is obtained:

$$\overrightarrow{e_j'} = P_{U'}\overrightarrow{e_j}. \tag{17}$$

The 2-norm of $\overrightarrow{e_j'}$ corresponds to how much the vector $\overrightarrow{e_j}$ is presented by the sub-space defined by $U'_{N\times N}$.

This orthogonal projection is used for two purposes. One is the subsequent quantification method of the dimension of ASS. The other is the quantification method of the effectiveness of the set of integral data.

2.3 Sensitivity

We use sensitivities of integral data with respect to nuclear data. Sensitivities are impact of change in nuclear data on integral data. A sensitivity S is defined as

$$S = \frac{\partial\, p/p}{\partial\, \sigma/\sigma}, \tag{18}$$

where p is integral data, and σ is nuclear data. In the present study, sensitivity is presented as a column vector whose size is the number of nuclear data.

2.4 Active Sub-Space

Active sub-space (ASS) is a sub-space spanned by only effective orthogonal basis components in an original space spanned by all the orthogonal basis vectors. As an example, let us consider a simple case that there are a number of vectors in a three-dimensional space and ASS spanned by these vectors. If those vectors almost exist on the plane including the origin within the original three-dimensional space, the dimension of this ASS is two.

In this study, we use ASS for the subsequent quantification method for the independency of data set.

2.5 Quantification method of independency of data set

Quantification process of independency of data set is described below.

First, we perform SVD with a matrix which is constructed by a set of vector data, and then obtain the orthonormal basis vectors. Second, for searching ASS, all vector data are orthogonally projected on sub-space spanned by the limited number of basis vectors. When all norms become enough close to unity, this sub-space can be regarded as ASS, and the dimension of this ASS corresponds to independency of the data set. In this study, we regard the norm value is enough close to unity when the value is larger than 0.99.

When we adopt the above concept to nuclear data testing with integral data, the matrix consists of sensitivity column vectors of a set of integral data. The number of the sensitivity column vectors correspond to the number

of integral data. By using the orthonormal basis vectors generated by SVD, we obtain the dimension of ASS of the sensitivities. The dimension means the independency of the set of integral data for verification of nuclear data.

2.6 Quantification method of the possibility of verification of individual nuclear data by using the set of integral data

If a nuclear data vector exists in ASS spanned by sensitivity vectors, this nuclear data can be presented by the set of sensitivity data which spans this ASS. This means that this nuclear data can be independently verified from the set of integral data. On the other hand, if a nuclear data vector does not exist on the ASS, we regard a norm of an orthogonally-projected vector of this nuclear data vector to the ASS as possibility of independent verification of this nuclear data.

3. Numerical Result

3.1 Numerical method

In this study, sensitivities of integral data with respect to nuclear data are calculated with a reactor physics code system CBZ, which is under development at Hokkaido University. Multi-group cross sections are obtained through resonance self-shielding calculations in homogeneous infinite media, and forward and adjoint angular neutron fluxes in spherical cores are calculated with a discrete-ordinate neutron transport solver SNR. With these neutron fluxes, sensitivities of neutron multiplication factors to reaction cross sections are calculated by the first-order perturbation theory. In this study, we use 280-energy group cross sections, and sensitivities of effective multiplication factor k_{eff} are considered. As nuclear data, only fission cross section of U-235 is considered.

3.2 Independency of two sets of integral data

First, let us consider a set of fictitious homogeneous bare spherical critical assemblies which are composed of U-235 and U-238. We prepare 94 different assemblies by changing U-235 enrichment from 7% to 100%. The size of each critical assembly is adjusted so as to make the multiplication factor unity. We calculate sensitivities of all these assemblies, and the size of a sensitivity matrix becomes 280×94.

For searching the dimension of ASS of the set of these integral data, the quantification method presented above is adopted

Figure 1 shows norms of orthogonally-projected vectors of each integral data on sub-spaces with different dimensions. In the case of a three-dimensional sub-space, all norms are larger than 0.99. This means that the number of dimensions of ASS, that corresponds to the independency of the set of integral data, is three in this data set.

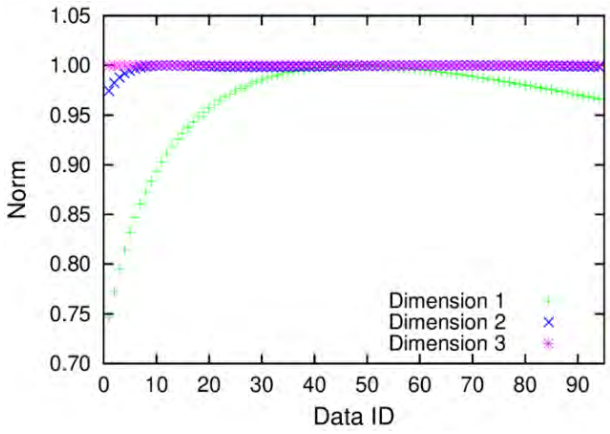

Fig. 1 Norm of orthogonal projected vectors of 94 integral data on sub-spaces with different dimensions

Second, we investigate the influence on independency by adding a new set of integral data. Additional integral data are also fictitious spherical critical assemblies with water reflector whose thickness is 20 cm. The assembly size is also adjusted to make the multiplication factor unity. As the same manner with the bare assemblies, 94 water-reflected assemblies are prepared by changing U-235 enrichment from 7% to 100%. We calculate sensitivities of these assemblies, and now the size of the new matrix is 280×188.

The quantification method is adopted to this new matrix. Figure 2 shows norms of orthogonally-projected vectors of 188 integral data to sub-spaces. This result shows that dimension of ASS becomes four. In other words, the independency of the set of integral data increases from three to four by addition of a new set of integral data to the original data set.

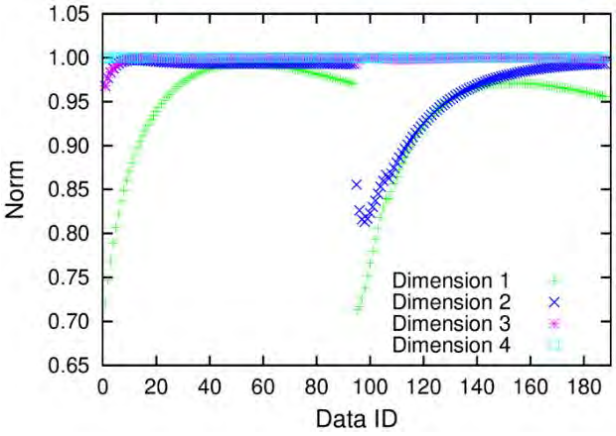

Fig. 2 Norm of orthogonal projected vectors of 188 integral data on sub-spaces with different dimensions

Figure 3 shows the orthonormal basis vectors of the four-dimensional ASS constructed from the 188 integral data.

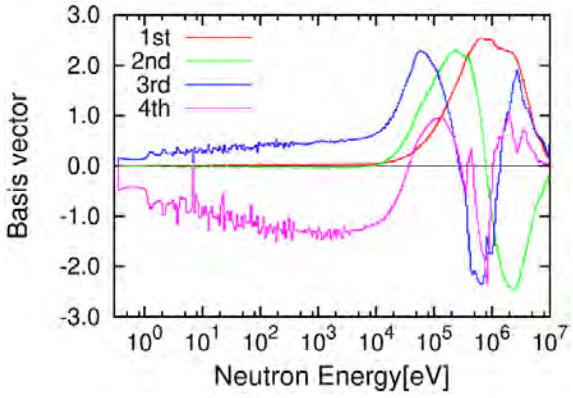

Fig.3 Basis vectors of four-dimensional ASS constructed by 188 integral data

Then, we quantify which additional integral data contribute to increase of independency. To do this we perform orthogonal projection of each of additional 94 integral data to the three-dimension ASS constructed by the original 94 integral data. When a norm is 0, this additional integral data is totally independent on the set of original 94 integral data and this additional integral data contributes to increase of the independency.

Figure 4 shows norms of orthogonally-projected vectors of each of integral data vectors of the additional 94 assemblies. This figure shows that the additional data with low enrichment relatively contribute to increase of the independency, and that the most efficient additional data is the assembly with enrichment of 10%. This is because this assembly has large fission reactions in thermal neutron energy.

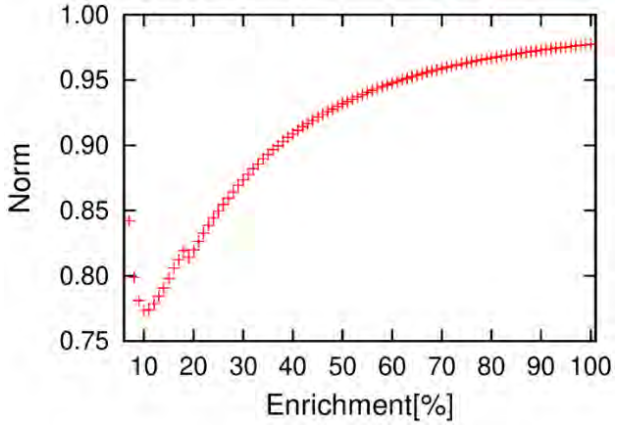

Fig. 4 Norm of orthogonal projected vectors of additional 94 integral data on ASS spanned by the original 94 integral data

3.3 Effectiveness of the set of integral data

For quantification of the possibility of verification of individual nuclear data by ASS of the set of integral data, the proposed method is adopted.

Figure 5 shows norms of orthogonally-projected vectors of each of nuclear data vector to the ASS spanned by the sensitivity vectors. This corresponds to the possibility of independent verification of individual nuclear data by using the set of integral data. Maximum norms are almost 0.3 in two cases in which one uses only bare assembly data and the other uses all the data. This result suggests that individual nuclear data verification is difficult by using these set of integral data.

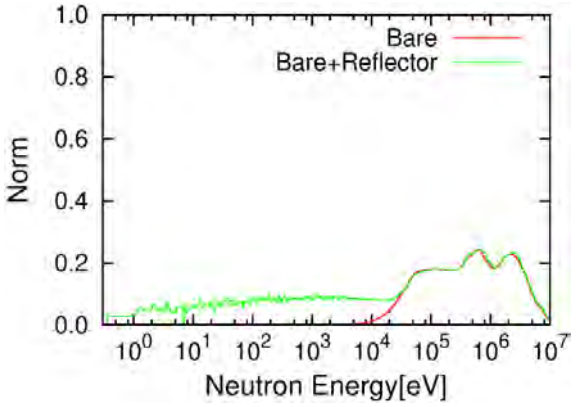

Fig. 5 Norm of orthogonal projected vectors of nuclear data vector on ASS

4. Conclusions

We have proposed the quantification method of the effectiveness of the set of integral data for verification of nuclear data by using SVD, the orthogonal projection and the concept of ASS. The effectiveness of the set of integral data means two things:

- The independency of the set of integral data
- The possibility of verification of individual nuclear data by the set of integral data

This study has treated two analysis conditions which are bare spherical critical assembly and that one plus spherical critical assembly with water reflector.

We could quantify above two things with two conditions. Concretely the independencies of the sets of 94 integral data and 188 integral data are three and four, respectively. Moreover, it is difficult to verify individual nuclear data by using these sets of integral data.

References

1. Meyer C, *Matrix Analysis and Applied Linear Algebra*, Society for Industrial and Applied Mathematics, Philadelphia, (2000).
2. Abdel-Khalik HS, et al., "Efficient subspace methods-based algorithms for performing sensitivity, uncertainty, and adoptive simulation of large-scale computational models," *Nucl. Sci. Eng.*, **159**, 256 (2008).

TS-07 Uncertainty Quantification and Data Assimilation

Proceedings of the Reactor Physics Asia 2019 (RPHA19) Conference
Osaka, Japan, Dec. 2-3, 2019

Estimated Criticality Lower-Limit Multiplication Factor Considering Neutronic Similarity and Uncertainties of Effective Multiplication Factor Using the Bootstrap Method (1) Theory

Takuto Hayashi[a,*], Fuga Nishioka[a], Tomohiro Endo[a], and Akio Yamamoto[a]
[a]*Nagoya University, Furo-cho, Chikusa-ku, Nagoya-shi, Aichi, 464-8603, Japan*
[*]Corresponding author: t-hayashi@fermi.energy.nagoya-u.ac.jp

Abstract

The present paper describes a calculation method for evaluation of the estimated criticality lower-limit multiplication factor (ECLLMF) considering neutronic similarity and uncertainties of effective multiplication factor (k_{eff}) using the bootstrap method. The normal distribution is assumed for a probability distribution with respect to calculation biases of k_{eff} to evaluate ECLLMF in the conventional method. An estimation method of ECLLMF was already developed using the bootstrap method, where the assumption of the normal distribution is not necessary. In this study, the calculation method for evaluation of ECLLMF using the bootstrap method is improved. The point of improvement is taking into account neutronic similarity between a target system and the criticality benchmark experiments, experimental uncertainties of benchmark data, and statistical uncertainties of k_{eff} by a continuous energy Monte Carlo code.

Key Words: **estimated criticality lower-limit multiplication factor, bootstrap method, neutronic similarity, experimental error, Monte Carlo code, statistical error**

1. Introduction

The estimated criticality lower-limit multiplication factor (ECLLMF) is the upper limit of the neutron multiplication factor where a target system may be judged subcritical [1]. The ECLLMF is evaluated from (1) many benchmark calculations using experimental data which are neutronically similar to a target system, and (2) statistically processing of calculated effective multiplication factors (k_{eff}) obtained by benchmark calculations. However, the statistical calculation method of the ECLLMF would be complicated and can be improved especially when a probability distribution of k_{eff} does not obey the normal distribution because the normal distribution is assumed in the conventional evaluation process.

Therefore, in order to propose a methodology without the assumption of the normal distribution, an evaluation method of the ECLLMF was developed using the bootstrap method, where the assumption of the normal distribution was not necessary [2]. In the previous study, the following issues remained to be addressed:

- Consideration of neutronic similarities between a target system and the criticality benchmark experiments in the evaluation process.
- Consideration of experimental uncertainties of benchmark data, statistical uncertainties of calculated k_{eff} by a continuous energy Monte Carlo code, and nuclear-data-induced uncertainties.

Hence, the present paper aims to develop a calculation method for evaluation of the ECLLMF taking into account (1) representative factor that incorporates the degree of neutronic similarity between a target system and a critical benchmark experiment system, (2) experimental uncertainties of benchmark data, and (3) statistical uncertainties of calculated k_{eff} by a continuous energy Monte Carlo code.

In section 2, the conventional calculation method of ECLLMF, where the assumption of the normal distribution is necessary, is briefly described. In addition, the improved calculation method of ECLLMF using the bootstrap method is proposed. Then, a numerical analysis is carried out for a bimodal distribution in order to verify the proposed method in section 3. Finally, concluding remarks are provided in section 4.

2. Theory

2.1 Conventional method

The calculated effective multiplication factors (k_{eff}) are assumed to follow the normal distribution in the conventional method. Then, the conventional estimated criticality lower-limit multiplication factor (ECLLMF) $k_{\mathrm{sub,t}}$ using the non-central *t*-distribution is calculated by [1]:

$$k_{\mathrm{sub,t}} = \bar{k} - \alpha_{\mathrm{t}} s, \tag{1}$$

where

$$\bar{k} = \frac{1}{n}\sum_{i=1}^{n} k_{\mathrm{eff},i}, \tag{2}$$

$$s^2 = \frac{1}{n-1}\sum_{i=1}^{n}\left(k_{\mathrm{eff},i} - \bar{k}\right)^2, (n \geq 2). \tag{3}$$

Note that $\bar{k}$ is the sample mean of $k_{\mathrm{eff},1}, k_{\mathrm{eff},2}, \ldots, k_{\mathrm{eff},n}$ obtained by the benchmark calculations for n criticality experiments; α_{t} is a margin value, and s is the sample standard deviation of $k_{\mathrm{eff},1}, k_{\mathrm{eff},2}, \ldots, k_{\mathrm{eff},n}$.

The margin value of α_{t} can be calculated using the properties of the normal distribution and the non-central *t*-distribution by setting p (excess probability of critical condition) and γ (success probability of setting ECLLMF). The value of p and γ are set individually by an analyst, *e.g.*, $p = 0.025$ and $\gamma = 0.975$. When n is sufficiently large, for example, α_{t} approaches 1.96 with $p = 0.025$. The value of α_{t} increases as n becomes smaller.

2.2 Proposed method

The bootstrap method is one of uncertainty evaluation methods and is used for evaluation of the confidence interval of the mean and the standard deviation of sample data or other statistical values [3], [4].

The ECLLMF using the bootstrap method without the assumption of the normal distribution was already developed [2]. In this method, the ECLLMF was estimated by generating new sets of samples through random sampling with replacement. From the viewpoint of the skewness and the kurtosis of a probability distribution of k_{eff}, the previous study was confirmed that the ECLLMF using the bootstrap method was more reasonable than $k_{\mathrm{sub,t}}$ when a probability distribution of k_{eff} did not obey the normal distribution.

In this study, the calculation method for evaluation of ECLLMF using the bootstrap method is improved. The point of improvement is taking into account (1) representative factor (c_k) that represents the degree of neutronic similarity between a target system and a critical benchmark experiment system, (2) experimental uncertainties of benchmark data (σ_{bench}), and (3) statistical uncertainties of calculated k_{eff} (σ_{calc}) by a continuous energy Monte Carlo code. The proposed method has an advantage that the improved ECLLMF can be equal to the previous ECLLMF using the bootstrap method when all representative factors are the same and uncertainties of k_{eff} can be regard as zero.

Calculation procedures of the ECLLMF using the bootstrap method $k_{\mathrm{sub,boot}}$ are as follows:

1. Obtain effective multiplication factors $k_{\mathrm{eff},1}, k_{\mathrm{eff},2}, \ldots, k_{\mathrm{eff},n}$, representative factors $c_{k,1}, c_{k,2}, \ldots, c_{k,n}$, experimental uncertainties of benchmark data $\sigma_{\mathrm{bench},1}, \sigma_{\mathrm{bench},2}, \ldots, \sigma_{\mathrm{bench},n}$, and statistical uncertainties of effective multiplication factors $\sigma_{\mathrm{calc},1}, \sigma_{\mathrm{calc},2}, \ldots, \sigma_{\mathrm{calc},n}$ by the benchmark calculations for n criticality experiments.
2. The experimental and statistical uncertainties of $k_{\mathrm{eff},i}$ are synthesized by:
$$\sigma_i = \sqrt{\sigma_{\mathrm{bench},i}^2 + \sigma_{\mathrm{calc},i}^2}. \tag{4}$$
3. A multi-modal distribution $p(x)$ is defined by a mixture of weighted n normal distributions [5]:
$$p(x) = \sum_{i=1}^{n} \frac{w_i}{\sqrt{2\pi\sigma_i^2}} \exp\left(-\frac{\left(x - k_{\mathrm{eff},i}\right)^2}{2\sigma_i^2}\right), \tag{5}$$
where the weighing factor w_i is determined by a linear model with respect to the representative factors $c_{k,i}$. The relationship between the representative factor and weight factor is represented by:
$$w_i = \max\left\{0, \frac{c_{k,i} - c_{k,\mathrm{acc}}}{c_{k,\max} - c_{k,\mathrm{acc}}}\right\}, \tag{6}$$
where the subscript i indicates the i th critical experiment; $c_{k,\max}$ is the maximum value of $c_{k,i}$; and $c_{k,\mathrm{acc}}$ is the acceptable minimum value of c_k. If the representative factors are not considered, $w_i = 1/n$, *i.e.*, each of critical experiments has the same weight.
4. Calculate the lower $100p$ percentile of the multi-modal distribution expressed by Eq. (5). The lower $100p$ percentile is defined by the value of a random variable when the cumulative distribution function matches. Hereafter, the percentile is called $k_{\mathrm{eff},p}$. For example, $k_{\mathrm{eff},p}$ can be evaluated using the Monte Carlo integration.
5. Generate a new set of resamples $k_1^{*b}, k_2^{*b}, \ldots, k_n^{*b}$ by the parametric bootstrap sampling based on the multi-modal distribution, where the superscript '$*b$' means the b th bootstrap sample. To consider the representative factors in this bootstrap sampling, the weighting factor w_i is used as the probability to select for the corresponding normal distribution $\mathcal{N}(k_{\mathrm{eff},i}, \sigma_i^2)$.
6. Calculate the bootstrap sample mean $\hat{k}^{*b}$ and the bootstrap sample standard deviation $\hat{s}^{*b}$ for the bth set of resamples, respectively.
7. Obtain $\hat{\mathbf{k}}^* = (\hat{k}^{*1}, \hat{k}^{*2}, \ldots, \hat{k}^{*B})$ and $\hat{\mathbf{s}}^* = (\hat{s}^{*1}, \hat{s}^{*2}, \ldots, \hat{s}^{*B})$ by repeating the procedure 5-6 in B times.
8. $\mathbf{k}_{\mathrm{sub,boot}} = (k_{\mathrm{sub,boot}}^1, k_{\mathrm{sub,boot}}^2, \ldots, k_{\mathrm{sub,boot}}^B)$ is obtained by:
$$\mathbf{k}_{\mathrm{sub,boot}} = \hat{\mathbf{k}}^* - \alpha_{\mathrm{boot}}\hat{\mathbf{s}}^*, \tag{7}$$
where the margin value α_{boot} is determined so that $k_{\mathrm{sub,boot},\gamma}$ reproduces $k_{\mathrm{eff},p}$ as presented in the following procedure 9. Here, $k_{\mathrm{sub,boot},\gamma}$ means the lower 100γ percentile of $\mathbf{k}_{\mathrm{sub,boot}}$ in ascending order.
9. Solve $f(\alpha_{\mathrm{boot}}) = 0$ using the bisection method [6], where the function $f(\alpha_{\mathrm{boot}})$ is defined by:
$$f(\alpha_{\mathrm{boot}}) = k_{\mathrm{sub,boot},\gamma} - k_{\mathrm{eff},p}. \tag{8}$$
In the bisection method, the iteration is performed

until $\left|k_{\mathrm{sub,boot},\gamma} - k_{\mathrm{eff},p}\right| < \varepsilon$ is satisfied. The convergence criteria ε is 10^{-7} because the sufficiently small ε should be set compared with the typical statistical errors (about 10^{-5}) in a continuous energy Monte Carlo code.

10. The ECLLMF $k_{\mathrm{sub,boot}}$ is finally obtained by:

$$k_{\mathrm{sub,boot}} = \bar{k} - \alpha_{\mathrm{boot}} s, \tag{9}$$

where the parameters $\bar{k}$ and s are the mean and the standard deviation of the multi-modal distribution expressed by Eq. (5), respectively.

3. Verification

A numerical analysis is carried out for the virtual k_{eff} which obey the bimodal distribution in order to verify the calculation method of the ECLLMF considering neutronic similarity and uncertainties of k_{eff} using the bootstrap method. Then, the verification of the proposed method is achieved by comparing the ECLLMF and the analytical solution. In this verification, the value of p and γ are 0.025 and 0.975, respectively.

A bimodal distribution means a weighted mixture of two normal distributions $\mathcal{N}\left(k_{\mathrm{eff},1}, \sigma_1^2\right)$, $\mathcal{N}\left(k_{\mathrm{eff},2}, \sigma_2^2\right)$. A probability density function of the bimodal distribution is obtained by Eq. (5). The mean and variance of the bimodal distribution μ, σ^2 are analytically obtained by:

$$\mu = \sum_{i=1}^{n} w_i k_{\mathrm{eff},i}, \tag{10}$$

$$\sigma^2 = \sum_{i=1}^{n} w_i \sigma_i^2 + \sum_{i=1}^{n} w_i \left(\mu - k_{\mathrm{eff},i}\right)^2, \tag{11}$$

where w_i is the weighting factor.

The probability distribution of a bimodal distribution with the calculation condition summarized in Table I is shown in Fig. 1.

Table I. Parameter of the bimodal distribution

No	$k_{\mathrm{eff},i}$	σ_i	w_i
1	0.990	0.007	0.6
2	1.009	0.004	0.4

μ	σ^2	σ
0.9976	0.0001224	0.0111

This verification can be also regarded as the following virtual conditions: calculated k_{eff} of the total criticality experiments obey the bimodal distribution; 60% of the total calculated k_{eff} obey the normal distribution $\mathcal{N}$ (0.990, 0.007^2) and the others obey the normal distribution $\mathcal{N}(1.009, 0.004^2)$.

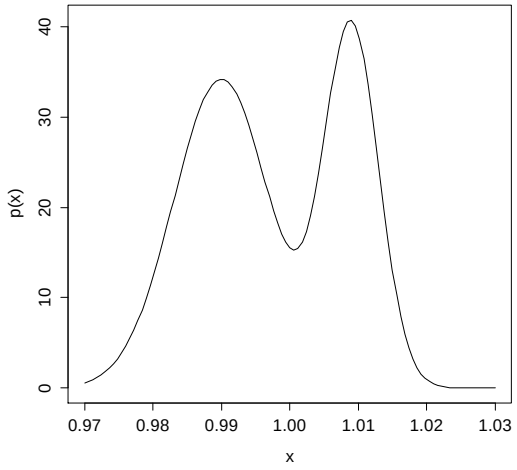

Fig. 1. Probability distribution of the bimodal distribution.

When the sample size is sufficiently large, ECLLMF approaches the lower $100p$ percentile of the bimodal distribution $k_{\mathrm{eff},p}$, thus a comparison between $k_{\mathrm{eff},p}$ and $k_{\mathrm{sub,boot}}$ is carried out for verification. Using the Newton method, $k_{\mathrm{eff},p}$ is calculated by the cumulative distribution function of the bimodal distribution, thus the numerical value of $k_{\mathrm{eff},p}$ is 0.977878. In addition, a comparison between a saturation value α_∞ and α_{boot} is carried out. The value of α_∞ can be analytically solved by:

$$\alpha_\infty = \frac{\mu - k_{\mathrm{eff},p}}{\sigma} = 1.78. \tag{12}$$

By changing the sample size, the estimation results of $k_{\mathrm{sub,t}}$ and $k_{\mathrm{sub,boot}}$, margin values of α_{t} and α_{boot}, and probabilities of ECLLMF exceeding $k_{\mathrm{eff},p}$ are shown in Fig. 2–4, respectively. In addition, probability distributions of 100 virtual experimental value k_{eff}, $k_{\mathrm{sub,t}}$, and $\mathbf{k}_{\mathrm{sub,boot}}$ include a blue dashed vertical line of $k_{\mathrm{eff},p}$ are shown in Fig. 5 as an example.

As shown in Fig. 2, the ECLLMF by $k_{\mathrm{sub,t}}$ did not approach $k_{\mathrm{eff},p}$ despite of the sufficiently large sample size. The ECLLMF by $k_{\mathrm{sub,boot}}$ was smaller than $k_{\mathrm{eff},p}$ when the sample size was small, then it approached $k_{\mathrm{eff},p}$ as the sample size became larger.

The differences between $k_{\mathrm{sub,t}}$ and $k_{\mathrm{sub,boot}}$ come from the differences in the margin values shown in Fig. 3. The conventional α_{t} value approached 1.96, while α_{boot} approached 1.78 in Fig. 3. Figure 4 indicates that the probability of ECLLMF exceeding $k_{\mathrm{eff},p}$ of the conventional method was not equal to the value of $(1-\gamma) = 0.025$. It means that the success probability of setting ECLLMF was not correctly set as γ in the conventional method. As can be seen from Fig. 5, the probability distribution of $k_{\mathrm{sub,t}}$ is shifted to the left direction (*i.e.*, the margin value of α_{t} is too large). This is caused by the assumption of the normal distribution for the virtual experimental value k_{eff} in the conventional method. On the contrary, the probability of ECLLMF exceeding $k_{\mathrm{eff},p}$ of the proposed method was always equal to $(1-\gamma)$ for any sample size. It means that the more appropriate

ECLLMF can be determined by the proposed method so that the success probability is equal to γ.

Consequently, it was confirmed that the proposed method was more reasonable than the conventional method when a probability distribution of k_{eff} obeyed the bimodal distribution. Another companion paper of this conference will report application results of estimation ECLLMF for more complicated probability distributions obtained by actual critical experiments.

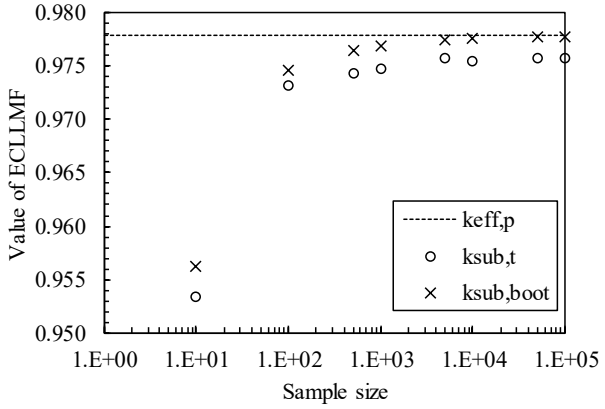

Fig. 2. Estimation results of $k_{\mathrm{sub,t}}$ and $k_{\mathrm{sub,boot}}$.

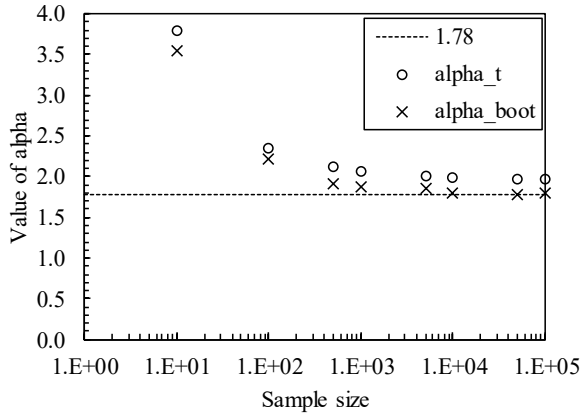

Fig. 3. Margin values of α_{t} and α_{boot}.

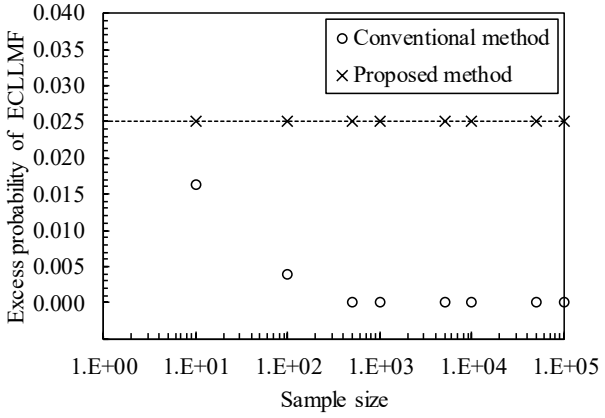

Fig. 4. Probabilities of ECLLMF exceeding $k_{\mathrm{eff},p}$.

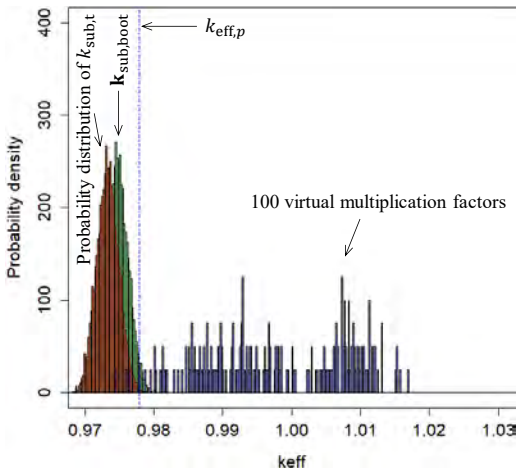

Fig. 5. Probability distributions of virtual experimental value k_{eff}, $k_{\mathrm{sub,t}}$, and $\mathbf{k}_{\mathrm{sub,boot}}$ include $k_{\mathrm{eff},p}$.

4. Conclusions

In the present paper, the calculation method using the bootstrap method was improved to evaluate the ECLLMF. The proposed ECLLMF was calculated taking into account neutronic similarity, experimental uncertainties of benchmark data, and statistical uncertainties of k_{eff} by a continuous energy Monte Carlo code. The numerical analysis was carried out for the virtual k_{eff} which obey the bimodal distribution in order to verify the proposed method. From the verification, it was confirmed that the proposed method was more reasonable than the conventional method when a probability distribution of k_{eff} obeyed the bimodal distribution.

The followings are future researches:

- Consideration of nuclear-data-induced uncertainties.
- Comparison of the proposed ECLLMF and a baseline upper-subcritical-limit obtained by Whisper-1.1 [7].

References

1. "Nuclear Criticality Safety Handbook, 2; English Translation," JAERI-Review-2001-028 (2001).
2. Hayashi T, Endo T, and Yamamoto A, "Calculation Method of Estimated Criticality Lower-Limit Multiplication Factor Using the Bootstrap Method," *Proc. M&C 2019*, Portland, OR, August 25-29, 2019, American Nuclear Society (2019).
3. Efron B, "Bootstrap Methods: Another Look at the Jackknife," *Ann. Stat.*, **7**, *1*, pp. 1-26 (1979).
4. Efron B and Tibshirani RJ, *An Introduction to the Bootstrap*, Chapman and Hall/CRC, Florida (1994).
5. Lindsay BG, *Mixture Models: Theory, Geometry and Applications*, **5**, Institute of Mathematical Statistics, Hayward, California (1995).
6. Burden RL and Faires JD, *Numerical Analysis, 3rd edition*, pp. 39-46, Brooks Cole, Boston, MA (2002).
7. Kiedrowski BC *et al.*, "Whisper: Sensitivity/Uncertainty-Based Computational Methods and Software for Determining Baseline Upper Subcritical Limits," *Nucl. Sci. Eng.*, **181**, *1*, pp. 17-47 (2015).

Proceedings of the Reactor Physics Asia 2019 (RPHA19) Conference
Osaka, Japan, Dec. 2-3, 2019

Estimated Criticality Lower-Limit Multiplication Factor Considering Neutronic Similarity and Uncertainties of Effective Multiplication Factor Using the Bootstrap Method (2) Application

Fuga Nishioka[a,*], Takuto Hayashi[a], Tomohiro Endo[a], and Akio Yamamoto[a]
[a]*Nagoya University, Furo-cho, Chikusa-ku, Nagoya-shi, 464-8603, Japan*
[*]Corresponding author: f-nishioka@fermi.energy.nagoya-u.ac.jp

Abstract

The present paper describes the calculation results of the estimated criticality lower-limit multiplication factor (ECLLMF) considering neutronic similarity and uncertainties of effective multiplication factor (k_{eff}) using the bootstrap method. A unit cell of a UO_2 sphere with a radius of 1.0 cm surrounded by a water moderator is considered as a target system. The proposed ECLLMF was calculated taking into account (1) representative factor that represents the degree of neutronic similarity between a target system and a critical benchmark experiment system, (2) experimental uncertainties of benchmark data, and (3) statistical uncertainties of calculated k_{eff} by a continuous energy Monte Carlo code. From the estimation results, it was confirmed that the distribution of k_{eff} and the ECLLMF change depending on the consideration of (1)–(3).

Key Words: **estimated criticality lower-limit multiplication factor, bootstrap method, neutronic similarity, experimental error, Monte Carlo code, statistical error**

1. Introduction

In our recent research, an evaluation method of the estimated criticality lower-limit multiplication factor (ECLLMF) was newly developed using the bootstrap method, where the assumption of the normal distribution is not necessary. The motivation and background of the present study are described in the companion paper [1].

The present paper describes the calculation results of the ECLLMF considering neutronic similarity and uncertainties of effective multiplication factor (k_{eff}) using the bootstrap method. A unit cell of a UO_2 sphere with a radius of 1.0 cm surrounded by a water moderator, where moderation ratio is almost optimum, is considered as a target system. The proposed ECLLMF is calculated taking into account (1) representative factor (c_k) that represents the degree of neutronic similarity between a target system and a critical benchmark experiment system, (2) experimental uncertainties (σ_{bench}) of benchmark data, and (3) statistical uncertainties (σ_{calc}) of calculated k_{eff} by a continuous energy Monte Carlo code.

In section 2, the calculation conditions of numerical analysis are described. In section 3, estimation results of ECLLMF using the conventional method and the proposed method are described. Finally, concluding remarks are provided in section 4. Detail calculation procedures are described in the companion paper [1].

2. Calculation Conditions

2.1 Calculation geometry and compositions

The numerical analysis was carried out for a unit cell of a UO_2 sphere with a radius of 1.0 cm surrounded by a 0.5 cm thickness of water moderator with the white boundary condition. Here, the moderation ratio is almost optimum. The calculation geometry model is shown in Fig. 1. Compositions of fuel and moderator are shown in Table I.

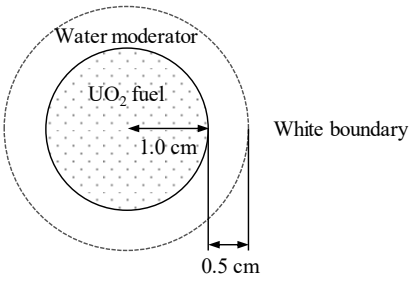

Fig. 1. Cell geometry and boundary condition.

Table I. Compositions of fuel (5 wt.%, 293 K) and moderator. (0.9970 g/cm^3, 293 K) [2]

	Element	Atomic number density ($\times 10^{24}$ atoms/cm^3)
Fuel	^{235}U	1.1757×10^{-3}
	^{238}U	2.2057×10^{-2}
	O	4.6465×10^{-2}
Moderator	H	6.6658×10^{-2}
	O	3.3329×10^{-2}

2.2 Selection of criticality benchmark experiment data

Whisper-1.1 [3] was used for benchmark calculations and a selection of critical experiment data contained in the International Criticality Safety Benchmark Evaluation Project (ICSBEP) Handbook [4]. The present study utilizes the calculated k_{eff} values selected by Whisper-1.1.

Effective multiplication factors $k_{\mathrm{eff},1}, k_{\mathrm{eff},2}, \ldots, k_{\mathrm{eff},n}$ obtained by the benchmark calculations for n critical experiments were corrected by subtracting the bias from the calculated k_{eff} value. Here, the bias is defined by subtracting unity from the experimental k_{eff} value.

For the target system in Fig. 1, the calculation conditions of MCNP6.2 [5] used in Whisper-1.1 are shown in Table II. The relationship between the representative factor (c_k) and weight factor (w) is represented by Eq. (1):

$$w_i = \max\left\{0, \frac{c_{k,i} - c_{k,\mathrm{acc}}}{c_{k,\max} - c_{k,\mathrm{acc}}}\right\}, \qquad (1)$$

where the subscript i indicates the i th critical experiment; $c_{k,\max}$ is the maximum value of $c_{k,i}$; and $c_{k,\mathrm{acc}}$ is the permissible minimum value of c_k. The value of $c_{k,\mathrm{acc}}$ is 0.6026 for the target system as shown in Fig. 1. The critical experiments whose representative factor $c_{k,i}$ is larger than the value of $c_{k,\mathrm{acc}}$ are selected by Whisper-1.1. For the critical experiments selected by Whisper-1.1, the weight factors w_i are summarized in Fig. 2. The total number of critical experiments (n) selected by Whisper-1.1 is 85. When the representative factors are not considered, $w_i = 1/n$.

The experimental uncertainties (σ_{bench}) of benchmark data, and the statistical uncertainties (σ_{calc}) of calculated k_{eff} are obtained from the Whisper-1.1 database. These uncertainties of k_{eff} are synthesized by Eq. (2):

$$\sigma_i = \sqrt{\sigma_{\mathrm{bench},i}^2 + \sigma_{\mathrm{calc},i}^2}. \qquad (2)$$

For the parametric bootstrap method in the evaluation of ECLLMF, the probability distribution of k_{eff} is expressed by the following multi-modal distribution $p(x)$, which is defined by a mixture of weighted n normal distributions:

$$p(x) = \sum_{i=1}^{n} \frac{w_i}{\sqrt{2\pi\sigma_i^2}} \exp\left(-\frac{\left(x - k_{\mathrm{eff},i}\right)^2}{2\sigma_i^2}\right). \qquad (3)$$

Table II. Calculation conditions for MCNP6.2.

Nuclear data library	ENDF/B-VII.1
Number of neutrons/cycle	100,000
Number of active cycles	500
Number of inactive cycles	100

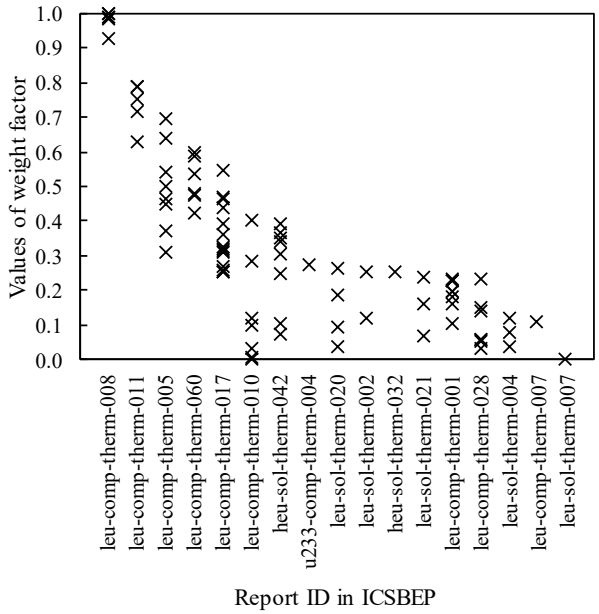

Fig. 2. Weight factors for each critical experiment selected by Whisper-1.1.

3. Estimation Results of ECLLMF

The conventional and proposed methods used the values of $p = 0.025$ (excess probability of critical condition), $\gamma = 0.975$ (success probability of setting ECLLMF) [6]. The total number of the bootstrap procedures (B) is 10^6. The number of bootstrap procedure (B) is equivalent to the number of the bootstrap samples. The values of $k_{\mathrm{sub,t}}$ and $k_{\mathrm{sub,boot}}$ mean ECLLMFs($= \bar{k} - \alpha s$) estimated by the conventional method based on the non-central t-distribution and by the proposed method using the bootstrap method, respectively. Note that $\mathbf{k}_{\mathrm{sub,boot}}$ in Figs. 3–6 which are described later means bootstrap distribution, not ECLLMF.

Values of $\bar{k}$, s, $k_{\mathrm{eff},p}$, α and ECLLMF are summarized in Table III. Note that $\bar{k}$ is the sample mean of $p(x)$ obtained by the benchmark calculations for n critical experiment; α is a margin value, and s is the sample standard deviation of $p(x)$. The value of $k_{\mathrm{eff},p}$ means the lower $100p$ percentile of $p(x)$ in ascending order.

For the following four cases, the random sampling results of probability density distributions for k_{eff} and $k_{\mathrm{sub,boot}}$ are shown in Figs. 3-6, respectively:

- Case 1: no considering representative factor c_k, without uncertainties σ_{bench} and σ_{calc} (Fig. 3)
- Case 2: considering c_k, without σ_{bench} and σ_{calc} (Fig. 4)

- Case 3: no considering c_k, with σ_{bench} and σ_{calc} (Fig. 5)
- Case 4: considering c_k, with σ_{bench} and σ_{calc} (Fig. 6)

Each of Figs. 3–6 includes a red solid vertical line of $k_{\text{sub,t}}$ and a blue dashed vertical line of $k_{\text{eff},p}$.

The estimated value of $k_{\text{sub,boot}}$ in Case 1 is slightly smaller than conventional $k_{\text{sub,t}}$ by 0.00032 $[\Delta k]$. This difference is caused by the difference of α between Case 1 and the conventional method, *i.e.*, the probability density distribution of k_{eff} does not necessarily obey the normal distribution. Here, an extension of Shapiro and Wilk's W test [7], which is a normality test, was carried out for a probability density distribution of k_{eff} and the obtained p-value was 2.99×10^{-7}. Since the p-value is smaller than 0.05, it was confirmed that the probability density distribution of k_{eff} did not obey the normal distribution.

The estimated value of $k_{\text{sub,boot}}$ in Case 2 is slightly smaller than that in Case 1 by 0.00023 $[\Delta k]$. When c_k is considered, k_{eff} with a small weight factor is rarely selected as a bootstrap sample. It is considered that the total number of effective bootstrap samples is reduced. Therefore, the value of α increased and the value of $k_{\text{sub,boot}}$ decreased in Case 2.

The estimated value of $k_{\text{sub,boot}}$ in Case 3 is smaller than that in Case 1 by 0.01185 $[\Delta k]$. By considering σ_{bench} and σ_{calc}, the probability distribution of k_{eff} changed, and the value of s increased. Therefore, the values of $k_{\text{eff},p}$ and $k_{\text{sub,boot}}$ decreased in Case 3.

The estimated value of $k_{\text{sub,boot}}$ in Case 4 is smaller than that in Case 1 by 0.01008 $[\Delta k]$, but larger than that in Case 3 by 0.00177 $[\Delta k]$. Since $\bar{k}$ and s are almost the same in Cases 3 and 4, it is considered that the difference in $k_{\text{sub,boot}}$ between Cases 3 and 4 is caused by the changes in the probability distribution shape (*e.g.*, kurtosis and skewness) of k_{eff} considering c_k, σ_{bench} and σ_{calc}.

Table III. Summary of $\bar{k}$, s, $k_{\text{eff},p}$, α and ECLLMFs.

Estimator	Conventional method	Case 1	Case 2
$\bar{k}$	0.99943	0.99943	0.99959
s	0.00243	0.00242	0.00249
$k_{\text{eff},p}$		0.99519	0.99519
α	2.3794	2.5219	2.6146
ECLLMF	0.99364	0.99332	0.99309

Estimator	Case 3	Case 4
$\bar{k}$	0.99943	0.99959
s	0.00389	0.00386
$k_{\text{eff},p}$	0.99170	0.99258
α	4.6156	4.2338
ECLLMF	0.98147	0.98324

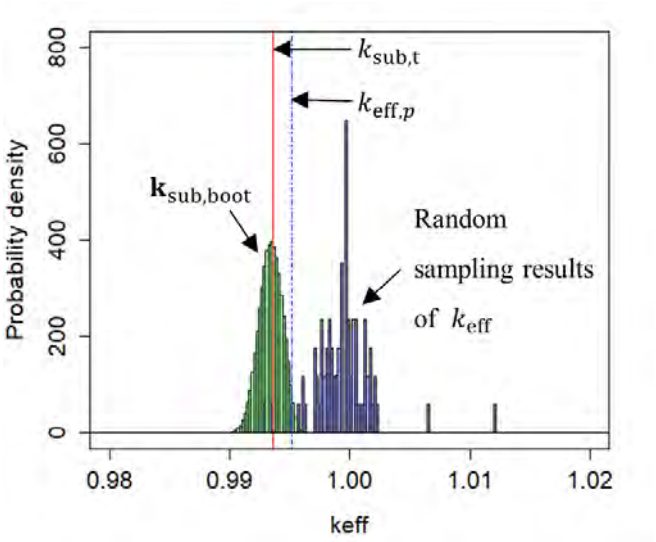

Fig. 3. Probability density distributions of random sampling results of k_{eff}, $\mathbf{k}_{\text{sub,boot}}$ and $k_{\text{sub,t}}$, $k_{\text{eff},p}$. (Case 1)

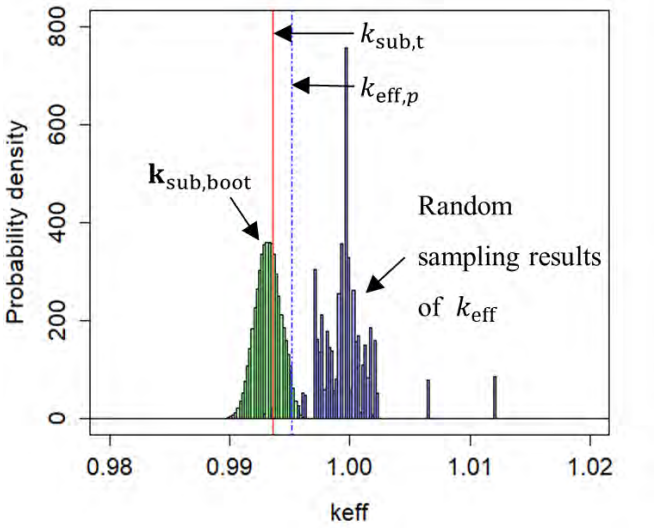

Fig. 4. Probability density distributions of random sampling results of k_{eff}, $\mathbf{k}_{\text{sub,boot}}$ and $k_{\text{sub,t}}$, $k_{\text{eff},p}$. (Case 2)

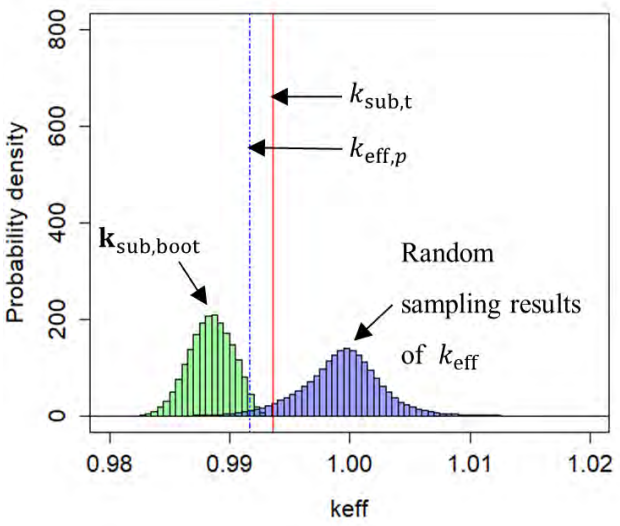

Fig. 5. Probability density distributions of random sampling results of k_{eff}, $\mathbf{k}_{\mathrm{sub,boot}}$ and $k_{\mathrm{sub,t}}$, $k_{\mathrm{eff},p}$. (Case 3)

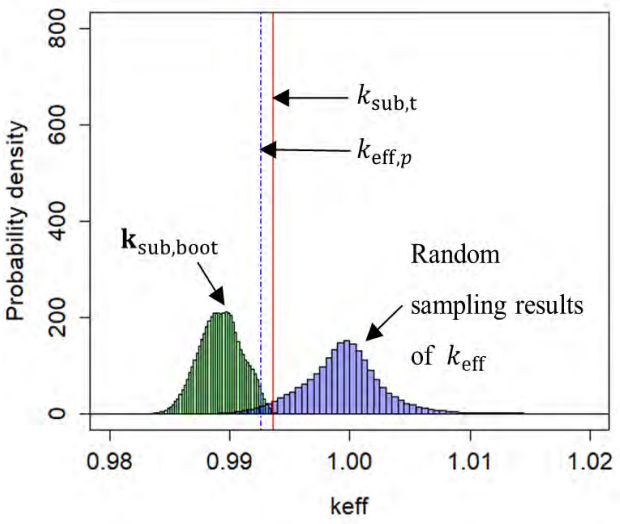

Fig. 6. Probability density distributions of random sampling results of k_{eff}, $\mathbf{k}_{\mathrm{sub,boot}}$ and $k_{\mathrm{sub,t}}$, $k_{\mathrm{eff},p}$. (Case 4)

4. Conclusions

The present paper aimed to calculate the ECLLMF considering neutronic similarity, and experimental and statistical uncertainties of effective multiplication factor (k_{eff}) using the bootstrap method. In this study, the proposed method was applied to a unit cell of a UO_2 sphere with a water moderator to confirm the validity. As a result, it was confirmed that the probability density distribution of k_{eff} and the ECLLMF change depending on the consideration of the neutronic similarity, and the experimental and errors. Thus, the proposed method enables to evaluate the ECLLMF taking into account the probability distribution shape of k_{eff}, which changes according to the neutronic similarity and the experimental calculation errors.

The future research is the evaluation of the ECLLMF for the molten core-concrete interaction (MCCI) products.

References

1. Hayashi T, Endo T, and Yamamoto A, "Calculation Method of Estimated Criticality Lower-Limit Multiplication Factor Using the Bootstrap Method," *Proc. M&C 2019*, Portland, Oregon, August 25–29, 2019, American Nuclear Society (2019).
2. Izawa K *et al*., "Infinite Multiplication Factor of Low-Enriched UO_2-Concrete System," *J. Nucl. Sci. Technol*., **49**(11), pp. 1043–1047 (2012).
3. Kiedrowski BC *et al*., "Whisper: Sensitivity/ Uncertainty-Based Computational Methods and Software for Determining Baseline Upper Subcritical Limits," *Nucl. Sci. Eng*., **181**(1), pp. 17–47 (2015).
4. "International Handbook of Evaluated Criticality Safety Benchmark Experiments," https://www.oecd-nea.org/science/wpncs/icsbep/handbook.html (2018).
5. "MCNP User's Manual – Code Version 6.2," https://laws.lanl.gov/vhosts/mcnp.lanl.gov/pdf_files/la-ur-17-29981.pdf (2017).
6. "Nuclear Criticality Safety Handbook, 2; English Translation," http://dx.doi.org/10.11484/JAERI-Review-2001-028 (2001).
7. Royston JP, "An Extension of Shapiro and Wilk's *W* Test for Normality to Large Samples," *Appl. Statist*., **31**(2), pp. 115–124 (1982).

Proceedings of the Reactor Physics Asia 2019 (RPHA19) Conference
Osaka, Japan, Dec. 2-3, 2019

Covariance-Oriented Sample Transformation Method for Uncertainty Analysis

Zhuojie Sui[a], Liangzhi Cao[a*], Chenghui Wan[a]

[a]*School of Nuclear Science and Technology, Xi'an Jiaotong University, Xi'an, Shaanxi,* 710049*, China*
[*]Corresponding author: caolz@mail.xjtu.edu.cn (Cao L.).

Abstract

In this paper, the method of Covariance-Oriented Sample Transformation (COST) has been proposed in the uncertainty analysis for reactor-physics modeling and simulation. As verification and application, the COST method has been applied in the nuclear-data uncertainty analysis for the TMI-1 pin-cell, propagating the nuclear-data uncertainties to the eigenvalue of the pin-cell. From the numerical result comparisons, it can be observed that the consistent uncertainty analysis results can be provided by COST with very small sample size, compared with the conventional sampling method with very huge sample size.

Key Words: Uncertainty analysis; COST; Minimum Sample Size

1. Introduction

The statistical sampling method is a widely capable technology for the Uncertainty Quantification (UQ) [1] of the reactor-physics modeling and simulation (M&S), especially for the non-linear systems. However, in those systems with multidimensional input parameters, the conventional sampling methods[2] always have a huge demand for sample size and are not able to propagate the uncertainty of input parameters completely, resulting in corresponding computational challenge and accuracy loss. Therefore, it is an issue waiting to be solved that how to notably reduce and determine the sample size of the input parameters on the basis of ensuring the consistent UQ results with those under infinite sample size and infinitesimal statistical fluctuations. In this context, through combining the most-basic ideas of the conventional sampling method and the Deterministic Sampling (DS) method [3-4], the Covariance-Oriented Sample Transformation (COST) has been proposed to generate multivariate normal distribution samples for uncertainty analysis.

2. Theory and Method

The input parameter uncertainties in the reactor-physics M&S are usually assumed to obey the normal distribution. Assume that the input parameter is $\boldsymbol{X}$ with the dimension of NV, the mean vector of $\boldsymbol{X}$ is $\boldsymbol{\mu}=[\mu_1, \mu_2,..., \mu_{NV}]^T$ and the input parameter covariance matrix is $\boldsymbol{\Sigma}$, then $\boldsymbol{X} \sim \boldsymbol{N}_{NV}(\boldsymbol{\mu}, \boldsymbol{\Sigma})$. The samples from general normal distribution are usually generated by multiplying the samples from the standard normal distribution by the transformation matrix, as shown in Eq.(1):

$$\boldsymbol{X}_S = \boldsymbol{A}\boldsymbol{Z}_S + \boldsymbol{V}; \qquad \boldsymbol{V} = \left[\overbrace{\boldsymbol{\mu}, \boldsymbol{\mu}, \ldots, \boldsymbol{\mu}}^{NS}\right] \tag{1}$$

where $\boldsymbol{X}_S$ is a sample set of the input parameter $\boldsymbol{X}$; $\boldsymbol{Z}_S$ is a sample set from the standard normal distribution $\boldsymbol{Z} \sim \boldsymbol{N}_{NV}(\boldsymbol{0}, \boldsymbol{I})$. $\boldsymbol{X}_S$ and $\boldsymbol{Z}_S$ have the same dimension $NV \times NS$ in which NS is the number of samples for each parameter of $\boldsymbol{X}$ and $\boldsymbol{Z}$. $\boldsymbol{A}$ is the transformation matrix with the dimension of $NV \times NV$. $\boldsymbol{V}$ represents the extended matrix of $\boldsymbol{\mu}$ with the dimension of $NV \times NS$.

For the determination of matrix $\boldsymbol{A}$, this paper presents a new method which is different from the conventional ones.

Firstly, based on the covariance information of the nuclear data in the evaluation nuclear database, the relative input-parameter covariance matrix $\boldsymbol{\Sigma}$ of the considered multi-group cross-section characterized can be constructed. Therefore, the joint probability density function (PDF) of the input parameters is determined as follows:

$$g(\boldsymbol{X}) = \frac{1}{2\boldsymbol{\pi}^{NV/2}\sqrt{|\boldsymbol{\Sigma}|}} exp\left(-\frac{1}{2}(\boldsymbol{X}-\boldsymbol{\mu})^T \boldsymbol{\Sigma}^{-1}(\boldsymbol{X}-\boldsymbol{\mu})\right) \tag{2}$$

where $\boldsymbol{X} = [\sigma_1, \sigma_2, \ldots, \sigma_{NV}]^T$, represents the input parameter vectors consisting of multi-group cross sections of all nuclides, reaction channels and energy groups that need to be analyzed, in which NV is the dimension of it; $\boldsymbol{\mu}$ is the mean vector of the input parameter. Then the eigenvalue decomposition of the matrix is used to diagonalize $\boldsymbol{\Sigma}$. The eigenvalues and corresponding eigenvectors are arranged in descending order. The number of non-zero eigenvalues, i.e. the rank of $\boldsymbol{\Sigma}$ is counted which can be denoted by r, and here, r is the minimum sample sizes required for convergence:

$$\boldsymbol{\Sigma} = \boldsymbol{U}\boldsymbol{\Lambda}_{\boldsymbol{\Sigma}}\boldsymbol{U}^T \tag{3}$$

Secondly, give a standard normal distribution population with the dimension equaling NV, which can

be denoted as $\boldsymbol{N_{NV}(0, I)}$. Given any sample size not less than r, the standard normal distribution is sampled by user-specified sampling technique to generate sample space characterized as $\boldsymbol{Z_S}$. It should be noted that the sample size should be big enough to fully describe the one-dimensional standard normal distribution when r is too small.

Then the users should calculate the sample covariance matrix of $\boldsymbol{Z_S}$ which can be characterized as $\boldsymbol{I^*}$, and the eigenvalue decomposition of the matrix is used to diagonalize $\boldsymbol{I^*}$. The number of non-zero eigenvalues, i.e. the rank of $\boldsymbol{I^*}$ is counted and can be denoted by k :

$$\boldsymbol{I^* = P\Lambda_{I^*} P^T} \tag{4}$$

Note that there is a condition $k \geq r$ that needs to be satisfied. If $k<r$, repeat this step to reproduce $\boldsymbol{Z_S}$ until the condition is met.

Thirdly, matrix $\boldsymbol{L}$ and matrix $\boldsymbol{R}$ are determined by the following formula：

$$\boldsymbol{L = P_k \Lambda_{I^*k}^{1/2}} \ ; \boldsymbol{R = U_k \Lambda_{\Sigma k}^{1/2}} \tag{5}$$

Then find an invertible matrix $\boldsymbol{F}$ which can transform $\boldsymbol{L}$ into the row simplest matrix. Meanwhile, a square matrix $\boldsymbol{S}$ of $NV \times NV$ is constructed based on $\boldsymbol{S} = \left(\boldsymbol{R} \ \vdots \ \boldsymbol{O}\right)$, whose order is equal to the dimension of the input parameter.

Finally, based on matrix $\boldsymbol{S}$ and $\boldsymbol{F}$, the transformation matrix $\boldsymbol{A}$ can be obtained by $\boldsymbol{A = SF}$ for linear transformation. Like the last step of the conventional sampling method, samples $\boldsymbol{X_S}$ are generated using Eq.(1) to propagate the input parameter uncertainties completely. Then the users can continue the next step of uncertainty analysis based on the sampling method.

3. Verification and Application

In order to verify the COST method in uncertainty analysis, the uncertainty analysis has been performed to the TMI-1 pin-cell, proposed by UAM[1]. In the process, the UNICORN code[5] has been applied to propagate the nuclear-data uncertainties to the eigenvalue of the TMI-1 pin-cell.

3.1 Sample characteristics and verification

For intuitive understanding the characteristics of samples generated by COST compared with those generated by conventional sampling method, two methods are used to sample the two-dimensional standard normal distribution $\boldsymbol{N_2(0, I_2)}$. The covariance matrix and distribution of the generated samples from an arbitrary random numerical experiment are shown in Table I.

It can be found that when the sample size increases from 30 to 20000, the sample covariance matrix generated by the conventional sampling method (i.e. LHS) is more likely to approximate the unit matrix $\boldsymbol{I_2}$, but there are still differences which can be the sources of errors in the subsequent uncertainty propagation. For COST, on the other hand, the sample covariance matrix can converge to the unit matrix $\boldsymbol{I_2}$ at an initial smaller sample size.

Table II shows the results of the sample verification in an arbitrary random numerical experiment based on ^{235}U-$\sigma_{(n,\gamma)}$ covariance matrix whose eigenvalue vector is $\boldsymbol{\lambda_\Sigma}$. Since the rank of the input parameter covariance matrix is 56, COST requires 56 samples, while the conventional sampling method is also given the same sample size for comparison. The top 20 largest eigenvalues are listed here while COST-Var($\boldsymbol{X_S^P}$) and LHS-Var($\boldsymbol{X_S^P}$) represent the variance of sample projection on corresponding eigenvectors by COST and conventional sampling method using LHS, respectively. From comparison shown in the table, the following conclusions can be drawn: the values of $\boldsymbol{\lambda_\Sigma}$ and COST-Var($\boldsymbol{X_S^P}$) are completely equal, hence the COST sample covariance matrix can fully map back to the target input parameter covariance matrix $\boldsymbol{\Sigma}$. This means the samples can carry all the information of the target covariance matrix which describes the uncertainty of input parameters. Furthermore, this phenomenon also means the uncertainty-calculation samples are generated correctly by COST method. However, in the conventional sampling method, the eigenvalue vector of $\boldsymbol{\Sigma}$ cannot be reconstructed through the sample, which means the sample loses part of the uncertainty information of the given input parameter.

3.2 Samples for uncertainty analysis

Figure 1 shows the performance of COST samples in the uncertainty analysis of TMI-1 pin at HFP conditions. The considered response is k_∞. In the figure, the starting point of COST curve is the minimum sample size point required by COST. The perturbation quantity of Direct Numerical Perturbation (DNP)[6] is set to 1%. LHS represents the conventional sampling method using Latin hypercube sampling technique. LHS-10000 represents the results of conventional sampling method (LHS) using 10000 samples as the rough reference value, although there are still some statistical fluctuations. It should be noted that all the points in Figure 1 are from an arbitrary random numerical experiment.

According to Figure 1, the following conclusions can be drawn:

(1) With the increase of the sample size, the uncertainty results curves of the response with respect to the sample size based on the COST method keep almost flat and the fluctuation range of them is very small, while the LHS method has notable statistical fluctuations and the curves fluctuate greatly.

(2) The minimum sample size can be determined by COST according to the input parameter covariance matrix in advance. Therefore, the computational cost of the sample-size test in conventional sampling method can be avoided.

(3) The consistent UQ results can be provided by COST with the minimal sample size, compared with the conventional sampling method with very huge sample size: Overall, the difference between COST results and LHS-10000 results is small in all cases, which are

within acceptable range. It is worth noting that the results of LHS-10000 are only taken as the rough reference value; In the first six cases, the results of COST and DNP are very close, even completely consistent. This means, the COST method can achieve high precision reconstruction of the covariance of input parameters through linear transformation, which will give a very good approximation of the propagated uncertainty. However, in the latter two cases, the differences between deterministic method and sampling method are obvious, especially for ^{238}U-$\sigma_{(n,elas)}$, $\sigma_{(n,inel)}$, $\sigma_{(n,2n)}$, $\sigma_{(n,f)}$, $\sigma_{(n,\gamma)}$, $\sigma_{(n,\nu)}$, the difference can account for 24.2% of COST and 23.6% of LHS -10000 results.

Table I. Sample distribution and sample covariance matrix of the two method

Sample size	Conventional sampling method (LHS)		COST	
	Sample covariance matrix	Sample distribution	Sample covariance matrix	Sample distribution
30	$\begin{bmatrix} 0.9410 & 0.2899 \\ 0.2899 & 1.0902 \end{bmatrix}$	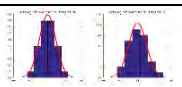	$\begin{bmatrix} 1 & 0 \\ 0 & 1 \end{bmatrix}$	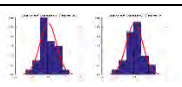
200	$\begin{bmatrix} 0.9921 & 0.1781 \\ 0.1781 & 1.0072 \end{bmatrix}$	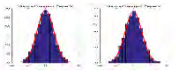	$\begin{bmatrix} 1 & 0 \\ 0 & 1 \end{bmatrix}$	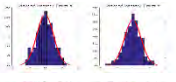
2000	$\begin{bmatrix} 1.0000 & -0.0412 \\ -0.0412 & 1.0023 \end{bmatrix}$	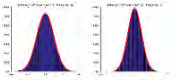	$\begin{bmatrix} 1 & 0 \\ 0 & 1 \end{bmatrix}$	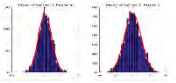
20000	$\begin{bmatrix} 1.0000 & 0.0140 \\ 0.0140 & 0.9999 \end{bmatrix}$	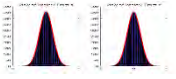	$\begin{bmatrix} 1 & 0 \\ 0 & 1 \end{bmatrix}$	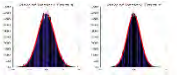

Table II. Sample verification results: Top 20 largest eigenvalues and variance of sample projection on corresponding eigenvectors of ^{235}U-$\sigma_{(n,\gamma)}$ input-parameter covariance matrix

Index	λ_Σ	COST-$Var(\boldsymbol{X}_S^p)$	LHS-$Var(\boldsymbol{X}_S^p)$	Index	λ_Σ	COST-$Var(\boldsymbol{X}_S^p)$	LHS-$Var(\boldsymbol{X}_S^p)$
1	1.189932053	1.189932053	1.350837908	**11**	0.001060731	0.001060731	0.000823979
2	0.601402038	0.601402038	0.709092319	**12**	0.000515916	0.000515916	0.000395084
3	0.066016454	0.066016454	0.055161019	**13**	0.000490640	0.000490640	0.000558967
4	0.033705620	0.033705620	0.031554108	**14**	0.000415083	0.000415083	0.000421806
5	0.009126260	0.009126260	0.011340763	**15**	0.000361361	0.000361361	0.000483240
6	0.004452515	0.004452515	0.005338535	**16**	0.000317896	0.000317896	0.000402570
7	0.004093384	0.004093384	0.003433930	**17**	0.000214704	0.000214704	0.000131445
8	0.002369551	0.002369551	0.002732174	**18**	0.000209785	0.000209785	0.000195423
9	0.001746378	0.001746378	0.001893451	**19**	0.000195123	0.000195123	0.000228734
10	0.001236687	0.001236687	0.000899516	**20**	0.000188628	0.000188628	0.000207613

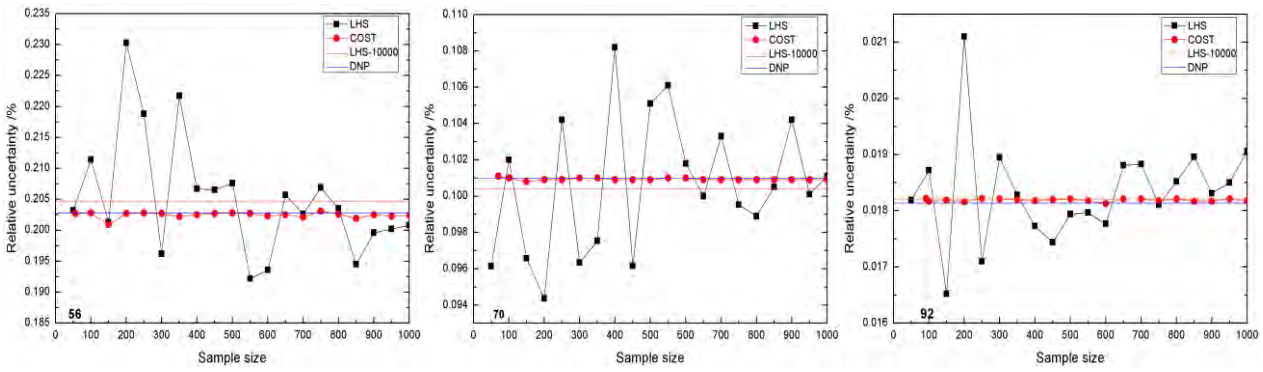

(a) ^{235}U- $\sigma_{(n,\gamma)}$ (b) ^{1}H- $\sigma_{(n,elas)}$,$\sigma_{(n,\gamma)}$ (c) ^{90}Zr- $\sigma_{(n,elas)}$,$\sigma_{(n,inel)}$,$\sigma_{(n,\gamma)}$

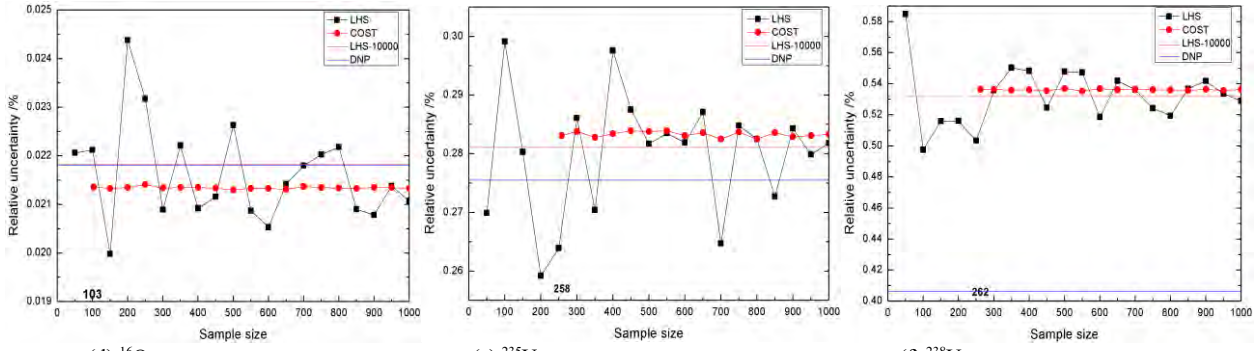

(d) ^{16}O- $\sigma_{(n,elas)}$,$\sigma_{(n,inel)}$,$\sigma_{(n,\gamma)}$,$\sigma_{(n,\alpha)}$ (e) ^{235}U- $\sigma_{(n,elas)}$,$\sigma_{(n,inel)}$,$\sigma_{(n,2n)}$,$\sigma_{(n,f)}$,$\sigma_{(n,\gamma)}$,$\sigma_{(n,\nu)}$ (f) ^{238}U- $\sigma_{(n,elas)}$,$\sigma_{(n,inel)}$,$\sigma_{(n,2n)}$,$\sigma_{(n,f)}$,$\sigma_{(n,\gamma)}$,$\sigma_{(n,\nu)}$

Fig. 1. Uncertainty analysis results of TMI-1-pin at HFP condition

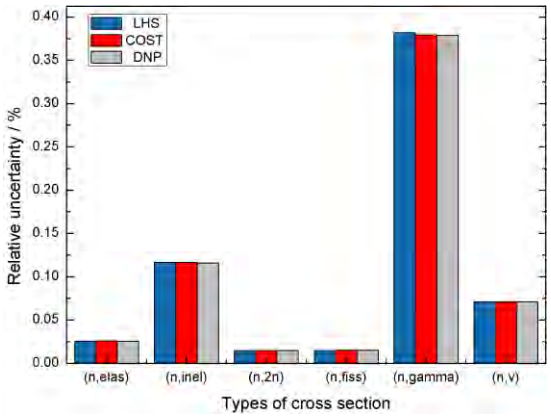

Fig. 2. Comparison of uncertainty results of different methods when the 6 reaction channels $\sigma_{(n,elas)}$, $\sigma_{(n,inel)}$, $\sigma_{(n,2n)}$, $\sigma_{(n,f)}$, $\sigma_{(n,\gamma)}$, $\sigma_{(n,\nu)}$ of ^{238}U are perturbed separately

In order to find the source of the difference, each reaction channel was analyzed separately, and the results are shown in Figure 2. In the figure, LHS represents the conventional sampling method, and the sample size used is 10000. Because the ranks of covariance matrices of $\sigma_{(n,inel)}$ and $\sigma_{(n,2n)}$are 12 and 2 respectively, which are too small to accurately describe the standard normal distribution, the sample size of them is set to 30 in COST. Therefore, for $\sigma_{(n,elas)}$, $\sigma_{(n,inel)}$, $\sigma_{(n,2n)}$, $\sigma_{(n,f)}$, $\sigma_{(n,\gamma)}$, $\sigma_{(n,\nu)}$, the sample size determined by COST is 51, 30, 30, 69, 51, 37 in turn. The perturbation quantity of DNP is set to 1%.

As can be seen from Figure 2, the uncertainty analysis results of the partial reaction channels obtained by the three methods are consistent. However, the cumulative uncertainty results of ^{238}U by DNP is smaller than the two sampling methods. This phenomenon shows that in DNP, although the global input parameter covariance matrix of the 6 reaction channels is used in calculating the uncertainty of k_∞ caused by ^{238}U when considering the correlation between reaction channels, the accuracy of the results is reduced by the low-order approximation of deterministic method.

4. Conclusion

In this paper, the COST method of generating multivariate normal distribution samples in uncertainty analysis has been proposed. By investigating the performance of samples generated by COST in the uncertainty analysis of UAM-TMI-1, the consistent uncertainty analysis results can be provided by COST with very small sample size, compared with the conventional sampling method with very huge sample size. It is clear that there are still some areas for COST method deserve further research and improvement. For example, if the users want to strictly guarantee the independence between nuclides, when many nuclides are considered, the number of computations will inevitably become very large.

Acknowledgements

This work is supported by the National Natural Science Foundation of China (Grant No. 11735011)

References

1. Ivanov K, Avramova M, Kamerow S, et al. Benchmarks for Uncertainty Analysis in Modeling (UAM) for the Design, Operation and Safety Analysis of LWRs. Volume I: Specification and Support Data for the Neutronics Cases (Phase I)[R]. OECD Nuclear Energy Agency, (2007).
2. Rochman D, Leray O, Hursin M, et al. Nuclear Data Uncertainties for Typical LWR Fuel Assemblies and a Simple Reactor Core[J]. Nuclear Data Sheets, 139:1-76, (2017).
3. Rahman S, Karanki D R, Epiney A, et al. Deterministic sampling for propagating epistemic and aleatory uncertainty in dynamic event tree analysis[J]. Reliability Engineering & System Safety, 175:62-78, (2018).
4. Sahlberg A., Ensemble for Deterministic Sampling with positive weights: Uncertainty quantification with deterministically chosen samples[D]. UPPSALA University, (2016).
5. Wan C, Cao L, Wu H, et al. Total sensitivity and uncertainty analysis for LWR pin-cells with improved UNICORN code[J]. Annals of Nuclear Energy, 99:301-310, (2017).
6. Ball M R, Novog D R Luxat J C. Analysis of implicit and explicit lattice sensitivities using DRAGON[J]. Nuclear Engineering and Design, 265(Complete):1-12, (2013).

Proceedings of the Reactor Physics Asia 2019 (RPHA19) Conference
Osaka, Japan, Dec. 2-3, 2019

Effectiveness of Subcritical Measurement at Solid Moderated KUCA Core for Reducing Nuclear Data-Induced Uncertainties in Other Light Water Reactor Analysis

Tomohiro Endo[a,*], Akio Yamamoto[a]
[a]*Nagoya University, Furo-cho, Chikusa-ku, Nagoya-shi, 464-8603, Japan*
[*]Corresponding author: t-endo@energy.nagoya-u.ac.jp

Abstract

This paper aims to clarify that the subcritical measurement at the solid moderated KUCA core is useful to reduce nuclide data-induced uncertainties of the effective neutron multiplication factors k_{eff} in other light water moderated systems. For this purpose, we pay attention to the prompt neutron decay constant α, which was measured by the Feynman-α method with the moving block bootstrap method for the deep subcritical KUCA core under the shutdown state without any external neutron source. The sensitivity analyses of α for the subcritical KUCA core and of k_{eff} for various light water moderated critical cores were carried out based on the first-order perturbation theory. Consequently, it is demonstrated that the nuclear data-induced uncertainties of k_{eff} can be reduced by the bias factor method using the measurement value of α, if the target k_{eff} value has a strong correlation with the measured α value in the subcritical KUCA core.

Key Words: **effective neutron multiplication factor, uncertainty, KUCA, subcritical measurement, prompt neutron decay constant, data assimilation**

1. Introduction

This study presents how effective the subcritical measurement at the solid moderated core of Kyoto University Criticality Assembly (KUCA) is to reduce the nuclear data-induced uncertainties of effective neutron multiplication factors k_{eff} for the light water reactor analysis.

In the field of the reactor physics, k_{eff} is an important core-characteristics-parameter to quantify the criticality. Using the numerical analysis such as the deterministic method or the Monte Carlo method, k_{eff} can be numerically predicted with uncertainties due to the following factors: (1) uncertainties of input parameters (*e.g.*, nuclear data, nuclide compositions, and geometries), and (2) errors of analytical modeling methods (*e.g.*, spatial and angular discretization, and energy collapsing in the deterministic method, or statistical error of the Monte Carlo method. Thus, Best Estimate Plus Uncertainty (BEPU) is an important subject to assure the quality of numerically predicted results. The data assimilation (DA) technique using actual measurement results (*e.g.*, the cross section adjustment method [1], and the bias factor method [2]) is effectively utilized to improve the prediction accuracy and precision of numerical results of k_{eff}.

Recently, to effectively utilize reactor-physics-experiment facilities, authors have been investigating DA using the subcritical measurement [3], instead of conventional critical experiments. In the previous study, it was demonstrated that the DA technique using the prompt neutron decay constant α measured at KUCA solid moderated core under the shutdown state can reduce the nuclear data-induced uncertainty of k_{eff} under the critical state. Namely, the effectiveness was confirmed for the just same core.

The purpose of this study is to clarify whether the subcritical measurement value of α in the polyethylene moderated core of KUCA is also effective for the criticality analysis for other light water-moderated reactors.

2. Subcritical Experiment and Sensitivity Analysis of α measured at KUCA

The zero-power reactor noise experiment was conducted in the A-core (A3/8" p36EU-NU) at KUCA under the shutdown state ($k_{\mathrm{eff}} \approx 0.937$) [4, 5]. Figure 1 shows the top view of the experimental core and the side view of the loaded fuel assembly. The core averaged ^{235}U enrichment was ~5.4wt%, which was adjusted by the unit fuel cell (one highly enriched uranium-aluminum alloy plate, one natural uranium plate, and three polyethylene plates). The deep subcriticality was achieved by fully inserting all the six control- and safety-rods and by unloading 3×3 fuel and reflector assemblies.

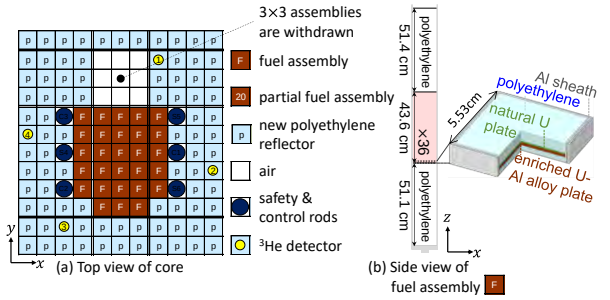

Fig. 1 Subcritical core geometry (A3/8" p36EU-NU).

The Feynman-α experiment was carried out during ~933.5 min with only inherent neutron sources, such as spontaneous fission of ^{238}U and (α,n) reaction of ^{27}Al due to α-decays of uranium isotopes. In other words, there is no external neutron source (*e.g.*, Am-Be and Cf source). To increase the detection efficiency and mitigate the higher-order mode components in the Feynman- α method, all the time-series data using four ^{3}He detectors were summed for the Feynman-α method. Using the moving block bootstrap method [4, 5], the measured value of α was obtained as 1618.5±6.5 (1/s) as shown in Fig. 2. In the bootstrap method, the sample size of bootstrap resamples was 1000 and the bootstrap correlation of $Y(T)$ between different neutron counting gate widths T were taken into account in the non-linear least square fitting procedure. Figure 2 indicates that the bootstrap histogram of α was well approximated by the normal distribution.

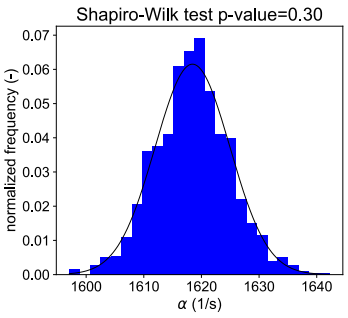

Fig. 2 Bootstrap histogram of α.

The sensitivity analysis (SA) of α with respect to the nuclear data was conducted based on the first-order perturbation theory, as proposed in the previous study [6]. For SA, the 56 neutron-energy group S_N calculations with P_2 anisotropic scattering using PARTISN [7]. The effective microscopic cross sections were evaluated by the ultra-fine energy group resonance calculation using SCALE6.2.3/CENTRM [8] with the ENDF/B-VII.1 library [9]. The calculation geometry was spatially discretized as shown in Fig. 3. The vacuum condition was used for all boundary because of the asymmetry in the experimental cores. The total number of discretized neutron-flight-directions was 384 (points/4π) by an improved variant of EO_N quadrature [10,11]. The numerical result of α was 1631.2 (1/s), which agreed well with the measurement value by comparison with nuclear data-induced uncertainty 10.0 (% $\Delta\alpha/\alpha$).

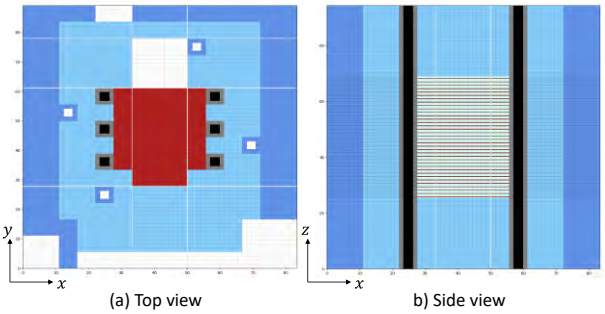

Fig. 3 Calculation geometry (A3/8" p36EU-NU).

3. Sensitivity Analysis of k_{eff} for Light Water Moderated Cores

First, using the Whisper1.1 [12], some critical experiments were picked up, according to the strength of nuclear data-induced correlation (or representative factor) between k_{eff} values of the KUCA subcritical core and various ICSBEP experiments [13]. Consequently, the following five light water moderated critical experiments were selected as shown in Fig. 4:

- LEU-COMP-THERM-007, Case 2
- LEU-COMP-THERM-039, Case 5
- LEU-COMP-THERM-002, Case 3
- LEU-COMP-THERM-009, Case 4
- LEU-COMP-THERM-010, Case 3

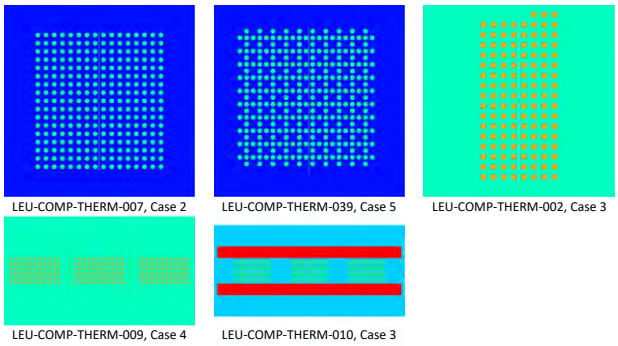

Fig. 4 Top view of selected ICSBEP benchmarks.

Furthermore, to investigate k_{eff} in the case of a commercial scale light water reactor, a preliminary numerical analysis of the BEAVRS Cycle 1 HZP benchmark was carried out based on the information specified in the document ver. 2.02 [14]. The ACE formatted libraries at the HZP condition (565.5K) were produced using the FRENDY [15].

Unlike in the case of SA of α using the deterministic codes, the SA of k_{eff} for these light water moderated cores was accomplished by the continuous energy Monte Carlo code MCNP 6.2 [16] with the ENDF-B/VII.1 library [9]. The relative sensitivity coefficients of k_{eff} with respect to the nuclear data (elastic+S(α,β), total inelastic, fission, (n,2n), (n,γ), (n,p), (n,d), (n,t), (n,^{3}He), (n,α), total fission ν, total fission χ) were evaluated using the iterated fission probability method. For the ICSBEP benchmarks, the total number of neutron

histories was 10^9, *i.e.*, neutron history per cycle=100000, active cycle=10000, and skip cycle=100. For the BEAVRS benchmark of which the dominance ratio is close to unity because of the large core geometry, the total number of neutron histories was the same but neutron history per cycle=1000000, active cycle=1000, and skip cycle=500.

4. Bias factor method using α

As discussed in the previous study [2], the nuclear data-induced correlation between the measurement and numerical values is a key parameter to reduce the uncertainties of numerically predicted results. Thus, using the sandwich formula with both the relative sensitivity coefficient matrices of α and k_{eff} ($\mathbf{S}_{\alpha,\sigma}$ and $\mathbf{S}_{k_{\mathrm{eff}},\sigma}$) as presented in Secs. 2 and 3, the correlation between α and k_{eff} can be evaluated as follows:

$$c_{\alpha,k_{\mathrm{eff}}} \equiv \frac{\mathbf{S}_{\alpha,\sigma}\boldsymbol{\Sigma}_\sigma\mathbf{S}_{k_{\mathrm{eff}},\sigma}^T}{\sqrt{\mathbf{S}_{\alpha,\sigma}\boldsymbol{\Sigma}_\sigma\mathbf{S}_{\alpha,\sigma}^T \times \mathbf{S}_{k_{\mathrm{eff}},\sigma}\boldsymbol{\Sigma}_\sigma\mathbf{S}_{k_{\mathrm{eff}},\sigma}^T}}, \quad (1)$$

where $\boldsymbol{\Sigma}_\sigma$ is the relative variance-covariance matrix of nuclear data. In this study, the 56 group SCALE covariance data (scale.rev08.56groupcov7.1) was used as $\boldsymbol{\Sigma}_\sigma$ [8]. Note that, in this study, $\mathbf{S}_{\alpha,\sigma}$ and $\mathbf{S}_{k_{\mathrm{eff}},\sigma}$ were calculated by the deterministic and the Monte Carlo methods, respectively; thus, the estimated correlation by Eq. (1) has an error owing to the difference in the analytical modeling method.

Table I summarizes the nuclear data-induced correlation between (1) the α value for the polyethylene moderated KUCA core and (2) the value for each of light water moderated benchmark problems. From Table I, the selected ICSBEP benchmarks have the strong correlation with the α value measured at the subcritical KUCA core, although the geometry of unit fuel cell (pin or plate-type cell) and the fuel forms (UO_2 or uranium-aluminum alloy) are different. The reason is that the relative variation in the sensitivity coefficients of α and k_{eff} with respect to the neutron energy are the almost the same each other in these cases, as presented in Fig. 5. On the other hand, the energy dependencies of the k_{eff}-sensitivity coefficients in the BEAVRS benchmark are different compared with other cases because the energy spectrum of neutron flux is different owing to the difference in the core temperature and the existence of boron in the borated water.

For supplemental information, the bias factor method using the measurement value of α was applied to check how small the nuclear data-induced uncertainty of k_{eff} can be reduced. By this DA, a priori nuclear data-induced variance of k_{eff} ($\mathbf{S}_{k_{\mathrm{eff}},\sigma}\boldsymbol{\Sigma}_\sigma\mathbf{S}_{k_{\mathrm{eff}},\sigma}^T$) is updated into a posteriori variance ($\mathrm{V}'_{k_{\mathrm{eff}}}$) as follows:

$$\begin{aligned}\mathrm{V}'_{k_{\mathrm{eff}}} &\approx \mathbf{S}_{k_{\mathrm{eff}},\sigma}\boldsymbol{\Sigma}_\sigma\mathbf{S}_{k_{\mathrm{eff}},\sigma}^T - \frac{\mathbf{S}_{k_{\mathrm{eff}},\sigma}\boldsymbol{\Sigma}_\sigma\mathbf{S}_{\alpha,\sigma}^T\mathbf{S}_{\alpha,\sigma}\boldsymbol{\Sigma}_\sigma\mathbf{S}_{k_{\mathrm{eff}},\sigma}^T}{\mathbf{S}_{\alpha,\sigma}\boldsymbol{\Sigma}_\sigma\mathbf{S}_{\alpha,\sigma}^T + \mathrm{V}_{\mathrm{exp},\alpha} + \mathrm{V}_{\mathrm{model},\alpha}} \\ &= \left\{1 - \frac{\mathbf{S}_{\alpha,\sigma}\boldsymbol{\Sigma}_\sigma\mathbf{S}_{\alpha,\sigma}^T\left(c_{\alpha,k_{\mathrm{eff}}}\right)^2}{\mathbf{S}_{\alpha,\sigma}\boldsymbol{\Sigma}_\sigma\mathbf{S}_{\alpha,\sigma}^T + \mathrm{V}_{\mathrm{exp},\alpha} + \mathrm{V}_{\mathrm{model},\alpha}}\right\}\mathbf{S}_{k_{\mathrm{eff}},\sigma}\boldsymbol{\Sigma}_\sigma\mathbf{S}_{k_{\mathrm{eff}},\sigma}^T, \end{aligned} \quad (2)$$

where $\mathrm{V}_{\mathrm{exp},\alpha}$ and $\mathrm{V}_{\mathrm{model},\alpha}$ are variances owing to the experimental errors and the analytical modeling errors, respectively. Based on the previous DA study [4], $\mathrm{V}_{\mathrm{exp},\alpha}$ and $\mathrm{V}_{\mathrm{model},\alpha}$ were determined to be 1.6×10^{-5} and 2.0×10^{-4}, respectively.

Table I. Results of the bias factor method using α.

Bench mark	$c_{\alpha,k_{\mathrm{eff}}}$ (-)	A priori k_{eff} -uncertainty $\sqrt{\mathbf{S}_{k_{\mathrm{eff}},\sigma}\boldsymbol{\Sigma}_\sigma\mathbf{S}_{k_{\mathrm{eff}},\sigma}^T}$ (%dk/k)	A posteriori k_{eff}-uncertainty $\sqrt{\mathrm{V}'_{k_{\mathrm{eff}}}}$ (%dk/k)
leu-comp-therm-007-002	-0.866	0.809	0.417
leu-comp-therm-039-005	-0.861	0.802	0.420
leu-comp-therm-002-003	-0.852	0.765	0.412
leu-comp-therm-009-004	-0.847	0.740	0.404
leu-comp-therm-010-003	-0.844	0.707	0.389
beavrs-cycle1-hzp	-0.254	0.565	0.546

Table I also provides nuclear data-induced uncertainties of k_{eff} before and after the bias factor method, *i.e.*, $\sqrt{\mathbf{S}_{k_{\mathrm{eff}},\sigma}\boldsymbol{\Sigma}_\sigma\mathbf{S}_{k_{\mathrm{eff}},\sigma}^T}$ and $\sqrt{\mathrm{V}'_{k_{\mathrm{eff}}}}$, respectively. As expected from Eq. (2), a posteriori uncertainty of k_{eff} becomes smaller, as the absolute value of the correlation $|c_{\alpha,k_{\mathrm{eff}}}|$ approaches to unity. Consequently, it was demonstrated that the stronger correlation results between α and k_{eff} result in the more efficient reduction of k_{eff}-uncertainty.

5. Conclusions

As clarified in this study, the subcritical measurement of α measured at the solid moderated KUCA core is useful to reduce nuclear data-induced uncertainties of k_{eff} in other light water moderated cores, if the correlation between α and k_{eff} is strong.

In this investigation, the sensitivity coefficients of α and k_{eff} were estimated by different numerical methods (*i.e.*, the deterministic and the Monte Carlo methods, respectively) because no existing continuous energy Monte Carlo code was available to carry out SA of α. This difference may degrade the correlation between α and k_{eff}, and the subsequent uncertainty reduction by DA. Thus, further research and development of numerical methodology of SA of a using the continuous Monte Carlo code are important to address this problem.

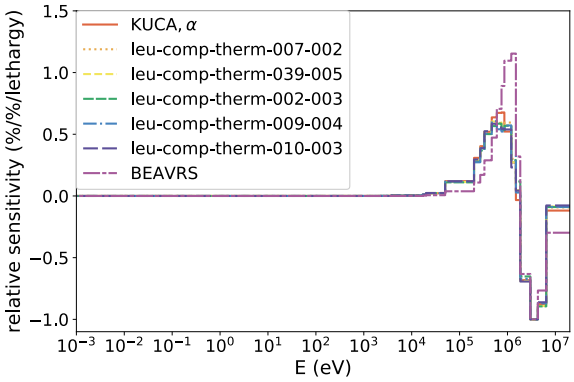

(a) ^{235}U: prompt χ_p for α, and total χ for k_{eff}

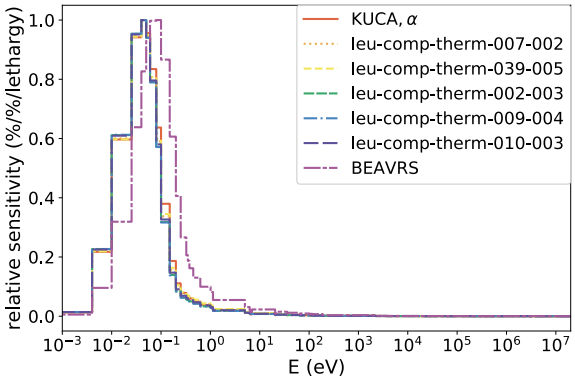

(b) ^{1}H: (n,γ)

Fig. 5 Comparison of sensitivity coefficients. The sensitivity coefficients are normalized by dividing the maximal or minimal value.

Acknowledgements

This work has been carried out in part under the Visiting Researcher's Program of the Research Reactor Institute, Kyoto University. The authors are grateful to all the technical staff of KUCA for their assistance during the experiment. This work was supported by the Japan Society for the Promotion of Science Grant-in-Aid for Scientific Research (C) [Grant Number 19K05328].

References

1. Yokoyama K, Kitada T, "Generalized Formulation of Extended Cross-section Adjustment Method based on Minimum Variance Unbiased Linear Estimation," *J. Nucl. Sci. Technol.*, **56**, *1*, 87 (2019).
2. Endo T, Watanabe T, Yamamoto A, "Bias Factor Method using Random Sampling Technique," *J. Nucl. Sci. Technol.*, **53**, *10*, 1494 (2016).
3. Endo T, Yamamoto A, "Data Assimilation using Subcritical Measurement of Prompt Neutron Decay Constant," *Proc. M&C2019*, Portland, Oregon, USA, August 25–29, 2019, American Nuclear Society (2019).
4. Endo T, Yamamoto A, "Comparison of Theoretical Formulae and Bootstrap Method for Statistical Error Estimation of Feynman-α Method," *Ann. Nucl. Energy*, **124**, 606 (2019).
5. Endo T, Yamamoto A, Yamanaka M, *et al.*, "Experimental Validation of Unique Combination Numbers for Third- and Fourth-order Neutron Correlation Factors of Zero-power Reactor Noise," *J. Nucl. Sci. Technol.*, **56**, *4*, 322 (2019).
6. Endo T, Yamamoto A, "Sensitivity Analysis of Prompt Neutron Decay Constant using Perturbation Theory," *J. Nucl. Sci. Technol.*, **55**, *11*, 1245 (2018).
7. Alcouffe RE, Baker RS, Dahl JA, *et al.*, "PARTISN: A Time-dependent, Parallel Neutral Particle Transport Code System," LA-UR-08-07258 (2008).
8. Rearden BT, Jessee MA (Eds.), "SCALE Code System," ORNL/TM-2005/39 Version 6.2.3 (2018).
9. Chadwick MB, Herman M, Obložinský P, *et al.*, "ENDF/B-VII.1 Nuclear Data for Science and Technology: Cross Sections, Covariances, Fission Product Yields and Decay Data," *Nucl. Data Sheets*, **112**, *12*, 2887 (2011).
10. Endo T, Yamamoto A, "Development of New Solid Angle Quadrature Sets to Satisfy Even- and Odd-Moment Conditions," *J. Nucl. Sci. Technol.*, **44**, *10*, 1249 (2007).
11. Endo T, Watanabe K, Chiba G, *et al.*, "Nuclear Data-induced Uncertainty Quantification of Prompt Neutron Decay Constant based on Perturbation Theory for ADS Experiments at KUCA," *J. Nucl. Sci. Technol.*, DOI: 10.1080/00223131.2019.1647893
12. Kiedrowski BC, Brown FB, Conlinet JL, *et al.*, "Whisper: Sensitivity/Uncertainty-Based Computational Methods and Software for Determining Baseline Upper Subcritical Limits," *Nucl. Sci. Eng.*, **181**, *1*, 17 (2015).
13. International Handbook of Evaluated Criticality Safety Benchmark Experiments, OECD-NEA, Paris, France, https://www.oecd-nea.org/science/wpncs/icsbep/handbook.html (2018).
14. Horelik N, Herman B, Ellis M, *et al.*, "MIT Benchmark for Evaluation and Validation of Reactor Simulations: Release ver. 2.02" MIT Computational Reactor Physics Group (2018).
15. Tada K, Nagaya Y, Kunieda S, *et al.*, "Development and Verification of a New Nuclear Data Processing System FRENDY," *J. Nucl. Sci. Technol.*, **54**, *7*, 806 (2017).
16. Werner CJ (Ed.), "MCNP User's Manual Code Version 6.2," LA-UR-17-29981 (2017).

Proceedings of the Reactor Physics Asia 2019 (RPHA19) Conference
Osaka, Japan, Dec. 2-3, 2019

Benchmark study of nuclear processed systems with NCA data

Satoshi Wada[a*], Kenichi Yoshioka[a] and Tsukasa Sugita[a,]
[a]*Toshiba Energy Systems & Solutions Corporation, 4-1 Ukishima-cho, Kawasaki-ku, Kawasaki 210-0862 Japan*
[*]Corresponding author: satoshi9.wada@toshiba.co.jp

Abstract

Critical experiment data of Toshiba Nuclear Critical Assembly were used to benchmark for FRENDY and NJOY codes, both with three neutron libraries: JENDL-4, ENDF/B-VII.1, and ENDF/B-VIII.0. The results obtained by using ACE-libraries processed by FRENDY and NJOY were in good agreements with the each other.

Key Words: **FRENDY, NCA, Benchmark study, NJOY**

1. Introduction

It is important to accumulate benchmarks that can be referred in the reactor physics studies *i.e.* testing new fuels, designing new cores, and code developments. Toshiba Nuclear Critical Assembly (NCA) started its operation in 1963, therefore, there are vast data available on the critical experiments. Those can be used as reference data when testing new fuel assembly concepts, void effect, or gadolinia effect [1]. Recently, a novel nuclear processed system, FRENDY, was developed by Japan Atomic Energy Agency (JAEA) [2]. FRENDY is expected to the evaluated nuclear data library JENDL. In addition, the latest JENDL and/or other evaluated nuclear data libraries will be able to use by FRENDY treating the GNDS [3] format and the MVP library. In this paper, two nuclear processed systems, FRENDY and NJOY [4-6] were evaluated by using the NCA critical-experiment data.

2. Critical Experiments

2.1 Toshiba Nuclear Critical Assembly

Critical experiments were conducted at the Toshiba Nuclear Critical Assembly (NCA). The main purpose of NCA is to develop and test new core and fuel assembly concepts and to develop new nuclear codes. The NCA is a light-water-moderated critical assembly that is allowed to operate with uranium-dioxide (UO_2) fuel rods of multiple enrichments. Also, three types of gadolinia-bearing UO_2 rods are available for the critical experiments. Fig. 1 shows the vertical cross-section of the NCA-core tank. The criticality of the NCA core can be adjusted by the water level. For designing light-water reactor (LWR) cores, void fractions and water densities are the key issues, therefore, void tubes are used in order to simulate hot 0% and 40% void conditions in the NCA as shown in Fig. 2. The cladding of fuel rods and void tubes are made of aluminum alloy.

2.2 Experimental cases

The experimental conditions are summarized in Table I, and the core configurations are shown in Fig. 3. These experiments simulated fuel assemblies of the boiling-water reactor (BWR): effects of the void fraction and the gadolinia were simulated in the experiments.

3. Critical Analysis

3.1 Calculation conditions

Calculations were carried out by using MCNP 6.2 code [7] with ACE libraries processed by FRENDY [2] and NJOY [4-6] with JENDL-4.0 [8], ENDF/B-VII.1 [9], and ENDF/B-VIII.0 [10]. In the current paper, the following conditions were used in the calculation: 20,000 particle histories for each batch; total batch of 6,050; 50 skip batch. The thermal scattering data is used only for hydrogen in H_2O with the following libraries;

1) ENDF/B-VI.8 thermal scattering data and JENDL-4.0 neutron library,
2) ENDF/B-VII.1 thermal scattering data and ENDF/B-VII.1 neutron library,
3) ENDF/B-VIII.0 thermal scattering data and ENDF/B-VIII.0 neutron library.

3.2 Calculation results

The calculation results are shown in Fig. 4. In the cases with higher void fraction, the neutron multiplication factor (k-effective) tended to overestimate the experimental data. The results obtained by JENDL-4.0 were smaller than that obtained by using the ENDF libraries. The FRENDY and NJOY results agreed within 0.1 %dk. The effect of the gadolinia-bearing rod was smaller than that of the void fraction.

4. Conclusions

The current paper evaluated two nuclear processed systems, FRENDY and NJOY, by using MCNP6.2 and critical experiment data obtained at the NCA. These calculation results are in good agreement with the ACE-format libraries processed by FRENDY and NJOY. The detailed evaluation results and discussions are planned to present in the conference.

Acknowledgements

The authors would like to thank Dr. K. Tada for kind support on the calculation with the FRENDY code.

References

1. Yoshioka K, et al., "CRITICAL EXPERIMENTS FOR BWR FUEL ASSEMBLIES WITH CLUSTER OF GADLINIA RODS," *Proc. PHYSOR 2014*, Kyoto, Japan, Sep. 28 – Oct. 3, 2014, Japan Nuclear Energy Society (2014) (CD-ROM).
2. Tada K, et al., "Development and verification of a new nuclear data processing system FRENDY," *J. Nucl. Sci. Technol.,* **54**, pp.806-817 (2017).
3. C. M. Mattoon, et. al, "Generalized Nuclear Data: a New Structure (with Supporting Infrastructure) for Handling Nuclear Data," *Nuclear Data Sheet*, **113**, pp. 3145-3171 (2012).
4. MacFarlane R. E., et al., "The NJOY Nuclear Data Processing System, Version 91," *LA-UR-12740-M* (1994).
5. MacFarlane R. E., et al., "The NJOY Nuclear Data Processing System, Version 2012," *LA-UR-12-27079* (2012).
6. MacFarlane R. E., et al., "The NJOY Nuclear Data Processing System, Version 2016," *LA-UR-17-200093-M* (2016).
7. Werner J., et al, "MCNP6.2 Release Notes," *LA-UR-18-20808* (2018).
8. Shibata K, et al., "JENDL-4.0: A New Library for Nuclear Science and Engineering," *J. Nucl. Sci. Technol.,* **48**, pp.1-30 (2011).
9. Chadwick M. B., et al., "ENDF/B-VII.1 nuclear data for science and technology: Cross section, covariances, fission product yields and decay data," *Nuclear Data Sheets,* **112(12)**, pp.2887-2996 (2011).
10. Brown D. A., et al., "ENDF/B-VIII.0: The 8th Major Release of the Nuclear Reaction Data Library with CIELO-project Cross Sections, New Standards and Thermal Scattering Data," *Nuclear Data Sheets,* **148**, pp.1-142 (2018).

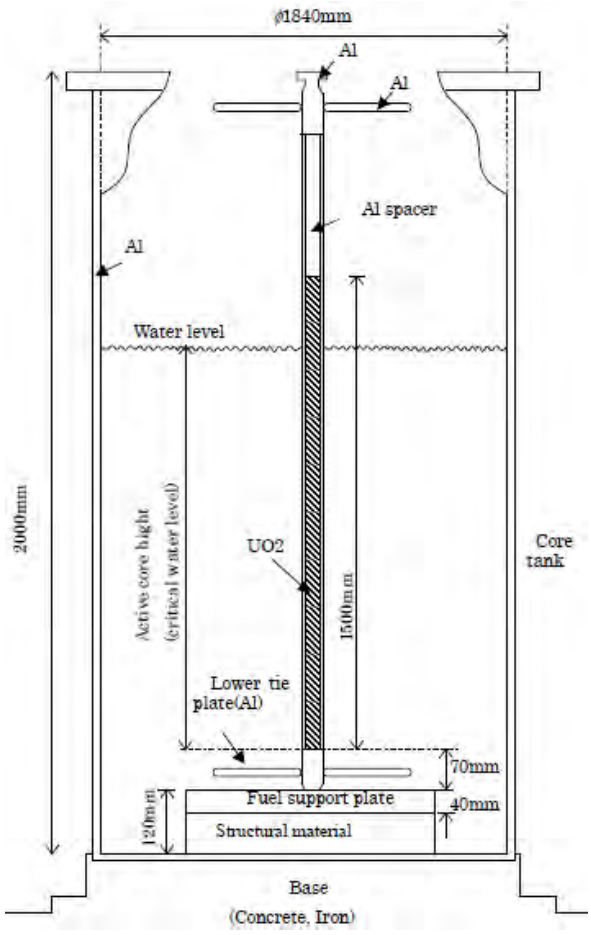

Fig. 1. Vertical cross section of NCA

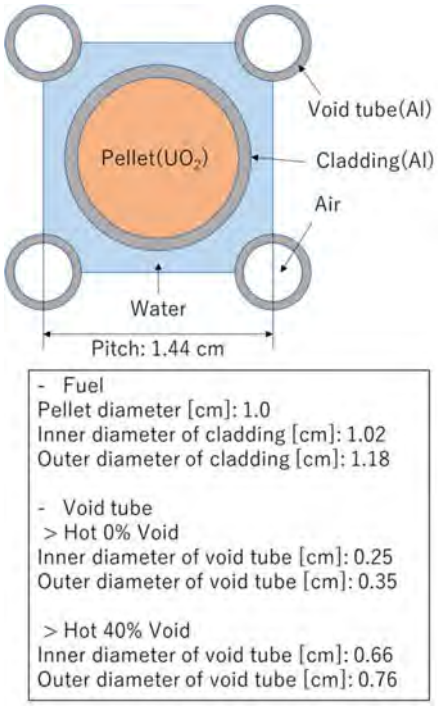

Fig. 2. Geometry of fuel rod and void tube

Table I. Summary of test cases

Case ID	Void fraction	Gadolinia condition	Critical water level (mm)
1	Cold	No gadolinia rod	1,137.9
2	Hot 0% Void	No gadolinia rod	907.4
3	Hot 40% Void	No gadolinia rod	1,019.3
4	Cold	With 5wt% gadolinia rod	949.6
5	Hot 0% Void	With 5wt% gadolinia rod	1,071.5
6	Hot 40% Void	With 5wt% gadolinia rod	951.8
7	Hot 0% Void	With 5wt% gadolinia rod	877.5
8	Hot 40% Void	With 5wt% gadolinia rod	968.9
9	Cold	With 10wt% gadolinia rod	966.1
10	Hot 0% Void	With 10wt% gadolinia rod	874.1
11	Hot 40% Void	With 10wt% gadolinia rod	1,182.4
12	Hot 40% Void	With 5wt% gadolinia rod	925.7
13	Cold	With 10wt% gadolinia rod	838.4
14	Hot 0% Void	With 10wt% gadolinia rod	935.9
15	Hot 40% Void	With 10wt% gadolinia rod	1,079.9
16	Cold	With 5, 15wt% gadolinia rod	1,026.1
17	Hot 0% Void	With 5, 15wt% gadolinia rod	1,176.9
18	Hot 40% Void	With 5, 15wt% gadolinia rod	1,060.0
19	Hot 40% Void	With 5, 15wt% gadolinia rod	969.8
20	Cold	With 10wt% gadolinia rod	963.8
21	Hot 0% Void	With 10wt% gadolinia rod	1,055.1
22	Hot 40% Void	With 10wt% gadolinia rod	1,195.8

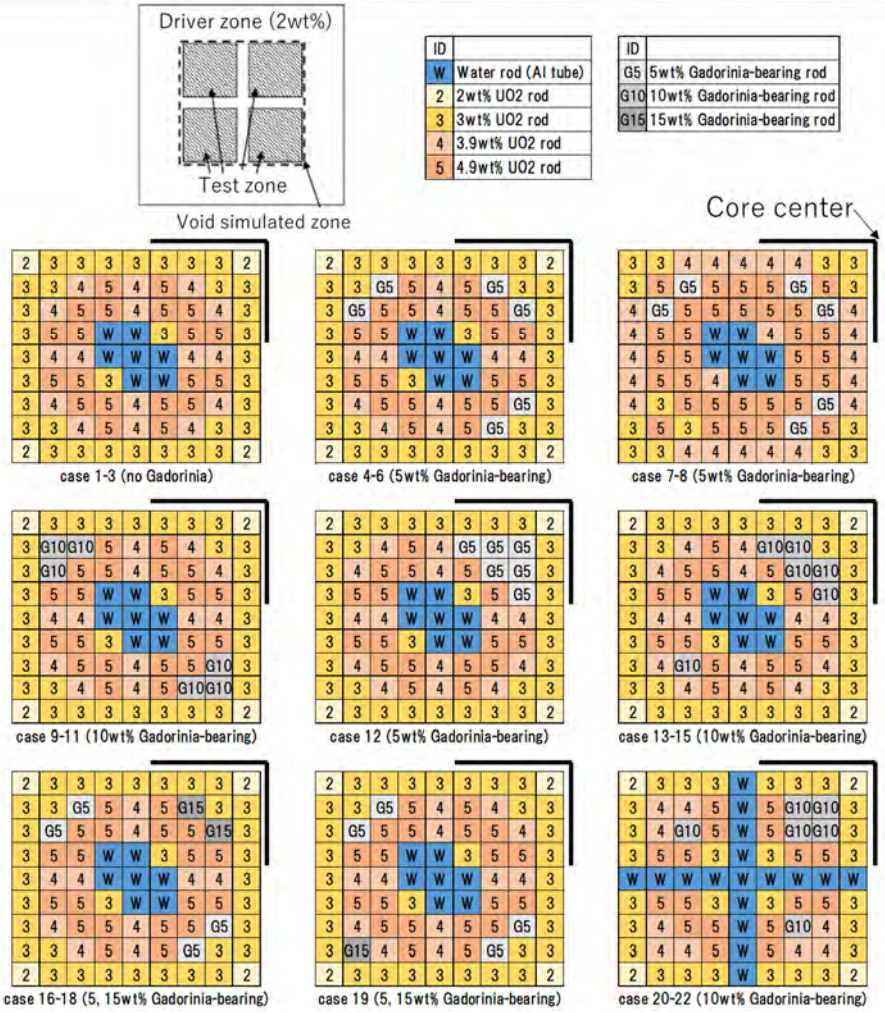

Fig. 3. Core configuration

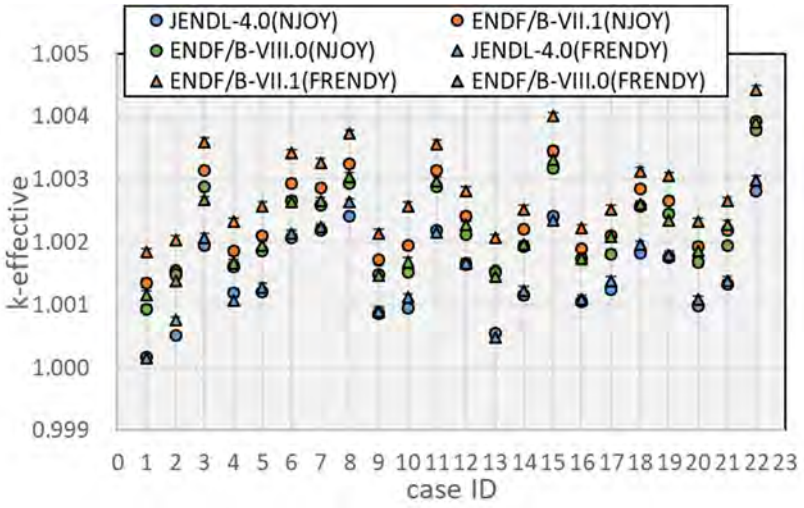

A) k-effective

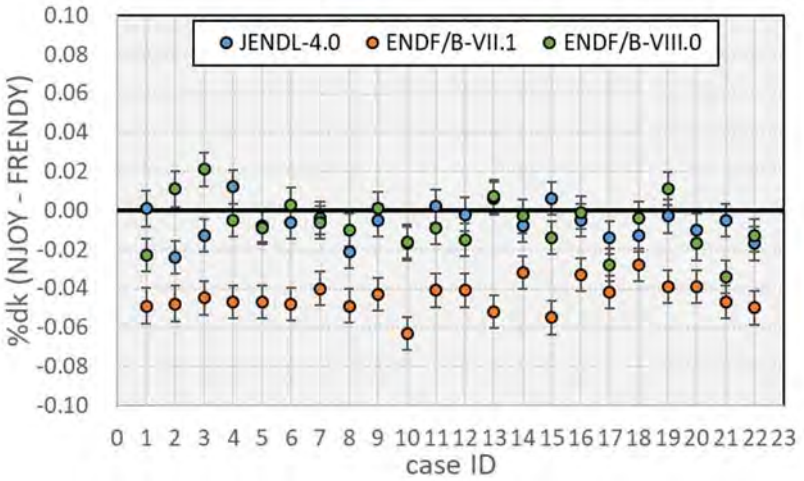

B) comparison of k-effective between using the NJOY and the FRENDY

Fig. 4. Calculation results

Proceedings of the Reactor Physics Asia 2019 (RPHA19) Conference
Osaka, Japan, Dec. 2-3, 2019

Sensitivity analysis for generalized response with RMC Code

Guanlin Shi*, Conglong Jia, Quan Cheng, and Kan Wang
Department of Engineering Physics
Tsinghua University, Beijing, China, 100084,
* shigl16@mails.tsinghua.edu.cn

Abstract

In this paper the generalized sensitivity analysis capability based on GEneralized Adjoint Response in Monte Carlo (GEAR-MC) method and direct perturbation (DP) method have been developed in the Reactor Monte Carlo Code RMC. The GEAR-MC method calculates the generalized sensitivity coefficient based on generalized perturbation theory. Whereas, the direct perturbation method is based on the definition of sensitivity coefficient. The newly developeded methods were verified by comparing the results of DP and GEAR-MC methods with the results of already implemented collision history-based method through Godiva and PWR pin cell benchmark problems. Results show that, in general, DP and GEAR-MC methods agree well with collision history-based method.

Key Words: **Monte Carlo, generalized sensitivity analysis, RMC**

1. Introduction

In past few years, sensitivity and uncertainty analysis has become a hot spot in reactor physics and several tools with sensitivity analysis capability are developed. For example, the TSUNAMI-3D [1] code of SCALE code package, McCARD [2], MONK [3], SERPENT2 [4], Open MC [5], MCNP6 [6] and Reactor Monte Carlo code (RMC) [7]. But only part of them have the ability to perform sensitivity analysis of generalized response function. In previous work, the collision history-based method has been implemented in RMC to compute generalized sensitivity coefficients. In this work, the GEAR-MC method put forward by C. Perfetti et al [8] and the direct perturbation method are implemented in RMC. And, the results computed by the GEAR-MC and direct perturbation methods have been compared with that computed by the collision history-based method.

2. Theory

2.1 Direct perturbation method

The sensitivity coefficient of response R is defined as

$$S_x^R = \frac{\delta R/R}{\delta x/x}, \tag{1}$$

where x is the cross section that need to be analyzed. Using central differences the following formula can be obtained

$$S_x^R = \frac{x}{R}\frac{R^+ - R^-}{x^+ - x^-}, \tag{2}$$

where x^+ and x^- represent the positive and negative perturbation for the nuclear data cross section x respectively. And R^+ and R^- are the corresponding results.

In practice, a multi-group structure perturbation factor library is prepared in advance. If we want 1% increase in elastic cross section then the data saved in perturbation factor library is 1.01. In transport canculation, the perturbation is introduced by multiplying the perturbation factor to the cross section. After perturbation, the elastic cross section will increase $\Delta\Sigma_s$. In order to keep balance, the total cross section will also increase $\Delta\Sigma_s$.

2.2 GEAR-MC method

GEAR-MC method is put forward to perform sensitivity analysis for the response function in the form of ratio of two reaction rates, which is expressed as

$$R = \frac{\langle \Sigma_1, \Psi \rangle}{\langle \Sigma_2, \Psi \rangle}, \tag{3}$$

where Ψ is the neutron flux, Σ_1 and Σ_2 are any kinds of nuclear data. $\langle\ \rangle$ is integration over some phase space.

The change of generalized response function to the nuclear data x is given by

$$\delta R = \left\langle \frac{\partial R}{\partial x}\delta x + \frac{\partial R}{\partial \Psi}\frac{\partial \Psi}{\partial x}\delta x \right\rangle. \tag{4}$$

So, the generalized sensitivity coefficient can be expressed as

$$S_x^R = \frac{\delta R/R}{\delta x/x} = \left\langle \frac{\partial R}{\partial x}\frac{x}{R} + \frac{\partial R}{\partial \Psi}\frac{\partial \Psi}{\partial x}\frac{x}{R} \right\rangle. \quad (5)$$

The first term on the right hand side of Eq. (5) is known as the direct term, it represents the influence of the perturbation of the nuclear data on the response function. And with a little mathematical manipulation, the direct term can be expressed as

$$\left\langle \frac{\partial R}{\partial x}\frac{x}{R} \right\rangle = \frac{\left\langle \frac{\mathrm{d}\Sigma_1}{\mathrm{d}x}\Psi x \right\rangle}{\langle \Sigma_1 \Psi \rangle} - \frac{\left\langle \frac{\mathrm{d}\Sigma_2}{\mathrm{d}x}\Psi x \right\rangle}{\langle \Sigma_2 \Psi \rangle}. \quad (6)$$

The second term on the right hand side of Eq. (4) is called indirect effect terms. It represents the impact of perturbation of nuclear data on the neutron flux and influences the response function further more. And it can be expressed as

$$\left\langle \frac{\partial R}{\partial \Psi}\frac{\partial \Psi}{\partial x}\frac{x}{R} \right\rangle = \frac{\left\langle \frac{\partial \Psi}{\partial x}\Sigma_1 x \right\rangle}{\langle \Sigma_1 \Psi \rangle} - \frac{\left\langle \frac{\partial \Psi}{\partial x}\Sigma_2 x \right\rangle}{\langle \Sigma_2 \Psi \rangle}. \quad (7)$$

In order to solve the indirect effect terms, The Boltzmann equation and the generalized adjoint equation will be used. The Boltzmann equation and generalized adjoint equation can be expressed as Eq. (8) and Eq. (9) respectively

$$k\mathrm{A}\Psi = \mathrm{M}\Psi, \quad (8)$$

$$(\mathrm{A}^* - \frac{1}{k}\mathrm{M}^*)\Gamma^* = \mathrm{Q}^*, \quad (9)$$

where superscript * denotes conjugation of symbols. Through perturbing the Boltzmann equation, Eq. (8) can be obtained

$$(k\mathrm{A} - \mathrm{M})\delta\Psi = (\delta\mathrm{M} - k\delta\mathrm{A})\Psi - \delta k\mathrm{A}\Psi. \quad (10)$$

Multiply Eq. (9) by $\delta\Psi$ and Eq. (10) by Γ^*, and then take the inner product respectively, we can get

$$\left\langle \Gamma^*(k\mathrm{A} - \mathrm{M})\delta\Psi \right\rangle = \left\langle \Gamma^*(\delta\mathrm{M} - k\delta\mathrm{A})\Psi \right\rangle - \delta k\left\langle \Gamma^*\mathrm{A}\Psi \right\rangle, \quad (11)$$

and

$$\left\langle \delta\Psi(\mathrm{A}^* - \frac{1}{k}\mathrm{M}^*)\Gamma^* \right\rangle = \left\langle \delta\Psi\mathrm{Q}^* \right\rangle. \quad (12)$$

Combine Eq. (11) and Eq. (12). We can derive that the indirect effect terms can be expressed as

$$\left\langle \frac{\partial R}{\partial \Psi}\frac{\partial \Psi}{\partial x}\frac{x}{R} \right\rangle = \left\langle x\Gamma^*(\frac{1}{k}\frac{\mathrm{dM}}{\mathrm{d}x} - \frac{\mathrm{dA}}{\mathrm{d}x})\Psi \right\rangle. \quad (13)$$

In order to solve the generalized adjoint flux, the GEAR-MC method is developed by C. Perfetti.

Multiply Eq. (10) by Γ^* and Eq. (9) by Ψ and integrating over some phase space, respectively, we can obtain

$$\left\langle \Gamma^* S \right\rangle = \left\langle \Psi\mathrm{Q}^* \right\rangle + \left\langle \Gamma^*\frac{1}{k}\mathrm{M}\Psi \right\rangle. \quad (14)$$

Assume the neutron source is point source, which can be expressed as

$$S = S_0\delta(\vec{P} - \vec{P_0}). \quad (15)$$

Substitute Eq. (15) into Eq. (14), the expression for the generalized adjoint flux at phase space P_0 can be obtained.

$$\Gamma^*(\vec{P_0}) = \frac{1}{S_0}\left\langle \Psi(\vec{P_0} \to \vec{r})\frac{1}{R}\frac{\partial R}{\partial \phi} \right\rangle + \frac{1}{S_0}\left\langle \Gamma^*(\vec{r})\frac{1}{k}\mathrm{M}\Psi(\vec{P_0} \to \vec{r}) \right\rangle. \quad (16)$$

The generalized adjoint flux includes two terms. The first term on the right hand side is called intra-generational term and it can be expressed as

$$\left\langle \Psi(\vec{P_0} \to \vec{r})\frac{1}{R}\frac{\partial R}{\partial \phi} \right\rangle = \frac{\Sigma_1\Psi(\vec{P_0} \to \vec{r})}{\langle \Sigma_1 \Psi \rangle} - \frac{\Sigma_2\Psi(\vec{P_0} \to \vec{r})}{\langle \Sigma_2 \Psi \rangle}. \quad (17)$$

It can be solved by using Contributon-Linked eigenvalue sensitivity/Uncertainty estimation via Track length importance Characterization (CLUTCH) method.

The second term on the right hand side is known as inter-generational term and it can be expressed as

$$\left\langle \Gamma^*(r)\frac{1}{k}\mathrm{M}\Psi(\tau_s \to r) \right\rangle = \Gamma_1^*F_1 + \Gamma_2^*F_2 + \Gamma_3^*F_3 + ... + 0. \quad (18)$$

It can be solved by using the method similar to iterated fission probability (IFP) method. But the difference is that in the IFP method only in asymptotic population the importance will be calculated whereas in GEAR-MC method the importance is calculated in both latent and asymptotic generation.

3. Results

To verify the RMC capability of calculating generalized sensitivity coefficients, the following linear response function is selected.

$$R = \frac{\iiint \Sigma_{\mathrm{f}}^{^{238}\mathrm{U}}(r,E)\Psi(r,E,\Omega)dEdrd\Omega}{\iiint \Sigma_{\mathrm{f}}^{^{235}\mathrm{U}}(r,E)\Psi(r,E,\Omega)dEdrd\Omega}. \quad (19)$$

The response is calculated in Godiva and UAM TMI PWR pin cell problems. The results of three methods are compared for Godiva problem. And only the results of GEAR-MC method and collision history method are compared for UAM TMI PWR pin cell problem.

3.1 Godiva benchmark

The energy-resolved F28/F25 sensitivity coefficients with regard to U-235 inelastic cross section, fission cross section, disappearance cross section and total cross section are presented in Fig. 1. In general, GEAR-MC method and collision history method agree well with each other.

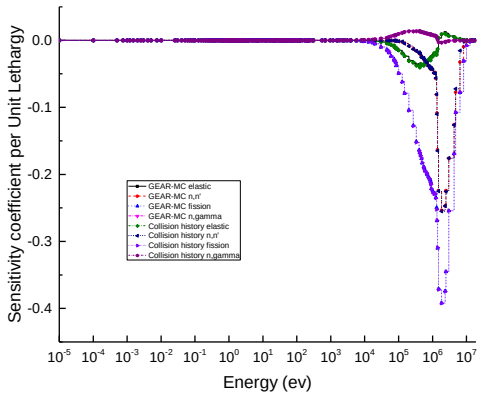

Fig 1. Sensitivity coefficients of ^{235}U

Some energy integrated sensitivity coefficients of ^{235}U are presented in Table I. As can be seen from the Table I, three methods agree well with each other and the GEAR-MC method could obtain lower variance than the collision history-based method. From Fig.1, it is easy to notice that the F28/F25 are more sensitive to the fission cross section of ^{235}U. This is mainly because the contribution from the direct term in Eq. (6).

3.2 UAM TMI PWR pin cell benchmark

Fig. 2 through Fig. 5 show the energy-resolved F28/F25 sensitivity coefficients with regard to ^{1}H n,gamma cross section, ^{235}U fission cross section and n,gamma cross section, ^{238}U inelastic cross section, fission cross section and ^{16}O elastic cross section respectively. From these figures we can also find that GEAR-MC method agree well with collision history method.

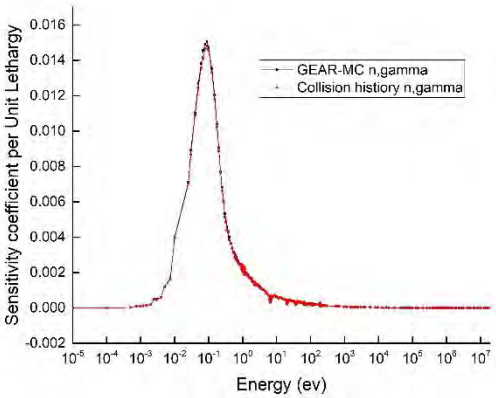

Fig 2. Sensitivity coefficients of ^{1}H

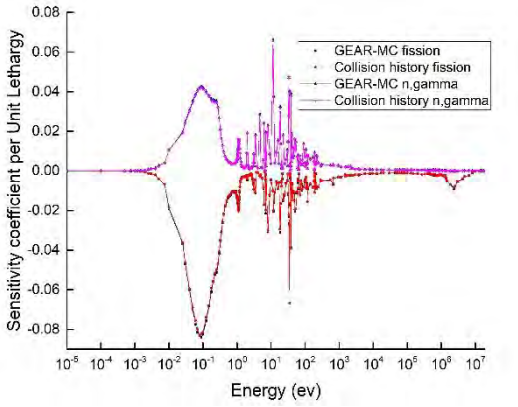

Fig 3. Sensitivity coefficients of ^{235}U

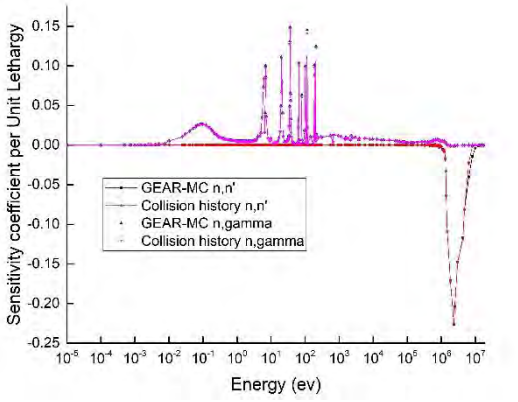

Fig 4. Sensitivity coefficients of ^{238}U

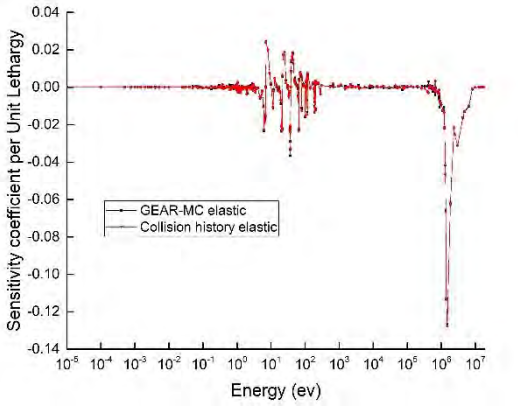

Fig 5. Sensitivity coefficients of ^{16}O

Some energy integrated sensitivity coefficients of this pin cell problem are presented in Table II. As can be seen from the Table II, relative differences between GEAR-MC method and collision history-based method are within 4%, which means GEAR-MC method generally agrees with

collision history-based method.

4. Conclusions

In this work the capability of computing generalized sensitivity coefficients based on the GEAR-MC method and direct perturbation method have been implemented in RMC. The Godiva benchmark and the UAM TMI PWR pin cell benchmark are used to verify the newly implemented methods. The results calculated by these two methods agree well with previously implemented collision history method..

Acknowledgements

This research is partially supported by China Scholarship Council, National Natural Science Foundation of China (GrantNo: 11475098).

References

1. Perfetti C M, Rearden B T, Martin W R. "SCALE Continuous-Energy Eigenvalue Sensitivity Coefficient Calculations." *Nucl. Sci. Eng.* **182**, pp.332–353, (2016).
2. Shim H J, Kim C H. "Adjoint sensitivity and uncertainty analyses in Monte Carlo forward calculations." *J. Nucl. Sci. Technol*. **05**, pp. 1453–1461(2011).
3. Baker C, Smith P N, Mason R, et al. "Calculating Uncertainty on k-effective with Monk 10." ICNC 2015, Charlotte, NC, September 13-17, (2015).
4. Aufiero, M., Bidaud, A., Hursin, M., et al. "A collision history-based approach to sensitivity/perturbation calculations in the continuous energy Monte Carlo code SERPENT." *Annals of Nuclear Energy.* **85**, pp. 245-258(2015).
5. Peng, Xingjie, et al. "Development of continuous-energy sensitivity analysis capability in OpenMC." *Annals of Nuclear Energy* **110**, pp. 362–383(2017).
6. Kiedrowski, Brian C., F. B. Brown, and P. P. H. Wilson. "Adjoint-Weighted Tallies for k-Eigenvalue Calculations with Continuous-Energy Monte Carlo." *Nuclear Science & Engineering the Journal of the American Nuclear Society* **168**(3), pp. 226-241(2011).
7. Qiu, Y., Aufiero, M., Wang, K., Fratoni, M. "Development of sensitivity analysis capabilities of generalized responses to nuclear data in Monte Carlo code RMC." *Annals of Nuclear Energy* **97**, pp. 142-152(2016).
8. Perfetti, Christopher M., and B. T. Rearden. "Development of a Generalized Perturbation Theory Method for Sensitivity Analysis Using Continuous-Energy Monte Carlo Methods." *Nuclear Science & Engineering the Journal of the American Nuclear Society* **182**(3), pp. 354-368(2016).

Table I. Energy integrated sensitivity coefficients of ^{235}U

Measurement	DP	GEAR-MC	Relative standard deviation	Collision history	Relative standard deviation	GERA-MC-Collision-history Relative difference (%)	DP-Collision-history Relative difference (%)
elastic	-7.60E-02	-7.34E-02	7.59E-03	-7.35E-02	1.02E-02	-0.14	3.40
inelastic	-3.33E-01	-3.44E-01	9.92E-04	-3.36E-01	1.22E-03	2.38	-0.89
fission	-8.52E-01	-8.62E-01	3.54E-04	-8.64E-01	3.58E-04	-0.23	-1.39
capture	3.90E-02	3.57E-02	8.50E-04	3.60E-02	2.68E-03	-0.83	8.33

Table II. Energy integrated sensitivity coefficients of different nuclide

Nuclide	Reaction	GEAR-MC	Relative standard deviation	Collision history	Relative standard deviation	Relative difference (%)
92235	fission	-2.80E-01	7.56E-04	-2.76E-01	1.27E-03	1.45
	capture	1.66E-01	3.53E-04	1.63E-01	8.30E-04	1.84
92238	inelastic	-2.26E-01	7.84E-04	-2.19E-01	1.21E-03	3.20
	capture	2.09E-01	4.01E-04	2.05E-01	7.94E-04	1.95
8016	elastic	-7.51E-02	9.56E-03	-7.60E-02	1.26E-02	-1.18
1001	capture	4.17E-02	3.89E-04	4.10E-02	1.60E-03	1.71

Proceedings of the Reactor Physics Asia 2019 (RPHA19) Conference
Osaka, Japan, Dec. 2-3, 2019

Uncertainty analysis of neutron parameters for NESTOR

Hongkuan LIAO, Qing LI, Yingrui YU*, Yuying HU

Science and Technology on Reactor System Design Technology Laboratory, Nuclear Power Institute of China, Chengdu, China

*Corresponding author: yuyr78@163.com

Abstract

Due to the complexity of the reactor system, many approximations are used in the nuclear design and calculations inevitably. The accuracy of the nuclear design software is closely related to the safety of the reactor design and operation. Besides, improving the accuracy is an effective way to excavating the economy of nuclear power plants. In this study, On the basis of the random sampling statistical analysis (RSSA) method, the uncertainty of control rod worth and boron concentration were obtained by comparing the measured values and the theoretical values modeled by NESTOR. The results indicate that the RSSA is feasible in the uncertainty analysis of nuclear design. As a result, the final computational uncertainty of the worth of control rod is ±7.447% and the final computational uncertainty of the boron concentration is ±49.71 ppm of NESTOR software.

Key Words: **NESTOR, Uncertainty Analysis, RSSA**

Nomenclature

μ_s	Average of samples
μ_p	Ensemble average
σ_s	Sample standard deviation
σ_p	Total standard deviation
N	Total number of samples
t	T distribution
χ^2	Chi square distribution
$X_{95/95}$	Under the limit of 95% confidence coefficient and 95% probability
$\mu_{p,95\%}$	Ensemble average of 95% confidence coefficient
$\sigma_{p,95\%}$	Total standard deviation of 95% confidence coefficient
$H(N_P)$	Owen factor[2]
β	Confidence level
γ	Probability level
CNP650	The PWR designed by China, consisting of 121 fuel assemblies, power rating of 1930MW[3].
NESTOR	A nuclear design software package designed by CNNC[4].
MWd/tU	Burnup unit
ARO	All Rod Clusters Out
D_{in}	Main regulating rod group D all in the core, while others all out of the core
P	Relative power of the core
BURNUP	Burnup in the core
CB	Boron Concentration
EFPD	Equivalent Full Power Day
ppm	10^{-6}（weight ratio）, using in soluble boron concentration
pcm	10^{-5}(Δ k/k)
ρ	The worth of control rod

1. Introduction

Uncertainty always exists in the engineering design such as the uncertainty of engineering system and the uncertainty of the environment[1]. So the uncertainty represents the credibility and trust of the system.

The reactor design is a typical and complex engineering design, and its uncertainty is very important to the thermal hydraulics analysis.

NESTOR nuclear design software package can be used to analyze full range of nuclear design contents. In this study, as important neutron parameters, the worth of the control rod and the boron concentration are chosen to be evaluated.

CORCA software is the core software of NESTOR, which is a 2D finite difference software. The theoretical values of the worth of control rod and the boron concentration are provided by CORCA, and the experimental measurements are used for the value comparison. After evaluating the applicability of RSSA by statistical analysis of the result, the uncertainty of the control rod worth and the boron concentration of NESTOR were given. The theoretical value of the control rod is obtained by simulating the ARO core state and the full insertion of the tested control rod group into the core state. The theoretical value of boron concentration is obtained by simulating the physical test state of the nuclear power plant once a month, and the considered state parameters include core power, control rod position, temperature and pressure.

2. Method and Code

Sensitivity and uncertainty analysis method could be divided into two categories which are the statistical analysis and the deterministic calculation. The most widely used statistical analysis method is the sampling method. In this study, we have quantified the influence of important plant state parameters with the parametric statistics method and the nonparametric statistics method[2].

2.1 Parametric Statistics

Normal distribution confidence limit method is a typical parametric statistics method. First of all, all the distribution characteristics of the input parameters should be confirmed. There are 3 steps in the method.

- Distribution test,
- Estimating the population mean and standard deviation,
- Analyzing the 95/95 limits.

Firstly, the distribution of samples would be tested by the test method such as χ^2 fitting testing[3]. The relationship among the mean and standard deviation of samples and the population would be presented as below if the test was passed.

$$\frac{\mu_s-\mu_p}{\sigma_s/\sqrt{N}}\sim t(N-1) \qquad \frac{(N-1)\sigma_s^{\,2}}{\sigma_p^{\,2}}\sim \chi^2(N-1) \tag{1}$$

Secondly, the population mean and standard deviation could be presented by the sample mean and standard deviation shown as Equation (2) and Equation (3).

$$\left[\mu_s-t_{\alpha/2}(N-1)*\sigma_s/\sqrt{N}\right]<\mu_p<\left[\mu_s+t_{\alpha/2}(N-1)*\sigma_s/\sqrt{N}\right] \tag{2}$$

$$\frac{\sigma_s^{\,2}*(N-1)}{\chi^2_{\alpha/2}(N-1)}<\sigma_p^{\,2}<\frac{\sigma_s^{\,2}*(N-1)}{\chi^2_{1-\alpha/2}(N-1)} \tag{3}$$

Thirdly, the 95/95 limit would be obtained as below.

$$X_{95/95}=\mu_{p,95\%}+H(N_P)\sigma_{p,95\%} \tag{4}$$

$H(N_p)$ is Owen factor. It is decided by the size of the sample space, which can be obtained by table look-up or calculation with the equation, as below .

$$H(N_P)=1.64485\times\frac{1+\sqrt{1-\left(1-\frac{1.3528}{N_P-1}\right)\frac{N_P-1}{N_P}}}{1-\frac{1.3528}{N_P-1}}$$

2.2 Nonparametric Statistics

The nonparametric statistics is to test the general characteristic to obtain the population tolerance limit under certain confidence and certain probability.

The process of quantifying the uncertainty of input parameters by the nonparametric statistics is shown in Fig. 1.

$$\text{input}\begin{pmatrix}(X)_1\\(X)_2\\\vdots\\(X)_N\end{pmatrix}\longrightarrow\text{operation matrix}\begin{pmatrix}(x_1,\ x_2,\ldots x_n)_1\\(x_1,\ x_2,\ldots x_n)_2\\\vdots\\(x_1,\ x_2,\ldots x_n)_N\end{pmatrix}$$

$$\xrightarrow{\text{code cacultion}}\text{output}\begin{pmatrix}Y_1\\Y_2\\\vdots\\Y_N\end{pmatrix}$$

Fig.1 the Process of Nonparametric Analysis

This method was presented by Wilks in 1941[4, 5]. Firstly, the important input parameters and their distribution should be determined, with sampling these parameters and obtaining the operation matrix. All the samples would generate the result of the output parameter after the code calculation. Then the tolerance limit could be obtained by sorting the output parameter.

For the single tolerance limit, the confidence and the probability should satisfy the condition described below.

$$\beta\le 1-\gamma^N \tag{5}$$

For the bilateral tolerance limit, the confidence and the probability should satisfy the condition as Equation (6).

$$\beta\le 1-\gamma^N-N(1-\gamma)\gamma^{N-1} \tag{6}$$

Based on the given confidence level βand probability level γ, the required number of samples N can be determined through the inequalities (5) and (6).

3. Uncertainty Analysis

In this section, the worth of control rod and the boron concentration are been analyzed. The theoretical model of plant was established by NESTOR software according to the operating status data of the nuclear power plant such as power, burnup, and boron concentration.

Samples are needed to be determined by sampling for RSSA method, but in this study, as the measured value of control rods coming from the start-up physical experiments of nuclear power plants, the measured boron concentration comes from the periodic physical test of the nuclear power plant once a month during the operation of plants which are obtained by chemical titration. It can be concluded that the calculation of control rod value and boron concentration is closely related to the uncertainty of reactivity calculation, but not to the specific state of the reactor core. Therefore, in this study, all the measured data is directly used to instead of sampling to obtain core status.

For RSSA method, relative or absolute deviation can be chosen as the object of uncertainty analysis according to the characteristics of the study, which will not affect the conclusions. In this study, the unit of control rod is pcm. As the value of each group of rods varies greatly, relative variation is used, $(p^{cal}-p^{mes})/p^{mes}$. As the concentration of boron varies with burnup, the absolute variation is used , $CB^{cal}-CB^{mes}$.

3.1 The worth of control rod

In order to ensure the conservativeness of the analysis results, there are totally 99 measured values of unit 1 to 4 of Qinshan II Nuclear Power Plant, unit 1 and unit 2 of Daya Bay Nuclear Power Plant are selected. And the 99 theoretical values of the measured states were obtained by NESTOR software. Then, the uncertainty of control rod worth was provided by comparing the theoretical values and measured values. Figure 2 presents the deviation of the theoretical values and measured values.

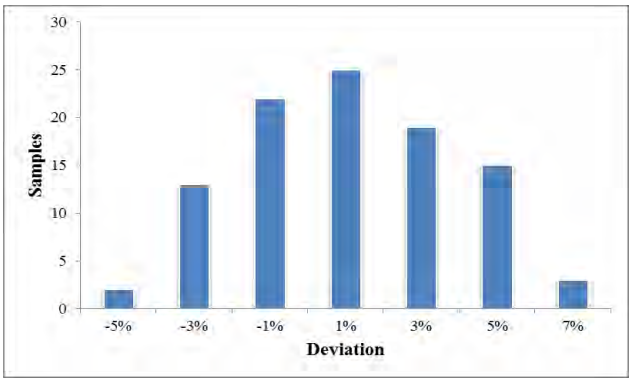

Fig. 2 Deviation of the Worth of the Control Rod

Table 1 Calculation data of χ^2 fitting testing

i	Span	pi	n*pi	ni	ni-n*pi	(ni-n*pi)2/n*pi
1	(-∞ , -5%]	0.046593	4.6127	2	-2.61	1.47985
2	(-5%,-3%]	0.109052	10.7961	13	2.20	0.44988
3	(-3%,-1%]	0.208947	20.6858	22	1.31	0.08350
4	(-1%,1%]	0.260961	25.8351	25	-0.84	0.02700
5	(1%,3%]	0.212480	21.0356	19	-2.04	0.19698
6	(3%,5%]	0.112772	11.1645	15	3.84	1.31769
7	(5% , ∞)	0.049194	4.8702	3	-1.87	0.71820
total	(-∞ , ∞)	1		99		4.2731

According to χ^2 fitting testing[3], as it is shown in Table 1, pi is the theoretical probability in the span, and n is the total number of samples. ni is the number of samples in actual range, and $(ni-n*pi)^2/(n*pi)$ means the divergence of each value interval. The total divergence $\sum_{i=1}^{k}(ni-n*pi)^2/(n*pi)$ is 4.2731, smaller than $\chi_\alpha^2(k-r-1)=\chi_{0.05}^2(4)=9.4877$. The degree of difference presents that the result meets normal distribution.

Thus, the bilateral tolerance interval of μ_p is [-0.651%, 0.729%], and the tolerance interval of σ_p is [0.0263, 0.0349]. The Owen factor $H(N_p)$ is 1.92499.

The upper limit under the condition of 95% confidence coefficient and 95% probability of the worth of control rod is 7.447%, and the lower limit is -7.369%.

The uncertainty of the worth of control rod is ±7.447%.

3.2 The boron concentration

Similar to the method of analyzing control rod worth, there are totally 112 measured values of unit 1 to 4 of Qinshan II Nuclear Power Plant. Unit 1 and unit 2 of Daya Bay Nuclear Power Plant are selected to analysis the uncertainty of the boron concentration calculated by NESTOR software. And the uncertainty of the boron concentration was provided by comparing the theoretical values and measured values of the 112 measured states. Figure 3 presents the deviation between the theoretical values and measured values.

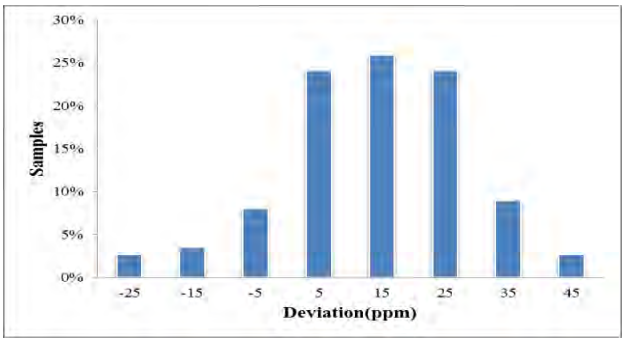

Fig. 3 Deviation of the Boron Concentration

The degree of difference presents that the result meets normal distribution. Thus, the bilateral tolerance interval of μ_p is [11.48 ppm, 17.70 ppm], and the tolerance interval of σ_p is [12.89, 16.79]. The Owen factor H(N_p) is 1.906487.

The upper limit under the condition of 95% confidence coefficient and 95% probability of the boron concentration is 49.71 ppm, and the lower limit is -20.60 ppm. The uncertainty of the boron concentration is ±49.71 ppm.

4. CONCLUSION

The computational uncertainty of important neutron parameters is very important to evaluate the economy and safety of nuclear power plants. In this study, the uncertainty of control rod worth and the boron concentration are analyzed. Finally the computational uncertainty of the worth of control rod is ±7.447% and the computational uncertainty of the boron concentration is ±49.71 ppm of NESTOR software.

It is proved that RSSA method is applicable to the uncertainty analysis of the neutron parameters; it can be applied to the uncertainty analysis of other neutron parameters such as moderator temperature coefficient and boron differential value in the future.

References

1. Wen Yao, Xiaoqian Chen, Wencai Luo, Michel van Tooren, Jian Guo, “Review of uncertainty-based multidisciplinary design optimization methods for aerospace vehicles,” *Progress in Aerospace Sciences*, 47(2011).
2. Glaeser H, “RS Method for uncertainty and sensitivity evaluation of code results and applications , “cience and Technology of Nuclear Installations, 2008.
3. Dovore, Jay L, Probability and Statistics for Engineering and Sciences, The Thomsom Corporation, 2004.
4. Wilks S S, Determination of sample sizes for setting tolerance limits[J], Heat Nuclear Technology,1995,112:355-358.
5. Wilks S S, Statistical prediction with special reference to the problem of tolenrance limits[J], The annals of mathematical statistics, 1942:400-409.

Proceedings of the Reactor Physics Asia 2019 (RPHA19) Conference
Osaka, Japan, Dec. 2-3, 2019

Comparison of Methods of Generating Covariance Matrix of Fission Yield

Keisuke Honta[a*] , Go Chiba[a]
[a]*Hokkaido University, Sapporo, Japan,*
[*]Corresponding author: keisukehon@eis.hokudai.ac.jp

Abstract

The modern evaluation method of generating covariance matrix of independent fission yields based on the generalized least square method is introduced, and uncertainties in nuclides number densities after nuclear fuel burnup are calculated using the generated covariance matrix and burnup sensitivities. In this work, calculations are performed using the pincell system as a preliminary study. Comparison with results based on the simple covariance generation method is made, and uncertainties of fission product nuclides number densities after burnup varies depending on the nuclides by switching the methods of generating covariance matrix of fission yields.

Key Words: **fission yield, uncertainty calculation, correlation**

1. Introduction

In evaluated nuclear data files, only variance is provided as uncertainty information on fission yield. In our research group, works on uncertainty propagation from fission yield to reactor physics parameters have been conducted [1], and fission yield covariance has been generated by a method adopted in the previous work by Katakura [2]. In the present paper, this method is referred to as Katakura's method. Katakura's method can approximately consider the fission yield covariance among fission product (FP) nuclides belonging to the same mass chain. In recent years, a new evaluation method for fission yield covariance matrices have been proposed by Fiorito et al [3]. This method is based on the Generalized Least Square (GLS) method. Under this circumstance, we introduce this new evaluation method, and compare results of uncertainty quantification with Katakura's method. Comparisons are made about FP nuclides number density uncertainty induced by fission yield uncertainties.

2. Theory

2.1 Basic equation of GLS

The GLS method is a method of revising the original input data by using new observable data dependent on the input data. In the field of nuclear reactor physics, it is used to adjust nuclear data using integral data. Basic equations used to adjust the nuclear data are shown in Eqs. (1) and (2) [4].

$$\widehat{\boldsymbol{T}} = \boldsymbol{T_0} + \boldsymbol{V_\sigma G^T}(\boldsymbol{V_{em}} + \boldsymbol{G V_\sigma G^T})^{-1}\left(\widetilde{\boldsymbol{R}} - \boldsymbol{R}(\boldsymbol{T_0})\right), \quad (1)$$

$$\widehat{\boldsymbol{V}} = \boldsymbol{V_\sigma} - \boldsymbol{V_\sigma G^T}(\boldsymbol{V_{em}} + \boldsymbol{G V_\sigma G^T})^{-1}\boldsymbol{G V_\sigma}. \quad (2)$$

By the GLS method, original nuclear data $\boldsymbol{T_0}$ is adjusted to $\widehat{\boldsymbol{T}}$, and the covariance matrix of the original nuclear data $\boldsymbol{V_\sigma}$ is updated to $\widehat{\boldsymbol{V}}$. In Eqs (1) and (2), $\boldsymbol{R}(\boldsymbol{T_0})$ is integral data predicted by using $\boldsymbol{T_0}$, $\boldsymbol{G}$ represents sensitivity of $\boldsymbol{R}(\boldsymbol{T_0})$ to $\boldsymbol{T_0}$, and $\widetilde{\boldsymbol{R}}$ is measured integrated data. The covariance matrix of $\widetilde{\boldsymbol{R}}$ and $\boldsymbol{R}(\boldsymbol{T_0})$ is represented as $\boldsymbol{V_{em}}$.

In the application of the GLS method to fission yield covariance matrix generation, independent fission yields are adjusted by using several physical constraint conditions.

2.2 GLS updating technique

The fission yield covariance matrix adjustment procedure using the GLS method which has five steps is shown in Fig. 1.

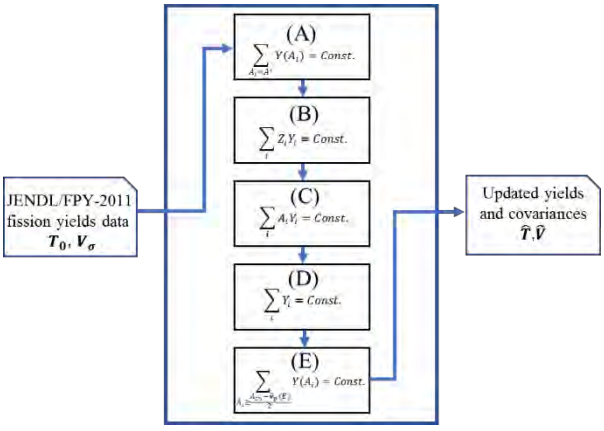

Fig. 1. Updating scheme used to adjust mean values and covariance matrix of fission yields

In the following, each of the five steps is described in detail. Note that we do not consider independent fission yields of light charged particles in the present study.

(A) Condition on chain yields

The first step is about a constraint of chain yields. A chain yield Ch_i represents the total yield for a given decay chain and is evaluated after both prompt and delayed neutron emissions, and i is a mass number of a stable nuclide at the end of this decay chain. A vector of chain yields $\boldsymbol{Ch}$ can be represented by independent fission yield vector $\boldsymbol{Y}$ and a matrix $\boldsymbol{D}$ as follows:

$$\boldsymbol{Ch} = \boldsymbol{DY}. \tag{3}$$

In the present study, the $\boldsymbol{D}$ matrix is created as follows. A square matrix corresponding to the number of nuclides whose size is 1,400 is prepared, and its diagonal component is 1 for stable nuclides and 0 for other nuclides. In the non-diagonal components of this matrix, the decay branching ratio from nuclide i to nuclide j given by the nuclear data is put to the (j, i) element of this matrix. After that, the matrix is multiplied iteratively. When there is no difference between before and after the multiplication, the matrix is regarded as the $\boldsymbol{D}$ matrix.

In this condition, a constraint of chain yields is posed. Sensitivity vector $\boldsymbol{G}$ in the adjustment equation is the $\boldsymbol{D}$ matrix itself.

(B) Condition on atomic number

$$\sum_i Z_i Y_i = Const. \tag{4}$$

Z_i and Y_i are the charge value and independent fission yield of fission product nuclide i, so this equation suggests that the number of protons is fixed. In the sensitivity vector $\boldsymbol{G}$, the entry becomes charge value of the corresponding nuclide.

(C) Condition on mass number

$$\sum_i A_i Y_i = Const. \tag{5}$$

A_i is the mass number of fission product nuclide i, so this equation suggests that the number of nucleons is fixed. In the sensitivity vector $\boldsymbol{G}$, the entry is the mass number of the corresponding nuclide.

(D) Condition on fission yield (1)

$$\sum_i Y_i = Const. \tag{6}$$

This equation suggests that the sum of independent fission yields is fixed. All the entries of the sensitivity vector $\boldsymbol{G}$ are unity.

(E) Condition on fission yield (2)

$$\sum_{A_i \geq \frac{A_{cn} - \bar{\nu}_p(E)}{2}} Y(A_i) = Const. \tag{7}$$

This equation suggests that the sum of independent fission yields of nuclides with large mass number is fixed. The sensitivity vector $\boldsymbol{G}$ in this case is 0 for nuclides with small mass number and 1 for nuclides with large mass number.

For the diagonal component of $\boldsymbol{V_{em}}$ for the condition (A), variance of the cumulative fission yields in JENDL/FPY-2011 are used. Note that non-diagonal components of $\boldsymbol{V_{em}}$ are 0 since no correlation is assumed among different chain yields. For the conditions (B) to (E), $\boldsymbol{V_{em}}$ are set as 0.01 % since these conditions should be strictly preserved.

In all the conditions, we assume $\widetilde{\boldsymbol{R}} = \boldsymbol{R}(\boldsymbol{T_0})$, so independent fission yield itself is not updated and only covariance matrix is updated in the present calculation. On the other hand, it is possible to give a condition that, for example, Eq. (7) becomes 2.0, but in such a case, it is not guaranteed that $\boldsymbol{T}$ becomes identical to $\boldsymbol{T_0}$.

3. Numerical Test

Independent fission yields of 23 fissile nuclides shown in Table I are considered in the present study. All the data are taken from JENDL/FPY-2011. Covariance matrix of these fission yield data are updated, and then using the updated covariance matrix, uncertainties of FP nuclides number densities after burnup in UO2 fuel with a uranium enrichment of 4.1 wt% and MOX fuel are calculated. The burnup is 45 GWD/t, and the number of target FP nuclides is 92.

All the calculations are carried out with a reactor physics code system CBZ, which is under development at Hokkaido University. Nuclear data-induced uncertainties of nuclides number densities after burnup are quantified by the so-called sandwich formula with sensitivities of nuclides number densities with respect to nuclear data. These sensitivities are calculated by a Burner module for pin-cell burnup calculations. In the Burner module the depletion perturbation theory considering spatial dependence is implemented [5]. Fuel burnup calculations are carried out with 107-group cross sections and a detailed burnup chain consisting of 1,400 fission product nuclides which are defined in JENDL/FPY-2011. Sensitivities of number densities of concerned 92 nuclides to half-lives, decay branching ratios and fission yields of all the fission product nuclides are calculated by the Burner module. For the sensitivity analysis of burnup calculation, the implicit effect has not been considered.

Table I. Fissile materials

Th-232	Pa-231	U-232	U-233	U-234
U-235	U-236	U-237	U-238	Np-237
Pu-238	Pu-239	Pu-240	Pu-241	Pu-242
Am-241	Am-242m	Am-243	Cm-242	Cm-243
Cm-244	Cm-245	Cm-246		

(With underline: fast fission Others: thermal fission)

4. Numerical Result

4.1 Changes in uncertainty due to correlation

Although the independent fission yield should be considered for correlation in nature, it is necessary to quantify the correlation in some way because it is not given in evaluated nuclear data files. Figure 2 shows FP nuclides number density uncertainty for two cases when the correlation of independent fission yield covariance is taken into account and not taken into account in the case of UO2 fuel at 45 GWD/t. Correlation is considered by Katakura's method. Forty-six (half of 92) nuclides are shown here due to page limitations. It is possible to confirm that the uncertainty decreases when considering the correlation among all the target FP nuclides [3].

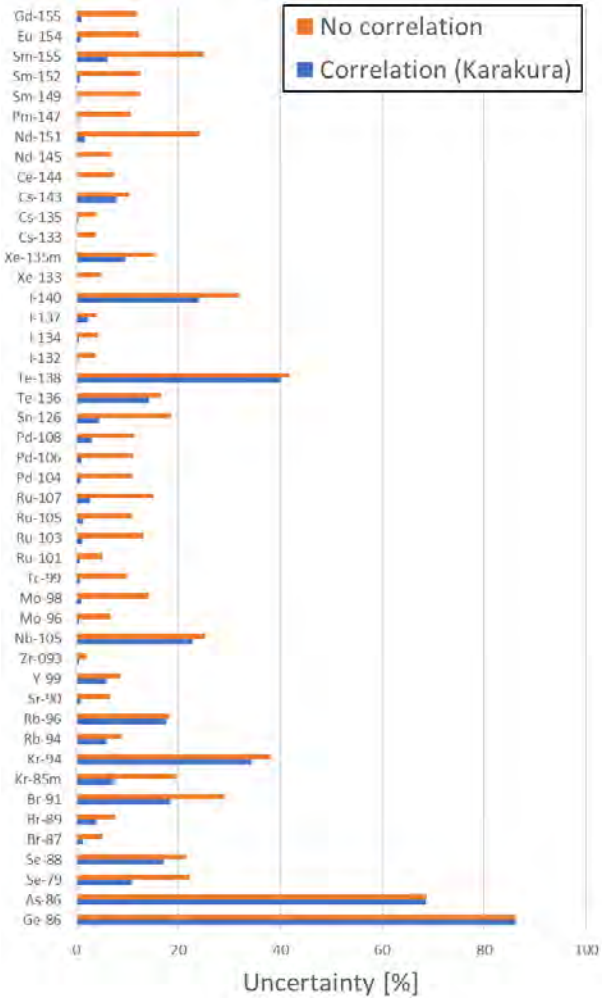

Fig. 2. FP nuclides number density uncertainty of UO2 at 45 GWD/t

4.2 Uncertainty difference due to covariance matrix generating method

The difference in the uncertainty of the FP nuclides number density after burnup using the conventional Katakura's method and the GLS method is shown in Fig. 3. The values in Fig. 3 are the results of difference between the GLS method and Katakura's method. As Fig. 2, forty-six (half of 92) nuclides are shown. According to Fig. 3, when using the GLS method, it can be seen that the uncertainty tends to increase. Furthermore when it increases, the difference is up to about 12 % in the case of MOX fuel. Also, looking at the difference due to fuel, the tendency of increase or decrease in uncertainty does not change, but there is a difference in degree.

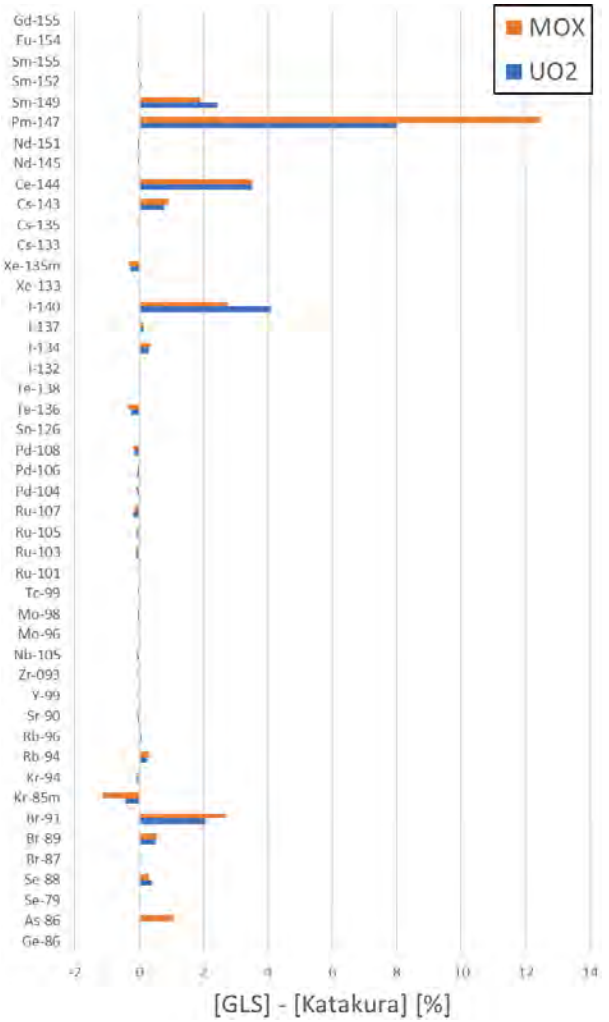

Fig. 3. Uncertainty difference due to adjustment method at 45 GWD/t

4.3 Impact assessment of each step in the GLS method

Figure 4 shows the contribution to FP nuclides number density uncertainty for every five steps in the GLS method in U-235 thermal fission case. Although the reduction effect of each step differs depending on the nuclide, it can be seen that the reduction effect of (A) chain yield condition is the largest. As shown in the reference [3], it is dominant that the influence of the (A) chain yield condition to update the covariance matrix.

4.4 Comparison of correlation coefficient by covariance matrix generation method

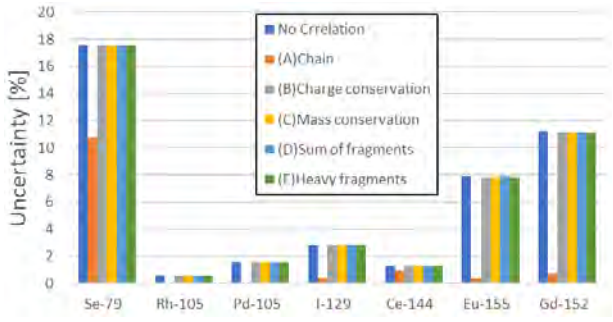

Fig. 4. Uncertainty reduction effect per step at U-235 thermal fission

The target is Ce-144, which has a relatively large difference between the two methods in Fig. 3, and the nuclide is important nuclide in the passive gamma method. Focusing on the sensitivity to fission yield of the nuclides number density after burnup, it is possible to grasp the difference due to the adjustment method by confirming the correlation coefficient matrix of the independent fission yields of the nuclides having relatively larger sensitivity. Table II describes the names of nuclides with a sensitivity of 1.0 % or more for Ce-144 nuclides in U-235 thermal fission yield. In Ce-144, all sensitive nuclides have the same mass, and it becomes Cs-144 → Ba-144 → La-144 → Ce-144 by a series of β^- decay. The adjusted correlation coefficient matrix of nuclides with these sensitivities is shown in Table II. Table III (a) and (b) show the result of the conventional Katakura's method and the GLS method, respectively. The GLS method weakens all negative correlations other than the correlation coefficient of each nuclide itself as compared with Katakura's method. In particular, the correlation coefficient between Ba-144 and La-144 is -0.805 in Katakura's method and -0.199 in the GLS method. This indicates that the negative correlation is significantly weakened.

Table II. Sensitivity of certain nuclides fission yield to Ce-144 fission yield in U-235 thermal fission

FP	Cs-144	Ba-144	La-144
Sensitivity	0.0384	0.3770	0.1010

Table III. Specific correlation coefficient matrix of U-235 fission yield after adjustment for Ce-144

(a) Katakura's method case

	Cs-144	Ba-144	La-144
Cs-144	1.000	-0.281	-0.103
Ba-144		1.000	-0.805
La-144			1.000

(b) The GLS method case

	Cs-144	Ba-144	La-144
Cs-144	1.000	-0.073	-0.037
Ba-144		1.000	-0.199
La-144			1.000

5. Conclusion

The new evaluation method of covariance matrix of independent fission yields has been introduced. Furthermore, the burnup calculation has been performed using the result given by the new method. As a result of comparing the evaluation methods, the uncertainty of FP nuclides number density after burnup have varied depending on the nuclides. In particular, when increasing, some have exceeded 10 % or more. In this work, calculations have been performed using the pincell system as an initial study, but in the future, it will be necessary to perform calculations close to reality, such as calculation of fuel assemblies, for evaluation.

Acknowledgements

This work was supported by the Nuclear Regulation Authority (NRA). Authors thanks to Dr. Toshihisa Yamamoto and Dr. Tatsuya Fujita for their helpful advices on this work.

References

1. Nihira S, Chiba G, "Uncertainty Quantification of Nuclides Number Densities after Fuel Depletion by Random Sampling Method," *Proc. Reactor Physics Asia 2017 Conference, RPHA2017*, Chengdu, China, Aug. 24-25, 2017 (2017).
2. Katakura J, "JENDL FP decay data file 2011 and fission yields data file 2011." JAEA-Data/Code 2011-025, Japan Atomic Energy Agency, (2012).
3. Fiorito L, et al., "Generation of Fission Yield Covariances to Correct Discrepancies in the Nuclear Data Libraries." *Ann. Nucl. Energy*, **88**, 12 (2016).
4. Dragt, JB, et al., "Methods of adjustment and error evaluation of neutron capture cross sections; application to fission product nuclides." *Nucl. Sci. Eng.* **62**, 117 (1977).
5. Chiba G, et al., "Development of a fuel depletion sensitivity calculation module for multi-cell problems in a deterministic reactor physics code system CBZ." *Ann. Nucl. Energy,* **96**, 313 (2016).

Proceedings of the Reactor Physics Asia 2019 (RPHA19) Conference
Osaka, Japan, Dec. 2-3, 2019

Application of Surrogate Modeling with Singular Value Decomposition for Design Basis Accident aiming Statistical Safety Analysis

Masaki Matsushita[a,*], Tomohiro Endo[a] and Akio Yamamoto[a]
[a]*Nagoya University, Furo-cho, Chikusa-ku, Nagoya-shi, 464-8603, Japan*
[*]Corresponding author: m-matsushita@fermi.energy.nagoya-u.ac.jp

Abstract

This study aims to reduce the computational cost by an accident analysis code (e.g., RELAP5/SCDAPSIM, MAAP, MELCORE) for statistical safety analysis. In order to reduce the computational cost, this study applies the reduced order modeling (ROM) with the singular value decomposition and the low-rank-approximation to time-series data obtained by a safety analysis code. Applying the ROM to the time-series data of RELAP5/SCDAPSIM, statistical safety analysis is carried out by the ROM instead of many RELAP5/SCDAPSIM calculations. This paper applies the ROM to the load rejection accident with an open failure of the turbine bypass valve for BWR, which is categorized as a design basis accident. The result of statistical safety analysis by ROM is almost consistent with that by RELAP5/SCDAPSIM. Therefore, statistical safety analysis by ROM is revealed applicable with reduction of calculations by RELAP5/SCDAPSIM from 1,000 to 135 in this study.

Key Words: **Statistical Safety Analysis**, **Singular Value Decomposition, Reduced Order Modeling, RELAP5/SCDAPSIM, Design Basis Accident, Load Rejection of BWR**

1. Introduction

This study presents the application of a surrogate model for the load rejection with an open failure of the turbine bypass valve, which is categorized as a design basis accident for BWR aiming statistical safety analysis.

After the severe accident at Fukushima Daiichi nuclear power plant in March 2011, the safety for nuclear power plant has been reaffirmed as the highest priority. In order to evaluate the safety, statistical safety analysis is carried out. In the statistical safety analysis, the uncertainty should be evaluated by calculations of a safety analysis code (SA-code). In general, random sampling can be used for the estimation of uncertainty. However, enormous number of samples is necessary for accurate prediction of the uncertainty, resulting in increase of the computational cost. Therefore, development of the surrogate model, which can rapidly reproduces the results of a SA-code, is desirable to evaluate the uncertainty through random sampling.

The reduced order modeling (ROM) with the singular value decomposition (SVD) and the low-rank-approximation (LRA) was developed in the previous study in order to reduce the computational cost for probabilistic safety margin analysis using a severe accident analysis code [1]–[2]. In the previous study, the ROM method is applied to the station black out with total loss of feedwater capabilities, which is categorized as a severe accident, to evaluate core damage frequency with a small computational cost. However, there are many accident scenarios in nuclear power plants. Therefore, it is desirable that the applicability of the proposed ROM method will be confirmed for various accident scenarios.

The purpose of this study is to apply the proposed ROM theory to a design basis accident (the load rejection with an open failure of the turbine bypass valve in a BWR) and to show the applicability of ROM for the statistical safety analysis.

2. Outline of ROM theory

This section briefly explains the concept of ROM with SVD and the application procedures of the ROM to the results of a SA-code.

2.1 Concept of ROM with SVD and LRA

The technique of SVD is widely used in the engineering field (*e.g.*, image compression and so on). SVD can decompose a matrix **A**, which consists of row vectors $\vec{a}_n$ $(1 \le n \le m)$, into three matrices as:

$$\mathbf{A} = \begin{pmatrix} \vec{a}_1 \\ \vec{a}_2 \\ \vdots \\ \vec{a}_m \end{pmatrix} = \mathbf{U}\mathbf{\Sigma}\,{}^{\mathrm{T}}\mathbf{V}, \qquad (1)$$

where $\mathbf{U} = (\vec{u}_1, \vec{u}_2, \dots, \vec{u}_m)$, $\mathbf{\Sigma} = diag(\sigma_1, \sigma_2, \dots, \sigma_m)$

and ${}^{\mathrm{T}}\mathbf{V} = {}^{\mathrm{T}}(\vec{v}_1, \vec{v}_2, \ldots, \vec{v}_t)$ contain the left singular vectors, the singular values, and the right singular vectors, respectively ($m \leq t$). By using these matrices with LRA, $\vec{a}_n$ in the matrix **A** is expressed as:

$$\begin{aligned} \vec{a}_n &= \sum_{i=1}^{m} u_{ni}\sigma_i \, {}^{\mathrm{T}}\vec{v}_i \\ &\approx \sum_{i=1}^{k} u_{ni}\sigma_i \, {}^{\mathrm{T}}\vec{v}_i, \end{aligned} \tag{2}$$

where k is the number of singular values considering in ROM ($m \gg k$), which is determined by a criterion (*e.g.*, the cumulative contribution ratio or the scree plot [3]); u_{ni} and σ_i is the the n-th element of i-th left singular vector and the i-th singular value, respectively. The above description also holds true for $m > t$.

From Eq. (2), any $\vec{a}_n$ in the matrix **A** can be expanded by linear combinations of representative right singular vectors. In other words, SVD and LRA can generate the dominant vectors, which cover overall characteristics of the matrix **A**. This property contributes modeling of the time-series results obtained by a SA-code [1].

2.2 Application of ROM to accident analysis results

A safety analysis code considers many input parameters due to the sophisticated modeling of physical phenomena that occurs in the accidents. Each input parameter should be ranked in the view of sensitivity for the accident in order to clarify the effect of input parameters. Therefore, preliminary sensitivity analyses of input parameters are desirable before construction of ROM. The number of sampling should be increased as the sensitivity of the input parameter becomes larger in order to accurately capture the effects of the input parameter for the analysis result.

The application procedures of the present method are as follows:

1. Sample *m* input parameters and perform *m* calculations by a SA-code The input parameters and the results are used to construct ROM.
2. Construct matrix **A** as shown in Eq. (1). Numbers of rows and columns are "the number of samples (*m*)" and "the number of time-steps in an analysis result (*t*)", respectively.
3. Apply LRA to matrix **A** after SVD. Then matrix **A** is decomposed as:
$$\mathbf{A} \approx \mathbf{U}'\mathbf{\Sigma}' \, {}^{\mathrm{T}}\mathbf{V}', \tag{3}$$
where $\mathbf{U}' = (\vec{u}_1, \vec{u}_2, \ldots, \vec{u}_k)$, $\mathbf{\Sigma}' = diag(\sigma_1, \sigma_2, \ldots, \sigma_k)$ and ${}^{\mathrm{T}}\mathbf{V} = {}^{\mathrm{T}}(\vec{v}_1, \vec{v}_2, \ldots, \vec{v}_k)$. The m simulation results are expanded using the right singular vectors obtained by SVD. (Eq. (2))
4. Set functions from correlation among the expansion coefficients $\vec{\beta}_i$ and input training data, where $\vec{\beta}_i$ is calculated by the left singular vectors and the singular values:
$$\begin{aligned} \boldsymbol{\beta} &= \mathbf{U}'\mathbf{\Sigma}' \\ &= \left(\vec{\beta}_1 \, \vec{\beta}_2 \, \cdots \, \vec{\beta}_i \, \cdots \, \vec{\beta}_k\right) \\ &= \begin{pmatrix} u_{11}\sigma_1 & u_{12}\sigma_2 & \cdots & u_{1k}\sigma_k \\ u_{21}\sigma_1 & u_{22}\sigma_2 & \cdots & u_{2k}\sigma_k \\ \vdots & \vdots & \ddots & \vdots \\ u_{m1}\sigma_1 & u_{m2}\sigma_2 & \cdots & u_{mk}\sigma_k \end{pmatrix}, \end{aligned} \tag{4}$$
Each element in the expansion coefficient $\vec{\beta}_i$ is represented by a function of input data used for training.
5. For "p" input parameter, which is not included in input data for training, the expansion coefficients $u_{pi}\sigma_i$ can be calculated by the function obtained in Step 4.
6. The time-series result for "p" input parameter can be predicted by the expansion coefficients obtained in Step 5 and the orthogonal basis ${}^{\mathrm{T}}\vec{v}_i$ as:
$$\vec{p} \approx \sum_{i=1}^{k} u_{pi}\sigma_i \, {}^{\mathrm{T}}\vec{v}_i, \tag{5}$$

3. Calculation Conditions

3.1 Safety analysis code and plant model

The RELAP5/SCDAPSIM code and the plant model of Lagna Verde Unit 1 and 2 (rated power: 1931MWth), which is BWR-5 designed by General Electric company, in Mexico are used.

3.2 Accident scenario

The accident scenario is the load rejection with an open failure of the turbine bypass valve. At $t = 0$ s, plant is a stable condition. However, the load rejection of turbine generator occurs at $t = 10$ s due to its failure or the mismatch between demand and supply, and so on. Then the turbine governor valve rapidly closes to protect turbine followed by the failure of turbine bypass valve to open. Therefore, the primary pressure rapidly increases resulting collapse of void in the core. Thus, plant power rapidly increases due to the void reactivity insertion. When the neutron flux exceeds 120% (relative value to rated power), the SCRAM signal is automatically dispatched. The accident is successfully terminated due to the negative Doppler feedback and the large negative reactivity by SCRAM.

In the above scenario, MCPR (Minimum Critical Power Ratio) is an important parameter in order to judge the integrity of the fuel. However, RELAP5/SCDAPSIM cannot evaluate MCPR due to the limitation of modeling. When power increases by reactivity insertion, the maximum heat flux in the core will become closer to the critical heat flux and MCPR has correlation with core power. From this consideration, the relative core power is used instead of MCPR in this study.

The total simulation time for the load rejection accident scenario is 30 seconds. The number of the time steps is 30 because the time step size of one second is applied to edit the results. The time-step size in RELAP5/SCDAPSIM calculations is automatically varied from 10^{-7} to 0.1 seconds.

3.3 Perturbed input parameters

Among many input parameters that have a significant/considerable effect in the load rejection accident, the uncertainty of reactivity parameters related to neutronic calculation (void, Doppler, and SCRAM reactivity) are considered due to their impact on the results. In this study, the uncertainty (1σ) of all input parameters is assumed as 10%, where it is known that the actual uncertainty would be around approximately 10 %. These reactivities are perturbed as Figures 1–3. The values of reactivities are based on those of typical BWRs and the perturbations are performed by multiplying a perturbation factor to reactivity. For ROM construction, the perturbation range of input parameters is $\pm 20\%$ to cover the uncertainty of input parameters within 2σ.

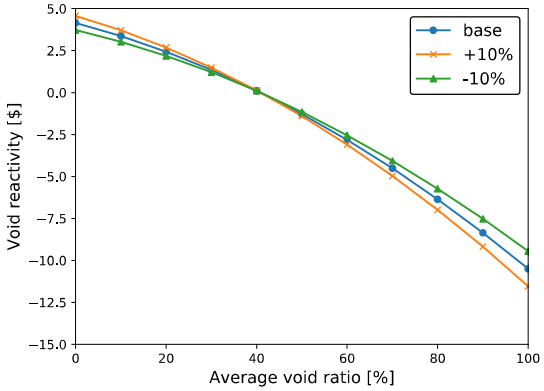

Fig. 1. The perturbation of void reactivity.

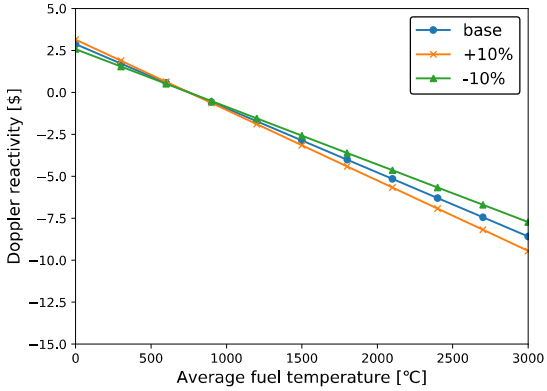

Fig. 2. The perturbation of Doppler reactivity.

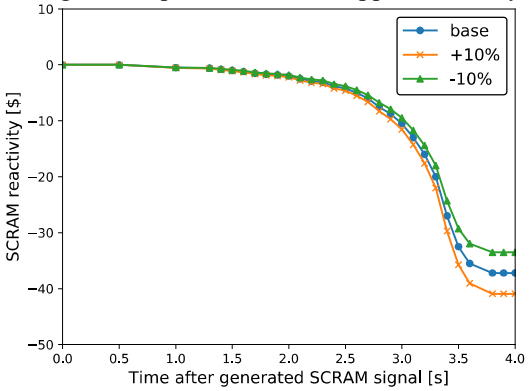

Fig. 3. The perturbation of SCRAM reactivity.

3.4 Procedures of ROM construction

The actual calculation procedures of ROM construction are as follows:

1. Perform sensitivity analysis of input parameters for the result obtained by RELAP5/SCDAPSIM (Eq.(6)). The sensitivity becomes smaller in the order of the void, SCRAM, and Doppler reactivity.
$$\frac{\Delta max\{f(x)\}}{\Delta x} \approx \frac{max\{f(base+\sigma_x)\} - max\{f(base)\}}{\sigma_x}, \quad (6)$$
where x is the input parameter (i.e., reactivity), f is a function of RELAP5/SCDAPSIM, and σ_x is the uncertainty of x.
2. The range 2σ of input parameters are divided into equal width based on Step 1. The void, SCRAM, and Doppler reactivity are divided into nine, five, and three, respectively.
3. By using $135\,(=9\times5\times3)$ combinations of input parameters, perform calculations of RELAP5/SCDAPSIM.
4. The input parameters and results are used to construct ROM. (Section *2.2.*) Note that the LinearNDInterpolator function of the Scipy package [4], which is the linear interpolation method, is used to estimate the expansion coefficient in ROM.
5. The number of k, which is the number of truncated bases in LRA, is determined by the scree plot, which is a criterion in the principal component analysis. In this analysis, $k = 27$ is used for ROM.

3.5 Procedures of statistical safety analysis

In order to validate the statistical safety analysis by ROM, the uncertainties of maximum power during the transient calculated by RELAP5/SCDAPSIM and ROM are compared. The procedures are described as follows:

1. Perform 1,000 times random sampling of input parameters. When the sampled values exceed the range of 2σ, resampling is performed since the range of input parameters covered by ROM is within 2σ and the extrapolation by ROM has low accuracy.
2. By using the 1,000 input parameters, ROM and RELAP5/SCDAPSIM calculations are carried out. Note that the identical input parameters are given for ROM and RELAP5/SCDAPSIM.
3. The average and the standard deviation of the ROM and RELAP5/SCDAPSIM results are estimated. Furthermore, the Pearson's correlation coefficient between ROM and RELAP5/SCDAPSIM results are also evaluated.

4. Results

Figure 4 shows the time-series data of core power in the base case, in which no uncertainty is considered for all reactivities. Figure 5 shows the histogram of the maximum power on output training data. ROM is constructed by using these 135 input and output training data.

Figure 6 and Table I show the comparison of

uncertainty estimated by ROM and RELAP5/SCDAPSIM. From Fig. 6, the maximum power estimated by ROM can approximately reproduce that by the RELAP5/SCDAPSIM. From Table I, ROM also can reproduce the average and the standard deviation obtained by many RELAP5/SCDAPSIM calculations. ROM results well reproduce those of RELAP5/SCDAPSIM.

However, there is a small difference between ROM and RELAP5/SCDAPSIM in Fig. 6 though identical input parameters are used. There are two possible reasons for the difference: 1. the lack of input training data to learn the behavior of the expansion coefficients and 2. the error of linear interpolation to estimate the expansion coefficients.

As a result, the reduction of computational cost by ROM will be possible. In this paper, the number of calculations by RELAP5/SCDAPSIM decreases from 1,000 to 135.

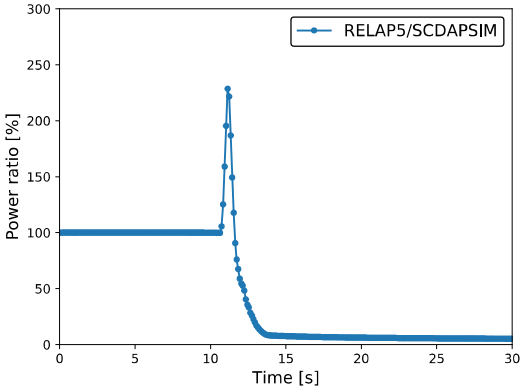

Fig. 4. Time-series data of power ratio in the base case.

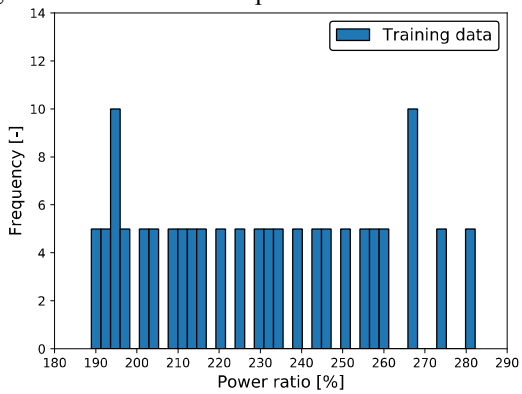

Fig. 5. The histogram of the maximum power for output training data (135 samples).

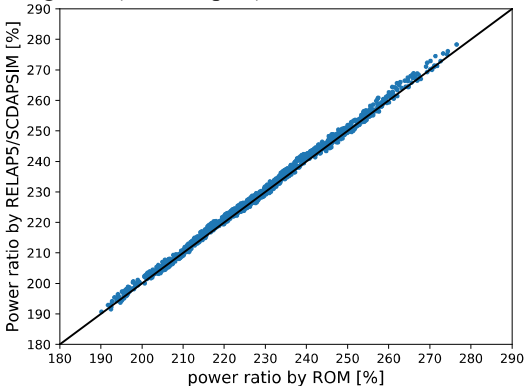

Fig. 6. Comparison of the maximum power between ROM and RELAP5/SCDAPSIM using 1,000 samples.

Table I. Comparison of average and standard deviation of maximum power during the transient. The correlation coefficient is also shown.

	ROM	RELAP
Average [%]	229.1	229.8
Standard deviation [%]	18.8	18.9
Correlation coefficient	0.999	

6. Conclusions

This study aims to reduce the computational cost by a SA-code for statistical safety analysis. In order to reduce the computational cost, the ROM is developed with SVD and LRA for time-series data obtained by a SA-code.

In this paper, ROM is constructed to estimate the maximum power in the load rejection accident for a BWR with an open failure of the turbine bypass valve, which is categorized as a design basis accident. The input parameters related to feedback and reactivity, which strongly affects the core power, is considered for the source of uncertainty. The reduction of computational cost by ROM will be possible since the maximum core power calculated by ROM is consistent with those by RELAP5/SCDAPSIM.

The following issues are considered as future problems; consideration of actual uncertainties in random sampling, consideration of additional input parameters for random sampling, and application to the other accident scenarios.

Acknowledgments

The RELAP/SCDAPSIM used in this study has been introduced by the funding of Nuclear Regulatory Authority (NRA) for the educational program of nuclear regulation and nuclear safety.

References

1. Matsushita M, Endo T, Yamamoto A, Kitao T, “Development of Reduced Order Model of Severe Accident Code for Probabilistic Safety Margin Analysis,” *Proc. PHYSOR 2018*, Cancun, Mexico, April 22–28, 2018, American Nuclear Society (2018) (USB).
2. Matsushita M, Endo T, Yamamoto A, “Surrogate Model of Severe Accident Analysis Code for SBO Aiming Probabilistic Safety Margin Analysis,” *Trans. Am. Nucl. Soc.*, **119**, p. 900, American Nuclear Society (2018).
3. Cattell RB, “The Scree Test for the Number of Factors,” *Multivariate behavioral research*, **1**, 2, p. 245, (1966).
4. “Scipy.org,” https://docs.scipy.org/doc/scipy/reference/generated/scipy.interpolate.LinearNDInterpolator.html?highlight=linearnd#scipy.interpolate.LinearNDInterpolator (access: 2019/5/21).

TS-08 Multiphysics Power Reactor Simulations

Proceedings of the Reactor Physics Asia 2019 (RPHA19) Conference
Osaka, Japan, Dec. 2-3, 2019

Preliminary Performance Assessment of the GPU Acceleration Module in a Pinwise Core Thermal Hydraulics Code ESCOT

Kyung Min Kim, Namjae Choi, Jaejin Lee, and Han Gyu Joo*
Seoul National University, 1 Gwanak-ro, Gwanak-gu, Seoul, 08826, Korea
*Corresponding author: skstr3182@snu.ac.kr

Abstract

Even though there have been significant advances in CPU computing power, whole-core multi-physics calculations still remain impractical for the industrial applications. Furthermore, as the development of the CPU technology is being challenged nowadays, heterogeneous computing is emerging as an alternative. This work suggests a strategy to accelerate pin-wise sub-channel T/H calculations on GPUs, which involves the solutions of linear systems, the manipulation of the equation of state, and the setup of the linear systems for the various components of the governing equations. A group of GPU acceleration methods were implemented in a drift-flux model based pin-wise sub-channel T/H code, ESCOT, which is being developed at Seoul National University. The performance results obtained with 4 GPUs for a OPR1000 quarter core appear comparable with the parallel calculation employing 104 CPU cores. It is demonstrated that even consumer-grade commercial GPUs can be used as an effective means in the sub-channel T/H calculation.

Key Words:
drift flux model, GPU, pressure equation, equation of state, BiCGSTAB

1. Introduction

As the CPU processing power had increased rapidly over the past decades, numerical solutions with higher resolutions and fewer approximations became more affordable and employable. In the reactor physics field, it had enabled whole-core multi-physics calculations by combining a high-fidelity neutronics code and a subchannel thermal-hydraulics (T/H) code. Current mainstream codes, which are CPU-based, include DeCART [1] coupled with MATRA [2], MPACT [3] coupled with COBRA-TF (CTF) [4], and nTRACER [5] coupled with ESCOT [6].

However, as the CPU technology faces the limitations due to the power consumption issue, researchers are now paying more attention to deploying heterogeneous computing powered by Graphics Processing Units (GPU) to achieve even higher performance. And so far it has succeeded in many computational physics fields. In keeping with this, nTRACER had also established a plan to offload entire core follow processes onto GPU. So far the neutronics solver has shown significant improvements in performance over the traditional CPU-based approach [7].

Therefore, as the next step, this research aims at extending the GPU acceleration capability of nTRACER to actual operational conditions that include T/H feedbacks. In order to achieve this goal, the GPU acceleration of the pin-wise core T/H code ESCOT is to be carried out. Especially, this paper focuses on optimizing the pressure equation solution, the evaluation of IAPWS-IF97 [8] steam table formulations, and the setup of linear system which had been the major challenges.

2. Scope of Research

Even though there exist efficient algorithms for massive parallelization of whole-core calculations on many-core systems, such systems are not yet practically affordable. Therefore, we continue to focus on planar decomposition strategy which, we think, is still an effective approach for practical whole-core calculations. Instead, we introduce GPUs to overcome the limitation of computing resources in a cost-effective way.

We expect that a moderate-sized cluster, which contains a dozen of nodes with multiple commercial GPUs in each node, will be affordable to most research and user groups, and we are focusing on developing algorithms that are most efficient for such small systems. Currently, we are building the *Soochiro 4* cluster in SNU, which is a representative form of our oriented system:

Table I. Specifications of the *Soochiro 4* cluster

# of Nodes	6
CPU	2 × Intel Xeon E5-2630 v4 20 Cores, 2.4 GHz (Boost)
GPU	4 × NVIDIA GeForce GTX 1080

Memory	8 × 16GB DDR4 RAM
Interconnect	Infiniband (56 Gbps)

To maximize the performance of multi-physics whole-core calculation in such small systems, tandem approach is favorable as in Fig. 1. Neutronics calculation requires binding each plane to a GPU, which will occupy most of the available nodes. If the T/H calculation can be carried out as fast as the neutronics iteration using the remaining resources, the T/H time can be fully hidden behind the neutronics time by the tandem manner.

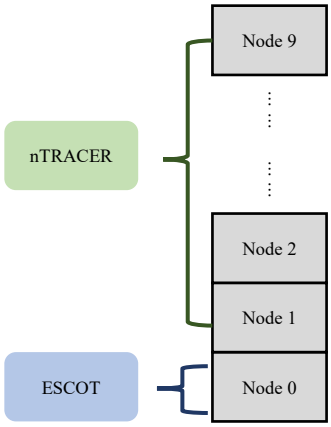

Fig. 1. Topology for the multi-physics simulation in tandem manner.

Therefore, this research targets to accelerate ESCOT code using only a single node to minimize the overhead from the T/H calculation by employing the tandem scheme.

3. Optimization Process

In this paper, only brief introductions and optimization strategies for the major bottleneck operations are presented. Full physical backgrounds and implementation schemes of ESCOT are explained in [6].

3.1 Pressure Equation

SIMPLEC [9] algorithm incorporates specific enthalpy, void fraction, and pressure to construct a linear system at a certain calculation node *(I,J)*. Of these three scalar quantities, the pressure linear system, which is solved every outermost iteration, has the form:

$$\left[1+\sum_{nb} b''_{nb}\right] P^{n+1}_{I,J} - \sum_{nb} b''_{nb} P^{n+1}_{nb} = s'_3 \quad , \tag{1}$$

where

b''_{nb} = coefficients for each pressure elements

$P^{n+1}_{I,J}$ = next time pressure of the node (I,J)

s'_3 = source element.

The coefficient matrix is septa-diagonal. Its diagonal dominance is very weak because the off-diagonal terms are much greater than unity. The CPU-based ESCOT employs BiCGSTAB in the PETSc [10] library by default.

Meanwhile, GPUs can exert their maximum performance when employing single precision units. BiCGSTAB algorithm, however, contains a couple of inner products and matrix-vector multiplications in each iteration, and single precision suffers from round-off errors in those reduction operations due to the ill-conditioned linear system. Therefore, several methods and preconditioners were investigated to replace or enhance BiCGSTAB, and solve the equation through the iterative refinement [7], but all of them failed or showed extreme performance degradation as follows:

Table II. Solutions tested using the iterative refinement

Solver	Preconditioner	Convergence
BiCGSTAB	ILU0	Converged
	SPAI [11]	Diverged
AAJ [12]		Converged Not feasible
AMG [13]		Diverged
BiCGSTAB(*l*) [14]		Diverged
IBiCGSTAB [15]		Diverged

As in Table II, all the attempts failed to converge except AAJ and BiCGSTAB with ILU0 preconditioner. However, the ILU0 preconditioner cannot be parallelized, because of the forward and backward substitutions. In addition, AAJ takes too much time to fully converge. So, it was determined that AAJ and BiCGSTAB with the ILU0 preconditioner are not practical to apply.

As a consequence of the investigation, it was confirmed that double precision approach to the pressure equation is indispensable. That being so, it became a main objective to optimize the double-precision BiCGSTAB so that the algorithm becomes the best-suited on GPU, instead of implementing new solvers or preconditioners. As follows are the conclusions of the optimization research:

(1) ELLPACK matrix format is much better than Compressed Sparse Row (CSR) format for the highly structured pressure equation matrix.
(2) BiCGSTAB with Jacobi (diagonal) preconditioner, which can be applied in parallel, outperforms BiCGSTAB without a preconditioner.
(3) All the linear algebra routines operating for the pressure matrix on GPUs are memory-bounded, so double precision calculations are only twice slower than single precision counterparts.

In the new BiCGSTAB solver, collective operations like inner products and l^2-norm are taken from CUBLAS, and the ELLPACK format matrix-vector multiplication and element-wise vector operations are implemented by manually tuned kernels.

3.2 Equation of State

ESCOT sets the mixture velocity, void fraction, specific enthalpy, and pressure as primary variables. Among these, mixture velocity and pressure are

calculated from solving each linear system, and the rest are solved for each calculation node. On the other hands, the other variables are designated as the secondary ones, which are determined by the equation of state (EOS) using the IAPWS-IF97 steam table. IAPWS-IF97 classifies the steam regions according to pressure and temperature, described in Fig. 2.

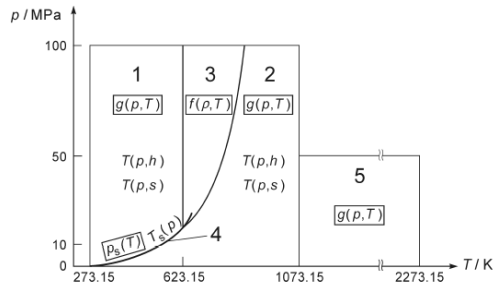

Fig. 2. Steam regions specified in IAPWS-IF97.

In real implementation, property functions require not only the base properties, but also the steam region of the properties. The region 1 and 2 are typical subcooled liquid and superheated vapor, but the region 3 is between the region 1 and 2, most of which is in the critical state and so algorithms are much more complex. The quantities in the region 1 and 2 consist of a set of multiple functions, in which dimensionless Gibbs free energy is calculated from expansions of polynomials, so it is one of the major calculation burdens.

In fact, since the EOS calculation is independent between meshes, coalesced access can be achieved, so it is suitable for the parallel execution scheme of GPUs. Moreover, IAPWS formulation for the steam table is a compute-intensive task, because it contains expansion of high order polynomials, which is also proper for GPUs. Although the steam table requires steam region of each calculation node, ESCOT utilizes and requires both liquid and vapor quantities and specifies the steam region, and therefore it is obvious that branch divergence barely occurs in the EOS procedure.

3.3 Linear System Setup

In the ESCOT algorithm, there are 4 linear systems that are set up every outer iteration, which are the axial and the radial momentum equations, the pressure equation and the scalar equation. For realistic problems, the number of the outer iterations is a hundred or over. Therefore, it is a severe burden unless hundreds of cores are employed in terms of the domain decomposition.

The linear system setup procedures, alike the EOS, are inherently independent between the meshes. However, in contrast to the EOS, they need much larger data than the EOS routines. Therefore, prefetch of global memory to each thread is done in the first stage and after that, registers are exploited mostly in the calculation to maximize flops.

4. Results and Discussion

Runtime and accuracy are compared between the original CPU-based and GPU-accelerated ESCOT for OPR1000 quarter core problem. In common, BiCGSTAB with the Jacobi preconditioner is used as the linear solver. The examinations were carried out on the *Soochiro 4* cluster, and the calculation conditions are summarized in Table III.

Table III. Calculation conditions

Version	CPU	GPU
# of calculation nodes	370,208 (11569 × 32)	
Compiler	Intel Fortran 17.0.4	PGI Fortran 18.10
Linear solver	Jacobi preconditioned BiCGSTAB (PETSc)	Jacobi preconditioned BiCGSTAB (Manual)
# of processors / devices	52 cores 104 cores	4 GPUs

As previously mentioned, the GPU-accelerated code was run using only a single node while CPU-based one used up all the available CPU cores. The results are summarized in Table IV and Table V. The three main bottlenecks are listed, and the rest are omitted.

Table IV. Time summary of 52 cores and 4 GPUs

Calculation	CPU	GPU	Speedup
Linear system setup	8.15s	3.82s	2.1
Equation of State	18.60s	5.93s	3.1
Solving the pressure equation	24.32s	32.30s	0.8
Total	73.76s	53.70s	1.4

Table V. Time summary of 104 cores and 4 GPUs

Calculation	CPU	GPU	Speedup
Linear system setup	4.21s	3.82s	1.1
Equation of State	9.78s	5.93s	1.7
Solving the pressure equation	15.77s	32.30s	0.5
Total	46.35s	53.70s	0.9

It can be observed that the linear system setup and the EOS procedures are fully parallelized so that they show good speed-up. Therefore, the GPU version outperforms 52 cores and is comparable with 104 cores.

However, in terms of solving the pressure equation, the GPU version could not exceed the CPU-based code even in 52 cores. This is due to cache utilization and memory bandwidth, which are the most notable differences between the two architectures. For the massive parallelization based on CPUs, the matrix is split into a number of small matrices, all of which can be loaded on CPU cache. For example, since the pressure matrix of the OPR1000 problem occupies 20 MiB memory, 52 and 104 cores can split it into 0.4 MiB and 0.2 MiB per processor, respectively, and these magnitudes are sufficiently small to be loaded on cache. However, the parallel strategy based on a couple of GPUs cannot get the data reside in cache, because size of the data is too big.

And in terms of bandwidth, multiple CPU cores are much faster than several GPUs, since all the data reside in cache for CPUs. Although each of cache bandwidth is lower than GPU global memory bandwidth, the memory is loaded through tens of cores for CPU, while only 4 GPUs load the data.

Next, the accuracy of the GPU-accelerated version was examined. Although not explained here, the iterative refinement strategy is employed in solving the axial momentum equation. However, it does not affect the solution as shown in Fig. 3 below. The figure shows the relative difference of outlet density in upper triangular part and outlet temperature in lower triangular part between solutions from CPU single core and 4 GPUs, respectively. It can be observed that magnitude of the relative difference is only 10^{-5}% order at best.

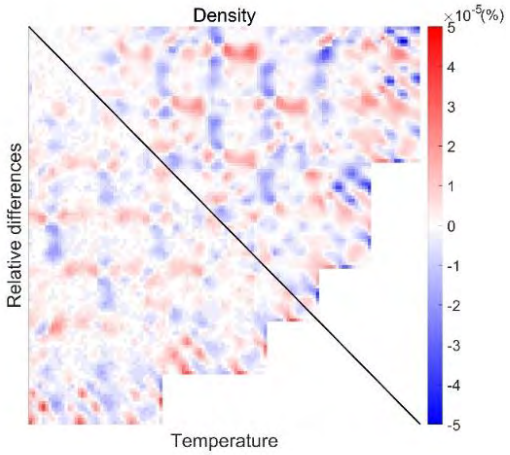

Fig. 3. Relative differences of outlet density and temperature

5. Conclusion

GPU acceleration capability has been implemented in ESCOT. The modules are still under development, so there exist yet under-optimized routines, such as the linear solver. Apart from this, the other main bottlenecks are sufficiently accelerated so that only a single computing node outperforms the many-core CPU performance. Also, the accuracy of the solutions from commercial GPUs were verified.

Still, the poor performance of the manually written BiCGSTAB solver should be enhanced to achieve the ultimate goal of the tandem coupling with the GPU-accelerated nTRACER. There are several ways to resolve it: 1) devising a new solver more proper for GPUs, 2) investigation of preconditioners which can be generated and applied in a parallel way, and significantly reduce the number of BiCGSTAB iterations. In order to carry out these tasks efficiently, the PETSc library will be used, which provides a variety of solvers and preconditioners for the GPU systems. Finishing the tasks will make it available to accomplish a whole-core steady-state calculation including T/H feedbacks within 5 minutes on a moderated-sized GPU cluster.

Acknowledgements

This research is supported by National Research Foundation of Korea (NRF) Grant No. 2016M3C4A795263 (Realization of Massive Parallel High Fidelity Virtual Reactor).

References

[1] J. Y. Cho, S. Yuk, “Massive Parallel Computation for an Efficient Whole Core Transport Calculation,” Transactions of the Korean Nuclear Society Spring Meeting, Jeju, Korea, May 17 - 18.
[2] H. Kwon et al., “Validation of a Subchannel Analysis Code MATRA Version 1.1,” KAERI/TR-5581/2014, Korea Atomic Energy Research Institute, 2014.
[3] B. Kochunas, T. Downar, Z. Liu, “Parallel 3-D Method of Characteristics in MPACT,” International Conference on Mathematics and Computational Methods Applied to Nuclear Science and Engineering, Sun Valley, Idaho, USA, May 5 - 9 (2013).
[4] R. Salko and M. Avramova, "COBRA-TF Subchannel Thermal-Hydraulics Code (CTF) Theory Manual-Revision 0," The Pennsylvania State University, 2015.
[5] Y. S. Jung et al., "Practical numerical reactor employing direct whole core neutron transport and subchannel thermal/hydraulic solvers," Annals of Nuclear Energy, vol. 62, pp. 357-374, 2013.
[6] J. Lee, A. Facchini., H. G. Joo, “Development of a Drift-Flux Model Based Core Thermal-Hydraulics Code for Efficient High-Fidelity Multiphysics Calculation,” Nuclear Engineering and Technology(2019), doi: 10.1016/j.net.2019.04.002
[7] N. Choi, J. Kang, H. G. Joo, “Preliminary Performance Assessment of GPU Acceleration Module in nTRACER,” Transactions of the Korean Nuclear Society Autumn Meeting, Yeosu, Korea, October 25 - 26.
[8] J. R. Cooper, “Revised Release on the IAPWS Industrial Formulation 1997 for the Thermodynamic Properties of Water and Steam,” International Association for the Properties of Water and Steam Publication, 2012.
[9] J. P. Van Doormaal, G. D. Raithby, “Enhancement of the SIMPLE Method for Predicting Incompressible Fluids Flow,” Numerical Heat Transfer, vol. no. 2, pp. 147-163, 1984.
[10] PETSc Team, "PETSc Users Manual," ANL-95/11 - Rev. 3.10, Argonne National Laboratory, 2018.
[11] M. J. Grote, T. Huckle, “Parallel Preconditioning with Sparse Approximate Inverses,” SIAM J. Sci. Compute., 18 (3) (1997), pp. 838-853.
[12] P. Pratapa, P. Suryanarayana, J. Pask, “Anderson Acceleration of the Jacobi Iterative Method: An Efficient Alternative to Krylov Methods for Large, Sparse Linear Systems,” Journal of Computational Physics, vol. 306, pp. 43–54 (2016).
[13] R. Gandham, K. Esler, Y. Zhang, “A GPU Accelerated Aggregation Algebraic Multigrid Method,” Computers & Mathematics with Applications, vol. 68, Issue 10, pp. 1151 – 1160, 2014.
[14] G. L. G. Sleijpen, D. R. Fokkema, “BiCGSTAB(L) for Linear Equations Involving Unsymmetric Matrices with Complex Spectrum,” Electronic Transactions on Numerical Analysis, vol. 1, pp. 11 – 32, 1993.
[15] L .T. Yang, R. P. Brent, “The Improved BiCGSTAB Method for Large and Sparse Unsymmetric Linear Systems on Parallel Distributed Memory Architectures,” Proceedings of the Fifth International Conference on Algorithms and Architectures for Parallel Processing, 2002, pp. 324 - 328.

Proceedings of the Reactor Physics Asia 2019 (RPHA19) Conference
Osaka, Japan, Dec. 2-3, 2019

BEAVRS Benchmark Analysis by a Whole Core Transport Code nTER

Ho Jin Park [a,*], Jin Young Cho[a]
[a] *Korea Atomic Energy Research Institute, 111, Daedeok-daero 989beon-gil, Daejeon, 34057, Korea*
[*] *Corresponding author: parkhj@kaeri.re.kr*

Abstract

The BEAVRS benchmark problem was solved by a newly developed whole core transport code, nTER (Neutron Transport Evaluator for Reactor) to verify its code systems through its core follow calculations. The nTER results for control rod worth, radial detector signal, and boron letdown curve during two cycles agree well with the measured data. Therefore, it is concluded that the nTER code is well developed in the terms of the solution accuracy for the high-fidelity nuclear parameter evaluation.

Key Words: **nTER**, **BEAVRS, Verification and Validation, Benchmark**

1. Introduction

A new transport code, nTER (Neutron Transport Evaluator for Reactor) [1], for direct whole core calculations was developed by Korea Atomic Energy Research Institute (KAERI) with the cooperation of Korea Hydro and Nuclear Power Central Research Institute (KHNP CRI). The nTER code uses radial method of characteristics (MOC) transport and the axial P_3 coupled method to obtain high-fidelity transport solutions. Moreover, the nTER code is equipped with up-to-date methodologies such as a radial MOC with anisotropic scattering source, high-performance computation based on node-wise MPI (Message Passing Interface) parallelization. The detailed methodologies and functionality of the nTER code are described in [1]. Recently, the various benchmark calculations such as C5G7 and VERA benchmark have been applied to examine the performance of the nTER code. The Benchmark for Evaluation and Validation of Reactor Simulations (BEAVRS) [2] was proposed by the Massachusetts Institute of Technology (MIT) computational reactor physics group, and this provides detailed specifications and various measurement data such as control rod bank worth, radial detector signal, isothermal temperature coefficients, and critical boron concentration (CBC) during two cycles. The BEAVRS solutions have been reported by various reactor physics codes such as VERA [3], nTRACER [4], SCALE/PARCS [5], MCS [6], and DeCART [7]. For this study, as an extension of the verification and validation (V&V) of the nTER code, a whole-core benchmark analysis for the BEAVRS benchmark was performed.

2. BEAVRS Benchmark Results by nTER

In the BEAVRS benchmark calculations, a ray-spacing of 0.05 cm, 2 polar angles of 90°, and 8 azimuthal angles of 90° were used for nTER MOC calculations. All nTER calculations were conducted with the newly-generated ENDF/B-VII.1 based PV05 47-group cross section library and the sub-group method.

2.1 Hot Zero Power Results by nTER

Table I compares the k_{inf}'s of two codes for fourteen 2D BEAVRS fuel assemblies (FAs), which consist of the BEAVRS cycle 1 and cycle 2 core. The root mean square (RMS) differences of the k_{inf} between the nTER and McCARD [8] reference solutions is about 63 pcm.

Table I. k_{inf} of BEAVRS 2D FA problems

Enri. w/o%	No. BA*	k_{inf} for 2D FA		
		McCARD	nTER	Diff (pcm)
1.6	0	0.99646	0.99749	103
2.4	0	1.13932	1.14043	85
	12	1.01575	1.01537	-37
	16	0.97742	0.97669	-77
3.1	0	1.22135	1.22263	86
	16	1.06547	1.06529	-16
	20	1.02975	1.02945	-29
	6	1.16459	1.16520	45
	15	1.08032	1.08043	9
3.2	0	1.23042	1.23179	17
	4	1.18869	1.18950	90
	8	1.14807	1.14848	57
	12	1.10825	1.10839	31
3.4	0	1.24916	1.25057	11

*BA=burnable absorber

Table II compares the control rod bank worth results by nTER for hot zero power (HZP) condition with the measured values. The benchmark sheets provide the

regulating rod and shutdown bank worth for each configuration. The calculated individual control rod bank worth agrees well with the measured one within 7.3%. Figure 1 shows the tilt-corrected FA-wise detector signal results from nTER. The relative RMS and maximum errors from C11 FA, which is the large tilt position, are 1.8% and 4.8%. Table III shows the isothermal temperature coefficients (ITC). The maximum error of ITC is 1.90 pcm/F°

Table II. Total and individual control rod bank worth

Case	Control rod bank worth (pcm)		
	Measured (M)	nTER (N)	Diff. (%) (M-N)/M
D in	788	784	0.5%
C with D in	1203	1256	-4.4%
B with D, C in	1171	1255	-7.2%
A with D,C,B in	548	508	7.3%
SE with All R in	461	467	-1.3%
Total	4171	4271	-2.4%

	H	G	F	E	D	C	B	A
		0.78	1.07	0.94	1.15	0.94	1.26	0.78
8	0.91	0.75	1.05	0.91	1.15	0.93	1.28	0.78
		-3.3%	-1.3%	-3.1%	0.0%	-1.0%	0.9%	-0.3%
		1.01	0.90	1.14	0.97	1.17	0.87	0.82
9		1.00	0.88	1.14	0.95	1.20	0.86	0.81
		-1.0%	-2.2%	-0.3%	-2.6%	2.7%	-1.1%	-0.6%
			1.14	0.97	1.21	0.98	1.24	0.73
10			1.13	0.96	1.20	0.97	1.28	0.72
			-0.5%	-0.8%	-0.6%	-1.5%	2.9%	-0.5%
				1.25		1.31		0.58
11				1.25	1.06	1.37	0.94	0.59
				0.4%		4.8%		1.3%
		Measured			1.34	1.20	0.96	
12		nTER			1.33	1.20	0.96	
		Diff			-0.8%	0.6%	0.0%	
						0.85	0.70	
13		RMS diff.	1.82%			0.85	0.71	
		Max.	4.84%			-0.2%	1.0%	

Fig. 1. Comparison of assembly-wise tilt-corrected detector signal.

Table III. Isothermal temperature coefficients

Case	Isothermal temperature coefficients (pcm/F°)		
	Measured (M)	nTER (N)	Diff. (M-N)
ARO	-1.75	-3.11	1.36
D in	-2.75	-4.65	1.90
C with D in	-8.01	-9.55	1.54

2.2 Cycle 1 and Cycle 2 Results by nTER

The BEAVRS benchmark provides two different types of boron letdown curves during cycle 1 and cycle 2 operations. One is based on the 100% hot full power (HFP) conditions while the other is based on the detailed calculations with variable parameters in detector measurements based on power history data. Figure 2 presents the 24 hour-averaged power history, time points in detector measurements, and control rod bank D positions for detailed calculations at cycle 1 and cycle 2.

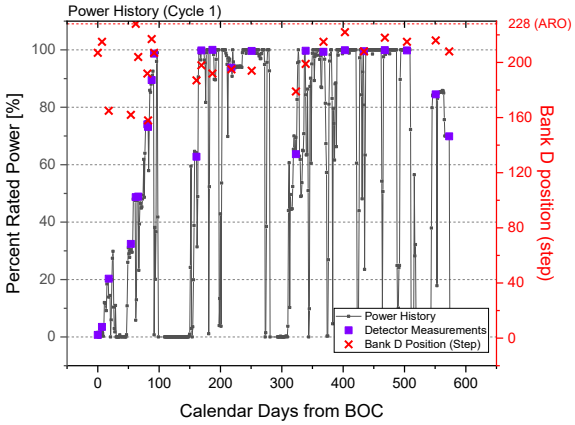

(a) cycle 1

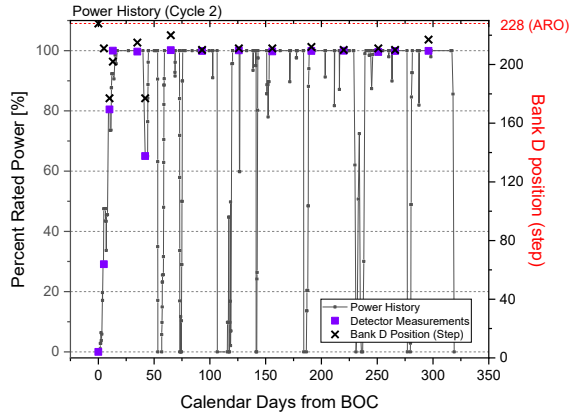

(b) cycle 2

Fig. 2. Power history and control rod bank positions

Figures 3 and 4 show the boron letdown curve calculated by 100% HFP condition. For cycle 1 and 2, the RMS errors of critical boron concentration are 8 and 4 ppm. During two cycles, it was observed that the CBC results from nTER agree reasonably well with the measurements. Figures 5 and 6 show the boron letdown curve calculated by the detailed calculation with variable parameters in detector measurements.

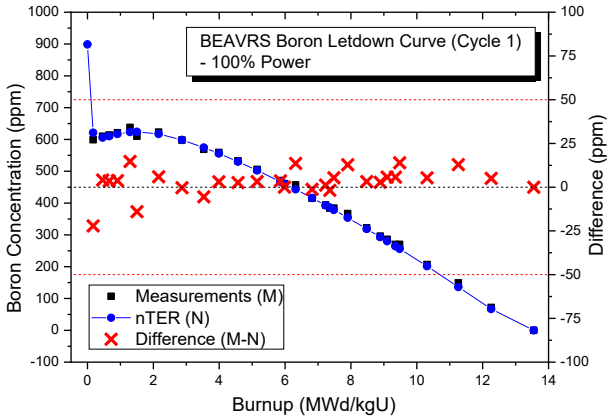

Fig. 3. Boron letdown curve for cycle 1 (100% Power)

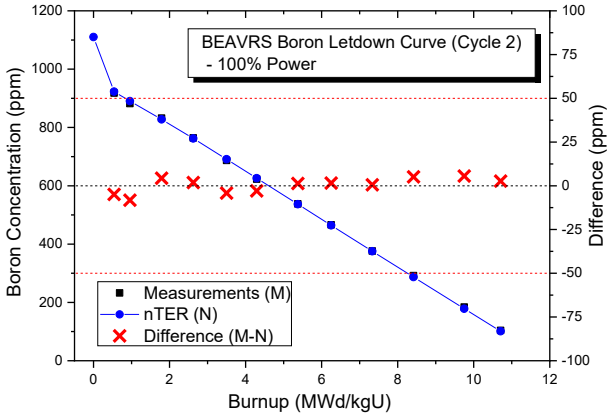

Fig. 4. Boron letdown curve for cycle 2 (100% Power)

For cycles 1 and 2, the RMS errors are 20 ppm. It is noted that the error at 12.34 MWd/kgU burnup (cycle 1) exceeds 50 ppm limits, which is well known as the typical acceptance criteria. However, the error of CBC at the same burnup point from CASMO/Simulate-3 calculations from the BEAVRS uncertainty quantification report is 46 ppm [9]. In the comparison of the PARCS results [5], it was the only point higher than 50 ppm. Therefore, a large error may come from the uncertainty of measurement, and the approximation of geometric model.

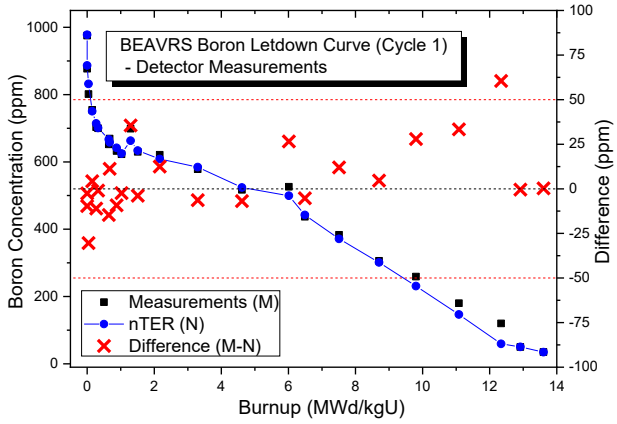

Fig. 5. Boron letdown curve for cycle 1 (detector measurements)

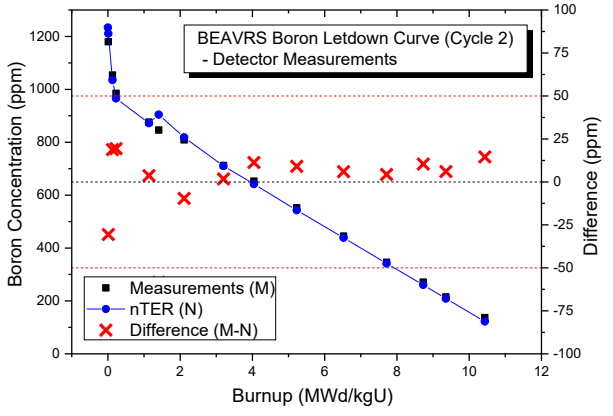

Fig. 6. Boron letdown curve for cycle 2 (detector measurements)

	H	G	F	E	D	C	B	A
		1.042	1.356	1.124	1.294	0.977	1.159	0.648
8	1.309	1.045	1.376	1.112	1.327	0.980	1.189	0.651
		0.3%	1.5%	-1.1%	2.6%	0.3%	2.6%	0.4%
		1.338	1.121	1.364	1.069	1.224	0.791	0.667
9		1.356	1.118	1.382	1.069	1.251	0.784	0.667
		1.3%	-0.3%	1.3%	0.0%	2.2%	-0.9%	-0.1%
			1.362	1.094	1.278	0.952	1.119	0.588
10			1.393	1.105	1.311	0.967	1.148	0.601
			2.3%	1.0%	2.6%	1.6%	2.6%	2.1%
				1.321				0.485
11				1.355	1.044	1.247	0.772	0.484
				2.5%		3.3%		-0.1%
		Measured					0.716	
12		nTER			1.143	0.983	0.720	
		Diff				3.8%	0.6%	
						0.651	0.512	
13		RMS diff.	1.93%			0.651	0.523	
		Max.	3.79%			0.0%	2.1%	

(a) 1.50 MWd/kgU (cycle 1)

	H	G	F	E	D	C	B	A
		1.031	1.042	1.053	1.124	1.028	1.001	0.762
8	1.243	1.032	1.059	1.057	1.132	1.016	0.985	0.772
		0.1%	1.6%	0.4%	0.7%	-1.2%	-1.6%	1.3%
		1.035	1.069	1.184	1.088		1.021	0.789
9		1.047	1.085	1.201	1.081	1.153	1.022	0.791
		1.1%	1.5%	1.4%	-0.6%		0.1%	0.3%
			1.219	1.079	1.259	1.069	1.052	0.712
10			1.234	1.074	1.269	1.044	1.035	0.705
			1.2%	-0.4%	0.8%	-2.4%	-1.6%	-0.9%
				1.317		1.226		0.552
11				1.308	1.063	1.219	0.961	0.536
				-0.7%		-0.6%		-2.8%
		Measured				1.070	0.791	
12		nTER			1.216	1.051	0.789	
		Diff				-1.8%	-0.3%	
						0.884	0.533	
13		RMS diff.	1.10%			0.874	0.526	
		Max.	2.77%			-1.2%	-1.1%	

(b) 10.43 MWd/kgU (cycle 2)

Fig. 7. Assembly-wise detector signal at various burnup step.

Figure 7 compares the calculated assembly-wise detector signals with the measurements at the time points in detector measurements. The relative RMS and maximum errors at 1.50 MWd/kgU (169 day) of cycle 1 are 1.9% and 3.8% and those at 10.43 MWd/kgU (296 day) of cycle 2 are 1.1% and 2.8%. The error of the nTER-calculated detector signals seems not to fluctuate with the burnup.

3. BEAVRS Benchmark Results by nTER/ESCOT

For convenient neutronics and thermal/hydraulics (T/H) coupling calculations, ESCOT [10] (Efficient Simulator of Core Thermal-Hydraulics) code was built in the nTER code. ESCOT is a drift-flux model (DFM) based pin-resolved T/H analysis with conducting equations for two-fluid analyses by adopting the mixture velocity. In the same manner as the nTER stand-alone (SA) calculations, the CBC calculations on the detailed calculations as shown in Fig. 5 was conducted by the nTER/ESCOT coupled (CO) calculations. To decrease the possibility of divergence or oscillations, under-relaxation scheme was adopted in the iterations between nTER and ESCOT as following equations:

$$P^{(k)} = (1-\alpha)\cdot P^{(k-1)} + \alpha \cdot f_N(P^{(k-1)}, T^{(k-1)}), \quad \ldots(1)$$

$$T^{(k)} = f_E(P^{(k-1)}, T^{(k-1)}). \quad \ldots(2)$$

where $P^{(k)}$ and $T^{(k)}$ are the pin-power distributions and temperatures at k-th iteration step and $f_N(P^{(k-1)},T^{(k-1)})$ and $f_E(P^{(k-1)},T^{(k-1)})$ indicate the nTER and ESCOT calculations using the pin-power distributions and temperatures at the previous iteration, respectively. Noted that the under-relaxation factor, α , was set as 0.7 for this study.

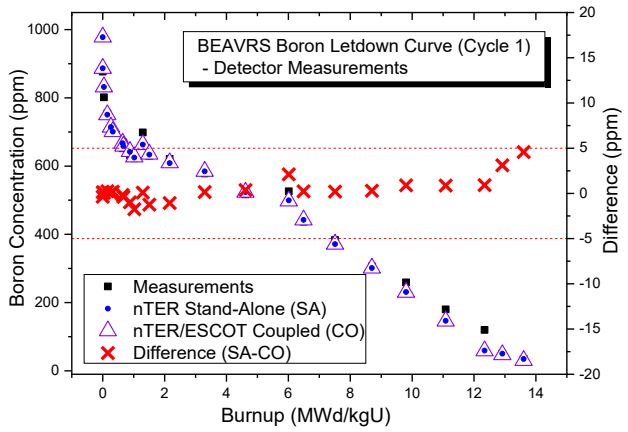

Fig. 8. Comparison of CBCs by SA and CO calculations (detector measurements)

	H	G	F	E	D	C	B	A
	0.923	0.763	1.063	0.919	1.155	0.928	1.275	0.771
8	0.935	0.764	1.063	0.918	1.153	0.926	1.271	0.769
	1.2%	0.2%	-0.1%	-0.1%	-0.2%	-0.2%	-0.3%	-0.3%
		1.013	0.886	1.149	0.954	1.203	0.861	0.805
9		1.014	0.886	1.148	0.952	1.201	0.859	0.803
		0.0%	-0.1%	-0.1%	-0.1%	-0.2%	-0.2%	-0.3%
			1.143	0.966	1.209	0.969	1.275	0.720
10			1.143	0.966	1.209	0.968	1.272	0.718
			-0.1%	0.0%	0.0%	-0.1%	-0.2%	-0.2%
				1.258	1.057	1.366	0.933	0.587
11				1.260	1.061	1.368	0.933	0.586
				0.2%	0.3%	0.1%	-0.1%	-0.2%
		SA			1.322	1.194	0.949	
12		CO			1.338	1.197	0.949	
		Diff			1.2%	0.3%	0.1%	
						0.841	0.701	
13		RMS diff.	0.39%			0.843	0.702	
		Max.	1.23%			0.2%	0.1%	

Fig. 9. Comparison of detector-signals by SA and CO calculations at 0 MWd/kgU (detector measurements)

Figures 8 and 9 compare the CBC and detector signal by SA calculations with those by CO calculations. The RMS and maximum difference of CBC between SA and CO are 1 ppm and 5 ppm. Noted that the difference between temperatures by nTER-equipped simple 1D T/H calculations and ESCOT elaborate drift-flux calculations is not largely affected in the behavior of CBC and detector-signal.

4. Conclusions

In this study, BEAVRS benchmark analyses were performed using the newly developed nTER transport code as the V&V tasks. It is noted that the nTER results for control rod bank worth, ITC, radial detector signal, and CBC during two cycles agree well with the measured data. Therefore, it is concluded that the nTER code is well developed in terms of solution accuracy for high-fidelity nuclear parameter evaluation. In addition, the multi-physics calculations by nTER/ESCOT code coupling were successfully performed in the same manner. The considerable difference between SA and CO results were not observed in CBC and detector signal.

Acknowledgements

This study was supported by KHNP CRI (Korean Hydro and Nuclear Power Central Research Institute).

References

1. J. Y. Cho et al., “Performance of a Whole Core Transport Code, nTER,” the 6th International Conference on Nuclear and Renewable Energy Resources (NURER2018), Ramada Plaza Jeju, Korea, 30 Sep. ~ 03 Oct. (2018).
2. N. Horelik et al., “Benchmark for Evaluation and Validation of Reactor Simulations,” MIT Computational Reactor Physics Group, rev03, 29 August, (2018).
3. B. S. Collins et al., “Simulation of the BEAVRS Benchmark using VERA,” International Conference on Mathematics & Computational Method Applied to Nuclear Science and Engineering (*M&C 2017*), Jeju, Korea, 16~20 Apr., (2017).
4. M. Ryu et al, “Solutions of the BEAVRS benchmark using the nTRACER direct whole core calculation code,” *J. Nucl. Sci. Technol.,* **52**, pp. 961-969, (2015).
5. P. Darnowski et al, “Analysis of the BEAVR PWR Benchmark using SCALE and PARCS,” *NUKLEONIKA*, **64**(3), 87, (2019).
6. Jiankai Yu et al, “Application of MCS/CTF/FRAPCON Multi-physics Coupling Code System in BEAVRS Cycle 1 Depletion Simulation,” *Transactions of the Korean Nuclear Society Autumn Meeting*, Yeosu, Korea, October 25-26, (2018).
7. H. J. Park et al., “BEAVRS Benchmark Analysis by DeCART Standalone and DeCART/MATRA Multi-Physics Code Coupling Calculations” M&C 2019, Portland, OR, August 25-29, (2019).
8. H. J. Shim et al., “McCARD: Monte Carlo Code for Advanced Reactor Design and Analysis,” *Nucl. Eng. Tech*., **44**, 161, (2012).
9. S. Kumar et al., “Integral Full Core Multi-Physics PWR Benchmark with Measured Data,” NEUP 14-6741, (2018).
10. J. Lee and H. G. Joo, “Preliminary Development of a Drift-Flux Model Based Pin-Resolved Core Thermal-Hydraulics Code for Dedicated Use in Efficient in High-Fidelity Neutronics Coupled Calculations,” Trans. Of the American Nuclear Society, Las Vegas, NV, USA, Nov. 6-10, (2016).

Proceedings of the Reactor Physics Asia 2019 (RPHA19) Conference
Osaka, Japan, Dec. 2-3, 2019

Initial Assessment of Anderson Acceleration on Pinwise Coupled Neutronics/Thermal-Hydraulics Code nTER/ESCOT

Jaejin Lee[a], Jin Young Cho[b] and Han Gyu Joo[a,*]
[a] *Seoul National University, 1 Gwanak-ro, Gwanak-gu, Seoul, 08826, Republic of Korea*
[b]*Korea Atomic Energy Research Institute, 111 Daedeok-daero 989Beon-gil, Yuseong-gu, Daejeon, 34057, Republic of Korea*

[*]Corresponding author: joohan@snu.ac.kr

Abstract

In order to improve the convergence behavior of the fixed-point iteration (Picard iteration) for neutronics/thermal-hydraulics coupled problems, Anderson acceleration is implemented in a pin-wise whole core analysis code nTER/ESCOT. The fixed-point map of Anderson acceleration is established for serially coupled whole core transport code and subchannel code. The performance of Anderson acceleration is examined with single assembly problems having low and high boron concentrations. The Anderson scheme shows the comparable convergence behavior to that of the optimum fixed-point iteration with under-relaxation factor.

Key Words: **Multiphysics, Fixed-point iteration, Anderson acceleration, Nonlinear problem, nTER, ESCOT**

1. Introduction

Pin-resolved whole core multiphysics calculations become more practical by the help of advanced computing resources and numerical methodologies. Especially, coupling a neutronics code and a thermal-hydraulics (T/H) code in pin-level is popular because their solutions have a strong inter-dependency in the Neutron Transport Equation[1]. For the scheme of coupling between physics, the fixed-point (or Picard) iteration (FPI) is widely used because of its ease of implementation. However, some convergence issues of the fixed-point iteration are raised when the physics are tightly coupled. Recently, the Jacobian-free Newton-Krylov (JFNK)[2] Methods have been suggested to resolve that problem, but calculating the residual of each system might require a bunch of modifications of codes. Moreover, a good preconditioner is essential for the excellent performance of JFNK methods, and it is opposite of the Jacobian-free feature.

For those reason, we apply Anderson acceleration (AA)[3] as an alternative coupling scheme to the fixed-point iteration. Anderson acceleration is a method which accelerates the convergence rate of the fixed-point iteration by utilizing secant information of previous iterations. The advantage of Anderson acceleration is that no extra information is required than the fixed-point iteration, so the physics codes can be treated as black boxes. In this study, the deterministic transport code nTER[4] embedded with the detailed two-phase subchannel T/H module ESCOT[5] is used as a test bed of Anderson acceleration. Firstly, the nTER/ESCOT multiphysics platform is introduced briefly. Secondly, the implementation of Anderson acceleration will be demonstrated. Lastly, the performance of Anderson acceleration compared to the fixed-point iteration will be presented with sample problems.

2. Coupling Scheme of nTER/ESCOT

nTER (Neutron Transport Evaluator for Reacotor) is a deterministics transport code under development by Korea Atomic Energy Research Institution (KAERI) with the cooperation of Korea Hydro and Nuclear Power Central Research Institute (KHNP-CRI). The 2D/1D method with the radial MOC and axial P_N solution is applied to nTER, and solutions are accelerated by the CMFD method. nTER is highly parallelized with MPI, as its domain can be decomposed by assembly-wise in a radial direction and plane-wise in an axial direction.

Although a built-in simplified T/H module was implemented in nTER, a detailed two-phase subchannel T/H code, ESCOT (Efficient Simulator of Core Thermal-hydraulics), is recently integrated in nTER for the high-fidelity analysis. ESCOT is a subchannel code developed by Seoul National University (SNU). The four equations drift-flux model is adopted for two-phase calculations, and numerical solutions are obtained by applying Semi-Implicit Method for Pressure Linked Equation (SIMPLE) algorithm. ESCOT is also MPI-based parallelized with the same domain decomposition scheme of nTER.

nTER and ESCOT are serially coupled where nTER is a main code and ESCOT takes charge of the T/H module of nTER. At each iteration of T/H feedback calculations, nTER provides pin-wise power distribution (q) to ESCOT. ESCOT performs its own calculation and returns T/H

solutions such as coolant densities (ρ_c), coolant temperatures (T_c), and fuel temperatures (T_f). nTER resumes the calculation after updating group constants. The flowchart of nTER/ESCOT is illustrated in Fig. 1.

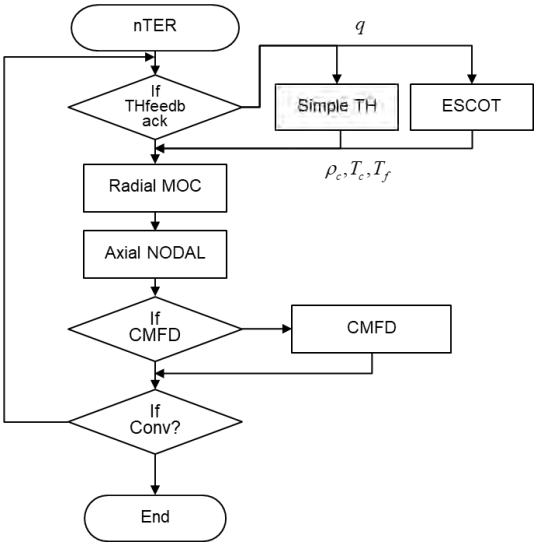

Fig 1. Flowchart of nTER/ESCOT

The above procedure is a typical fixed-point iteration with the Gauss-Seidel scheme as shown in Table I. The solution function f and g can be corresponded to nTER and ESCOT solution algorithm respectively. The solution vector **x** which is solutions of nTER and inputs of ESCOT refers power profile q. Likewise, the solution vector **y** consists of ρ_c, T_c, and T_f.

Table I. Fixed-point iteration with Gauss-Seidel scheme

Given $\mathbf{x}^0$, $\mathbf{y}^0$
for k=0,1,....
Solve $\mathbf{x}^{(k+1)} = f(\mathbf{x}^{(k)}, \mathbf{y}^{(k)})$
Solve $\mathbf{y}^{(k+1)} = g(\mathbf{x}^{(k+1)}, \mathbf{y}^{(k)})$
end

3. Implementation of Anderson Acceleration

In this chapter, the algorithm of Anderson acceleration is presented, and the implementation process in the code is explained.

3.1 The Anderson acceleration method

In many scientific applications, a system of nonlinear equation can be generally expressed as below:

$$F(\mathbf{x}) = 0, \quad F : \mathbb{R}^n \to \mathbb{R}^n . \tag{1}$$

The eq. (1) can be rearranged to an equivalent a fixed-point problem as follows:

$$\mathbf{x} = G(\mathbf{x}), \quad G : \mathbb{R}^n \to \mathbb{R}^n . \tag{2}$$

Based on the above definition, the algorithm of Anderson acceleration can be expressed as Table II.

Table II. Algorithm of Anderson acceleration

Given $\mathbf{x}^0$ and $m \geq 1$,
Set $\mathbf{x}^1 = G(\mathbf{x}^0)$.
for k=1,2,....
Set $m_k = \min\{m, k\}$.
Compute $G(\mathbf{x}_k)$ and let $f_k = G(\mathbf{x}_k) - \mathbf{x}_k$.
Set $F_k = [f_{k-m_k}, ..., f_k]$
Determine $\alpha^{(k)} = [\alpha_0^{(k)}, ..., \alpha_{m_k}^{(k)}]^T$ that solves

$$\begin{cases} \min\limits_{\alpha=[\alpha_0,...,\alpha_{m_k}]^T} \left\| F_k \alpha \right\|_2 \\ \text{s.t.} \sum\limits_{i=0}^{m_k} \alpha_i = 1 \end{cases} .$$

Set $\mathbf{x}_{k+1} = \sum\limits_{i=0}^{m} \alpha_i^{(k)} G\left(\mathbf{x}_{k-m_k+i}\right)$.
end

Here, m is the storage depth which determines how many histories of previous iterations will be stored, so Anderson-m denotes the algorithm of Table II having specific m. The idea of Anderson acceleration is to determine the solution at (k+1)-th iteration as a linear combination of G where the coefficients make the norm of residual vectors the minimum value. The least-squares problem can be solved by QR decomposition. The detail derivation and algorithm are described in [6,7]

3.2 Construction of the fixed-point map

In order to implement Anderson acceleration to the nTER/ESCOT code, the fixed-point map G has to be constructed for the system[8]. Firstly, the solution function of nTER is defined as below:

$$\mathbf{x}_N^{(n+1)} = g_N(\mathbf{x}_N, T_c, \rho_c, T_f) \tag{3}$$

where subscript N means nTER, and superscript (n+1) denotes the next iteration while the notation for the current iteration is omitted. The solution vector $\mathbf{x}_N$ contains group scalar fluxes and eigenvalue. The pin powers can be calculated by multiplying the scalar fluxes and kappa-fission cross sections, so that process can be expressed with a transfer function τ:

$$q^{(n+1)} = \tau_{E,N}(\mathbf{x}_N^{(n+1)}) \tag{4}$$

where subscript E denotes ESCOT, so [E,N] implies that the solutions are transferred from nTER to ESCOT. The solution function of ESCOT can be defined as same manner:

$$\mathbf{x}_E^{(n+1)} = g_E(\mathbf{x}_E, q^{(n+1)}) . \tag{5}$$

The solution vector $\mathbf{x}_E$ contains main variables of T/H solutions such as velocities, pressure, and water properties at each subchannel. Extracting essential T/H solutions from the $\mathbf{x}_E$ can be expressed with followed transfer functions:

$$T_c^{(n+1)} = \tau_{N,E,T_c}\left(\mathbf{x}_E^{(n+1)}\right) \quad (6)$$

$$T_f^{(n+1)} = \tau_{N,E,T_f}\left(\mathbf{x}_E^{(n+1)}\right) \quad (7)$$

$$\rho_c^{(n+1)} = \tau_{N,E,\rho_c}\left(\mathbf{x}_E^{(n+1)}\right). \quad (8)$$

Therefore, the fixed-point map G can be constructed as:

$$\begin{pmatrix} q^{(n+1)} \\ T_f^{(n+1)} \\ T_c^{(n+1)} \\ \rho_c^{(n+1)} \end{pmatrix} = G\begin{pmatrix} q \\ T_f \\ T_c \\ \rho_c \end{pmatrix} = \begin{pmatrix} \tau_{E,N}\left(g_N\left(T_c,\rho_c,T_f\right)\right) \\ \tau_{N,E,T_c}\left(g_E\left(q^{(n+1)}\right)\right) \\ \tau_{N,E,T_c}\left(g_E\left(q^{(n+1)}\right)\right) \\ t_{N,E,T_c}\left(g_E\left(q^{(n+1)}\right)\right) \end{pmatrix}. \quad (9)$$

The eq. (9) can be further simplified by eliminating q, because it only depends on ρ_c, T_c, and T_f. Finally, the following fixed-point map is derived as:

$$\begin{pmatrix} T_f^{(n+1)} \\ T_c^{(n+1)} \\ \rho_c^{(n+1)} \end{pmatrix} = G\begin{pmatrix} T_f \\ T_c \\ \rho_c \end{pmatrix} = \begin{pmatrix} \tau_{N,E,T_c}\left(g_E\left(\tau_{E,N}\left(g_N\left(T_c,\rho_c,T_f\right)\right)\right)\right) \\ \tau_{N,E,T_c}\left(g_E\left(\tau_{E,N}\left(g_N\left(T_c,\rho_c,T_f\right)\right)\right)\right) \\ t_{N,E,T_c}\left(g_E\left(\tau_{E,N}\left(g_N\left(T_c,\rho_c,T_f\right)\right)\right)\right) \end{pmatrix}. \quad (10)$$

4. Performance Examination with Single Assembly Problems

The performance of Anderson acceleration is examined with single assembly problems. The configuration of the assembly is a typical PWR 16x16 rod array as shown in Fig. 2. The axial computational nodes are constructed by diving 4.4 m height into 26 non-uniform planes. Typical Hot Full Power (HFP) conditions of PWRs are applied as 15.5 MPa outlet pressure, 296 °C inlet temperature, and 15.9 MWth of power. Two different boron concentrations, 0 ppm and 1,000 ppm, are used to simulate different feedback effects.

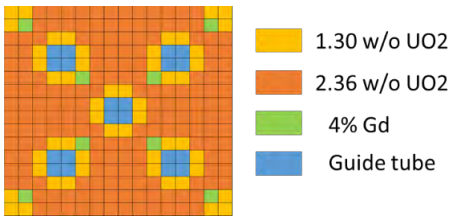

Fig. 2. Material configuration of a single assembly problem

Fig. 3 shows that how the axial power profiles are changed as the fixed-point iteration goes. Because coolant with low boron concentration has a strong negative Moderator Temperature Coefficient (MTC), the axial power shape is down-shifted and more vigorous changes are observed.

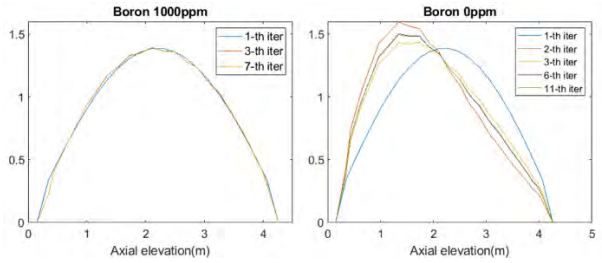

Fig. 3. Axial power profile change by fixed-point iteration

For the fixed-point iteration, the under-relaxation factors are applied for fuel temperatures as below:

$$T_f = \omega T_{new} + (1-\omega)T_{old}. \quad (11)$$

In case of Anderson acceleration, storage depth of 1 and 2 are applied. The norm 2 of fission source pseudo error of MOC is monitored to investigate the convergence rate, and it is illustrated in Fig. 4 and Fig. 5. The convergence criterion is set to 10^{-5}.

The major results can be found in Fig. 4, Fig5, Table III, and Table IV. The eigenvalues are agreed within 2 pcm difference. The optimum under-relaxation factor of FPI is different by 1.0 and 0.7 for 1,000 ppm and 0 ppm case respectively, so it can be considered that the optimum under-relaxation factor of the FPI would be varied by the characteristics of a problem. Anderson-1 shows comparable performance with that of the optimum FPI in both cases, while Anderson-2 does only for 1,000 ppm case.

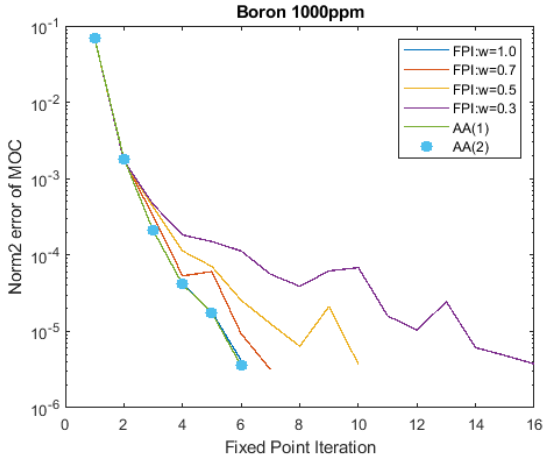

Fig. 4. Norm 2 of fission source errors by FPI and AA of Boron 1,000 ppm case

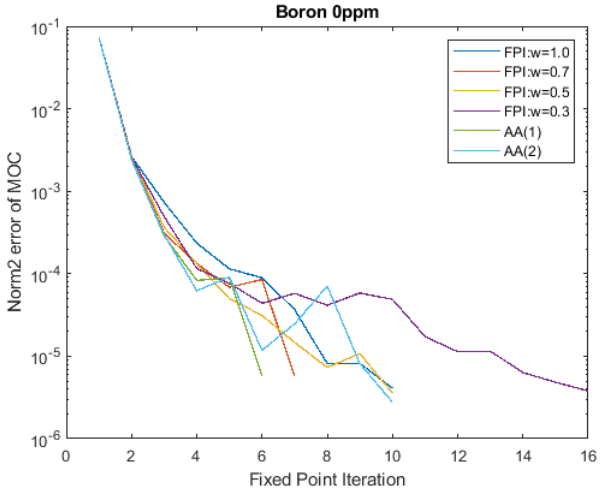

Fig. 5. Norm 2 of fission source errors by FPI and AA of Boron 0 ppm case

Table III. Result comparison of FPI and AA of boron 1,000 ppm case

	k-eff	$\Delta\rho$ (pcm)	Rel. Pin Power diff. (Max/RMS, %)	# of FPI
FPI w=1.0	0.96470	Ref.	Ref.	6
FPI w=0.7	0.96470	0	0.14/0.06	7
FPI w=0.5	0.96470	0	0.14/0.05	10
FPI w=0.3	0.96469	1	0.21/0.10	16
AA-1	0.96471	-1	0.10/0.02	6
AA-2	0.96470	0	0.10/0.02	6

Table IV. Result comparison of FPI and AA of boron 0 ppm case

	k-eff	$\Delta\rho$ (pcm)	Rel. Pin Power diff. (Max/RMS, %)	# of FPI
FPI w=1.0	1.09060	Ref.	Ref.	10
FPI w=0.7	1.09059	1	0.45/0.24	7
FPI w=0.5	1.09062	-2	0.48/0.32	10
FPI w=0.3	1.09062	-2	0.72/0.46	16
AA-1	1.09059	1	0.89/0.58	6
AA-2	1.09061	-1	0.43/0.23	10

6. Conclusions

In order to improve the convergence behavior of fixed-point iteration in neutronics-T/H coupled calculations, Anderson acceleration is implemented to nTER/ESCOT. Through the performance examinations in two different boron concentrations, it was figured out that Anderson acceleration can follow the optimum performance of the under-relaxed FPI, so we can expect the improved convergence behavior of nonlinear iterations by Anderson acceleration without heuristic scanning.

However, the deteriorated performance of higher order Anderson acceleration is a remaining issue, so it will be studied in the future. Moreover, the applicability of Anderson acceleration will be widely investigated for core size problems and depletion calculations.

Acknowledgements

This work was supported by Korea Atomic Energy Research Institution (KAERI) and funded by Korea Hydro and Nuclear Power Central Research Institute (KHNP CRI)

References

1. Kochunas R., et al., "VERA Core Simulation Methodology for Pressurized Water Reactor Cycle Depletion," *Nucl. Sci. Eng.*, **185** (2017)
2. Knoll D.A. and Keyes D.E., "Jacobian-free Newton-Krylov Methods: a Survey of Approaches and Applications," *J. Comput. Phys.*, **193**, 357-397 (2004)
3. Anderson D.G., "Iterative Procedures for Non-linear Integral Equations," *J. ACM 12*, **547**, 547-560 (1965)
4. Cho J.Y., et al., "Performance of a Whole Core Transport Code, nTER," *NURER2018*, Jeju, Korea, Sep. 30 – Oct. 03 (2018)
5. Lee J., et al., "Development of a drift-flux model based core thermal-hydraulics code for efficient high-fidelitymultiphysics calculation," *Nucl. Eng. and Tech*, https://doi.org/10.1016/j.net.2019.04.002 (2019)
6. An H., et al., "Anderson Acceleration and Application to the Three-Temperature Energy Equations," *J. Comput. Phys.,* **347**, 1-19 (2017)
7. Walker H.F., "Anderson Acceleration: Algorithms and Implementations", Research Report, MS-6-15-50, Worcester Polytechnic Institute Mathematical Sciences Department (2011).
8. Toth A., et al. "Local Improvement Results for Anderson Acceleration with Inaccurate Function Evalutions," *SIAM J. Sci. Comput.*, **39**(5), 47-65 (2017)

Proceedings of the Reactor Physics Asia 2019 (RPHA19) Conference
Osaka, Japan, Dec. 2-3, 2019

Pin-by-Pin Multi-physics Analysis and Evaluation of the Critical Heat Flux (CHF) in a PWR Core

Jaeha Kim, Khurrum Saleem Chaudri, and Yonghee Kim*
Department of Nuclear and Quantum Engineering, KAIST, 291 Daehak-ro, Yuseong-gu, 34141, Republic of Korea
*Corresponding author: yongheekim@kaist.ac.kr

Abstract

A diffusion-based pin-by-pin neutronics and sub-channel thermal hydraulics coupled code system has been developed. The pin-by-pin neutronics calculations are performed using HCMFD algorithm while the sub-channel thermal hydraulics solution is provided by the START code. It is shown that a steady-state pin-by-pin coupling analysis can be performed within a reasonably short time with the code system. With the sub-channel T/H coupling, the radial power peaking factor in a converged solution becomes 1.26 as compared to 1.46 for uncoupled case. Similarly, the Critical Heat Flux Ratio (CHFR) gives a value of 1.78 for converged coupled solution as compared to 1.62 for non-coupled solution, hence showing more margin of safety.

Key Words: **HCMFD algorithm, START code, Neutronics-T/H coupling, Pin-by-pin diffusion analysis, Sub-channel T/H analysis**

1. Introduction

In view of the safety and operational margin of nuclear reactors, accurate pin-wise power distribution is essential and a lot of efforts are being made for more accurate 3-D pin-power information. However, the massive computational loads for a high-fidelity solution is always a major obstacle.

In our research group, the Hybrid Coarse-Mesh Finite Difference (HCMFD) algorithm [1] and the GET Plus SPH (GPS) methods [2] are suggested to carry out pin-by-pin neutronics calculations accurately in a short time. Similarly, the START code [3] provides capability to carry out sub-channel based thermal hydraulics calculations for large LWR core in a relatively short time. In this study, HCMFD algorithm based code has been coupled with the START code to perform whole-core pin-by-pin neutronics/thermal-hydraulics coupled calculations for a large LWR core.

Critical Heat Flux Ratio (CHFR), ratio of Critical Heat Flux (CHF) to local heat flux, is a very important safety parameter for reactor design and safety. Conservative value estimation for CHFR is done based on hot channel values. Effect of coupled calculation on CHFR prediction is studied in this work.

2. Methodology

2.1 HCMFD Algorithm

In the HCMFD algorithm, two CMFD (Coarse-Mesh Finite Difference) methods are nonlinearly coupled with the nodal expansion method (NEM) applied on pin-level. To enable an efficient parallel computing, the whole domain is decomposed into subdomains, the fuel assemblies in a LWR.

The global balance is governed by solving the global eigenvalue problem with the one-node CMFD method, represented by Eq. (1).

$$A_{cmfd}^{global}\Phi_{cmfd}^{global} = \frac{1}{k}F_{cmfd}^{global}\Phi_{cmfd}^{global}, \quad (1)$$

Φ_{cmfd}^{global} : global node-averaged fluxes,
A_{cmfd}^{global} : global system matrix,
F_{cmfd}^{global} : global fission source operator,
k : multiplication factor.

Then the global balance information is transferred to each subdomain in terms of the boundary conditions, the fixed fission source and incoming currents on the boundary.

The local fixed source problems, represented by Eq. (2), are solved by the conventional two-node CMFD method based on NEM, with the given boundary conditions. The solutions of the local problems are then homogenized for the following global calculation.

$$M_i^{local}\phi_i^{local} = S_i^{local}, i = 1,2,...N, \quad (2)$$

ϕ_i^{local} : i-th node local fluxes,
M_i^{local} : i-th node local system matrix,
S_i^{local} : i-th node local fixed source.

In this HCMFD framework, the whole-core pin-by-

pin analysis can be performed very effectively by an efficient parallel computing in a local-global non-linear iterative scheme as shown in Fig. 1. More details of the work can be found in the reference [1].

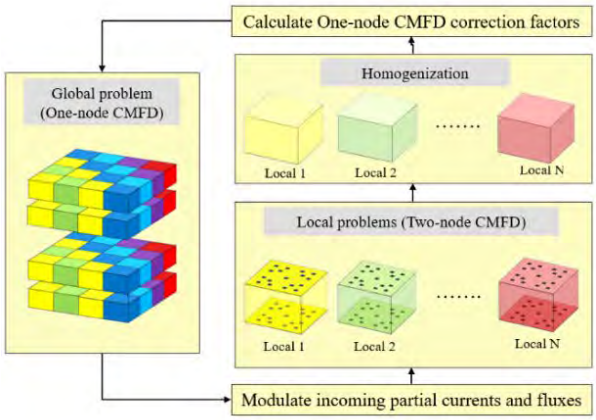

Fig. 1: Schematic diagram of the HCMFD algorithm

2.2 START code

The START (Steady and Transient Analyzer for Reactor Thermal Hydraulics) code is an in-house developed code to perform sub-channel thermal hydraulics analyses for LWRs. Special emphasis is on fast execution of the code to perform coupled neutronics/thermal hydraulics analysis in a reasonable time. OpenMP parallelization is applied to several parts of the code.

The START code is based on homogeneous two-phase model. Basic conservation equations (mass, momentum and energy), based on sub-channel formulation, are solved using marching algorithm. Newton-Raphson iterations determine pressure drop for axial and radial pressure drop used in axial and lateral momentum equations. Time-dependent solution is based on an implicit scheme. The START code solution has been validated against PSBT benchmark. More details of the work can be found in the reference [3]. Various correlations and model used in the START code are given in Table I.

CHFR is determined using local conditions. EPRI correlation is used for calculation of CHF value. Relevant correction factors such as grid spacer correction factor and effect of non-uniform axial heat flux are also included in calculations.

Table I: Correlations and models used in START code

Parameter	Correlation
Two-phase friction multiplier	Armand Correlation
Grid spacer pressure drop	K. Rehme Model
CHF Prediction	EPRI Correlation
HTC (Single phase/subcooled and saturated nucleate boiling)	Dittus-Boelter/ Dittus+Thom

2.3 HCMFD/START Coupled Analysis

As the START code is written in a modular form, it has been integrated into the HCMFD code as a T/H module. The main program and START module continuously interchange required data in each neutronics and T/H calculation, and do feedbacks for a converged multi-physics solution. Detailed list of data interchanged is introduced in Table II.

Table II: Flow of data in coupled analysis

Data flow	List of data
HCMFD → START	Pin-by-pin linear power.
START → HCMFD	Coolant temperature, Coolant density, Fuel temperature.

Meanwhile, a module for fuel temperature analysis has been added. It performs a 1-D cylindrical fuel temperature analysis using the rod-centered coolant temperature and corresponding surface heat transfer coefficient. The effective fuel pin temperature is simply calculated by using a 30/70 weighted average of fuel centerline and fuel surface temperature [4]. The obtained pin-by-pin fuel temperature data is then transferred to HCMFD for the T/H feedback. The cross-section feedback is done by Eq. (3) with the cross-section derivatives prepared in advance.

$$\Sigma(T_f,T_c,D_c)=\Sigma^{ref}+\frac{\partial\Sigma}{\partial\sqrt{T_f}}\Delta\sqrt{T_f}+\frac{\partial\Sigma}{\partial T_c}\Delta T_c+\frac{\partial\Sigma}{\partial D_c}\Delta D_c+\frac{\partial^2\Sigma}{\partial D_c^{\,2}}(\Delta D_c)^2 \quad (3)$$

The coupled analysis is initiated by execution of HCMFD code with constant values for fuel temperature, coolant temperature, and coolant density followed by T/H calculations. After every START run, convergence is checked for coolant temperature, density, fuel temperature, and linear power. Iterations continue until the convergence criteria is met. Flow chart for coupled calculations is shown in Fig. 2.

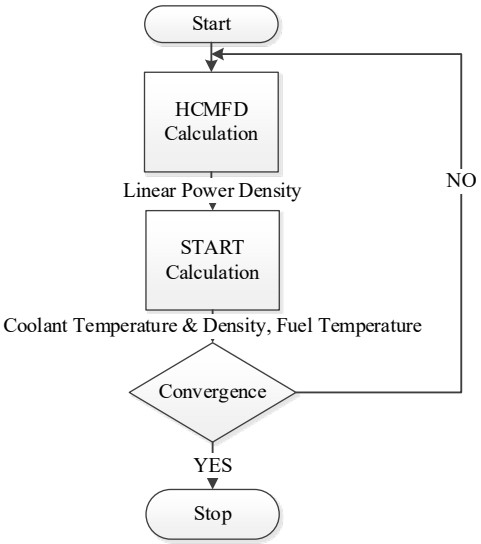

Fig. 2: Flow chart for coupled calculations

3. Numerical Results

In this work, all calculations are performed with 40 cores on Intel Xeon Gold 6148 CPUs (2.40 GHz). To assess the computational performance of the coupled code system, an arbitrary OPR-1000(Optimized Power Reactor, 1000MW)-size core was analyzed. The fuel loading pattern with 6 types of assemblies (A0, B0, B1, B2, C0, C1) is shown in Fig. 3. A total of 177 fuel assemblies of 16 by 16 fuel pins is present in the core. The core has an active height of 3.81 m which is divided into 19 axial segments. The assembly geometry is shown in Fig. 4, and the pin-wise cross-sections are generated by pin-cell homogenization in each assembly lattice model using a 2-D transport code, DeCART2D [5] varying the temperature conditions. The baffle surrounding the fuel assemblies is also appropriately considered in the core model. The pin-wise discontinuity factors are applied over the whole core.

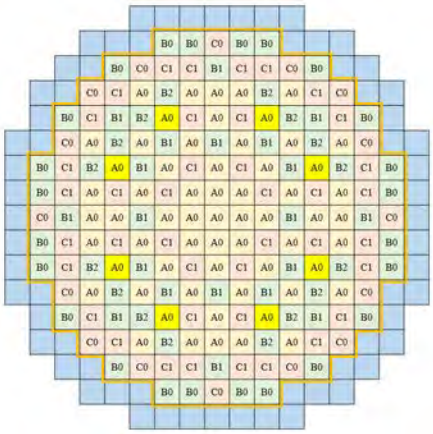

Fig. 3: Fuel loading pattern

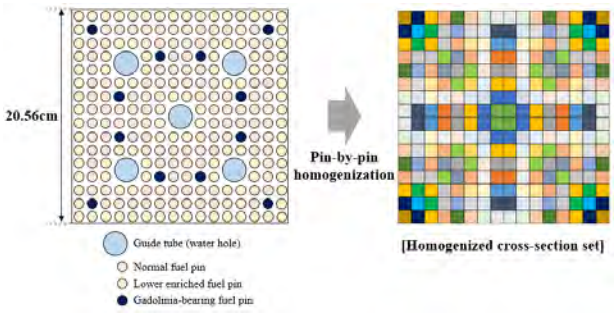

Fig. 4: Assembly geometry and pin-cell homogenization

For convergence criteria, it is observed that maximum linear power error shows slowest convergence. Especially the points near the bottom or top of reactor core, where the power density is small, show larger deviations in relative error. For a maximum linear power error of less than 0.1%, maximum deviation in coolant temperature, density, and fuel temperature is already below 0.1%. So from all the nodes, maximum linear power error needs to be below 0.1% in order for coupled calculations to stop.

For speedy convergence and avoiding oscillations in the solutions, under relaxation factor (URF) is applied when thermal hydraulics parameters are transferred to HCMFD. Initially, a URF value of 0.5 is applied. This helps dampening the oscillations in power profile and achieve convergence in less number of iterations, as shown by previous studies [6]. The variation in linear power density (radial average value) for the 19 axial nodes during coupled process is shown in Fig. 5.

It is seen that after fourth iteration, the values are quite close to each other showing convergence of solution is being approached. In Fig. 5, it can be seen that 1st iteration profile is perfectly chopped cosine type, which we expect due to use of constant T/H parameters, as compared to bottom-skewed profile obtained after convergence of coupled solution.

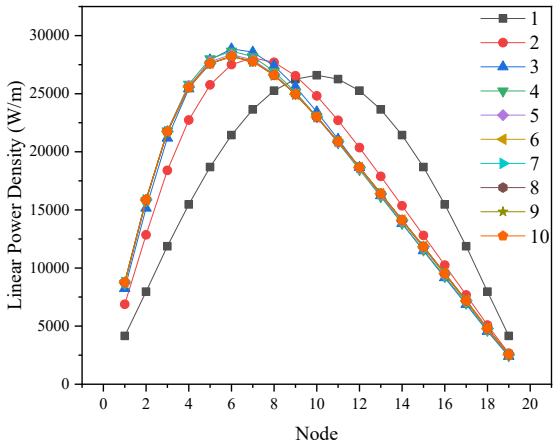

Fig. 5: Linear power density variation during iterations

Convergence behavior of various parameters with iteration number is shown in Fig. 6.
It is observed that reactivity (pcm), shows a value of less than 5 pcm at 9th iteration. For converged solution i.e. 10th iteration, a reactivity difference of less than 2 pcm is obtained. The accumulated variation in k-eff is -771 pcm from the initial condition.

Critical Heat Flux Ratio (CHFR) shows an increase in value with coupled iterations, hence greater margin of safety. Initial value of CHFR was 1.62 that converges to a value of 1.78 at 10th iteration. Due to bottom-skewed converged power profile, location of CHFR also shifts accordingly.

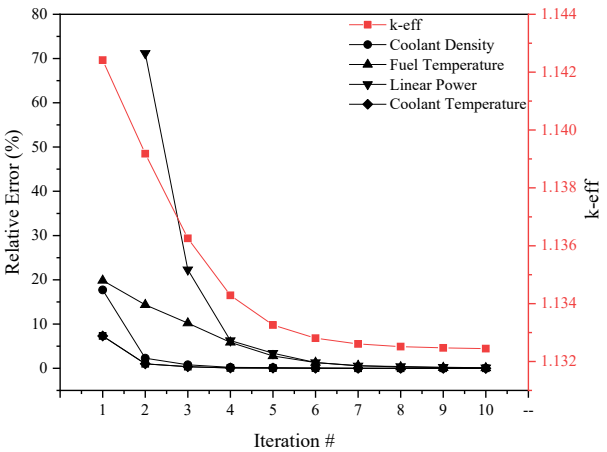

Fig. 6: Convergence behavior of various key parameters

Radial power shape for converged solution is shown in Fig. 7. The converged power profile becomes more evenly spread in the core rather than just peaking at the center, and then falling off quickly for peripheral assemblies. Radial assembly peaking factor values of 1.43 and 1.35 are obtained for initial core and converged core respectively.

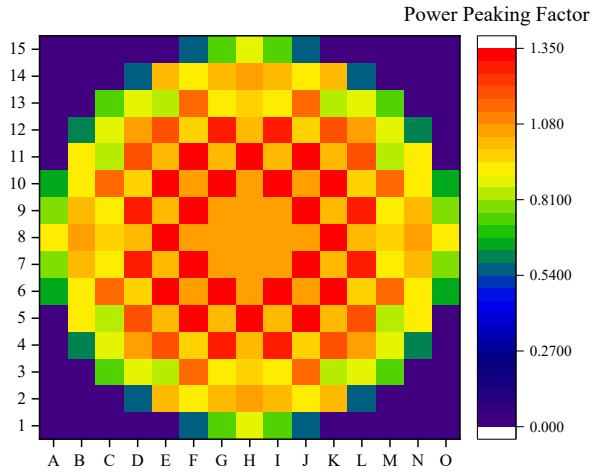

Fig. 7: Assembly-wise radial power peaking profile

Calculation time for the simulation is of particular interest. Both the codes, HCMFD and the START code, have computational times less than a minute for whole core calculation. In order to further decrease the computational time, part of thermal hydraulic solution (flow rates and pressure drops) from previous iteration was used as an initial guess for current iteration. This caused a significant decrease in computational time once the solution started to approach convergence.

Individual code timing in each iteration, reported in Table III, confirms this. The overall calculation time for coupled codes to produce a converged solution turn out to be 203 seconds for 10 coupled iterations. Both HCMFD and START show very good parallel efficiency of values above 70%. Calculation time for fuel temperature analysis module is negligible (approx. 3.0 sec for 10 iterations) showing very good parallel performance.

Table III: Computing time

Iteration #	HCMFD		START	
	CPU time (sec)	Parallel efficiency (%)	CPU time (sec)	Parallel efficiency (%)
1	8.642	71.5	15.743	87.1
2	15.706	74.8	13.596	89.9
3	13.908	75.3	11.610	93.2
4	9.950	75.2	10.838	94.7
5	10.712	74.9	10.499	95.6
6	9.748	75.0	10.385	95.7
7	7.580	75.4	10.331	95.9
8	3.092	75.6	10.311	95.9
9	4.543	74.8	10.293	95.9
10	2.971	75.5	10.276	96.0
Total (sec)	203.460			

4. Conclusions

Whole-core pin-by-pin coupled neutronics/thermal hydraulics simulation for an OPR-1000 core has been carried out using in-house codes. Pin-by-pin neutronics calculations are carried out using HCMFD algorithm while sub-channel thermal hydraulics solution is carried out using the START code. The simulations have shown that within a very reasonable time (~3.5 minutes), with a small commercial cluster system, pin-by-pin scale coupled simulations are possible. Coupled solution effect can be seen in radial power profile which is showing a radial power peaking value of 1.35 for converged core as compared to 1.46 for initial core. Similarly, CHFR value of 1.78 is obtained for converged coupled case as compared to 1.62 for standalone calculation. Clearly bottom-skewed axial power profile as compared to assumed chopped cosine also shows need and importance of coupled calculations for design and safety analyses. The location of CHF also shifted from E8 to F10 for initial and converged solution respectively.

Acknowledgements

This work was supported by the National Research Foundation of Korea (NRF) Grant funded by the Korean Government (MSIP) (NRF-2016R1A5A1013919).

References

1. J. Kim and Y. Kim, “Development of 3-D HCMFD algorithm for efficient pin-by-pin reactor analysis,” *Ann. Nucl. Energy*, vol. 127, pp. 87–98, May (2019)
2. H. Yu, J. Kim, and Y. Kim, “Pinwise Diffusion Solution of Partially MOX-Loaded PWRs with the GPS (GET PLUS SPH) Method,” *Nucl. Sci. and Eng.*, June (2019).
3. K. S. Chaudri, J. Kim, and Y. Kim, “Development and validation of a fast sub-channel code for LWR multi-physics analyses,” *Nucl. Eng. Technol.*, February (2019).
4. T. Kozlowski and T. J. Downar, “PWR MOX/UO2 Core Transient Benchmark Final Report,” *NEA/NSC/DOC*, p. 20 (2006)
5. “DeCART 2D v1.0 User's Manual,” KAERI/TR-5116/2013, Korea Atomic Energy Research Institute (2013)
6. C. L. Waata, “Coupled neutronics thermal hydraulics analysis of a high-performance light-water reactor fuel assembly” (2006)

Proceedings of the Reactor Physics Asia 2019 (RPHA19) Conference
Osaka, Japan, Dec. 2-3, 2019

Functional Expansion Tallies in Monte Carlo High Fidelity LWR Analysis

Bamidele Ebiwonjumi, Hyunsuk Lee, Peng Zhang, Deokjung Lee*
Department of Nuclear Engineering, Ulsan National Institute of Science and Technology, 50 UNIST-gil, Eonyang-eup, Ulju-gun, Ulsan, 44919, Korea
*Corresponding author: deokjung@unist.ac.kr

Abstract

Functional expansion tallies (FETs) are implemented in the Monte Carlo code MCS to improve the fidelity of multi-physics (MP) solution of light water reactor (LWR) problems. Neutronics (N) parameters (spatial flux or power) are expanded in a set of orthogonal basis functions (Legendre and/or Zernike polynomials) and the coefficients of the functional expansions are determined from the Monte Carlo (MC) simulations. With the coefficients, the required distribution is reconstructed continuously in space. Moreover, thermal-hydraulic (TH) quantities (fuel temperature, coolant density) obtained from the TH calculations of MCS are integrated into polynomial functions and their coefficients are calculated. Coupled MP simulation results are presented in this paper using a three-dimensional (3D) PWR fuel pin. FETs coefficients of power are transferred to the TH solver. Then the power distribution is reconstructed for the TH calculations. Subsequently, the coefficients of fuel temperature/coolant density are returned as feedback, and the fuel temperature/coolant density profiles are reconstructed for the next neutronic cycle. The results obtained with the coefficients demonstrates promise of the FETs for high fidelity MP coupled calculations.

Key Words: **MCS, functional expansion tallies, Legendre polynomials, Zernike polynomials, Multiphysics, high fidelity**

1. Introduction

MC methods have the advantage to utilize continuous-energy cross-sections, and model arbitrary complex geometry with very few approximations. However, MC methods are well suited for the estimation of integral quantities and to determine quantities of interest in a given volume or point. To estimate a distribution (spatial flux or power), the geometry of the problem is discretized, and the integrated quantity is determined in each bin. The fidelity of this discrete representation is usually improved by using finer bins. However, small bin size means that small number of neutrons contribute to the tally bin, and a large bin score standard deviation. Large number of particle histories are thus needed to obtain finer distributions and decrease the bin-wise standard deviation. Large particle histories also imply increased run time. One of the solution to the aforementioned problem is to use functional expansion tallies (FETs) [1].

2. Monte Carlo Code MCS

MCS is a 3D continuous-energy MC code under development at the Ulsan National Institute of Science and Technology (UNIST), for the purpose of high fidelity large scale power reactor analysis [2]. MP coupling in MCS allows the modeling of thermal-hydraulics and fuel behavior feedback [3], with fuel depletion, on-the-fly doppler broadening of cross-sections, S(α, β) data and doppler broadening rejection correction. MCS employs the conventional MC tally bins to estimate neutronic parameters using the collision and track-length estimators. MCS does not contain FET capabilities and are currently being implemented as detector tallies and for MP calculations.

3. Functional Expansion Tallies

FETs enables the continuous representation of spatial distributions. The discrete representation is limited to the zeroth moment. FETs produce high order moments based on a set of orthogonal basis functions, which can be used to reconstruct the spatial distribution. A given distribution can be expressed as a functional expansion according to Eq. (1)

$$F(\xi) = \sum_{n=0}^{\infty} a_n k_n f(\xi) \quad (1)$$

where ξ denote the spatial variable, $\{f(\xi)\}_0^{\infty}$ forms a complete set of orthogonal basis functions, k_n is the normalization constant, a_n represent the expansion coefficients given by Eq. (2), in which $\rho(\xi)$ is a weighting function.

$$a_n = \int F(\xi) f(\xi) \rho(\xi)\, d\xi \quad (2)$$

3.1 Legendre polynomials

Legendre polynomials can be used to express the axial distribution of flux, power, fuel temperature and coolant density in a fuel pin. Legendre polynomials are defined in Eq. (3) [4]

$$P_{n+1}(\xi) = \frac{(2n+1)\xi P_n(\xi) - nP_{n-1}(\xi)}{n+1} \quad (3)$$

with $P_0(\xi) = 1$ and $P_1(\xi) = \xi$ and n is the polynomial order. Legendre polynomials are orthogonal in [-1, +1] and the orthogonality relation is shown in Eq. (4).

$$\int_{-1}^{1} P_i(\xi) P_j(\xi) d\xi = \frac{2}{2i+1}\delta_{ij} \quad (4)$$

with $\delta_{ij} = 1$ for $i = j$ and $\delta_{ij} = 0$ otherwise. The normalization constant is given by Eq. (5) and the weighting function for Legendre polynomials is 1.

$$k_n = \frac{2n+1}{2} \quad (5)$$

3.2 Zernike polynomials

Zernike polynomials can be used to represent the radial distributions on unit disks. They have been used in optics and are defined in Eq. (6) as the product of radial and azimuthal polynomials [5]. Application of Zernike polynomials to FETs can be found in [6-7].

$$\begin{aligned} Z_n^m(r,\theta) &= R_n^m(r)\cos(m\theta) && m > 0 \\ Z_n^m(r,\theta) &= R_n^m(r)\sin(m\theta) && m < 0 \\ Z_n^m(r,\theta) &= R_n^m(r) && m = 0 \end{aligned} \quad (6)$$

where n and m are the order of the radial and azimuthal polynomials respectively. The radial polynomial is defined in Eq. (7). Zernike polynomials are orthogonal in [0, 1]. The orthogonality relations are shown in Eq. (8a) and (8b) for $m \neq 0$ and $m = 0$ respectively. The normalization constants are presented in Eq. (9). Only the radial functions corresponding to $m = 0$ are considered in this work.

$$R_n^m(r) = \sum_{s=0}^{\frac{n-m}{2}} \frac{(-1)^s (n-s)!}{s!\left[\frac{n+m}{2}-s\right]!\left[\frac{n-m}{2}-s\right]!} r^{n-2s} \quad (7)$$

$$\int_0^1 \int_0^{2\pi} Z_n^m(r,\theta) Z_{n'}^{m'}(r,\theta) r dr d\theta = \frac{\pi}{2n+2}\delta_{n,n'}\delta_{m,m'} \quad (8a)$$

$$\int_0^1 \int_0^{2\pi} Z_n^m(r,\theta) Z_{n'}^{m'}(r,\theta) r dr d\theta = \frac{\pi}{n+1}\delta_{n,n'}\delta_{m,m'} \quad (8b)$$

$$k_n^m = \begin{cases} \frac{2n+2}{\pi}, & m \neq 0 \\ \frac{n+1}{\pi}, & m = 0 \end{cases} \quad (9)$$

3.1.1 Evaluation of expansion coefficients

The expansion coefficients in Eq. (2) are an integral quantity. They can be estimated in a Monte Carlo simulation. With a collision estimator, the coefficients of tallied quantity $F(\xi)$ are shown in Eq. (10).

$$a_n = \frac{1}{N}\sum_{i=1}^{N} \frac{w_i F(\xi_i)}{\Sigma_t(\xi_i)} f_n(\xi_i) \quad (10)$$

where n is the nth coefficient of the expansion, N is the number of histories, w_i is the weight of particle i prior to collision, Σ_t is the total macroscopic cross section, and $f(\xi)$ represents the Legendre and/or Zernike polynomials evaluated at the collision point. By applying the appropriate normalization constant, the continuous distribution can be reconstructed according to Eq. (1). It should be noted that the particle position must be transformed to the Legendre and/or Zernike space as shown in Eq. (11) and Eq. (12), where the problem geometry spans the axial and radial regions, $z_{min} \leq z \leq z_{max}$ and $0 \leq r' \leq R$, respectively.

$$\xi = 2\frac{z - z_{min}}{z_{max} - z_{min}} - 1 \quad (11)$$

$$r = \frac{r'}{R} \quad (12)$$

4. Numerical Tests

The FETs are tested on a 3D fuel pin to verify the implementation. The pin-cell test employ reflective boundary conditions in the *x*, *y* directions and black boundary conditions in the *z* direction. The pin-cell is a 3.0 wt.% ^{235}U, 400cm long fuel pin with 0.41195 cm radius. All materials are 293.6 K and moderator density is 0.7 g/cm^3. 200 inactive cycles, 200 active cycles and 500,000 neutron histories were simulated. Fig. 1 shows the continuous axial power distribution in the fuel pin reconstructed with 10th order Legendre polynomials and compared to the discrete representation tallied in 24 axial nodes. FETs are also collected using the convolution of 10th order Legendre and Zernike Polynomials. The continuous power distribution in the *r-z* direction of the fuel pin is presented in Fig. 2. Power in the right-hand side is higher than in the left-hand side because the right-hand side is nearer to the boundary of the fuel pin where there is increased fission power due to the fuel's closeness to the moderator.

With the same pin-cell, coupled MP simulation was performed with FET coefficients. Coefficients of power are transferred to the TH solver and the power distribution is reconstructed for the TH calculations. The fuel temperature and coolant density are obtained respectively by solving the heat conduction and mass/energy conservation equations with the reconstructed power distribution. Moreover, the TH results are then integrated into Legendre and Zernike polynomial functions according to Eq. (13) with coefficients determined from Eq. (14). Subsequently, coefficients of fuel temperature and coolant density are returned as feedback. Then the fuel temperature and coolant density profiles are then reconstructed for the next neutronic cycle. An example of the fuel temperature reconstructed from coefficients is shown in Fig. 2. MP simulation results based on the

coefficients are presented in Fig. 3. The temperature and density distributions are compared in order to verify the MP results based on coefficients with those obtained with the discrete power/temperature/coolant density distributions. Fig 3 illustrates the comparison of the power, average fuel temperature, maximum fuel temperature, coolant density and temperature distribution respectively. The power distribution has been normalized to the total system power. The MCS/FET results are reconstructed from polynomial coefficients. The MCS/TH1D results are those obtained with the discrete representations of power, fuel temperatures and coolant densities. The axial MCS/FET fuel temperature and coolant density/temperature distributions used during the simulation are reconstructed using 10th order Legendre polynomial coefficients and the radial fuel temperature is reconstructed with 4th order Zernike polynomial coefficients at all axial levels. The *k-eff* of MCS/FET is 8 pcm less compared to MCS/TH1D (see Table I), and this difference is within one standard deviation of the quadratically combined *k-eff* uncertainty.

$$F(r,\theta,z) = \sum_{l=0}^{L}\sum_{n=0}^{N}\sum_{m=-n}^{n} c_{n,l}^{m} Z_n^m(r,\theta)P_l(z) \quad (13)$$

$$c_{n,l}^{m} = \int_{-1}^{1} dz \int_{0}^{1} dr \int_{0}^{2\pi} d\theta\, F(r,\theta,z) Z_n^m(r,\theta)P_l(z) \quad (14)$$

6. Conclusions

FETs are presented in this paper as an alternative approach to improve the fidelity of MC LWR analysis. Spatial distributions of N-TH parameters are expanded in a set of orthogonal basis functions including Legendre and Zernike polynomials. The coefficients of the functional expansions are evaluated and then used to reconstruct the distribution continuously during a MP simulation. Good agreement is obtained when compared to the discrete case which demonstrates that the FETs can be applied in MP coupled calculations. The results presented in this paper are preliminary and foundational to the future work which includes neutron transport through materials of continuously varying properties, application of the FETs to MP calculations of fuel assembly and ultimately large scale commercial PWRs.

Acknowledgements

This work was partially supported by the National Research Foundation of Korea (NRF) grant funded by the Korea government (MSIT). (No. NRF-2019M2D2A1A03058371). This research was partially supported by the project(L18S015000) by Korea Hydro & Nuclear Power Co. Ltd..

References

1. Griesheimer DP, Martin WR, Holloway JP, "Estimation of Flux Distributions with Monte Carlo Functional Expansion Tallies," *Rad. Prot. Dos.*, **115**, 428 (2005).
2. Lee H, "Development of a New Monte Carlo Code for Large-Scale Power Reactor Analysis," (PhD thesis), Ulsan National Institute of Science and Technology, Ulsan (2019).
3. Yu J, Lee H, Lemaire H, et al., "MCS based Neutronics/Thermal-hydraulics/Fuel-performance Coupling with CTF and FRAPCON," *Computer Physics Communications*, **238**, 1 (2019).
4. Abramowitz M, Stegun IA, *Handbook of Mathematical Functions: with Formulas, Graphs, and Mathematical Tables*, Courier Corporation (1964).
5. Wang JY, Silva DE, "Wave-front Interpretation with Zernike Polynomials," *Applied Optics*, **19**, 1510 (1980).
6. Ellis M, "Methods for Including Multiphysics Feedback into Monte Carlo Reactor Physics Calculations," (PhD thesis), Massachusetts Institute of Technology (2017).
7. Wendt B, Kerby L, et al., "Advancement of functional expansion capabilities: Implementation and optimization in Serpent 2," *Nucl. Eng. Des*, **334**, 138 (2018).

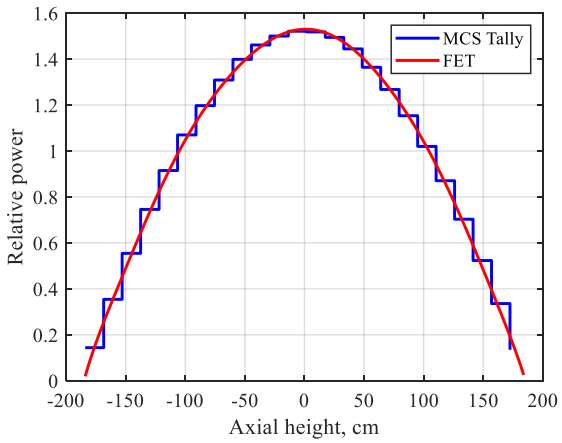

Fig. 1. Comparison of axial power distribution in a fuel pin.

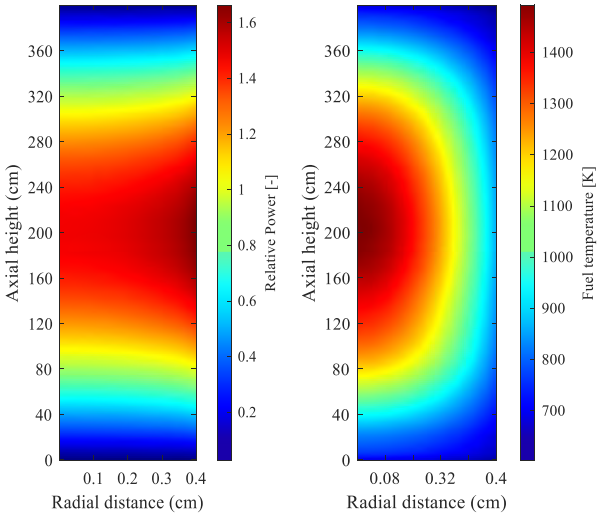

Fig. 2. Continuous power/fuel temperature distribution.

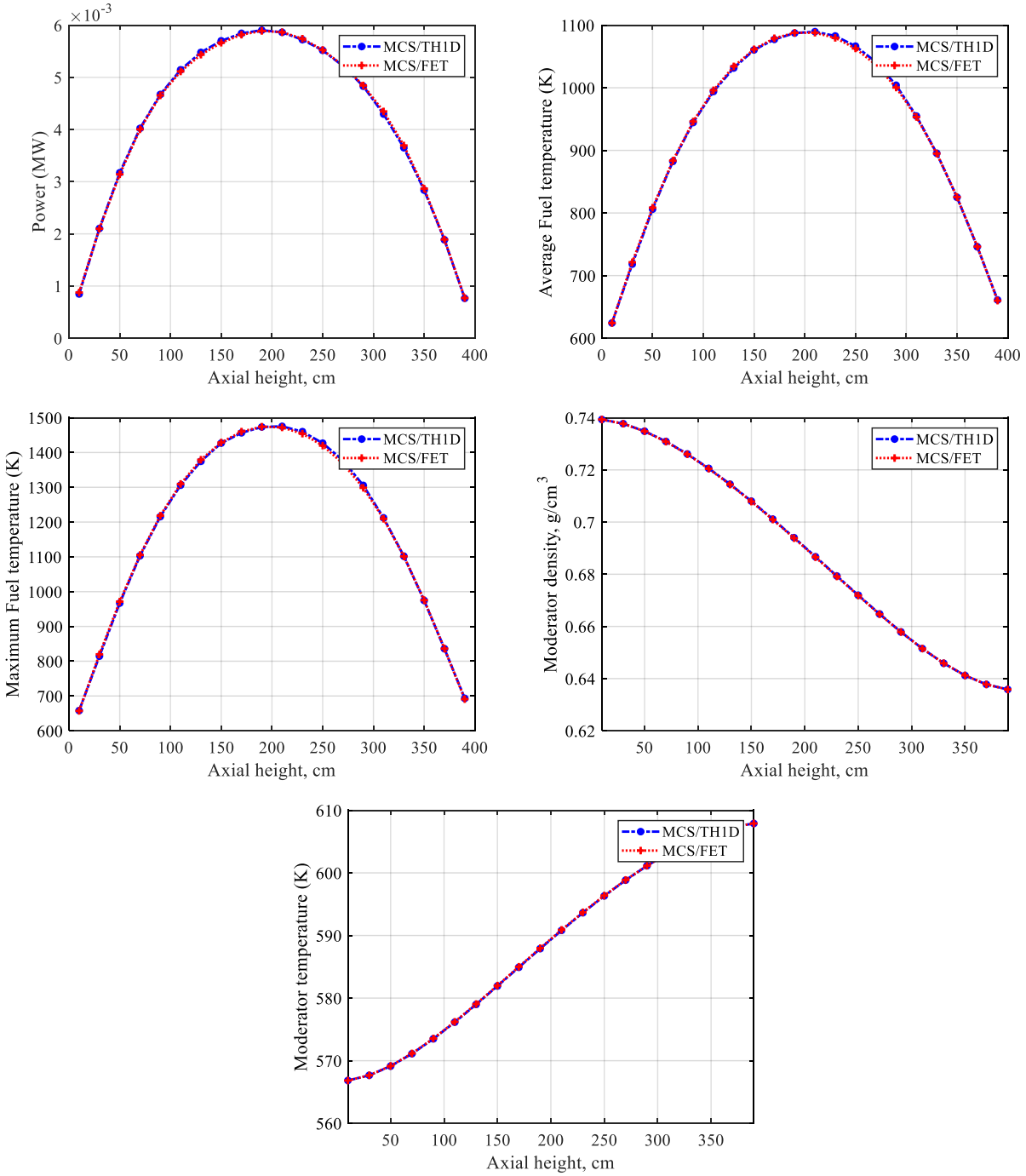

Fig. 3. Comparison of axial distribution of power, fuel temperature, coolant density and temperature.

Table I. Comparison of the Fuel Pin *k-eff* Values

MCS/TH1D	1.10022 ± 7.52317E-05
MCS/FET	1.10014 ± 7.78896E-05
Δk (pcm)	-8.00000E-05 ± 1.08290E-04

Proceedings of the Reactor Physics Asia 2019 (RPHA19) Conference
Osaka, Japan, Dec. 2-3, 2019

Hybrid Parallelism of Internal Coupling Method between Monte Carlo Code RMC and Sub-channel Thermal-Hydraulic Code CTF

Kaiwen Li[a], Shichang Liu[b], Juanjuan Guo[a] and Kan Wang[a,*]
[a]*Department of Engineering Physics, Tsinghua University, 100084 Beijing, CHINA*
[b] *School of Nuclear Science and Engineering, North China Electric Power University, 102206, Beijing, CHINA*
[*]Corresponding author: wangkan@mail.tsinghua.edu.cn

Abstract

Internal coupling interface for the CTF Thermal-Hydraulics code developed in the RMC Monte Carlo code has been implemented for multi-physics simulations on nuclear reactors. Fixed-point iteration scheme is utilized to take the Thermal-Hydraulic feedback into account during the neutronic transport calculation in RMC. This paper introduces the scheme of internal coupling, the novel hybrid parallelism method and the validation results based on a simple single fuel pin test case and a checkerboard 2-by-2 assemblies case. The results demonstrated the accuracy and parallel capability of the coupling system.

Key Words: **RMC, CTF, Internal Coupling, Hybrid Parallelism**

1. Introduction

Multi-scale and multi-physics high-fidelity analysis on large PWRs and other reactors has become a significant issue nowadays. With years of efforts all around the world, including the rapid development of high performance computing, it is more and more practical to conduct full-core pin-by-pin multi-physics simulation.

Therefore, many attempts to couple neutronics transport codes with thermal hydraulics codes have been taken over the world. The MOC code MPACT[1] in CASL[2] project has been coupled with CTF[3] to build a multi-physics coupling system based on deterministic neutron transport method[4]. This coupling system has been successfully applied to analysis on large commercial LWRs to obtain pin-wise distributions of neutronic parameters and thermal hydraulic parameters. Besides, another deterministic code nTRACER[5] has been coupled with CTF and MATRA[6].

For Monte Carlo method, efforts have been made to reduce the time and memory consumption and these years, coupling systems based on Monte Carlo method are being established around the world. MCNP[7] developed by LANL has been coupled with FLICA[8] by KIT in 2011, Serpent 2 has been coupled with SubChanFlow by KIT in 2015[9], MC21 has been coupled with CTF in 2017[10], and MCS developed by UNIST has been coupled with CTF in 2018[11].

In the aspect of Neutronics-Thermal-Hydraulics coupling, REAL (Reactor Engineering Analysis Laboratory) group in Tsinghua University, Beijing, China, has made a lot of progress based on the state-of-art Monte Carlo code RMC. RMC is a continuous-energy Reactor Monte Carlo neutron, photon and electron transport code developed by REAL group in Department of Engineering Physics at Tsinghua University, Beijing, China[12]. On-the-fly treatment of temperature dependent cross section, including improved Gauss-Hermite Quadrature Method in resolved resonance regions(RRR), on-the-fly probability table interpolation in unresolved resonance regions(URR) and on-the-fly sab interpolation in thermal energy regions, has been well developed[13]. Moreover, RMC has become the first Monte Carlo code that accomplished the fully two-cycle simulation of BEAVRS benchmark with COBRA-EN[14].

RMC has already been successfully coupled with CFD code CFX in 2012[15] and sub-channel thermal hydraulic code COBRA-EN in 2015[16]. In 2017, Guo's work has implemented the coupling between RMC and CTF with a hybrid coupling scheme[17].

COBRA-TF (CTF), Coolant Boiling in Rod Arrays-Two Fluid, is a sub-channel thermal-hydraulic code designed specially for Light Water Reactor (LWR) vessel and core analysis. CTF is developed and improved by Reactor Dynamics and Fuel Modeling Group (RDFMG) in North Carolina State University (NCSU)[3].

Hybrid coupling method has been successfully applied to the simulation of VERA Benchmark Problem 6 to 9. However, to fully make use of the capability of both RMC and CTF, internal coupling method has to be developed.

Compared to hybrid coupling with CTF, internal coupling method has some advantages listed below:

- Data transferred between RMC and CTF by memory, which may avoid the truncation and save the disk I/O time.
- Precise 3D power distribution is served as the heat source for CTF, instead of the reconstruction from 2D radial distribution and 1D axial distribution read from CTF input files. Therefore, for some situations where

the power distribution is far from symmetric, internal coupling will give more precise description and consequently more accurate results.

- RMC and CTF are regarded as two functions or modules rather than two programs in the internal coupling system, thus on some batch platforms like Tianhe-2 and Sunway-Taihu Light HPC Clusters, the neutronic and TH calculation is integrated into one job rather than several separated jobs, which may reduce the queueing time.

The preprocessing procedure of CTF is required only once in the internal coupling method, while several runs are essential in hybrid coupling method.

2. Methodology

2.1 Coupling Scheme

When the TH feedback is not considered, the neutron transport equation can be interpreted as Equ. (1).

$$L\phi + R\phi = \frac{1}{k}F\phi, \qquad (1)$$

where L is the loss operator, R is the removal operator, F is the fission operator and k is the eigenvalue, that is, the multiplication factor of the reactor.

In Equ. (1), operator L, R, F are all functions of macro cross sections, which vary according to the temperature distribution $T(\vec{r})$ and number density distribution $N(\vec{r})$. Therefore, from the multi-physics aspect, the neutron transport equation evolves to Equ. (2) below.

$$L(T,N)\phi + R(T,N)\phi = \frac{1}{k}F(T,N)\phi, \qquad (2)$$

The temperature distribution $T(\vec{r})$ and number density distribution $N(\vec{r})$ can be obtained from thermal hydraulic calculation. In Equ. (3), ψ is the power distribution, and TH(ψ) represents the thermal hydraulic equations operator when the power distribution is ψ. Equ. (4) is the flux to power distribution process.

$$TH(\psi)(T,N) = 0, \qquad (3)$$

$$P(\phi) = \psi, \qquad (4)$$

In the coupling system, Equ. (2)(3)(4) are coupled together. There are different methods to handle those equations. For example, some regard the TH feedback as a perturbation while others may recommend to use Jacobian or Jacobian-Free Newton Krylov method. The most straightforward and practical method, however, is Picard iteration method. In this work, Picard iteration method is chosen, and the iteration process can be clarified as below:

$$L\left(T^{(n)},N^{(n)}\right)\phi^{(n)} + R\left(T^{(n)},N^{(n)}\right)\phi^{(n)} = \frac{1}{k^{(n)}}F\left(T^{(n)},N^{(n)}\right)\phi^{(n)}, \qquad (5)$$

$$P\left(\phi^{(n)}\right) = \psi^{(n)}, \qquad (6)$$

$$TH\left(\psi^{(n)}\right)\left(T^{(n+1)},N^{(n+1)}\right) = 0, \qquad (7)$$

where $n = 0,1,2,\ldots$.

Equ. (5)(6) can be solved by a neutron transport code and Equ. (7) can be handled by a thermal hydraulic code. The initial temperature distribution T and number density distribution N are set even practically.

The data transferred between those two modules are power distribution ψ, temperature distribution T (both fuel temperature and moderator temperature distribution included) and number density distribution N (especially the number density distribution of the coolant). Fig. 1 below demonstrates the data transfer in Picard iteration process.

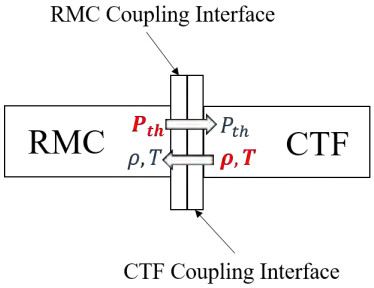

Fig. 1. Schematic diagram of coupling method: data transfer between neutronic transport code RMC and sub-channel code CTF.

From the experience, the influence of TH feedback on eigenvalue k_{eff} is no more than 1000pcm, typically 200pcm for the full core, thus the single physics solution obtained from the first iteration is not too far from the coupling one. Due to the negative reactivity coefficient of TH feedback and the local convergence of Picard iteration method, we may get a pretty good approximation after only a few iterations.

2.2 Convergence Criteria

When the solution is closer to the actual one, the change of TH feedback will become smaller and smaller, thus due to the continuity of the equations, the flux calculated from the neutronics code will be similar to the previous one. Therefore, the convergence criteria of Picard iteration is set to the 2-order norm of the relative change of flux distribution ϕ.

$$\left\| \frac{\phi^{(n+1)} - \phi^{(n)}}{\phi^{(n)}} \right\| < \epsilon, \qquad (8)$$

ϵ can be set at some figure of the same order of the standard deviation of neutron flux ϕ. In addition, to terminate from too many iterations, a maximum of iteration number can also be defined.

2.3 MPI/OpenMP Hybrid Parallelism

To distribute the heavy work to thousands or even more CPUs, MPI mechanism is used to communicate between those processes. However, the memory stack for each process is isolated and when burnup is involved, all the material data should be copied to each process, which may exceed the limit of physical resources. Therefore,

shared memory mechanism is utilized and the OpenMP library is utilized. Currently, RMC has accomplished the MPI/OpenMP hybrid parallelism and in this work, this mechanism is extended to the coupling module.

To include CTF into the MPI/OpenMP hybrid parallelism scheme, some detailed analysis and the usage of MPI sub-communicator and group are needed – some of the MPI processes are reorganized as a sub-communicator to handle the CTF work while others waiting for the TH feedback.

When OpenMP is also involved, a more complicated but innovative method is taken. For instance, in Fig. 2, the maximum number of process is 3 due to the memory limit, but the number of assemblies is 4. As there is no OpenMP support in CTF, the number of MPI processes required by parallel CTF is 4, the same as the number of assemblies. In this innovative method, 4 processes are created but to reduce the memory usage, Proc. 3 will not cooperate in the calculation of RMC, thus less memory is consumed by this process.

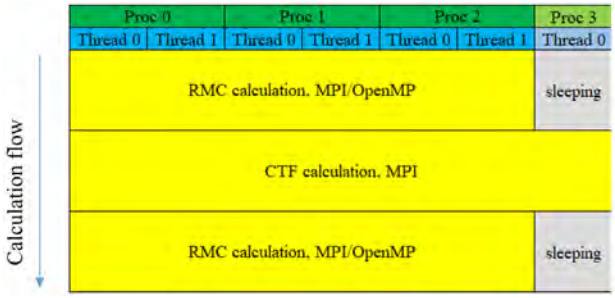

Fig. 2. An example for demonstrating the innovative hybrid coupling method for internal coupling between RMC and CTF.

2.4 Cross Compilation

Cross compilation is required, for RMC is written in C++ while CTF in Fortran. Therefore, techniques like "extern "C"" in C++ and "name bind" in Fortran are used. The cross compilation treatment is successfully tested both under GNU and Intel (R) compilers.

3. Simulation Results and V&V

Comparisons between hybrid coupling and internal coupling on some test cases are performed to verify the correctness of the implementation of internal coupling. And to validate the coupling system, the 2-by-2 assemblies case proposed in Yu's work[11] is used to compare RMC/CTF coupling and MCS/CTF coupling. As not all parameters are described in [11]. , there may be slight difference between results calculated by MCS/CTF and here calculated by RMC/CTF.

3.1 Single Fuel Pin Case

A typical PWR fuel pin case is used to demonstrate the capability of internal coupling between RMC and CTF. Comparison between hybrid coupling and internal coupling is performed to verify the correctness as the hybrid coupling method has been validated by many cases before.

The single pin has a length of 400 cm and is axially divided into 20 sections in the CTF model. The radius of the fuel pellet is 0.41195 cm and the inner and outer radius of the cladding is 0.41875 and 0.47585 cm. The pitch of the pin is 1.26 cm.

In the neutron transport calculation, 200 inactive and 200 active cycles with 50,000 histories per cycle are simulated respectively in hybrid coupling and internal coupling.

Table I. Eigenvalue results from different cases.

Case	keff	std
w/o TH feedback	1.130519	0.000246
Hybrid coupling	1.120219	0.000244
Internal coupling	1.120033	0.000241

Table I gives the eigenvalues and their standard deviation calculated in three cases. Significant overestimation of eigenvalue as large as 1000pcm can be observed without TH feedback, while the difference between hybrid and internal coupling methods is only 18.6pcm, less than the standard deviation, which verifies the correctness of the internal coupling between RMC and CTF.

3.2 Checkerboard 2-by-2 assemblies case

This checkerboard case is proposed in Yu's work to demonstrate the capability of MCS and CTF coupling [11]. The simulation results from RMC/CTF internal coupling method are compared with those from MCS/CTF coupling system to validate our coupling system.

The four assemblies in this case are the same except for the enrichment – the top left and bottom right has an enrichment of 1.30 w%, while the other two of 2.36%.

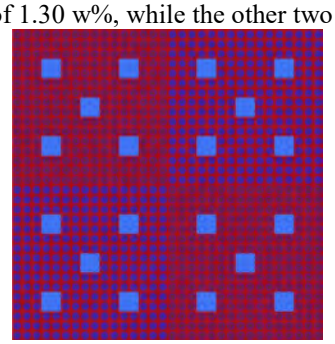

Fig.3. The radial profile of the 3D checkerboard 2-by-2 assemblies case[11].

Fig.3 shows the geometry of the case. The blue blocks contain guide tubes.

100 inactive and 100 active cycles are simulated and the number of neutrons per cycle is 500,000. In this

summary, the comparison of eigenvalue and radial power distribution are shown below in Table II and Fig. 4.

Table II. Eigenvalue results from different coupling systems (w/ cross flow). To keep the number of digits the same, results from RMC/CTF are rounded from 6 digits to 5.

Case	keff	std
MCS/CTF	1.12095	0.00008
RMC/CTF	1.12104	0.00006

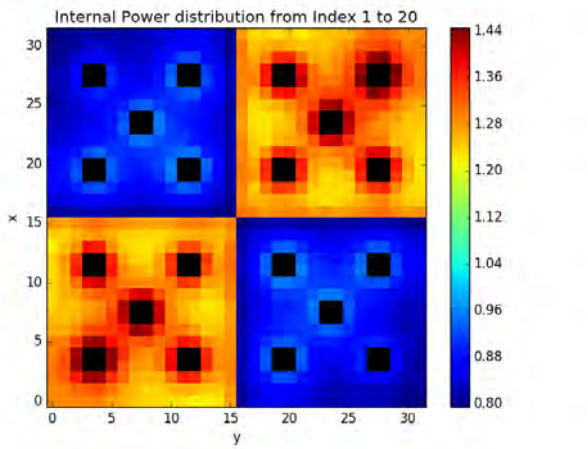

Fig. 4. Radial power distribution from RMC/CTF coupling.

Compared with the results from MCS/CTF, the difference of eigenvalue is only 9pcm, and the radial power distributions of the two coupling systems are almost the same, which validates the internal coupling method implemented between RMC and CTF.

4. Conclusion

Internal coupling between the RMC neutronics code and the CTF sub-channel thermal-hydraulic code has been successfully implemented and MPI and OpenMP hybrid parallelism is supported. Verification and validation for this internal coupling system is firmly guaranteed by the consistence with hybrid coupling and the MCS/CTF coupling system, which enables the coupling system to be competitive for high-fidelity full-core pin-by-pin multi-physics simulation.

Reference

1. Kochunas, B., et al. *Overview of development and design of MPACT: Michigan parallel characteristics transport code*. 2013.
2. Turinsky, P.J. and D.B. Kothe, Modeling and simulation challenges pursued by the Consortium for Advanced Simulation of Light Water Reactors (CASL). Journal of Computational Physics, 2016. 313: p. 367--376.
3. Salko, R.K. and M.N. Avramova, COBRA-TF Subchannel Thermal-Hydraulics Code (CTF) Theory Manual–Revision 0. Consortium for Advanced Simulation of Light Water Reactors, CASL-U-2015-0054, 2015.
4. Kochunas, B., et al., Demonstration of Neutronics Coupled to Thermal-Hydraulics for a Full-Core Problem using COBRA-TF/MPACT. CASL Document CASL-U-2014-0051-000, 2014.
5. Ryu, M., et al., Solution of the BEAVRS benchmark using the nTRACER direct whole core calculation code. Journal of Nuclear Science and Technology, 2015. 52(7-8): p. 961--969.
6. Yoo, Y.-J., D.-H. Hwang, and Others, Development of a subchannel analysis code MATRA applicable to PWRs and ALWRs. Nuclear Engineering and Technology, 1999. 31(3): p. 314--327.
7. Briesmeister, J.F., MCNP-A General Monte Carlo N-Particle Transport Code, Version4A. LA-12625, 1993.
8. Aniel, S., et al. FLICA4: Status of numerical and physical models and overview of applications. 2005.
9. Daeubler, M., et al., High-fidelity coupled Monte Carlo neutron transport and thermal-hydraulic simulations using Serpent 2/SUBCHANFLOW. Annals of Nuclear Energy, 2015. 83: p. 352-375.
10. Kelly Iii, D.J., et al., MC21/CTF and VERA multiphysics solutions to VERA core physics benchmark progression problems 6 and 7. Nuclear Engineering and Technology, 2017. 49(6): p. 1326--1338.
11. Yu, J., et al., Preliminary coupling of the Thermal/Hydraulic solvers in the Monte Carlo code MCS for practical LWR analysis. Annals of Nuclear Energy, 2018. 118: p. 317--335.
12. Wang, K., et al. RMC-A Monte Carlo code for reactor core analysis. 2014. EDP Sciences.
13. Liu, S., et al., Development of on-the-fly temperature-dependent cross-sections treatment in RMC code. Annals of Nuclear Energy, 2016. 94: p. 144-149.
14. Wang, K., et al., Analysis of BEAVRS two-cycle benchmark using RMC based on full core detailed model. Progress in Nuclear Energy, 2017. 98: p. 301-312.
15. Li, L.-S., H.-M. Yuan, and K. Wang, Coupling of RMC and CFX for analysis of pebble bed-advanced high temperature reactor core. Nuclear Engineering and Design, 2012. 250: p. 385-391.
16. Liu, S.C., et al. Study of neutronics and thermal-hydraulics coupling with RMC COBRA-EN system. 2015.
17. Guo, J., et al., Coupled neutronics/thermal-hydraulics analysis of a full PWR core using RMC and CTF. Annals of Nuclear Energy, 2017. 109: p. 327-336.

Proceedings of the Reactor Physics Asia 2019 (RPHA19) Conference
Osaka, Japan, Dec. 2-3, 2019

NECP-X and CTF Solutions to VERA Benchmark

Bo Wang[a, *], Zhouyu Liu[a] and Liangzhi Cao[a]
[a]*Xi'an Jiaotong University, No.28 Xianning West Road, Xi'an, Shaanxi, 710049, P.R.China*
[*]Corresponding author: 756958413@qq.com

Abstract

An internal coupling scheme was proposed for the coupling between high-fidelity neutronics code NECP-X and sub-channel thermal hydraulic code CTF. CTF was involved in NECP-X as a shared library object and driven by NECP-X, NECP-X and CTF have their communicator, respectively. Coupling data was transferred via code memory rather than files. NECP-X/CTF was applied to VERA benchmark. The results were compared with other high-fidelity coupling systems. The numerical results shown that internal coupling method is an effective way for reactor core simulation and is accurate enough.

Key Words: **NECP-X; CTF; coupling calculation; VERA Benchmark**

1. Introduction

With the growth of computing capability, the coupling of high-fidelity neutronics and sub-channel thermal hydraulic becomes more and more popular worldwide. Coupling data is passed through computer memory in internal coupling method, there are higher transform efficiency and more complete iteration data, but usually two codes need to be modified to meet the requirements for internal coupling. Usually an interface transferring rod power from neutronics code to thermal hydraulic code and an interface transferring thermal hydraulic variable from thermal hydraulic code are needed.

In this paper, NECP-X and CTF are combined with the internal coupling approach. First CTF is compiled to a shared library using CMake tool, then the shared library is linked in NECP-X using CMake tool when compiling NECP-X. Note that the preprocessor of CTF is used to generate the input files of CTF, which is designed for pressurized water reactor in a quick and less error-prone manner.

This paper is organized as follows: in Section 2, NECP-X, CTF are introduced in brief, respectively; in Section 3, the coupling method is described, including coupling approach, data transform method and mesh mapping; the coupling results of VERA benchmark are listed and compared in Section 4; finally the conclusions and future work are presented in Section 5.

2. Coupling codes

2.1 High-fidelity neutronics code NECP-X

NECP-X is a new high-fidelity neutronics code developed by NECP laboratory at Xi'an Jiaotong University. The 69-group cross sections library for transport calculation and continuous energy cross sections library for resonance calculation are used; a pseudo-resonant-nuclide subgroup method is implemented; there are four methods for anisotropic scattering: the P0 isotropic approximation, the outflow transport approximation, the inflow transport approximation and the high order scattering method; the hybrid transport method based on 2D MOC and 1D SN is adopted in NECP-X, multi-group CMFD acceleration and multi-level parallel method have been extended to the transport calculation; a closed channel T/H model without cross flow based on pin level has been developed and coupled into NECP-X; the transient calculation and depletion based on the predictor-corrector quasi-static method also are implemented in NECP-X.

2.2 Sub-channel thermal hydraulic code CTF

COBRA-TF is a code developed originally in 1980 by Pacific Northwest Laboratory under sponsorship of the NRC, began as a T/H rod-bundle analysis code. The code uses a two-fluid modeling approach with consideration for three separate, independent flow fields; fluid film, vapor, and liquid droplets. Both sub-channel and 3D Cartesian forms of 9 conservation equations are available for PWR modeling. COBRA-TF includes a wind range of T/H models crucial to accurate LWR safety analysis including, but not limited to, flow regime dependent two-phase heat transfer, inter-phase heat transfer and drag, droplet breakup, and quench-front tracking.

CTF is an improved version of COBRA-TF developed and maintained by RDFMG at PSU and NCSU [1]. There are three symmetry models in CTF, including quarter-core mirror symmetry, quarter-core rotational symmetry and eighth-core symmetry. The domain decomposition method has been realized in CTF with assembly as the smallest unit based on MPI.

3. Coupling method

In this section, the internal coupling approach is described in Section 3.1, the radial mesh mapping is shown in Section 3.2, the parallel coupling and call logic are discussed in Section 3.3.

3.1 The coupling approach

CMake, gfortran and BLAS/LAPACK libraries are needed prior the CTF building, PETSc and MPICH libraries are necessary if the parallel option is on. To couple with other neutronics codes, a CTF_Coupling_Interface has been developed. When processing the building, firstly this interface is built as a shared library object via modifying the CTF CMakeLists file, then the shared library object is included and linked in NECP-X. All data is passed through the interface in coupling.

3.2 The mesh mapping

Fig. 1 shows the neutronics and thermal hydraulic model to a quarter core. The pin power generated by NECP-X is flat source region level, but pin power transferred to CTF is homogenized in a fuel pin and the power profile inside the fuel rod is constant as Fig. 2 shown. Fig. 3 shows the T/H variable exchange, CTF can solve the 3D heat conduction equations to obtain fine temperature distribution inside a fuel rod, but just the volume-averaged fuel temperature is used in NECP-X now.

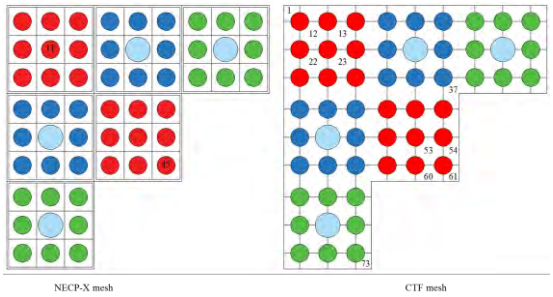

Fig. 1. Model of quarter core.

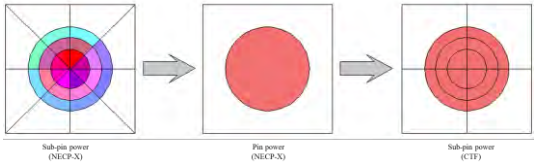

Fig. 2. Pin power transform between NECP-X and CTF.

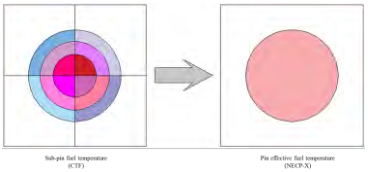

Fig. 3 Thermal hydraulic variable transform.

3.3 Parallel coupling and call logic

The minimum spatial decomposition unit in NECP-X is quarter assembly, while the minimum unit in CTF is assembly, so actually the number of cores needed for neutronics calculation is large than the number for T/H calculation. The whole flow chart is given in Fig. 4 to illustrate the details of coupling process.

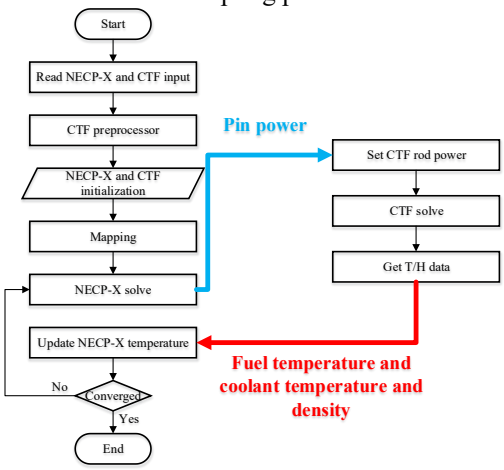

Fig. 4. Flow chart of coupling calculation.

4. Numerical results

4.1 VERA 6

VERA #6 is a PWR fuel assembly case at HFP conditions [2]. The axial model of NECP-X is as Fig. 5 shown. The convergence criteria is listed in Table 1.

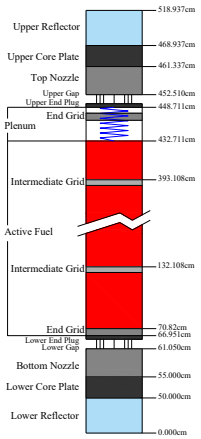

Fig. 5. Axial model of NECP-X.

Table 1. Convergence criteria

Parameters	Value
Keff	1 pcm
Fuel rod temperature	1 K
Cladding temperature	1 K
Coolant temperature	1 K

The keff results comparison [3] with other high-fidel ity codes are listed in Table 2.

Table 2. Keff Comparison

Code	Value	Difference
MC21/CTF	1.16424±0.00003	0
MPACT/CTF	1.16361	-63
NECP-X/CTF	1.16289	-135

Fig. 6 shows the axial integral power comparison with MPACT/CTF, the outlet temperature is compared in Fig. 7, the maximum fuel rod temperature is shown in Fig. 8, last some typical channels and typical fuel rods results are compared in Fig. 9 and Fig. 10.

Fig. 6. Comparison of axial power

Fig. 7. Outlet temperature comparison.

Fig. 8. Averaged fuel temperature at 25th layer.

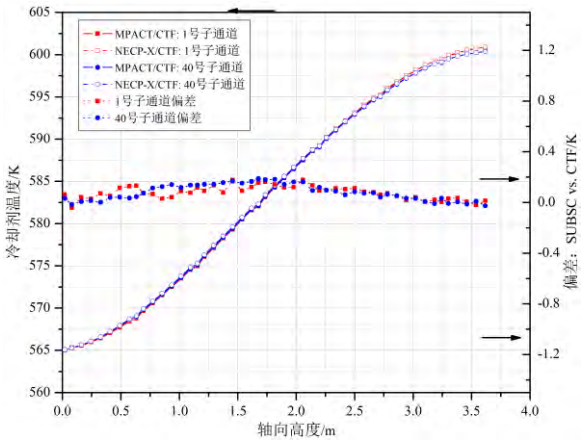

Fig. 9. Comparison of 2 channels.

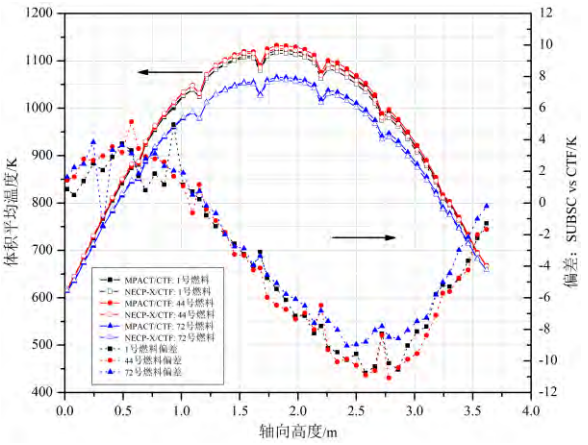

Fig. 10. Comparison of 3 fuel rod.

4.2 VERA 7

VERA 7 is run a full power and nominal flow condition. The core is at beginning of life and hot full power conditions, including nominal power and flow. The geometry is identical with VERA 5 except for the position of Bank D. The soluble boron concentration is calculated to keep the core criterial.

The criterial boron concentration results are compared in Table 3, the radial assembly normalized power is compared in Fig. 11.

Code	CBC (ppm)	Difference (ppm)
MC21/CTF	854.5	-
RMC/CTF	848	-6.5
NECP-X/CTF	850.5	-4

	H	G	F	E	D	C	B	A	
8	1.1179	1.0302	1.1156	1.0564	1.1571	1.0531	1.0487	0.7558	MC21/CTF
	1.1020	1.0178	1.1024	1.0465	1.1481	1.0517	1.0524	0.7653	NECP-X/CTF
	-1.4188	-1.1994	-1.1839	-0.9361	-0.7746	-0.1365	0.3516	1.2600	Relative difference (%)
9	1.0299	1.1081	0.9828	1.1475	1.0795	1.1549	1.0119	0.8558	
	1.0178	1.0948	0.9728	1.1372	1.0738	1.1535	1.0186	0.8682	
	-1.1706	-1.1990	-1.0208	-0.8957	-0.5249	-0.1224	0.6650	1.4454	
10	1.1148	0.9825	1.1310	1.0740	1.1844	1.1210	1.0552	0.7646	
	1.1024	0.9728	1.1203	1.0667	1.1792	1.1226	1.0613	0.7757	
	-1.1130	-0.9906	-0.9444	-0.6772	-0.4408	0.1400	0.5809	1.4542	
11	1.0556	1.1471	1.0740	1.1798	1.0774	1.1184	0.9865	0.6335	
	1.0465	1.1372	1.0667	1.1727	1.0750	1.1200	0.9961	0.6420	
	-0.8610	-0.8611	-0.6772	-0.5977	-0.2194	0.1391	0.9781	1.3493	
12	1.1566	1.0793	1.1850	1.0777	1.2377	0.8650	0.8914		
	1.1481	1.0738	1.1792	1.0750	1.2389	0.8683	0.9015		
	-0.7317	-0.5065	-0.4912	-0.2472	0.1001	0.3868	1.1325		
13	1.0537	1.1557	1.1219	1.1193	0.8654	0.8656	0.6073		
	1.0517	1.1535	1.1226	1.1200	0.8683	0.8732	0.6124		
	-0.1933	-0.1915	0.0597	0.0586	0.3404	0.8806	0.8450		
14	1.0492	1.0128	1.0565	0.9876	0.8923	0.6077			
	1.0524	1.0186	1.0613	0.9961	0.9015	0.6124			
	0.3038	0.5756	0.4572	0.8656	1.0305	0.7786			
15	0.7563	0.8565	0.7653	0.6343					
	0.7653	0.8682	0.7757	0.6420					
	1.1931	1.3625	1.3614	1.2215					

Fig. 11. The radial assembly normalized power

The core coolant temperature distribution is shown in Fig. 12 and the outlet coolant density and coolant density distribution are shown in Fig. 13.

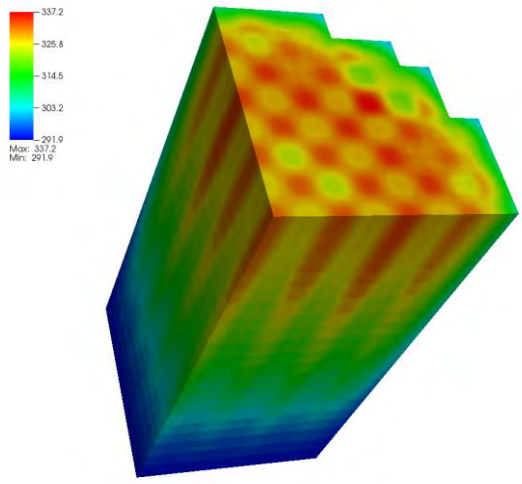

Fig. 12. The coolant temperature distribution.

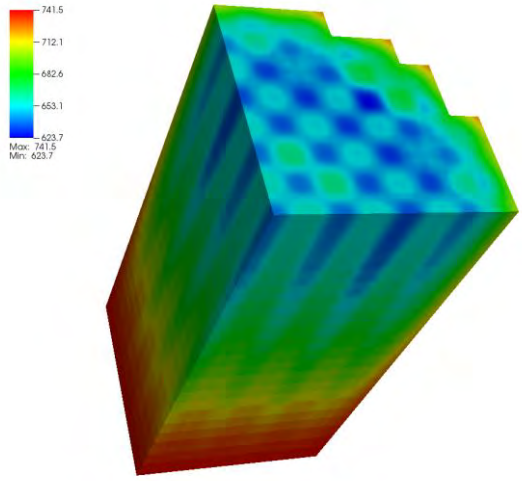

Fig. 13. The coolant density distribution.

6. Conclusions

An internal coupling approach is applied to high-fidelity neutronics code NECP-X and sub-channel TH code CTF. All coupling data is transferred via computer memory, and the different parallel communicators are used for different codes. The coupling system is used into VERA N/TH coupling benchmark and numerical results show that the coupling system can simulate the PWR and works well.

Acknowledgements

This work was supported by National Natural Science Foundation of China No. 11605130, 11605128, 11775169.

References

[1] Salko, Robert & Wysocki, Aaron & Avramova, M. & Toptan, Aysenur & Porter, N. & Blyth, T. & Dances, C. & Gomez, A. & Jernigan, C. & Kelly, J. (2016). CTF Theory Manual.

[2] GODFREY A T. "VERA core physics benchmark progression problem specifications," Oak Ridge National Laboratory, CASL-U-2012-0131-004, 2013.

[3] KELLY III D J, et al. "MC21/CTF and VERA multiphysics solutions to VERA core physics benchmark progression problems 6 and 7," Nuclear Engineering and Technology, 49, pp. 1326-1338(2017).

KURNS REPORT OF
INSTITUTE FOR INTEGRATED
RADIATION AND NUCLEAR SCIENCE,
KYOTO UNIVERSITY

発行所　京都大学複合原子力科学研究所
発行日　令 和 1 年 11 月
住所　　大阪府泉南郡熊取町朝代西 2 丁目
　　TEL（072）451- 2300